DENOISING AND SEGMENTATION OF ECHOCARDIOGRAPHIC IMAGES IN MULTILPE VIEWS

Ph.D. THESIS

by

NAGASHETTAPPA BIRADAR

DEPARTMENT OF ELECTRICAL ENGINEERING
INDIAN INSTITUTE OF TECHNOLOGY ROORKEE
ROORKEE – 247667 (INDIA)
APRIL, 2015

DENOISING AND SEGMENTATION OF ECHOCARDIOGRAPHIC IMAGES IN MULTILPE VIEWS

A THESIS

Submitted in partial fulfilment of the requirements for the award of the degree

of

DOCTOR OF PHILOSOPHY

in

ELECTRICAL ENGINEERING

by

NAGASHETTAPPA BIRADAR

DEPARTMENT OF ELECTRICAL ENGINEERING
INDIAN INSTITUTE OF TECHNOLOGY ROORKEE
ROORKEE – 247667 (INDIA)
APRIL, 2015

INDIAN INSTITUTE OF TECHNOLOGY ROORKEE
ROORKEE

CANDIDATE'S DECLARATION

I hereby certify that the work which is being presented in this thesis entitled **"DENOISING AND SEGMENTATION OF ECHOCARDIOGRAPHIC IMAGES IN MULTILPE VIEWS"** in partial fulfilment of the requirements for the award of the Degree of Doctor of Philosophy and submitted in the Department of Electrical Engineering of the Indian Institute of Technology Roorkee, Roorkee is an authentic record of my own work carried out during a period from July, 2011 to April, 2015 under the supervision of Dr. M. L. Dewal, Professor, Department of Electrical Engineering, Indian Institute of Technology Roorkee and Dr. Manoj Kumar Rohit, Professor, Department of Cardiology, Post Graduate Institute of Medical Education and Research, Chandigrah.

The matter presented in this thesis has not been submitted by me for the award of any other degree of this or any other Institute.

(**NAGASHETTAPPA BIRADAR**)

This is to certify that the above statement made by the candidate is correct to the best of our knowledge.

(M. L. Dewal)
Supervisor

(Manoj Kumar Rohit)
Supervisor

Date: _____

INSTITUTE ETHICS COMMITTEE

Postgraduate Institute of Medical Education and Research, Chandigarh

Prof. O.N. Bhakoo
Chairman

Prof. Dheeraj Gupta
Convener

Cand/13/463/29/7/13

No: PGI/IEC/2013/2033-34
Date: 25/07/2013

CONTACT

Phone:
+91 172 2756820

Email:
iecpgi@gmail.com

Dr. Manoj Kumar,
Additional Professor
Dept. of Cardiology
PGIMER, Chandigarh.

Title: Analysis of Echocardiographic Images.

Project No: P-446

Dear Dr. Dutta,

We received five copies of your above mentioned project proposal, submitted by **Mr. Nagashettappa Biradar** is pursuing his Ph.D under your guidance, which has been assigned the project number **P-446**. The project was discussed in the meeting of the Institute Ethics committee held on 23.07.2013. After due consideration and discussion, your project was **APPROVED**.

It is understood that the study will be conducted under your direction strictly as per the submitted protocol. Any deviations from the approved protocol and study documents must be sent to the Ethics Committee for re-approval. Any adverse reaction or condition noted during the study period should be reported to the Ethics Committee immediately. A report of the study should be sent to the Ethics Committee yearly.

Justice Jhanji /Dr. BN Goswami (Alternate members), Dr. Savita Malhotra and Dr. Vanita Jain did not attend the meeting.

All future correspondence with respect to this project must mention **the project number.**

Kind Regards

Yours sincerely,

(Dheeraj Gupta)

Copy to: Prof.-in-charge, Medical Education Cell, PGIMER, Chandigarh.

ABSTRACT

Echocardiography is the most commonly used first-line imaging modality in the assessment of cardiac chamber and valvular abnormalities. The valvular abnormalities can be classified as regurgitation and stenosis. Aortic regurgitation (AR) is a valvular disorder due to the retrograde flow of blood from the aortic valve into the left ventricle during the diastole. The aetiologies and the consequences of AR are diagnosed using transthoracic echocardiographic (TTE) images acquired in parastrenal long axis (PLAX), parasternal short axis (PSAX), apical four chamber (A4C), apical two chamber (A2C) and apical five chamber (A5C) views. The Doppler imaging modalities such as continuous wave Doppler (CWD) and color Doppler echocardiography along with conventional B-Mode (brightness mode) and M-Mode (motion mode) images are used hand-in-hand to detect the prevalence of regurgitation, better understanding of the mechanism of regurgitation and quantification of severity along with its repercussions. But the technical research is more concentrated on despeckling, and segmentation of good quality B-Mode images acquired in a particular view from healthy adults. Hence, it is necessary to study the applications of despeckling and segmentation techniques for TTE images acquired in multiple views from patients diagnosed with AR. Current research work attempts to overcome the existing caveats by integrated processing of B-Mode, CWD, and color Doppler echocardiography images. The work looks for the best denoising and segmentation techniques suitable for different modalities of echocardiographic imaging in multiple views.

Based on the exhaustive technical and clinical literature review, the following research objectives have been framed: 1) To propose despeckling methods for the B-Mode TTE images of aortic valve and cardiac chambers acquired in multiple views using different windows. 2) Comparative analysis of state-of-the-art despeckling techniques and texture features for the B-Mode and CWD images. 3) To propose delineation techniques for tracing the outer spectrum of CWD images. 4) Comparative analysis of segmentation techniques using the TTE images acquired in multiple views and windows. These research objectives are accomplished in the following manner.

Speckle noise present in cross sectional TTE images makes it difficult to consistently perform delineation of the cardiac structure. It is necessary to suppress noise and enhance contrast without altering the fine details present in the images. To address the issue of speckle noise, six despeckling techniques are proposed in this thesis. The first proposed technique is based on multiscale techniques. The multiscale techniques are employed for speckle noise in the logarithmic domain, considering the approximated additive noise model of despeckling. The transformation of images into the logarithmic domain, application of shrinkage techniques and bringing the image back into the original space are the three common steps for all multiscale techniques. Eight shrinkage techniques are analyzed for

despeckling of TTE images in multiple views. The performances of logarithmic multiscale techniques are compared with adaptive and diffusion based filtering techniques. The denoised images are enhanced using Butterworth filter. The integrated effects of denoising and enhancement are tested on active contour, region, watershed and edge based segmentation techniques. Further, to make use of the advantages of M-band wavelets, it is proposed to combine M-band ridgelet with neighborhood coefficient thresholding for the despeckling of TTE images. The thresholds of coefficients are computed using neighborhood coefficient thresholding technique and reconstructed to obtain the denoised images.

The second proposed despeckling technique is known as the hybrid triangulation moving average (TMAV) fuzzy filter. The performance of TMAV filter is fine tuned for despeckling of TTE images by combining it with adaptive Wiener filter. Four fuzzy filters have been analyzed in the logarithmic domain for speckle noise reduction. The despeckling performances of all the four fuzzy filters are fine tuned by combining them individually with adaptive Wiener filter. The integrated fuzzy filter is the third proposed despeckling technique which is the improved version of hybrid TMAV fuzzy filter. It is based on the integration of geometric, Wiener and fuzzy filters. The hybrid homomorphic fuzzy (HHF) is the fourth proposed technique which is the combination of logarithmic fuzzy filter and anisotropic diffusion filter. The diffusion based methods are known for speckle noise suppression, and edge preservation capability but they do not perform well when the noise contamination in the images is high. The fuzzy filters have superior figure of merit in comparison to anisotropic diffusion filters. The advantages of anisotropic diffusion and fuzzy filters are integrated in the proposed HHF filter.

The hybrid posterior sampling based Bayesian estimation (PSBE) is the fifth proposed technique for despeckling of TTE images. The performance of logarithmic PSBE technique degrades considerably for images contaminated with high amount of noise. To address this issue, an additional adaptive filter is embedded into logarithmic PSBE and is known as the hybrid PSBE technique. The contrast of output images are enhanced using Butterworth filter. The effects of denoising and enhancement on segmentation are studied using three basic techniques namely the edge, region and multistage watershed. The extreme total variation bilateral (ETVB) is the sixth proposed technique for denoising of TTE images of the cardiac structures. The regularizer term of the total variation (TV) filter is replaced with the bilateral (BL) term in the proposed ETVB filter. The true information is incorporated in the algorithm using Bayesian inference and probability density function. Applications of gradient projection based restoration methods have been analyzed for speckle noise reduction of TTE images.

In an effort to define the best despeckling filter for the B-Mode, CWD and color Doppler images in multiple views, a comparative study is under taken in this thesis. The applications of 48 filters are analyzed for the B-Mode, CWD, MM, and color Doppler images where the performance analysis is in terms of sixteen image quality metrics, visual quality assessment

and clinical validation. Both, traditional and blind assessment parameters are computed for assessment of noise suppression, edge and structure preservation. The despeckling filters are grouped into eight type's namely local statistics, fuzzy, Fourier, multiscale, nonlinear iterative, total variation, nonlocal mean and hybrid filters.

It has been observed that the median filter and Gaussian low pass filter are more commonly used for reduction of noise in the CWD images. The applications of state-of-the-art despeckling filters have not been extensively analyzed for the CWD images. Therefore, applications of despeckling filters analyzed for B-Mode images have also been analyzed for the CWD, pulse wave Doppler (PWD), M-Mode and color Doppler images. The despeckling performance of filters have also been compared in terms of 65 texture features computed from the denoised B-Mode, M-Mode, CWD, and color Doppler echocardiographic images. The set of features include five first order statistical (FOS), 26 spatial gray level dependence matrix (SGLDM), four gray level difference statistics (GLDS), four statistical feature matrix (SFM), six Laws texture energy measures (LTEM), four fractal dimension, two Fourier power spectrum and five neighborhood gray tone difference matrix features. All the texture features have been computed before and after the application of despeckling filters.

The segmentation of original and the pre-processed B-Mode, CWD and color Doppler images is taken up as the next objective. This objective looks for the best delineation technique for each modality image in multiple views. Initially, synthetic images with different amount of intensity in-homogeneity have been delineated using segmentation techniques based on various variants of the edge, region, watershed, fuzzy, active contour and level set techniques. The applications of these techniques are analyzed for the contouring of synthetic, color Doppler, B-Mode and CWD images. The objective of segmenting the B-Mode images is to trace the inner boundaries of left ventricle (LV) and aortic valve (AV) along with the leaflets of AV and mitral valve (MV). The B-Mode images acquired in two parasternal and three apical windows are used for analysis of segmentation techniques. The color Doppler images in PLAX and A5C are segmented to trace the outer boundary of regurgitant jet area. The outer spectrum of the CWD images is traced using multiple segmentation techniques.

To begin with, the edge, region and multi-stage watershed segmentation techniques are analysed. The performances of these techniques are improved by combining them with filters. The existing techniques such as wavelet based scale multiplication edge detection (SMED) approach, intuitionistic fuzzy divergence (IFD) based edge detection, soft thresholding, topological derivative based delineation, Magagnin and Kiruthika method have been employed for tracing the outer boundaries of the images. Further, the techniques based on active contour and level set have been employed for tracing the boundaries in the presence of intensity in-homogeneity. This set of techniques includes methods such as reaction diffusion, region scalable fitting (RSF), global minimization of active contour

(GMAC), Laplacian fitting energy, statistical and variational multiphase level set (SVMLS) approach, active contour without edges, selective binary and Gaussian filtering regularized level set. The manually segmented B-Mode images are compared with results obtained on application of local region based active contour segmentation technique. The estimated parameters on manual segmentation are compared with those obtained on application of semi-automated segmentation.

The analysis of segmentation techniques for CWD images is carried out using filtered as well original noisy images. The Gaussian and median filters used in Kiruthika method, Magagnin method and reaction diffusion (RD) based active contour method are replaced by the despeckling techniques in the proposed modifications for these three delineation techniques. These basic filters are replaced by ten despeckling filters such as DsFlsmv, DsFmedian, DsFhmedain, DsFad, DsFsrad, DsFlsminsc, DsFhomog, DsFWiener, DsFhomog and DsFgf4d. Further, performances of the modified RD method with various despeckling filters are tested using low contrast images with higher intensity in-homogeneity. The boundaries traced show that embedding of despeckling filter as replacement for the Gaussian filter in the RD method can be employed in the delineation of CWD images even in the presence of intensity in-homogeneity.

ACKNOWLEDGEMENTS

I express my deep gratitude to Dr. M.L.Dewal, Professor, Department of Electrical Engineering, Indian Institute of Technology Roorkee, Roorkee, and Dr. Manoj Kumar Rohit, Additional Professor, Department of Cardiology, Post Graduate Institute of Medical Education and Research, Chandigrah, for their valuable guidance throughout my research work. Their minute technical and clinical discussions, their everlasting moral support and their faith have lead to the completion of my thesis work. Apart from the above mentioned qualities, their immense concern during tough and good times of my PhD is indeed very memorable and highly appreciable.

I would like to extend my gratitude and heartfelt thanks to Dr. S. P. Srivastava, Professor and Head, Department of Electrical Engineering, for extending all necessary facilities to pursue my research work. I also express my thanks to Dr. Pramod Agarwal, Professor, Department of Electrical Engineering and Dean (Academics) and Dr. Vinod Kumar, Deputy Director and Professor, Department of Electrical Engineering, Indian Institute of Technology Roorkee, Roorkee, for extending all necessary facilities during their tenure as Head of the Department, Department of Electrical Engineering, Indian Institute of Technology Roorkee. I extend my sincere thanks to the members of student research committee Prof. Vinod Kumar, Prof. R. S. Anand, Prof. G. N. Pillai and Prof. Sanjeev Manhas for their valuable suggestions and assistance during my study period at IIT Roorkee. I wish to thank Prof. M. K. Vasantha for acting as a father like figure and a local guardian at IIT Roorkee. His slogan of “Happy Time” really kept us going else it would have been a herculean task to complete research. I also extend my sincere thanks to Professor Aoske Nandi, Chair and Head, Department of Electronics and Computer Engineering, Brunel University and Dr. Rangaraj M. Rangayyan, Professor, Department of Electrical Engineering, University of Calgary, for the thought provoking discussion of current research and challenges and inspiring to pursue research. I also express my gratitude towards Dr. Constantinos S. Pattichis, Professor of Computer Science at University of Cyprus for motivating to work in the field of despeckling of ultrasound images.

I express my thanks towards my parent institute Bheemanna Khandre Institute of Technology (BKIT), Bhalki for deputing me to pursue research at IIT, Roorkee. I express my gratitude and thanks to Dr. B. B. Lal, Principal, and Er. Ishwar Khandre, Chairman, BKIT, Bhalki. I also sincerely acknowledge the help provided by AICTE, New Delhi for pursuing research under Quality Improvement Programme. I am indebted to the faculty members of Department of Electrical Engineering, Indian Institute of Technology Roorkee, Roorkee, and Department of Electronics and Communication Engineering, BKIT, Bhalki for their encouragement in hard times, which contributed directly or indirectly in a significant way towards completion of this thesis.

I am quite blessed and lucky to be working with wonderful team of research scholars at IIT, Roorkee. I acknowledge the help rendered by my fellow researchers Dr. Subrahmanyam, Murala, Dr. K.T. Raju, Mr. Jayendra Kumar, Mr. Deep Gupta, Mr. Nagendra H., Mr. Guruswamy, Mr. Subramanya M. B., Mr. Santosh Desai, Mr. Chandra Shekar, Dr. Govardhan, Dr. Anil Gonde, Mr. Prateek Dolas, Mr. Sachin Singh, Mr. Pratul Arvind, Mr. Arvind R. Yadav, Mr. Arun Balodi, Mr. Yogesh Sariya, Mr. Roshan Kumar, Mr. Bhavik Patel, Mr. Nandkishore K., Smt. Sandeep Kaur, Dr. Mohammad Arif, Dr. Yatindra, Dr. H.S. Bhaduria, and Mr. sanjay Kumar who never hesitated in lending a helping hand and made my stay at IIT,Roorkee most memorable one. I extend my thanks to all whom I have missed to mention.

I extend my thanks to office superintendent Mr. Mohan Singh, and other staff members particularly Mr. Rishab Verma, Mr. Shushil Kumar, Mr. Amir Ahmed, Mr. Mahaveer Prasad, and all others who were quite helpful during my stay at IIT, Roorkee. I also wish to thank Mr.Rajiv Gupta, Mr. Dinesh Kumar, Mr. Jogeshwar Prasad, and Mr. Veer Chand, staff of Applied Instrumentation (AI) lab and Instrumentation and signal processing (ISP) Lab.

I am highly indebted to my beloved parents and in-laws for their unconditional support, encouragement and maintained family in my absence without troubling me any time. It was quite difficult last phase of my research as I lost my mother in the flag end. I acknowledge her love and support. I owe at lot to my wife Sarojani, my son Shashank, daughter Nidhi, my sister-in-law Smt. Archana and her son Abhishek, for their understanding, unwavering patience and encouragement, as the current research work is culmination of sacrifices and support rendered by them, for which I shall ever remain indebted. I thank my elder and younger brothers for their moral support and taking care of parents and family obligations. I thank my all friends and relatives especially to Dr. Sanjay Kumar Gowre, Mr. Sanjeev Gogga, Mr. Sharanbasappa Belamgi, Mr. Dhiraj Deshpande, Mr. Vijay Kumar Katgi, Mr. Sanjay Kulkarni, Dr. Ashok Vangere, Prof. A. M. Bhavikatti, Mr. Maharudra Nelagi, and Mr. Sunil Sangame for taking care of my society and intuitional responsibilities. I also thank the entire BKIT family.

Lastly, but not least by any measures I am thankful to the GOD for bestowing good health and cheers, strength and confidence for completing the work.

(Nagashettappa Biradar)

CONTENTS

LIST OF FIGURES

LIST OF TABLES

LIST OF ACRONYMS

ATV	Anisotropic Total Variation
AD	Anisotropic Diffusion
AFTV	Adaptive Fidelity Total Variation
ATMED	Asymmetrical Triangulation Median
AR	Aortic Regurgitation
ARJW	Aortic Regurgitant Jet Width
AI	Aortic Insufficiency
AS	Aortic Stenosis
A2C	Apical Two Chamber
A4C	Apical Four Chamber
A4CD	Apical Four Chamber Diastole
A4CS	Apical Four Chamber Systole
A5C	Apical Five Chamber
A5CD	Apical Five Chamber Diastole
A5CS	Apical Five Chamber Systole
AV	Aortic Valve
AVA	Aortic Valve Area
AVC	Aortic Valve Complex
AMVL	Anterior Mitral Valve Leaflet
Ao	Aorta
AWMF	Adaptive Weighted Median Filter
BL	Bilateral Filter
BFAC	Balloon Force Active Contour
B-Mode	Brightness Mode
BShrink	Bayes Shrink
BT	Block Thresholding
BPFA	Beta Process Factor Analysis
CD	Color Doppler
CO	Cardiac Output
CED	Coherence Enhancing Diffusion
CT	Computed Tomography
CSA	Cross Sectional Area
CV	Chan & Vese
CWD	Continuous Wave Doppler
EROA	Effective Regurgitant Orifice Area
ECG	Electrocardiogram
ETVB	Extreme Total Variation Bilateral
DsF	Despeckling Filter
DsFgf4d	Geometric Filter
DsFhomog	Maximum Homogeneity Filter
DsFad	Anisotropic Diffusion
DsFhomo	Homomorphic Filter
DsFlsminsc	Minimum Speckle Index Filter
DsFlsmv	Local Statistics Mean Variance
DsFmedian	Median Filter
DsFhmedian	Hybrid Median
DsFsrad	Speckle Reducing Anisotropic Diffusion

DsFWiener	Wiener Filter
DRLSE	Distance Regularized Level Set Evolution
DPAD	Detail Preserving Anisotropic Diffusion
DWT	Discrete Wavelet Transform
FBL	Fast Bilateral Filter
FIF	Fourier Ideal Filter
FBF	Fourier Butterworth Filter
FoM	Figure Of Merit
FOS	First Order Statistics
FPI	Feature Preserving Index
GHT	Generalized Hough Transform
GLDS	Gray Level Difference Statistics
GLM	Generalized Likelihood Ratio Filtering Method
GW	Geometric Wiener
GVF	Gradient Vector Field
GMAC	Global Minimization Active Contour
HHF	Hybrid Homomorphic Fuzzy
HFBF	Homomorphic FBF
HTMAV	Hybrid Triangulation Moving Average
HTMED	Hybrid Triangulation Median
HATMED	Hybrid Asymmetrical Median
IE	Infective Endocarditis
IVC	Inferior Vena Cava
IOWT	Interscale Orthogonal Wavelet Threshold
IVS	Intera-Ventricular Septum
IFD	Intuitionistic Fuzzy Divergence
LAMF	Local Adaptive Median Filter
LET	Linear Expansion Of Threshold
LA	Left Atrium
LTEM	Laws Texture Energy Measures
LSE	Level Set Evolution
LSF	Level Set Function
LV	Left Ventricle
LVEDV	Left Ventricle End Diastole Volume
LVESV	Left Ventricle End Systole Volume
LVEF	Left Ventricle Ejection Fraction
LVEDD	Left Ventricle End Diastole Diameter
LVESD	Left Ventricle End Systole Diameter
LVOT	Left Ventricular Outflow Tract
M-Mode	Motion Mode
MPT	Multiscale Product Threshold
MS	Mitral Stenosis
MR	Mitral Regurgitation
MBR	M-Band Ridgelet
MPT	Multiscale Product Threshold
MSE	Mean Square Error
MRI	Magnetic Resonance Imaging
MV	Mitral Valve
NDT	Non-Destructive Testing

NMSE	Normalized Mean Square Error
NSS	Neighborhood Shrinkage Using SURE
OCT	Optical Coherence Tomography
OBNLM	Optimized Bayesian Nonlocal Mean
PIG	Poisson Inverse Gradient
PDE	Partial Difference Equation
PSBE	Posterior Sampling Bayesian Estimation
PPB	Probabilistic Patch Based
PISA	Proximal Iso-volumetric Surface Area
PHT	Pressure Half Time
PMVL	Posterior Mitral Valve Leaflet
PLAX	Parasternal Long Axis
PLAXS	Parasternal Long Axis Systole
PLAXD	Parasternal Long Axis Diastole
Pshrink	Probability Shrinkage
PSAX	Parasternal Short Axis
PSNR	Peak Signal To Noise Ratio
PLOW	Patch Based Locally Optimal Wiener
PWD	Pulse Wave Doppler
PW	Posterior Wall
RD	Reaction Diffusion
RF	Regurgitant Fraction
RHD	Rheumatic Heart Disease
RNLA	Ripplet Using Nonlinear Approximation
RA	Right Atrium
RV	Right Ventricle
RVOT	Right Ventricle Outflow Tract
ROF	Rudin, Osher And Fatmi
ROI	Region Of Interest
RMSE	Root Mean Square Error
SAR	Synthetic Aperture Radar
SFM	Statistical Feature Matrix
SGLDM	Spatial Gray Level Dependence Matrix
SMED	Scale Multiplication Edge Detection
STJ	Sino-Tubular Junction
SSI	Speckle Suppression Index
SSIM	Structural Similarity Index
SURE	Stein’s Unbiased Risk Estimation
SV	Stroke Volume
TMED	Triangulation Median
TMAV	Triangulation Moving Average
TV	Total Variation
TTE	Transthoracic Echocardiography
TEE	Transoesophageal Echocardiography
US	Ultrasound
VCW	Vena-Contracta Width
VFC	Vector Field Convolution
2D	Two Dimensional

CHAPTER 1: INTRODUCTION

This chapter describes the cardiac structure, and the imaging modalities employed for the assessment of valvular abnormalities. The advantages and disadvantages of echocardiographic imaging along with the importance of acquiring images in multiple views using various acoustic windows are discussed. The need for pre-processing of transthoracic echocardiographic images, the state-of-the-art techniques employed for speckle noise reduction and segmentation are highlighted in the literature review presented. The major objectives of current research work are also being outlined.

1.1 Motivation

Medical imaging modalities provide effective mapping of different body tissues under pathological conditions resulting in different image patterns. These patterns reflect the status of the biological tissues through images that are employed in the routine clinical practice for the medical diagnosis and treatment planning. The computer-aided pre/post-processing and analysis of medical images encompass a number of potential areas such as image acquisition, noise reduction, enhancement, compression, automated/semi-automated delineation and image based visualization. The basic purpose of medical image analysis is to obtain scientific knowledge of various diseases and their impact on other anatomical structures to administer suitable treatment, intra-operative navigation and surgical planning [1-12].

The sustained effort of researchers is reflected by various medical imaging modalities available for acquiring the exceptional views of various organs in multiple views. The imaging modalities such as X-ray, computed tomography (CT), ultrasound (US), and magnetic resonance imaging (MRI) are available for diagnosis [4, 5, 13-16]. Among the available medical imaging modalities, the images acquired from the US B-scans are widely used in diagnosis due to its cost effectiveness, portability, acceptability and safety it offers. Due to the ability to aid human visualization of human tissues without deleterious effect, the US B-scan imaging has been widely employed in imaging soft tissues such as that of heart, kidney, liver, lungs, prostate, spleen, uterus, kidney, carotid artery, and bone fractures. The US of heart is known as echocardiography. The technical advances due to extensive research in modern electronics and biomedical image processing have revolutionized state-of-the-art of the US based machines in the recent years [5, 7, 17-19]. The modernization has increased the computational power drastically enhancing the efficiency of the doctors in accurate disease diagnosis. These days the US machines are available in the doctors' offices, emergency departments, ambulances and operation theatres. The US systems are used in cardiology, detection of renal disorders, breast cancer detection, prostate cancer detection, gynaecology complications, etc. [5, 7, 14, 20-28].

The echocardiographic images are affected by shadowing from the lungs, reflection of signal from the ribcage and respiration of the patient. Artifacts are often introduced due to the probe motion and incorrect gain settings. The low gain settings may eliminate certain structures and using high gain settings can mask structures which lead to significant wrong diagnosis. A large number of images are obtained for better reconstruction but it lengthens the time of acquisition and introduces motion artifacts [22, 29-36]. It is operator-dependent and often significant training is required to acquire good quality and correct data. Manually analysis is a herculean task, it is quite laborious, time consuming with inter/intra-personal variations. The huge data is acquired during the diagnosis at various stages. It is difficult to manually analyse the acquired data due to the poor quality of images and drawbacks of the imaging modalities. It is quite challenging to derive the necessary information from the acquired data by the doctors and technicians. Also, the manual analysis is a subjective methodology, it compromises on the accuracy of diagnosis and severity estimation. It is very difficult to reproduce quantitative measurements. All these reasons have made computer aided diagnosis all that important and have triggered requirement for software based techniques for automatic analysis of the medical images [12, 37-55].

The B-Mode echocardiographic images have attracted the attention of many researchers for noise reduction, enhancement or automated segmentation compared to M-Mode, continuous wave Doppler, color Doppler, and pulse wave Doppler echocardiographic images. The research in this area is mostly being reported for echocardiographic images acquired from healthy individual in a particular view and window. The valve and chamber specific image processing and analysis techniques during various stages of valvular abnormalities are very few. Further, it is observed that no single Doppler based imaging scheme can provide all information necessary for precise assessment of prevailing abnormality in the heart. Hence, this research work is taken up to address issues pertaining to disease specific analysis of the images acquired in multiple acoustic windows employing various Doppler based echocardiographic modalities along with B-Mode images [12, 13,17, 19, 56]. The basics of heart anatomy, imaging modalities and diagnosis of valvular abnormalities are introduced in this chapter along with a comprehensive literature review on denoising and segmentation of echocardiographic images.

1.2 Introduction

The heart is a specialized muscular structure that contracts regularly and continuously. It provides oxygenated blood to the entire human body. It is strongly protected through its placement in the ribcage between the right and left lungs. Normally age, physical size and the

prevailing abnormality dictate the heart size of that individual. The size of heart in a normal and healthy adult is the size of his clenched fist. The heart weighs between 200 to 425 grams. On an average, the heart beats of a healthy individual about 100,000 times every day. The pericardium surrounds the heart and it is a double layered structure. The heart's major blood vessels are covered by the outer layer of the pericardium. These blood vessels are connected to various structures of the body. The pericardium's inner layer is attached to the heart muscles. A fluid coating separates the layers of membrane, and allows the dynamic motion of the heart [3, 57].

1.3 Cardiac structure

The heart as a structure consists of four chambers and four valves functioning synchronously. The left atrium and right atrium constitute the upper chambers whereas the lower chambers are known as left and right ventricles. Left and right chambers of the heart are separated by a wall of muscle called septum. The area of septum that divides the atria is called inter-atrial septum and the area that separate the ventricles is called the inter-ventricular septum. The four valves of heart synchronously regulate the flow of oxygenated and de-oxygenated blood. The tricuspid valve (TV) regulates flow of blood between the right atrium and the right ventricle whereas the pulmonary valve regulates blood flow from the right ventricle (RV) into the pulmonary arteries which carry blood to the lungs to pick up oxygen. The mitral valve (MV) allows oxygenated blood from the lungs, passing through the left atrium into the left ventricle. Lastly, the aortic valve (AV) allows the oxygenated blood from the left ventricle (LV) into the aorta, the body's largest artery, where oxygenated blood is delivered to the rest of the body [3, 57].

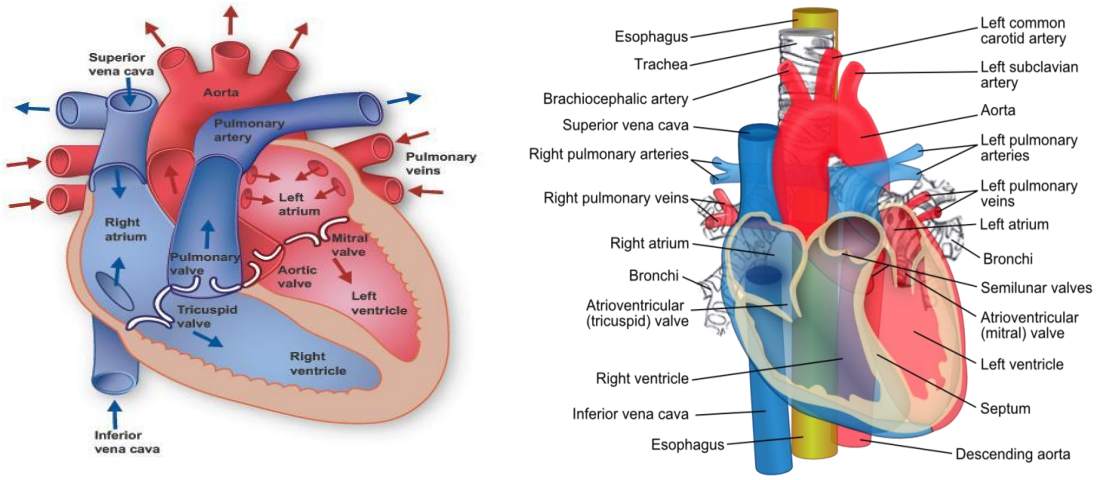

Figure 1.1 Cardiac structure: a. direction of flow of blood across chambers and valves, b. parts of the cardiac structure (Image courtesy: www.studyblue.com, en.wikipedia.org)

In Figure 1.1, the arrow shows the direction of blood flow through the chambers and valves in the heart. The blood enters the right atrium (RA) of the heart from the superior and

inferior vena cava. From the RA, blood is pumped into the RV. From the RV, blood is pumped to the lungs through the pulmonary arteries. The oxygenated blood from the lungs passes through the pulmonary veins into the left atrium (LA). The LV pumps the blood to the rest of the body through the aorta. In order for the heart to function properly, the blood must flow only in one direction and that is controlled by the valves. The ventricles have inlet valve from the atria and outlet valve leading to the arteries. A normal valve opens and closes, in exact coordination with the pumping action of the atria and ventricles [3, 57].

Each atrio-ventricular valve consists of an irregular ring of membranous tissue those are attached to the heart wall over a ring-shaped region called the annulus as shown in Figure 1.2. Distinct lobes of this membranous tissue are referred to as leaflets. The free edges of the leaflets are tethered by thin tendons, the chordae tendineae and to the papillary muscles, which are specialized muscles on the inner side of the ventricle wall. The right atrio-ventricular valve is known as the tricuspid valve, with the name reflecting the three-leaflet structure. The left atrio-ventricular valve is called the mitral valve because the two-leaflet structure resembles a miter, a type of headgear worn by catholic bishops.

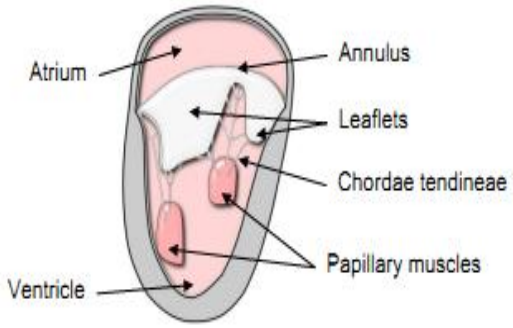

Figure 1.2 Major constituents of an atrio-ventricular valve: the leaflets, annulus, chordae tendineae and papillary muscles

The semi-lunar valves consist of three half-moon-shaped leaflets that are attached to the walls of their respective outflow vessels as shown in Figure 1.3. The region at which two adjacent leaflets join and meet the vessel wall is called a commissure. The left semi-lunar valve is called the aortic valve, reflecting its location in the ascending aorta, and the right semi-lunar valve is called the pulmonary valve, taking its name from pulmo, the Latin word for the lung.

1.4 The aortic valve

The aortic valve (AV) is situated between the left ventricular outflow tract (LVOT) and the aorta as shown in Figure 1.4. It allows the LV to eject blood into the aorta during systole while

preventing regurgitation during diastole. It is a highly layered specialized complex structure functionally adaptive to the cells and the extra cellular matrix [3].

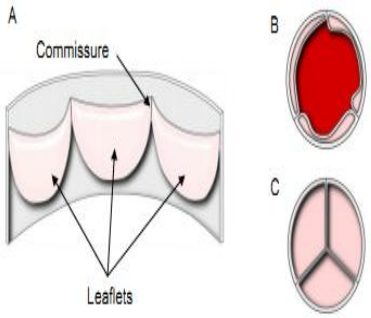

Figure 1.3 Semi-lunar valve: a. axial cutting of outflow vessel between leaflets and unrolling, b. top view of transverse section of outflow vessel distal to the open valve, and c. from top view of transverse section of outflow vessel distal to the closed valve

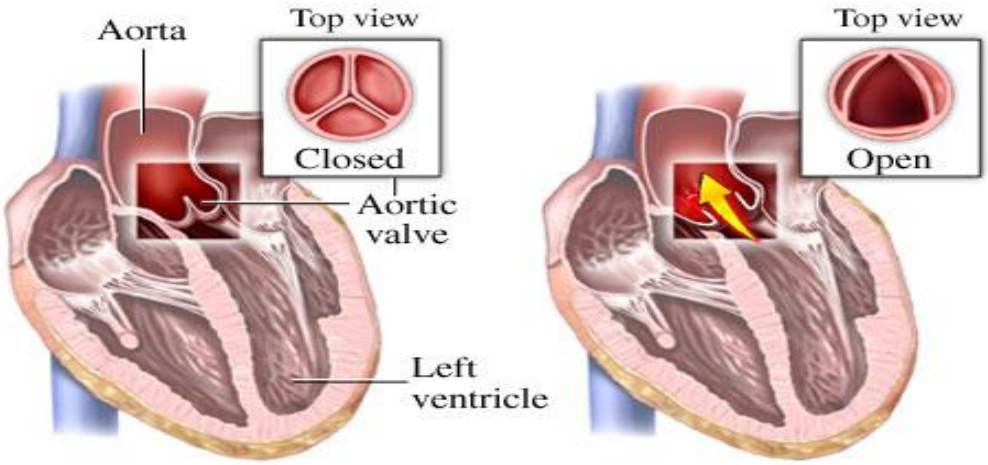

Figure 1.4 Opening and closing of normal AV
(Image courtesy: www.medicinenet.com)

1.4.1 The AV cusp structure

The AV cusps or leaflets are thin, flexible structures that come together and close the valve during diastole. The AV is composed of three cusps of roughly equal area. These cusps open against the aortic wall during systole to a triangular orifice as shown in Figure 1.4. During the diastole, they close rapidly and completely under minimal reverse pressure. The size of orifice area in a normal adult is 3.0 to 4.0 cm^2. The cell in the valve structure plays a crucial role in the durability and functioning.

There are two broad categories of cells found in the AV: (i) endothelial cells on the surface of the cusps and (ii) interstitial cells that populate the body of the valve cups and form an integral network along with the extracellular matrix. The endothelial cells populate the

surface of the AV cusp and are responsible for maintaining a non-thrombogenic blood contact surface, as well as transmit nutrient, biochemical and mechanical signals to the interstitial cells. The endothelial cells form single cell mono-layers on both the cusp surfaces, and possess cell junctions similar to arterial endothelial cells.

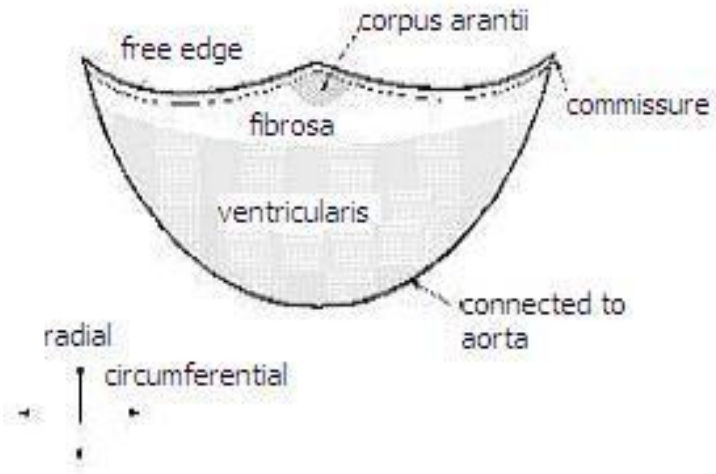

Figure 1.5 Anatomy of a cusp (Image courtesy: http:// heartlab.robarts.ca).

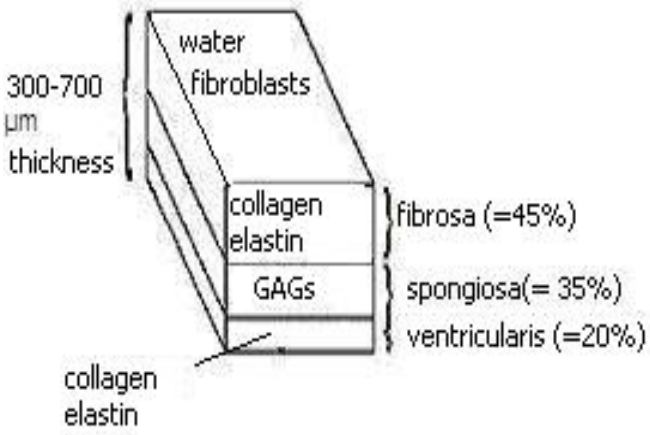

Figure 1.6 Cross sectional view of a cusp (Image courtesy: http:// heartlab.robarts.ca)

The interstitial cells are a heterogeneous and dynamic population of specific cell types that have several unique characteristics. These cells are responsible for constant renewal and turnover of the extracellular matrix “scaffold”. As these cusps cycle, there are substantial and repetitive changes in size and shape. In particular, the AV cusps have nearly 50% greater area in diastole than in systole. The curved base portion connects the cusp to the aortic wall.

The sinuses of valsalva are three elliptical depressions behind each cusp, which together with the cusps form the functional unit of the aortic valve. The left and right sinuses contain

Ostia that lead into the left and right main coronary arteries. The third sinus does not feed a coronary artery and is named the non-coronary sinus. Figure 1.5 shows a single aortic valve cusp. At the top of the cusp is the free edge, the part of the cusp that is freely movable during the blood flow. Just in from the free edge along the upper portion of the cusp is the coaptation region, which is the portion that joins the neighbouring cusps. A cross-sectional view of an aortic valve cusp is shown in Figure 1.6. The inflow surface, known as ventricular is predominantly collagenous with radially aligned elastic fibers. The central region called as spongiosa is composed of loosely arranged collagen and glycosamaminoglycans. The outflow surface, commonly called as the fibrosa, is composed of the circumferentially aligned and densely packed collagen fibers. They are largely arranged parallel to the cusp free edge.

1.5 Aortic valve diseases

The AV diseases are common among the adult population and approximately two percent of the people suffer because of these valvular abnormalities [58]. The AV diseases can be grouped as genetic or completely epigenetic abnormalities. The genetic disorders are either inherited from parents or they occur during cardiogenesis. The valvular diseases may be acquired as a consequence of other pathologies also, such as renal failure. The degenerative AV disease may be characterized by the valvular structural changes such as increase in the thickness, stiffness and calcification of the leaflets resulting in the mal-functioning of the aortic valve complex (AVC) being manifested as either aortic stenosis, regurgitation or both. The exact reason of valvular disease vary depending on the various pathological conditions such as congenital heart defects, ventricular septal defects, herited disorders, acquired pathologies and epigenetic causes.

The commonly observed congenital heart defects include the bicuspid aortic valve, ventricular septal defects, and coarctation of aorta. The ventricular septal defects result in the circulation shunts that severely impair the normal unidirectional blood flow. The heterogenic connective tissue disorders, improper valve tissue development and common connective tissue abnormalities fall under the category of heritable AV disorders. The acquired diseases may be due to the bacterial infections that cause lesions on the valve leaflets [58].

The rheumatic heart disease (RHD) and the infective endocarditis (IE) are the two major acquired valvular diseases. The RHD commonly results as a consequence of the rheumatic fever which is known as post-streptococcal multisystem disease characterized by the chorea, migratory arthritis and subcutaneous nodules. Endocarditis can involve the heart muscle, heart valves, or lining of the heart. It is often reflected in the form of inflammation of these parts of the heart. The IE is a seditious-like reaction caused by the presence of a variety of bacterial

vegetations on valve leaflets. The majority of valvular diseases are not diagnosed in the childhood but may occur later with no apparent aetiology. Late-onset of the valvular disease is blanket terms, which encompass a variety of symptoms, including the valvular stenosis, regurgitation, tissue calcification and degeneration. Aortic valve disease can be broadly categorized into two categories: (i) aortic stenosis and (ii) aortic regurgitation [58].

1.5.1 Aortic stenosis

Aortic stenosis (AS) is an acquired or a congenital narrowing of the AV orifice which results in the obstruction of the LVOT with increase in the resistance to blood flow from the LV to the aorta. It occurs when the valve opening is reduced during systole resulting in a larger pressure gradient between the ventricle and the aorta. The LV has to generate an increased pressure in order to overcome the increased after-load caused by the stenotic valve and eject blood out of the ventricle at the same cardiac output. The valvular stenosis is characterized by the greater left ventricular pressure in comparison to the aortic pressure during left ventricular ejection. The common causes of the AS are degeneration of aortic valve leaflets, congenital valve malformations and inflammation such as the rheumatic fever. The consequences of severe AS results are i) reduced ventricular stroke volume, ii) increased end-systolic volume, and iii) a compensatory increase in end-diastolic volume and pressure. Due to the increased pressures generated by the LV, the myocardium of the ventricle undergoes hypertrophy. This may be observed as thickening of the left ventricular walls [58].

1.5.2 Aortic regurgitation

The second category of the AV disease is aortic regurgitation (AR) or aortic insufficiency (AI). The AR is the backflow of blood from the ascending aorta into the outflow tract of the LV during the diastole where the AV is completely closed and the MV is fully open. The phenomenon of regurgitation is because of incompetence of the AV or malfunctioning of the valvular apparatus (e.g., leaflets, annulus of the aorta) resulting in retrograde flow of blood into the left ventricular chamber. It occurs when the AV fails to close completely and blood flows back into the LV after ejection into the aorta is complete (after the heart sound S2) [3, 6, 9, 57-60].

Normally, there is a brief period of isovolumic relaxation after the AV closes (the mitral valve is also closed at this point). However, when the AV is leaky, the ventricle begins to fill from the aorta after the incomplete closure of the AV. This leads to an increase in the ventricular volume prior to the opening of the MV and normal ventricular filling. As a result the blood leaves the aorta in two directions (back into the heart as well as down the aorta).The aortic diastolic pressure falls more rapidly thereby leading to a decrease in the arterial diastolic pressure. As

the ventricle fills from both the aorta and the LA, there is a large increase in left ventricular volume and pressure (increased preload) [3, 6, 57-60]. The increased preload causes the LV to contract more forcefully thereby increasing ventricular (and aortic) systolic pressure and increasing stroke volume to help compensate for the regurgitation. The increase in ventricular end-diastolic pressure, however, also leads to an increase in left atrial pressure, which can result in pulmonary congestion and edema.

Regurgitation coupled with enhanced LV stroke volume, results in a characteristic widening of the aortic pulse pressure [3, 6, 9, 57-60]. The prevalence of AR in the patients presenting for aortic valve replacement (AVR) suggests that the cusp prolapse is one of the common causes of AR. Regurgitation can be grouped into three types namely:

Type I: Enlargement of the aortic root with normal cusps structure

Type II: Cusp prolapse or fenestration

Type III: Poor cusp tissue quality or quantity

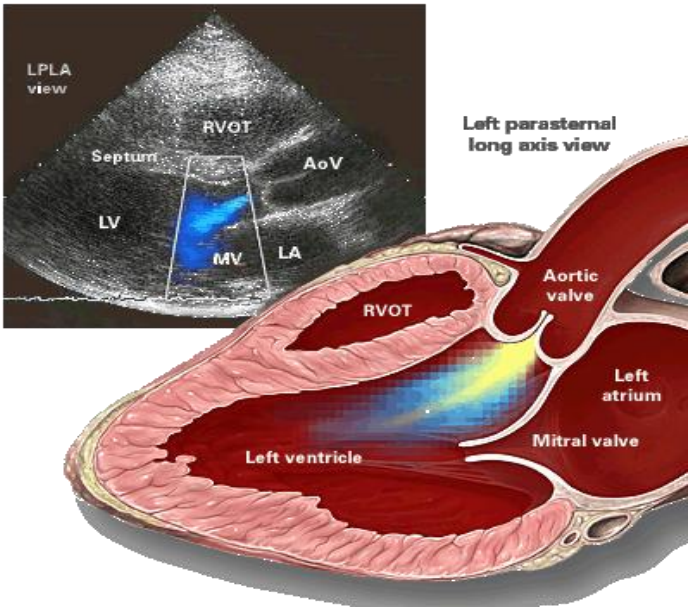

Figure 1.7 Radiologic characteristics of aortic regurgitation
(Image courtesy: www.yale.edu/imaging/echo_atlas/entities/aortic_regurgitation.html)

The estimated number of patients with the RHD in India was 734 million at risk and 0.06–0.46 million cases reported in 2008. Adjusted to the entire US population, the data suggest that the prevalence of any valvular diseases was 2.5%. Within this sample, 0.4% of the patients had AS, 0.5% with AR, 0.1% had mitral stenosis and 1.7% had mitral regurgitation [1]. In the early stages of AR, there would be a large increase in the pressures across the LV and the LA. The

increase in the LV and LA volume, result in a large pressure rise. Over time, with long-standing regurgitation, the LA and the LV dilate so that the increased volume does not lead to steep increase in the pressure. Due to the extra effort, the LV has to go through, the blood slump leads to its dilation and hypertrophy. As with the AS, patients with severe AR may have to undergo valve replacement therapy or repair [9, 57, 59, 60]. The radiologic characteristics of the AR are shown in Figure 1.7.

Aortic regurgitation is the leading cause of death. The earlier the regurgitation is detected, the better the treatment can be provided. However, early detection requires an accurate and reliable diagnosis which should also be able to distinguish normal and abnormal valve functioning. The valvular regurgitation can result in LV dysfunction in 25% of the AR patients with no symptoms of abnormality being exhibited [61]. Hence, assessment of the LV systolic and diastolic function using imaging modalities such as the conventional two dimensional (2D) B-Mode, cross sectional echocardiographic images and three Doppler echocardiography modalities, play a vital role in the management of regurgitation [61].

The role of non-invasive imaging and, in particular, of echocardiography has been pivotal in understanding the complexity of the AV complex and measuring the severity of the valve lesion. The Doppler echocardiographic modalities such as the B-Mode, color Doppler, continuous wave Doppler and M-mode are used hand-in-hand for assessment of the aetiologies and consequences of aortic regurgitation. The poor US viewing windows make the task further challenging for the cardiologist in the case of patients with mild regurgitation and severe LV dysfunction [61]. A contrast enhancing dye is being injected to help better visualization of the cardiac chamber boundaries in the patients with poor acoustic viewing windows [62]. The contrast of images may be enhanced by combining the data acquired from various probe positions. But it is a cumbersome activity, and is still in the research stage, hence it is clinically not available [3, 6, 57, 59, 62]. There is also need for early identification of severity so that medical or surgical intervention can be offered before the functioning of cardiac structure becomes irreversible.

1.5.2.1 Causes of aortic regurgitation

The regurgitation across the AV can be because of the mal-coaptation of aortic leaflets, abnormalities associated with their supporting structures (aortic root and annulus) or both. The abnormalities that primarily affect the AV leaflets include the presence of two leaflets or four leaflets (i.e. bicuspid and quadricuspid aortic valves, respectively) in place of normal three leaflets, the congenital abnormalities, the RHD, the connective tissue or inflammatory diseases

and the usage of anorectic drugs. The dysfunction of the annulus or the aortic root can be due to the aortic root dilation, aortic dissection and various connective tissue diseases. The morphologies characterizing the aortic dilation may consist of enlargement of aortic root, ascending aorta and the proximal aortic arch or the root ascending and proximal aortic arch enlargement. This increase in the size might occur at more than one point. A bicuspid AV is commonly associated with dilation of the aortic root in addition to the congenital leaflet abnormality. Finally, chronic severe AR of any cause can lead to progressive enlargement of the aortic root and further worsening of AR over time [9, 57, 59, 60].

1.5.2.2 Physical signs and symptoms of aortic regurgitation

Most often the progress of AR is quite gradual and cardiac structure attempts to compensate for this problem on its own. No major signs or symptoms are being presented or may be visible and observed for many years, and mostly the patient is unaware of this prevailing abnormal condition. But, as the severity of regurgitation progresses and increases, the signs and symptoms are visible. These may consist of weakness and fatigue, shortness of breath, pain in the chest accompanied with discomfort or tightness, giddiness, rapid or fluttering pulse and palpitations of heart and swelling of the ankles [6, 16, 58].

1.5.2.3 Physiology of AR

In a normal healthy adult, the AV opens when the pressure in the LV is higher than pressure in the aorta, allowing the blood to be ejected from the LV into the aorta during ventricular systole. The amount of blood ejected is known to as the stroke volume (SV). Under the normal conditions, about 50 to 70% of the blood is ejected from the filled LV into the aorta which in turn is being used by the body. This is known as the 'ejection fraction'. At the end of ventricular systole, the pressure in the LV decreases as it relaxes and then begins to fill up with blood from the LA. This relaxation of the LV results in the fall of its pressure. When the pressure in the LV falls below the pressure in the aorta, the AV will close, preventing blood in the aorta from moving back into the LV [6, 16, 58].

1.5.2.4 Pathophysiology of AR

The return of blood from the AV into the LV during the diastole results in the undesired hemodynamic changes and appearance of the heart. During regurgitation, when the pressure in the left ventricle falls below the pressure in the aorta, the AV may not be able to completely close. This results in leakage of the blood from the aorta into the LV. The amount of blood that flows back through the AV during regurgitation is referred to as the regurgitant fraction (RF).

The diastolic blood pressure in the aorta is decreased with an increase in the pulse pressure as a consequence of regurgitation.

The LV size, function and the hemodynamic would be normal for the patients with mild AR. In acute severe AR, the equilibration of the LV and aortic pressures might be observed with the left atrial pressure being elevated and may also result in the pulmonary edema. But, in the case of chronic, severe and compensated AR, the LV dilatation might be observed with the EF maintained in the normal range. A systolic arterial hypertension and wide pulse pressure may also be observed. The filling pressures of the LV might be normal or higher by a fraction [6, 16, 58].

1.6 Assessment of aortic regurgitation

The imaging modalities such as cardiac auscultation, chest X-ray, electrocardiograms (ECG), magnetic resonance imaging (MRI) and echocardiography (B-Mode, M-Mode, CWD, PWD, and color Doppler), are used for assessment of aortic regurgitation [6, 16, 58]. Cardiac auscultation is the most commonly used screening test employed to determine the presence or the absence of AR. The classical auscultatory finding of AR is a blowing decrescendo diastolic murmur being heard best along the left sternal border. An isolated systolic murmur is common in the patients with moderate or mild AR. The murmur is best heard when the patient is comfortably seated and leans forward with breath held in expiration. The murmur would be soft and rarely shown excitement in investigating it thoroughly. The apex beat is normally down and left inclined. A chest X-ray can reveal the hypertrophy of the LV and dilatation of the aorta. An ECG can assist in the assessment of systolic dysfunction in chronic AR. The ECG contains reliable information about the structural and functional alterations of the ventricular myocardium in chronic AR. The cardiac chamber catheterization can also assist in locating the left ventricular dysfunction.

The echocardiography is the most important imaging tool employed in the diagnosis of cardiac and valvular abnormalities. The images in echocardiography are constructed based on the concepts of Doppler shift exhibited by the US waves on passing through the heart. Each of the Doppler imaging modality employs a different mechanism in which the US signals are transmitted, received and images are reconstructed and displayed on the computer screen. An echocardiogram will assist the clinicians in the assessment of cardiac anatomy, detection of the presence and severity of valvular abnormalities, aetiologies and consequences of the valvular regurgitation, and the dynamic functioning of the heart in totality.

The B-Mode echocardiographic images are used in analysing the consequences of valvular abnormalities by measuring the chamber and valvular dimensions, studying the

changes in the shape of constituents of cardiac structure, detection and localization of valvular vegetations, assessment of congenital abnormalities and demonstration of morphological changes in the valve due to abnormalities. The severity of AR may be determined by measuring the pressure half time (PHT) using CWD absed echocardiography. The pulse wave Doppler (PWD) echocardiography is employed in the measurement of flow velocity integral of the aortic outflow volume and mitral inflow volume. The Doppler color flow mapping is widely used in identification the severity of valvular regurgitation and stenosis [6, 16, 58].

Doppler heart sounds (DHS) are one of the most important sounds produced by blood flow, valves motion and vibration of the other cardiovascular components. However, the factors such as calcification or obesity often result in a diagnostically unsatisfactory Doppler techniques assessment and, therefore, it is sometimes necessary to assess the spectrogram of the Doppler shift signals to elucidate the degree of the disease. Cardiac magnetic resonance imaging (MRI) provides highly accurate assessment of LV volumes, mass, and ejection fraction. It can also give an excellent visualization of the aortic root and the ascending aorta. But, the usefulness of the cardiac MRI is limited by the long acquisition times, patient access during scanning and the cost constraints. The exercise testing is useful as a measure of functional capacity when it is unclear whether symptoms are present. However, exercise LV ejection fraction is often abnormal in asymptomatic patients with severe AR and does not to provide any additional prognostic information when the LV size under the resting state and function are known. The AV morphology is evaluated using the parasternal short axis (PSAX) view images whereas the LVOT diameter and aortic annulus, sinus and sino-tubular junction (STJ) diameters are measured in the parasternal long axis (PLAX) view.

No single method provides an entirely accurate quantitative assessment of the severity of valvular regurgitation, and the complex interaction of anatomic and hemodynamic variables can add to these potential difficulties. Although the echocardiographic images provide important clinical information necessary but the physician has to intelligently integrate and correlate data acquired from various echocardiographic modalities in different views using different acoustic windows. Combination of different parameters computed using different modality images are employed in quantifying the severity of AR because no single method provides the necessary quantitative information. Assessment of AR requires an integrated approach, acquiring of data through various acoustic windows and views, visualizing the cardiac structures at various points and positions, and making use of all available information and comparing them [12, 13, 19, 56, 58, 63].

1.7 Ultrasound

The term ultrasound (US) can encapsulate all acoustics of frequencies larger than the upper threshold which a human ear can intercept (f > 20 kHz). In clinical imaging, the US refers to 1-20 MHz range [22]. The image obtained depends on the transmission of acoustic pulses into the human body and their interaction with the tissue medium. An US signal is transmitted into the body, these sound waves are reflected back and the machine decodes the reflected echo by interpreting its strength and timing. The amplitude of the signal is the strength of the sound wave transmitted and received back. The magnitude of the reflected US signal determines the brightness and the intensity displayed on the computer screen [3, 7, 14, 17, 64].

The high reflectivity is observed across the bones and is displayed as white on the gray scale whereas the low reflectivity from the muscular tissues is shown as gray and no reflection is depicted as black. The image produced from the reflected US signal is dependent on the time lag between the transmitted signal and the received US signal. The propagation speed of the sound wave is the speed with which it travels in a given medium. The speed is computed depending on the medium density and stiffness. A list consisting of the propagation speed through various tissues is tabulated in Table 1.1. The average speed through soft tissue is 1540 m/s. The acoustic impedance shows the amount of resistance offered to the travelling sound wave through the medium. The reflection of the US wave depends on the difference in the acoustic impedance of two tissues across a boundary [7].

Table 1.1 Propagation speed through various tissues

Material	Acoustic impedance(x10^6)	Velocity (m/s)	Material	Acoustic impedance(x10^6)	Velocity (m/s)
Air	0.004	330	Lung	0.18	650
Bone	7.80	4080	Soft tissue	1.58	1540
Liver	1.69	1550	Fat	1.34	1459
Muscle	1.68	1580	Blood	1.65	1575

The difference in the acoustic impedance at various points on the boundary determines the amount of sound energy reflected and transmitted. As and when the wave finds a difference in the impedance some of the signals are transmitted and some may be reflected. The amount of the wave reflected in dependent on difference in the impedance. The smaller variations result in a smaller amount of reflected energy, large differences will have a large amount of reflected energy and no reflections are observed when there is no difference in the impedance. The higher the difference in the acoustic impedance the greater will be the amount of energy reflected. The energy dispersion by the reflected sound wave results in a weaker transmitted

wave in comparison to the original wave and this reduction is known as attenuation. The frequency of the wave and the distance a pulse travels determine the amount of attenuation in that medium. Larger the distance a given pulse travels, the higher would be the amount of attenuation. The cause of attenuation can be the absorption, scattering or reflection.

The quality of the image depends on the resolution. The spatial resolution is defined as the shortest distance between two discrete points where the object points can be clearly differentiated. The axial resolution is defined as the ability to make a clear distinction between closely spaced points along the axis of the beam and is estimated based on the pulse length. A transducer operating at high frequency gives a better axial resolution than low frequency transducers. The lateral resolution reflects the ability to distinguish between the closely placed points side by side.

Echocardiography has emerged as the most important imaging modality employed in the diagnosis of aortic regurgitation. The assessment of AR severity is accomplished by integrating information obtained by employing four Doppler echocardiography modalities in various acoustic windows and views. Two dimensional (2D) B-mode, M-mode, continuous wave Doppler (CWD), pulse wave Doppler (PWD) and color Doppler echocardiography images are being used hand-in-hand for the diagnosis and assessment of AR [19].

1.8 Viewing of the cardiac structure

The echocardiography based studies and analysis are carried out using sophisticated ultrasound machines. In transthoracic echocardiography (TTE), the US signals of various frequencies are transmitted from the probe placed on the patient's anterior chest wall. The patient lies in the left lateral position and a jelly is applied on the transducer to ensure that the good quality images are acquired. The ECG (electrocardiograph) is simultaneously recorded along with B-Mode echocardiographic images. The echocardiographic examination may span for a period of 15-20 minutes.

1.8.1 Echocardiographic windows and views

The echocardiographic images are acquired in various views using different acoustic windows each view provides specific details which the other views fail to show. There are several standard positions on the chest wall for placing the probe, commonly known as echo windows, which allow the good penetration of the ultrasound signals without too much absorption and attenuation.

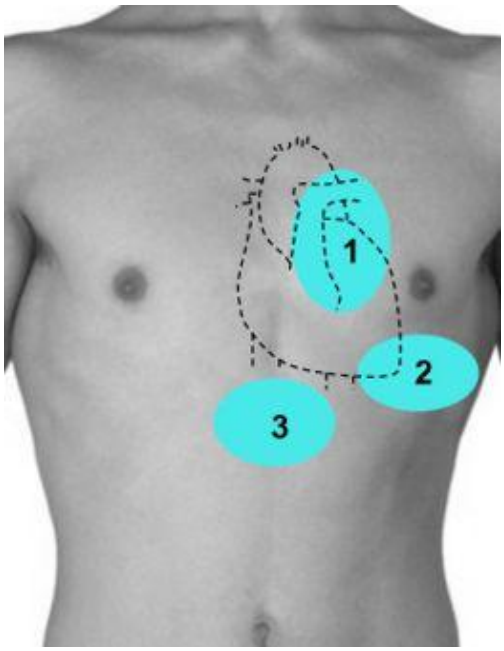

Figure 1.8 Echocardiographic windows: 1) Parasternal, 2) Apical, and 3) Subcostal window (Image courtesy: web.stanford.edu/group/ccm_echocardio/cgi-bin/mediawiki/index.php)

There are three major echocardiographic windows, which are used in the visualization of cardiac structure, namely: parasternal window, apical window and subcostal window. The subcostal window is also known as the subxyphoid window. The major windows are pictorially shown in Figure 1.8 for better understanding of the process of image acquisition. In the parasternal window, the images can be acquired either using long axis or in short axis. In the short axis the image can be acquired at four levels namely: base of the cardiac structure (level of AV), level of MV, left ventricular papillary muscles and left ventricular apex.

In the apical window the images are acquired in apical 4 chamber (A4C) view, apical 2 chamber (A2C) view and apical 5 chamber (A5C) view. In the subcostal window the images are viewed as subcostal 4 chamber view, subcostal short axis view and subcostal inferior vena cava view. The use of parasternal and apical window in viewing various parts of the cardiac structure, the position of the transducer during each view, the common abnormalities being diagnosed by measuring various parameters are tabulated in Table 1.2.

1.8.2 Parasternal window

The transducer is placed at the left sterna edge in the 2^{nd}-4^{th} intercostals space to acquire the image in the left parasternal window. The images are acquired in either the long axis view or short axis view where the ‘axis’ refers to the plane in which the US signal beam moves through

the heart. The images acquired using the parasternal window in the long axis and short axis are shown in Figure 1.9, and Figure 1.10, respectively.

Table 1.2 Two dimensional echocardiographic windows

Position of transducer	Acronym	Structure viewed	Abnormalities viewed	Measurements
Parasternal window				
2^{nd} -4^{th} intercostals space	PLAXS PLAXD	AV, Ao, RV, IVS, LV, AMVL, PMVL,	Dilatation of aortic root, dissection of aorta, leaflet calcification thickening of leaflets and septum, vegetation, mobility	Diameter of aortic annulus, Sinus of Valsalva, STJ,AVA,
2^{nd} -4^{th} intercostals space(90^0 rotated)	PSAXS PSAXD	AV,RV,PA,LA (AV level)	Bicuspid/tricuspid AV, aneurysm of SOV, atrial septal defect, thickening of valve, calcification	Number of cusps, aortic root dimension, LA diameter
Apical window				
Cardiac apex	A4CS A4CD	LV,LA,RV,RA,MV,TV, septum,	LA,LV,RA,RV hypertrophy, wall motion abnormality, MV calcification,	LVEDV,LVESV, MV annulus diameter
Cardiac apex (angled)	A5CS A5CD	Ao, LV, LA, RA, RV	Calcification of AV and MV, changes in LV,LVOT	Aortic outflow velocity, SV,CO
Cardiac apex (angled)	A2CS A2CD	LV,MV	Chamber enlargement, thickening of IVS,	LV EF, LV area, LVEDD, LVESD

1.8.2.1 Parasternal long axis (PLAX) view

The parasternal long axis (PLAX) view is useful for measuring the size and contractility of the right and the left ventricle, to study the functioning of aortic and mitral valve and to assess the morphological and structural changes. The PLAX view can also be used to observe the regurgitation mechanism and assesses the severity through the color Doppler echocardiography. While acquiring the images in PLAX view, the notch on the probe should be directed towards the sternum, at 9-10 o'clock position. The pictorial representation of an image in PLAX view is shown in Figure 1.9. The following parts of the cardiac structure are observed in PLAX.

i) Inter-ventricular septum (IVS) and posterior wall (PW): The thickness and contractility of IVS and PW can be assessed.

ii) Right ventricle (RV): The right ventricle is located on the top in PLAX view. The right ventricle outflow tract (RVOT) can also be seen in this view.

iii) Left ventricle (LV): The LV is seen in this view below the inter-ventricular septum. The size along with wall thickness of the LV is best measured in the PLAX view.

iv) Mitral valve (MV): The PLAX also happens to be the best view to observe the structure of the MV and study the dynamics of anterior and the posterior MV leaflets.

v) Aortic valve (AV): The openings of the aortic cusps are visually seen.

vi) Aortic root (AoR): The aortic annulus, dimensions of sinus of valsalva and aortic root can be measured.

vii) Left atrium (LA): It should be the same diameter as that of the aortic root

viii) Descending aorta: Desc Ao.

ix) Pericardium: It is the most echoic structure which appears very bright.

The images acquired in the apical window are useful in evaluating in LV and RV function, estimation of valvular regurgitation and stenosis, and measuring the LV diastolic function.

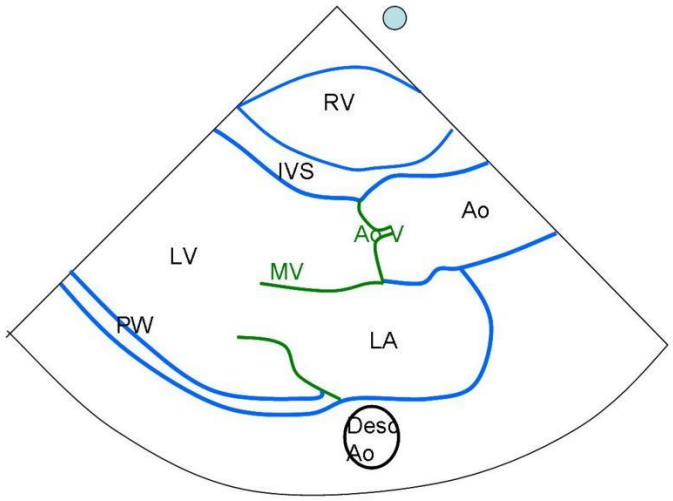

Figure 1.9 Parasternal long axis (PLAX) view
(Image courtesy: web.stanford.edu/group/ccm_echocardio/cgi-bin/mediawiki/index.php/)

1.8.2.2 Parasternal short axis (PSAX) view

The position of the transducer in PSAX view is at the same place as that of PLAX view except that the transducer is rotated by 90 degree where the marker dot points to the left shoulder. With the change in the angle of the transducer placed on the chest wall, many short axis view images can be acquired. However there are four standard levels used during the diagnosis of abnormalities and study of the cardiac structure. The angulations of probe at the base to the apex for acquiring of the PSAX view images are called as “bread loafing”. The image in the PSAX is pictorially shown in Figure 1.10. The opening and closing of the AV, tricuspid valve and the pulmonic valve can be visualized in the PSAX view along with the structural changes in the LA and RV. At the pulmonary artery level the pulmonary artery, pulmonary valve, right ventricular outflow tract (RVOT) are seen whereas at the aortic valve level the AV cusps, LA, inter-atrial septum, tricuspid valve and the RVOT can be observed. The MV orifice, MV leaflets and ventricular septum are visible in the mitral valve level whereas the antero-lateral papillary

muscle (PM), postero-medial PM, anterior wall, lateral wall, inferior wall and IV septum can be visually observed at the papillary muscle level in the PSAX view.

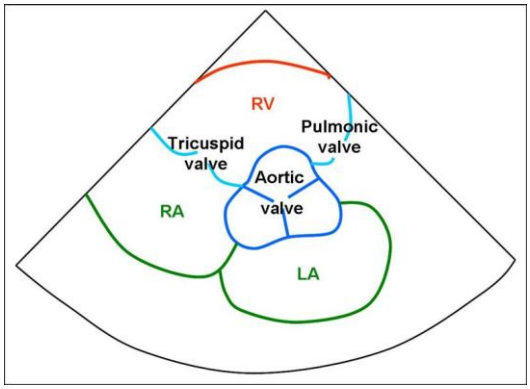

Figure 1.10 Parasternal short axis (PSAX) view
(Image courtesy: web.stanford.edu/group/ccm_echocardio/cgi-in/mediawiki/index.php/)

1.8.3 Apical Window:

The pictorial representation of images acquired using the apical window in four chamber view, five chamber and two chamber view are shown in Figure 1.11 and Figure 1.12, respectively.

1.8.3.1 Apical 4 chamber (A4C) view

The four chambers and two valves of the heart are visualized in apical 4 chamber (A4C) view. The images acquired in A4C view are useful in evaluating the LV and RV function, estimation of valvular regurgitation and stenosis and measuring the LV diastolic function. The images in this view are also employed for visually observing the apex of LV, studying the diastolic function and stenosis of the mitral valve and estimating the ejection fraction. The transducer is placed at the apex of the heart in this view. The marker dot direction points towards the left shoulder in the A4C view. The structures seen in A4C include left and right ventricle, left and right atrium, mitral valve, tricuspid valve, inter ventricular (IV) and inter-artial (IA) septum, LV apex, lateral wall LV, and free wall RV.

1.8.3.2 Apical 5 chamber (A5C) view

The images are acquired in apical 5 chamber by tilting the transducer in A4C view downward. The fifth chamber included in A5C is the AV and the ascending aorta. It is neither ventricular nor the artial chamber as the name suggests. The images in A5C will assist in the diagnosis of AS or AR. It addition to the structures seen in A4C, LVOT, AV and proximal aorta are seen in A5C.

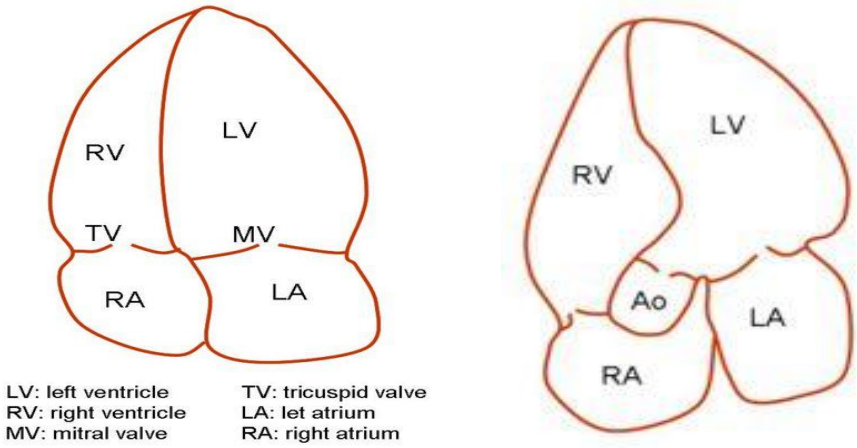

Figure 1.11 Apical 4 chamber view and apical five chamber view
(Image courtesy: web.stanford.edu/group/ccm_echocardio/cgi-bin/mediawiki/index.php/)

1.8.4 Subcostal window

The images are acquired by placing the transducer under the xiphisternum with the marker dot position pointing towards the left shoulder. The position of the transducer is rotated by 90 degree when compared to the apical views. This window is useful in the diagnosis of lung diseases, observing the inferior vena cava (IVC), interartial septum and the abdominal aorta.

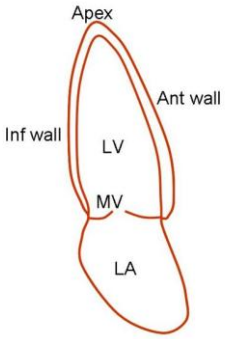

Figure 1.12 Apical two chamber view
(Image courtesy: web.stanford.edu/group/ccm_echocardio/cgi-bin/mediawiki/index.php/)

1.9 Echocardiographic imaging techniques

The three commonly used echocardiographic imaging techniques in the clinical practice are 1) 2D or cross sectional B-Mode images, 2) Motion or M-Mode and 3) Doppler techniques such as a) Continuous wave Doppler (CWD), b) Pulsed wave Doppler (PWD) and c) Color Doppler. Each of the echocardiographic imaging modalities are briefly described below:

1.9.1 2D Echocardiography

The 2D echo provides the cross-sectional view of the tissues in time. The snapshots of the tissues in cross section are acquired in quick succession and are displayed on the TV screen. The 2D echocardiographic images can be acquired in various windows and views, to observe the real time functioning and dynamics of the cardiac chambers, cardiac valves, and various blood vessels. The ultrasound beam is swept across the area of interest to create a 2D image. The probe rotates the beam at certain angles to scan the area. The reflected US signals are combined to obtain the image from the desired area. The 2D echocardiographic images play an important role in the diagnosis of valvular abnormalities and cardiac structure based studies. Some of the important applications of the 2D echocardiography are: i) study of the heart anatomy and structural relationships, ii) study of valvular and cardiac chamber abnormalities, iii) study of dynamics of heart in real time in different acoustic windows, iv) computing the stroke volume, cardiac output, volume and ejection fraction, v) study of valvular architecture like number of leaflets, size of orifice, size of leaflets, vi) proper positioning of the M-Mode image and Doppler echo, vii) assist in image guided interventions and viii) diagnosis of intra-cardiac masses, and pericardial diseases.

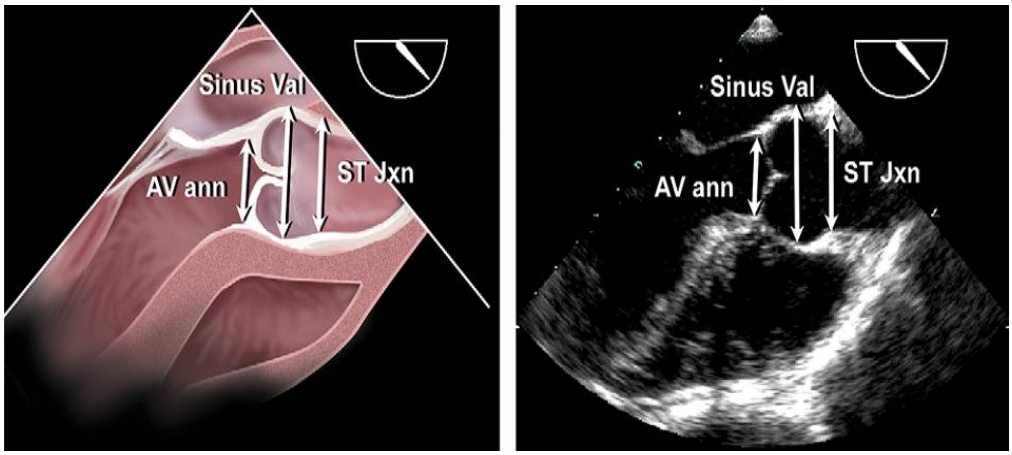

Figure 1.13 Measurement of aortic root diameters at aortic valve annulus (AV ann) level, sinuses of valsalva (Sinus Val) and sino-tubular junction (ST Jxn) from long axis view

The aortic root and the proximal ascending aorta are visualized in the parasternal long axis acoustic window. The 2D TTE images of LVOT and aortic root are acquired in different views by varying the intercostals spaces and at various distances from left sternal border. The useful images are also acquired from the patients in the right parasternal views with right lateral decubitus position. Some of the important measurements are carried out at: 1) aortic valve annulus (the pivot point of the aortic leaflets), 2) the maximal diameter in the sinuses of valsalva

and 3) sino-tubular junction (the transition between the sinuses of valsalva and the tubular portion of the ascending aorta). The measurements performed using the PLAX views are shown in Figure 1.13 and Figure 1.14.

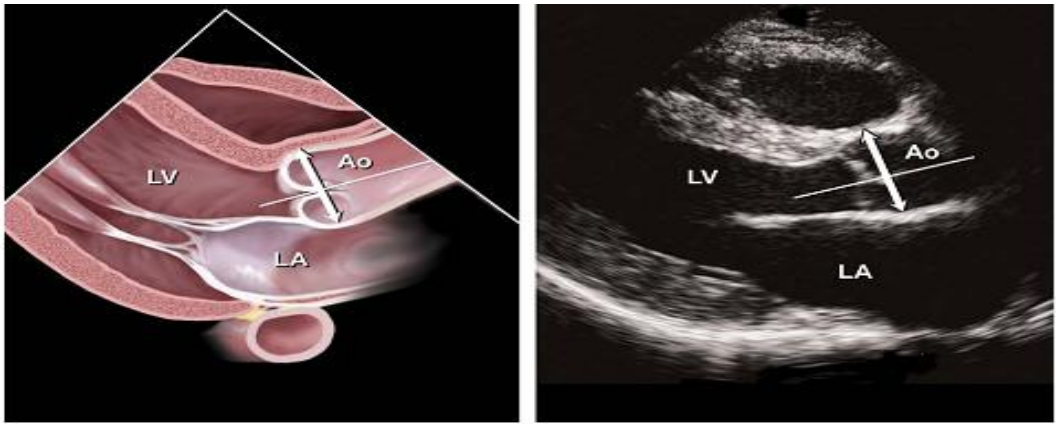

Figure 1.14 Measurement of aortic root diameter at sinuses of valsava from 2D PLAX view

The dimensions of aortic annulus are computed at the base of the AV leaflets. The AV annular diameter is estimated between the hinge points of the AV leaflets in the parasternal or apical long-axis views. The ascending aorta can also be observed in the long-axis. The short-axis view of the ascending aorta may also convey useful information for the diagnosis. The amount of dilatation and the diameter of the aortic root at the sinuses of valsalva are heavily influenced by the age of the person and the body surface area. The dilatation of aortic root is a strong reflection of progress, presence and occurrence of the aortic insufficiency.

1.9.2 Doppler techniques

Other than the B-Mode TTE images, the Doppler images acquired using CWD, PWD, and color Doppler modalities are employed by the clinicians in routine clinical diagnosis, not as a substitution but as complementary task. A brief description of Doppler based imaging modalities and “Doppler effect” is provided in the next few paragraphs.

1.9.2.1 Doppler effect

The Doppler effect is observed and employed by human beings in everyday life such as train sounding the horn nearing to railway platforms. It is observed that the pitch of the horn increases (high frequency) when nearing the platform and decreases (low frequency) as it passes by. This shows that the fundamental nature of the sound wave depends on the relative motion of the listener and the sound source. The frequency change known as the Doppler shift

depends on the speed of the automobile and the frequency of the horn sound. The reflected US signal from a tissue interface provides the information regarding the depth and reflectivity of tissue. The concept of Doppler effect is being employed in the estimation of blood flow velocity where the change in reflected frequency occurs due to the motion of blood cells or tissue of the cardiac structure. A shift in the frequency occurs due to relative motion of the source, reflected and the received sound waves where the transducer used is the source and also the receiver with the red blood cells acting as the reflector. The Doppler shift in the frequencies is proportional to the ratio of the velocity of blood to the speed of the sound and to the original frequency. It is observed that maximum velocity information can be obtained when the US beam is aligned parallel to the direction of flow of blood.

A direct relationship exists between the peak velocity of blood flow and the pressure gradient measured across a stenotic valve. The velocity information computed using Doppler evaluations can act as complementary information to the data acquired using the standard 2D B-Mode (brightness) echocardiography and M-Mode (motion mode) echocardiography. The reflected US signal provides flow velocity information and also its direction. In the conventional practice, the velocities towards the transducer are shown above the baseline whereas the velocities away from the transducers are depicted below the baseline. The returned Doppler US signal is the spectral tracing of the velocity being displayed on time axis. The intensities of the Doppler signals are displayed on a gray-scale as darker shades of the gray. A large number of red blood cells moving at a particular velocity are displayed as dark shade on the Doppler spectrum whereas cells travelling at higher velocity are shown in light shade.

The three Doppler modes commonly used in the clinical practice are continuous wave Doppler (CWD) echocardiography, pulse wave Doppler (PWD) echocardiography and color Doppler echocardiography. In CWD two piezoelectric crystals are employed, one each for transmission and reception without any time delay. The PWD echocardiography uses a single crystal for emitting a burst of US and then receives after a particular time gap.

1.9.2.2 Continuous wave Doppler (CWD) echocardiography

The conventional CWD imaging can record variations at very high velocities, but cannot precisely locate the jet in space. The CWD imaging modality is normally employed for computing the trans-valvular gradients based on peak velocity estimation. One or a group of elements are transmitted and another set receive continuously as shown in Figure 1.15 in CWD imaging. The velocities along the line are being detected and are used to measure high flow velocities during valvular regurgitation. The trans-valvular gradients can be quantified precisely

based on peak velocity estimation using the CWD imaging modality. A positive signal can be visualized at the start with the AV closure and a down slope is observed during diastole. The down slope is a measurement of the rate of pressure decay between aorta and the LV. A steep down slope is considered to be the reflection of severe regurgitation.

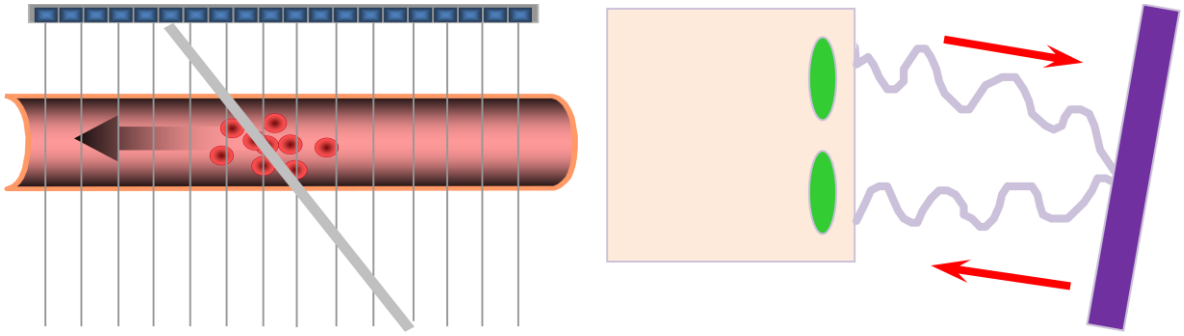

Figure 1.15 Working of CWD based echocardiography

1.9.2.3 Pulse wave Doppler (PWD) echocardiography

The PWD imaging can be used to precisely locate the abnormal flows in the space, but due to the problem of aliasing, the true velocities cannot be recorded. The recording of peak velocities is almost not possible in most of the abnormal jets as the high velocities results which often results in aliasing. As a result, the PWD is commonly employed for identifying the location of turbulent jets but this test would be quite laborious and time consuming as tedious mapping is necessary for detecting the precise location and the size of an abnormal jet. In clinical practice, the pulse-wave method is used for detection of regurgitation in the LVOT.

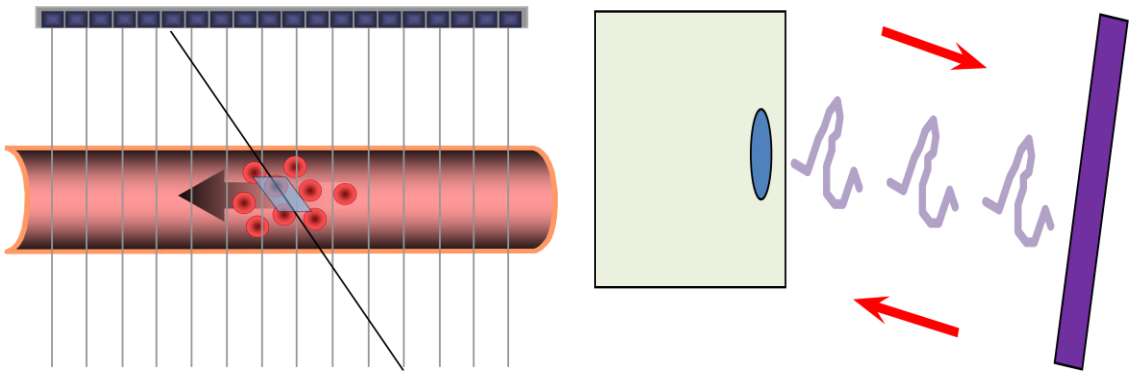

Figure 1.16 Working of PWD based echocardiography

A single or group of pulses are being used in the transmission and reception of PWD images as shown in Figure 1.16. The elements are transmitted and the machine waits to receive returning echoes and decode them. The time delay between transmission and reception of

sound waves directly relates to the depth of the targeted reflectors. The shift in the frequencies are converted into velocity and displayed as a strip on the output image.

1.9.2.4 Color Doppler echocardiography

In color Doppler based imaging modality, the real time blood flow is displayed as a color overlay over the 2D B-Mode image. Many range gates are employed along many color lines to estimate the frequency shift of blood flow and this is converted into velocity. The unique advantage of color Doppler imaging over the conventional PWD is its capability to display the normal or abnormal blood flow directly onto the echocardiographic images. The tedious mapping techniques used in the PWD imaging are not necessary in color Doppler imaging. But, the color Doppler based flow imaging also fails in accurately recording the high velocity information. In addition, aliasing occurs on similar lines as being observed using PWD imaging approach and the peak velocities cannot be precisely estimated in the diseased states. The color Doppler echocardiography is a sensitive technique employed in the diagnosis of valvular stenosis and regurgitation. This technique allows visualization of flow disturbance and its pattern into the LV. The aortic regurgitant jet appears as a mosaic flow because of aliasing and turbulence in the LVOT and this jet originates from the AV.

The color Doppler flow imaging is employed for assessment of valvular regurgitation severity such as the AR, AS, mitral regurgitation (MR), mitral stenosis (MS), by measuring the size of the vena contracta (VC). The colors being displayed on the flow map image convey useful information regarding the direction of blood flow. The red color is assigned for flow towards the transducer and blue for the blood moving away from the transducer. The combinations of colors are also employed to display the turbulent flow during regurgitation which allows the clinician to make discrimination between the normal and the abnormal flow.

The effective regurgitant orifice area (EROA) can be computed in the apical long-axis view by making use of the maximal VC width (VCW) imaged in early diastole. The width of the VC is considered to be the smallest diameter of the narrowest portion of the region just distal to the orifice at the junction of the proximal flow–convergence region. The width of the vena contracta (VC-W) reflects the degree of valvular regurgitation. The exact size and shape of the VC are important parameters in the quantification of regurgitant lesions. The EROA is a marker of regurgitant lesion severity, less dependent on the hemodynamic variations than regurgitant volume and regurgitant fraction (RF). The EROA corresponds hydro-dynamically to the area of the VC, which is the smallest area of regurgitant flow through the valve, which is significantly smaller than jet size. Some of the reasons for erroneous overestimation of the EROAs are

imaging at low frequency, poor lateral resolution and reverberations induced by the chest wall [65]. Aortic regurgitant jet width (ARJW) is one of the reliable indicators for aortic regurgitation severity. The imaging modalities, their advantages, disadvantages, concept and parameter estimated, as discussed in the above paragraphs, are tabulated in Table 1.3 for quick reference.

Table 1.3 Imaging modalities in 2D B-Mode echocardiography

Parameter	Method	Concept	Advantages	Limitations
Anatomic				
LV size	2D	Dilation of LV due to volume overload	Normal size excludes chronic significant AR	Enlargement due to other causes
Aortic leaflets	2D	Thickening, vegetations and perforations of the leaflets	Simple, abnormal in severe AR	Poor accuracy, defect under estimation
Doppler				
Jet width in LVOT	Color	Increased regurgitant flow reflected as a larger color signal	Simple, sensitive and quick screening for AR	Inaccurate with noncircular jets
Jet width/LVOT Width (%)	Color	Cross sectional area of jet V/s LVOT width	Simple, sensitive and quick to screen for AR	Inaccurate with eccentric jets, assumes LVOT size to be normal
CSA Jet/CSA LVOT (%)	Color	Cross sectional area of jet V/s cross sectional area of the LVOT		
Vena contracta width (cm)	Color	The point of maximal flow convergence	Simple, quantitative, feasible to measure	Inaccurate for multiple, complex jets
Jet density	CW	The more flow, the denser the Doppler signal	Simple	Qualitative; complementary data only
Jet deceleration rate (PHT)	CW	Rate of equalization between diastolic pressure and LVDP	Simple	Not specific, influenced by other factors
Diastolic flow reversal	PW	Regurgitation due to retrograde flow into the LV	Simple	Not specific, may be because of other factors
PISA method	Color	Blood converging on regurgitant orifice forms hemispheric shells	Provides both EROA and regurgitant volume	Feasibility limited by far field imaging, multiple jet
Flow quantification				
Regurgitant volume	2D PW	Difference between flow through regurgitant and a normal valve	Quantitative method, valid for multiple lesion	Multiple measurement, error in valve diameter

1.9.3 Advantages of echocardiographic imaging

The echocardiography, a US imaging technique is a real time, safe, secure, powerful, non-invasive and portable, painless, no ionizing radiation, economical, concurrent, needing no special environment and is clinically readily accessible technique, widely used in diagnosis of valvular diseases like aortic stenosis and insufficiency because of its continuing improvements in the image quality.

1.9.4 Disadvantages of echocardiographic imaging

Echocardiography is an operator-dependent technique and thus the usefulness of imaging depends on the operating skills of the technician or cardiologist trying to visualize the condition of the patient's heart. Therefore echocardiographic imaging requires rigorous training and experience. Even well-trained experts may have a high inter-observer and intra-observer variations during the diagnosis [62] as even till date manual racing is necessary to compute the phsical size of the chambers and valves.

Therefore, semi-automated and automatic detection would play a crucial role in the detection of cardiac chamber size and valvular abnormalities. The amount of penetration is also a major limitation in imaging using US signals. The images obtained fail to reflect the prevailing abnormalities at a greater depth in the cardiac chamber and valves. Further, the echocardiographic images are not complete tomographic slices which make analysis very difficult. The nonlinear characteristics of US, the low signal-to-noise ratio, reverberations, poor visibility, poor contrast and speckle noise make it extremely difficult to accurately and reliably assess the severity of AR. The limitations of color Doppler echocardiography include the following: operator dependency, patient morphological characteristics, and insufficient sonication window.

1.10 Literature review

The US based echocardiographic images suffer from the interference induced due to the fluctuating backscattered echoes of the randomly distributed scatters, known as the speckle. It is the fine grained texture-like pattern observed in the echocardiographic images in all cross-sectional views and windows. The speckle is regarded as a multiplicative noise that results in obscuring of the fine image details. The speckle is common to all imaging systems using coherent waves for illumination, such as the synthetic aperture radar, and optical coherent tomography. In echocardiography, the speckle noise is prominent in all the cross-sectional views [66], and its effect is far more significant than additive noise sources such as sensor noise [33]. The basic description of speckle in the literature is based on the characterization of laser speckle by Goodman [67]. The granular echo is not because of any blood structure but arises due to fluctuation scattering from the randomly distributed blood cells [68]. The speckle pattern does not depend on the properties of the scattering medium [69].

The speckle noise reduction techniques employed image enhancement can be broadly grouped into image averaging or compounding and image filtering methods [70]. The averaging filtering techniques suffer due to the loss of the spatial resolution. Compounding techniques combine two or more images of the same imaged area [71]. The filtering techniques can be either working in the spatial domain or the frequency domain. Severe blurring is being observed on application of linear spatial filters along with loss of the important diagnostically useful features [72].

1.10.1 Adaptive and SAR filters

A large number of nonlinear filtering techniques such as median filter, and adaptive weighted median filter (AWMF) had been advocated for noise reduction. The edges are preserved on

application of these filters but noisy pixels are retained along with loss of fine details. The AWMF was proposed for maximum speckle noise reduction in uniform areas and also preserve edges and features [73]. The other set of filters were based on the local statistical parameters such as the mean, maximum, minimum, and average values. The Wiener filter, proximity based filter [74], and order statistic filters were also tested noise reduction in the images. A directional median filter was proposed by Czerwinski *et al.* [75] for speckle noise reduction in the US image of pig muscle. The performance of this filter was reported to be superior in comparison to AWMF and block median filter [75].

The multiplicative noise is also present in synthetic aperture radar (SAR) images. A local adaptive median filter (LAMF) based on the local statistics was proposed by Qiu *et al.* [76] for suppression of speckle noise in the SAR images. Performance of the LAMF was evaluated in terms of speckle suppression index (SSI), speckle image statistical analysis (SISA), edge enhancing index (EEI), feature preserving index (FPI), and image detail preserving coefficient (IDPC) [76]. The adaptive filters such as the Lee filter [77], Kaun *et al.* filter [78], Frost *et al.* filter [79] and their enhanced versions [80] were initially experimented using the SAR images. The working of the SAR filters has been based on the coefficient of variations unlike the median or the mean filters.

The other aspect to be taken into account was the dependence of filter performance on the size and shape of the filtering window. These filters can preserve the edges but do not enhance them as required in most of the medical US based applications. They have also been analysed for speckle noise reduction of the US images of kidney, liver, carotid artery and heart. Lee advocated a minimum mean square error (MMSE) based local mean and variance filter for speckle noise suppression and contrast enhancement [77, 81] in the SAR images. The performance was analysed by artificially embedding additive and multiplicative noise in the standard test images [81]. Ozcan *et al.* [82] embedded a wavelet based filter with the Lee and Wiener filter for speckle noise reduction of optical computed tomography (OCT) images. The result analysis revealed the performance of hybrid filter was superior in terms of PSNR in comparison to the original Lee, wavelet and Wiener filter. The performance of SAR filters namely the Lee filter [77], Kaun *et al.* filter [78], Frost *et al.* filter [79] and their enhanced versions [80] were analysed by Finn *et al.* [22] for the TTE images acquired in one view. The performance of these filters can be analysed for the CWD, PWD, MM and CD images acquired in multiple views.

1.10.2 Diffusion based filters

The concept of heat diffusion was employed in the design of anisotropic diffusion (AD) filters for suppression of noise in images. The AD filter is an iterative method for smoothing the image. It is a nonlinear, partial differential Equation (PDE) based filtering method that encourages diffusion in the homogeneous region while inhibiting diffusion at the edges [83]. In diffusion filtering, noise at the edges cannot be successfully eliminated. To overcome this problem, the concept of coherence-enhancing diffusion based on diffusion tensors models was in [84]. But the coherence-enhancing diffusion models are not commonly used for image denoising as undesired ripples might be induced in the filtered image. The nonlinear coherent diffusion (NCD) method of [85] was a tensor valued AD scheme for the removal of speckle noise.

The noise suppression and edge enhancement based on instantaneous coefficient of variation was advocated by Yu and Acton [35]. This technique was based on modifications of AD filter [83] and was known as speckle reducing anisotropic diffusion (SRAD) filter. It preserved the edges by inhibiting diffusion across the edges and allowing diffusion on either side of each of the edge. The performance of the filter was reported in terms of figure of merit (FoM), mean preservation and variance reduction. Further the performance of the SRAD filter was compared with homomorphic AD filter, enhanced Frost, and enhanced Lee filter for the SAR images. The SRAD filter suppresses the noise but gives in the inverse diffusion at boundaries of the US images. Various modifications were suggested by various authors to improve the performance of the SRAD filter. One way of improving performance was to employ a larger number of neighbourhood pixels [23]. A detail preserving anisotropic diffusion (DPAD) method was proposed in [86] to estimate the equivalence between the threshold controlling level of diffusion and variation in noise coefficient by incorporating various modifications to the SRAD filter. This method was initially tested using the SAR images. An oriented speckle reducing anisotropic diffusion (OSRAD) was proposed in [87] for enhancing the capability of varying diffusion with direction to speckle adaptive diffusion filtering. The four neighbouring pixel template in the SRAD filter was replaced by a new template of larger size to compute the diffusion term [23].

Liu and Liu [88] proposed a different approach for the construction of diffusion tensor using a four directional derivative based AD for noise reduction in the standard test image of Lena and a synthetic test image. A modified nonlinear complex diffusion filter was proposed by Saini *et al.* [89] by modifying the diffusion coefficient and time step size for speckle noise reduction in echocardiographic images acquired from patients diagnosed with mitral regurgitation (MR).

The nonlinear AD based filters can preserve the edges along with intra-region smoothing. These filters may result in incomplete noise suppression and blurring of weak edges if the time step considered is large for noise suppression in the US images. It might be necessary that the output image of the AD filter be post-processed using techniques such as viscous levelling to further improve the quality of the denoised image.

1.10.3 Transform domain filters

The image in the spatial domain is projected into frequency domain on application of transforms such as wavelet [24, 26, 90-93], M-Band ridgelet [94], curvelets, ripplet [95, 96] and others. The de-correlation, sparseness and multi-resolution properties of the wavelets play a vital role in despeckling techniques. The major advantages of the wavelets based techniques are the image can be decomposed and processed either at coarse or fine resolution levels, employ thresholding techniques to suppress or enhance the coefficients of interest, and coefficients can be processed independent of each other. The wavelet based thresholding techniques are commonly referred to as the shrinkage techniques. The hard and soft thresholding techniques [97, 98] are commonly employed either individually or combined with other techniques for speckle noise reduction. However, the other techniques such as probability based shrinkage (ProbShrink) [99], Bayesian shrink (BayesShrink), block thresholding (BlockShrink), multiscale product threshold (MPT) [100], stein's unbiased risk estimation using linear expansion of threshold (SURELET) [101], interscale orthonormal wavelet thresholding (IOWT) [102], neighbourhood shrinkage combined with SURE (NeighShrinkSURE) [103], M-Band ridgelet [94], and nonlinear approximation based ripplet (RNLA) [95] which are the state-of-the art filters, which have not been extensively analysed for the echocardiographic images. Hence, these denoising techniques can be analysed for the TTE images using logarithmic transformations.

The wavelet based shrinkage techniques use the logarithmic transformation to convert the multiplicative noise into approximated additive noise [104-106]. The logarithmic transformation of image helps in enhancing the weak backscatters along with decreasing the dynamic range in the US images [107]. The homomorphic filtering results in higher resolution of denoised images in comparison to linear filters [108]. Zong *et al.* [32, 33] proposed a homomorphic, soft and hard threshold based wavelet shrinkage technique for noise reduction and feature enhancement of echocardiographic images acquired in short axis [32, 33]. The performance of the technique was compared with median filter, homomorphic Wiener filter, wavelet shrinkage filter and discrete wavelet transform (DWT) based filter [32, 33].

The multiplicative noise was treated as additive white noise and various wavelet thresholding techniques be applied for the logarithmically transformed echocardiographic image [33]. The Bayesian error estimation was combined with wavelet thresholding for noise reduction. Achim *et al.* [34] integrated the Bayesian estimation, and wavelet decomposition as a homomorphic filter for speckle noise reduction in the US images of kidney and urinary bladder. The noise reduction was achieved using three major steps. The input image was subjected to logarithmic transformation and then decomposed at various scales using 2D wavelet transform. The image and noise at various scales were respectively modelled using the symmetric alpha-stable and Gaussian processes. In the third step, Bayesian processors based on symmetric alpha-stable prior were constructed at each scale for speckle noise suppression and optimal feature extraction [34]. The performances of the median filter, homomorphic Wiener filter, soft thresholding, hard thresholding and minimization of Bayesian error based denoising were compared in terms of mean square error (MSE), signal to MSE (SMSE) and beta metric (β) [34].

Badalyan and Bazulin [109] had demonstrated the importance of the homomorphic filter in improving the resolution and overall quality of non-destructive test (NDT) US images of weld joints [109]. Gupta *et al.* [110] employed soft thresholding of wavelets coefficients for noise reduction in the US image of kidney. The shrinkage method based on the Gaussian distribution model was applied to the sub-band wavelet coefficients. This technique was proposed as a variant of the BayesShrink based shrinkage method. Gupta *et al.* [110] compared the performance of their Bayesian based denoising technique with median filter and homomorphic filter in terms of SMSE, correlation coefficient (ρ) and beta metric (β). Zhang, Li, and You [111] advocated a matched filter based on double-sided thresholding for the diagnoisis of proliferative diabetic in the retina of eyes. Multi-correlation based filtering was advocated by Zhang *et al.* [112] for diagnosis of red lesions in the retina. Michailovich and Tannenbaum [113] proposed a modified homomorphic technique for speckle noise reduction in the US images of human kidney, carotid artery and urinary bladder. The images were pre-processed before projecting them into the logarithmic space and subjecting to wavelet thresholding. The correlation between the image samples was reduced by subjecting the image to spectral equalization. The spectral equalized image was subjected to outliner-shrinkage process for suppression of spiky components of the additive noise.

The performance of three filters in homomorphic domain namely, the total variation (TV) filter, the AD filter and wavelet filter were analysed by computing normalized mean square error (NMSE), speckle-SNR, and β in [113]. Several multiscale shrinkage functions were proposed by Rabbani *et al.* [105] based on local mixture of priors for modelling of the logarithmically

transformed US images of liver and carotid artery in the complex wavelet domain. Sudha *et al.* [114] proposed a weighted variance and multiscale product threshold (MPT) estimation for speckle noise reduction for the US images of obstetric sonography. The performance of filters such as Lee, Kaun *et al.*, Forst *et al.*, VisuShrink, and BayesShrink and the proposed method were analysed in terms of PSNR and MSE [114].

The combination of DWT and adaptive filter was proposed for speckle noise reduction in vitro B-scan image of pig heart [115]. The despeckling was performed by separating the input image into two parts employing an adaptive filter followed by transformation into wavelet domain and soft thresholding of the coefficients [115]. The Generalized likelihood method (GLM) using the wavelets was proposed for noise reduction in the US and the MRI images. The correlation among the features was employed for preliminary coefficient classification followed by thresholding [116]. The wavelet based technique was combined with anisotropic diffusion filter known as the nonlinear multiscale wavelet diffusion (NMWD), for speckle noise suppression as well as edge enhancement for the echocardiographic images in A4C and the US image of liver [36]. A directive filtering based on the modified Gabor functions employing 2D directive filter bank was proposed by Dantas and Costa [117] for speckle noise reduction in B-Mode images of breast. The performances of wavelet pyramid and Laplacian pyramid were compared in terms of contrast enhancement and speckle noise suppression in the US images [118]. The performance of wavelet pyramid was superior for speckle noise suppression whereas the Laplacian pyramid stood out for the X-ray and mammographic images [118].

1.10.4 Total variation and bilateral filter

A maximum a posterior (MAP) estimator was employed for obtaining functional minimiser corresponding to the denoised image to be recovered [119]. This variational approach was used for reduction of multiplicative noise in the SAR images [119]. Gilboa *et al.* [120] proposed an adaptive fidelity based total variation (AFTV) filter resulting in better performance in comparison to anisotropic diffusion and total variation filter. A multi-grid nonlinear method based on TV regulation was employed for speckle noise suppression along with structure preservation in the echocardiographic images by Sheng *et al.* [121]. Tomasi and Manduchi [122] proposed a non-iterative method for smoothing of the noisy images with the edges preserved by combining the nearby image values. Tang *et al.* [123] proposed a speckle reducing bilateral filter that could work well in both high and low intensity regions for the US images of cattle follicle. An improved bilateral filter (IBF) was advocated by Zhang *et al.* [124] by reducing the two parameters to one and increasing the contribution of adjacent pixels which were employed to approximate the

current pixel. The combination of bilateral filter and total variations filter may be analysed for the B-Mode TTE images acquired in the multiple views and modalities. The regularization term of the TV filter may be replaced with the bilateral term to improve filtering characteristics of the filters.

1.10.5 Nonlocal mean (NLM) filters

The nonlocal filters do not make any assumption on the location of pixels in the image during denoising a particular pixel. The weight assigned to a pixel in the restoration process does not depend on the distance between the current pixel and others. The nonlocal mean (NLM) algorithm, estimates each pixel value as a weighted average of other similar noisy pixels. However, the core problem with NLM is that it cannot exploit the smoothness of the edge contour that can separate the white from black regions [125]. Buades *et al.* [126] employed image patches to extract relevant features for additive noise reduction.

The Bayesian framework was proposed by Coupe *et al.* [125] to derive a nonlocal mean filter for speckle noise reduction in the US images. An extension of the nonlocal mean filter was proposed by Deledalle *et al.* [127]. The noise reduction process was shown to be the “weighted maximum likelihood estimation” problem. The weights were derived using a data driven process. This probabilistic patch based filter was advocated for speckle noise reduction in the SAR images. Guo *et al.* [128] combined the maximum likelihood estimation and nonlocal filter in their proposed modified nonlocal (MNL) filter for speckle noise reduction in the echocardiographic images. As TTE images suffer from speckle noise, the NLM and PPB filters might find applications. Analysis of nonlocal filters might be taken up for the TTE images.

1.10.6 Comparative analysis of despeckling filters

Sheng and Xia [129] had compared the performances of seven filters using five performance parameters namely edge enhancing index (EEI), speckle suppression index (SSI), image detail preserving coefficient (IDPC), feature preserving index (FPI) and speckle image analysis. The applications of filters such as the mean, median, Lee-sigma, local region filter, Lee, Frost, and MAP filter have been analysed in [129]. A comparative analysis of ten despeckling filters for the US images of carotid artery was carried out by Loizou *et al.* [27, 130, 131]. The performance analysis of the filters was being reported in terms of image quality metrics (IQM), texture feature analysis and visual quality assessment. The filters analysed by Loizou *et al.* [27, 130, 131] were based on the wavelet denoising, median filtering, homomorphic filtering, anisotropic diffusion, local statistics, non-coherence diffusion, homogeneity of pixels and geometric filtering.

It was being pointed by Loizou *et al.* [27, 130, 131] that the filters employed by them for carotid artery images may find applications in despeckling of the TTE images.

Mateo *et al.* [26] analysed the performances of median, adaptive median, Fourier ideal, Fourier Butterworth, wavelet and homomorphic filters for the US images of kidney in terms of MSE, SNR, PSNR and β. The authors have reflected in their paper that the research should move in the direction of fine tuning the existing filters, look for their variants which can result in better noise suppression and edge preservation. They have also pointed out that researchers should look in for the combination of different filters, either in series or parallel combination, which may result in better edge preserved denoised images [26]. The performance of Lee, Kaun, Frost, homomorphic anisotropic diffusion, homomorphic Wiener, SRAD and hybrid filter were comparatively analysed for the speckle noise reduction in holographic images by Srivastava *et al.* [132] in terms of nine parameters namely MSE, normalized MSE (NMSE), PSNR, speckle index (SI), SNR, effective number of looks (ENL), ρ, structural similarity index (SSIM) and execution time [132]. Tay *et al.* [133] compared the despeckling performance of filters such as the Lee filter, Wiener, SRAD, AWMF, wavelet and squeeze box filter (SBF) for B-Mode cardiac US images in terms of despeckling assessment index and SSIM.

The importance of despeckling filters was demonstrated using balloon force active contour (BFAC) based image segmentation. The US images were denoised using the filters such as the Lee filter, adaptive Wiener filter, SRAD filter and others. The pre-processed images were subjected to the BFAC based segmentation. The delineation results showed superior performance using denoised images in comparison to segmentation of unprocessed B-Mode US images [133]. Applications of fifteen despeckling filters based on wavelet denoising, local statistics and anisotropic diffusion were analysed for echocardiographic images in terms of computational complexity, preservation of edges, overall image quality and improvement in contrast by Finn *et al.* [22]. The IQM consisted of estimation of parameters such as FoM, SSIM and edge region MSE, contrast-to-noise ratio (CNR) and SNR [22]. The pre/post-processing techniques employed for reduction of various artifacts and enhancement techniques were comprehensively reviewed by Ortiz *et al.* [14].

The applications of three despeckling techniques namely adaptive, AD and wavelets filters were analyzed in [14]. Elamvazuthi *et al.* [134] compared the performance of anisotropic diffusion, median, Wiener, average, wavelet and hybrid filters for the US images of bone fracture in terms of PSNR. A hybrid filter based on the combination of wavelet, anisotropic diffusion and Wiener, was also analyzed for the noise reduction in the US images of bone. The performance of hybrid filter was superior compared to other filters in terms of visual quality.

The comparative analysis of despeckling filters for the US images of breast was being reported by Zhang *et al.* [135]. The denoising characteristics of eleven filters such as the NLM filter, PPB filter, GLM filter, SRAD filter, Lee, Frost *et al.* filter, DPAD filter and four other filters were analysed in terms of PSNR, MSE, SSIM and FoM along with the visual quality. Hence, comparative analysis of despeckling filters for the B-Mode, CWD, and colour Doppler images can be taken up.

1.11 Segmentation

The computer-aided image segmentation plays a crucial role in accurate delineation and computing the size of various parts of heart during the diagnosis. It also plays a vital role in locating the pathology, and assists in the image-guided interventions [19, 37, 38, 136-140]. The segmentation approaches based on thresholding, edge, region, hybrid, texture, active contour, level set, clustering, active shape models, active appearance models and machine learning techniques have been proposed by various authors for automated, or semi-automated delineation of images [58, 93, 141]. In spite of advancement in image processing and analysis techniques even today assessment of severity of valvular abnormalities is carried out by manually tracing of images acquired in a particular view and region of interest.

An overview of segmentation techniques employed for the B-Mode TTE images is shown in Table 1.4 highlighting the pre-processing filter employed, and window in which the images were acquired. The Table 1.4 reflects that methods based on region, edge, watershed, active contour, snakes, level set, fuzzy, clustering, and neural networks are commonly used in segmentation of images acquired in a particular view only. This shows that there is a scope for the analysis of segmentation techniques for images acquired in multiple views using various echocardiographic imaging modalities. A brief review of segmentation techniques proposed for the US images are presented in the next sub-sections.

1.11.1 Snake

The active contour based segmentation techniques are commonly employed for finding the boundaries of the LA and LV. The deformable models based on the energy optimization are referred to as balloons, snakes and active contour models. The snake algorithm is also extensively employed in segmentation of anatomical structures such as lungs, kidney, cerebrum, brain, liver and spine, acquired using various imaging modalities like the US, MRI, CT and X-ray.

Table 1.4 Overview of segmentation techniques used for B-Mode TTE images

Year	Ref.	Delineation Technique	Purpose	Pre-processing	Type of image
1987	[203]	Haralick's method of edge detection	Tracing of endocardial and epicardial borders	Gaussian filter	Phantom image
1988	[142]	Edge detection by thresholding	Ventricular contour detection	Mexican Hat filter	PLAX, A4C
1996	[136]	Canny edge detection and active contour	Tracing of endocardial and epicardial borders	Gaussian filter	PSAX
1998	[204]	Active contours guided optical flow estimates	Tracking the boundaries of MV leaflets, AV and LV	Kalman filter	PLAX, A4C
2000	[205]	Multiscale Fuzzy-clustering	Assessment of LV function	AD filter	3D Echo
2002	[206]	K-means clustering algorithm and self-organizing maps	Measurement of fetal heart structures	Median filter	A4C
2003	[43]	Multiscale level set framework	Segmentation of endocardial boundaries	Gaussian filter	A2C
2004	[150]	Multiscale directional edge map and snakes	Boundary of the left ventricle	Adaptive smoothing	A4C
2004	[207]	Edge detection using Sobel compass gradient mask	Generate contour line of endocardium border	Median filtering	PSAX
2005	[45]	Prior knowledge based Geodesic active contour	Segmentation of cardiac valve structure	--	A4C
2006	[208]	Fuzzy reasoning and Canny edge detection	Determine the boundaries and edginess of each pixel	SRAD	A4C
2005	[209]	Shape based snake model combined with GHT	Segmentation of left ventricle	Gaussian filter	A4C
2006	[210]	Deformable contour along with Otsu thresholding	Segmentation: endocardial surface	4 different filters	PSAX, PLAX
2006	[172]	watershed and morphological operation along with snake	Boundary detection of the left ventricle	Adaptive Smoothing	A4C
2007	[211]	Otsu thresholding, morphological operations	Detection of myocardium infarction	Median filtering	A2C
2007	[212]	Deformable contour algorithm	Segmentation of heart muscle	Adaptive filtering	A2C
2008	[174]	Localizing region based active contour	Region based delineation achieved in a local way	Particle filtering	X-ray of LV
2008	[47]	Active contour embedded with temporal information	Dropout and speckle noise reduction and delineation	Gaussian filter	PSAX
2008	[48]	Artificial neural network	Delineation of boundaries of left ventricle	Histogram equalization	A4C
2008	[177]	Watershed/Region filter with temporal information	Segmentation of left ventricle	High boost filter	A2C
2009	[12]	Active Contour , Hough transformation	Segmentation of left ventricle	Gaussian and AD filter	PSAX
2009	[213]	Neural Network	Segmentation of heart cavities	Median, average filter	A4C
2009	[214]	Center-based approach, Fuzzy-based technique	LV boundary detection	DWT soft thresholding	PSAX
2010	[156]	Level set with preprocessing	Automatic segmentation of four heart cavity	Phase symmetry Morphological	A4C
2011	[54]	Level set without edges	Heart shape segmentation	AD filter, edge enhancement	A4C
2011	[50]	Phase symmetry approach: Comparative analysis	Extract simultaneously all heart cavities	Histogram equalization, AMF	A4C
2011	[52]	Local phase based level set	Capture LV boundaries	Cauchy kernels	A4C
2011	[51]	Weighted radial edge filtering with adaptive recovery	Automatic segmentation of endocardial boundary	Recursive adaptive filter	PSAX
2012	[215]	Confidence maps	US shadow detection	Gaussian kernel	A4C
2012	[182]	Geometrically constrained level-set	Segment whole myocardium	--	A2C, PSAX

The energy function consists of an external and an internal force component. The sum of these two forces known as the total force function is iteratively optimized during delineation

process. The external energy is computed using image gradient. This energy is said to be sensitive towards image degradations such as the speckle noise, dropouts and other artifacts.

The speckle noise and dropout disrupt wall boundaries and lead to errors in detection. Various difficulties are encountered while using active contours for images with boundary concavities like those in TTE images. Initialization is important in active contour based segmentation but poor initialization results in premature convergence at some local energy minimum point and fails to capture the features of interest in the US images. The major drawback of simple initialization is the large number of iterations needed for convergence due to poor shape approximation. A poorly placed shape may never give in a right desired delineated boundary. It is therefore necessary to make active contour based techniques more versatile and robust to speckle noise, intensity in-homogeneity, low-contrast and other inherent artifacts present in the TTE images. Segmentation techniques were proposed for addressing the issue of intensity in-homogeneity in the MRI images during segmentation. These techniques may find applications for segmentation of the TTE image in multiple views. As observed in Table 1.4 the median and Gaussian filters are employed during boundary tracing process. Attempts can be made to replace the Gaussian and median filters with the despeckling filters as the performance of SRAD, hybrid median, adaptive Wiener and others are superior in comparison to the basic filters.

Lamberti *et al.* [142] employed a Mexican hat filter for image smoothing prior to ventricular contour detection. The method consisted of image windowing, pre-smoothing, contour detection, and finally display of the delineated contour being superimposed on the original image. Xu and Prince [143] proposed the gradient vector flow (GVF) based active contour segmentation technique. It was shown that the GVF results in a larger capture range and could move the snakes into the boundary concavities. Some of the drawbacks of GVF field were high computational cost, parameter sensitivity, and noise sensitivity along with unclear relationship between the capture range and other parameters. Ghiachetti [144] used several levels of low-pass filters for reduction of noise prior to model based constrained contour evolution. The snake algorithm and optical flow estimation along with filtering techniques were used for contour delineation of the echocardiographic images. Chen *et al.* [145] combined the early vision modelling with snake model for segmentation of the US images while suppressing the speckle noise. The early vision model was employed for estimating the distance map. This estimated map was used as an image force, to move the discrete snake elements for better noise suppression and accurate convergence of the delineated contour. Hamarneh and Gustavsson [146] embedded the prior knowledge of the LV shape into the active contour method for

segmenting the echocardiographic images. Jacob *et al.* [147] employed a shape space based active contour technique for segmentation of the LV and tracking the myocardial boundaries of the echocardiographic images. A temporal Kalman filter was employed for extraction of the periodic motions. The Kalman filter was employed by Abolmaesumi and Sirouspour [148] during the cavity boundary delineation of the US images.

Hang *et al.* [149] embedded GVF in the geodesic active contour model for segmentation of the echocardiographic images. The images were pre-processed using a geometric filter prior to segmentation. It was considered that the deformable model with the GVF as an external force could capture both sides of the boundaries. Cheng *et al.* [150] presented a technique of adding morphological operations in the snake based segmentation for automatic LV boundary detection from a sequence of echocardiographic images. The automatic localization of ROI provided an initial contour for the snake deformation. A multi-scale directional edge map was employed for effective suppression of the speckle noise. A method for segmenting the MV leaflets in echocardiographic images was presented by S´ebastien Martin *et al*. [151]. The motion of the valve and the muscle were captured by employing two contours. The curve fitting techniques resulted in initial boundaries. The finer boundaries were obtained using snakes.

Li and Acton [152] proposed vector field convolution (VFC) based active contour to address the issues such as noise sensitivity, limited capture range, and poor convergence of the concavities. The major drawback of the VFC based segmentation was that the weak edges were snowed under the strong edges along with the noise. Stoitsis *et al.* [153] employed Hough transform for the initialization of active contours. The contour estimation was achieved by deformation of the initial curve based on the gradient vector flow field. The performance of method which combined Hough transform and active contour was improved by adopting an optimal thresholding method for the gradient field. The thresholding parameters and the size of the morphological operator were shown to have a positive impact on the segmentation results.

Fang *et al.* [47] incorporated temporal information into active contours to address issues of dropout and speckle noise encountered during segmentation in the TTE images. The ventricular boundaries of echocardiographic images were assumed to be made up of both strong and weak segments. Li and Acton [152] proposed the Poisson inverse gradient (PIG) based initialization approach for segmentation using the parametric active models. The energy was estimated using the external force field assisted in the computation of the initial contour. The PIG based segmentation fails when the maximum distance between the edges is larger than the minimum distance between the edges and noise/clutter. Marsousi *et al.* [155] combined external forces with adaptive node insertion and multi-resolution strategy for segmentation of endocardium in

the echocardiographic images. The localized parameter estimation was included for matching of the parameters of every point with the regional information.

1.11.2 Level set

The geodesic active contours with the level-set representation have become the basis of many boundary-driven segmentation techniques being advocated in the last decade. The gradient computed using the geodesic active contour model was sensitive to noise as the differentiation of gray levels tends to magnify noise [20, 156-158]. Many researchers have proposed various techniques and modifications to existing techniques for enhancement in the accuracy of segmentation methods and making them robust to noise, discontinuity and in-homogeneity. The idea of level set evolution (LSE) was proposed by Osher *et al.* [92, 159]. The velocity term of the LSE was based on the edges. It consisted of two components namely the regularity component and the edge detection component. The regularity component was employed for determining the shape of the contour whereas the edge detection component attracted the contour towards the edges. The delineation process was performed considering the zero level set of a scalar function. The gradient was used to stop the evolution process during the delineation using level set frame work.

The region based models were advocated by Mumford *et al.* [160] which relied on the statistical information of the image intensity to minimize the energy function. The velocity function was restricted to be piecewise constant function by Chan and Vese [64, 161, 162] and this was a particular case of minimal partition problem. Chan and Vese [64] advocated an active contour based segmentation model based on the concepts of level set method and Mumford-Shah [160] delineation technique. The curve evolution in the CV model was based on the concept of energy minimization in place of edge-function being employed to stop the evolving curve. The geometric models were initially proposed by Caselles *et al.* [163] and Malladi *et al.* [164]. The level sets techniques were in line with the energy-based deformable methods. Caselles *et al.* [163] introduced stopping function in level set allowing the contour to stop on edges. The geodesic active contour is an extension of geometric active contours. It allows tracing of a stable boundary when the image gradients suffer from large variations. The major advantage of level set based delineation was the ability to handle changes in shape and topology during evolution process [165, 166].

Quite often the boundaries of echocardiographic images are discontinuous at more than one place, and with missing borders due to signal dropouts and smeared boundaries. In these situations it is challenging to identify the true boundaries accurately. The contour fitting process

is equivalent to determining the geodesics of the minimal distance curves using the minimization of intrinsic energy. The conventional level set segmentation technique with the arc length minimiser has often failed to reach the desired segmentation because it was difficult to control the regularization term in the presence of speckle noise and low contrast of echocardiographic images.

Kotropoulos and Pitas [167] and Kotropoulos *et al.* [168] employed parallel segmentation and L_2 mean based filtering approach for delineation of the US B-Mode images. Klinger *et al.* [169] used mathematical morphology based for segmentation of B-Mode echocardiographic images. The advantages of computer aided algorithms for segmentation of various anatomical structures were reviewed by Pham *et al.* [170] along with their drawbacks. The impact of intensity in-homogeneity and noise during delineation of medical images such as the MRI were also highlighted. The segmentation techniques like thresholding based, region growing, clustering and artificial neural networks were analyzed for MRI brain images, MRI image of the LV and digital mammographic images. Lin *et al.* [43] proposed a learned shape template based segmentation technique for boundary tracing of A4C TTE images. The boundaries extracted at the coarse level were used as initial contour for boundary delineation at finer scales. The method was advocated assuming closed contour for all A4C images but this may not be the case always; discontinuities may be present. The noise present in the TTE images was smoothed by increasing the Gaussian pyramid level. Shao *et al.* [171] have compared various methods which make use of filtered US images for delineation of prostate boundaries. The authors have reported that filtered images result in better and faster delineation in comparison to the unprocessed images. They have also reviewed the performances of edge based, texture based and model based segmentation techniques for ultrasonographic images of prostate. The edge based techniques were employed for delineation of pre-processed images. The noise was suppressed using maximum filter and other smoothing filters.

Shang *et al.* [45] embedded region and shape prior of the cardiac valves into the geodesic active contour for segmentation of the MV leaflets. The segmentation technique was implemented using the level set framework. The region prior constrained the evolution of zero level set and the shape prior pulled the curve to the ideal contour. Cheng *et al.* [172] combined directional edge map, watershed transform, morphological operations and snake deformation to delineate the boundaries in A4C. The multi-scale directional edge map was employed for despeckling of echocardiographic images. Hough transform was employed on Gaussian filtered B-mode US images of carotid artery for arterial lumen segmentation.

The global threshold based on the histogram was used during the edge detection and morphological operations for merging smaller discontinuities. The images were subjected to Gaussian filter for removing the noise present in the image in [173]. Lankton and Tannenbaum [174] proposed the local region based active contour to meet the segmentation challenges posed by heterogeneity of objects and intensity in-homogeneity in the medical US images. The background and foreground were represented in terms of smaller local regions instead of global considerations. The segmentation technique was optimized by considering each individual point separately. This was followed by forward or backward movement based on minimum or maximum energy being computed at every point. But, the local region based delineation was sensitive to initialization. The number of iterations required was high compared to global region based techniques. Zhang *et al.* [175] proposed a mechanism for simultaneous bias correction and segmentation in the presence of intensity in-homogeneity. The method was based on the concept that intensities in-homogeneity in the local regions were separable which might have been inseparable considering the entire image. The K-means clustering and level set segmentation in variational framework were employed in the algorithm for segmentation of X-ray, CT and MRI images with intensity in-homogeneity. Li *et al.* [154] proposed minimization of energy based on region scalable fitting (RSF) to deal with the problems encountered during segmentation due to the presence of intensity in-homogeneity. The data fitting energy was computed from the intensity information derived from two sides of the local regions by employing contours and two fitting functions. The computed energy was embedded into the variational level set framework for deriving energy minimization necessary in curve evolution.

Sheng *et al.* [176] proposed a shape based snake model for segmentation of MV leaflet and the LV using images acquired in A4C. The generalized Hough transformation (GHT) and template matching techniques were embedded into the shape based segmentation model for delineation. The GHT was employed for computing the initial contour. The elastic deformation energy was used for deforming the contour based on the local minima estimation. The image processing techniques such as thresholding, filtering, watershed transforms and radial search were combined with temporal information for tracing the boundaries of the LV in echocardiographic images by Lacerda *et al.* [177]. Wu *et al.* [48] proposed an artificial neural network (ANN) based boundary detection technique for the echocardiographic image in the presence of speckle noise.

The authors of [48] had also reviewed the performances of five techniques highlighting the pre-and post processing techniques employed by various authors. To reduce the processing time, the region of interest was manual selected and results obtained on application ANN were

compared with manually traced contours. Fernandez- Caballero and Vega-Riesco [12] analyzed the performances of segmentation methods based on Hough transform and active contour for automatic LV boundary tracing. The analysis was carried out using the TTE images acquired in the PLAX and PSAX. These images were pre-processed followed by gradient detection and gradient smoothing.

Zheng *et al.* [178] proposed a delineation technique which was said to be robust to initialization with simultaneous segmentation and bias correction. The intensity distribution was modelled as Gaussian distribution by varying the mean and variance. The level set methods result in irregularities during curve evolution process which lead to numerical errors and destroy the stability of evolution. This issue has often been overcome using the concept of re-initialization. But the re-initialization procedure gives rise to new questions such as when to apply, how to apply and perform. To address these issues Li *et al.* [179] proposed the concept of distance regularized level set evolution (DRLSE). The regularity of the level set function was intrinsically maintained during the level set evolution. The distance regularization effect eliminated the need for re-initialization avoiding induced numerical errors.

The TTE images were pre-treated and then subjected to phase symmetry algorithm [50]. This was followed by application of the geometric deformable model for contouring the chambers of heart. The pre-processing step and the level set based segmentation were simultaneously used across four cardiac chambers. The performances of automated technique were compared with manually segmented image. The segmented image was post processed to remove the left over smaller regions in the delineated image. Skalski and Turcza [54] proposed an algorithm based on level set without edges for estimating the cardiac chamber shape in echocardiographic images. The ROI was computed automatically by employing Hough transform. The TTE images were pre-processed using the AD filter in order to improve the image quality prior to computing the ROI. Bansod *et al.* [51] proposed a weighted radial edge filtering based semiautomatic segmentation algorithm for delineation of endocardial contours in the PSAX view. The weighted radial edge filtering algorithm was employed in conjunction of adaptive dropout recovery for a semi-automatic tracing of the boundaries of heart chambers in the 2D TTE. Saini *et al.* [180] detected the boundaries of the LV and the LA using the Netwon-Raphson method. The speed of contour convergence was enhanced and the number of iterations reduced by incorporating Newton- Raphson method. Silverstre Silva *et al.* [181] proposed phase symmetry based automatic segmentation technique for paediatric echocardiographic images. A logarithmic based stopping function was employed in the level set evolution process.

Further, the authors of [181] compared the performances of phase symmetry technique with the methods such as the modified level set, and watershed technique, along with manual contours traced by two practicing cardiologist. Dietenbeck *et al.* [182] proposed a technique for tracing the inner and outer boundaries of myocardium in four views. The level set model was constrained by a shape formulation that could allow delineation of both contours. Belaid *et al.* [52] proposed a level set propagation based technique to capture the LV boundaries. A modified speed term based on local phase and local orientation was derived from the monogenic signal to make the algorithm robust to attenuation artifacts. The global minimization active contours (GMAC) methods were proposed by Bresson *et al.* [183] to eliminate re-initialization by combining the TV model with the CV model. The unification of the denoising and segmentation procedures resulted in the global minimization solution for the active contours subject to intensity homogeneity constraint. The GMAC may be applied to some variational LSF with specific forms like reaction diffusion (RD) [184]. A diffusion term is embedded into the conventional LSE Equation in the reaction diffusion based segmentation by Zhang *et al.* [184]. A solution of the RD Equation is piecewise constant with different phase fields and also happens to the solution of the LSE Equation.

1.11.3 Comparative analysis of segmentation techniques

Hammoude [37] reviewed techniques which were employed at various stages during the segmentation of endocardium boundaries. The paper reviewed the methods employed in data acquisition, pre-processing, segmentation, border identification, post processing, and evaluation methods. Noble *et al.* [185] compared segmentation techniques used in the medical US images such as echocardiography, intravascular US, transrectal US, US images acquired in gynaecology and obstetrics, and breast US. Further, highlighting the important role played by segmentation techniques in clinical decision making, Noble [5] had reviewed various tissue characterization and segmentation techniques available in the literature for the US images. Shrimali *et al.* [25] compared six segmentation techniques commonly used for delineation of the US images. The advantages and limitations of thresholding, edge based, region growing, region split and merge, hybrid, texture based and deformable model were highlighted by Shrimali *et al.* [25]. An overview of trends in the US image segmentation based on neural networks, statistical shape model, discrete region competition, level set, hybrid watershed, texture and shape prior, their advantages and limitations were also reported. Noble *et al.* [4] reviewed the state of the art techniques available for US image analysis, bringing out the significance of image despeckling, enhancement, segmentation and image registration in image guided interventions.

A comprehensive review of LV segmentation techniques for TTE images was carried out by Wu and Nicolosi [138]. The pre and post processing techniques employed by various were also documented. But the paper do not speak of experimental results obtained using various techniques for images acquired in various views. Das and Banerjee [186] had reviewed the applications of parametric contour model in delineation of the MV leaflets and the LV along with wide range of applications.

1.12 CWD image denoising and segmentation

The current US machines have inbuilt software which can provide accurate peak velocity, velocity time integral and gradients from a manually traced velocity envelope. The peak velocity estimated from the manually traced envelope can result in an error of approximately larger than 25%, even by the most experienced clinicians [187]. The Doppler spectra exhibit large variations in the envelope shape and image appearance under various disease conditions and state of the cardiac valves. The automation of CW Doppler images may result in faster processing, uniformity in the results with increased objectivity, and more accurate estimation of valvular abnormalities.

Mo *et al.* [31] studied the statistical properties of the CWD signals by making of the data acquired across the carotid artery. Based on their study, they had concluded that the granular structures observed in CWD spectrograms were similar to those of the US B-mode images. Hall *et al.* [188] proposed a model based image processing scheme for automatic estimation of the E-wave from velocity profiles acquired across the mitral valve. Gong *et al.* [189] proposed a multi-stage automated system for processing of the CWD spectrograms acquired at the AV and the MV. The automatic scheme consisted of pixel grouping, thresholding and the median filter, which generated the velocity profiles and reduced the background noise from spectrograms of aortic outflow and mitral inflow spectrograms. Thresholding was applied on the denoised images instead of direct application on the CWD images. Tschirren *et al.* [40] proposed an image processing based automated scheme for tracing the boundaries of the spectra and to determine the maximum blood velocity. A Gaussian low pass filter was used for suppression of noise and the horizontal details were detected by computing maximum gray level projection, taking into account all pixels with certain threshold value. A nonlinear Laplacian edge detector was used for detecting the edges; this edge detector was not very sensitive to the noise and was superior compared to the Sobel filter. Jansson *et al.* [190] highlighted the importance of speckle noise reduction in automated spectra boundary tracing. A model based on autocorrelation function was proposed for predicting the frequency separation among the uncorrelated speckle.

Krger and Evans [191] advocated a prototype for tracking the changes in the blood velocity. The returning Doppler profile signals were evaluated in terms of the SNR and total power. The need for proper steering of the US beam was studied to improve the SNR. The automatic tracking of Doppler signals resulted in doubling of the effective beam width of the transducer. Shechner *et al.* [192] proposed a scheme of integrating the Sobel operator, Laplacian edge detector, low pass filter, edge linking and curve fitting procedures for automatic tracing of the MV spectrograms. Greenspan *et al.* [193] employed a Gaussian kernel for noise reduction and the contrast stretching procedure for enhancing the visual outlook of CWD spectrogram acquired across the MV. The significance of reducing noise and edge detection in automatic delineation of CWD spectra was also highlighted [193].

Doherty *et al.* [194] proposed a parametric method for computing envelope in Doppler umbilical US images with varying levels of SNR. The Doppler signal was assumed to be consisting of multidimensional time series components infected with noise for the estimation of velocity spectrum curve. The waveform fitting was performed through optimization of cross correlation of Doppler signal and a periodic reference function. Magagnin *et al.* [195] proposed a image processing based semi-automatic scheme for delineation of the pulsed Doppler spectrum acquired from the patients suffering of rheumatoid arthritis. A horizontal and a vertical Sobel filter were employed for the detection of the baseline and scale factor from the spectrograms, respectively. The CWD spectrograms were divided into overlapping regions followed by computation of the histograms and threshold automatically for each region. The outliers present in the processed image were removed using a median filter. The deformable structures in Doppler images were detected using a “probabilistic, hierarchical, and discriminant” i.e. the “PHD framework” by Zhou *et al.* [196]. Wang *et al.* [197] proposed a shape driven model for automatic outer boundaries tracing for pulsed Doppler images. A discrete Kalman filter was introduced for recursively estimating the velocity envelopes. The statistical shape model and Kalman filter were used for adaptive weight estimation and envelope tracing. Park *et al.* [198] employed a series of detector for locating objects and shape information to segment the MV inflow patterns [198]. Kiruthika *et al.* [199] proposed a method to trace the boundaries of the CWD images acquired from patients diagnosed with AR. The method consisted of median filtering, contrast enhancement, Gaussian filtering, morphological operations, intensity adjustment and Canny edge detection. An adaptive pulse coupled neural network (PCNN) with adaptive thresholding was employed by Li *et al.* [200] for removing speckle noise from Doppler blood flow spectrograms. They had concluded that removal of noise is essential and the preliminary step necessary in spectrogram automation [200].

Combinations of two median filters were employed for reduction of noise from the spectrum image by Kalinic *et al.* [201]. Syeda-Mahmood *et al.* [202] proposed a clinical decision support system for identification of spectrum shape patterns for various valvular diseases using content based image retrieval. An overview of automatic or semi-automatic segmentation techniques employed for extraction of cardiac structure boundaries are tabulated in Table 1.4 highlighting the views in which the images were acquired, the filter employed, the concept and method of delineation. The Table 1.4 highlights that the research is concentrated on segmentation of images acquired in only one view either in PLAX, PSAX, or A4C. However, as pointed in the earlier section, the clinicians views the cardiac structure in more than one view, employing one or more acoustic windows in B-mode, M-mode, CWD, PWD, and color Doppler imaging modalities during the study and diagnosis of cardiac and valvular abnormalities.

1.13 Clinical literature review

Tribouilloy *et al.* [216] proposed a method for assessment of AR by measuring the width of vena contracta (VCW) and effective regurgitant orifice area (EROA). Shipton *et al.* [217] had concluded that the AR results from the disease affecting the aortic root or aortic leaflets, preventing their normal closure. Doppler echocardiography would provide information about the AV morphology and aortic root size, and a semi-quantitative estimate of the severity of AR [217]. Willett *et al.* [218] proposed assessment of AR by color Doppler imaging of the VC. The visual grading of valvular regurgitation by Doppler color flow mapping technique was inaccurate because various hydrodynamic variables and instrument settings affect color flow jet display. The VCW and area correlate well with regurgitant fraction (RF) and regurgitant volume [218]. Vinereanu, Ionescu and Fraser [219] proposed a scheme for assessment of AR using the images acquired in PLAX. It was concluded that single plane area–length method would tend to overestimate the LV volumes and ejection fraction (EF) in asymptomatic patients with severe AR. Heidenreich *et al.* [220] had concluded that a systolic murmur could be a clue to the presence of AR and should be used in conjunction diastolic murmur in the diagnosis of valvular disorders.

Sarano and Tajik [221] have described AR as a unique valvular disease resulting in both left ventricular volume overload and pressure overload. A simple and reliable measurement would be the VC, the width of the regurgitant flow at the orifice, and the size of the orifice [221]. Surenderanath *et al.* [222] reported that measuring the severity of AR was necessary due to the typical progression of aortic valve disease and intervention before deterioration of the LV function.

Further, they pointed to the sub-optimal acoustic windows present in the echocardiography imaging along with the need for Doppler alignment, and geometric assumptions [222]. Maganti *et al.* [223] had concluded that a single method would not be providing all the data necessary for accurate quantitative assessment of the valvular regurgitation, and the complex interaction of among the anatomic and hemodynamic variables. The combination of preload and after-load excess may lead to the progressive LV dilatation. The echocardiography images were used as a diagnostic tool for assessing the LV dimensions, volumes, and ejection fraction. It was also employed in the morphological assessment of the aortic valve, annulus, and root. The color flow and spectral Doppler echocardiography were then used to further the quantification of valvular regurgitation [223].

The morphology of the AV was analyzed in the PSAX view in [224]. The diameter of the LVOT, aortic annulus, the sinus and the STJ were determined in the PLAX view. The CWD recordings through the AV were obtained for estimating the peak and mean trans-aortic pressure gradients. Finally, the color Doppler echocardiography was employed for locating the presence of regurgitant valve [224]. This integrated study was employed for estimation of the valvular regurgitation being observed after transcatheter AV implantation (TVAI). Recke [225] from their studies had concluded in clinical practice the ECG and the echocardiographic imaging should complement each other to overcome inherent limitations pertaining to sensitivity of both methods. Based on their research Simpson and Miller [226] had recommended that 3D TTE should be regarded as a complementary tool to 2D TTE but not as a substitution.

The literature review presented in the earlier paragraphs suggest the following: The recommendations by European Society of Echocardiography, American Society of Echocardiography, and British Society of Echocardiography suggest that the integrated processing of TTE images is necessary as images acquired in multiple views using different windows and US based imaging modalities are employed in the study of heart anatomy and various abnormalities of the cardiac structure. But, most of the research is concentrated on the images acquired in a particular view and modality. The B-Mode images assist in the study of anatomy of the heart and analyze of the consequences of the valvular abnormalities. The images in PLAX provide information of the AV, MV, RV and LVOT whereas the PSAX view show the all the three leaflets of AV. The images in A4C provide information on the structure of ventricles, and auricles along with the dynamic motion of the MV during diastole and systole. The AV can be visually seen in A5C which is not possible using the A4C and A2C views. The CWD spectrums are employed for computing the flow velocities whereas the color Doppler is useful in estimation of the regurgitant jet area and the VCW.

This again reflects that the information available in a particular view cannot represent all necessary information and anatomy of the cardiac structure. Hence, it would be mandatory for the clinicians to visually observe the cardiac structure in multiple views employing various echocardiographic imaging modalities, looking for the prevalence or absence of valvular and cardiac chamber abnormalities accurately. Hence, this research was taken up to study computer aided processing for the TTE images acquired in multiple views (PLAX, PSAX, A4C, A5C and A2C) and multiple echocardiographic imaging modalities (B-Mode, M-Mode, CWD, PWD, and color Doppler).

The literature review of speckle noise reduction techniques point out the following: 1) There are many multiscale based techniques which are not extensively used for noise reduction with edge preservation in the TTE images of the AV and cardiac chambers. The wavelet based GLM filter and various shrinkage techniques can be analysed for noise reduction in the TTE images [2, 94, 99, 100, 116, 227]. 2) The posterior sampling based Bayesian estimation (PSBE) was employed for speckle noise reduction in OCT images [228]. This may find an application for noise suppression and enhancement in the TTE images. 3) The fuzzy triangulation filters are extensively used for suppression of additive noise. These filters may be analysed, with or without any modifications, for reduction of multiplicative noise in the echocardiographic images using approximated noise model [229]. 4) The duality based total variation filters have been proved to be effective in restoration of images [230]. These filters were not tested using the TTE images hence a work has been taken up to analyze performances in terms of noise suppression and edge preservation. 5) It is observed that the most recent review of filtering techniques for TTE images carried out by Finn *et al.* [22]. The filters such as the NLM, PPB, PSBE, TV, and fuzzy filters, were not included in the review of despeckling filters for the TTE images. Hence, a work has been taken up in this research to study the filtering characteristics of eight types of filters including those filters analyzed by Loizou *et al.* [27,130, 131] for the US images of carotid artery. 6) The performances of filters were analyzed using traditional image qulaity metrics. It is necessary to preserve the edges, and the images should be clinically accepted. The edge preservation in the preprocessed images are estimated in terms of beta metric, speckle suppression index, and other parameters in the current work along with clinical grading. The performances of despeckling filters are estimated in terms of 16 IQM along with clinical grading. 7) The median and Guassian filters are commonly employed for the preprocessing of the CWD images. The applications of filters advocated for the B-Mode images are not extensively explored for CWD images. Hence, work has been taken up to study applications of despeckling filters for the CWD, PWD, and color Doppler images.

8) The texture features of B-Mode images acquired in PLAX, PSAX, A4C, A5C, and A2C, CWD images, and color Doppler images, would play a vital role in computing the severity of valvular regurgitation. The 65 texture features computed by Loizou *et al.* [27,130,131] for the US images of carotid artery are estimated for TTE images in multiple views using various echocardiography based imaging modalities.

The segmentation of the TTE images is concentrated on the images acquired in only one view by most of the reseachers. But during clinical diagnosis, images acquired in multiple views, using different echocardiographic modalities, are manually segmented to compute various parameters from the traced ROI. It would be therefore necessary to study the applications of segmentation techniques for images in multiple views as each view presents a different set of challenges and hurdles during either semi-automatic or automated process of delineation. The TTE images are of low constrast and have intensity in-homogeneity. The current research studies applications of segmentation techniques in the presence of intensity in-homogeneity for low contrast TTE images in five views using two acoustic windows.

The boundaries of the CWD images are traced using the edge and region based techniques. The applications of active contour based techniques for boundary tracing of CWD spectrum is not fully explored and reported in the literature . The current research work studies the applications of watershed transform, texture filters and active contours in segmentation of CWD images. It is observed that Gaussian filters were being used for reduction of noise in the CWD images prior to the application of segmentation technique. But, despeckling filters are superior in comparison to the Guassian and median filters in terms of both noise suppression and edge preservation. Therefore, these filters may be replaced by despeckling filters, in the process of delineating the outer boundaries of CWD images, in the presence of intensity homogeneity.

The color Doppler images are help in visualizing the process of regurgitation and estimating its severity. The severity is estimated by manual tracing of the regurgitant jet area observed in the LVOT. To overcome the disadvantages of manual segmentation it is proposed to trace the regurgitant jet area in the A5C and PLAX view, employing all the segmentation techniques being analysed for the B-Mode and CWD images.

1.14 Objectives of present study

Assimilating the discussions in the earlier paragraphs, taking into account the Literature review presented in the above background, and discussions with the clinicians, the major objectives of the present research work were framed and are enlisted below: 1) To propose denoising

techniques for B-Mode echocardiographic images of aortic valve and cardiac chambers acquired in multiple views using different windows. 2) Comparative analysis of state-of-the-art despeckling techniques for the B-Mode and CWD images. 3) To propose delineation techniques for tracing the outer spectrum of CWD images. 4) Comparative analysis of segmentation techniques using the TTE images acquired in multiple views and windows.

1.15 Organization of the thesis

The current thesis consists of six chapters. The first chapter introduces the basic concepts of echocardiographic imaging, different views and windows of acquiring images, the drawbacks of echocardiographic imaging, literature review of denoising and segmentation techniques, the scope for research, and the objectives of current research work.

Chapter 2 speaks of six proposed despeckling techniques for B-Mode images acquired in multiple views. The implementation of multiscale in the logarithmic domain, hybrid posterior sampling based Bayesian estimation filter, hybrid triangulation median filter, integrated fuzzy filter, hybrid homomorphic fuzzy filter, and extreme total variation bilateral filter, are described followed by result analysis. The impact of denoising and enhancement of images during segmentation are also brought out in this chapter.

Chapter 3 brings out a comparative analysis of eight types of despeckling filters for the B-Mode images. The performance of 48 despeckling filters are analysed in terms of sixteen image quality metrics, visual quality assessment and clinical validation.

Chapter 4 describes the despeckling techniques for the CWD and color Doppler images. The texture features extracted from the despeckled B-Mode images in PLAX, PSAX, A4C, A5C, and A2C, CWD images and color Doppler are compared in this chapter.

Chapter 5 deals with segmentation of B-Mode, CWD and color Doppler images. The delineation techniques are analysed for the images in multiple views and modalities. The boundaries of AV, LV, RV, AV leaflets, MV leaflets, outer spectrum of CWD and the regurgitant jet area in color Doppler images are segmented in the presence of low contrast and intensity in-homogeneity.

Chapter 6 presents an assimilation of the proposed work highlighting the contributions put-in by the candidate and his supervisors. It also points out the way forward for the current research work on denoising and segmentation of TTE images in multiple views.

CHAPTER 2: DESPECKLING OF B-MODE ECHOCARDIOGRAPHIC IMAGES

This chapter describes the proposed despeckling filters analysed for speckle noise reduction in B-mode transthoracic echocardiographic (TTE) images acquired in multiple view and windows. The chapter begins with introduction to the phenomenon of speckle formation in the ultrasound imaging, followed by noise modelling, image quality metrics (IQM), and image database employed in the analysis of filters performance for the TTE images in multiple views. The proposed despeckling techniques are described and analysed in terms of the IQM, visual quality assessment and clinical validation. This chapter describes multiscale techniques, hybrid posterior Bayesian estimation filter, hybrid fuzzy filter, integrated fuzzy filter, hybrid homomorphic fuzzy filter, and extreme total variation bilateral filter proposed for the noise reduction and edge preserved despeckling filters for the TTE images.

2.1 Introduction

The imaging modalities such as the transthoracic echocardiography (TTE) [22, 31, 32, 33, 37, 54, 66] and optical coherence tomography (OCT) [82, 228, 232], employ the coherent waves for illumination; suffer due to the presence of speckle noise. Speckle is a fine grained textural pattern observed in B-mode TTE images acquired using various acoustic windows and views [22]. The multiplicative noise is prominent in all the cross-sectional views [22, 66] and its adverse impact is severe compared to additive noise [22, 33]. The despeckling filters are employed for reduction of speckle noise while retaining edges and structure of the cardiac structure. The suppression of speckle noise in the TTE images with edge and structure preservation is a herculean image pre-processing problem which is addressed by various researchers.

The speckle noise omnipresent in the TTE images may introduce spurious ‘false-fine’ structures, camouflage the small gray level differences of the imaged medium leading to hazy boundaries, scale-down the contrast of the image and all these abrogating the human interpretation [4, 7, 14, 22, 26, 32, 33, 231]. The processes of automatic segmentation are slowed down due to speckle noise [22, 23, 231]. All coherent systems are blessed with presence of speckle noise, which severely affects the system performance [22, 23, 228, 231, 232]. The contrast of the TTE is very poor [4, 22, 36], hence endocardial trabeculae or papillary muscle are quite often treated as the left ventricular (LV) boundary leading to the under estimation of the LV volume and mass [8, 36]. Thus, there comes the necessity and need to despeckle and enhance [4, 14, 22, 23, 26, 29, 32, 33, 35, 36, 77, 83, 231] the TTE images for accurate location, diagnosis, analysis and interpretation of valvular abnormality accurately in real time. The cutback of speckle noise improves the overall image quality and also the boundary characterization [4, 22].

This chapter presents the applications of various despeckling filtering for the TTE images acquired in two parasternal and three apical views. The chapter begins by speaking of speckle noise and evaluation parameters, followed by description of proposed despeckling techniques and analysis of results. This chapter presents six techniques proposed for despeckling of the TTE images acquired from the adult patient diagnosed with aortic regurgitation. Section 2.2 deals with the brief description of eight multiscale techniques analysed in the logarithmic domain for despeckling of the TTE images. The performances of these filters are compared with two adaptive and four iterative despeckling techniques. The posterior sampling based Bayesian estimation (PSBE) is analysed for the TTE images along with proposed hybrid PSBE in Section 2.3. The proposed hybrid triangulation moving average (TMAV) filter is analysed in Section 2.4 followed by the proposed integrated fuzzy filter, which is the combination of fuzzy, geometric and Wiener filter, is described in Section 2.5. The hybrid homomorphic fuzzy (HHF) filters are analysed in Section 2.6. The regularization term of the total variation is replaced by the bilateral filter. This proposed filter is known as extreme total variation bilateral (ETVB) filter and is explained in Section 2.7.

2.1.1 Modelling employed for denoising

The modelling of multiplicative speckle noise is a tough task since it is the product of noisy and noise free components unlike the additive noise which is sum of these two components. The noise is modelled either as multiplicative or approximated as additive as in the case of most of the wavelet based despeckling filtering techniques. The speckle noise is modelled as

$$f(x,y) = g(x,y)n(x,y) \tag{2.1}$$

where $g(x,y)$ is noise free image, $f(x,y)$ is the acquired image and $n(x,y)$ is the multiplicative noise, x and y are the variables indicating the spatial locations [32]. The process of converting multiplicative noise to approximated additive noise is being met with by taking the logarithm of the input image as follows

$$\begin{aligned} \log[f(x,y)] &= \log[g(x,y)n(x,y)] \\ &= \log[g(x,y)] + \log[n(x,y)] \end{aligned} \tag{2.2}$$

The above Equation 2.2 can be rewritten as

$$f_{xy} = g_{xy} + n_{xy} \tag{2.3}$$

where $f_{xy} = \log[f(x,y)]$, $g_{xy} = \log[g(x,y)]$ and $n_{xy} = \log[n(x,y)]$. The Equation 2.3 makes way for application of various denoising techniques developed for additive white Gaussian noise, to

be tested on TTE images inherent with multiplicative speckle noise. In these methods the input is logarithmically transformed, $f(x,y) = \log(f(x,y))$ and denoised output is obtained by taking the exponential of the reconstructed image, $\hat{g}(x,y) = \exp(T_{WS}(\log(f(x,y))))$, where T_{WS} are thresholding methods. The discrete wavelet transform (DWT) of a noisy image $f = g + n$ can be represented as $W_j^d f = W_j^d g + W_j^d n$ where $W_j^d g$ and $W_j^d n$ are the DWT of original image and additive noise respectively. The denoising techniques studied and analyzed in this are briefly discussed in the following sections.

The multiscale despeckling based on wavelet transforms can be classified into wavelet shrinkage, the Bayesian framework, or those based on the correlation between coefficients. The shrinkage technique suppresses the coefficients representing the noise while retaining the coefficients that likely to represent the required features. In wavelet based hard thresholding the coefficients greater than a defined threshold are retained while others are set to zero. The wavelet soft thresholding attempts to avoid the discontinuities. The adaptive thresholding try to improve the performance by adding additional local information of the images such as the edge identification into despeckling techniques. The Bayesian based thresholding were specifically designed for a particular type of noise and therefore they may not be suitable for other imaging modalities. The major disadvantage of wavelet despeckling in the Bayesian framework was the computation of the prior distributions of the noise-free image, but no noise free TTE images are available as the speckle noise is inherent in the US images.

2.1.2 Evaluation of denoising techniques

The performances of multiscale, iterative and adaptive denoising techniques are evaluated on both clinical TTE and standard images. In standard images, the denoised image is compared to reference noise free image. In clinical TTE images, no reference noise free image exists hence the performance metrics are measured using the original speckled image as the reference image. Thus the results obtained using synthetic images can be considered ideal ones whereas those of clinical images are relative to the noisy input.

2.1.2.1 Image quality metrics for performance evaluation

The performances of denoising techniques are evaluated using 16 image quality metrics. The performance evaluation is first carried out using the traditional parameters such as the signal to noise ratio (SNR) [26], peak signal to noise ratio (PSNR) [26], mean square error (MSE) [22, 26], correlation coefficient (ρ), normalized correlation coefficient (NCC), root mean square error (RMSE), normalized mean square error (NMSE), Laplacian mean square error (LMSE),

normalized error summation (Err3,Err4) and geometric average error (GAE). The edge preservation is estimated by calculating the Prat's figure of merit (FoM) [22], beta metric (β) [26, 113] and image quality index (IQI) [27]. The structural similarity is assessed using the structural similarity (SSIM) index [22]. The visual quality is estimated by looking all finer details and texture information in the denoised images in comparison to original images. Finally the clinical validation of the denoised images is carried out by analysis of the grades awarded by the clinicians for the processed images. The error measuring parameters are computed using two images. The details of these parameters are available in [27].

The SNR measures the performance using the original image f_{org} and denoised image f_{den} , and it indicates the amount of reduction in noise after denoising. The displacement of edge pixel between original image and the denoised image are measured using FoM. The SSIM is employed to quantify the preservation of structural content of original image after denoising. The value of SSIM equal to 1 indicates that the structural information is intact else there is a loss of information. Some of the parameters like PSNR, MSE, β, image quality index (IQI) are also important in evaluation and these are defined below

$$\mathrm{PSNR}(f_{den}, f_{org}) = 20 \mathrm{x} \log_{10}\left(\frac{255}{\sqrt{\mathrm{MSE}(f_{den}, f_{org})}}\right) \tag{2.4}$$

$$MSE(f_{den}, f_{org}) = \frac{1}{MN}\sum_{i=1}^{M}\sum_{j=1}^{N}(f_{den} - f_{org})^2 \tag{2.5}$$

$$\mathrm{SNR} = 10\log_{10}\left(\frac{\mathrm{var}(f_{org})}{MSE(f_{den}, f_{org})}\right) \tag{2.6}$$

$$\mathrm{FoM}(f_{den}, f_{ref}) = \frac{1}{\max(N_{den}, N_{ref})}\sum_{j=1}^{N_{den}}\frac{1}{1+\gamma d_j^2} \tag{2.7}$$

$$\rho(f_{den}, f_{org}) = \frac{\sum_{i=1}^{M}\sum_{j=1}^{N} f_{den} f_{org}}{\sqrt{\sum_{i=1}^{M}\sum_{j=1}^{N} f_{den}^{\ 2}}\sqrt{\sum_{i=1}^{M}\sum_{j=1}^{N} f_{org}^{\ 2}}} \tag{2.8}$$

$$\beta = \frac{D(\Delta f_{den} - \bar{\Delta} f_{org}, \Delta f_{org} - \bar{\Delta} f_{org})}{\sqrt{D(\Delta f_{den} - \bar{\Delta} f_{den}, \Delta f_{den} - \bar{\Delta} f_{den}) D(\Delta f_{org} - \bar{\Delta} f_{org}, \Delta f_{org} - \bar{\Delta} f_{org})}} \tag{2.9}$$

$$\mathrm{SSIM}(f_{org}, f_{den}) = \frac{1}{M}\sum\frac{(2\mu_{f_{org}}\mu_{f_{den}} + c_1)(2\sigma_{f_{org}f_{den}} + c_2)}{(\mu_{f_{org}}^2 + \mu_{f_{den}}^2 + c_1)(\sigma_{f_{org}}^2 + \sigma_{f_{den}}^2 + c_2)} \tag{2.10}$$

$$SSI = \frac{\sqrt{VAR(f_{den})}}{Mean(f_{den})} \frac{Mean(f_{org})}{\sqrt{VAR(f_{org})}} \tag{2.11}$$

$$SMPI = Q \frac{\sqrt{VAR(f_{den})}}{\sqrt{VAR(f_{org})}} \tag{2.12}$$

with $Q = K + \left|\text{Mean}(f_{den}) - \text{Mean}(f_{org})\right|$, $K = \frac{\max(\text{Mean}(f_{den})) - \min(\text{Mean}(f_{den}))}{\text{Mean}(f_{org})}$

Where γ is the scalar multiplier being utilized as penalization factor with typical value 1/9, n_d and n_r are the number of pixels in original and processed images respectively, d_j is the Euclidean distance, Δf_{den} and Δf_{org} represent the filtered version of original and processed images, pixel mean intensities in the region Δf_{den}, Δf_{org} are represented by $\bar{\Delta} f_{den}$ and $\bar{\Delta} f_{org}$ respectively, c_1 and c_2 are constants, $\sigma_{f_{org}} \sigma_{f_{den}}$ and $2\mu_{f_{org}} \mu_{f_{den}}$ are the standard deviations and means of TTE images compared, $\sigma_{f_{org}\, f_{den}}$ represents the covariance, $c_1, c_2 \leq 1$ are the constants, N_{den} and N_{ref} are the number of pixels in original and processed images respectively.

2.1.2.2 Clinical TTE images

The TTE images used in current research are acquired using Philips I33 machine with S5 probe at Echo Lab, Postgraduate Institute of Medical Education and Research (PGIMER), Chandigarh, India. In the present experimentations, the B-Mode images acquired in the PLAX, PSAX, A4C, A5C, and A2C are pre-processed and delineated using various despeckling and segmentation techniques. The causes of valvular abnormalities and their consequences are visually seen using different acoustic windows. The PLAX images are used to study the dynamics of leaflets, to look for any calcification, perforation, thickening, prolapse and dissection of the leaflets. The variations in the size and the shape of LV, LA, RV, and RA, due to valvular stenosis and regurgitation are observed in A4C, A2C and A5C views. The information acquired using the parasternal and apical windows are integrated by the cardiologist for assessment of aetiologies and the consequences of valvular abnormalities, to decide on the future course of treatment or medication [2, 3]. Experiments are conducted on 1000 B-Mode TTE images acquired in the PLAX, PSAX, A4C, A5C and A2C views.

2.2 Multiscale techniques for despeckling of TTE images

The concepts of hard and soft thresholding [97,98] are extensively being used in despeckling of the US images in the logarithmic domain. Guo *et al.* [233] proposed a wavelet based

thresholding method for reduction of the speckle noise in logarithmically transformed synthetic aperture RADAR (SAR) images. The discrete dyadic wavelet transform were used by Zong *et al.* [33]. The Daubechies wavelets of length four and soft thresholding were employed for suppression of noise. The wavelet hard and soft thresholding were together used by Zong *et al.* [32] for speckle noise reduction in logarithmic domain for TTE images in parasternal short axis (PSAX). The multiplicative noise was approximated as a Gaussian noise in the logarithmic domain. Saevarsson *et al.* [234] used hard thresholding in curvelet domain for suppression of multiplicative noise. It was reported that edges were preserved but despeckling in the singular and the smooth areas presented problems. Khare *et al.* [235] employed soft thresholding of wavelet coefficients for reduction of salt and pepper, speckle and Gaussian noise in medical images. The threshold was computed based on the median, standard deviation and mean of the image to be processed. Yue *et al.* [36] had integrated the wavelet and the AD filter concepts for speckle noise suppression and enhancement of the echocardiographic images in the A4C.

It is observed that many of the wavelet based despeckling techniques employ hard thresholding, soft thresholding or their combination for noise suppression [32, 33, 233, 235]. The other combinations such as soft thresholding and the AD filter have also been experimented with aim of suppressing maximum amount of noise while preserving edges, structure and resolution of the images [36, 110, 236]. The results have shown that hard thresholding may cause oscillations during reconstruction and the soft thresholding may affect the accuracy of the denoised image [237].

The multiscale techniques implemented in the logarithmic domain are based on additive noise model. The transformation of image using logarithmic operation, thresholding and projecting the image back to the spatial domain are the common steps observed in all wavelet shrinkage techniques using various thresholding methods. The use of logarithmic operation decouples the multiplicative components of the acquired signal into independent individual noise-free and noise components [26, 110]. The desired features are separated from noisy features using the logarithmic transformation [33]. The noisy components are treated as white Gaussian noise [34].

In the quest, looking for best multiscale denoising technique, it is observed that applications of many shrinkage techniques are not exclusively analysed using the TTE images acquired in multiple views and windows [99, 101-103, 120, 227, 238, 239]. There are wavelet thresholding techniques which were proposed in the homomorphic domain for the US images [26, 32, 33, 110, 240]. Therefore, it is felt that various shrinkage techniques, not analysed for the TTE images, can be tapped in for suppression of speckle noise. It is proposed to analyse

the multiscale techniques, in the logarithmic domain, for the TTE images acquired in the two parasternal and three apical views. The logarithmic based shrinkage techniques are referred to as LM*x*E schemes, where 'L' represents the logarithmic projection of the input images, 'M*x*' refers to the shrinkage technique, and 'E' stands for the exponential operation using which the images are brought back to the spatial domain.

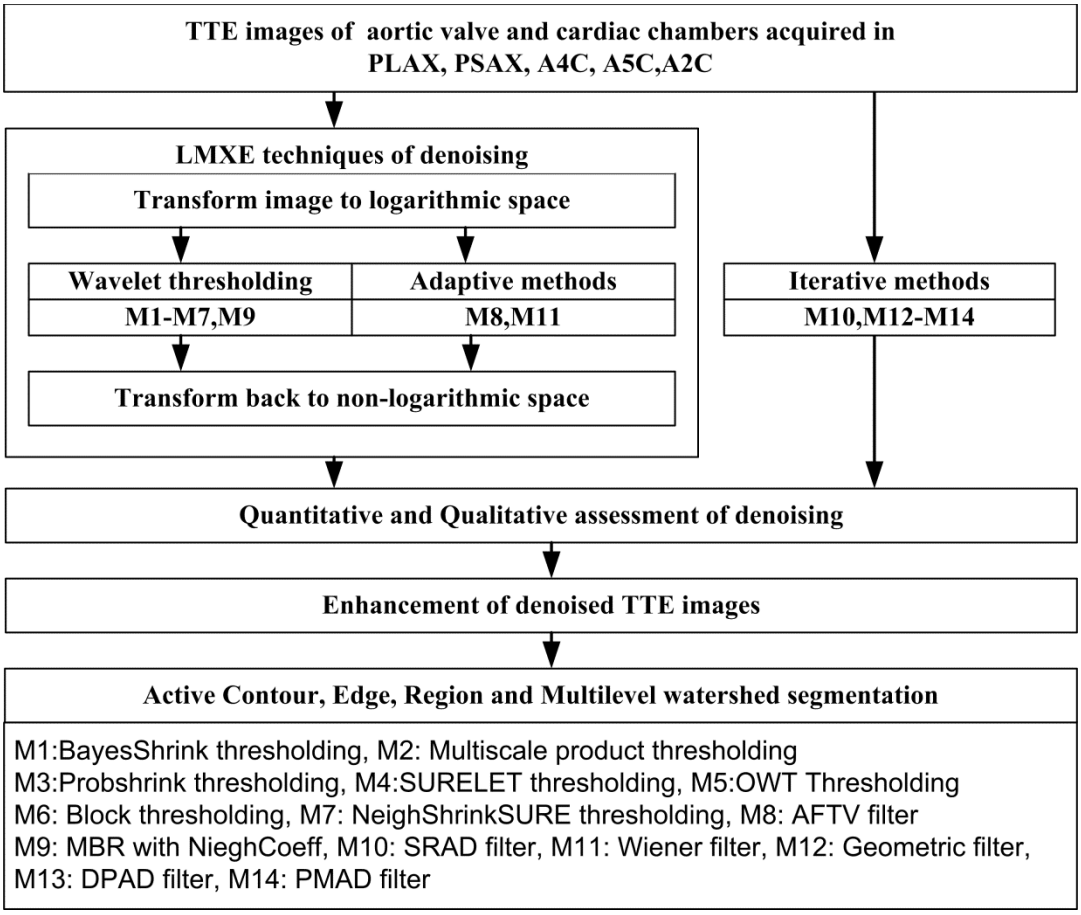

Figure 2.1 Methodologies for analysis of multiscale techniques in log domain

The wavelet based shrinkage techniques analyzed in the logarithmic domain for the TTE images consists of : (i) 'Stein's unbiased risk estimation (SURE)' embedded with the 'linear expansion of threshold (LET)' SURELET [101], (ii) neighbourhood shrinkage combined with the SURE, NeighShrinkSURE (NSS) [103], (iii) Block thresholding (BlockShrink) [239], (iv) multiscale product thresholding (MPT) [100,238], (v) probability based shrinkage (ProbShrink) [99], (vi) Bayesian shrinkage (BayesShrink) [227], (vii) inter-scale orthonormal wavelet thresholding (IOWT) [102], (viii) Bivariate thresholding using DWT (HDWT), (ix) Bivariate thresholding using dual tree discrete wavelet transform (HDTDWT) [241] and (x) Curvelet with hard thresholding [242].

The performances of the multiscale techniques were compared with (i) the AD filter proposed by Perona and Malik [83], (ii) speckle reducing anisotropic diffusion (SRAD) filter [35], (iii) adaptive fidelity term based total variation filter (AFTV) [120], (iv) adaptive Wiener filter [79], (v) detail preserving anisotropic diffusion (DPAD) filter [86], (vi) adaptive geometric filter [244], and (vii) Generalized likelihood ratio filtering method (GLM) based on wavelet transformation [116]. Most of the multiscale methods work in logarithmic domain for multiplicative noise reduction applications. But there are some methods such as generalized likelihood method (GLM) and M-band ridgelet which are based on multiplicative noise model. Methods based on both additive and multiplicative noise model are briefly explained in this section. The multiscale filtered images are further enhanced using the Butterworth filter as suggested in [245]. The integrated effect of denoising and enhancement during segmentation are studied using the edge, region, watershed, and active contour techniques. The proposed method of analyzing the multiscale techniques for noise reduction in the TTE images is shown using Figure 2.1. The multiscale techniques are briefly explained in the following sections.

Table 2.1 Available on-line resources for denoising

Ref.	Method	Name of filter with available on-line resources
[227]	LM1E	BayesShrink:http://my.fit.edu/~kozaitis/MATLAB/code/denoiseBayes2D.m
[100]	LM2E	MPT: http://www4.comp.polyu.edu.hk/~cslzhang/code/MI.rar
[99]	LM3E	ProbShrink: http://telin.ugent.be/~sanja/
[101]	LM4E	SURELET: http://www.laurent-duval.eu/Codes/Surelet_tlbx.zip
[102]	LM5E	OWT: http://bigwww.epfl.ch/demo/suredenoising/MATLAB/OWT_SURELET.zip
[239]	LM6E	BlockShrink:http://www.mathworks.in/MATLABcentral/fileexchange/24430-blockshrink-denoising/content/DenoiseFun.m
[103]	LM7E	NeighShrinkSURE:http://www.mathworks.in/MATLABcentral/fileexchange/20705-neighshrinksure-denoising
[120]	M8	AFTV: http://visl.technion.ac.il/~gilboa/PDE-filt/tv_denoising.html
[86]	M13	DPAD:http://www.mathworks.in/MATLABcentral/fileexchange/36906-detail-preserving-anosotropic-diffusion-for-speckle-filtering--dpad-
[241]	HDWT	Bivariate: http://eeweb.poly.edu/iselesni/WaveletSoftware/denoise2.html

2.2.1 Bayes thresholding (M1)

The sub-band adaptive, data driven wavelet shrinkage known as the Bayes thresholding, works in the Bayesian framework employing the general Gaussian distribution (GGD) based prior on the wavelet coefficients. The Bayes thresholding is commonly called as the BayesShrink [227], and it is referred as the method M1. The method in the logarithmic domain is represented as LM1E. The computation GGD depends on the standard deviation (σ_X) and the shape parameter (β) rendering sub-band adaptive threshold $T_B(\sigma_X)$.

This is mathematically represented in Equation 2.13 [227]:

$$GG_{\sigma x,\beta}(x) = C(\sigma_x, \beta)\exp\{-[\alpha(\sigma_x, \beta)|x|]^{\beta}\}, -\infty < x < \infty, \sigma_x > 0, \beta > 0 \quad (2.13)$$

where $\alpha(\sigma_x, \beta) = \sigma_x^{-1}\left[\frac{\Gamma(3/\beta)}{\Gamma(1/\beta)}\right]^{1/2}$, $C(\sigma_x, \beta) = \frac{\beta.\alpha(\sigma_x, \beta)}{2\Gamma(1/\beta)}$ and $\Gamma(t) = \int_0^{\infty} e^{-u}u^{t-1}du$ is gamma function. The soft threshold is estimated by minimizing the error function computed using the Bayesian risk estimation

$$r(T) = E(\hat{X} - X)^2 = E_X E_{Y|X}(\hat{X} - X)^2 \quad (2.14)$$

Where $X \approx GG_{\sigma x,\beta}$, $\hat{X} = \eta_T(Y), Y \mid X \sim N(x, \sigma^2)$. On application of the DWT, the transformed images are $Y = X + V$, where $Y = Wf$, $X = Wg$ and $V = Wn$, W is the wavelet coefficient like the dyadic orthogonal wavelet, $f = \log(f)$, $g = \log(g)$ and $n = \log(n)$. This phenomenon results in an estimate of denoised image $\hat{g} = \exp(W^{-1}\hat{X})$, where $\hat{X} = (\hat{T}_B(\log(f(x, y))))$. The sub-band dependent threshold are computed using the relation given below [227]

$$\hat{T}_B(\sigma_X) = \hat{\sigma}^2 \big/ \hat{\sigma}_X \quad (2.15)$$

where $\hat{\sigma}_X = \sqrt{\max(\hat{\sigma}_Y^2 - \hat{\sigma}^2, 0)}$ with $\hat{\sigma} = \frac{Medain(|Y_{ij}|)}{0.6745}$ and Y_{ij} Є wavelet subband HH_1.

The variance of *Y*, σ_Y^2 is computed by

$$\sigma_Y^2 = \frac{1}{n^2}\sum_{i,j=1}^{n} Y_{ij}^2 \quad (2.16)$$

The steps employed in the implementation of the BayesShrink based denoising in the logarithmic domain are shown in Figure 2.2.

2.2.2 Adaptive multiscale product thresholding (M2)

The adjacent subbands are multiplied for the amplification of features of interest and abridging the noisy ones [100]. Wavelet coefficients are considered for further processing when the multiscale product is greater than the adaptive threshold value. Mathematically, the process of multiscale product thresholding (MPT) is represented as $Z_j^d = P_j^d f = W_j^d f.W_{j+1}^d f$, where W_j^d are wavelet coefficients, $d = x, y$, specifying the directions. The estimated product threshold would consists of two components represented as $P_j^x f(x,y) = W_j^x f(x,y).W_{j+1}^x f(x,y)$ and $P_j^y f(x,y) = W_j^y f(x,y).W_{j+1}^y f(x,y)$, respectively in the horizontal and the vertical directions.

An appropriate adaptive threshold $t_p^d(j)$ can be computed and imposed on Z_j^d for the elimination noise and estimating the significant image structures. The adaptive threshold are computed using Equation 2.17

$$t_p^d(j) = \mu_\varepsilon^d(j) / \mu_g^d(j) \tag{2.17}$$

where $\mu_\varepsilon^d(j) / \mu_g^d(j)$ is the ratio of intensity of noise against signal in the multiscale product threshold with $\mu_g^d(j) = \mu_f^d(j) - \mu_n^d(j)$, $\mu_n^d(j) = \rho_{j+1}.\sigma_j.\sigma_{j+1}$, ρ is the correlation coefficient, and σ is the standard deviation. The estimation of noise free signals is based on $\mu_f^d(j) = E[Z_j^d]$, estimation of noise $\mu_n^d(j) = E[V_j^d]$ with estimation of multiscale product $\mu_g^d(j) = E[W_j^d g.W_{j+1}^d g]$, Z_j^d is multiscale product, V_j^d is the scale product and W_j^d is wavelet coefficients. The threshold of significant coefficient is estimated using the relation [100]

$$\hat{W}_j^d f(x,y) = \begin{cases} W_j^d f(x,y), & P_j^d f(x,y) \geq t_p^d \quad j \\ 0 & P_j^d f(x,y) < t_p^d \quad j \end{cases} \tag{2.18}$$

where *j=1,2,……..J*; and *d=x, y,* $W_j^d f(x,y)$ is the wavelet coefficient obtained.

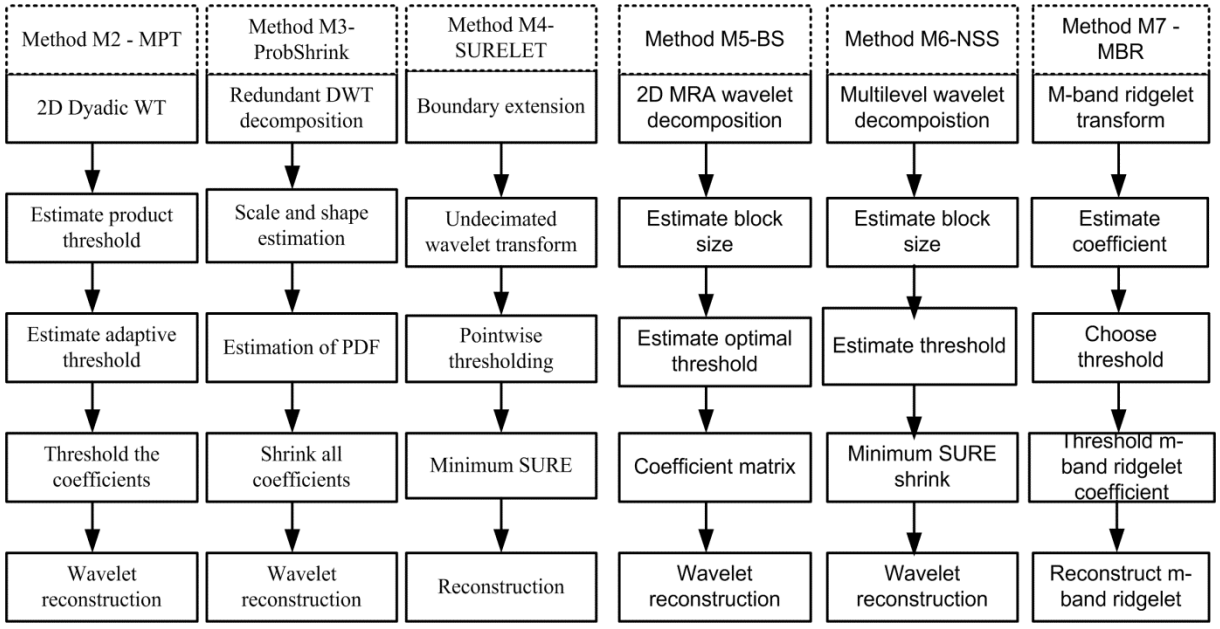

Figure 2.2 Steps in multiple multiscale denoising techniques

A 2D dyadic wavelet transform is applied to the logarithmically transformed image. The MPT and adaptive thresholds are computed. The significant wavelet coefficients are identified by comparing the product thresholds with the adaptive thresholds. The wavelet transform

employed in the implementation behaves like a canny edge detector. The steps employed in the implementation of the MPT based denoising in logarithmic domain are shown in Figure 2.2.

2.2.3 ProbShrink method of denoising (M3)

The generalized Laplacian prior based probability evaluation is used for estimation of the noise free components in the signal and is represented as [99]

$$p(g) = \frac{\lambda\beta}{2\Gamma\left(\frac{1}{\beta}\right)} \exp\ -\lambda|g|^{\beta} \tag{2.19}$$

where $\Gamma(x)$ represents the Gamma function, $\Gamma(x) = \int_0^{\infty} t^{x-1}e^{-t}dt$, $\lambda > 0$ is known as scale factor and β presents the shape parameter. The wavelet coefficients are multiplied with estimated probability of the signal containing vital information of interest. Estimation of the probabilities alleviated the need for preliminary edge detection. Each of the coefficients is shrunk in the subband using adaptive function with the probability that they represented significant information. If the signal does not have "signal of interest", it is represented by H_0. The "signal of interest" in the signal is labelled as H_1 with threshold T for $g = \log(g)$ and is defined as, $H_0 : |g| \le T$, $H_1 : |g| > T$. This method of denoising is known as the ProbShrink [99]. The probability based shrinkage is computed using the relation in Equation 2.20.

$$\hat{g} = P(H_1|y)y = (\mu\eta/1+\mu\eta)y \tag{2.20}$$

where $\mu\eta$ represented the likelihood ratio, $\mu = P(H_1)/P(H_0)$, $\eta = p(f|H_1)/p(f|H_0)$ and $f = \log(f)$. The image in the logarithmic is decomposed into the subbands using DWT. All the specifications for subband adaptive shrinkage are incorporated in the designed estimator, and μ is expressed as

$$\mu = \frac{P(H_0)}{P(H_1)} = \frac{1-\Gamma_{inc}\left((\lambda T)^{\beta}, \frac{1}{\beta}\right)}{\Gamma_{inc}\left((\lambda T)^{\beta}, \frac{1}{\beta}\right)} \tag{2.21}$$

The expression in Equation 2.21 can be written as

$$\mu = P(H_1)/P(H_0) = \exp(-\lambda T)/\ 1-\exp(-\lambda T) \quad \text{for } \beta = 1 \tag{2.22}$$

These values are combined with

$$p(f\ |\ H_0) = \int_{-\infty}^{\infty} \phi(f-g;\sigma) f(g\ |\ H_0)dg \tag{2.23}$$

$$p(f \mid H_1) = \int_{-\infty}^{\infty} \phi(f-g;\sigma) f(g \mid H_1) dg \tag{2.24}$$

with zero mean Gaussian density of $\phi(f;\sigma)$ with standard deviation σ. The shape and the scale parameter for generalized Laplacian prior for noise-free wavelet coefficients are estimated from the noisy histogram. The probability density function (PDF) of coefficient magnitudes, averaged coefficients and probability of each coefficient in the subbands are calculated, followed by ProbShrink shrinkage.

2.2.4 SURELET (M4)

The clean image requirement for the estimation of the MSE is overcome using the SURELET [101]. This is employed for an efficient and fast denoising of the images. The optimization is performed in the image domain with the extension of boundaries leading to improvement in the PSNR. This technique is the combination of minimum risk estimation using SURE and linear expansion of thresholds (LET). The process of SURELET estimation can be represented in Equation 2.25

$$\mathrm{F}(f) = \sum_{k=1}^{K} a_k \mathrm{F}_k(f) \tag{2.25}$$

where a_k are computed by minimization of loss (SURE). The loss is estimated using Equation 2.26.

$$\in = \frac{1}{N} \left\| \mathrm{F}(f) - f \right\|^2 + \frac{2\sigma^2}{N} \mathrm{div}[\mathrm{F}(f)] - \sigma^2 \tag{2.26}$$

which is the unbiased estimation of the MSE and this is estimated by Equation 2.27

$$\varepsilon(\in) = \frac{1}{N} \left\| \mathrm{F}(f) - \mathrm{x} \right\|^2 \tag{2.27}$$

for $f(x,y) = \log(f(x,y))$ and $f_{denoised} = \exp(T_{SLET}(\log(f_{orginal}(x,y)))$, where T_{SLET} is SURELET based denoising. Filter bank based SURELET is analyzed with overlapping factor equal to 3, redundancy=3 and the down sampling factor N=4. The estimated coefficients a_k are the solution for linear set of Equations, the system is represented by

$$\sum_{t=1}^{K} \underbrace{\mathrm{F}_k(f)^{\mathrm{T}} \mathrm{F}_l(f)}_{[\mathrm{M}]_{k,l}} = \underbrace{\mathrm{F}_k(f)^{\mathrm{T}} f - \sigma^2 \mathrm{div}\{\mathrm{F}_k(f)\}}_{[c]_k} \text{ for } k = 1,\ldots,K \tag{2.28}$$

$$\Updownarrow$$

$$\mathrm{Ma=c}$$

Let $\mathrm{D}= d_{i,j\ (i,j)\in[1;L]\times[1;N]}$ represent decomposition and $\mathrm{R}= r_{i,j\ (i,j)\in[1;N]\times[1;L]}$ leading to the ideal reconstruction $\mathrm{DR}=\mathrm{Id}$.The thresholding is represented as $\Theta\ w = \theta_i\ w_{i\ i\in[1;L]}$.The point-wise denoising technique is of the form $\hat{g} = \mathrm{F}(f) = \mathrm{R}\Theta(\mathrm{D}_f)$. Incorporating LET with SURE the algorithm can be rewritten as

$$\mathrm{F}(f) = \sum_{k=1}^{K} a_k \underbrace{\mathrm{R}\Theta_k(\mathrm{D}f)}_{\mathrm{F}_k(f)} \tag{2.29}$$

where $\Theta_k(.)$ is point-wise thresholding. The denoising is performed point-wise using SURELET, and the threshold is calculated using the relation given below [101]:

$$\theta_i(w) = \mathrm{a}_{\mathrm{i},1} t_1(w) + \mathrm{a}_{\mathrm{i},2} t_2(w)\text{, where } t_1(w) = w \text{ and } t_2(w) = w(1 - e^{-(\frac{w}{3\sigma})^8}) \tag{2.30}$$

2.2.5 Interscale orthonormal wavelet thresholding (M5)

The interscale orthonormal wavelet thresholding (IOWT) [102] is a parameterized denoising technique which alleviates the necessity of a statistical design model. This method uses the observation that no shift can be seen between the features of bandpass $\mathrm{LH_j}$ and lowpass $\mathrm{LL_j}$ subbands when the group delay is the same, else leading to some variations. To balance for the shift due to group delay, the lowpass subband is filtered in three bandpass directions using gain delay compensated (GDC) filters. The inter-scale and intra-scale correlations between various coefficients of different subbands with increased redundancy help in obtaining better denoising. No assumptions are being made on the existence of clean image. The MSE is estimated using SURE without any apriori information of noise free image. The goal is to find the denoising function that minimizes the MSE [102]

$$\mathrm{MSE} = \left\langle \left| \theta(f) - g \right|^2 \right\rangle = \left\langle \theta(f)^2 \right\rangle - 2\left\langle g\theta(f) \right\rangle + \left\langle g^2 \right\rangle \tag{2.31}$$

The general form of denoising function is [102]

$$\theta(f) = \sum_{k=1}^{K} a_k \varphi_k(f) \tag{2.32}$$

where φ is the basis function. The basis function determines the shape of denoising and has properties like differentiability, anti-symmetric and linear behaviour for large coefficients. The point-wise function is being used as the denoising function given by [102]

$$\theta(f) = \sum_{k=1}^{K} a_k f e^{-(k-1)\frac{f^2}{2T^2}} \tag{2.33}$$

A reliable statistical analysis is being ensured by preventing denoising in subbands where number of samples is below 256. The frequency responses of analysis and GDC filters are computed followed by 2D wavelet transformation of the gray scale, resized log transformed echo image. The image in the logarithmic domain is filtered using an adaptive filter followed by interscale prediction. The image is denoised using interscale SURELET.

2.2.6 Block thresholding (BlockShrink) (M6)

The risk estimation based on SURE does not take into consideration the neighbouring coefficients of the pixel during thresholding and hence it is considered to be less adaptive to the data [239]. Thresholding is applied to entire block in block thresholding, instead of each element at each level individually. Either all the wavelets coefficients within the block are retained or all are set to zero. The SureShrink based denoising does not take into consideration the neighboring coefficients of a pixel under consideration hence it can be said that it is less adaptive to data [239]. The major hurdles in block thresholding are the constant block size and at each resolution level correlation is not taken into consideration. The other issues are selection of wavelet type and resolution level.

2.2.7 NeighShrinkSURE (M7)

Major hurdles in block thresholding are a) constant block size and b) correlation is not taken into consideration at all levels. These difficulties are encountered by estimating the optimal threshold and block size by incorporating SURE with NeighShrink resulting in NeighShrinkSURE. Adaptive block size and threshold are estimated using Stein's unbiased risk estimation. The threshold value is compared with sum of the squares of all the wavelet coefficients for each block (S_b^2) [103,239]

$$S_b^2 = \sum_{i \in ib1} \sum_{j \in jb1} w_{ij}^2 \tag{2.34}$$

where $ib_1 = \{i : (b_1 - 1)L + 1 \le i \le b_1 L, \quad jb_2 = \{j : (b_2 - 1)L + 1 \le i \le b_2 L.$

If S_b^2 is less than or equal to the estimated threshold, the coefficients are laid to rest (discarded) with zero value or else a breather (enhanced) is added through the Equation 2.35 [103, 239]

$$\hat{\theta}_{ij} = w_{ij}\left(1 - \frac{\lambda}{S_{b1,b2}^2}\right)_+ \tag{2.35}$$

for $i \in ib_1$, $j \in jb_2$. The estimated total risk is represented as [103, 239]

$$SURE(w, \lambda, L^2) = \sum_{b_1 b_2 = 1}^{m} SURE(w_{b_1 b_2}, \lambda, L^2) \tag{2.36}$$

The greatest threshold λ^s and the block size L^s are acquired by minimizing $SURE\ w,\lambda,L^2$ specifically by [103, 239]

$$\lambda^s, L^s = \arg\min_{\lambda,L} SURE(w,\lambda,L^2) \tag{2.37}$$

The coefficient to be denoised is placed at the centre of square neighbouring window. The optimal threshold is estimated using Stein's loss estimation. The NeighShrink shrinkage [103, 239] is computed using the relation

$$\hat{\theta}_{ij} = w_{ij}\beta_{ij} \tag{2.38}$$

where $\beta_{ij} = \frac{1-\lambda^2}{S_{ij}^2}$, $S_{ij}^2 = \sum_{k,l\in B_{ij}} w_{kl}^2$, λ is the threshold.

The detail subbands are extracted and thresholding is reinforced. The optimal threshold, optimal neighbourhood size and thresholding of noisy subband are estimated using NeighShrink. A 2D wavelet with subband thresholding at various level of decomposition is used in the 'NeighShrinkSURE' filter. The results obtained with noise variance equal to 0.01 for 2 level of wavelet decomposition are considered for comparisons with other denoising techniques.

2.2.8 Curvelet based denoising

The curvelet transform is a multi-scale transform with frame element indexed by the scale and the location parameter [13, 242, 247]. Unlike the wavelets, curvelets are well localized not only in position and scale but also in orientation. This transform is effective in noise reduction with edges well preserved along the curves since the curvelet pyramid consists of elements with high degree of directional specificity. Curvelet based denoising methods preserved the edges perfectly, however, these methods also generated some visual distortion and fuzzy edges in the homogeneous regions of the image [242]. They consist of the combinations of ridgelet and spatial bandpass filters. They have variable width, length and anisotropy. The image can be represented at different scales, permitting the removal of different amount of noise at different scales.

The ridgelet are combined with spatial band pass filter for isolation at various scales. The curvelet transform can be used for effective denoising as it can preserve the edges. The ridgelet transform is able to capture line-singularities of the image, but could not approach the curve-singularities very effectively. The ridgelet posses a global length, so a variable width can be embedded in the curvelets along with a variable length resulting in the required variable anisotropy.

Candes *et al.* [247] had proposed fast discrete curvelet transform (FDCT) which is widely employed for image denoising applications. The curvelet based denoising technique can deliver edge preservation perfectly, but may also generate visual distortion and fuzzy edges in homogeneous regions of the denoised image. The steps used in the implementation of curvelet based denoising are a) application of forward curvelet transformations, b) thresholding of the coefficients and c) reconstruction using the inverse curvelet transformation. Denoising is performed in logarithmic domain using soft thresholding with five curvelet subbands and ridgelet scale L= [*3 4 4 5*] from fine level to coarse level. The minimum local window size of local ridgelet is taken as 16 [242].

2.2.9 Generalized likelihood method (GLM) of filtering

GLM is a multiscale denoising technique based on the multiplicative model of speckle noise. It emphasizes on the visual outlook of the image whereas techniques like SRAD concentrate only on edge preservation [22, 116]. An initial classification of the coefficients is carried out based on the correlation among the prominent features across various resolution scales non-iteratively. This initial coefficient classification is employed for the estimation of statistical distribution of the features of interest and noise. The spatial adaptation is achieved using a local spatial activity indicator in the wavelet domain. It uses non-decimated wavelet transform, with equal number of coefficients at each resolution scale.

2.2.10 Iterative denoising techniques

Anisotropic diffusion filter is a nonlinear, partial differential Equation (PDE) based technique that promotes diffusion in homogeneous region while holds back at edges [22, 35, 83, 86]. The major advantage of nonlinear diffusion is speckle noise reduction can be carried out directionally by edge function and edges get enhanced. In order to get rid of limitations of the AD filter, Yu and Acton [35] proposed the SRAD filter. The diffusion function is controlled by instantaneous coefficient of variation (ICOV) and it is represented as ratio between standard deviation to mean. Detail preserving anisotropic diffusion (DPAD) method [86] estimates the equivalence between threshold, controlling the level of diffusion and the variation in noisy coefficient by incorporating various modifications to SRAD [22]. A larger neighbourhood for estimating the local statistical parameters are incorporated in DPAD calculations. Geometric filter [22, 27,130, 131, 244] works on increasing or decreasing the values of neighbourhood pixels based on their relative values. It works on the principle that images are made up of valleys and narrow walls. This filter tears down the walls and fills up the valleys.

Thus, the weak edges to be preserved get smeared. The intensities of the pixels located at the centre of the 3×3 window are compared with eight neighbours. Depending on intensity values of neighbourhood pixels the value is either incremented or decreased so that the values stands out compared to others. The size of moving window in this study is set to 3×3 with number of iteration equal to 2.The visual quality of the image improves on application of geometric filter on noisy images but the same time image is smoothed considerably. Some of the edges and finer details are mostly lost on application of geometric filter. In this study the following parameters are considered for PMAD filter: number of iterations=10 to 60, diffusion constant=30, rate of diffusion=0.25 and spatial neighborhood of pixel=8. The coefficient of variation = 0.02 and number of iterations =30 are considered for analysis of SRAD. The SRAD filter, the adaptive Wiener filter, geometric, DPAD and the PMAD filters are represented by method numbers from M10 to M14, respectively.

2.2.11 Adaptive fidelity based total variation (M8)

The image texture provides lots of critical information but this is almost lost on application of denoising methods like the AD filter. To overcome such drawbacks, image denoising based on total variation with adaptive fidelity term is proposed by Gilboa, Zeevi and Sochen [120]. The adaptive fidelity term controls the amount of denoising by measuring local variance in the image. The denoising is performed in two phases. In the first phase the texture and the noise are isolated using scalar total variation with λ =1. During the second phase local power constraints estimated using the local variance are placed on the output of first phase.

2.2.12 Enhancement

The Butterworth filter is able to reduce noise with preservation of edge. No ringing effects are induced in the image due to the denoising process. The performance is superior compared to the median filter and average filter [245, 248]. A Butterworth filter is employed for enhancement of TTE images. The general form of an nth order Butterworth filter is defined in terms of transfer function as [245, 248]

$$H(u,v) = \frac{1}{1+[D(u,v)/D_0]^{2n}} \tag{2.39}$$

where $D(u,v) = [(u-P/2)^2 + (v-Q/2)^2]^{1/2}$ with $P \geq 2M-1, Q \geq 2N-1$.

2.2.13 Proposed schemes of denoising using multiple multiscale techniques

The multiscale techniques M1 to M7, DWT and DTDWT with hard and soft thresholding are experimented by projecting the input image in the logarithmic domain. Various steps incorporated in the study of multiscale techniques are in accordance to the description available in the respective reference papers. The proposed methodology of using the multiscale techniques for reduction of noise is shown in Figure 2.1. The resources available on the internet and those provided by various authors are tabulated in Table 2.1 for quick reference. The steps used in the implementation of multiscale techniques are shown in Figure 2.2. The proposed schemes of denoising using multiple multiscale techniques along with other techniques are briefly described below.

2.2.13.1 Logarithmic BayesShrink (LM1E)

In LM1E, the log transformed image is decomposed using a multilevel 2D wavelet transform. The data driven threshold are estimated followed by the soft thresholding. The image is reconstructed using inverse transformation. The LM1E method of denoising generated large threshold values for the TTE images. To address this issue the images are pre-processed before application of LM1E filter.

2.2.13.2 Logarithmic MPT (LM2E)

A 2D dyadic wavelet transform is applied to the image in the logarithmic domain. The multiscale product and adaptive thresholds are estimated by making use of steps shown in Figure 2.2. The significant wavelet coefficients are identified by comparing the product thresholds with adaptive thresholds. The inverse wavelet transformation is followed by the exponential operation.

2.2.13.3 Logarithmic ProbShrink (LM3E)

The logarithmic transformed image is decomposed into subbands using the DWT. The shape and the scale parameter for the generalized Laplacian prior and the noise-free wavelet coefficients are estimated from histogram. The probability density function (PDF) of coefficient magnitudes, averaged coefficients and probability of each coefficient in the subbands are calculated, then ProbShrink based wavelet shrinkage is being performed. These steps are followed by wavelet reconstruction.

2.2.13.4 Logarithmic SURELET (LM4E)

The loss estimation based on SURE (Stein’s unbiased risk estimation) combined with the LET is analysed in the logarithmic domain using the LM4E filter. The boundaries are extended followed

by wavelet transformation, before application of the LM4E filter. Point-wise thresholding is performed based on minimization of the SURE and the LET. The wavelet reconstruction is followed by the exponential operation. The steps employed in the implementation of LM4E are shown in Figure 2.2.

2.2.13.5 Logarithmic IOWT (LM5E)

A reliable statistical analysis may be ensured by preventing denoising in the subbands where number of samples is below 256. The essential number of iterations and number of dyadic scales for a given size of signal are to be computed. The frequency responses of analysis and gain delay compensated signals are computed. This is followed by the 2D wavelet transformation of the image which is converted into gray scale, resized, and projected into the logarithmic space. The image is denoised using interscale SURELET and reconstructed using inverse wavelet followed by exponential operation.

2.2.13.6 Logarithmic BlockShrink (LM6E)

The detail subbands are extracted and for each of the subblock the optimal threshold are estimated. The thresholded coefficients matrix is formed and the image is reconstructed. The exponential of the reconstructed image is taken to move the image into non-logarithmic domain.

2.2.13.7 Logarithmic NeighShrinkSURE (LM7E)

The detail subbands are extracted and subband thresholding is reinforced with calculation of the optimal threshold, optimal neighborhood size and thresholding of noisy subband using NeighShrink. The thresholded subbands are reconstructed and denoised image is obtained. The steps employed in the implementation of LM7E filter are shown in Figure 2.2.

2.2.13.8 M-band Ridgelet (M9)

The combination of M-band wavelet and Ridgelet known as M-Band Ridgelet (MBR) is proposed for analysis and classification of texture of standard natural test images [94]. Texture is preserved using MBR transformations. The bottleneck of 2D wavelet and ordinary ridgelet transforms are overcome using the MBR based filter. The issue of concern using the wavelets is the signal could be decomposed only with same bandwidth in the logarithmic scale. The MBR overcomes the disadvantages of the wavelet and ridgelet. In this thesis, it is proposed to use the MBR based filter with neighbor coefficient (NeighCoeff) thresholding [249] for speckle noise reduction in the TTE images. Before application of the MBR transforms the images are pre-processed.

The steps used in the MBR based despeckling are as follows:

Step 1: Load TTE image, resize and convert it into gray scale

Step 2: Apply the 2D-FFT and partition into slices.

Step 3: Apply the inverse 1D-FFT on each slice.

Step 4: Apply the 1D M-band wavelets on each slice.

Step 5: Get the M-band ridgelet responses.

Step 6: Apply NeighCoeff thresholding algorithm on the M-band ridgelet responses.

Step 7: Reconstruction of M-Band ridgelet to obtain the desired denoised image

The NeighCoeff thresholding is performed taking into consideration a reference point and its neighbor for length *L=3*. The NeighCoeff thresholding takes into account the neighbouring MBR coefficients. In this method, size of the neighbor varies depending on the coefficients.

$$S_{i,j}^2 = \sum_{m=-N}^{N} MRT_{i,j+m}^2; \quad N = N_0 - i \tag{2.40}$$

Here *j* is the level in M-band decomposition and the size of neighbour is (2N+1). N_0 can be selected based on the size of image and the support of M-band ridgelet coefficients:

$$MRT_{i,i} = \begin{cases} MRT_{i,j}\left(1 - \dfrac{\alpha\lambda^2}{S_{i,j}^2}\right) & if\ S_{i,j}^2 \geq \alpha\lambda^2 \\ 0 & else \end{cases} \tag{2.41}$$

where λ is given by *2log* (*m*) and α adjusts the threshold value in the denoising process.

Steps employed in the implementation of the MBR based despeckling

Step 6.1: Apply M-Band ridgelet transform to the noisy image, obtain the scaling coefficients and M-band ridgelet coefficients.

Step 6.2: Choose the threshold by employing Equation 2.40 and Equation 2.41 and apply thresholding to the MBR coefficients (leave the scaling coefficients alone).

Step 6.3: Reconstruct scaling coefficients and the MBR coefficients and obtain the denoised image.

The adaptive Wiener filter, represented as LM11E in this section, is implemented in logarithmic domain using MATLAB inbuilt function "*Wiener2*". The size of window is set either as 3×3, 5×5, 7×7, 9×9. The methods M8 to M10 and M12 to M14 are implemented considering the multiplicative noise model. The parameters and procedure incorporated in the implementation and analysis of these filters are according to the results discussed in [24, 26, 90-93, 99-103, 227, 239, 242]. The algorithms and the MATLAB functions provided by the authors of methods

M1 to M7 are being used for studying the applications and analysis of multiscale techniques in the logarithmic domain for the TTE image denoising. The name of the shrinkage technique along with the references, acronyms used for addressing them and on-line link for available resources are tabulated in Table 2.1 for quick reference.

2.2.14 Results and Discussion

Experimental results obtained for noisy Barbara image using logarithmic multiscale techniques (LM1E to LM7E) are depicted in Figure 2.3 and visual quality comparisons are shown in Figure 2.4. The performance of wavelet hard thresholding (WTHT), wavelet soft thresholding (WTST) and translation invariant wavelet transform with soft thresholding (TIWT) are compared with other logarithmic methods in Figure 2.3. The noise in Barbara image is effectively removed with structure well preserved using method LM7E as observed in Figure 2.4. Denoising performance of multiple multiscale techniques in the logarithmic domain (LM1E to LM7E, and LM11E) are initially studied and analyzed on 10 TTE images (I_1-I_{10}) where image I_1 is the AV in PSAX, I_2 is the AV in PLAX, I_3 is the LV in A4C, I_4 is the AV in A5C, I_5 is LV in A2C during systole and I_6 to I_{10} are images acquired during diastole.

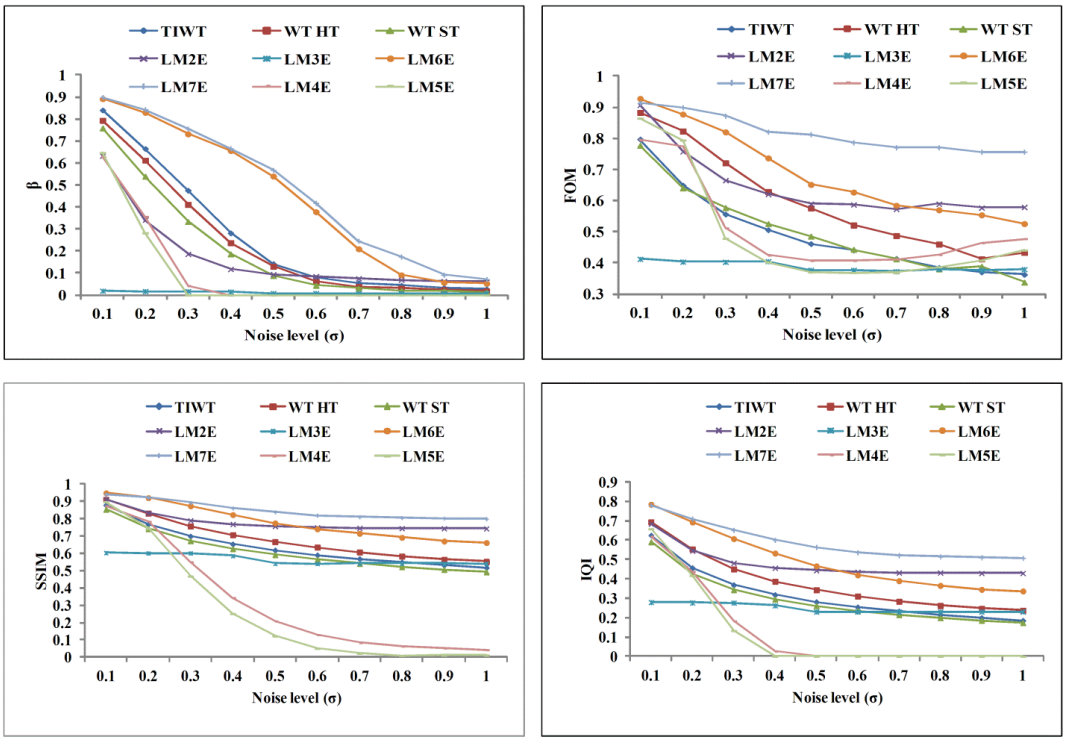

Figure 2.3 Comparison of IQM at various values of noise variance for Barbara image

Figure 2.4 Comparison of visual quality of Barbara image after denoising. a. Noisy image, b.LM1E, c.LM2E, d.LM3E, e.LM4E, f.LM5E, g.LM6E, h.LM7E, i.LM8E

The results obtained for the TTE images using all logarithmic methods are depicted in Figure 2.5. The performances of LM6E and LM7E are compared with M10, M12 to M14 in Figure 2.6. The performances of multiscale techniques for noisy Barbara image are tabulated in Table 2.2. The IQM obtained for all denoising techniques using 1000 TTE images are tabulated in Table 2.3 and Table 2.4. Table 2.3 presents a comparison of edge preservation and other parameters in terms of mean and standard deviation (mean ± std) and Table 2.4 contains various error values in denoised TTE images specified in-terms of MSE, RMSE, LMSE, NAE, Err3, Err4 and MD. The denoised images obtained on application of multiscale techniques are depicted in Figure 2.7 (PSAX view), Figure 2.8 (PLAX view), Figure 2.9 (A4C view) and Figure 2.10 (A5C

view). The clinical validation of denoised images is shown in Table 2.5. The denoised images obtained on using the MBR based filter are shown in Figure 2.11.

LM2E filter: The images are smoothed using the LM2E filter with partial loss of the texture information. It is observed that the PSNR stationed at 22.49 dB with σ≥0.7 for the Barbara image. The PSNR for LM2E filter is superior compared to despeckling techniques such as LM3E, LM5E, M8, M9, M12, M14, GLM and curvelet. It is observed that the FoM and the SSIM are greater than 0.9, indicating good edge preservation. The MSE for all TTE images I_1-I_{10} are in the range 27 to 35. The visual quality assessment reveal that the images are over smoothed, with the structure intact but the finer details lost. The IQI is moderate for all TTE and standard test images on application of LM2E filter. The clinical validation reveals that the results of LM2E filter is not completely acceptable for them. The visual qualities of denoised TTE images in multiple views, on application of LM2E are shown in Figure 2.7 to Figure 2.10.

LM3E: A window size of 3×3 is employed in the LM3E filter for experimentations at various noise levels with sym8 based dyadic wavelet transform at level 2. The values of PSNR, ρ, IQI, and FoM are better compared to the LM5E filter. The visual quality of denoised image is poor as noise is retained in the image. The values of β≤0.1 and IQI ≤0.3 speak of the poor quality of the denoised images. The edges are blurred, they are not preserved. But it is necessary to preserve the edges in the medical even after pre-processing for accurate diagnosis but this may not be possible using the LM3E filter. The visual qualities of denoised TTE images in multiple views, on application of LM3E are shown in Figure 2.7 to Figure 2.10.

Table 2.2 Comparison of IQM for Barbara image using multiscale and other techniques

Method	BETA	IQI	FOM	SSIM	ρ	PSNR	SNR	MSE	RMSE	LMSE	GAE	ERR3
LM1E	0.743	0.715	0.893	0.916	0.997	28.41	45.05	93.72	9.68	0.475	0.059	12.30
LM2E	0.629	0.671	0.894	0.912	0.996	27.15	42.52	125.42	11.20	0.607	0.059	15.67
LM3E	0.086	0.527	0.757	0.816	0.992	23.61	35.45	282.98	16.82	0.992	0.089	22.67
LM4E	0.931	0.802	0.934	0.955	0.999	32.69	53.60	35.03	5.92	0.136	0.037	7.41
LM5E	0.857	0.770	0.930	0.946	0.998	30.53	49.29	57.52	7.58	0.274	0.046	9.63
LM6E	0.856	0.719	0.911	0.935	0.998	30.17	48.56	62.58	7.91	0.275	0.050	9.76
LM7E	0.920	0.793	0.934	0.953	0.999	31.56	51.34	45.44	6.74	0.195	0.041	8.54
M8	0.725	0.684	0.706	0.888	0.996	27.32	42.9	120.5	10.98	0.687	0.071	13.1
M9	0.070	0.513	0.693	0.808	0.990	23.03	34.29	323.51	17.99	0.995	0.095	24.32
M10	0.798	0.725	0.873	0.921	0.997	28.09	44.4	100.98	10.05	0.372	0.067	12.1
LM11E	0.785	0.704	0.889	0.918	0.997	28.79	45.8	85.86	9.266	0.383	0.056	11.7
M12	0.406	0.546	0.739	0.794	0.991	20.42	29.1	590.8	24.31	1.102	0.146	31.8
M13	0.828	0.761	0.865	0.931	0.998	29.55	47.3	72.10	8.491	0.361	0.054	10.4
M14	0.754	0.704	0.88	0.896	0.996	26.46	41.1	147.03	12.13	0.531	0.073	15.6
HDTDWT	0.910	0.767	0.927	0.944	0.999	31.53	51.28	45.74	6.76	0.179	0.041	8.59
HDWT	0.866	0.749	0.916	0.933	0.998	30.39	49.00	59.49	7.71	0.252	0.047	9.87
WTHT	0.678	0.651	0.748	0.881	0.995	25.91	40.04	166.85	12.92	1.187	0.086	15.10
TIWT	0.842	0.625	0.804	0.879	0.996	26.41	41.04	48.72	12.20	0.443	0.072	15.58
GLM	0.682	0.605	0.789	0.874	0.995	26.14	40.50	158.29	12.58	0.639	0.070	16.48
Curvelet	0.676	0.650	0.750	0.882	0.995	25.92	40.06	166.52	12.90	1.196	0.086	15.08

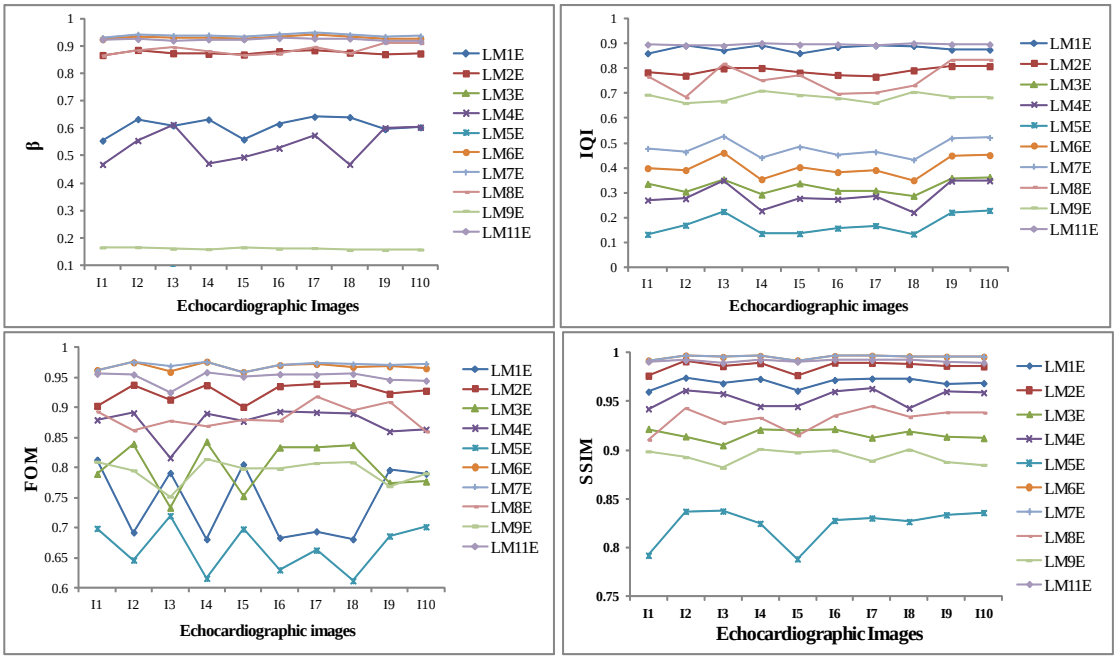

Figure 2.5 Comparison of IQM for TTE images using multiscale techniques

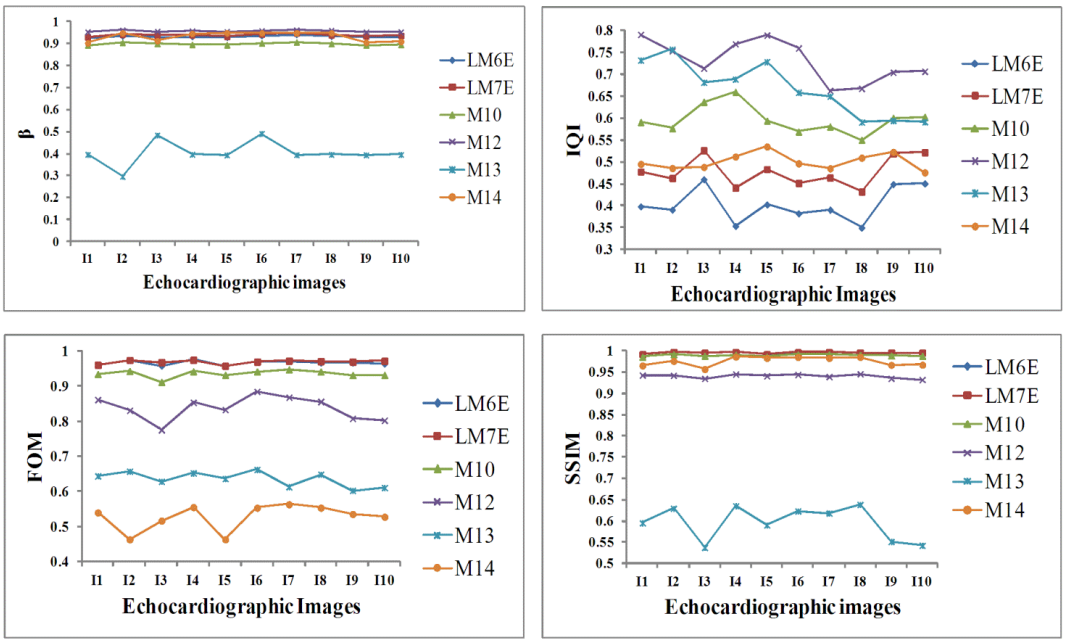

Figure 2.6 Comparison of multiscale and iterative techniques for TTE images

LM4E: The performance of the LM4E filter is good when operated for very smaller values of noise variance. But for the higher values of σ, the threshold values generated are unwarrantedly very large, leading to the induction of spurious edges in the denoised image. At σ=0.001, 0.01, 0.1, 0.2, the maximum pixel value in thresholded images are 253.3, 275.3, 487.7, and 3.3×10^3 respectively. At higher noise level improvements are observed on combining LM4E filter with adaptive Wiener filter with 3×3 windows.

LM5E: The IQM for the LM5E filter are on similar lines of the LM4E filter. The visual qualities of denoised TTE images in multiple views, on application of LM4E and LM5E are shown in Figure 2.7 to Figure 2.10.

LM6E: The wavelet with symmlet 8 is used for wavelet transformation. The PSNR for the LM6E filter is highest among the multiple multiscale techniques. The MSE is least, and ρ almost equal to 1, β= 0.93, FoM=1 and SSIM=1. The LM6E filter operating at various values of σ resulted in good noise suppression and edge preservation.

Table 2.3 Comparison of IQM for TTE images using multiscale techniques (mean ±std)

Method	BETA	IQI	FOM	SSIM	NCC	PSNR(dB)	SNR(dB)
LM1E	0.54±0.01	0.88±0.01	0.91±0.01	0.94±0.01	0.87±0.05	25.50±0.30	23.29±4.09
LM2E	0.87±0.01	0.62±0.02	0.93±0.02	0.99±0.01	0.97±0.01	33.08±0.52	37.47±1.16
LM3E	0.049±0.02	0.307±0.03	0.774±0.03	0.899±0.01	0.851±0.06	23.365±0.36	19.023±3.92
LM4E	0.85±0.04	0.39±0.04	0.99±0.01	1.00±0.00	0.99±0.03	35.53±1.57	41.86±3.99
LM5E	0.497±0.05	0.402±0.05	0.913±0.04	0.980±0.01	1.02±0.01	26.16±1.44	24.61±4.50
LM6E	0.986±0.01	0.422±0.05	0.985±0.01	0.998±0.00	0.996±0.01	42.542±2.33	57.377±0.94
LM7E	0.964±0.01	0.510±0.05	0.97±0.01	0.99±0.00	0.99±0.03	37.08±0.79	45.46±0.87
M8	0.78±0.02	0.67±0.03	0.67±0.06	0.90±0.01	0.93±0.03	28.53±0.12	29.11±4.32
M9	0.16±0.01	0.67±0.02	0.80±0.02	0.90±0.01	0.84±0.05	23.55±0.32	17.95±2.15
M10	0.95±0.00	0.61±0.02	0.97±0.01	1.00±0.00	0.98±0.00	36.35±0.29	43.48±1.53
LM11E	0.97±0.01	0.87±0.01	0.95±0.01	0.99±0.01	0.99±0.01	40.02±0.81	51.35±0.98
M12	0.99±0.01	0.95±0.00	0.96±0.01	1.00±0.00	1.00±0.00	46.96±0.83	65.41±1.11
M13	1.00±0.00	0.71±0.02	1.00±0.00	1.00±0.00	1.00±0.00	52.07±2.63	74.92±3.24
M14	0.86±0.01	0.52±0.02	0.64±0.04	0.93±0.01	0.96±0.01	30.53±0.36	31.85±1.50
GLM	0.987±0.01	0.64±0.02	0.98±0.01	1.00±0.00	1.00±0.00	41.33±0.38	53.97±2.30

Table 2.4 Comparison of error based IQM for TTE images using multiscale techniques

Method	MSE	RMSE	LMSE	GAE	ERR3	ERR4	MD
LM1E	183.85±13.02	13.55±0.47	0.81±0.01	0.14±0.03	27.86±0.58	42.06±0.59	226.34±5.52
LM2E	32.18±3.83	5.66±0.34	0.24±0.02	0.08±0.01	10.89±0.22	16.95±0.21	172.4±0.01
LM3E	300.68±26.21	17.33±0.74	1.01±0.01	0.21±0.05	33.97±0.81	50.41±0.79	271.72±0.05
LM4E	19.34±7.67	4.33±0.81	0.37±0.11	0.05±0.02	12.63±2.25	8.35±1.36	117.60±41.90
LM5E	166.75±60.49	12.73±2.19	3.15±0.97	0.06±0.01	44.33±13.10	95.46±37.91	169.5±92.6
LM6E	4.19±2.54	1.97±0.55	0.04±0.02	0.03±0.00	3.38±0.65	4.99±0.66	47.21±2.64
LM7E	12.94±2.37	3.58±0.33	0.11±0.01	0.06±0.01	6.64±0.32	10.44±0.27	102.4±3.81
M8	91.25±2.51	9.55±0.13	0.47±0.04	0.16±0.04	25.75±1.20	17.21±0.59	214.77±14.72
M9	287.6±22.15	16.95±0.63	0.98±0.01	0.23±0.03	33.56±1	50.04±1.03	246.4±4.33
M10	15.12±1.02	3.89±0.13	0.14±0.01	0.06±0.00	10.12±0.06	6.96±0.08	74.33±0.26
LM11E	6.57±1.20	2.55±0.24	0.05±0.01	0.05±0.01	3.87±0.23	5.04±0.23	28.31±1.97
M12	3.33±0.25	2.15±0.11	1.01±0.00	1.02±0.00	2.64±0.11	2.99±0.10	5.03±0.60
M13	3.47±0.29	0.66±0.20	0.01±0.00	0.01±0.00	2.12±0.54	1.35±0.37	19.73±4.34
M14	57.74±4.67	7.59±0.31	0.28±0.02	0.15±0.01	15.25±0.23	11.63±0.26	84.13±1.79
GLM	4.80±0.46	2.19±0.10	0.01±0.01	0.02±0.01	5.40±0.15	8.95±0.20	62.3±0.17

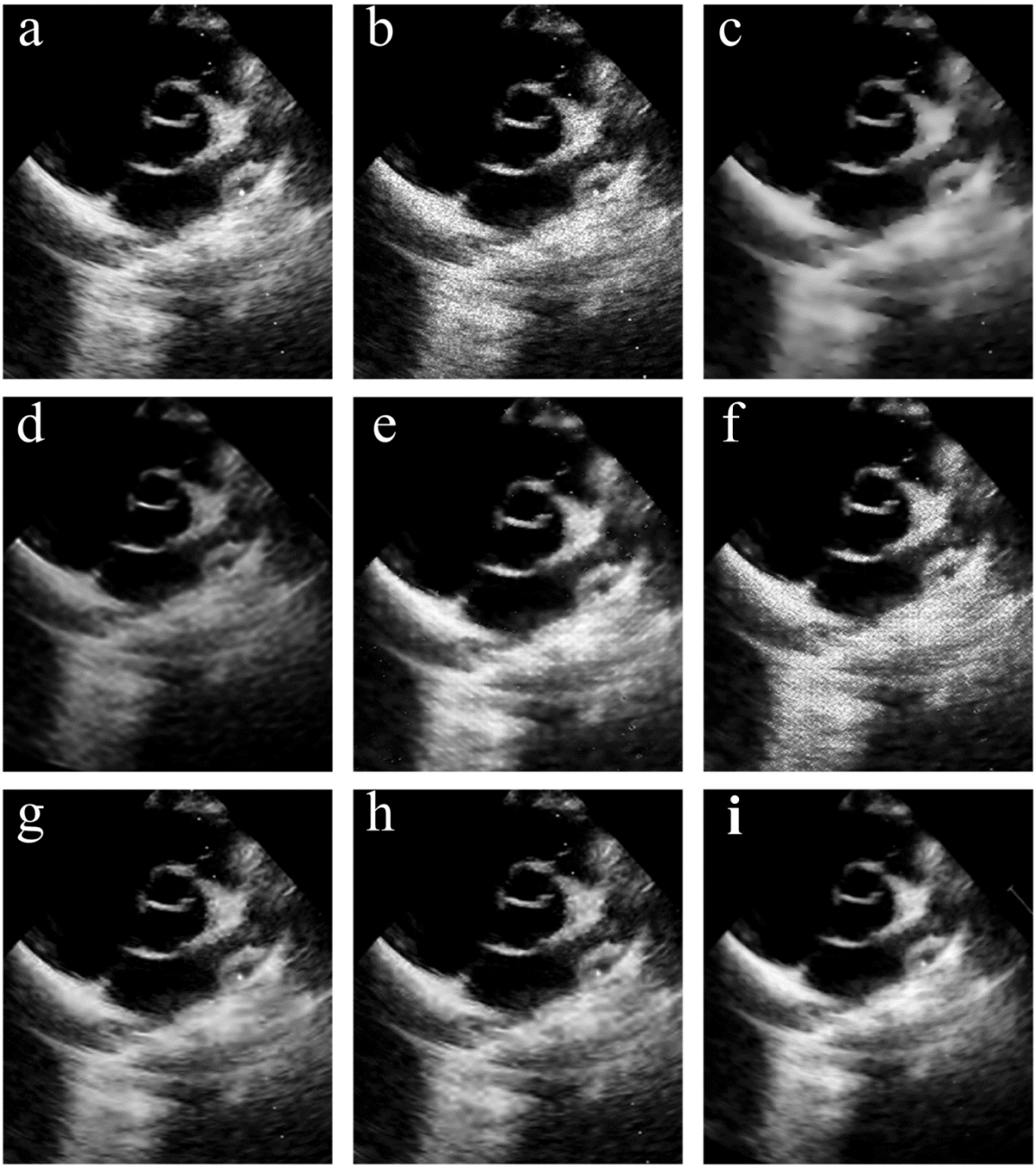

Figure 2.7 Denoising of TTE images in PSAXD view using multiscale techniques. a. Original image, b.LM1E, c.LM2E, d.LM3E, e.LM4E, f.LM5E, g.LM6E, h.LM7E, i.M8

LM7E: The wavelet decomposition is at level 2 with sym8 type of filter is employed during the analysis of LM7E filter. The performance of the LM7E filter is superior compared to other methods. The IQM such as the FoM, SSIM, ρ and β are all almost equal to one, which reflect superior performances compared to other methods. The PSNR is higher than the non-homomorphic methods considered for comparison. The variation of β between LM7E and LM6E is about 0.01 with ρ and FoM quite similar but the values of MSE is lesser using the LM7E filter.

The PSNR is around 4dB higher, MSE is lesser by 17 for LM7E filter compared to M10, M12 and M14. The values of β, ρ and FOM of LM7E filter are similar compared to the SRAD filter (fractionally around 0.04 higher using the LM7E filter).

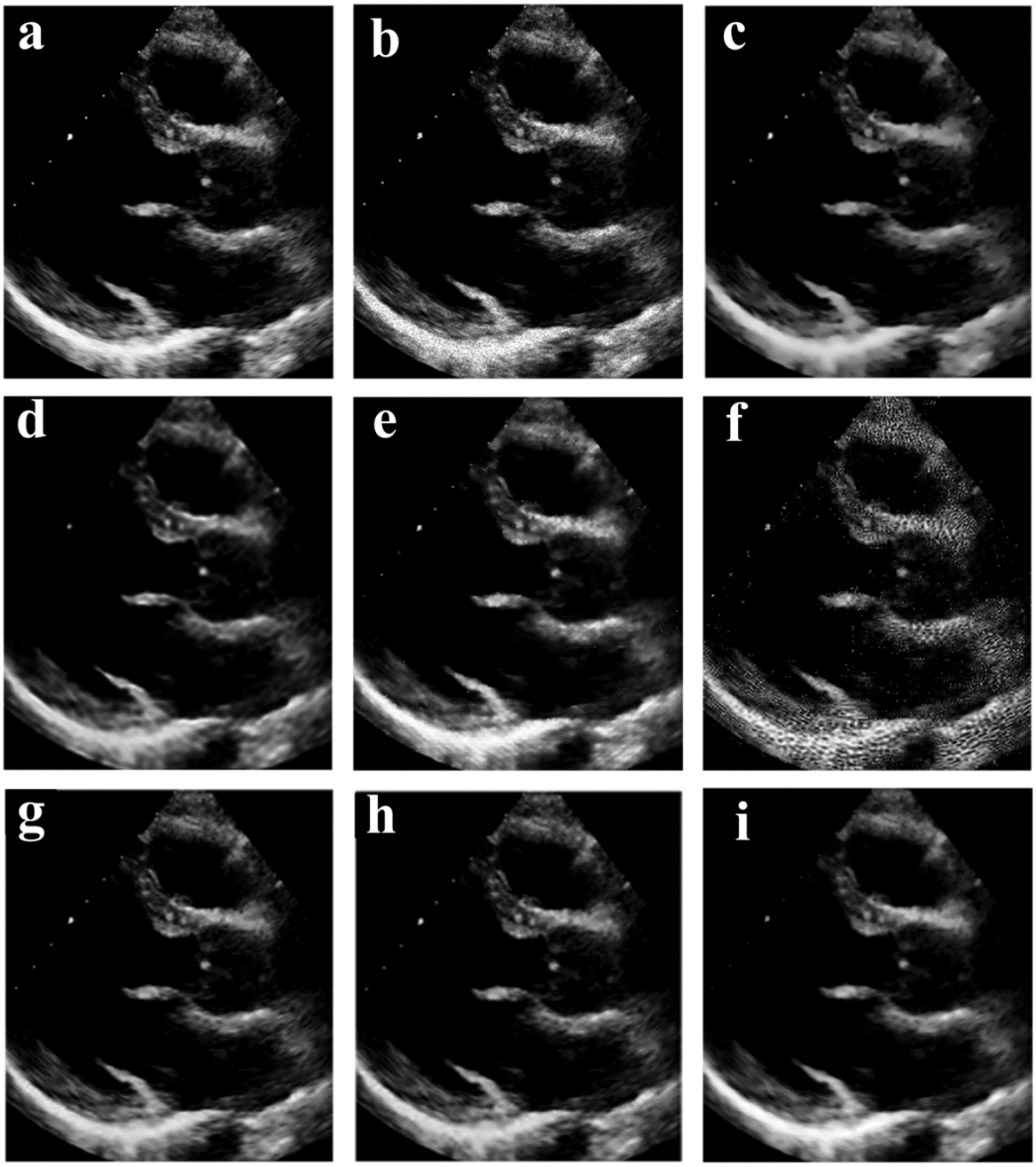

Figure 2.8 Denoising of TTE images in PLAXD using multiscale techniques. a. Original image, b.LM1E, c.LM2E, d.LM3E, e.LM4E, f.LM5E, g.LM6E, h.LM7E, i.M8

M8: The performance analysis shows that the application of M8 filter results better edge preserved images with β≈0.8, FoM≈0.9, MSE≈40-63. Noise reduction specified using PSNR

values are greater for M8 filter compared to the GLM, M14, M12, M9 and curvelet based filters. The IQI and β value obtained using LM4E to LM7E filters are better compared to M8 filter. The visual qualities of denoised TTE images in multiple views, on application of M8 filter are shown in Figure 2.7 to Figure 2.10.

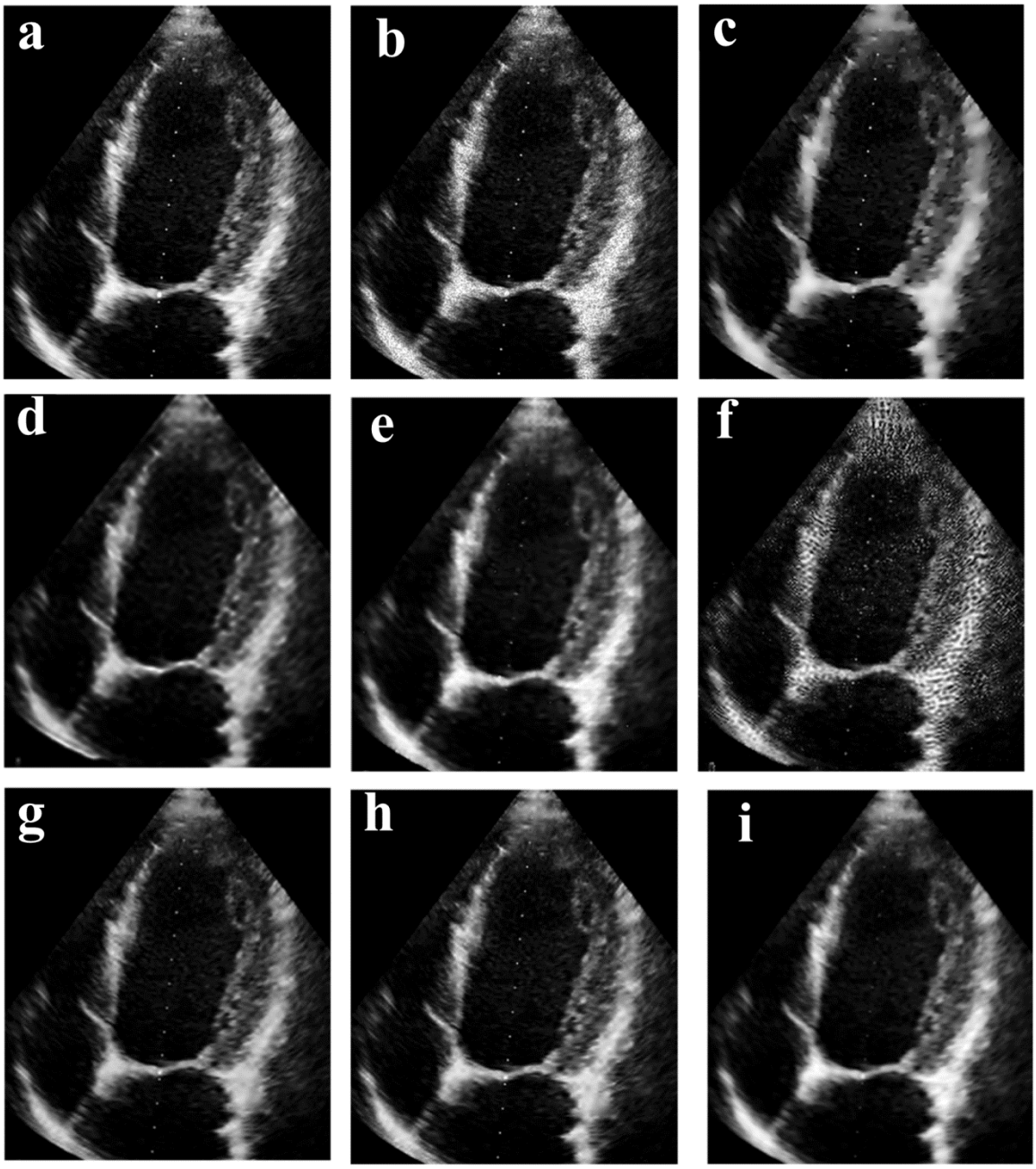

Figure 2.9 Denoising of TTE images in A4C using multiscale techniques. a. Original image, b.LM1E, c.LM2E, d.LM3E, e.LM4E, f.LM5E, g.LM6E, h.LM7E, i.M8

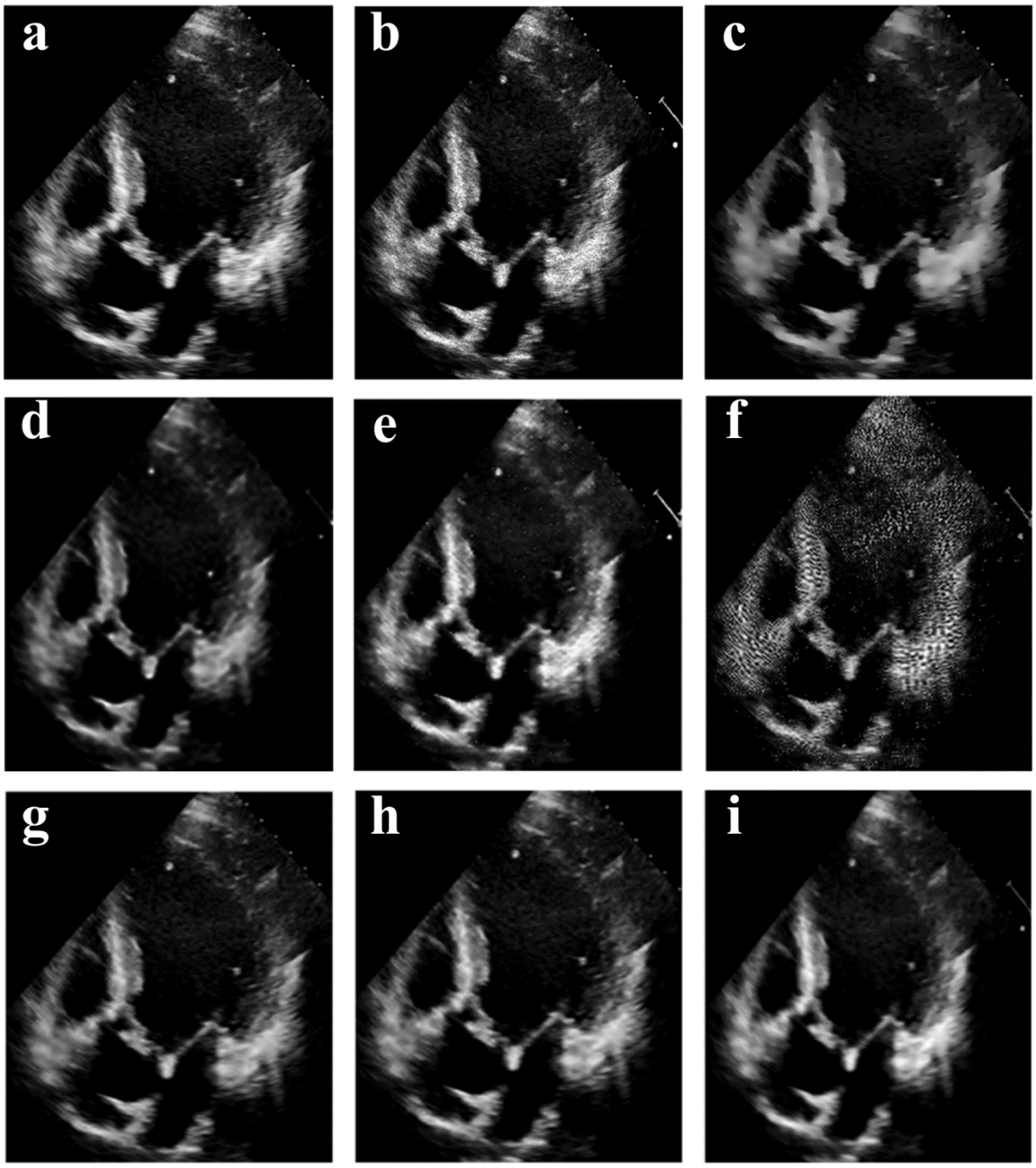

Figure 2.10 Denoising of TTE images in A5C using multiscale techniques. a. Original image, b.LM1E, c.LM2E, d.LM3E, e.LM4E, f.LM5E, g.LM6E, h.LM7E, i.M8

M9: The IQI obtained using the proposed M9 filter is superior in comparison to LM1E, LM3E, LM4E, LM5E, LM6E and non-homomorphic methods M10 and M12. The performance of LM9E filter is better compared to the M5 filter in terms of all IQM. But the SSIM is lesser than LM1E to LM8E except in the case of M5. The images are smoothed and the finer details in the TTE images are lost. The denoised images obtained on application of the MBR filter are shown in

Figure 2.11. The smoothing of TTE images is observed in second row of Figure 2.11 on application of the MBR filter.

Clinical validation: The validation of denoised images is carried out by grading of images by four clinical practitioners at PGI, Chandigrah. The grading of images is based on visual perception and preservation of contents in the image.

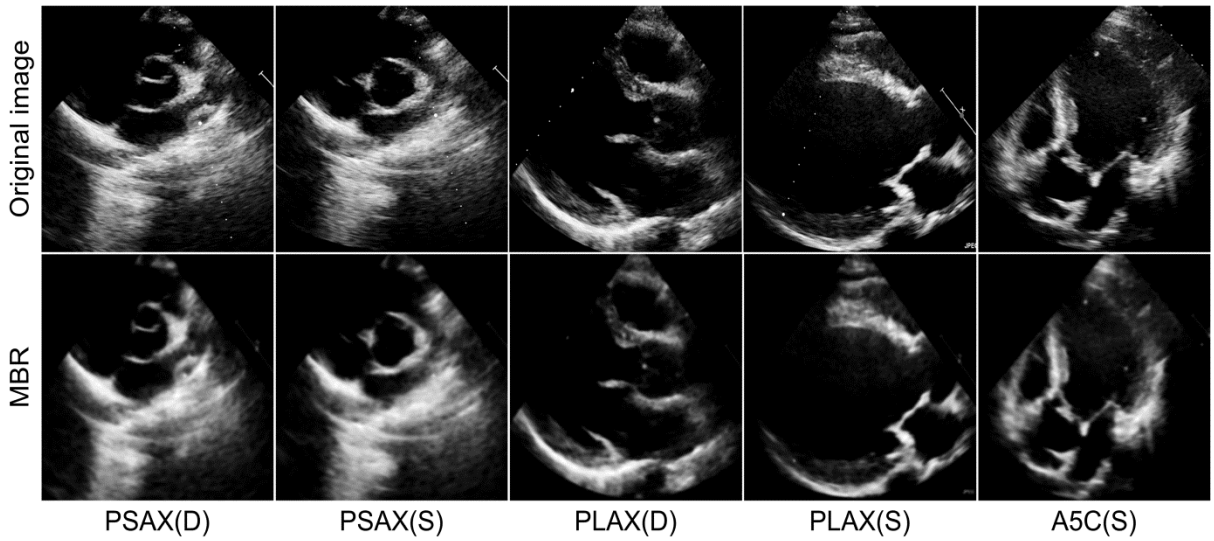

Figure 2.11 Visual qualities of TTE images on application of MBR filter

Table 2.5 Grading of denoised images by clinicians

Filter Name	Grade	Filter Name	Grade
LM2E, PMAD	4	LM6E, M8, Wiener filter	7
LM1E, LM5E	5	LM7E, GLM, DPAD	8
LM4E, SRAD	6	Geometric filter	9

The team of evaluators consisted of a senior experienced clinical practitioner working as Professor in Department of Cardiology, and the other three are post-graduate students at PGI, Chandigrah. Grading is carried out by awarding values from 1 to 10; 1 signifies bad quality and 10 for highest visual quality of the image. The average grades of each method are tabulated in Table 2.5. The grading reveals that LM6E, LM7E, LM11E, GLM, DPAD, geometric, and AFTV filters are acceptable while LM2E, LM1E and LM5E filters are not completely acceptable.

Comparison of multiple multiscale techniques

The values of PSNR obtained for standard test images at various noise levels show that the performance of LM4E filter and LM6E filter are superior compared to all multiscale schemes.

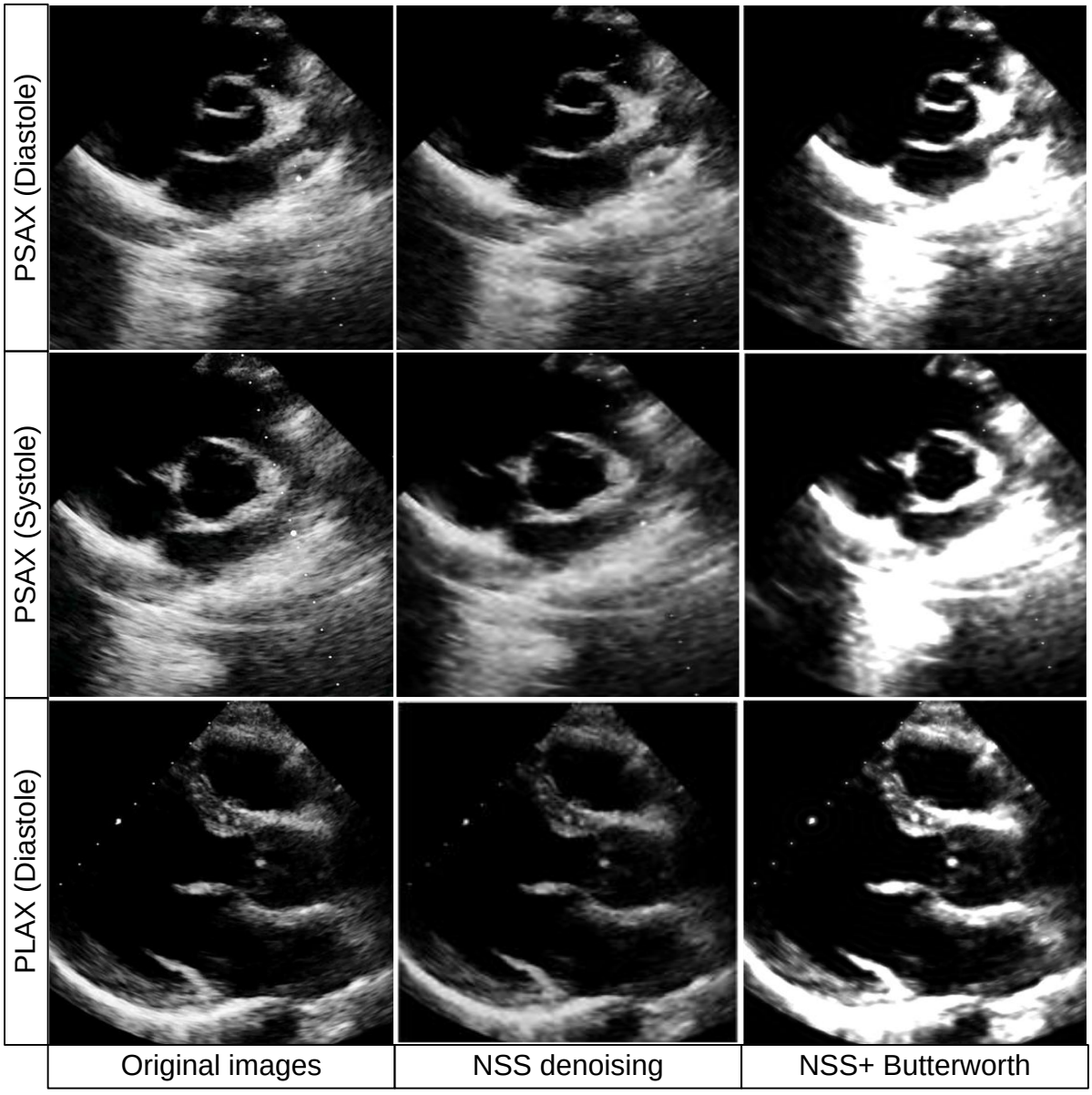

Figure 2.12 Visual qualities of denoised and enhanced images

The visual quality of LM6E filter and LM7E filter are better superior compared to the LM4E filter in terms of finer details preservation. In case of the TTE images the edge preservation is better using LM7E filter compared to other techniques. The values of FoM, β, SSIM, and NCC are almost equal to one. This means that edges and structures are well preserved using LM7E filter. The values of FoM for M2, M4, M6, M7 and M8 filter are greater than 0.85 which show good edge preservation in these methods. The β for the LM2E, LM6E and LM7E filters are 0.87, 0.93 and 0.93 respectively, representing high edge preservation. The MSE of denoised images for methods based on M6 and M7 filters are minimum compared to others. The IQI for LM1E,

LM2E, LM8E and LM9E filters are 0.9, 0.8, 0.9 and 0.7, respectively indicating that the correlation, luminance and contrast of the images are well maintained. Based on these observation it may be concluded that the overall performance of LM6E and LM7E filters are superior among the multiscale and iterative despeckling techniques.

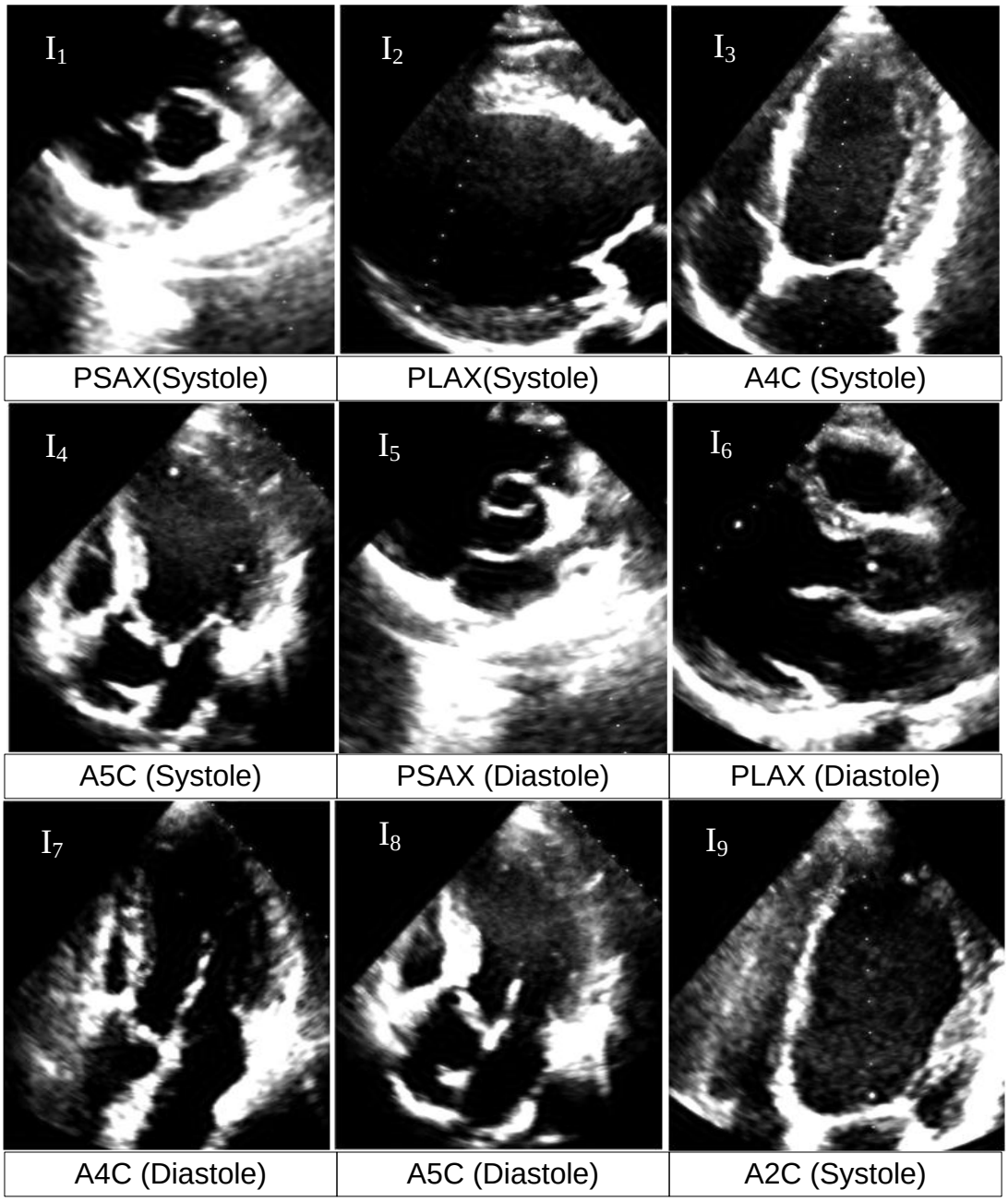

Figure 2.13 Visual qualities of TTE images using LM7E and Butterworth filters

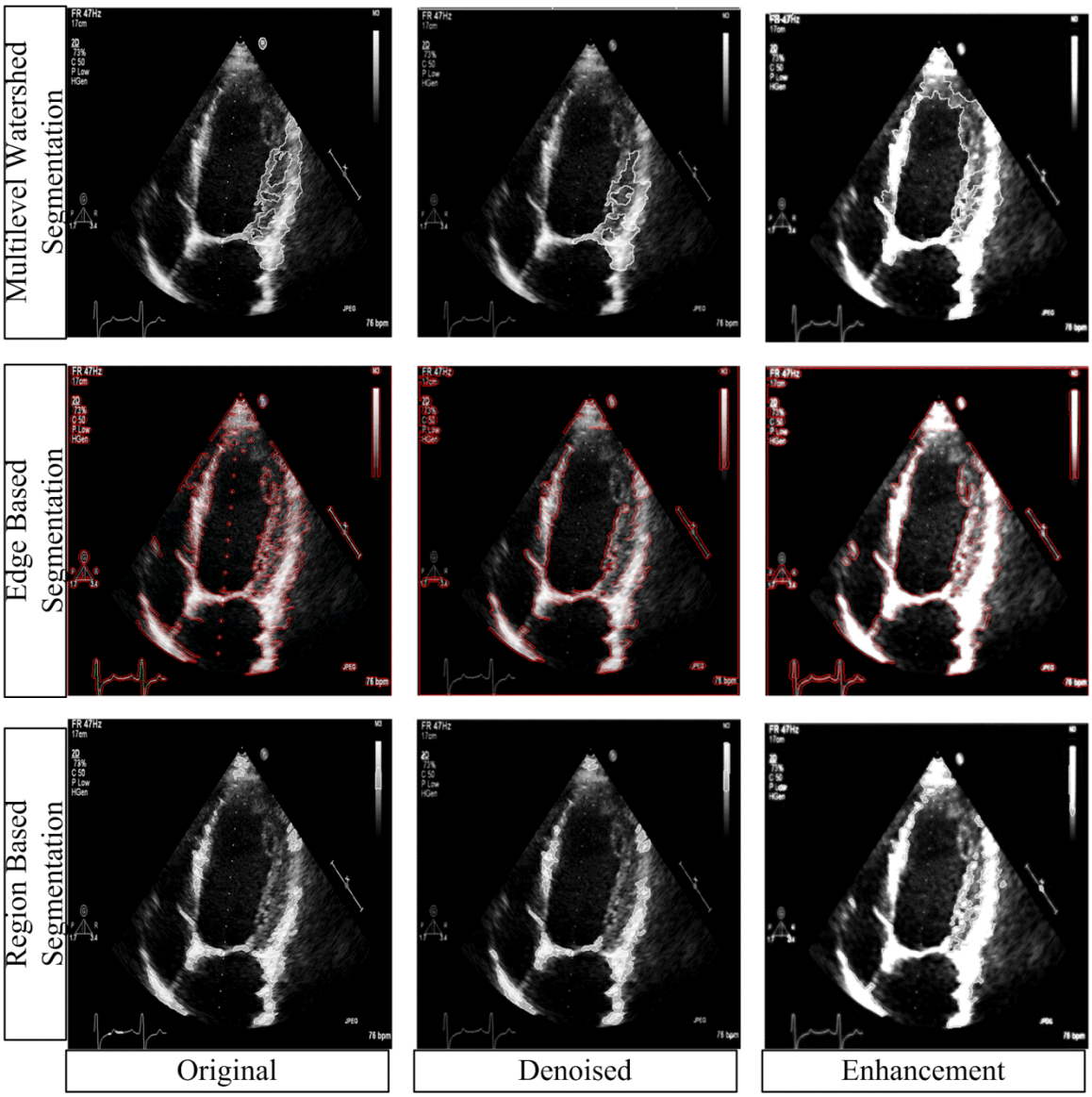

Figure 2.14 Multilevel watershed, edge and region based segmentation, First column original images, second column denoised images and third column enhanced images

Comparison of multiscale techniques with other denoising methods

The values of β and FoM are better using LM7E filter compared to M8, M9, M10, M12 and M14 filter for standard test images and the TTE images. Also the performance of LM7E filter is on-par with DPAD and geometric filter in-terms of β and FoM value. The values of PSNR is 2.9 dB to 37.5 dB for filters such as the M7, M10, M11 and M12 filters compared to the values in the range (44.5dB to 46.2dB) for M6. The SSIM ≥ 0.98 for LM6E, LM7E, M10 and M11 filters, FOM ≥ 0.96 for M6 and M7 filters while it is between 0.91 to 0.95 for M10 and M11 filters, and MSE < 15 for LM6E and LM7E filters. The β is 0.92 to 0.94 for M6 and M7 filters and 0.89 to 0.91 for the M10 and M11 filter but it is 0.95 for the geometric filter. Based on these comparisons a

conclusion is made i.e. the performance of LM7E and LM6E filters are better compared to most of the non-wavelet based techniques.

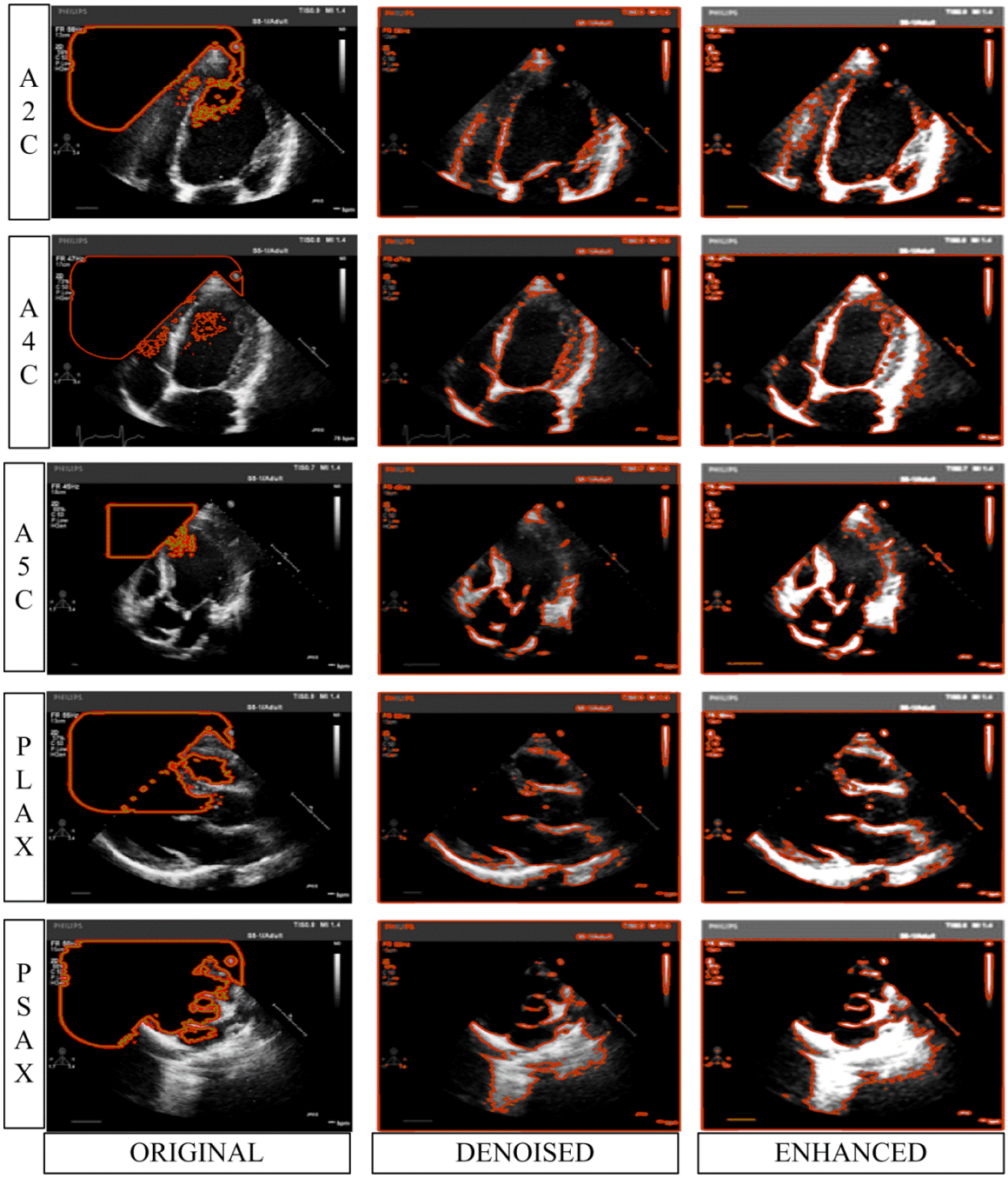

Figure 2.15 Active contour based segmentation, First column original images, second column denoised images and third column enhanced images

The boundaries are delineated using region growing based segmentation method and tracing are acceptable. But seed and threshold selection are difficult for the low contrast images

like those of the TTE. The cardiac boundaries traced using multilevel watershed segmentation is better compared to other edge and region growing methods but this method at times leads to over segmentation. It is also observed that the boundaries are better traced and more complete in the enhanced images compared mere denoised images. The enhanced images are compared with the original and denoised images in Figure 2.12 and Figure 2.13. The effects of denoising and enhancement on boundary detection using multilevel watershed, region and edge based segmentation combined with morphological operations are shown in Figure 2.14 for A4C view. The application of active contour segmentation based on images acquired in parasternal and apical views are shown in Figure 2.15.

The Chan-Vese model [64] of active contour segmentation with manual selection of initial contour is employed for delineation of the cardiac structures boundaries and the results are shown in Figure 2.15. The original images are shown in the first column, the second and third column contain the denoised and enhanced images, respectively. The denoised image is passed through another filter and the obtained enhanced images are shown as “enhanced” images in Figure 2.15. Careful observation reveals that enhancement of images helps in accurate inner and outer cardiac and valvular boundaries delineation which is visible in the denoised images. The enhancement of images seems to be resulting in complete contour based boundaries whereas discontinuities in the delineated contours are observed in multilevel watershed segmentation of denoised images. The performance of active contour based segmentation is better compared to region, edge and watershed transform based segmentation. The complete contours are traced using enhanced images in comparison to original and denoised images.

2.3 Hybrid posterior sampling based Bayesian estimation Filter

Various authors have employed Bayesian estimation in reduction of noise. Achim *et al.* [34] proposed Bayesian estimation in the homomorphic domain for reduction of speckle noise in the US images of kidney. Hua *et al.* [236] integrated wavelet Bayesian despeckling with regularization based on the Markov random field for reduction of noise in the SAR images. The local weighted average is computed using the Bayesian estimator, which assisted in computing the noise free component. An optimal threshold for wavelet shrinkage based on Bayesian formulation was proposed by Gupta *et al.* [110]. The sub-band wavelet coefficients were modelled using generalized Gaussian distribution (GGD). The optimum threshold is estimated by minimizing the Bayes’ risk function. The resultant threshold is computed as the ratio of sub-band standard deviation to the noise variance multiplied by proportionality constant [110].

The optical coherence tomography (OCT) images like SAR and the US techniques are also affected by speckle noise [22, 82, 228, 232]. The logarithmic based posterior sampling Bayesian estimation (PSBE) was employed in cutback of speckle noise present in rodent retinal OCT images [228]. As stated earlier, the TTE images also suffer from ill effects of speckle noise. It is felt that the PSBE technique can be tapped in for noise reduction in the TTE images. It is also observed that the performance of PSBE technique degraded drastically for noisy TTE images. It was pointed out by Mateo *et al.* [26] that the sequential or parallel combinations of filters would fine tune the despeckling characteristics of filters. Taking into consideration the conclusions of Mateo et al. it is proposed to embed PSBE with Wiener filter. To address the issues, it is proposed to embed spatially adaptive Wiener filter at various stages like before transforming image into logarithmic space, or after logarithmic operation or both before and after logarithmic transformation, followed by PSBE and exponential operation in each of the cases. These techniques are known as hybrid PSBE filters. They are briefly described in this sub-section. The complete details of the PSBE technique are available in [228, 232].

2.3.1 Posterior sampling Bayesian estimation (PSBE)

This method is based on the conditional posterior sampling approach with Bayesian estimation for the denoising of speckle noise present in the rodent retinal OCT images [228]. In this technique, the noise free details are computed using the Bayesian least square error computations using the conditional posterior sampling and then the average squared error is minimized. The unknown target distribution is anticipated employing an indirect scheme from a recognized preliminary likelihood distribution *Q*. Let a random position s' in the initial site s and it is computed depending upon the preliminary probability distribution $Q(s' \mid s)$ defined as [228]

$$Q(s' \mid s) = 1/2\pi\sigma_{spatial}\, e^{-(\|s'-s\|^2/2\sigma^2_{spatial})} \tag{2.42}$$

where $\|s'-s\|^2$ is the Euclidean distance squared between s' & s, and $\sigma_{spatial}$ is the spatial variance. The preliminary probability has tendency of producing sites in the close proximity of initial site s. The new site s' is taken into consideration with local mean $\mu(s)$ and noise variance σ^2 if the condition brought out using Equation 2.43 [228] is satisfied. This step is repeated to incorporate maximum number of sites in the neighborhood of the initial site s

$$|\mu(s) - \mu(s')| < 2\sigma \tag{2.43}$$

The weights at each site are computed using Equation 2.44 [228]

$$w(s_i' \mid s) = \exp(-\left|\mu(s) - \mu(s')\right| / 2\sigma^2) \tag{2.44}$$

A weighted histogram approach is employed for evaluation of the posterior distribution [228] with δ (.) as the Dirac delta function and Z is normalization term. The posterior evaluation is represented in Equation 2.45 as

$$\hat{P}(g_l(s) \mid f_l(s)) = \left(\sum_{k=\Omega} w(s_k' \mid s)\delta(g_l - f_l(s_k')) \right) / Z \tag{2.45}$$

The minimized Bayesian least square estimation is computed as [228]

$$\hat{g}_l(s) = \int p(g_l(s) \mid m_l(s)) g_l(s) dg_l(s) \tag{2.46}$$

The image is transformed into the logarithmic space in accordance to Equation 1.2 and a new site s' is drawn based on Equation 2.42. The local mean $\mu(s)$ confined to the neighbourhood with its centre at s is estimated. A 7×7 region centred at s is utilized in computation of the local mean and variance in all the experimentations. The inclusion of the site s' as the realization of posterior sampling is based on satisfactory realization of the conditional sampling proposed by Equation 2.43. It is assumed that the local mean provides the initial estimate of noise free data. This determines the enclosure of the site s' as realization of the posterior distribution with conditional sampling. The procedure of conditional sampling is recursively performed, so that maximum number of sites could be incorporated in the computation of the image with zero noise. The weights for each site to be embedded in sampling are computed using Equation 2.44, which is based on Gibbs likelihood function. The weighted histogram estimation is followed by the normalization of the histogram bin. This estimation is utilized in posterior distribution and this is represented in Equation 2.45. The accumulated weights for each of the sites are those of the acquired information.

The generalized Bayesian estimation using Equation 2.47 is performed followed by the exponential operation. Thus obtained denoised images are used for IQM estimation and analysis of the PSBE filter for the TTE images. Butterworth filter is employed for the enhancement of the TTE images [245, 249]. This filter is able to suppress the noise with preservation of edge. No ringing artifacts are induced in the image during enhancement process, and the performance is superior compared to the median filter and average filter. This Butterworth filter is also used for enhancement of the US images [245], hence in this thesis it is being employed for contrast enhancement of the TTE images of the aortic valve.

2.3.2 Proposed hybrid PSBE schemes (N1-N4)

The performance of logarithmic based PSBE filter [228] is considerably degraded when the TTE images are very noisy or the images are embedded or simulated with high speckle noise. To overcome this problem a spatially adaptive Wiener filter is sequentially combined with PSBE filter. The Wiener filter is used for despeckling of the US images [80, 110, 116, 248]. The Wiener filter is very effective and optimum in denoising of additive noise and the performance of Wiener in homomorphic domain is on par with other denoising techniques [11, 32, 104-109, 113, 116]. This filter enhances the outskirt of the spectrum, and is the optimal filter for US images [11]. The Wiener filter is also known for its restoring characteristics [80, 248]. The performance of PSBE filter is superior in comparison to others methods. Hence, the PSBE filter and the adaptive Wiener filter are combined in the logarithmic domain and are referred to as hybrid PSBE filter. The proposed modifications incorporated in the PSBE filter are tabulated in Table 2.6.

The image is projected into the logarithmic space, filtered using adaptive Wiener filter, and subjected to PSBE. This hybrid scheme is represented as method N1. This hybrid scheme is very effective at all noise levels. The performance of the filter improved, when the noisy image is pre-filtered using adaptive Wiener filter and subjected to PSBE in the logarithmic domain. This scheme is known as method N2. The edge preservation improved further when Wiener filter is embedded both before and after log transformation followed by the PSBE filter. This modification is represented as represented as N3. The modified method N3 introduces over-smoothing at lower noise levels. The denoised images obtained using N3 method followed by adaptive Wiener filtering is represented as scheme N4. The edge preservation and reduce distortion are further enhanced in scheme N4. This scheme also leads to over-smoothing but most of the IQM improve in N4 scheme. In all the four modifications suggested, the implementation of the PSBE filter is on the similar lines as explained earlier.

Table 2.6 Hybrid PSBE techniques for denoising of TTE images

Method	Author	Name of the method	Type	Modification
N [228]	Wong, Mishra, Bizheva and Clausi [228]	PSBE	LSE	Embed Wiener filter
N1	First proposed hybrid PBSE method: Logarithmic transformation+ adaptive Wiener filtering + PSBE +exponential			
N2	Second proposed hybrid PBSE method: Adaptive Wiener filtering + Logarithmic transformation+ PSBE +exponential			
N3	Third proposed hybrid PBSE method: Adaptive Wiener filtering + N1			
N4	Fourth hybrid PBSE method: N3+ Adaptive Wiener filtering			

The proposed modifications look similar but with exclusion or inclusion of Wiener filtering at a particular point as shown in Table 2.6. The denoised images are enhanced using Butterworth filter. The enhanced TTE images would aid automated process of tracing the boundaries.

2.3.3 Results

The performances of hybrid PSBE schemes are compared with the PSBE filter. The methods are analyzed for denoising of TTE images of the AV and cardiac chambers in five views. As pointed out in the earlier sections, many researchers speak of noise reduction in terms of PSNR, SNR, and MSE, but not the edge preservation on application of filters.

Table 2.7 Comparison of PSNR for PSBE and hybrid PSBE methods

Echo image	**σ^2**	**PSNR for PSBE at various values of spatial variance**									**Proposed methods**			
		0.1	0.2	0.3	0.4	0.5	0.6	0.7	0.8	0.9	N1	N2	N3	N4
I1	0.05	26.6	26.8	27.8	**28.4**	28.1	27.6	26.9	26.4	25.8	**29.4**	**28.9**	**29.5**	**29.2**
	0.1	23.8	24.1	25.2	26.2	**26.4**	26.4	26.0	25.6	25.2	**27.3**	**26.9**	**27.5**	**27.4**
	0.2	21.1	21.2	22.4	23.5	24.0	**24.1**	24.1	24.0	23.7	**25.2**	**24.5**	**25.5**	**25.4**
	0.3	19.5	19.6	20.8	21.6	22.0	22.1	**22.1**	22.0	22.0	**23.5**	**22.2**	**23.7**	**23.5**
I2	0.05	26.9	28.4	29.2	**29.3**	28.5	27.7	26.9	26.2	25.6	**30.0**	**28.9**	**29.5**	**29.0**
	0.1	25.3	25.5	26.5	27.2	**27.2**	26.6	26.1	25.5	25.1	**27.9**	**26.9**	**27.7**	**27.4**
	0.2	22.5	22.7	23.8	24.8	24.9	**25.0**	24.5	24.3	23.9	**25.7**	**24.8**	**25.6**	**25.5**
	0.3	20.9	21.1	22.0	22.9	**23.1**	23.0	23.0	22.8	22.5	**24.0**	**22.9**	**24.0**	**24.0**
I3	0.05	27.4	27.6	28.5	**28.7**	28.1	27.4	26.6	26.0	25.5	**29.5**	28.5	**29.0**	**28.7**
	0.1	24.5	24.7	25.8	**26.7**	26.5	26.2	25.8	25.3	24.9	**27.4**	26.6	**27.3**	**27.2**
	0.2	21.7	21.9	23.1	23.9	24.3	**24.4**	24.1	23.8	23.6	**25.2**	**24.4**	**25.2**	**25.2**
	0.3	20.1	20.3	21.4	22.1	22.4	**22.5**	22.4	22.1	22.1	**23.6**	22.3	**23.5**	**23.7**
I4	0.05	28.3	28.6	29.4	**29.4**	28.8	27.9	27.2	26.6	25.9	**30.3**	29.3	**29.7**	29.4
	0.1	25.5	25.8	26.8	27.4	**27.6**	26.9	26.4	25.9	25.4	**28.1**	27.3	**28.0**	27.8
	0.2	22.7	22.9	24.1	25.0	25.2	**25.1**	24.9	24.7	24.4	**26.1**	25.2	**26.0**	**25.9**
	0.3	21.0	21.3	22.3	23.0	23.5	**23.5**	23.3	23.1	23.0	**24.6**	**23.6**	**24.7**	**24.6**

Table 2.8 Comparison of β for PSBE and hybrid PSBE filters

Echo image	**σ^2**	**Beta metric for PSBE at various spatial variance**									**Proposed methods**			
		0.1	0.2	0.3	0.4	0.5	0.6	0.7	0.8	0.9	N1	N2	N3	N4
I1	0.05	0.51	0.52	0.54	0.59	**0.62**	0.62	0.58	0.52	0.45	**0.66**	**0.81**	**0.83**	**0.84**
	0.1	0.38	0.39	0.42	0.46	0.50	**0.52**	0.50	0.45	0.38	**0.55**	**0.73**	**0.74**	**0.75**
	0.2	0.28	0.27	0.30	0.33	0.37	0.38	**0.39**	0.34	0.30	**0.43**	**0.55**	**0.54**	**0.55**
	0.3	0.22	0.22	0.25	0.27	0.29	0.30	**0.30**	0.26	0.23	**0.33**	**0.35**	**0.38**	**0.38**
I2	0.05	0.63	0.60	0.62	0.67	**0.69**	0.67	0.63	0.56	0.48	**0.72**	**0.82**	**0.84**	**0.84**
	0.1	0.46	0.46	0.49	0.54	0.58	**0.58**	0.56	0.50	0.43	**0.62**	**0.75**	**0.76**	**0.76**
	0.2	0.33	0.34	0.36	0.41	0.44	**0.46**	0.44	0.40	0.35	**0.50**	**0.61**	**0.59**	**0.61**
	0.3	0.27	0.27	0.29	0.32	0.35	**0.36**	0.35	0.32	0.28	**0.39**	**0.44**	**0.43**	**0.44**
I3	0.05	0.56	0.57	0.60	0.64	**0.66**	0.66	0.61	0.54	0.47	**0.71**	**0.82**	**0.83**	**0.84**
	0.1	0.44	0.44	0.47	0.52	0.55	**0.56**	0.53	0.48	0.42	**0.60**	**0.74**	**0.76**	**0.76**
	0.2	0.31	0.32	0.35	0.38	0.41	**0.43**	0.42	0.38	0.33	**0.47**	**0.61**	**0.57**	**0.58**
	0.3	0.25	0.26	0.28	0.31	0.33	**0.34**	0.33	0.29	0.25	**0.36**	**0.40**	**0.40**	**0.42**
I4	0.05	0.59	0.59	0.63	0.66	**0.68**	0.67	0.62	0.55	0.47	**0.73**	**0.83**	**0.83**	**0.83**
	0.1	0.45	0.46	0.48	0.53	0.57	**0.57**	0.55	0.49	0.42	**0.62**	**0.75**	**0.76**	**0.76**
	0.2	0.33	0.33	0.36	0.40	0.42	**0.44**	0.43	0.39	0.34	**0.49**	**0.59**	**0.58**	**0.59**
	0.3	0.26	0.27	0.28	0.30	0.35	**0.35**	0.34	0.31	0.27	**0.40**	**0.44**	**0.44**	**0.45**

But it is necessary to speak of the edge preservation and distortion of the images as edges provide important details. The edge preservation and distortion can be measured using the FoM, β and SSIM [23, 35, 231]. The performance of PSBE filter and hybrid PSBE filters are first tested using standard gray scale test images. And later the performance is evaluated for the denoising of the TTE images of the AV and cardiac chamber.

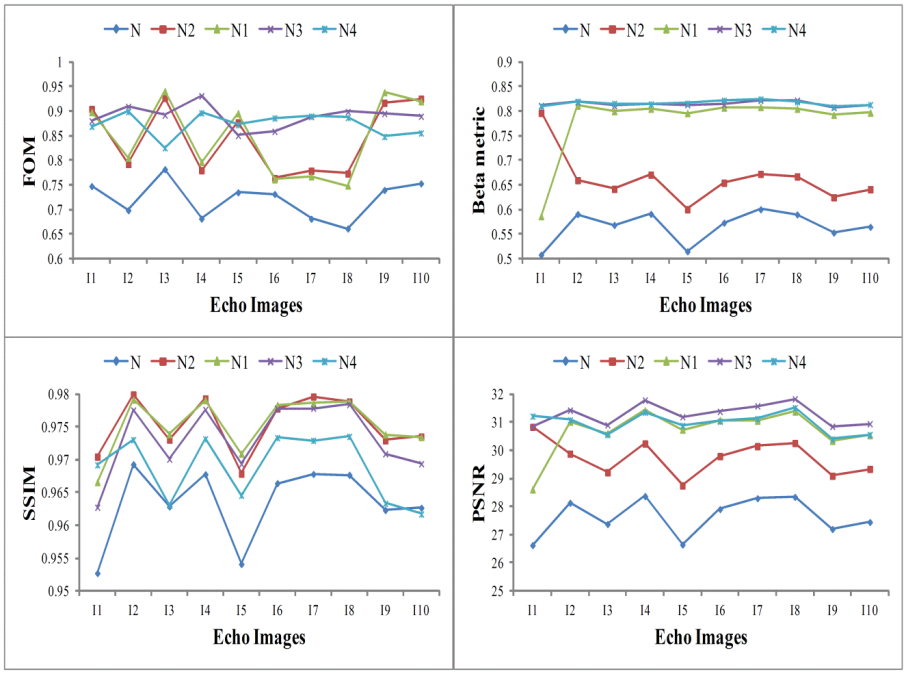

Figure 2.16 Comparison of IQM for TTE images using PSBE and hybrid PSBE filters with σ^2 =0.05 and $\sigma_{spatial}$ =0.1

Table 2.9 Comparison of ρ for PSBE and hybrid PSBE filters

Echo image	σ^2	Correlation coefficient for PSBE at various spatial variance											Proposed methods			
		0.1	0.2	0.3	0.4	0.5	0.6	0.7	0.8	0.9	1	2	N1	N2	N3	N4
I1	0.05	0.98	0.98	0.98	**0.99**	0.98	0.98	0.98	0.98	0.97	0.97	0.95	**0.99**	**0.99**	**0.99**	0.99
	0.1	0.96	0.96	0.97	0.98	**0.98**	0.98	0.98	0.97	0.97	0.97	0.95	**0.98**	**0.98**	**0.98**	**0.98**
	0.2	0.92	0.92	0.94	0.95	0.96	0.96	**0.97**	0.97	0.96	0.96	0.95	**0.97**	**0.97**	**0.98**	**0.98**
	0.3	0.89	0.89	0.91	0.93	0.94	0.95	0.95	**0.96**	0.95	0.95	0.94	**0.96**	**0.96**	**0.96**	**0.96**
I2	0.05	0.97	0.98	0.98	**0.98**	0.98	0.98	0.97	0.97	0.96	0.96	0.93	**0.99**	0.98	0.99	0.98
	0.1	0.96	0.96	0.97	0.97	**0.97**	0.97	0.97	0.96	0.96	0.96	0.93	**0.98**	0.98	0.98	0.98
	0.2	0.92	0.92	0.94	0.95	0.96	**0.96**	0.96	0.96	0.95	0.95	0.92	**0.97**	0.97	0.97	0.97
	0.3	0.89	0.89	0.91	0.93	0.94	0.94	**0.94**	0.94	0.94	0.94	0.92	**0.95**	0.95	0.95	0.96
I3	0.05	0.98	0.98	0.98	**0.98**	0.98	0.98	0.98	0.97	0.97	0.97	0.94	**0.99**	0.99	0.99	0.99
	0.1	0.96	0.96	0.97	0.97	**0.98**	0.97	0.97	0.97	0.97	0.96	0.94	**0.98**	0.98	0.98	0.98
	0.2	0.92	0.92	0.94	0.95	0.96	**0.96**	0.96	0.96	0.96	0.96	0.94	**0.97**	0.97	0.97	0.97
	0.3	0.89	0.89	0.91	0.93	0.94	0.94	0.95	**0.95**	0.95	0.95	0.93	**0.96**	0.95	0.96	0.96
I4	0.05	0.98	0.98	0.98	**0.98**	0.98	0.98	0.97	0.97	0.96	0.96	0.93	**0.99**	0.98	0.99	0.98
	0.1	0.96	0.96	0.97	0.97	**0.97**	0.97	0.97	0.96	0.96	0.96	0.93	**0.98**	0.98	0.98	0.98
	0.2	0.92	0.92	0.94	0.95	0.96	**0.96**	0.96	0.96	0.95	0.95	0.92	**0.97**	0.96	0.97	0.97
	0.3	0.89	0.89	0.91	0.92	0.93	0.94	0.94	**0.94**	0.94	0.94	0.92	**0.95**	0.95	0.96	0.96

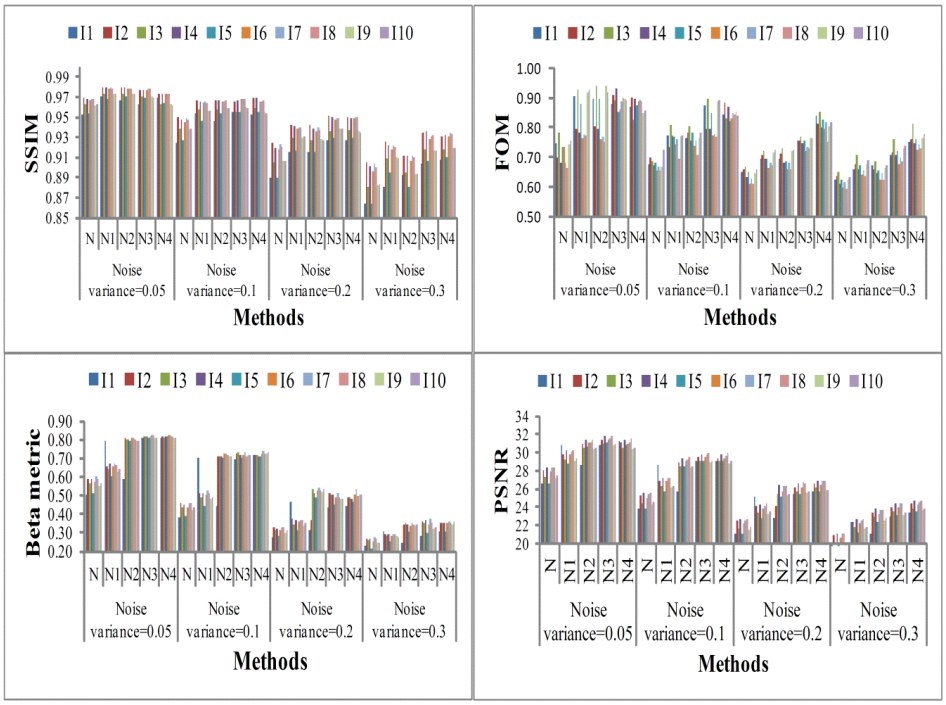

Figure 2.17 Comparison of IQM for PSBE and hybrid PSBE for at different values of noise variance

Table 2.10 Comparison of SSIM for PSBE and hybrid PSBE filters

Echo image	σ^2	SSIM for PSBE at various spatial variance											Proposed methods			
		0.1	0.2	0.3	0.4	0.5	0.6	0.7	0.8	0.9	1	2	N1	N2	N3	N4
I1	0.05	0.95	0.95	0.96	0.96	0.95	0.95	0.95	0.94	0.94	0.93	0.88	0.96	0.96	0.96	0.96
	0.1	0.92	0.93	0.93	0.93	0.93	0.93	0.93	0.92	0.92	0.92	0.87	0.94	0.94	0.95	0.94
	0.2	0.89	0.89	0.89	0.89	0.89	0.89	0.89	0.89	0.89	0.89	0.85	0.92	0.90	0.92	0.92
	0.3	0.86	0.86	0.87	0.86	0.86	0.86	0.85	0.85	0.85	0.85	0.82	0.89	0.86	0.89	0.89
I2	0.05	0.95	0.97	0.97	0.97	0.96	0.96	0.95	0.94	0.94	0.93	0.87	0.97	0.97	0.97	0.96
	0.1	0.95	0.95	0.95	0.95	0.95	0.94	0.93	0.93	0.93	0.92	0.87	0.96	0.95	0.96	0.95
	0.2	0.92	0.93	0.93	0.92	0.92	0.91	0.91	0.91	0.90	0.90	0.85	0.94	0.92	0.93	0.93
	0.3	0.90	0.91	0.90	0.90	0.89	0.88	0.88	0.88	0.87	0.87	0.83	0.91	0.88	0.91	0.92
I3	0.05	0.96	0.96	0.96	0.96	0.96	0.95	0.94	0.94	0.93	0.92	0.86	0.97	0.96	0.96	0.95
	0.1	0.94	0.94	0.94	0.94	0.94	0.93	0.93	0.92	0.92	0.91	0.85	0.95	0.94	0.95	0.94
	0.2	0.91	0.91	0.91	0.91	0.90	0.90	0.89	0.89	0.89	0.88	0.83	0.92	0.90	0.92	0.92
	0.3	0.88	0.88	0.88	0.87	0.87	0.86	0.86	0.85	0.85	0.85	0.81	0.90	0.86	0.90	0.90
I4	0.05	0.97	0.97	0.97	0.97	0.96	0.96	0.95	0.95	0.94	0.93	0.88	0.97	0.97	0.97	0.97
	0.1	0.95	0.95	0.95	0.95	0.95	0.94	0.94	0.93	0.93	0.92	0.88	0.96	0.95	0.96	0.95
	0.2	0.92	0.92	0.92	0.92	0.92	0.91	0.91	0.91	0.91	0.90	0.86	0.94	0.92	0.94	0.93
	0.3	0.90	0.90	0.90	0.89	0.89	0.89	0.88	0.88	0.87	0.87	0.84	0.91	0.89	0.92	0.92

Comparison of hybrid PSBE filters and PSBE filter: The proposed experimentations are performed on the TTE images of the AV and LV. The images in A2C, A4C, A5C, PSAX, and PLAX, are represented as (I_1 to I_5) during diastole and (I_6 to I_{10}) in systole respectively during the analysis of the performance. The results are tabulated in Table 2.7 to Table 2.12 and plotted in Figure 2.16. The images were added with variable amount of speckle noise using MATLAB function "*imnoise*". The spatially adaptive filtering is performed using the MATLAB function

"Wiener*2*". The PSBE filter and hybrid PSBE filters are experimented for spatial sigma (0.1 to 1), window size (3×3, 7×7), and the number of samples as 70 to 150, sigma factor is ≥0.8.

Table 2.11 Comparison of MSE for PSBE and hybrid PSBE filter

Echo image	σ^2	MSE for method N at various spatial variance											Proposed
		0.1	0.2	0.3	0.4	0.5	0.6	0.7	0.8	0.9	1	2	N1
I1	0.05	141.2	134.9	107.1	**94.5**	101.5	114.2	132.0	150.5	169.3	186.6	315.3	**75.1**
	0.1	271.2	255.9	194.7	156.6	**148.4**	150.6	164.6	180.6	197.9	211.7	335.9	**121.4**
	0.2	509.6	489.4	371.1	291.6	261.2	**251.6**	252.9	261.7	277.0	282.8	403.2	**197.5**
	0.3	734.7	708.0	546.9	452.6	411.1	397.0	**396.5**	407.8	408.0	418.1	524.0	**290.1**
I2	0.05	133.2	95.0	78.1	**77.1**	92.1	111.6	133.5	156.4	178.7	199.0	354.5	**65.7**
	0.1	190.5	181.3	144.9	**124.0**	126.5	141.2	161.4	183.1	200.9	219.4	372.7	**106.1**
	0.2	362.0	345.9	269.1	215.5	**208.2**	213.1	230.3	239.7	262.4	281.5	426.1	**175.8**
	0.3	529.9	508.3	407.9	336.3	**320.8**	322.9	333.6	344.1	363.3	373.5	514.9	**261.4**
I3	0.05	119.3	114.1	92.7	**88.3**	100.3	119.4	142.2	163.6	183.5	203.9	349.6	**72.3**
	0.1	231.0	218.2	169.5	**140.4**	144.1	155.2	171.9	192.5	212.7	229.2	372.9	**118.5**
	0.2	439.7	417.1	320.5	263.8	243.9	**237.6**	254.3	270.9	280.8	302.2	435.8	**198.3**
	0.3	638.2	603.4	473.5	399.1	376.9	**367.5**	376.9	397.7	405.3	423.0	538.9	**282.8**
I4	0.05	95.1	89.7	**73.5**	73.9	86.3	104.3	124.2	143.8	165.2	184.1	318.3	**60.1**
	0.1	183.9	172.2	134.6	**117.5**	119.1	131.3	149.3	168.9	185.5	204.7	334.5	**100.5**
	0.2	348.6	334.9	253.6	205.7	**196.0**	199.4	209.3	221.0	236.3	252.9	383.2	**160.9**
	0.3	510.6	480.5	381.5	323.1	**292.2**	294.6	306.3	318.3	328.4	343.9	459.7	**223.7**

Table 2.12 Comparison of FoM for PSBE and hybrid PSBE filters

Echo image	σ^2	FoM for PSBE filter at various spatial variance											Proposed methods			
		0.1	0.2	0.3	0.4	0.5	0.6	0.7	0.8	0.9	1	2	N1	N2	N3	N4
I1	0.05	0.75	0.76	0.78	0.80	0.84	0.86	0.90	0.88	0.83	0.86	0.80	0.88	0.90	0.91	0.88
	0.1	0.67	0.68	0.69	0.70	0.71	0.73	0.76	0.78	0.81	0.84	0.77	0.82	0.83	0.86	0.82
	0.2	0.65	0.64	0.66	0.67	0.67	0.68	0.69	0.72	0.73	0.75	0.77	0.73	0.73	0.80	0.84
	0.3	0.62	0.63	0.63	0.64	0.65	0.65	0.66	0.69	0.70	0.72	0.78	0.72	0.71	0.76	0.81
I2	0.05	0.77	0.69	0.70	0.71	0.73	0.75	0.77	0.78	0.82	0.82	0.77	0.80	0.82	0.91	0.88
	0.1	0.68	0.68	0.69	0.71	0.72	0.71	0.76	0.74	0.76	0.77	0.78	0.76	0.77	0.83	0.87
	0.2	0.65	0.64	0.66	0.67	0.68	0.69	0.70	0.72	0.74	0.75	0.80	0.74	0.74	0.81	0.81
	0.3	0.63	0.62	0.63	0.63	0.64	0.66	0.67	0.69	0.70	0.72	0.72	0.71	0.70	0.76	0.81
I3	0.05	0.74	0.74	0.77	0.80	0.85	0.85	0.90	0.91	0.90	0.88	0.73	0.90	0.93	0.86	0.81
	0.1	0.67	0.66	0.68	0.70	0.72	0.74	0.76	0.78	0.81	0.83	0.75	0.84	0.82	0.87	0.81
	0.2	0.65	0.66	0.67	0.68	0.70	0.70	0.70	0.71	0.75	0.75	0.76	0.75	0.74	0.81	0.81
	0.3	0.63	0.63	0.64	0.65	0.65	0.67	0.69	0.70	0.71	0.73	0.76	0.74	0.72	0.77	0.82
I4	0.05	0.66	0.66	0.68	0.70	0.71	0.73	0.75	0.77	0.81	0.84	0.79	0.81	0.80	0.92	0.89
	0.1	0.65	0.66	0.66	0.68	0.70	0.71	0.70	0.76	0.73	0.75	0.79	0.74	0.75	0.82	0.87
	0.2	0.62	0.62	0.62	0.64	0.65	0.67	0.69	0.69	0.72	0.73	0.79	0.72	0.71	0.78	0.84
	0.3	0.60	0.60	0.60	0.61	0.63	0.64	0.64	0.66	0.68	0.69	0.76	0.68	0.66	0.72	0.77

The IQM such as the FoM, β, ρ, SSIM, PSNR and MSE are plotted in Figure 2.16, at noise variance σ^2=0.05 with spatial sigma $\sigma_{spatial}$=0.1, Wiener filter size as 3×3. The analysis of performance parameters shown in Figure 2.16 reveal that the hybrid PSBE filter are more robust to noise in compared to PSBE filter. All the six IQM are superior for hybrid PSBE filter in comparison to PSBE filter. It is observed that the edges and structure are well preserved with

maximum noise suppression as reflected by the values of β, FOM, and SSIM are greater than 0.8, MSE is quite small, with higher values of PSNR and SNR.

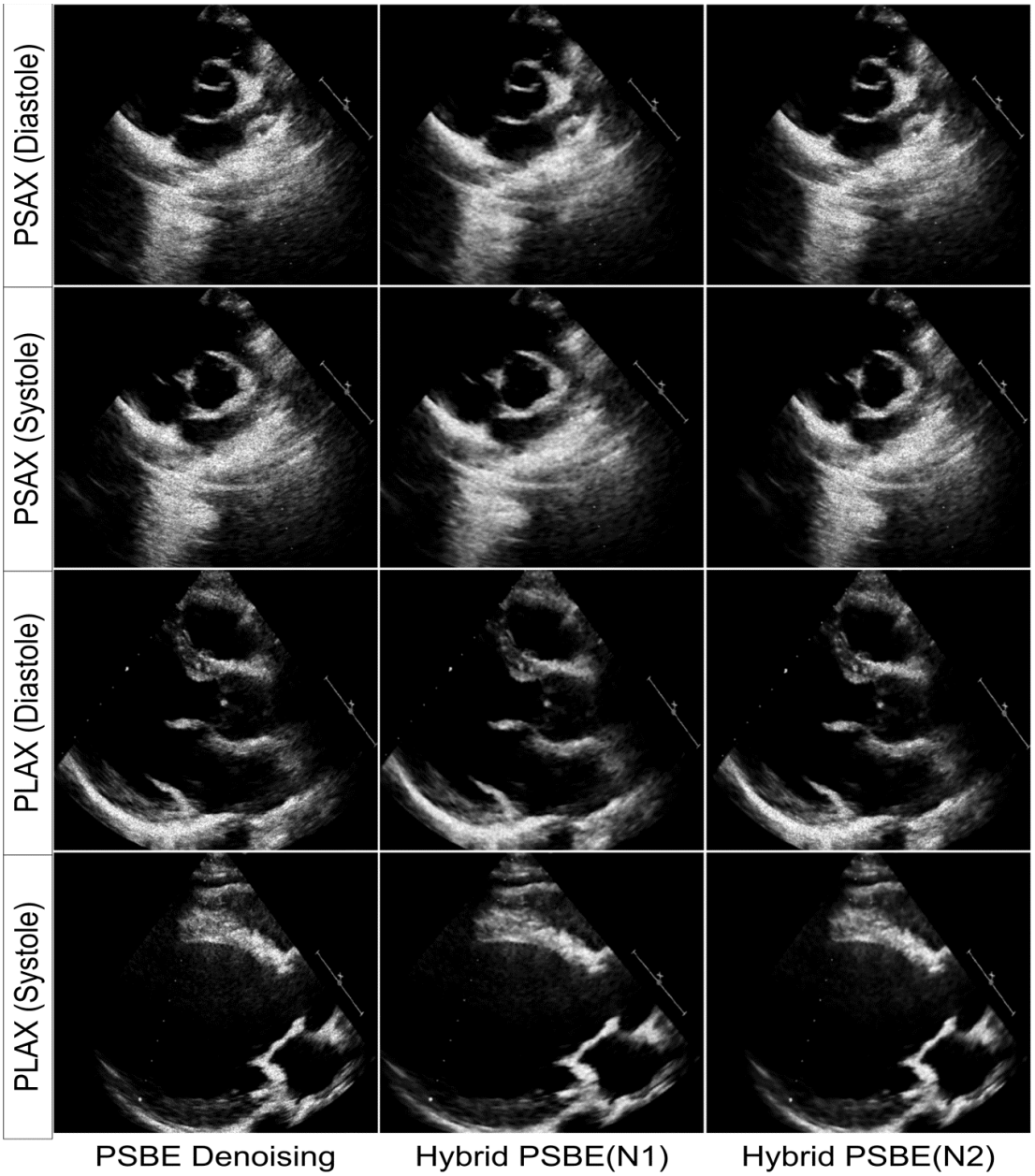

Figure 2.18 Denoising of TTE images by PSBE and hybrid PSBE filters (N1 and N2)

The values of IQM at various noise levels are shown in Figure 2.17. The comparisons in Figure 2.17 show improvement in denoising performance using the hybrid techniques. The IQM values for each hybrid filter are tabulated in Table 2.7 to Table 2.12. These IQM were estimated at various values of noise variance with spatial sigma varied in steps of 0.1. The performance of

filter is best for spatial sigma between 0.3-0.6 at all levels of noise. It is observed that the performance of the hybrid PSBE filters is superior in comparison to PSBE filter.

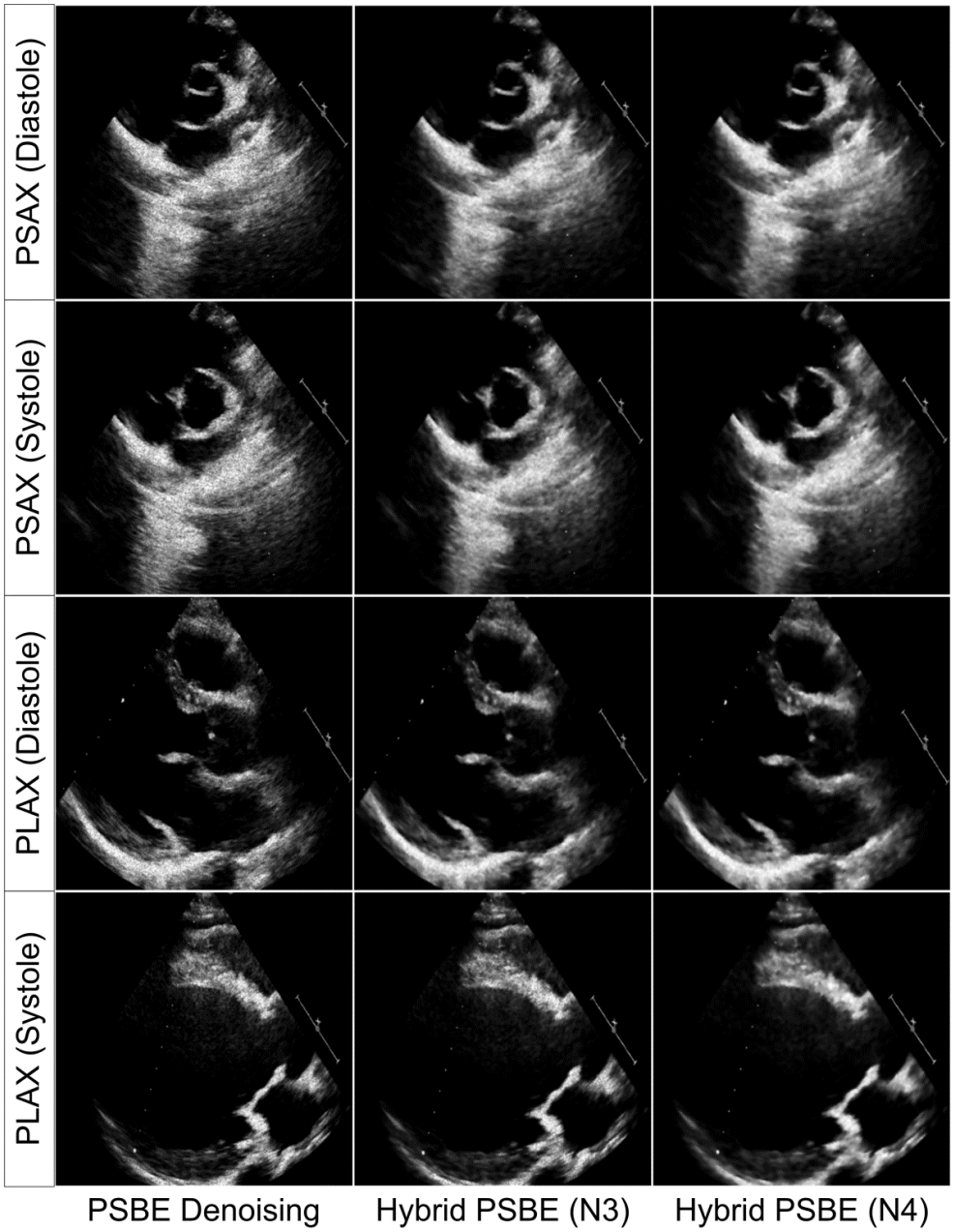

Figure 2.19 Denoising of TEE images by PSBE and hybrid PSBE filters (N3 and N4)

The visual quality of the TTE images stood out using PSBE filters as shown in Figure 2.18 to Figure 2.20. The edges and structure of TTE images are well preserved. Further, it is noticed that the texture is well preserved in the proposed hybrid PSBE schemes like N1 and N2 filter whereas smoothing is observed in N3 and N4 schemes. The overall image structure is well

preserved using all PSBE schemes. The denoised images are enhanced using a Butterworth filter. The hybrid PSBE filter of N1 scheme works well at all noise levels. Improvements are observed in the values of MSE, PSNR, ρ , β , and SSIM, using filter N1 in comparison to PSBE filter but no improvement are seen in the FoM. All these observations are based on the bold face values in the Table 2.7 to Table 2.12. The visual quality comparisons show improvement in the visual outlook with texture and structure of the images well preserved.

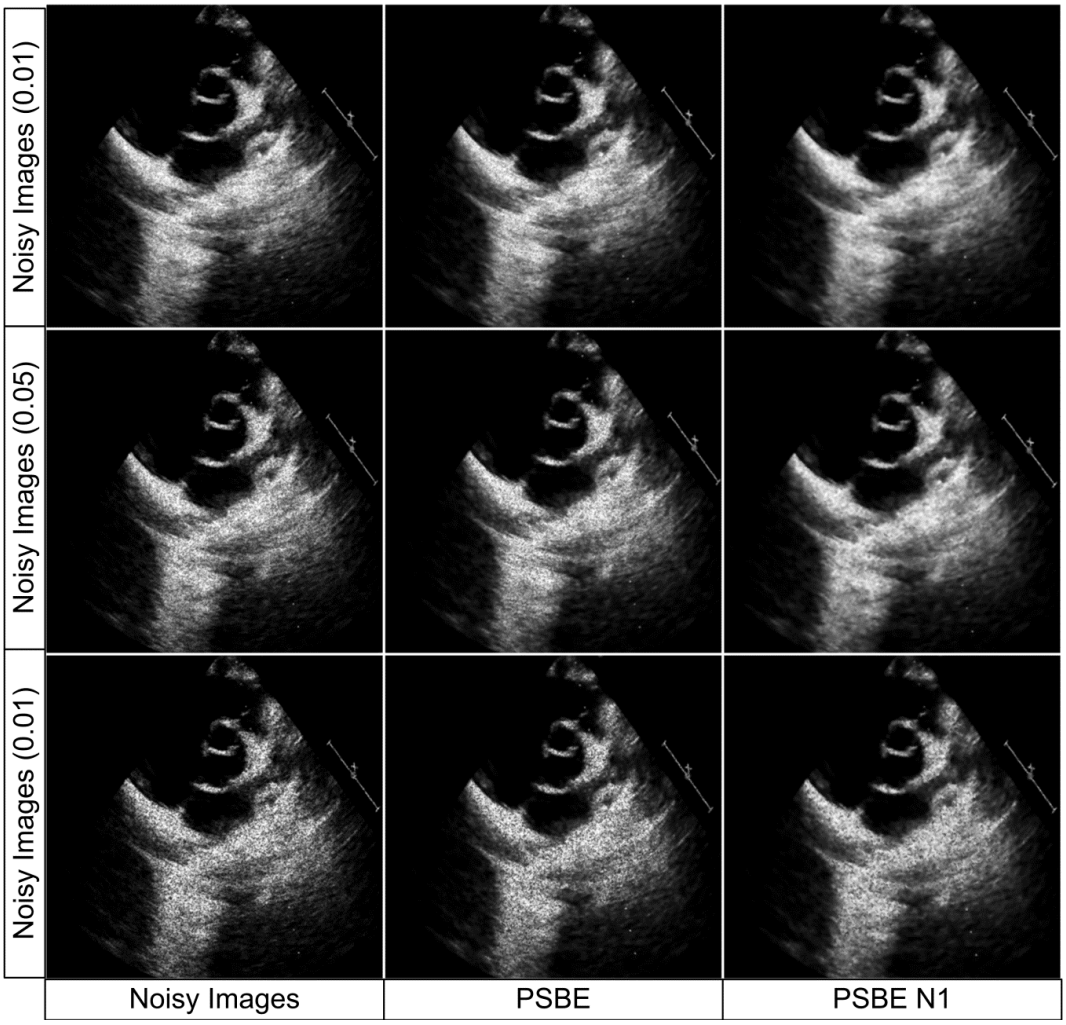

Figure 2.20 Denoising of TTE images of AV in PSAX by PSBE and hybrid PSBE

The IQM such as β , FoM and SSIM are superior for N2 filtering scheme compared to N and N1 filters but with decreased PSNR, and ρ . It is observed that the values of PSNR, β and FoM are superior for N3 filter in comparison to N2, N1 and N4 filter but with marginal decrease in ρ . The values of β and FOM are superior for N4 filter but over smoothing are observed. The denoised TTE images on application of PSBE and hybrid PSBE filters are shown in Figure 2.18.

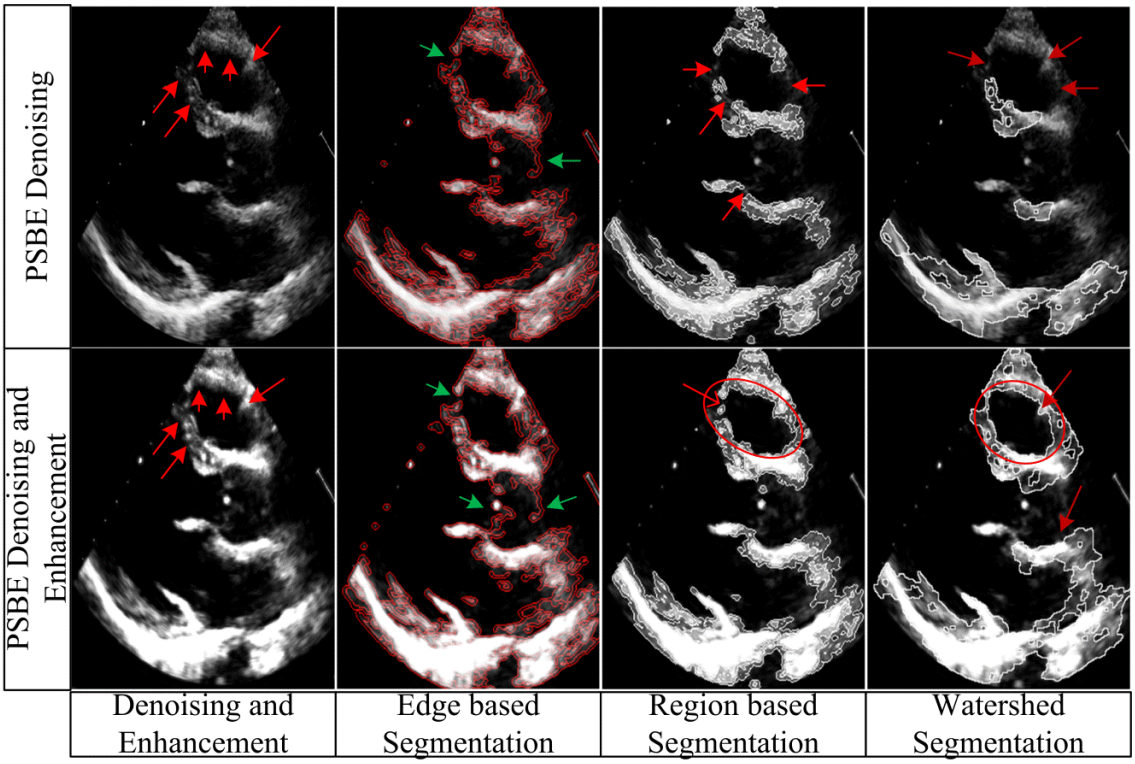

Figure 2.21 Denoising, Enhancement and Segmentation of TTE images of AV in PSAX

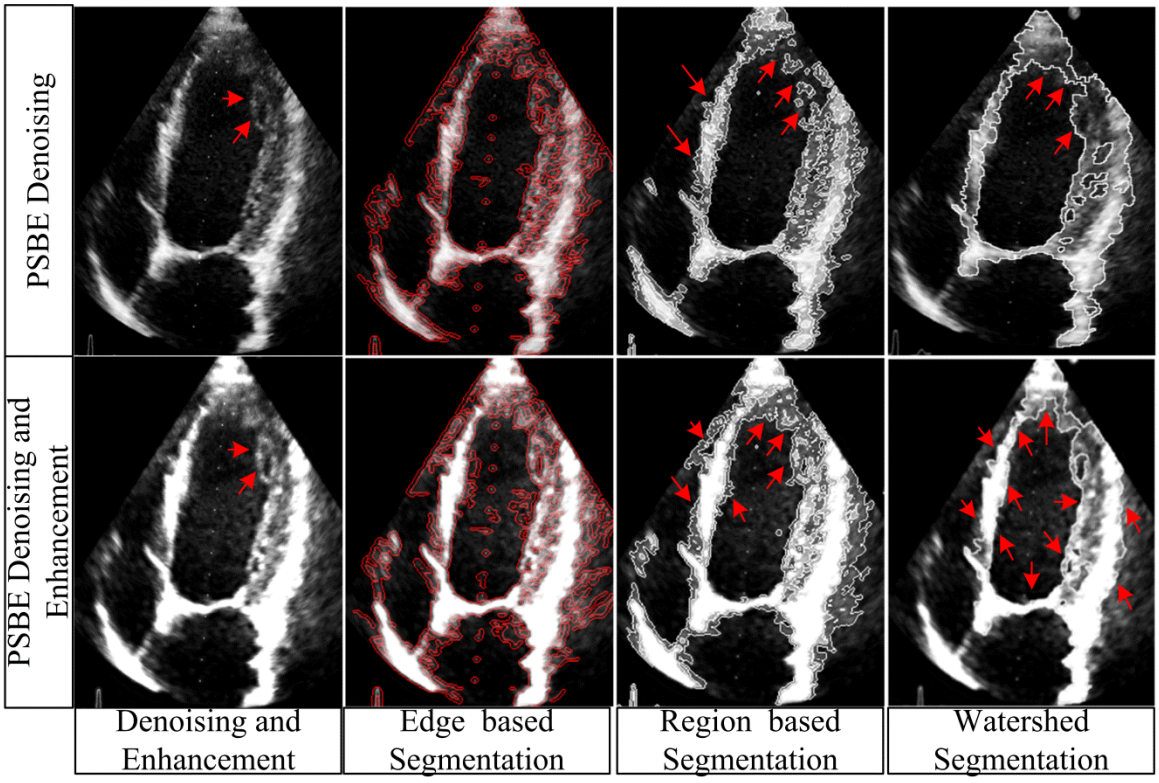

Figure 2.22 Denoising, Enhancement and Segmentation of LV in A4C view

The results of hybrid filter N1 and N2 are shown in Figure 2.18 and N3 and those of N4 filters shown in Figure 2.19. The visual quality of the hybrid filter N2 is superior in comparison to hybrid filter N1 and PSBE filter. Further, the performance of N4 is superior in comparison to N3, N2, N1 and PSBE filter at higher levels of noise. But, at lower noise levels the performance of PSBE filter is superior compared to the hybrid PSBE filters. The performance of PSBE and hybrid PSBE filters at various noise levels are shown in Figure 2.20. This Figure 2.20 reveals that the performance of PSBE filter is superior in comparison to hybrid PSBE filters at lower noise levels. But, at higher noise levels, additional filter being added is justified as the performance of hybrid filter is better compared to the PSBE filter.

The effect of PSBE filter and Butterworth filter in segmentation of TTE images are shown in Figure 2.21 and Figure 2.22. The impact of denoising and enhancement on the edge, region and watershed based segmentation of TTE images shown in Figure 2.21 and Figure 2.22. The enhanced images result better in cardiac and valvular boundaries tracing compared with the original and denoised images alone. The Figure 2.21 shows segmentation of PLAX images whereas the results in Figure 2.22 are images in A4C view. The performance of multistage watershed segmentation is better in comparison to boundary tracing using the edge and region based delineation.

2.4 Hybrid fuzzy filters

The fuzzy filters based on the concepts of moving average and median are proven to be effective in reducing various types of noise [229, 250] but they are not extensively explored for multiplicative noise reduction in TTE images. The performance of these filters were reported only in-terms of the MSE and number of looks (ENL) in [229, 250], but in medical imaging applications it would be necessary to preserve the edges [26]. To address the issue of speckle noise reduction in TTE images in general and fine tune the characteristics of fuzzy filter in particular, a despeckling technique based on the sequential combination of triangulation moving average (TMAV) filter with adaptive Wiener filter in logarithmic domain is proposed, and analyzed. The median filter can effectively suppress the speckle noise but the edges get blurred and they are not preserved across the image boundaries [229, 250]. The triangulation fuzzy filters with moving average center can preserve image sharpness. The block diagram of the proposed scheme for hybridization of fuzzy filter is shown in Figure 2.23.

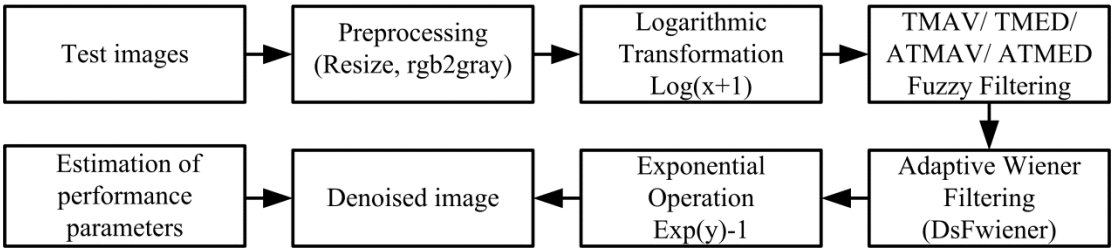

Figure 2.23 Denoising using hybrid TMAV filter

The median value for the fuzzy triangulation with median center (TMED) filter [229, 250] are defined by Equation 2.47 and Equation 2.48

$$F[f(i+r,j+s)=\begin{cases}1-\dfrac{|f(i+r,j+s)-f_{med}(i,j)|}{f_{mm}(i,j)}, & for\,|f(i+r,j+s)-f_{med}(i,j)|\le f_{mm}(i,j)\\ 1, & for\ f_{mm}=o\end{cases}\right\} \quad (2.47)$$

$$f_{mm}(i,j)=\max[f_{\max}(i,j)-f_{med}(i,j),\ f_{med}(i,j)-f_{\min}(i,j)] \quad (2.48)$$

The maximum, minimum, median and moving average values are respectively represented by $f_{\max}(i,j)$, $f_{\min}(i,j)$, $f_{med}(i,j)$ and $f_{mav}(i,j)$ with $s,r\in A$, the window at indices (i,j).

The output of the fuzzy filters is estimated using Equation 2.49 [229, 250] given below:

$$y(i,j)=\frac{\sum_{(r,s)\in A}F[f(i+r,j+s)].f(i+r,j+s)}{\sum_{(r,s)\in A}F[f(i+r,j+s)]} \quad (2.49)$$

where $F[f(i,j)]$ is the window function defined in terms of fuzzy membership functions and "A" is area. The asymmetrical triangulation median (ATMED) filter with median center (ATMED) [229, 250] is defined by Equation 2.50 below:

$$F\ \ f(i+r,j+s)\ =\begin{cases}1-[f_{med}(i,j)-f(i+r,j+s)]/\ f_{med}(i,j)-f_{\min}(i,j), \\ \quad for\ \ f_{\min}(i,j)\le f(i+r,j+s)\le f_{med}(i,j)\\ 1-[f(i+r,j+s)-f_{med}(i,j)]/[f_{\max}(i,j)-f_{med}(i,j)], \\ \quad for\ f_{med}(i,j)\le f(i+r,j+s)\le f_{\max}(i,j)\\ 1, \quad for\ f_{med}(i,j)-f_{\min}(i,j)=0\,or\,f_{\max}(i,j)-f_{med}(i,j)=0\end{cases}\right\} \quad (2.50)$$

The details of the TMAV filter and ATMAV filter based on symmetrical and asymmetrical moving average center respectively are available in [229, 250].

2.4.1 Proposed hybrid TMAV filter

The block diagram of proposed hybrid triangulation moving average fuzzy filter is shown in Figure 2.23 and each step is described below:

Step 1: Consider a standard noise free image, resize it to 512×512, convert to gray scale and induce speckle noise (only for standard images).

Step 2: Project image into the logarithmic space according to Equation 1.2. This step would be represented as *f*=log *(double* (*f*) +1)*;* where *f* is a noisy image.

Step 3: The median value are estimated using fuzzy triangulation membership function with moving average center (TMAV) defined by Equation 2.51 and Equation 2.52 with different window and padding size.

$$F\ f(i+r,j+s)=\begin{Bmatrix} 1-\dfrac{\left|f(i+r,j+s)-f_{mav}(i,j)\right|}{f_{mv}(i,j)}, \\ for\left|f(i+r,j+s)-f_{mav}(i,j)\right|\le f_{mv}(i,j) \\ 1,\ for\ f_{mv}=0 \end{Bmatrix} \tag{2.51}$$

$$f_{mv}(i,j)=\max[\,f_{\max}(i,j)-f_{mav}(i,j),\ f_{mav}(i,j)-f_{\min}(i,j)] \tag{2.52}$$

The maximum, minimum and moving average values are represented by $f_{\max}(i,j)$, $f_{\min}(i,j)$ and $f_{mav}(i,j)$ respectively, with $s,r\in A$, the window at indices (i,j).

Step 4: The output of the fuzzy TMAV filter is computed using Equation 2.49.

Step 5: Output of filter is passed through adaptive Wiener filter with different window size.

Step 6: The output of fuzzy filter is projected back to the spatial domain using exponential operation which is represented by *Ydenoised=exp(y)-1*.

Step 7: The IQM are computed followed by analysis of the results.

The above steps were repeated for different noise levels, images and window size. The window size considered for experimentations included 3×3, 5×5, 7×7 and 9×9. All experimentations are performed using standard test images of Lena, Mandrill, Cameraman, Barbara, Monarch, Woman dark hair and House of size 512×512 [127]. The synthetic noise is embedded to each of these images using MATLAB inbuilt function "*imnoise*".

2.4.2 Results

The SSIM and FoM of the proposed hybrid TMAV filter are compared with fuzzy TMAV filter and Wiener filter in Table 2.13. The analysis of results tabulated in Table 2.13 and Table 2.14 reveals that the adaptive Wiener filter in logarithmic domain is superior compared to the TMAV filter in terms of SNR and PSNR.

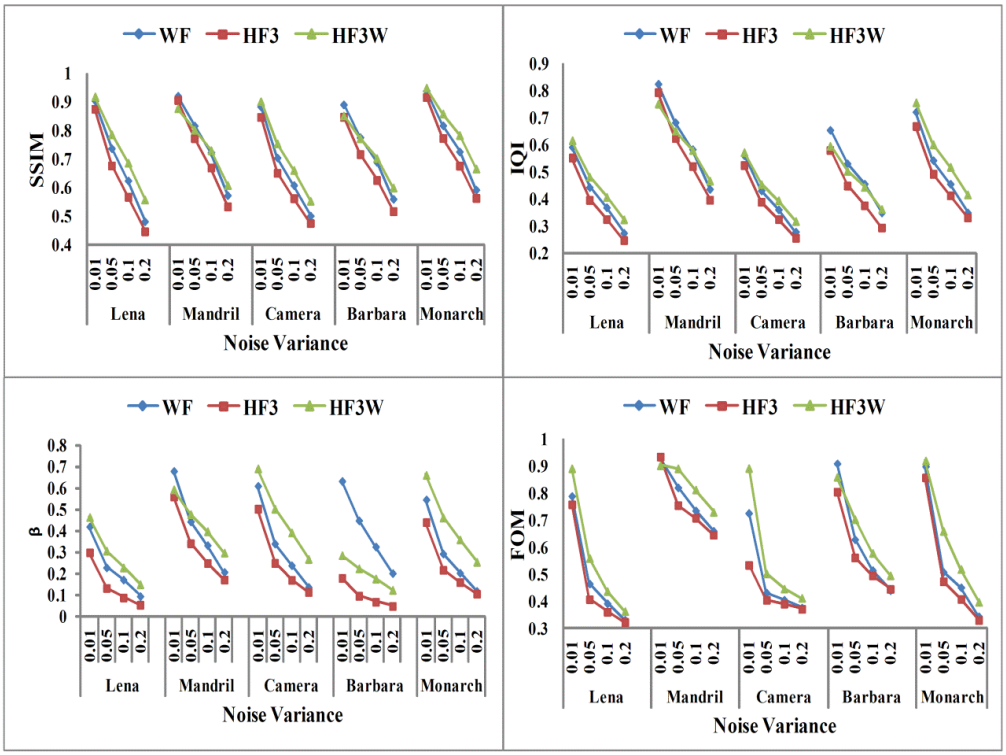

Figure 2.24 Denoising using fuzzy and hybrid fuzzy filters

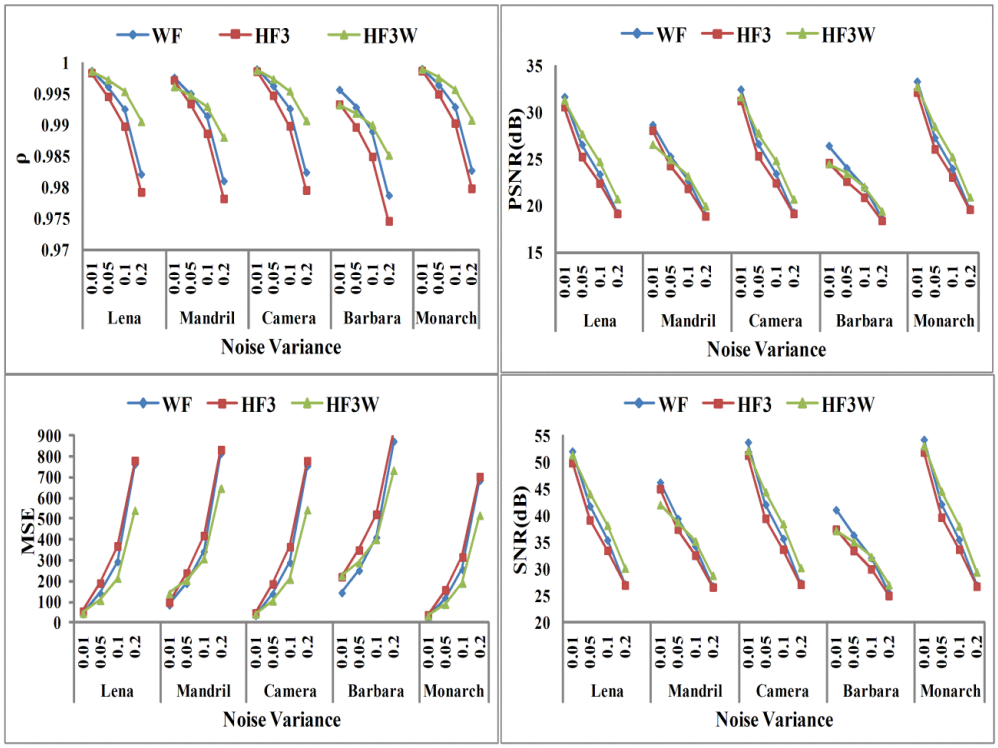

Figure 2.25 Denoising using fuzzy and hybrid fuzzy filters

Figure 2.26 Denoising using fuzzy and hybrid fuzzy filters

The performance of fuzzy filter is superior in-terms of IQI, SSIM and FoM. It is also observed that performance of the proposed hybrid TMAV filter is superior in comparison to the fuzzy filter and Wiener filter in terms of both edge preservation and noise reduction. The values of SSIM, FoM, IQI and ρ are enhanced on integration of fuzzy filter with the Wiener filter. The denoising results obtained for noise variance equal to 0.1 are compared in Table 2.13 and Table 2.14. The IQM obtained at various values of noise variance for proposed hybrid TMAV filter are shown in Figure 2.24 and Figure 2.25. The improvements in the IQM are observed for proposed hybrid TMAV filter.

Table 2.13 Comparison of values of SSIM and FoM for hybrid TMAV filter

Metric		SSIM				FoM			
Image		Lena	Monarch	House	Dark Hair	Lena	Monarch	House	Dark Hair
Noisy Image		0.5733	0.6742	0.4569	0.6173	0.3833	0.4440	0.3393	0.3792
Geometric Filter		0.6451	0.7527	0.5412	0.7506	0.3943	0.4848	0.3556	0.3982
Wiener Filter (WF)		0.7394	0.8192	0.6512	0.7978	0.4913	0.5517	0.3896	0.4285
HF filters	HF1 (TMED)	0.7407	0.8073	0.7101	0.8325	0.5600	0.6417	0.4317	0.4903
	HF2	0.7618	0.8427	0.7086	0.8415	0.5936	0.6903	0.4607	0.5301
	HF3 (TMAV)	0.8356	0.8855	0.8238	0.9126	0.8219	0.8536	0.5101	0.6259
	HF4	0.7985	0.8680	0.7506	0.8701	0.6152	0.7771	0.4970	0.5561
HFW filters	HF1W	0.7787	0.8318	0.7583	0.8614	0.6173	0.7560	0.4933	0.5346
	HF2W	0.7895	0.8571	0.7425	0.8681	0.6136	0.7800	0.5049	0.5692
	HF3W	0.8576	0.8862	0.8445	0.9206	0.8338	0.8547	0.5727	0.7481
	HF4W	0.8175	0.8753	0.7885	0.8860	0.6945	0.8531	0.5151	0.5921

Table 2.14 Comparison of values of SNR and MSE for hybrid TMAV filter

Metric		SNR				MSE			
Image		Lena	Monarch	House	Dark Hair	Lena	Monarch	House	Dark Hair
Noisy Image		26.37	26.46	26.29	27.25	849.08	738.90	1024.86	669.94
Geometric Filter (GF)		31.44	31.64	31.21	32.80	473.44	406.80	581.95	353.56
Wiener Filter (WF)		41.99	42.41	43.26	42.34	140.63	117.80	145.30	117.84
HF filters	HF1 (TMED)	34.91	32.69	39.04	35.04	317.74	360.56	236.12	273.02
	HF2 (ATMED)	41.25	40.32	45.66	43.20	153.17	149.71	110.21	106.75
	HF3 (TMAV)	39.20	37.25	44.83	41.63	193.78	213.31	121.30	127.85
	HF4 (ATMAV)	41.19	39.83	45.79	41.81	154.23	158.46	108.54	125.28
HFW filters	HF1W	35.73	33.10	39.85	35.49	289.02	343.88	215.08	259.23
	HF2W	41.89	39.66	46.57	44.18	145.45	161.67	99.26	95.41
	HF3W	39.33	36.69	44.96	41.64	190.86	227.51	119.44	127.79
	HF4W	41.97	39.02	46.51	42.04	154.46	173.99	99.91	122.01

Over smoothing is observed at the lower noise levels in comparison to higher levels. The FoM and IQI obtained are two times of the noisy image. The value of $\rho \geq 0.99$ for all the images shows that the input and output values are highly correlated. Based on the analysis of results in Table 2.13 and Table 2.14, it can be concluded that embedding of Wiener filter and the TMAV filter, edge preservation and structural similarity can be enhanced. The visual quality of denoised image using TMAV filter and proposed filters are compared in Figure 2.26 for noise variance equal to 0.1. Large amount of noise is retained in the denoised images. The noise reduction is more pronounced using the proposed hybrid TMAV filter as clearly observed from Figure 2.26. The IQM of the hybrid TMAV filter is compared with denoising techniques in Table 2.13 and Table 2.14.

2.5 Integrated fuzzy filters

The applications of the filters such as median, adaptive weighted median (AWM), and moving average (MAV) filters are known for removing the additive noise but their application on the US images are less explored [26,229, 250]. The working of AWM filter depends on the window size

and weight adjustment [26, 73, 228]. It operates normally using a fixed window size thereby restricting the enhancement phenomenon. It can result in the smeared image boundaries. The geometric filter [244] based on the image morphology preserves the edges which is not observed using the TMAV filter. But the issue of concern using the geometric filter is the noise retained in the filtered image.

The Wiener filter based on the minimization of MSE is also employed in the additive noise reduction applications. It is used for speckle noise reduction in the logarithmic domain and has become reference technique for many researchers for comparison of results obtained by their respective methods or modifications [116, 134]. According to psychophysics, the human eye may not function as minimum MSE estimator, in fact allows noise leading to sharp intensity changes. The applications of fuzzy filters along with geometric, Wiener, the combination of geometric-Wiener, the combination of geometric-fuzzy, and the proposed integrated fuzzy (i.e. geometric-Wiener-fuzzy) filter are analysed in this sub-section.

2.5.1 Proposed integrated fuzzy filters

The fuzzy filters can be employed to suppress noise in the logarithmic domain. But the edges were not fully preserved. The geometric filter is known for edge preservation when employed for speckle noise reduction. Therefore, it is proposed to combine the edge preservation capabilities of geometric filter and noise reduction capabilities of Wiener filter into the fuzzy filters. During the implementation of fuzzy filters such as TMED, ATMED, TMAV and ATMAV, as shown in Figure 2.27, the output of geometric-Wiener filtered image is logarithmically transformed, and passed through TMAV or TMED fuzzy filter. The output of fuzzy filter is transformed to the non-logarithmic domain using the exponential operation.

Initially, experiments are conducted to study the applications of geometric filter (GF), Wiener filter (WF) and combination of the GF and WF resulting in GW filter. Analysis of the GF, WF and GW filter is followed by the study of fuzzy filters in the logarithmic domain. The TMED, ATMED, TMAV and ATMAV fuzzy filters are numbered as F1, F2, F3 and F4, respectively. The sequential combination of geometric filter and fuzzy filter are represented as GF1, GF2, GF3 and GF4. The combination of geometric-Wiener filters with fuzzy filters, known as integrated fuzzy filters, are represented as GWF1, GWF2, GWF3 and GWF4 where F1 to F4 are fuzzy filters and W represents the Wiener filter. The geometric filter is used for denoising of the TTE images with different number of iterations. The Wiener filter is used at the end of iteration during the integration of geometric and Wiener filters. The geometric filter is embedded with the fuzzy

filters in the second set of experiments. Finally, the geometric-Wiener filter is combined with the fuzzy filters as shown in Figure 2.27 and the steps are explained below.

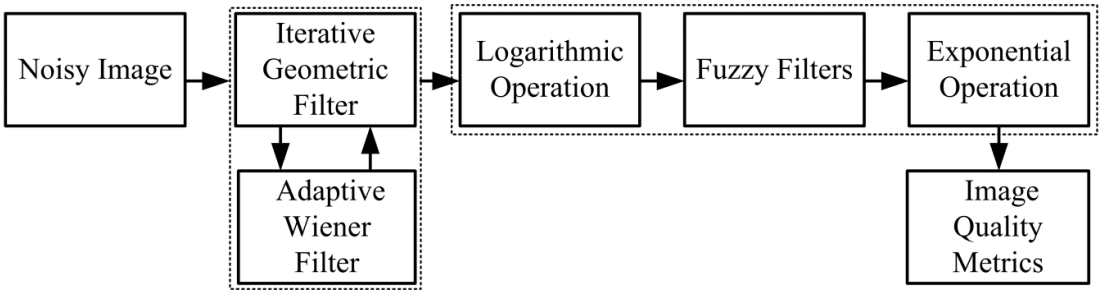

Figure 2.27 Block diagram of the proposed integrated fuzzy filter

The steps incorporated for the implementation of integrated fuzzy filters are

Step 1: Consider a standard noise free image, resize it to 512x512, convert it to gray scale and embed speckle noise. In case of the TTE images, no artificial noise is added as they inherit speckle noise.

Step 2: The images are denoised using GW filter with different number of iterations. During iterative process, the output of geometric filter image is subjected to Wiener filtering.

Step 3: The noise filtered image is projected into the logarithmic domain.

Step 4: Image in the logarithmic domain is filtered using the fuzzy filter. The output of the fuzzy filter is estimated using Equation 2.50.

Step 5: The output of fuzzy filter is projected back to the non-logarithmic space.

Step 6: Computation of the IQM, visual quality assessment and clinical validation.

The inbuilt function "Wiener*2*" is employed for implementation of Wiener filter. The window size of Wiener filter is considered as 3×3. The above steps are being repeated for different levels of noise artificially added to the noise free images and for different window size of fuzzy and Wiener filters varying in the range 3×3, 5×5, 7×7 and 9×9. Further, all the steps are repeated using the TMED, ATMED, TMAV and ATMAV filters. In each of the experiments, the step 4 is different. Each of the fuzzy filters is based on different membership function.

2.5.2 Results

All experimentations are performed using several standard test images such as Lena, Mandrill, Cameraman, Barbara, Monarch, Woman dark hair and House of size 512×512 [127]. The applications of the geometric filter, Wiener filter, and combination of geometric-Wiener, combination of geometric-fuzzy and integrated fuzzy filters are analyzed for the TTE images. The performance of the geometric, Wiener, the geometric-Wiener, fuzzy, geometric-fuzzy and

geometric-Wiener-fuzzy filters are analyzed in terms of the IQM followed by visual quality assessment.

Table 2.15 Comparison of IQM for fuzzy, geometric-fuzzy and integrated fuzzy filters

Noise	Method	FoM	SSIM	IQI	β	ρ	SNR	PSNR	MSE
0.01	F1	0.7514	0.8659	0.4917	0.0755	0.9966	43.25	27.28	121.56
	GF1	0.8259	0.8697	0.4947	0.0931	0.9966	43.38	27.34	119.84
	GWF1	**0.8671**	**0.8905**	**0.5431**	**0.1518**	**0.9968**	**43.82**	**27.57**	**113.81**
	F2	0.7590	0.8750	0.5530	0.3016	0.9984	49.94	30.62	56.31
	GF2	0.7932	0.8835	0.5652	0.3284	0.9985	50.57	30.94	52.35
	GWF2	**0.8819**	**0.9202**	**0.6163**	**0.4552**	**0.9988**	**52.16**	**31.73**	**43.62**
	F3	0.9066	0.9221	0.6002	0.0807	0.9982	48.62	29.97	65.51
	GF3	0.9099	0.9228	0.6002	0.0701	0.9982	48.87	30.09	63.66
	GWF3	0.8689	0.9106	0.5918	0.0675	0.9980	47.86	29.59	71.50
0.05	F1	0.4435	0.6930	0.3646	0.0080	0.9931	35.16	23.24	308.48
	GF1	0.4563	0.6993	0.3665	0.0001	0.9933	36.00	23.65	280.30
	GWF1	**0.5597**	**0.7816**	**0.4293**	0.0284	**0.9956**	**41.01**	**26.16**	**157.29**
	F2	0.4023	0.6781	0.3990	0.1315	0.9946	39.24	25.28	192.90
	GF2	0.4239	0.6845	0.4049	0.1374	0.9950	39.96	25.64	177.63
	GWF2	**0.5149**	**0.7707**	**0.4755**	**0.2384**	**0.9970**	**44.35**	**27.83**	**107.16**
	F3	0.5465	0.7950	0.4647	0.0888	0.9968	41.18	26.25	154.31
	GF3	0.5383	0.8021	0.4704	0.0878	0.9969	42.46	26.89	133.17
	GWF3	**0.5990**	**0.8032**	**0.4762**	0.0910	**0.9969**	**44.26**	**27.79**	**108.27**
0.1	F1	0.3627	0.5671	0.2869	0.0230	0.9864	27.36	19.34	757.23
	GF1	0.3659	0.5757	0.2924	0.0152	0.9869	28.34	19.83	676.50
	GWF1	**0.4419**	**0.6865**	**0.3661**	-0.0003	**0.9932**	**36.92**	**24.12**	**252.01**
	F2	0.3693	0.5691	0.3265	0.0854	0.9898	33.53	22.42	372.49
	GF2	0.3660	0.5776	0.3341	0.0860	0.9904	34.32	22.81	340.12
	GWF2	**0.4535**	**0.6728**	**0.4067**	**0.1670**	**0.9948**	**39.73**	**25.52**	**182.38**
	F3	0.4040	0.6821	0.3833	0.0764	0.9940	33.35	22.33	380.09
	GF3	0.4020	0.6927	0.3903	0.0732	0.9943	34.75	23.03	323.62
	GWF3	**0.4634**	**0.7163**	**0.4148**	**0.0868**	**0.9953**	**40.22**	**25.77**	**172.35**
0.2	F1	0.3164	0.3917	0.1851	0.0174	0.9626	17.42	14.36	2380.26
	GF1	0.3141	0.4038	0.1932	0.0176	0.9654	18.41	14.86	2124.11
	GWF1	**0.3750**	**0.5611**	**0.2952**	**0.0180**	**0.9872**	**30.73**	**21.02**	**513.91**
	F2	0.3283	0.4495	0.2518	0.0582	0.9794	27.09	19.20	781.68
	GF2	0.3294	0.4549	0.2564	0.0552	0.9802	27.79	19.55	721.01
	GWF2	**0.3798**	**0.5643**	**0.3381**	**0.1162**	**0.9906**	**34.49**	**22.90**	**333.25**
	F3	0.3399	0.5072	0.2695	0.0474	0.9833	22.78	17.05	1283.26
	GF3	0.3479	0.5172	0.2752	0.0486	0.9847	24.04	17.67	1110.79
	GWF3	**0.3845**	**0.5952**	**0.3376**	**0.0725**	**0.9912**	**34.04**	**22.67**	**351.27**

The performance of these filters at various noise levels are tabulated in Table 2.15. The results in Table 2.15 reveal that performance of the GF filters are superior compared to the fuzzy filters. These results are further improved in case of proposed integrated fuzzy filter in comparison to results of the fuzzy and geometric-fuzzy filters. The IQM such as the FoM, SSIM, IQI, β, ρ, SNR and PSNR values are highest for the GWF filters in-comparison to the fuzzy and geometric-fuzzy filters. The SNR and PSNR are higher by 2dB, for the GWF2 compared to GF2 filter at all noise levels.

Table 2.16 Comparison of IQM for different images with noise variance equal to 0.01

Methods	FoM						ρ				
	Lena	Darkhair	Blonde	Peppers	Mandrill	Barbara	Lena	Darkhair	Blonde	Peppers	Mandrill
GF	0.7382	0.5140	0.7329	0.6516	0.9020	0.7529	0.9964	0.9966	0.9964	0.9964	0.9962
WF	0.7380	0.5894	0.8024	0.9513	0.9208	0.8481	0.9987	0.9986	0.9985	0.9987	0.9961
GW	0.7705	0.6128	0.8370	0.8373	0.9363	0.8723	0.9988	0.9988	0.9986	0.9991	0.9978
GF1	0.8495	0.6000	0.9045	0.8303	0.9000	0.8239	0.9968	0.9986	0.9944	0.9824	0.9904
GF2	0.7576	0.5736	0.9193	0.9085	0.9077	0.8444	0.9985	0.9991	0.9979	0.9979	0.9945
GF3	0.8639	0.6972	0.9123	0.8927	0.8956	0.8824	0.9980	0.9993	0.9968	0.9922	0.9933
GWF1	0.8596	0.7679	0.8416	0.8661	0.8457	0.8043	0.9968	0.9990	0.9947	0.9838	0.9906
GWF2	0.8874	0.7108	0.9004	0.9087	0.8954	0.8279	0.9988	0.9994	0.9982	0.9981	0.9940
GWF3	0.8727	0.7510	0.8647	0.8806	0.8509	0.8957	0.9980	0.9993	0.9967	0.9925	0.9925
Methods	IQI						SSIM				
	Lena	Darkhair	Blonde	Peppers	Mandrill	Barbara	Lena	Darkhair	Blonde	Peppers	Mandrill
GF	0.5079	0.4683	0.5108	0.4718	0.7405	0.6825	0.8331	0.8793	0.8287	0.8393	0.9146
WF	0.5885	0.5816	0.6017	0.7470	0.7458	0.7019	0.8998	0.9190	0.8972	0.8622	0.7598
GW	0.6001	0.6107	0.6103	0.6683	0.8326	0.7048	0.9065	0.9281	0.9028	0.9139	0.9259
GF1	0.5412	0.5514	0.5973	0.5776	0.5439	0.4920	0.8898	0.9248	0.6942	0.6859	0.5551
GF2	0.5667	0.5912	0.6826	0.7031	0.6677	0.5919	0.8847	0.9213	0.7902	0.8174	0.6834
GF3	0.5900	0.6471	0.7137	0.7002	0.6406	0.5891	0.9108	0.9550	0.8094	0.8105	0.6527
GF4	0.6130	0.6482	0.7355	0.7429	0.6738	0.5900	0.9191	0.9710	0.8425	0.8605	0.6886
GWF1	0.5429	0.6177	0.6356	0.6357	0.4984	0.4949	0.8899	0.9458	0.7463	0.7510	0.5239
GWF2	0.6157	0.6448	0.7396	0.7558	0.6348	0.5821	0.9205	0.9440	0.8477	0.8720	0.6560
GWF3	0.5908	0.6520	0.6917	0.6972	0.5638	0.5890	0.9109	0.9530	0.8032	0.8171	0.5884
GWF4	0.6128	0.6488	0.7339	0.7486	0.6241	0.7503	0.9186	0.9463	0.8412	0.8624	0.6452
Methods	MSE						RMSE				
	Lena	Darkhair	Blonde	Peppers	Mandrill	Barbara	Lena	Darkhair	Blonde	Peppers	Mandrill
GF	131.76	106.06	150.66	132.06	141.35	131.60	11.48	10.30	12.27	11.49	11.89
WF	45.99	42.07	58.53	49.31	139.63	86.45	6.78	6.49	7.65	7.02	11.82
GW	44.57	36.35	57.37	34.60	79.17	90.04	6.68	6.03	7.57	5.88	8.90
GF1	113.90	46.09	226.43	627.27	347.98	351.54	10.67	6.79	15.05	25.05	18.65
GF2	52.21	29.51	83.38	76.40	198.78	217.05	7.23	5.43	9.13	8.74	14.10
GF3	71.33	21.59	128.04	279.79	242.21	248.31	8.45	4.65	11.32	16.73	15.56
GF4	47.88	21.75	84.00	112.34	198.04	248.41	6.92	4.78	9.17	10.60	14.07
GWF1	114.28	31.75	210.18	577.60	335.33	355.50	10.69	5.63	14.50	24.03	18.31
GWF2	43.69	20.26	73.73	69.65	213.93	221.41	6.61	4.50	8.59	8.35	14.63
GWF3	71.29	21.01	132.31	269.16	267.95	254.04	8.44	4.58	11.50	16.41	16.37
GWF4	48.03	19.74	84.27	110.90	222.33	106.03	6.93	4.44	9.18	10.53	14.91
Methods	ERR3						ERR4				
	Lena	Darkhair	Blonde	Peppers	Mandrill	Barbara	Lena	Darkhair	Blonde	Peppers	Mandrill
GF	13.30	12.73	13.93	13.41	13.48	13.50	14.80	14.72	15.24	14.96	14.77
WF	8.26	8.50	9.29	8.76	14.25	11.73	9.63	10.27	10.85	10.46	16.44
GW	8.09	7.83	9.22	7.25	10.84	11.94	9.41	9.41	10.77	8.52	12.66
GF1	16.09	9.24	21.85	41.96	23.19	25.72	21.78	12.03	28.88	57.94	27.39
GF2	8.98	6.88	12.12	12.22	17.57	20.67	10.87	8.19	15.65	16.89	20.89
GF3	12.07	6.23	16.67	29.40	19.31	21.77	15.97	8.04	22.41	42.65	22.76
GF4	9.18	6.34	12.72	16.29	17.52	21.96	11.60	8.02	16.46	22.78	20.78
GWF1	16.09	8.15	21.27	40.47	22.78	25.96	21.73	11.33	27.99	55.96	26.79
GWF2	8.61	5.73	11.82	12.05	18.14	20.89	10.78	6.88	15.33	16.67	21.36
GWF3	12.04	6.17	16.36	27.95	20.17	22.16	15.89	8.00	21.39	40.22	23.55
GWF4	9.22	5.68	12.71	16.03	18.42	13.44	11.67	6.88	16.40	22.15	21.60

Table 2.17 Comparison of parameters for different images with noise variance equal to 0.01

Methods	LMSE						β			
	Lena	Darkhair	Blonde	Peppers	Mandrill	Barbara	Lena	Darkhair	Blonde	Peppers
GF	6.410	22.745	2.419	11.595	3.321	0.882	0.326	0.167	0.484	0.197
WF	1.255	5.895	0.615	0.287	0.654	0.384	0.412	0.141	0.603	0.783
GW	1.101	4.585	0.581	1.267	0.603	0.390	0.431	0.143	0.618	0.442
GF1	1.967	4.289	2.891	6.751	1.462	1.323	0.150	0.012	-0.203	-0.526
GF2	1.059	2.076	0.910	0.478	0.929	0.983	0.330	0.121	0.358	0.626
GF3	1.137	1.664	1.545	3.038	1.074	1.033	0.067	0.083	-0.056	-0.269
GF4	0.833	1.754	0.894	0.766	0.925	1.056	0.411	0.092	0.364	0.487
GWF1	1.971	2.432	2.297	5.948	1.241	1.322	-0.15	-0.002	-0.28	-0.57
GWF2	0.794	1.178	0.763	0.408	0.881	0.998	0.455	0.202	0.489	0.713
GWF3	1.136	1.283	1.355	2.726	1.022	1.034	0.067	0.103	-0.068	-0.289
GWF4	0.837	1.061	0.896	0.775	0.900	0.906	0.406	0.214	0.369	0.487
Methods	SNR(dB)						PSNR(dB)			
	Lena	Darkhair	Blonde	Peppers	Mandrill	Barbara	Lena	Darkhair	Blonde	Peppers
GF	42.55	43.26	42.48	42.67	42.15	42.10	26.93	27.88	26.35	26.92
WF	51.97	52.56	50.86	54.30	47.18	45.40	31.64	32.53	30.54	32.74
GW	43.82	50.50	38.91	29.15	34.26	33.57	27.57	31.49	24.58	20.16
GF1	43.79	53.73	39.55	29.86	34.58	33.47	27.55	33.11	24.90	20.51
GF2	50.59	54.37	47.58	47.43	39.13	37.76	30.95	33.43	28.92	29.30
GF3	52.14	57.64	48.65	48.24	38.49	37.58	31.73	35.06	29.45	29.70
GF4	47.88	57.08	43.86	36.16	37.41	36.59	29.60	34.79	27.06	23.66
GWF1	47.89	57.32	43.57	36.50	36.53	36.39	29.60	34.91	26.91	23.83
GWF2	51.35	57.67	47.52	44.08	39.16	36.45	31.33	35.02	28.89	27.63
GWF3	51.32	57.86	47.49	44.20	38.15	43.87	31.32	35.18	28.87	27.68
GWF4	51.70	51.29	50.69	51.24	42.19	45.75	31.50	31.89	30.46	31.20

The following are the highlights of the results tabulated in Table 2.15: 1) the performance of F3, GF3 and GWF3 filters are superior in terms of edge preservation compared to filtering based on F1 and F2. The IQM values of FoM, SSIM, IQI, and β are higher for these filters suggesting better edge preservation. 2) The noise reducing capabilities of F2 based filters are better compared to the F1 and F2 filters. The higher values of SNR and PSNR with lesser MSE reveal this point suggesting better noise reduction using the F2, GF2 and GWF2 filter. 3) Improvement in the IQM is observed using the integration of geometric with fuzzy and geometric-Wiener-fuzzy filters. Enhancement is observed in performance of the GF filters compared to the fuzzy filters, and the GWF filters in comparison to the GF filters. The results suggest that proposed methods are superior compared to others.

The analysis of the results tabulated in Table 2.16 and Table 2.17 reveal that the performances of fuzzy filters are on the similar lines as discussed earlier. The IQM obtained for noise variance equal to 0.01 are tabulated in Table 2.16. The results in terms of the FoM, ρ, IQI, SSIM, MSE, RMSE, ERR3 and ERR4 are tabulated in Table 2.16. The IQM such as LMSE, β, SNR and PSNR are shown in Table 2.17. It is observed that the performances of geometric-

Wiener filter are superior in comparison to the geometric filter. The values of FoM ≥ 0.75, ρ ≥ 0.99 and SSIM ≥ 0.9 for the GWF filters indicate superior edge and structure preservation.

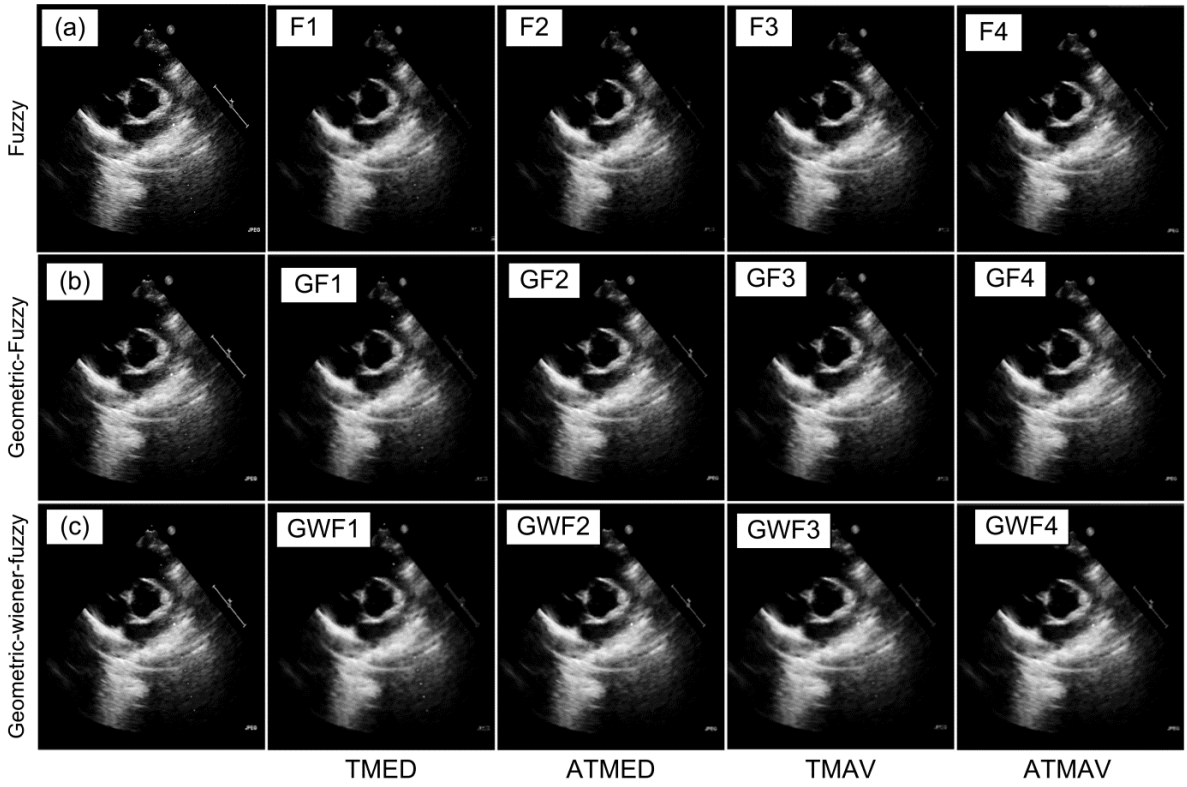

Figure 2.28 Denoised TTE images: a) Original image, b) geometric filter, c) geometric-Wiener filter, F1 to F4: TMED, ATMED, TMAV, ATMAV, and GF1 to GF4: geometric fuzzy filters, GWF1 to GWF4: Geometric-Wiener-Fuzzy filters

The values of IQI are enhanced using the GWF filters as observed in Table 2.16. The performance of geometric-Wiener filter is best in terms of SSIM. The value of SSIM is higher compared to SSIM for all fuzzy, GF and GWF filters. The MSE is reduced by more than two times using GW and GWF filters for all images at noise variance equal to 0.01. The RMSE, LMSE, ERR3 and ERR4 are also reduced using the GW and the GWF filters. The values of β are greater than 0.7 using Wiener and GWF2 filter whereas all other methods the value is less than 0.5. The improvement in value of β is observed using the GW, GF and GWF filters. The values for SNR and PSNR tabulated in Table 2.17 reveal that the performance of GF1 is enhanced by more than 2dB in the GWF1 filter. The performance of GF4 filter is enhanced by more than 4dB using proposed GWF4 filter. The overall result analysis reveals that the performances of proposed integrated filters are superior in terms of edges and structure preservation with maximum noise suppression.

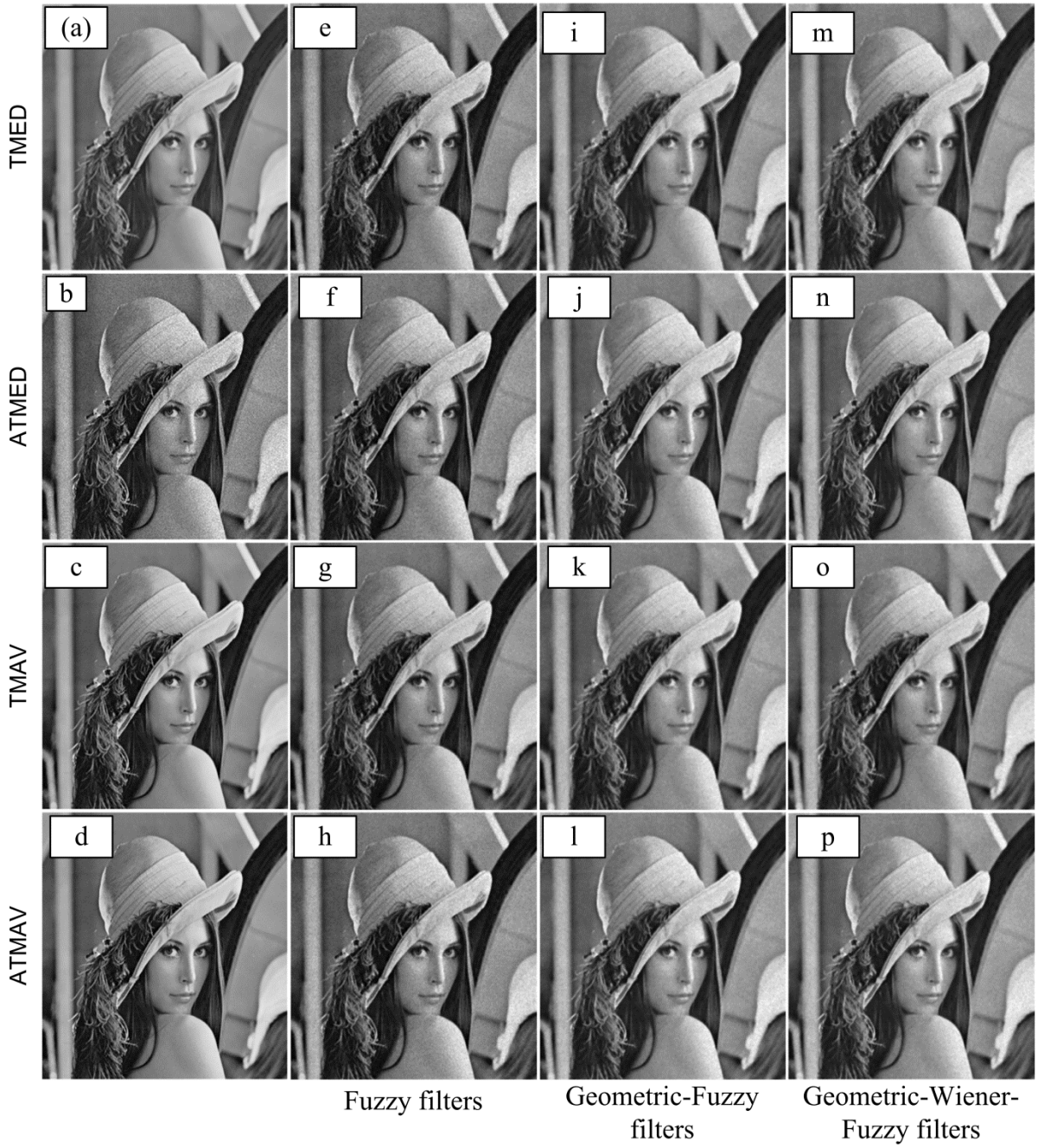

Figure 2.29 Visual quality comparison of denoised Lena image for noise level equal to 0.01: a) Original noise free image, b) Noisy image c) Geometric filter, d) Geometric-Wiener filter, e) to h) :F1 to F4 filter, i) to l): GF1 to GF4 filter, m) to p): GWF1 to GWF4 filter

The visual qualities of denoised TTE images and standard test image are shown in Figure 2.28 and Figure 2.29, respectively. The visual quality of denoised images obtained using the GWF filters are compared to the fuzzy filters (F1 to F4), and Geometric-fuzzy (GF1 to GF4) filters. It is observed that large amount of noise is retained in fuzzy filters. Noise reduction is more pronounced using GW and GWF filters. The clinical validation of denoised images is

carried out as already discussed for the multiscale techniques and TMAV fuzzy filter. Denoised images based on GF, GWF and GW filters are acceptable for the doctors whereas the denoised images obtained using TMED filter and GF1 filters were not appreciated.

2.6 Hybrid homomorphic fuzzy filters

The performances of hybrid TMAV filter and integrated fuzzy filters are further improved by sequential combination of the homomorphic fuzzy (HF) filter with the AD filter. The idea of sequential combination of filters is advocated by Mateo *et al.* during the analysis of basic filters for the US images of kidney. The proposed sequential combination of the HF filter and the AD filter is called as hybrid homomorphic fuzzy (HHF) filter. Further the performance of the HHF filter is compared with seventeen denoising techniques. The Out of the seventeen techniques, ten methods is experimented in the logarithmic domain, and seven other methods in non-homomorphic domain. The nonlinear fuzzy filters are defined using different membership functions. The fuzzy membership points out to the degree of similarity and belongingness of each element to the defined fuzzy set. Three fuzzy filters based on the concepts of median and MAV filters are analyzed in the homomorphic domain and represented as the HF filters. As pointed out in the earlier sections the weighted median filter (WMF) can effectively suppress the speckle noise but the edges are not well preserved [229, 250], whereas the fuzzy filters can preserve the image sharpness when employed for denoising. The triangulation median filter (TMED), asymmetrical TMED (ATMED) filter and triangulation moving average filter (TMAV) are formulated in using the equations described below [229, 250]

$$F[f(i+r,j+s)]=\begin{cases}1-\dfrac{|f(i+r,j+s)-f_{med}(i,j)|}{f_{mm}(i,j)}, & for\,|f(i+r,j+s)-f_{med}(i,j)|\le f_{mm}(i,j)\\ 1, & for\ f_{mm}=o\end{cases} \quad (2.53)$$

$$f_{mm}(i,j)=\max[f_{\max}(i,j)-f_{med}(i,j),\ f_{med}(i,j)-f_{\min}(i,j)] \quad (2.54)$$

$$F[f(i+r,j+s)]=\begin{cases}1-[f_{med}(i,j)-f(i+r,j+s)]/f_{med}(i,j)-f_{\min}(i,j), \\ \quad for\ \ f_{\min}(i,j)\le f(i+r,j+s)\le f_{med}(i,j)\\ 1-[f(i+r,j+s)-f_{med}(i,j)]/[f_{\max}(i,j)-f_{med}(i,j)], \\ \quad for\ f_{med}(i,j)\le f(i+r,j+s)\le f_{\max}(i,j)\\ 1, \quad for\ f_{med}(i,j)-f_{\min}(i,j)=0\ or\ f_{\max}(i,j)-f_{med}(i,j)=0\end{cases} \quad (2.55)$$

$$F[f(i+r,j+s)]=\begin{cases}1-|f(i+r,j+s)-f_{mav}(i,j)|/f_{mv}(i,j), \\ for\,|f(i+r,j+s)-f_{mav}(i,j)|\le f_{mv}(i,j)\\ 1,\ for\ f_{mv}=o\end{cases} \quad (2.56)$$

$$f_{mv}(i,j)=\max[f_{\max}(i,j)-f_{mav}(i,j),\ f_{mav}(i,j)-f_{\min}(i,j)] \quad (2.57)$$

where the maximum, minimum, median value and moving average value are respectively represented by $f_{\max}(i,j)$, $f_{\min}(i,j)$ $f_{med}(i,j)$ and $f_{mav}(i,j)$ with $s,r \in A$, the window at indices (i,j). The output of the fuzzy filter is computed using Equation 2.50 [229, 250].

2.6.1 Proposed hybrid homomorphic fuzzy filter

The performances of the fuzzy filter in the homomorphic domain are fine tuned by sequentially adding a SRAD filter, thus embedding advantages of both filters in the new one. The proposed hybrid homomorphic fuzzy (HHF) filter along with all other homomorphic and non-homomorphic filtering methods are shown in Figure 2.30. The basic steps incorporated during the implementation are shown in Figure 2.30.

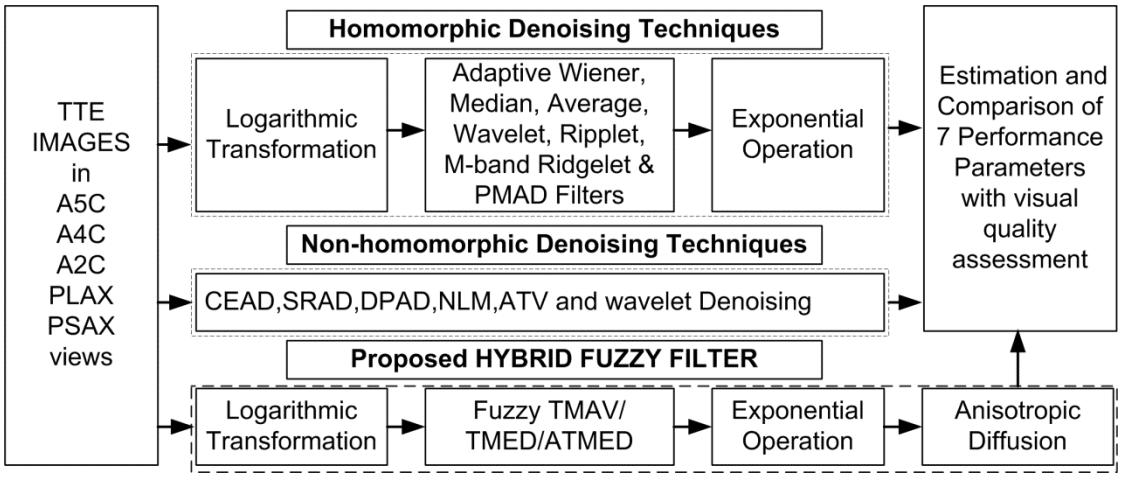

Figure 2.30 Homomorphic and Non-homomorphic despeckling techniques

The input TTE image is transformed into the logarithmic domain and moving average are computed using TMAV membership functions defined by Equation 2.56 and Equation 2.57. The output of fuzzy filter is computed using Equation 2.50. The exponential operation brings the image to the spatial domain. The output of the HF filter using TMAV membership function is taken as input to the AD filter resulting in the fine tuned despeckled image.

2.6.2 Results

The performances of the TMED, ATMED and TMAV filters are analyzed using the standard test images of size of 512×512 each. Speckle noise is added into the standard test images. The results are obtained in-terms of PSNR, SSIM and FoM which are tabulated in Table 2.18.

Table 2.18 Performance parameters comparison for standard test images

Image	σ^2	PSNR(dB)			SSIM			FOM		
		ATMED	TMED	TMAV	ATMED	TMED	TMAV	ATMED	TMED	TMAV
Lena	0.01	**30.66**	27.28	29.98	0.8756	0.8657	**0.9217**	0.7349	0.7252	**0.9102**
	0.05	25.28	23.25	**26.25**	0.6787	0.6928	**0.7947**	0.4199	0.4166	**0.5338**
	0.1	**22.51**	19.30	22.34	0.5685	0.5666	**0.6856**	0.3685	0.3573	**0.4082**
	0.2	**19.19**	14.36	17.00	0.4488	0.3915	**0.5048**	0.3295	0.3133	**0.3448**
	0.3	**16.75**	10.84	12.96	**0.3702**	0.2328	0.3252	**0.3100**	0.2951	0.3074
Mandrill	0.01	**28.10**	25.12	27.29	0.9064	0.8736	**0.9168**	**0.9362**	0.9238	0.9244
	0.05	24.38	22.39	**24.87**	0.7765	0.7577	**0.8399**	0.7837	0.7956	**0.8611**
	0.1	**21.92**	19.22	21.86	0.6724	0.6436	**0.7528**	0.7057	0.6938	**0.7706**
	0.2	**18.90**	14.48	16.92	0.5348	0.4409	**0.5698**	0.6488	0.6176	**0.6653**
	0.3	**16.60**	10.82	12.89	**0.4289**	0.2404	0.3583	**0.6223**	0.6006	0.6185
Cameraman	0.01	**31.10**	27.31	30.15	0.8536	0.8587	**0.9175**	0.5777	0.6882	**0.9217**
	0.05	25.36	23.27	**26.30**	0.6558	0.6742	**0.7707**	0.4092	0.4081	**0.5110**
	0.1	22.48	19.60	**22.57**	0.5668	0.5720	**0.6667**	0.3904	0.3932	**0.4338**
	0.2	**19.25**	14.50	17.15	0.4799	0.4318	**0.5194**	0.3734	0.3620	**0.3878**
	0.3	**16.83**	10.82	12.96	**0.4215**	0.3050	0.3820	**0.3624**	0.3454	0.3552
Barbara	0.01	**24.73**	22.76	24.19	0.8468	0.8010	**0.8612**	0.8370	0.8276	**0.8989**
	0.05	22.69	20.95	**22.76**	0.7180	0.6955	**0.7810**	0.5577	0.5898	**0.6995**
	0.1	**20.92**	18.39	20.62	0.6295	0.5972	**0.7015**	0.4903	0.4814	**0.5580**
	0.2	**18.44**	14.17	16.54	0.5163	0.4377	**0.5534**	0.4466	0.4158	**0.4567**
	0.3	**16.41**	10.91	12.90	**0.4331**	0.2742	0.3740	**0.4148**	0.3928	0.4066
Monarch	0.01	**27.79**	20.63	23.55	**0.8499**	0.6737	0.8163	**0.9424**	0.9014	0.9166
	0.05	26.15	23.80	**27.01**	0.7747	0.7886	**0.8640**	0.4747	0.5103	**0.6586**
	0.1	**23.09**	19.70	22.75	0.6800	0.6758	**0.7757**	0.4070	0.3848	**0.4908**
	0.2	**19.64**	14.72	17.39	0.5612	0.4927	**0.6094**	0.3322	0.3061	**0.3566**
	0.3	**17.27**	11.26	13.39	**0.4785**	0.2977	0.4139	0.3110	0.2683	0.2938

The results show that the performance of HF filter based on ATMED was superior in comparison to other techniques in terms of the IQM such as the PSNR, MSE and SNR. It is also observed that the SSIM and FoM for the HF filter based on TMAV is superior in comparison to the HF filter based on TMED and ATMED. The high values of SSIM and FoM indicate lesser distortion and higher edge preservation using the HF filter with TMAV. Hence, the HF filter with TMAV is considered in the further experimentations and it is fine tuned using the SRAD filter. Similar experiments were carried out for the TTE images but no noise is added to these images. It is observed that the results are similar to those discussed in earlier for the standard test images.

Results obtained using the proposed HHF filter are compared with the HF filter using the TMAV and SRAD filter in terms of the IQM in Figure 2.31 and Figure 2.32 and visual quality comparisons in Figure 2.33. The IQM such as the PSNR, MSE, SNR and ρ, for HFF filter are superior in comparison to the HF filter and the SRAD filter. The average PSNR for the HHF filter

is higher by 3.7 dB compared to the SRAD filter and 9.3 dB for the HF filter. The MSE is 8 times lesser for the HHF filter compared to the HF filter and 3.6 times lesser compared to the AD filter.

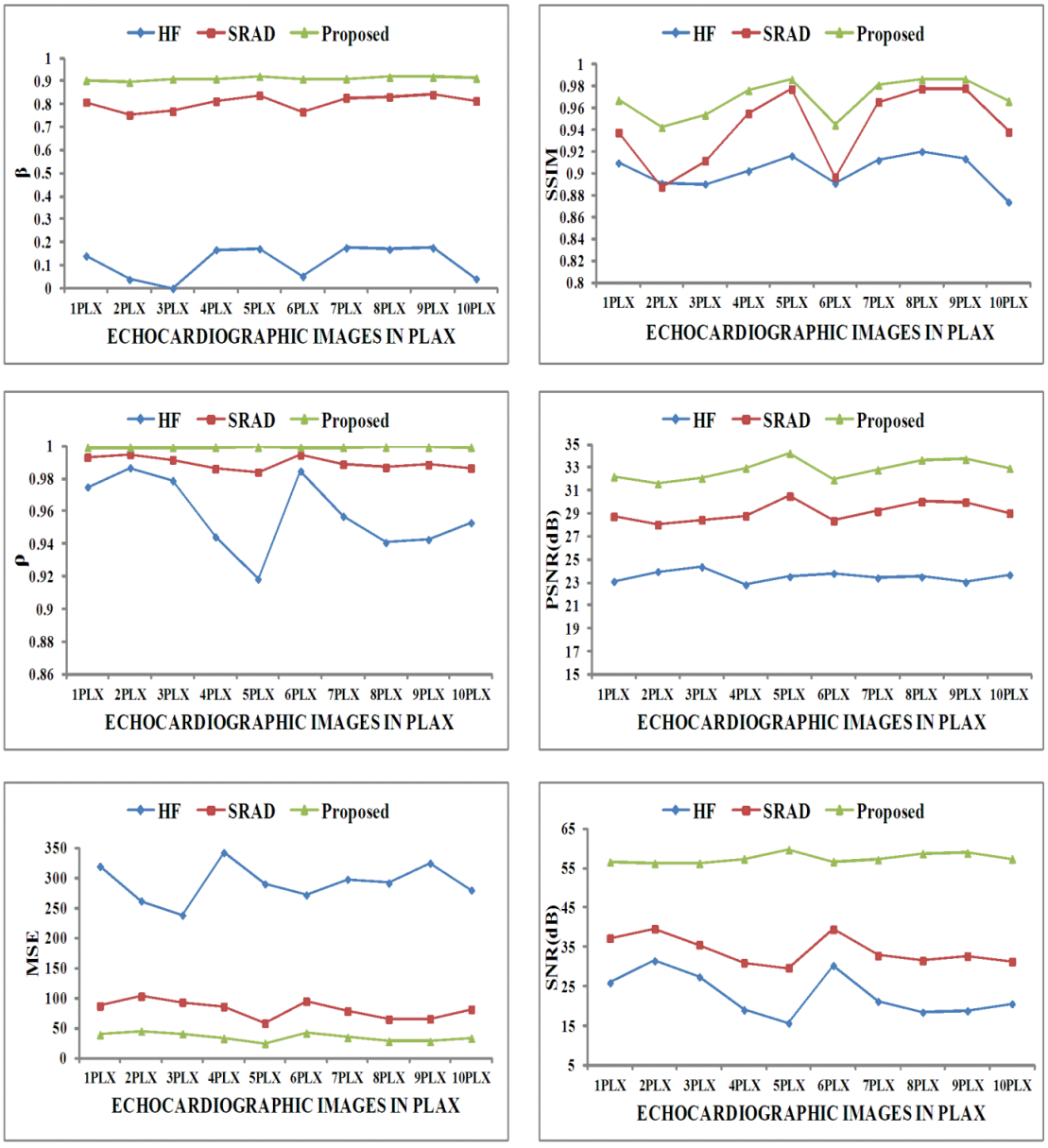

Figure 2.31 IQM for the TTE images in PSAX using HF, SRAD and proposed HHF filter

The value of ρ is on an average 0.04 and 0.01 times higher compared to the HF filter and the SRAD filter, respectively. The SNR is 1.7 times and 2.5 times higher compared to the SRAD filter and HF filter, respectively. Observing the value of β in Figure 2.31 reveals that $\beta<0.2$ for the HF filter and $\beta>0.92$ for the HHF filter which reveals that β value is increased by 9 times using HHF filter in comparison to HF filter and 1.14 times higher compared to SRAD filter.

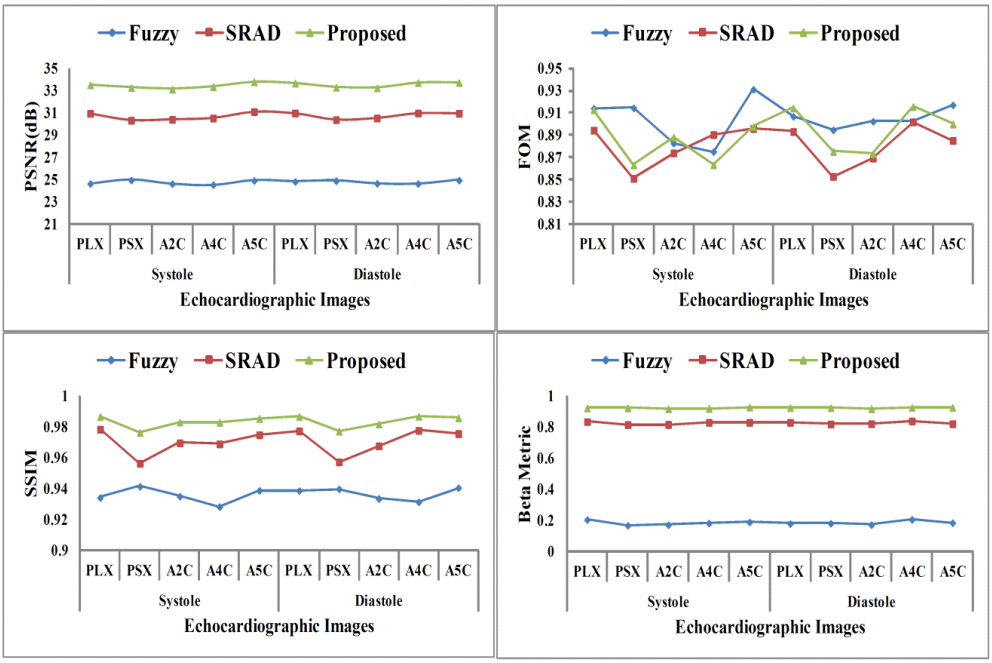

Figure 2.32 IQM for the TTE images in multiple views using HF, SRAD and proposed HHF filter

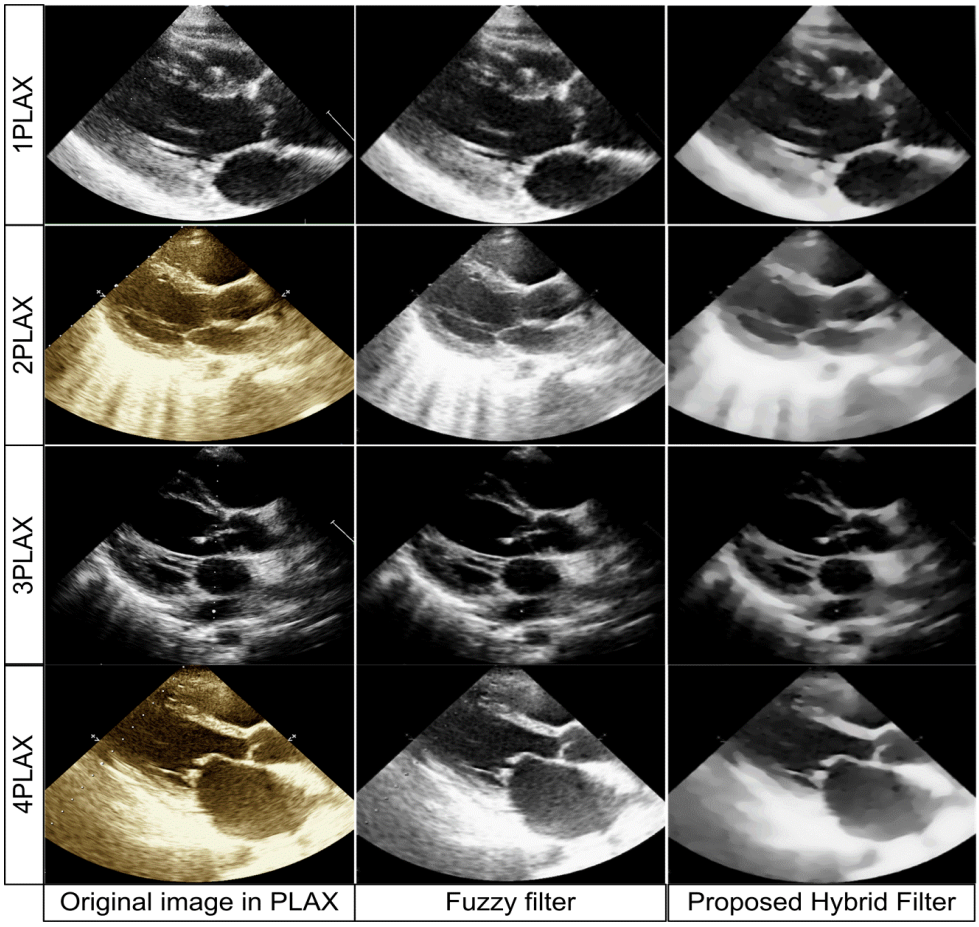

Figure 2.33 Visual quality of TTE images on application of fuzzy and hybrid fuzzy

The visual quality assessments are reported using Figure 2.33 and Figure 2.34. It is observed that the overall structure of the images are well preserved using the proposed HHF filter. The IQM such as β, FoM, SSIM, ρ, PSNR, MSE and SNR are superior using the proposed HHF filter in comparison to the TMAV filter and SRAD filter.

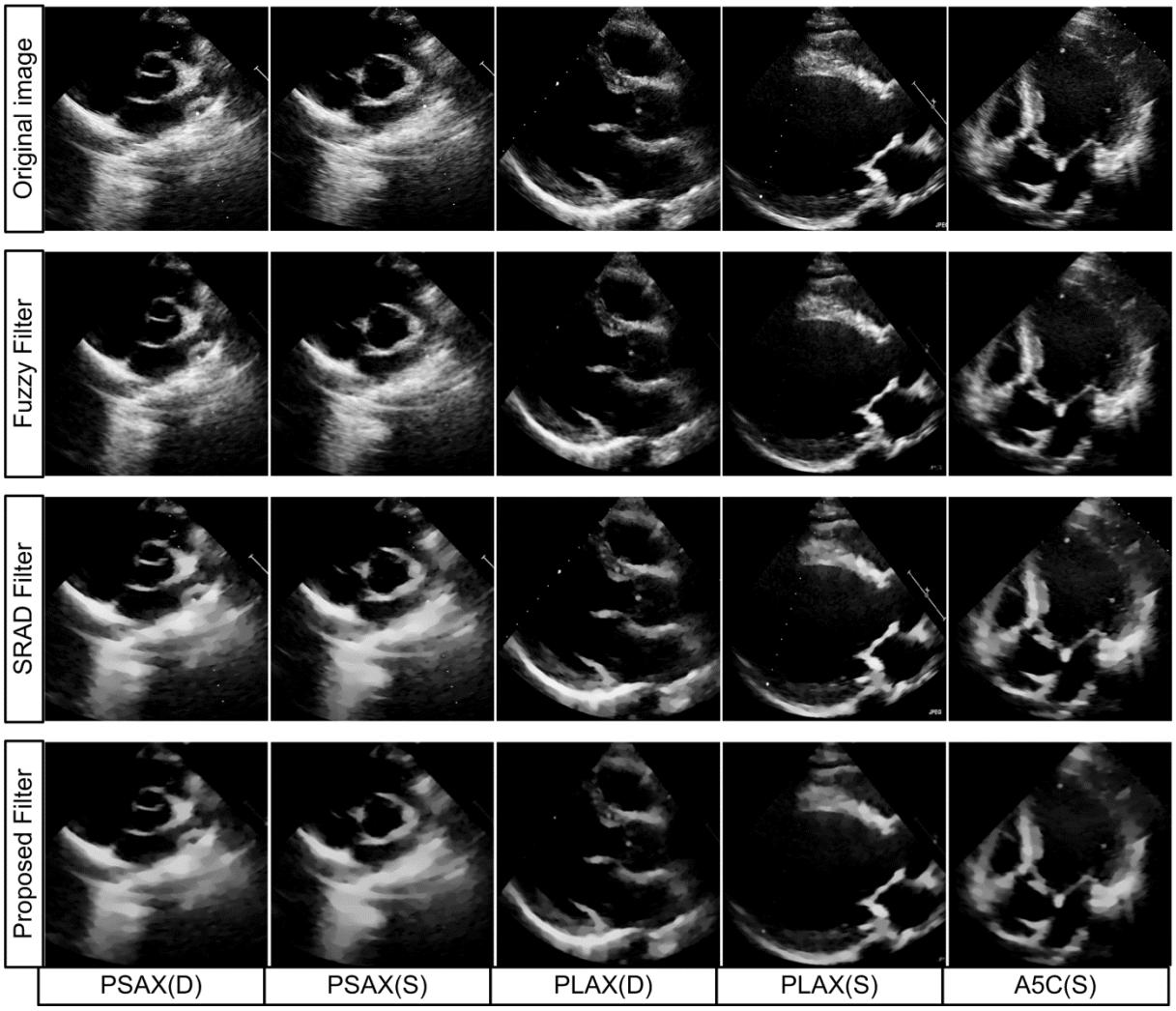

Figure 2.34 Visual qualities of TTE images in multiple views using fuzzy and hybrid fuzzy

2.7 Extreme total variation bilateral filter

Various despeckling techniques based on the principles such as the multiscale [22, 26, 90-93, 116, 130-135], diffusion [22, 35, 83, 86, 131, 135], nonlocal mean (NLM) [125-127,135], total variation (TV) [119-121, 230, 252-254], bilateral [122, 255-261] and fuzzy techniques [229, 250] are available for noise reduction. The despeckling applications of the TV are not extensively reported for the TTE images in multiple views. The recent review papers on the US images [22, 26, 27, 130, 131, 134, 135] have not brought out the applications of TV based despeckling

methods. Hence, work is taken up to study on the applications of TV based noise reduction methods integrated with bilateral filter and prior information for despeckling of the TTE images acquired in various views.

The concept of total variation can be employed in applications such as the image denoising, deblurring, inpainting and others, ever since the idea proposed by Rudin, Osher and Fatemi (ROF) [119-121, 178, 230, 251-255, 259]. The issues of concern, during usage of the TV in noise reduction are loss of contrast, loss of geometry and the staircase effects, under various situations [253-255, 259]. To address these issues, modified versions of the TV filter and various new techniques have come into existence such as anisotropic total variation (ATV), isotropic total variation (ITV) [251], adaptive fidelity total variation (AFTV) [120], duality based gradient projection algorithms [230], the TV as a local filter [253], replacement of L^2 norm with L^1 norm in the fidelity term [259], and others. Zhu *et al.* [230] had studied the applications of the duality based gradient projection (GP) restoration algorithms including the Barzilai–Boorwein (BB) methods. The performances of these filters were analyzed in terms of tolerance, number of iterations and the CPU time. The applications of all methods analysed in [230] are employed for speckle noise reduction in this thesis. Ertas *et al.* [258] combined denoising features of the TV and NLM for reduction of artifacts in 3D iterative image reconstruction. The TV is employed for suppression of background noise while the NLM filter for reduction of out-of-focus blur. The performances of filters were analyzed using SSIM, RMSE and SNR. The concept of edge and texture preservation is not addressed in [258].

The objective in this section is analyze the performances of the TV filter [252] and its variants such as the AFTV [120], ATV, ITV [251] filters along with the proposed extreme total variation bilateral (ETVB) filter, the duality based gradient projection methods [230], DsF [27, 130, 131], Fourier filters [26], NLM filters [125-127] and fast bilateral filter [256] in terms of the IQM. The intensity variations within a tissue or an organ are not as prominent as at their boundaries. The rapid variations are noticed at the boundary walls of the tissues and organs. Therefore, minimization of the TV might significantly improve the image quality, edge preservation and noise reduction [258]. The TV based denoising is effective in suppression of noise but fails to preserve finer details [258]. To address this issue, the extreme total variation bilateral (ETVB) filter is proposed and analysed in this thesis.

2.7.1 Bilateral filter

The bilateral filter is known for smoothing of images with preservation of the edges. The applications of bilateral filter have drastically increased ever since its naming as Bilateral by

Tomasi Manduchi [122-124, 255-257, 260, 261]. One of the basic and most important applications of the bilateral filter is image denoising. It can also be used in applications such as the tone mapping, contrast enhancement, image fusion, compression of artifacts, mesh smoothing, image interpolation, optical flow mapping, depth map estimation, medical imaging and video enhancement. The popularity of bilateral filters can be attributed to 1) simplicity in formulation, 2) efficiency dictated by selection of only two parameters and 3) high computational speed [256, 261]. It works by estimating the weighted average of the neighboring pixels. The basic theme is a pixel will have influence on another pixel if it is located in its nearby vicinity and had similar value [257, 260]. The bilateral filter [122] is defined as $BL[f]_p = \frac{1}{W_p}\sum_{q\in S} G_{\sigma_s}(\| p-q \|)\times G_{\sigma_r}(\| f_p - f_q \|)\times f_p$, where W_p is the normalization factor and it is computed as $W_p = G_{\sigma_s}(\| p-q \|)\times G_{\sigma_r}(\| f_p - f_q \|)$.

The parameters σ_s and σ_r along with window size dictate the amount of denoising which can be achieved using Bilateral filter [122]. The weighted average can be computed based on the range and distance of the Gaussian kernels with G_{σ_r} as the range Gaussian and G_{σ_s} is the spatial Gaussian. The spatial Gaussian decreases the influence of distant pixels whereas the range Gaussian helps in reducing the influence, when the intensity values are different. The final weight is product of temporal (spatial) and distant weights [122, 257, 260]. Kornprobst *et al.* [260] and Paris *et al.* [255] have recommended a linear dependence defined as $\sigma_r = 1.95\sigma_n$, where σ_n represents the local noise level [255, 260]. The optimal value of σ_s is relatively insensitive to noise present compared to σ_r. The kernels are normalized, the sum of coefficients is 1, and centre pixel value of the kernel would be largest and kernel might be of any form.

The input image is used for the estimation of spatial and range weights, followed by multiplication of these values resulting in edge preservation and smoothing. Initially, texture map and block discontinuity maps are generated. The distant component is estimated using the texture map and the range components are estimated using block discontinuity maps. Each of the pixel value is substituted by weighted average of its neighbor. Each pixel is penalized by two components i.e. spatial component penalized the distant pixel and range component penalizes the pixel with different intensity values. Integration of the range and the spatial components ensure that only similar pixels in the neighborhood contribute towards the final pixel values. Thus, the bilateral filter delivers a despeckled image with contours and edges all well preserved.

2.7.2 Duality based algorithms for total variation

The denoising applications of the following algorithms are analyzed along with the proposed ETVB filtering scheme: Chambolle algorithm, Chan-Golub-Mulet (CGM) algorithm, gradient projection with constant length (GPCL), GP with backtracking line search (GPLS), sequential quadratic programming with spectral BB(SQPBB), primal-dual hybrid gradient (PDHG), GP with BB (GPBB), GP with cyclic BB (GPCBB), GPPB with safeguarding (GPPBsafe), GPPB with monotone version of BB step length (GPPBNM), GP with adaptive BB (GPABB) and GPBB, SQPBB, GPABB with different number of cycles such as M2 for two cycles, M3 for three cycles. The values of various parameters in implementation of duality based GP algorithms are based on the analysis and discussion in [230], constant fidelity term is 0.045, fixed step length is 0.248, and maximum number of iterations is 5 in all the implementations. The complete details of duality based GP algorithms are available in [230] and the MATLAB code provided by authors of [230] are being used.

2.7.3 Proposed extreme total variation bilateral filter

Total variation based denoising results in better edge preservation and reduction of noise. But the smaller and finer details may be lost on application of the TV regularizer [230, 259]. The noisy pixels in the flat regions may be presumed as edge pixels, resulting in false noisy edges. It would be desirable that the regularization term is adaptive to achieve better denoising characteristics with edges and structure well preserved [261]. The regularization term of the TV filter is replaced by bilateral term to overcome the drawbacks of total variation. The reasons for selection of bilateral filter as TV regularization term are: 1) TV itself cannot preserve the feature information and smooth them while denoising, so a term is to be used in order to preserve the edges while denoising and bilateral fulfils this requirement. 2) Also, the regularizer term in TV gives a unique solution, same is the case with the bilateral term, which also results in a unique solution. The proposed algorithm is explained in this section. The Equation 1.2 can be rewritten as

$$f_{xy} = T_{xy} + \eta_{xy} \tag{2.58}$$

Where f_{xy} is a noisy image, T_{xy} is the true information, which is considered as the prior knowledge and used by extreme total variation bilateral (ETVB). Here ETVB is replacing the regularizer term of total variation method with the Bilateral filtering term and incorporate the prior term in order to denoise the noisy image. The total variational technique [253] removes the noise in the image according to the following Equation 2.59

$$u_{den} = \arg\min_u \int_{\Omega} (u - f)^2 dx + \lambda \int_{\Omega} |\nabla u| dx \tag{2.59}$$

where u_{den}, f and λ are denoised, input image and smoothing factor, respectively. Solving Equation 2.29 using Euler- Lagrange and gradient descent method [252]

$$\frac{(f-u)}{\sigma_{fu}^2} + \lambda * div\left[\frac{\nabla u}{|\nabla u|}\right] = 0 \tag{2.60}$$

σ_{fu} is the factor which defines the Gaussian range of f in which u can lie, where $div\left[\frac{\nabla u}{|\nabla u|}\right]$ is the regularizer term and on replacing it with the bilateral filtering term $\tilde{u}(k)$ defined in Equation 2.61, substituting it in Equation 2.60 results in Equation 2.62, which are given as follows:

$$\tilde{u}(k) = \frac{\sum_{p \in N(k)} G_c(\| p-k \|) \times G_s(\| u(p)-u(k) \|) \times u(p)}{\sum_{p \in N(k)} G_c(\| p-k \|) \times G_s(\| u(p)-u(k) \|)} \tag{2.61}$$

Where $G_c(\| p-k \|)$ is the closeness smoothing function $e^{-x^2/2\sigma_c^2}$ and $G_s(\| u(p)-u(k) \|)$ is the feature preserving weighing function $e^{-x^2/2\sigma_s^2}$ which penalize the large variations in intensities, $N(k)$ is neighborhood of k, for every k[th] pixel in the noisy image. Substituting Equation 2.61 in Equation 2.60 results in the following modified method of denoising

$$\frac{(f-u)}{\sigma_{fu}^2} + \lambda \times \tilde{u}(k) = 0 \tag{2.62}$$

The concept of prior knowledge is introduced in the traditional TV method, where the prior refers to say generalized information about an object. The usage of prior knowledge is considered to be an inverse problem of obtaining the noise free image from the noisy data. There can be many different ways using which the estimated image can be computed from the noisy image (i.e. having the wide range of possibilities). So, more the given prior knowledge about the object, the more we can constrain the possibilities and better the prediction can be made. Here the prior information (t) is incorporated by using the Bayesian inference and probability density function (PDF). PDF make use of the Directed Acyclic Graph (DAG) based upon the Markov property. The graph is interpreted as, given the parent having two children, good or bad, and when the evil is taken off from the bad then it leads to the good and enlightenment. Similarly, removal of noise from the noisy image leads to the estimated results and both the input and denoised image depends exclusively upon the true knowledge. Given

the true and input information, the probability of the possible output denoised image is defined as

$$P(u / f \cup t) = \frac{P(f \cup t / u) * P(u)}{P(f \cup t)} \tag{2.63}$$

When the dependencies of true knowledge are incorporated then Equation 2.63 can be rewritten as:

$$P(t,u / f \cup t) = P(f \cup t / u) * P(t / u) * P(u) \tag{2.64}$$

This is called as the A-posterior and aim is to maximize this estimation i.e. the maximization of *u*, defined in Equation 2.65, is likely to be both f and t

$$u = \arg\max_u P(t,u / f \cup t) \tag{2.65}$$

which is the Maximum A-posterior Probability (MAP), and the energy of this function is given as: Energy=negative log of A-posterior: which is to be minimized and this leads to Equation 2.66

$$E(u) = \min_u \sum_{i=1}^{n} \frac{(f_i + t_i - u_i)^2}{2 \times \sigma_{ft}^{\ 2}} + \sum_{i=1}^{n} \frac{(t_i - u_i)^2}{2 \times \sigma_{tu}^{\ 2}} + \sum_{i=1}^{n} \lambda \times |u_i - u_{i+1}| \tag{2.66}$$

When solved using the E-L and optimization method leads to the following Equation 2.67 which is referred to as extreme total variation bilateral (ETVB) filtering scheme.

$$0 = \frac{(f + t - u)}{\sigma_{ft}^2} + \frac{(t - u)}{\sigma_{tu}^2} + \lambda . \frac{\sum_{p \in N(k)} G_c(\| p - k \|) \times G_s(\| u(p) - u(k) \|) \times u(p)}{\sum_{p \in N(k)} G_c(\| p - k \|) \times G_s(\| u(p) - u(k) \|)} \tag{2.67}$$

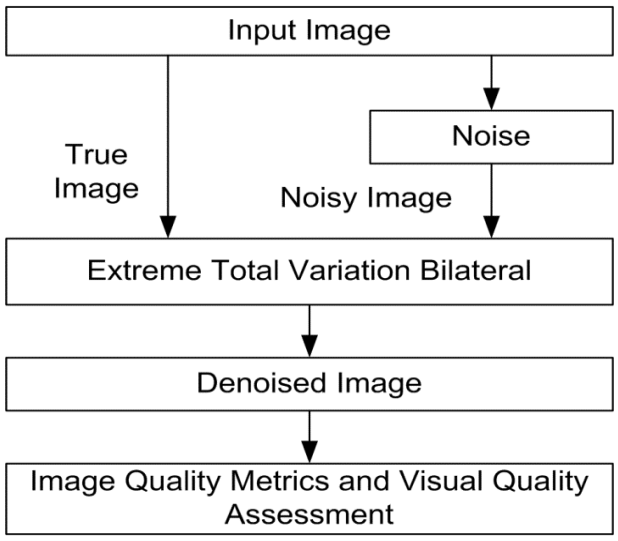

Figure 2.35 Block diagram of ETVB filtering scheme

The proposed method of denoising is shown in Figure 2.35. The noise free image is embedded with speckle noise. The noise free image and noisy image are subjected to extreme total variation bilateral filter with prior knowledge of noise free image. The regularization term of total variation are replaced with bilateral filter. The prior information of input image is embedded into total variation based denoising.

2.7.4 Results

The image quality metrics and visual quality based results are presented in this section. Denoising performances in terms of edge preservation are tabulated in Table 2.19 and using traditional parameters in Table 2.20, for total variation based techniques. The results in Table 2.19 are of Barbara image artificially embedded with speckle noise of variance 0.01, 0.05 and 0.1, using imnoise. The traditional image quality metrics for Barbara image, with noise variance 0.01, are shown in Table 2.20. The results obtained using replacement of TV term with BL term without taking into account the prior information are represented as “TV+BL” and “TV+BL+True” considers true information, results are named as “ETVB”.

Table 2.19 Comparison of TV based filters in terms of edge preservation

Metrics	**IQI**			**SSIM**			**BETA**			**FoM**		
Variance	0.01	0.05	0.1	0.01	0.05	0.1	0.01	0.05	0.1	0.01	0.05	0.1
ROF[253]	0.672	0.441	0.332	0.886	0.701	0.593	0.703	0.397	0.285	0.736	0.495	0.459
AFTV[120]	0.680	0.450	0.341	0.887	0.703	0.592	0.717	0.401	0.292	0.718	0.523	0.454
GPPB_M2F[230]	0.584	0.539	0.480	0.852	0.793	0.717	0.527	0.455	0.344	0.794	0.721	0.581
GPPB_M3F[230]	0.580	0.539	0.482	0.848	0.793	0.715	0.454	0.436	0.341	0.787	0.725	0.573
CGM[230]	0.541	0.520	0.470	0.845	0.806	0.727	0.573	0.461	0.347	0.763	0.773	0.594
Chambolle [230]	0.644	0.556	0.484	0.883	0.794	0.705	0.710	0.495	0.359	0.845	0.668	0.552
GPCL[230]	0.559	0.521	0.467	0.853	0.799	0.720	0.371	0.386	0.324	0.786	0.747	0.578
GPLS[230]	0.554	0.523	0.458	0.852	0.799	0.722	0.350	0.395	0.316	0.777	0.736	0.588
PDHG[230]	0.563	0.527	0.476	0.844	0.796	0.718	0.525	0.437	0.335	0.759	0.733	0.590
SQPBB_M2[230]	0.594	0.539	0.484	0.857	0.794	0.720	0.581	0.466	0.343	0.778	0.702	0.590
SQPBB_M[230]	0.594	0.537	0.483	0.857	0.793	0.717	0.577	0.459	0.345	0.770	0.716	0.582
SQPBB_NM2[230]	0.578	0.540	0.482	0.851	0.798	0.716	0.571	0.467	0.347	0.794	0.751	0.573
SQPBB_NM[230]	0.575	0.537	0.479	0.849	0.794	0.715	0.569	0.464	0.346	0.782	0.719	0.580
GPBBsafe[230]	0.559	0.530	0.478	0.843	0.795	0.718	0.508	0.446	0.337	0.768	0.733	0.574
GPABB[230]	0.586	0.538	0.480	0.853	0.794	0.717	0.527	0.455	0.341	0.775	0.734	0.591
GPBB_N3alt[230]	0.561	0.526	0.476	0.844	0.794	0.719	0.491	0.436	0.344	0.764	0.740	0.589
GPBB_N2alt[230]	0.558	0.533	0.479	0.843	0.798	0.719	0.500	0.450	0.344	0.754	0.757	0.593
GPBB_Nalt[230]	0.549	0.528	0.475	0.841	0.793	0.715	0.493	0.454	0.341	0.771	0.716	0.583
GPBB_NM[230]	0.559	0.527	0.477	0.843	0.793	0.717	0.499	0.448	0.339	0.779	0.748	0.599
GPBB_M[230]	0.565	0.526	0.476	0.851	0.797	0.717	0.438	0.428	0.336	0.771	0.753	0.592
GPBB_M3[230]	0.558	0.517	0.468	0.850	0.799	0.721	0.409	0.400	0.329	0.784	0.765	0.580
ATV[252]	0.654	0.539	0.450	0.904	0.783	0.682	0.734	0.467	0.328	0.877	0.591	0.491
ITV [252]	0.684	0.539	0.439	0.916	0.774	0.669	0.773	0.458	0.322	0.906	0.566	0.482
TV+BL	0.951	0.855	0.788	1.000	1.000	1.000	0.982	0.914	0.834	0.961	0.953	0.891
ETVB	0.967	0.895	0.839	1.000	1.000	1.000	0.989	0.949	0.898	0.963	0.959	0.946

Table 2.20 Traditional parameters for Barbara image using TV based filters

Methods	SNR	PSNR	MSE	RMSE	ERR3	ERR4	MD	LMSE	NAE	SC	NK
ROF[253]	41.48	26.63	141.33	11.89	14.01	15.75	74.48	0.910	0.079	0.994	0.9989
AFTV[120]	42.24	27.01	129.46	11.38	13.48	15.24	77.40	0.780	0.074	0.997	0.9978
GPPB_M2F	38.49	25.13	199.36	14.12	18.68	22.49	80.39	0.798	0.077	1.021	0.9838
GPPB_M3F	38.24	25.01	205.25	14.33	18.96	22.81	88.67	0.822	0.077	1.021	0.9838
CGM	38.73	25.25	193.97	13.93	18.34	22.06	79.71	0.756	0.077	1.024	0.9826
Chambole	40.61	26.19	156.22	12.50	16.58	20.07	76.02	0.657	0.069	1.018	0.9863
GPCL	38.45	25.11	200.49	14.16	18.62	22.38	84.30	0.863	0.078	1.021	0.9837
GPLS	38.37	25.07	202.18	14.22	18.69	22.45	80.56	0.879	0.079	1.021	0.9835
PDHG	38.49	25.13	199.38	14.12	18.60	22.34	87.18	0.780	0.077	1.022	0.9835
SQPBB_M2	38.75	25.26	193.58	13.91	18.46	22.27	84.21	0.776	0.075	1.021	0.9839
SQPBB_M	38.78	25.28	192.81	13.89	18.42	22.21	80.54	0.775	0.075	1.020	0.9842
SQPBB_NM2	38.60	25.19	196.96	14.03	18.56	22.35	79.54	0.780	0.076	1.021	0.9837
SQPBB_NM	38.56	25.17	197.90	14.07	18.60	22.39	80.78	0.781	0.077	1.021	0.9838
GPBBsafe	38.24	25.01	205.33	14.33	18.89	22.69	85.43	0.808	0.078	1.021	0.9834
GPABB	38.50	25.14	199.30	14.12	18.69	22.52	83.81	0.800	0.077	1.021	0.9837
GPBB_N3alt	38.29	25.03	204.05	14.28	18.82	22.62	84.70	0.806	0.078	1.022	0.9830
GPBB_N2alt	38.19	24.98	206.42	14.37	18.95	22.78	85.58	0.813	0.078	1.022	0.9831
GPBB_Nalt	38.14	24.96	207.67	14.41	18.98	22.80	87.46	0.818	0.079	1.021	0.9836
GPBB_NM	38.21	24.99	206.08	14.36	18.94	22.76	84.99	0.813	0.078	1.022	0.9833
GPBB_M	38.39	25.08	201.79	14.21	18.75	22.56	81.28	0.829	0.078	1.021	0.9835
GPBB_M3	38.35	25.06	202.76	14.24	18.77	22.57	81.71	0.842	0.078	1.021	0.9837
ATV[252]	43.23	27.50	115.63	10.75	14.00	16.86	68.76	0.506	0.062	1.016	0.9885
ITV [252]	44.86	28.32	95.78	9.79	12.63	15.19	63.20	0.427	0.058	1.013	0.9906
TV+BL	62.17	85.11	0.001	0.01	0.02	0.02	0.06	0.036	0.026	0.992	1.0038
ETVB	65.35	86.70	0.001	0.01	0.01	0.02	0.05	0.022	0.021	0.991	1.0042

Table 2.21 Image quality metrics for proposed method ETVB

IQM	Lena			Woman Dark hair			Woman Blonde			Mandrill		
Noise	0.01	0.05	0.1	0.01	0.05	0.1	0.01	0.05	0.1	0.01	0.05	0.1
IQI	0.946	0.817	0.722	0.955	0.882	0.826	0.952	0.837	0.739	0.981	0.924	0.867
SSIM	1.000	1.000	1.000	1.000	1.000	1.000	1.000	1.000	1.000	1.000	1.000	1.000
BETA	0.949	0.786	0.639	0.871	0.577	0.425	0.971	0.869	0.766	0.955	0.804	0.675
FoM	0.945	0.937	0.944	0.881	0.897	0.882	0.971	0.901	0.846	0.963	0.965	0.949
MSE	0.000	0.000	0.001	0.000	0.000	0.000	0.000	0.000	0.001	0.000	0.001	0.001
SNR	66.12	58.70	52.55	73.21	61.76	55.08	72.66	61.51	55.21	58.69	56.80	51.50
RMSE	0.011	0.017	0.024	0.006	0.012	0.018	0.011	0.020	0.029	0.020	0.023	0.031
PSNR	87.21	83.50	80.42	92.02	86.30	82.96	87.55	81.97	78.82	81.98	81.04	78.38
ERR3	0.013	0.020	0.028	0.008	0.016	0.023	0.013	0.023	0.033	0.023	0.026	0.035
ERR4	0.015	0.023	0.032	0.010	0.018	0.027	0.014	0.026	0.037	0.025	0.029	0.038
AD	0.004	0.003	0.004	0.000	0.000	0.001	0.003	0.002	0.001	0.014	0.006	0.004
SC	0.976	0.978	0.975	0.994	0.997	1.001	0.992	0.996	1.005	0.948	0.976	0.980
NCC	1.012	1.011	1.012	1.003	1.001	0.999	1.004	1.001	0.997	1.027	1.012	1.009
MD	0.059	0.073	0.094	0.047	0.065	0.085	0.061	0.081	0.101	0.063	0.073	0.090
LMSE	0.100	0.534	1.259	0.249	1.453	3.362	0.053	0.254	0.544	0.091	0.497	1.085
GAE	0.019	0.029	0.042	0.014	0.026	0.036	0.013	0.025	0.036	0.029	0.032	0.045

Figure 2.36 Despeckling of Lena image using various TV based methods

The gradient projection based TV methods have IQI less than 0.6 whereas methods such as ROFTV, AFTV, Chambolle, ATV and ITV have IQI greater than 0.65. The performance of TV+BL and ETVB are superior in comparison to all total variation based methods tabulated in Table 2.19 with IQI ≥ 0.95. Structural similarity index, $(SSIM)_{ATV,\ ITV} \geq 0.9$ whereas $(SSIM)_{TV+BL}$ and $(SSIM)_{ETVB}$ are equal to one. Edge preservation parameter β is 0.989 and 0.982 using ETVB and TV+BL, respectively. The methods such as ROFTV, AFTV, ATV and ITV have the β

value less than 0.77 and gradients projection filters less than 0.6. The performance of TV+BL and ETVB are superior in terms of IQI, SSIM, β and FoM compared to all TV methods tabulated in Table 2.19. These results reveal better edge preservation obtained employing the proposed method. Table 2.20 reveals that traditional image quality metrics are enhanced many fold compared to performances of other total variation based methods. The enhancement in traditional parameters in Table 2.20 show superior noise reduction capabilities of proposed integration of bilateral filter and prior information into total variation based denoising technique.

Table 2.22 Image quality metrics of denoised TTE images

TV+BL										
Image	**IQI**	**SSIM**	**BETA**	**NK**	**FoM**	**SNR**	**RMSE**	**LMSE**	**NAE**	**MD**
PSAX(S)	0.7399	1.00	0.9955	0.9951	0.9666	64.05	0.0055	0.0090	0.0239	0.0519
PLAX(S)	0.7215	1.00	0.9958	0.9941	0.9613	63.34	0.0049	0.0083	0.0262	0.0519
A4C(S)	0.7720	1.00	0.9955	0.9941	0.9818	63.04	0.0054	0.0090	0.0275	0.0519
A5C(S)	0.7899	1.00	0.9959	0.9929	0.9733	62.54	0.0049	0.0082	0.0262	0.0519
A2C(S)	0.7657	1.00	0.9953	1.0000	0.9340	63.51	0.0055	0.0093	0.0275	0.0520
PSAX(D)	0.7376	1.00	0.9955	0.9953	0.9565	64.36	0.0054	0.0090	0.0237	0.0519
PLAX(D)	0.7043	1.00	0.9958	0.9940	0.9637	63.44	0.0050	0.0084	0.0251	0.0519
A4C(D)	0.6882	1.00	0.9962	0.9932	0.9596	62.58	0.0049	0.0075	0.0270	0.0530
A5C(D)	0.7029	1.00	0.9963	0.9912	0.9721	60.73	0.0046	0.0074	0.0289	0.0519
Extreme total variation bilateral (ETVB)										
Image	**IQI**	**SSIM**	**BETA**	**NCC**	**FoM**	**SNR**	**RMSE**	**LMSE**	**NAE**	**MD**
PSAX(S)	0.7469	1.00	0.9966	0.9957	0.9720	66.51	0.0048	0.0068	0.0207	0.0453
PLAX(S)	0.6972	1.00	0.9969	0.9949	0.9662	65.80	0.0042	0.0063	0.0228	0.0453
A4C(S)	0.7497	1.00	0.9966	0.9948	0.9699	65.48	0.0047	0.0068	0.0239	0.0453
A5C(S)	0.7410	1.00	0.9969	0.9939	0.9772	65.00	0.0042	0.0062	0.0228	0.0453
A2C(S)	0.7558	1.00	0.9965	0.9999	0.9439	65.98	0.0047	0.0070	0.0239	0.0452
PSAX(D)	0.7449	1.00	0.9966	0.9959	0.9630	66.81	0.0047	0.0068	0.0206	0.0453
PLAX(D)	0.7395	1.00	0.9968	0.9948	0.9690	65.90	0.0043	0.0063	0.0218	0.0453
A4C(D)	0.6953	1.00	0.9972	0.9941	0.9667	65.05	0.0043	0.0057	0.0234	0.0460
A5C(D)	0.7350	1.00	0.9970	0.9942	0.9772	65.35	0.0042	0.0060	0.0224	0.0453

The performance of ETVB technique for images such as Lena, Woman Dark hair, Woman Blonde, and mandrill are tabulated in Table 2.21 at various noise levels. The performance of proposed methods is on similar lines as discussed for Barbara image in earlier paragraphs. High values of IQI, SSIM, and β themselves speak of superiority of the proposed techniques in terms of edge preservation. LMSE, MSE, RMSE, and MD are all less than 1 and drastically reduced in comparison to all techniques tabulated in Table 2.22. The performances of ETVB method are compared with other state-of-art technique in Table 2.23.

Table 2.23 Comparison with proposed technique with other state-of-art technique

Method	IQI	SSIM	β	ρ	FoM	MD	LMSE	MSE	SNR	RMSE	PSNR
DsFlsminsc	0.518	0.818	0.073	0.991	0.811	128.0	1.114	286	35.36	16.91	23.57
DsFlsmv	0.724	0.913	0.813	0.997	0.889	66.04	0.405	94.5	44.98	9.72	28.38
DsFWiener	0.714	0.918	0.781	0.997	0.852	62.33	0.393	86.2	45.78	9.29	28.78
DsFgf4d	0.546	0.794	0.407	0.991	0.778	170.0	1.103	594	29.01	24.38	20.39
DsFad	0.493	0.803	0.475	0.994	0.663	98.77	0.802	241	36.82	15.54	24.30
DsFsrad [131]	0.704	0.903	0.794	1.000	0.874	76.80	0.544	125	42.51	11.20	27.14
DsFhmedia	0.626	0.868	0.486	0.995	0.848	113.1	0.813	166	40.05	12.91	25.91
DsFhomog	0.597	0.852	0.298	0.993	0.805	104.2	0.944	230	37.23	15.18	24.50
DsFmedian	0.566	0.834	0.173	0.993	0.769	181.2	1.062	234	37.10	15.30	24.44
FBL [257]	0.751	0.951	0.962	0.999	0.888	30.43	0.093	32.4	54.29	5.69	33.03
FBF [26]	0.705	0.891	0.771	0.997	0.719	61.01	0.453	99.5	44.53	9.97	28.15
FIF[26]	0.671	0.881	0.761	0.996	0.709	67.12	0.634	130	42.21	11.40	26.99
GLM[116]	0.754	0.924	0.781	0.997	0.885	86.32	0.445	84.1	45.99	9.17	28.88
OBNLM [125]	0.784	0.962	0.924	0.998	0.934	56.21	0.165	81.9	46.22	9.05	29.00
PPB [127]	0.743	0.954	0.918	0.999	0.910	83.54	0.164	40.8	52.27	6.39	32.02
TV+BL	0.951	1.000	0.982	1.000	0.961	0.063	0.036	0.00	62.17	0.01	85.11
ETVB	0.967	1.000	0.989	1.000	0.963	0.054	0.022	0.00	65.35	0.01	86.70

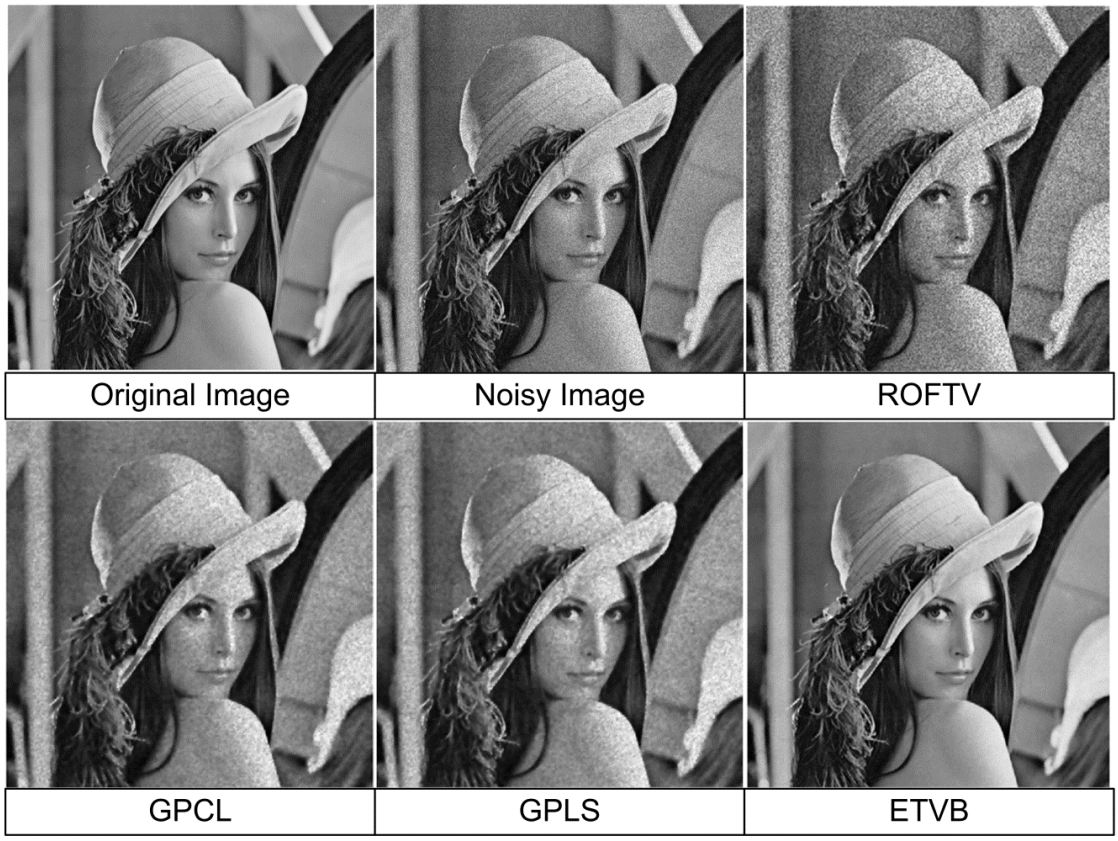

Figure 2.37 Despeckling of Lena image using TV, GPCL, GPLS and ETVB filters

Figure 2.38 Despeckling of Barbara image using various TV based filters

The performance of proposed ETVB technique for TTE images are tabulated in Table 2.22. IQI≥0.7, SSIM≈1, BETA≥0.99, and FoM≥0.9 show that the edges and structure are preserved. The error in the denoised images in terms of parameters such as RMSE, LMSE, NAE and MD are less than 1, which indicates superior noise reduction in the denoised images. The visual qualities of the denoised images are displayed in Figure 2.36, to Figure 2.38. The texture of denoised image is compared in Figure 2.38 using zoomed version of Barbara image

on application of various despeckling techniques. It is noticed that GP based methods lead into suppression of finer details. Speckle noise is removed but the edge and texture information is lost in the due process.

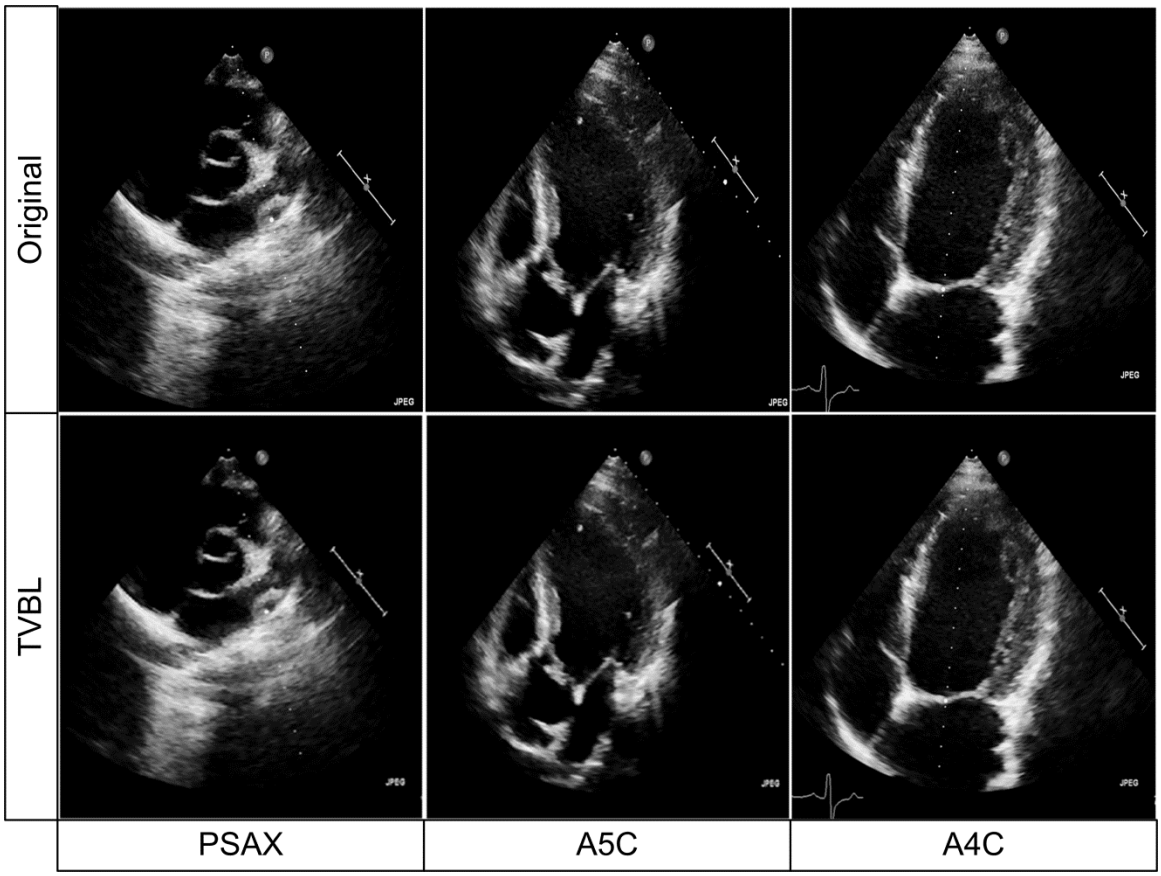

Figure 2.39 Despeckling of TTE image in multiple views using various TVBL filter

The ROF TV method results in loss of texture accompanied with retention of noise in textured and smooth parts of the image respectively. The NLM based filter performance is visually superior compared to TV based methods but on certain instances it also leads to over-smoothing and noise retention. The analysis of images depicted in Figure 2.36 shows the visual quality of Lena image is enhanced on application of proposed filter. The contrast of images is reduced using TV based methods and this is evident on observing all images shown in Figure 2.36. A small amount of noise is retained in most of the TV based methods such as AFTV, ROFTV, ATV, ITV, and gradient projection TV methods. Almost all noise is removed using the proposed methods.

The texture of image is retained using proposed methods as evident from Figure 2.38. A part of Barbara image is shown in Figure 2.38, where texture of the image is different from the homogenous regions. The texture of the image is lost using CGM, FIF, Chambolle and DsFad,

gradient projection based TV partly preserve the texture. Texture of the images are fully preserved on application of methods such as NLM, PPB, DsFlsmv, and proposed ETVB method. ROF TV results in loss of texture information in parts such as scarf, chair and trouser. A small amount of noise is retained in smooth regions such as cheek and chin. The NLM based filter leads in over-smoothing in certain parts such as upper part of the arm. This particular effect is observed when the patch size is large and over-smoothing is reduced in cases of smaller patches. The drawbacks of ROF TV, NLM and PPB filters are overcome using ETVB filtering scheme. The visual qualities of denoised TTE images are analyzed using images shown in Figure 2.39. It is observed that the required finer details retained in the despeckled TTE images and the quality of image is acceptable for the clinicians.

2.8 Summary

The TTE images acquired in multiple views were despeckled using the proposed techniques. The first proposed technique is based on the logarithmic multiscale techniques. Eight multiscale techniques were analysed in the logarithmic domain. The analysis revealed that the NeighshrinkSURE (NSS) represented as LM7E stood out among the multiscale techniques in terms of noise suppression and edge preservation. The implementation of PSBE filter and its improved version, known as hybrid PSBE filter is the second proposed scheme. The third proposed technique is based on combining the TMAV filter with Wiener filter to fine tune the performance of fuzzy filter. The performance of hybrid TMAV filter was further improved by integrating fuzzy, Wiener and the geometric filter. This technique is called as integrated fuzzy filter whose performance is superior in comparison to geometric, Wiener and four fuzzy filters. The advantages of anisotropic diffusion and fuzzy filters are combined in the fifth proposed filter known as hybrid homomorphic fuzzy filters. The performance of HHF filter is analysed for the images acquired in two parasternal and three apical views.

CHAPTER 3: COMPARATIVE ANALYSIS OF DESPECKLING TECHNIQUES

In this chapter a comparative analysis of despeckling techniques for the B-mode transthoracic echocardiographic images is being presented in terms of image quality metrics, visual quality assessment and clinical validation. The thrust areas of analysis were speckle noise suppression with edge and structure preservations. The performance of 48 filters, grouped into eight types are analysed in terms of traditional and blind-source IQMs for the TTE images. The objective of comparative analysis is to identify best within class and inter-class filter in terms of noise suppression and clinical acceptance.

3.1 Introduction

Transthoracic echocardiography (TTE) is a non-invasive, clinically preferred technique and quite popular because of low cost, and portability [3-10, 22]. The visual qualities of the TTE images in the multiple views and windows play an important role in the study of aetiologies and the impact of valvular abnormalities. But, as pointed earlier, the visual interpretation and automated computer aided analysis are hindered by the poor quality of the images [5, 12, 14, 17-20, 39-47]. The shadowing, low contrast, reverberations and speckle noise make it fuzzy in locating the abnormalities and consistent measurement [4, 5, 54, 58, 180,182, 201]. The TTE images acquired using the cross sectional windows and views have higher amount of noise in them [22]. An overview of despeckling methods employed for noise reduction in the US images of breast [135], kidney [26], bone [96, 134], heart [22] and carotid artery [27, 131] is available in Table 3.2 with all abbreviations in Table 3.1. The concept, merits and demerits of each filter are brought out in Table 3.3.

Many researchers analysed and compared the performance of despeckling techniques [22, 26, 27, 80, 130, 131, 134, 135, 263, 264] for various types of US images. Mateo *et al.* [26] compared image quality metrics (IQM) of median filter, adaptive median filter, homomorphic wavelet filter with soft thresholding, Fourier Ideal Filter (FIF) and Fourier Butterworth Filter (FBF) for the US images of kidney. Finn *et al.* [22] compared 15 despeckling filters based on local statistics, wavelet, synthetic aperture radar (SAR) filters and image geometry on the TTE images. Elamvazuthi *et al.* [134] analyzed filters such as the Wiener, average, median, anisotropic diffusion (AD), wavelet and the combination of wavelet filter with Wiener filter for suppression of speckle noise in the US images of bone fracture. Zhang, Wang and Cheng [135] had compared the performances of nonlocal mean (NLM) filters with local adaptive, anisotropic, hybrid and multiscale techniques on the US images of breast. Loizou *et al.* [27,130, 131] had compared applications of 10 denoising filters for reduction of speckle noise in carotid artery.

Table 3.1 List of abbreviations used in Chapter 3

Acronym	Full form	Acronym	Full form	Acronym	Full form
ATV	Anisotropic total variation	DsFsrad	Speckle reducing anisotropic diffusion	NSS	Neighborhood shrinkage using SURE
AFTV	Adaptive fidelity total variation	DsFWiener	Wiener filter	OCT	Optical coherence tomography
BShrink	Bayes shrink	DPAD	Detail preserving anisotropic diffusion	OBNLM	Optimized Bayesian nonlocal Mean
BT	Block thresholding	FBL	Fast bilateral	PPB	Probabilistic patch based
BPFA	Beta process factor analysis	FIF	Fourier ideal filter	PShrink	Probability shrinkage
CED	Coherence enhancing diffusion	FBF	Fourier Butterworth filter	PSBE	Posterior sampling based estimation
DsF	Despeckling filter	GLM	Generalized likelihood method	PLOW	Patch based locally optimal Wiener
DsFhomog	Maximum homogeneity	HTMAV	Hybrid triangulation moving average	RNLA	Ripplet using nonlinear approximation
DsFad	Anisotropic diffusion	HTMED	Hybrid triangulation median	SURE	Stein's unbiased risk estimation
DsFhomo	Homomorphic	IOWT	Interscale orthogonal wavelet threshold	TMED	Triangulation median
DsFlsminsc	Minimum speckle index	MPT	Multiscale product threshold	TMAV	Triangulation moving average
DsFlsmv	Local statistics mean variance	MBR	M-Band ridgelet	TTE	Transthoracic echocardiography
DsFhmedian	Hybrid median	MRI	Magnetic resonance imaging	US	Ultrasound

Table 3.2 An overview of despeckling filters

Method name	Reference and type of image	Method name	Reference and type of image
Local statistics based techniques		**Nonlinear techniques**	
Lee [77, 81], Kaun [78], Frost [79, 265]	[22]-**TTE** image in PLAX and PSAX, [77- 79, 265]-SAR images, [135]- US Breast [27, 131]- US Carotid artery	CED[84]	[84]-CT bone, [131]- Carotid artery
		DsFad [83]	[27, 131]- US Carotid artery, [22]- **TTE**
		DsFsrad [35], DsFhmedian [27, 131]	[27, 131]- US Carotid artery, [22]- **TTE**
DsFlsminsc, DsFlsmv [27, 130, 131]	[27, 131]- US image of Carotid	DPAD[86], Level set diffusion [266]	[135]-US image of Breast
DsFWiener [27, 130, 131]	[27, 131]- Carotid artery, [134]- Bone fracture	DsFgf4d [27, 131], DsFhomo	[135]- Breast, [22]-**TTE**, [27, 131]- Carotid
BL [256]	[135]- Breast US	DsFhomog [27, 131], DsFmedian [27, 131]	[27, 131]- Carotid artery
Fuzzy filtering techniques		**Multiscale techniques**	
TMED,TMAV,ATMED,ATMAV [229, 250]	[229, 250]-Synthetic	BayesShrink [227], OWT [102]	[100-103, 227]-Synthetic images [100]-MRI image of liver
Fourier Filters[26]		ProbShrink [99], NSS [103]	
FBF,FIF,HFBF, HFIF [26]	[26]- US image of Kidney	SURELET [101], MPT [100]	
Total variation		GLM [116]	[135]-US Breast, [22]- **TTE** , [116]- MRI
AFTV [120], ROF [120, 252], ATV [251]	[120, 253]-Standard , [252]-MRI	MBR [94]	[267]- US bone fracture
Aujol et al. [119]	[119]-Synthetic and SAR images	RNLA [95]	[96]- US bone fracture
Shock filter [268]	[268]- Standard images	PSBE [228]	[228]- OCT image of rat retina
Nonlocal mean techniques		**Hybrid techniques**	
OBNLM [125, 126], PPB[127]	[135]-US image of Breast	HTMAV, HATMV,HTMED, GW	[251]- Standard images
Sparse & dictionary learning [269,277]	BPFA [269], Sparse[277]	Synthetic images [270]	

Table 3.3: Concept, merits and demerits of despeckling filters

Method	Concept	Merits	Demerits
Lee [22, 77]	Estimating central pixel intensity based on the average pixel intensity and coefficient of variation with minimization of the mean square error	Spatially adaptive filters, visual enhancement, structure of the image well preserved	Allow noisy edges to persist, sharp features not retained, limited noise reduction, induce blocky effect
Kaun et al. [22, 78]	Similar to the Lee filter but based on the different weighing function	Structure well preserved, spatially adaptive filters, enhancement	Poor noise reduction, over-smoothing, details are lost, blurring of edges, poor performance in homogeneous regions
Frost et al. [22, 79, 270]	Noise free image is computed by convolving noisy image with a defined mask	Adaptive least squares estimation, better noise suppression, Texture is preserved	Sharp features are not retained, significant loss in image detail, blurring of image at boundaries
Local statistics mean variance [27, 130,131]	Use the first order statistics like mean and variance of each pixel neighborhood	Image quality enhanced, mean and median values preserved, texture feature well preserved	Computational time depends on size and shape of the window and number of iterations,
Wiener [27, 131]	Pixel-wise adaptive Wiener technique, restoration of image based on mean square error	Superior noise suppression, enhance the optical sensitivity evaluation	Smoothing of the texture information, not suitable for statistical analysis
Minimum speckle index [27, 131]	Estimate the most homogeneous area around neighborhood of each pixel , centre pixel in window is replaced by smallest speckle index in a sub-mask	May be employed in improving the classification accuracy and outcome of statistical analysis	Edges not well preserved, reduction in the image quality, over-smoothing of the image, finer details lost
Fast bilateral [256]	Works based on the spatial locations and similarity of pixel values and its neighbors, each pixel value is replaced by weighted average of its neighboring pixels.	Feature preserving filter, Smoothing with edge preservation, Simple in its formulation	Not designed to deal with textured regions, undesired “staircasing effect”, computational cost is high
Triangulation median [229]	Median value is computed using symmetrical triangular fuzzy filter	Simple, edges are well preserved	Output is noisy, texture is lost , edges are partially preserved
Asymmetrical triangulation median [229,250]	Median value is computed using asymmetrical triangular fuzzy filter	Edges and structures are well preserved	Texture is partially preserved but with some loss of details, further degradation at high noise level
Triangulation moving average [229,250]	Moving average value is estimated using symmetrical triangular fuzzy filter	Higher noise suppression compared to TMED filter	Reduction in the contrast, Sensitive to size of the window and padding
Fourier ideal filter[26]	Suppresses all frequencies higher than the cut-off frequency	High noise suppression	Image blurring, texture lost, sensitive to cut-off frequency, finer details lost
Fourier Butterworth filter[26]	Fourier transformation, Butterworth filtering, transforming the image back to the spatial domain	Significant reduction in speckle, eliminates Gibbs effects, low computational complexity	Smaller details are lost, Sensitive to cut-off frequency and order of the filter
Homomorphic fourier Butterworth filter [26]	Logarithmic transformation based Fourier Butterworth filter	Increase in contrast, attenuating low frequencies enhances the edges	Texture is not preserved, image blurring, sensitive to cut-off frequency and order of the filter
Homomorphic Fourier ideal filter[26]	Logarithmic transformation based Fourier ideal filter	High noise suppression	image blurring, texture lost, sensitive to cut-off frequency
Probability based shrinkage[99]	Estimating the probability of noiseless subband data based on the Laplacian prior	Alleviates the need for preliminary edge detection	Generation of large coefficients in the edgy regions

Posterior sampling based Bayesian estimation [228]	Conditional posterior sampling approach is employed for estimation of posterior distribution of noise free pixel	Noise is suppressed with structure preservation, dynamic learning of noise distribution, contrast enhanced	Homogeneous regions are blurred, higher execution time
Block thresholding [239]	Divide subband into equal square blocks and estimate block size and threshold based on the loss estimation	Neighboring coefficients of the pixel are taken into account	Fixed block size and threshold
NeighShrinkSURE [103]	Estimation of optimal threshold and window size in every subband using Stein's unbiased risk estimation.	Effective noise suppression, edge preservation in logarithmic domain	Smoothing of finer details, reduction in the contrast
Generalized likelihood ratio method [22, 116]	Initial coefficient classification is used for estimating the statistical distribution of the features of interest.	Improved noise suppression with details well preserved	Small amount of noise retained, generate wavelet related artifacts
Orthonormal wavelet thresholding [102]	Denoising process is parameterized as sum of nonlinear unknown weights followed by SURE.	Alleviating the necessity for the design of a statistical model	Introduce visual artifacts, generate large coefficients in edgy regions
Ripplet with nonlinear approximation [95, 96]	Generalization of curvelet transforms by incorporating addition support and degree parameters	Avoiding the artifacts of ringing nature, representing shape of object	Texture of the not preserved, sensitive to the number of coefficients to be retained, reduction in contrast the image
SURELET[101]	Loss estimation based on Stein's unbiased risk estimation (SURE) integrated with linear expansion of threshold (LET)	Requirement of the clean image for the estimation of MSE is overcome	Generates spurious values at higher levels of speckle noise
Multiscale product thresholding [100]	Adjacent subbands are multiplied to exploit interscale dependencies.	Significant edges are well preserved, and enhanced	Redundancy present in the image not considered, over-smoothing
M-band ridgelet [94, 267] with thresholding	Based on the combination of m-band wavelet and ridgelet known as m-band ridgelet.	Better energy compaction, performs better than wavelets, enlarging high frequency components	Smoothing of the images, selection of optimal threshold
Optimized Bayesian nonlocal mean [125, 135]	Make use of redundancy, attempt to identify features to be retained and noise to be eliminated by averaging, metrics governed by patches surrounding each pixel	Feature preserving filter, Performance better than spatial image denoising algorithms	Ringing artifacts around the edges, regions are over-smoothed due to patch jittering effect, time consuming
Probabilistic patch based [127, 135]	Generalization of Euclidean distance used in NLM , incorporating 'weighted maximum likelihood estimation	Better balance is being achieved between point-wise estimator accuracy and error	Higher computational time, over-smoothing of the homogeneous regions
Patch based locally optimal Wiener [271]	Patches are compared looking for photometric and geometric similarity, exploiting redundancy present	Visual outlook enhanced, edges and structures well preserved	Fractional loss of textural information along with smoothing of images
BPFA [269]	Non-parametric Bayesian dictionary based method employing the truncated beta-Bernoulli technique	High noise suppression and edge preservation	Computational time very high, reduction in the brightness of the image
Hybrid TMED	Integration of Wiener and Fuzzy filter based on TMED	Edges are preserved, improvement in noise reduction compared to TMED	Sensitive to the size and shape of the window and amount of padding
Hybrid ATMED	Integration of Wiener and Fuzzy filter based on ATMED	Improves noise reduction capabilities of ATMED	Noise is retained in the denoised images
Hybrid TMAV	Integration of Wiener and Fuzzy filter based on TMAV	Noise suppression improved, quality of images superior compared to TMAV	Noise removal takes place but with some blurring and loss of texture
Geometric Wiener	Combination of geometric and Wiener filter	High noise suppression	Smoothing of the edges near the boundaries

Adaptive fidelity total variation [120]	The amount of denoising in a particular region is controlled using fidelity term, acts according to the contents of region.	Image denoising with texture preservation	Texture information are excluded, smaller details lost, restoration is not uniform
Rudin, Osher and Fatemi total variation [120, 253]	Regularizer allows discontinuities whereas oscillations are not allowed to creep-in, uses L^1 norm of the gradient	Edges preserved, smooth regions are effectively reconstructed	Loss of geometry, inability to handle texture dta, “staircasing effect”, texture data systematically “washed out”,
Anisotropic total variation [251]	Preferential direction of edge detection to boost them during reconstruction, anisotropic version of ROF TV model	Efficient , small amount of data required for the reconstruction of the image	Not simple to compute variation, inability to deal with textured data
Aujol et al. [119]	Maximum-A posteriori regularizer based estimator is employed for estimating the functional minimizer reflecting the denoised image	Edge and structure are largely preserved while suppressing noise	Poor visual outlook of the image
Shock filter [269]	Application of dilation or erosion operations depending on the pixel belonging to minimum or maximum zone	High noise suppression, structure of the image well preserved	Poor edge preservation and visual outlook
Median filtering [26, 27, 131]	Pixels replaced by the median value in the window	Retains sharp edges, increase the intensity of the images, exploits contribution of all pixels	Extra computational burden, edge blurring, thin lines and sharp corners lost
Hybrid median [26, 27, 131]	Estimate the median outputs obtained using median filtering with three different windows	Edges are preserved with improvement in the visual outlook of the image	Smoothing of the images, computational burden
Maximum homogeneity[26, 27, 131]	Maximum homogeneity around a pixel in the neighborhood	No tuning of the thresholds required, assists in automatic interpretation of pixels	Smoothing of the images, smaller details lost
Homomorphic [26, 27, 131]	Image logarithmically transformed, FFT is computed, denoised followed by IFFT and exponential operation	Sharpening of features and suppression of noise	Certain details are lost, texture not fully preserved
Geometric filter [27, 131, 244]	Image geometry using complementary hulling principle, centre pixel is incremented or decreased based on the neighboring pixel values	Effective speckle noise suppression and edge preservation	Small amount of speckle noise is retained
Speckle reducing anisotropic diffusion [22, 27, 35, 131]	Inhibit diffusion across edges, allow diffusion on either side of the edge , diffusion controlled by instantaneous coefficient of variation (ICOV)	Intra-region smoothing is combined with edge preservation	Low contrast edges smeared, speckle pattern improperly retained in bright regions
Level set diffusion [267]	The coefficient of variation is combined with the geodesic snake for denoising of multiplicative noise	High noise Suppression with edge preservation	Reduction in the brightness of the image with loss of texture features
Anisotropic diffusion [22, 27, 35, 83, 131]	Encourages diffusion in the homogeneous region while inhibits diffusion at edges	Intra-region smoothing and edge preservation, impressive for non-textured images	Dependent on the shape of the energy function, noise at edges are retained, degrades contrast, obscure edges
Detail preserving anisotropic diffusion [86, 135]	Estimating the equivalence between threshold controlling level of diffusion and variation in noise coefficient, diffusion function is modification of Kaun et al. filter	Requires lesser computational time compared to SRAD, strong speckle suppression	Low contrast edges are smeared, Retaining subtle features is quite difficult
Coherence enhancing diffusion [22, 84]	Based on the concept of embedding diffusion tensors into diffusion models	Simultaneously enhance edges while smoothing images	Undesired ripples introduced

The authors in [27, 130, 131] have pointed out that the despeckling filters considered by them may find applications for the TTE image despeckling. Therefore, in the current study the applications of despeckling techniques analyzed by Loizou *et al.* [131], Mateo *et al.* [26], along with other types of filters are explored. The despeckling performances are compared in terms of noise reduction and edge preservation for the TTE images. An overview of the despeckling filters tabulated in Table 3.2 shows that applications of many techniques are not explored for the TTE images. The filters such as the bilateral [122-124, 255-257, 260, 261, 273], detail preserving anisotropic diffusion (DPAD) [86, 135], fuzzy [158, 229, 274], local statistics (LS) [27, 130,131, 265, 270, 275], M-band ridgelet (MBR) [94, 267], NLM [125,126, 135], probabilistic patch based (PPB) [127, 135, 271], total variation (TV) [252-254, 259], ripplet [95, 96], sparse representation [269, 272, 277] and wavelet shrinkage [90, 92, 99, 101-103, 278-280, 299], were not included in the most recent review of despeckling methods for the TTE images by Finn *et al.* [22].

This thesis presents analysis of 48 despeckling filters. These filters are grouped into eight types. The analysis is in terms of 16 IQM along with the visual quality assessment and clinical grading. The edge and structure preservation are discussed at length taking the clinicians perspective into consideration. All the despeckling techniques are briefly described in next few sections followed by the analysis of their performances for the TTE images in multiple views. An overview of various despeckling filters analysed are tabulated in Table 3.2 with suitable reference which will provide overall picture of all filters in analysed in this chapter. It would be quite difficult to provide all details of 48 filters hence it is being attempted to present only the most required details in this chapter. The complete details of all filters are available in the references mentioned against each filter in Table 3.2 and Table 3.3.

3.2 Types of despeckling techniques

Eight types of despeckling techniques are analysed for the TTE images acquired in two parasternal and three apical views. A total of 48 filters are analysed for both standard noisy images and the TTE images acquired from adult patients diagnosed with aortic regurgitation. In clinical practice, the TTE images are visually seen in PLAX, PSAX, A4C, A5C and A2C during study of the aetiologies and consequences of aortic regurgitation. The eight types of filters are tabulated in Table 3.2 for quick overview. The Table 3.2 includes the 48 filters analysed in this chapter for the B-mode TTE images of aortic valve and cardiac chambers. The concept of each of the filters with their merits and demerits along with references are tabulated in Table 3.3. Some of the details of these filters are provided in the next sub-section. The eight types of filters namely 1) local statistics, 2) fuzzy, 3) Fourier, 4) total variation, 5) nonlocal mean, 6) nonlinear iterative, 7) multiscale and 8) hybrid filters are briefly described in following sub-sections from 3.2.1 to 3.2.8. The results are analysed in section 3.3.

3.2.1 Local statistics based filters

This class of filter includes the adaptive SAR filters (Lee filter, Kaun *et al.* filter and Frost *et al.* filter) [22, 76-82] the despeckling filter (DsFlsmv, DsFlsminsc, and DsFWiener) [27, 130, 131] and bilateral filter [122-124]. The local statistics filters (Kuan *et al.* filter, Frost *et al.* filter, and Lee filter) are known for speckle noise suppression, but the sharp features are not well preserved. The general form of first order local statistics based filters [27, 131] is given by

$$f_{denoised} = \bar{g}_{x,y} + W_{x,y}(g_{x,y} - \bar{g}_{x,y}) \tag{3.1}$$

where $g_{x,y}$ is the noisy pixel value, $\bar{g}_{x,y}$ is local mean value, $f_{denoised}$ are the estimated denoised pixel values in the window, $W_{x,y}$ is the weighing factor where $W \in [\mathbf{0},\mathbf{1}]$ and x,y are co-ordinates of the pixel.

3.2.1.1 SAR despeckling filters

The despeckling techniques such as the Lee filter, Kaun *et al.* filter, Frost *et al.* filter, minimum speckle index filter, and Wiener filters are briefly introduced in this sub-section. The Lee filter is an adaptive noise reduction technique based on the multiplicative noise model. The working of SAR filters such as the Lee filter [22, 77, 135] are based on an assumption that the mean and variance of pixels would be equal to local mean and the variance of all pixels within the processing window. The output image would be obtained by computing the central pixel intensity based on the average pixel intensity and the coefficient of variation in the filter window. The general formulation of Kaun *et al.* filter [22, 78, 135] is same as the Lee filter but has different weighting function. In Frost *et al.* filter, the noise free image was obtained by convolving the original noisy image with a mask [22, 265].

3.2.1.2 Despeckling based on local statistics (DsFlsmv, DsFlsminsc, DsFWiener)

The despeckling filter (DsFlsmv) is based on local statistical parameters such as the mean and the variance of the neighborhood [27, 131]. The filter functions on the additive noise model. The output of the DsFlsmv filter is computed using the weighing factor [27, 131] defined as in Equation 3.2

$$W_{x,y} = \frac{(1 - \bar{g}^2\sigma^2)}{(\sigma^2 + \sigma_n^2)} \tag{3.2}$$

where σ^2 and σ_n^2 are the variance of the moving window and the entire image, respectively [27, 131]. The value of σ_n^2 is computed as $\sigma_n^2 = \sum_{x=1}^{p} \sigma_p^2 \big/ \bar{g}_p$ where σ_p^2, and $\bar{g}_p$ are the variance and the mean of noise in the selected window, respectively and *p* represents index of all the windows in the entire image [27, 131]. The noise variance is computed using the logarithmically compressed image. This was based on the computation of the average noise

variance for various windows with dimensions considerably higher than the processing filter window [27, 131]. The despeckling filter based on minimum speckle index is known as homogenous mask area filtering and is abbreviated as DsFlsminsc (despeckling filter-local statistics minimum speckle index) [27, 131]. It works by looking for the most homogeneous area in a 5×5 neighborhood around each pixel using a 3×3 subset window. The average gray value of the 3×3 mask with smallest speckle index C is taken as a substitution for the centre pixel of the 5×5 neighborhood and C is computed as

$$C = \sigma_s^2 \big/ \bar{g}_s \tag{3.3}$$

where $\bar{g}_s$ and σ_s^2 are the mean and the variance of the 3×3 window. The smallest speckle index in the window represents the most homogenous sub-window. The Wiener filter is abbreviated as DsFWiener and is based on mean square error [27, 131].The weighing factor of adaptive Wiener filter can be estimated using the Equation 3.4

$$W_{x,y} = (\sigma^2 - \sigma_n^2) \big/ \sigma^2 \tag{3.4}$$

where σ^2 and σ_n^2 are the variance of the moving window and the entire image, respectively [27, 131].

3.2.1.3 Bilateral filter

Bilateral filters not only preserve the edges, but also smooth the images when used as a noise reduction technique [96, 255-257, 261, 273]. They are comprised of range and domain filters. The nonlinear characteristic of range filters increases the computations. To overcome this problem, modifications have been proposed by various researchers such as the new class of bilateral filters known as constant time bilateral. The constant time filters make use of polynomial range kernels. Further improvements are achieved using raised cosine kernel as proposed by Chaudary *et al.* [256]. The general form of the bilateral filter based on raised cosine kernel is given by

$$\hat{f}(x) = \frac{\sum_{|n| \le M} d_n(x) \bar{g}_n(x)}{\sum_{|n| \le M} d_n(x) \bar{h}(x)_n} \tag{3.5}$$

where $h_n(x) = exp(jn\gamma f(x))$, $g_n(x) = f(x)h_n(x)$ are the auxiliary images, $f(x)$ is the image to be processed, $\gamma = \pi \big/ 2T$ with T representing the range, $d_n(x) = c_n \, exp(-jn\gamma f(x))$, $\Phi(s) = \sum_{|n| \le M} c_n \, exp(jn\gamma s)$, $\Phi(f(x-y) - f(x)) = \sum_{|n| \le M} d_n(x) \, exp(jn\gamma f(x-y))$, with range kernel, c_n are the coefficients of trigonometric function and M is the kernel degree. The coefficients and auxiliary images are obtained from input image. The raised cosine kernel based constant time bilateral filter is employed for averaging each of the auxiliary images [256].

3.2.2 Fuzzy filter

The weighted median filter effectively suppresses the speckle noise but the edges are not well preserved [229, 250]. The fuzzy filters preserve image sharpness and the edges. Fuzzy filters such as fuzzy filter based on triangular function with median (TMED) center, asymmetrical triangular function with median (ATMED), triangular moving average (TMAV) center and asymmetrical triangular moving average (ATMAV), are analyzed in the logarithmic domain.

3.2.3 Fourier filtering

The filters of this category are based on the Fourier transformation. Here the images are transformed from the spatial domain into the frequency domain and vice versa. The lower frequencies represent the slowly changing regions whereas the higher frequencies represent the fast changing regions (the edges). A low pass Fourier ideal filter (FIF) is defined as a filter which passes all frequencies within the cut-off frequency without any attenuation and completely attenuates frequencies above cut-off value. The Fourier Butterworth filter (FBF) reduces noise with the edges preserved [26, 245, 248]. The homomorphic FIF (HFIF) and homomorphic FBF (HFBF) are implemented using the following steps. The input image is projected into logarithmic domain and subjected to fast Fourier transform (FFTs). The image in the Fourier domain is filtered using ideal or Butterworth filter, followed by inverse FFT transforms (IFFT). Finally, the image is projected back into the non-logarithmic space.

3.2.4 Multiscale techniques

The maintenance of spatial relation among the pixels, reduced computational burden, excellent localization characteristics and simplicity in application are the key features of wavelet transforms (WT). But, the major disadvantages of the WT are the oscillations, the shift variance, aliasing and the lack of directionality. The wavelet coefficients have the tendency to oscillate around singularities making singularity extraction difficult. Any wavelet coefficient processing (filtering, and thresholding) may spoil the delicate balance between the forward and the inverse transform, leading to artifacts in the reconstructed image. The lack of directional selectivity may pose complication in modelling and processing of the image features like ridges and edges. The time complexity is on the move in usage of wavelet-based despeckling techniques due to the DWT and IDWT operations to be performed.

Multiscale techniques are being effectively used for additive and multiplicative noise reduction [90, 92, 99,101-103, 278-280, 299]. These techniques are popularly called as thresholding or wavelet shrinkage. Most of the wavelet based noise reduction methods work in logarithmic domain. Each input is projected into logarithmic space, subjected to denoising and projected back to the non-logarithmic space. The wavelet shrinkage techniques implemented in the logarithmic domain were very extensively discussed in Chapter 2.

3.2.4.1 Logarithmic wavelet shrinkage techniques

The following techniques are analysed in this category of filters using the log and exponential operations along with various thresholding techniques. The Bayes thresholding is experimented in the logarithmic domain for suppression of speckle noise in the standard test images and clinical TTE images. This technique is referred to as BayesShrink [227]. The multiscale product thresholding, known as the MPT filter, based on multiplication of the DWT at adjacent scales, is analysed for reduction of noise in the TTE images [100]. In the probability based shrinkage, known as the ProbShrink, the wavelet coefficients are multiplied with the probability of signal containing information of interest [99]. The combination of loss estimation using Stein's unbiased risk estimation (SURE) and linear expansion of threshold (LET), known as SURELET [101] is also analysed for reducing speckle noise using the approximated additive noise model. The interscale orthonormal wavelet thresholding (IOWT) [102], and block thresholding are also analysed in the logarithmic domain. The combination of neighbourhood shrinkage and SURE, known as the NSS filter [103] is studied in the logarithmic domain.

3.2.4.2 M-Band Ridgelet (MBR)

The combination of M-Band wavelet and ridgelet is known as M-Band Ridgelet (MBR) [94, 267]. The MBR is embedded with NeighCoeff thresholding [250] for speckle noise reduction. The ridgelet transform have been employed in applications such as denoising of images, extraction of features and classification based on texture features. This transform overcomes the limitations of the wavelets. But, two band wavelet transformations have to be performed in the randon domain to obtain the ridgelet transform. These transform are capable of analysing only the low frequency signals, they fail at higher frequencies [94, 267]. In this thesis, M-Band ridgelet transform is employed for despeckling of the TTE images using the M-Band wavelet decomposition in the randon domain. The M-Band wavelet decomposition assists in enlargement of high frequency components.

3.2.4.3 Generalized likelihood ratio filtering method (GLM)

The generalized likelihood method (GLM) for filtering was proposed by Pizurica *et al.* [116]. It is a multiscale denoising technique based on the multiplicative model of speckle noise. An initial classification of the coefficients is carried out based on correlation among the prominent features across various resolution scales non-iteratively. This initial coefficient classification is employed for the estimation of statistical distribution of the features of interest. The spatial adaptation is achieved using a local spatial activity indicator in the

wavelet domain. It uses non-decimated wavelet transform, with equal number of coefficients at each resolution scale.

3.2.4.4 Posterior sampling Bayesian estimation (PSBE)

The posterior sampling Bayesian estimation was employed for speckle noise reduction in the OCT images [228]. In logarithmic PSBE, noise free image details are estimated using Bayesian least square error calculations using conditional posterior sampling and then the average squared error was minimized. The unknown destination distribution is anticipated by sampling a recognized preliminary probability distribution. The posterior distribution is computed by means of a weighted histogram approach [228].

3.2.4.5 Ripplet with nonlinear approximation (RNLA)

The generalization of the curvelet transform at higher dimension is known as ripplet transform. This transform is embedded with support and degree parameters [95, 96]. These transforms were advocated for efficient representations of the images or 2D signals at various scales and directions. The Fourier transforms are efficient in representing only smooth images but fail to perfectly represent images containing edges. The ripplet transform provide an efficient representation of the edges in the 2D images. The ripplet transform can be employed in various image processing applications such as image restoration, image compression and image denoising. The wide range of applications of ripplet transform is because of its characteristics such as anisotropy, fast coefficient decay, high directionality, good localization and multi-resolution [95, 96]. The extracted ripplet coefficients are arranged in the descending order followed by approximation of the signal by the largest coefficient and measurement of reconstruction error. The Ripplet forward transformation in the discrete domain is of the form as represented in Equation 3.6

$$R_{j,\vec{k},l} = \sum_{n_1=0}^{M-1} \sum_{n_2=0}^{N-1} f(n_1,n_2)\overline{\rho_{j,\vec{k},l}(n_1,n_2)} \tag{3.6}$$

where $\rho_{j,\vec{k},l}$ is the mother wavelet function, $f(n_1,n_2)$ is the image to be processed and the Ripplet coefficients are represented by $R_{j,\vec{k},l}$.

3.2.5 Total variation

The total variation (TV) based denoising is based on the concept that the integral of absolute gradient of the noisy image would be high, resulting in high total variation. The images with smaller variation are considered to be better denoised with high detail preservation [251-253]. The denoised image $f_{denoised}$ obtained by minimizing the quadratic term with the TV regularization is given by Equation 3.7

$$f_{denoised} = arg\,min_u \int_\Omega (f-u)^2 dx + \lambda \int_\Omega |\nabla f| dx \tag{3.7}$$

where the quadratic data term $\int_{\Omega}(f-u)^2 dx$ fits f in u according to the least square fit, $\int_{\Omega}|\nabla f|dx$ is the regularization term (denoising function) and λ is the weighting parameter which is the measure of smoothness. The parameter λ plays an important role in the effectiveness of denoising. No denoising is observed when the value of λ is equal to zero, the input and output are the same. The effectiveness increases with increase in value of λ and as it tends one.

3.2.5.1 Adaptive fidelity total variation (AFTV)

The image textures provide lot of critical information but are lost on application of methods like PMAD. To overcome such drawbacks, image denoising using TV with adaptive fidelity term was proposed by Gilboa, Zeevi and Sochen [120]. Adaptive fidelity term controls the amount of denoising by measuring the local variance in the image. The denoising is performed in two phases. In the first phase the texture and the noise are isolated using scalar total variation method of denoising with λ=1. During the second phase the local power constraints estimated using local variance are placed on the output of first phase.

3.2.5.2 Anisotropic total variation (ATV)

The anisotropic filtering and total variation are known for their ability to identify and preserve the edges in the denoised image [251]. The edges are preserved at the cost of induction of additional structure due to noise in the anisotropic filter. The total variation based filter results in stair-casing effects, leading to gradual changes in the contrast of the homogeneous regions structures, especially across the corners and the edges. To overcome these drawbacks, AD and TV filters are combined resulting filter known as the anisotropic total variation (ATV) filter. The ATV based on the split Bregman algorithm is analysed for speckle noise reduction with edges preserved in the TTE images. The Bergman iterations are employed during denoising process because it quickly converges, needs to solve lesser number of unconstrained problems, λ remains constant and avoids numerical instabilities [252].

3.2.6 Nonlinear iterative filters

The qualities of denoised images depend on number of iterations and nonlinear technique in this class of filters. The following filters are considered in nonlinear iterative filters category for performance analysis: DsFgf4d, DsFad, DsFsrad, DsFhomog, DsFmedian [27, 131], CED [22, 84, 131] and DPAD [86, 135] filters. The DsFgf4d [22, 27,130, 131, 244] filter works either by increasing or decreasing the values of neighborhood pixels depending on their relative values. It is based on the assumption that the images are made up of valleys and narrow walls. The intensity of pixel located at the center of a 3×3 window is compared with

eight neighbors. Depending on intensity values of the neighborhood pixels the value is either incremented or decremented so that the values stand out compared to others.

3.2.6.1 Diffusion based despeckling techniques (DsFad, DsFsrad, CED, and DPAD)

The anisotropic diffusion filter is a nonlinear partial differential Equation (PDE) based filtering technique which promotes diffusion in the homogeneous regions while it holds back at edges [22, 27, 35, 83, 130, 131, 264]. In DsFad filter [22, 83, 131] it is not important to know the power spectrum or the noise pattern, it can automatically remove the noise. The diffusion function employed to control image smoothing in the AD filter is based on the image gradient, and may not be unsuitable to despeckling of images with multiplicative speckle noise. In diffusion based filtering, the noise at edges could not be successfully removed. In order to overcome this issue, the concept of diffusion tensors into the diffusion models was advocated, and this class of diffusion is referred to as the coherence enhancing diffusion (CED) models. The diffusion tensor is based on the gradients in x and y directions. The Gaussian filter is employed for removing the variations due to the presence of noise. The CED can simultaneously enhance edges and smoothen given image. Therefore, CED based techniques can be employed for image enhancement. But it may result in undesired ripples in the filtered image [22, 84, 131].

The concept of coherence during diffusion is expressed in terms of eigenvalues and eigenvectors. In DsFsrad [22, 35, 131] the gradient based edge discriminator is replaced with a discriminator better suited for speckle. The diffusion function is controlled by instantaneous coefficient of variation (ICOV) and this is the ratio between standard deviation to the mean [22, 35, 131] defined as:

$$q(x,y;t) = \frac{std\{f(x,y;t)\}}{\bar{f}(x,y;t)} \tag{3.8}$$

where statistical values are estimated using a nearest four neighbor window. Diffusion function utilized is of the form represented in Equation 3.9 [22, 35]

$$c[q(x,y;t), q_0(t)] = (1+((q^2(x,y,t) - q_0^2(t))/q^2(x,y,t)(1+q_0^2(t)))^{-1} \tag{3.9}$$

where q_0 represents the ‘speckle scale function’.

The detail preserving anisotropic diffusion (DPAD) filter was proposed in [86] to estimate the equivalence between threshold controlling level of diffusion and variation in the noise coefficient [22, 35]. A larger neighborhood for estimating the local statistical parameters was incorporated in the DPAD filter for accurate computations.

3.2.6.2 Nonlinear despeckling filters (DsFhomog and DsFmedian)

The filter based on estimation of maximum homogeneity over a pixel neighborhood is known as DsFhomog filter [27, 131]. This filter estimates homogeneous neighborhood around every

pixel by taking into account the pixels belonging to processed neighborhood. Median filter (DsFmedian-Despeckling median filter) is a nonlinear filtering technique [27, 131]. The noisy pixel is replaced by the median value without taking into account the local image features like the presence of an edge.

3.2.7 Nonlocal mean filter (OBNLM, PPB)

The nonlocal means (NLM) algorithm by Buades *et al.* [126] estimates each pixel value as a weighted average of other, similar noisy pixels. As in the bilateral filter, NLM estimates each pixel value using a weighted average of other pixel values in the image. It uses a similarity based on the resemblance of the pixels' neighborhoods in high-dimensional space. Furthermore, in contrast to the bilateral filter, in which only the vicinity of each pixel contributes to the estimate, in NLM all pixels may contribute. The basic idea behind nonlocal means is creation of metric governed by patches around each pixel [125-127, 135]. The features of interest are selected by comparing image patches. The patterns surrounding each pixel are compared instead of intensity of each pixel.

The redundancy present in the image is put to use in optimized Bayesian nonlocal means (OBNLM) based image denoising [125, 135]. The value of each pixel in NLM is estimated by calculating the weighted average of all other pixels in the entire image based on the similarity resemblance criteria of all the neighboring pixels, leading to superior denoising performance in comparison to local statistics based denoising [125]. The search window size, similarity window size and h-parameter responsible for control of filter size, dictate the performance of the NLM filter. The core issue concerning the NLM filter like wavelet thresholding is that it cannot fully exploit the smoothness of the edge contour which can separate the white and the black regions. Therefore, there is scope for improvement in its performance. The most prominent feature of the NLM is the weighted averaging of pixels based on the neighborhoods which produced a decay rate that was superior to those linear filters. The NLM based estimators are local and do not exploit the global similarities.

3.2.7.1 Probabilistic patch based (PPB) filter

The patch based filters are the state-of-art noise reduction methods employed in the US image pre-processing [127, 135]. In denoising based on the NLM filter, the Euclidean distance is computed between the patches. The generalization of this distance was proposed in [127] using probabilistic patch-based (PPB) method incorporating 'weighted maximum likelihood estimation (WMLE)'. The weight $w(s,t)$ in the PPB filter, between patch *s* and patch *t* with *i* iterations is defined as in Equation 3.10 [127, 135]

$$w(s,t) = exp\left\{-\sum_{k}\left[\frac{2L-1}{h}\log\left(\frac{f_{s,k}}{f_{t,k}}+\frac{f_{t,k}}{f_{s,k}}\right)+\frac{1}{T}\frac{\left|\hat{f}_{s,k}^{i-1}-\hat{f}_{t,k}^{i-1}\right|^2}{\hat{f}_{s,k}^{i-1}\hat{f}_{t,k}^{i-1}}\right]\right\} \tag{3.10}$$

where trade-off between noise suppression and fidelity estimation is achieved through parameters *h* and *T*, $f_{t,k}$ and $f_{s,k}$ are the k^{th} pixel amplitude, where their previous values are $\hat{f}_{t,k}^{i-1}$ and $\hat{f}_{s,k}^{i-1}$ for patch *t* and *s* respectively.

3.2.8 Hybrid filters

The hybrid median filter is abbreviated as DsFhmedian (despeckling filter-hybrid median) filter. It is an extension of the DsFmedian (despeckling filter-median). The median values are calculated using three different window shapes namely normal shape, x-shape and cross shape [27, 131]. All four fuzzy filters namely TMED, ATMED, TMAV, and ATMAV filters in are combined with Wiener filter and these filters are known as hybrid fuzzy filters [229, 250]. The performance of geometric filter is improved by combining it with Wiener filter. During iterative processing, the output of the geometric filter is subjected to Wiener filtering for removal of noise retained.

Table 3.4 Overview Image Quality Metrics

Metrics	Name of Metrics	Reference	Concept/Significance
SNR	Signal to noise ratio	[22, 131]	Computing of the level of speckle before and faster processing
PSNR	Peak signal to noise ratio	[26, 27, 131, 134, 135]	Measurement of objective difference between two images
MSE	Mean square error	[22, 26, 131, 267]	Mean difference between original and despeckled image
ρ	Correlation coefficient	[267]	Measurement of closeness between original and processed image
RMSE	Root mean square error	[27, 131]	Square root of squared error average over a window
AD	Average difference	[27, 131]	Mean difference divided by the size of the image
SC	Structural content	[27, 131]	Measurement of similarity, for identical images the value should be 1
LMSE	Laplacian mean square error	[27, 131]	Obtain the edge features of the image
MD	Maximum difference	[27, 131]	Maximum difference between original and processed image
Err3	Normalized error summation	[27, 131]	Error summation using the Minkowski metric, norm of dissimilarity between original and despeckle image
Err4	Normalized error summation	[27, 131]	
NAE	Normalized average error	[27, 131]	Measure of error prediction accuracy
NCC	Normalized cross correlation	[27, 131]	Measurement of alignment before and after despeckling
SSIM	Structural similarity index	[22, 131, 135, 267, 268]	Similarity between original and denoised image
FoM	Figure of merit	[22, 135]	Measurement of edge displacements between the processed and the original image
β	Beta metric	[26, 96, 113]	Objective criteria for measuring edge preservation
IQI	Image quality index	[27, 131]	Models distortion as combination of luminance of distortion, loss of correlation, and contrast distortion

3.3 Results

The performances of 48 despeckling filters are analyzed in terms of IQM, visual quality and clinical grading. The selections of input parameters for each filter are based on the discussions in various research papers [94-103, 130, 131, 134, 135, 267]. The combination of input parameters which resulted in the best despeckling, i.e., noise suppression (high PSNR and SNR, low MSE, RMSE, LMSE, MD, and AD), edge preservation (IQI, β, and FoM

≈1), structural similarity (SSIM≈1) and clinical grading (maximum value on the scale of 10, good ≥ 7 else clinically not acceptable) are considered. The significance of each IQM is highlighted in Table 3.4 along with reference and expansion of the acronym. The list of input parameters employed in the analysis of filter performance are Tabulated in Table 3.5 for quick reference. All other combinations of input parameters were also tested on the standard noisy images. Some of the important parameters used for implementation of each filter are tabulated in Table 3.5. The visual qualities of despeckled standard test images are shown in Figure 3.1 to Figure 3.6 and their TTE counterparts in Figure 3.7 to Figure 3.12. The quantitative performance parameters for noisy standard images are tabulated in Table 3.6 to Table 3.12 and for TTE images in Table 3.13 to Table 3.15. The MATLAB code provided by the authors of the following papers [27, 86, 95, 99-103, 116,119, 120, 125, 127, 130, 131, 256] are used in testing of despeckling filters with suitable selection of parameters for standard and TTE images.

Table 3.5 Input parameters for despeckling techniques

Reference	Method	Parameters
[22, 77, 79, 81]	Lee, Kaun et al., Frost et al.	Window size=5x5
[21, 27,131]	DsFlsminsc	Window size =5x5, iterations=2 , also with 3x3, 7x7,and 9x9
	DsFlsmv	Window size=5x5, iterations=2, also with 3x3, 7x7,and 9x9
	DsFWiener	Window size=5x5, iterations=1, also with 3x3, 7x7,and 9x9
[256]	FBL	Width of spatial Gaussian=10, width of range Gaussian=20,tol=0.01
[229, 250]	Fuzzy filter	Window size=3x3, padding, also with 5×5, 7×7,and 9x9
[26]	FIF/HFIF	f_c =500, also with f_c =100, 1000
	FBF/HFBF	Order=2, f_c =500, also with f_c =100, 1000
[227]	BayesShrink	haar wavelet, level =2
[99]	ProbShrink	Window size=3x3, level=2, sym8 wavelet
[101]	SURELET	Down sampling N=4, overlap factor K=3, redundancy =3
[103]	NSS	Level =3, wtype = sym8
[100]	MPT	Scale number =2, C=12
[22, 116]	GLM	window size=3×3, level=2, K=3
[94]	MBR	m-band M=3, alpha=5000
[95]	RNLA	Support c=1,degree d=3
[228]	PSBE	Sigma spatial=0.01, window size=21x21, samples=100
[120]	AFTV	Iterations=3, λ=0, time step =0.2
[252]	ROF	Time step= 0.25, Number of iterations = 5
[251]	ATV	Iterations=2, λ=1 , time step=0.2,
[22, 83, 131]	DsFad	Diffusion constant =30, rate of diffusion=0.25,iterations=20
[22, 35]	DsFsrad	Iterations=30,time step=0.02, rho=1
[22]	CED	Iterations=20,time step=0.02, Diffusion constant =20
[86]	DPAD	Iterations=30,time step=0.02, Cu noise estimation
[21, 27, 131]	DsFgf4d	Window=3x3, iterations=2
	DsFhomog	Window=3x3
	DsFmedian	Window=5x5,iterations=3
[125, 135]	OBNLM	Search area=23x23,block size=15x15,smoothing parameter h=0.4
[127, 135]	PPB	Iterations=4, α=0.8, T=2, search area=23x23, patch size=7×7
[21, 27, 131]	DsFhmedian	Window=5x5,iterations=2
[27, 131].	Hybid Fuzzy	Fuzzy and Wiener window size=3x3

Local statistics filters: The visual qualities of the denoised images on applications of local statistics and SAR based filters such as Lee, Kaun *et al.*, Frost *et al.*, DsFlsmv, DsFWiener, DsFlsminsc and FBL filters, are shown in Figure 3.1 and Figure 3.7 respectively for standard

and TTE images. The values of IQM obtained using these filters are tabulated in Table 3.6, Table 3.12, Table 3.13 and Table 3.14. The performance parameters tabulated in Table 3.6 were obtained at various noise levels (σ^2=0.01, 0.05, and 0.1) for Lena and Barbara image. The output of Kaun *et al.* and Lee filter induce visual artifacts. The application of Frost et al. filter results in the loss of texture information and over-smoothing.

Table 3.6 Comparison of IQM using local statistics filters

Methods	MSE						SNR					
	Lena			Barbara			Lena			Barbara		
	0.01	0.05	0.1	0.01	0.05	0.1	0.01	0.05	0.1	0.01	0.05	0.1
Lee	51.27	129.4	234.9	262.1	295.1	432.9	50.75	42.71	37.53	36.12	35.09	31.76
Kaun	48.01	137.6	254.4	160.2	263.3	404.5	51.32	42.18	36.84	40.39	36.08	32.35
Frost	92.26	106.0	130.9	288.8	298.9	322.3	45.65	44.44	42.61	35.27	34.97	34.32
DsFlsmv	37.47	169.6	435.0	117.2	220.9	438.0	53.47	40.36	32.18	43.10	37.60	31.66
DsFWiener	45.92	207.4	390.9	86.68	261.8	456.1	51.71	38.61	33.11	45.73	36.13	31.30
DsFlsminsc	85.39	127.7	186.5	286.0	328.6	388.5	46.32	42.82	39.53	35.36	34.15	32.70
FBL	57.86	424.0	1060	92.17	446.2	1030	49.70	32.40	24.44	45.19	31.50	24.22
	IQI						**SSIM**					
Lee	0.511	0.425	0.358	0.474	0.458	0.401	0.911	0.826	0.741	0.763	0.767	0.714
Kaun	0.544	0.434	0.363	0.550	0.505	0.439	0.917	0.801	0.705	0.845	0.797	0.726
Frost	0.526	0.468	0.431	0.493	0.463	0.438	0.888	0.837	0.782	0.794	0.768	0.737
DsFlsmv	0.639	0.424	0.313	0.691	0.563	0.446	0.934	0.770	0.631	0.903	0.821	0.724
DsFWiener	0.590	0.421	0.350	0.702	0.539	0.453	0.901	0.708	0.600	0.916	0.774	0.684
DsFlsminsc	0.553	0.450	0.393	0.517	0.447	0.400	0.903	0.802	0.719	0.816	0.756	0.700
FBL	0.545	0.332	0.251	0.668	0.492	0.385	0.908	0.679	0.540	0.913	0.767	0.655
	Beta Metric						**FoM**					
Lee	0.409	0.208	0.118	0.471	0.373	0.222	0.874	0.792	0.603	0.685	0.736	0.689
Kaun	0.419	0.204	0.130	0.603	0.413	0.270	0.892	0.613	0.492	0.897	0.801	0.656
Frost	0.269	0.223	0.211	0.304	0.275	0.273	0.778	0.805	0.688	0.731	0.752	0.771
DsFlsmv	0.510	0.207	0.132	0.785	0.471	0.323	0.883	0.550	0.424	0.865	0.675	0.550
DsFWiener	0.407	0.151	0.101	0.782	0.460	0.306	0.728	0.430	0.383	0.878	0.584	0.514
DsFlsminsc	0.195	0.152	0.114	0.071	0.054	0.039	0.844	0.639	0.506	0.834	0.749	0.680
Fast BL	0.416	0.143	0.098	0.768	0.395	0.276	0.776	0.447	0.354	0.829	0.572	0.484
	Time						**RMSE**					
Lee	32.54	32.64	32.59	32.62	32.62	32.59	7.160	11.37	15.32	16.18	17.17	20.80
Kaun	32.90	32.62	32.57	33.08	34.14	34.09	6.929	11.73	15.95	12.65	16.22	20.11
Frost	26.27	26.19	27.35	26.26	27.55	27.47	9.605	10.29	11.44	16.99	17.29	17.95
DsFlsmv	0.536	0.526	0.525	0.515	0.518	0.516	6.121	13.02	20.85	10.83	14.86	20.92
DsFWiener	0.065	0.040	0.039	0.040	0.041	0.040	6.776	14.40	19.77	9.310	16.18	21.35
DsFlsminsc	20.13	19.69	19.96	19.65	19.73	19.65	9.240	11.30	13.65	16.91	18.12	19.71
Fast BL	2.003	1.857	2.041	1.993	2.002	2.002	7.606	20.59	32.56	9.601	21.12	32.10
	PSNR						**NCC**					
Lee	31.03	27.01	24.42	23.95	23.43	21.76	0.996	0.99	0.981	0.987	0.979	0.968
Kaun	31.32	26.74	24.07	26.08	23.92	22.06	0.997	0.992	0.983	0.991	0.982	0.972
Frost	28.48	27.88	26.96	23.52	23.37	23.04	0.991	0.988	0.98	0.978	0.974	0.964
DsFlsmv	32.39	25.84	21.74	27.44	24.69	21.71	0.995	0.993	0.984	0.987	0.983	0.975
DsFWiener	31.51	24.96	22.20	28.75	23.95	21.53	0.998	0.994	0.986	0.993	0.987	0.976
DsFlsminsc	28.82	27.07	25.42	23.57	22.96	22.23	0.996	0.992	0.983	0.983	0.976	0.966
Fast BL	30.51	21.86	17.87	28.48	21.64	18	0.993	0.99	0.985	0.989	0.984	0.978

Denoising is accompanied with check box effects in the Lee and Kaun et al. filters. As the kernel size is increased, output image appeared to blurry using the DsFls and DsFlsminsc filters, the texture information is not preserved. Smoothing of the background is observed using Lee, Kaun *et al.*, Frost *et al.*, and DsFlsminsc filters. The noise is effectively

suppressed using the DsFlsmv, DsFWiener and FBL filters with the structures and edges well preserved. Lee filter output showed high noise suppression but output appeared to be somewhat blurred.

Figure 3.1 Visual quality comparisons for local statistics filters at σ=0.1: (a) Original image, (b) Noisy image [40.06, 0.652, 12.09], (c) Lee [36.12, 0.512, 16.19], (d) Kaun et al. [40.39, 0.4933, 12.659], (e) Frost et al. [35.27, 0.499, 16.99], (f) DsFlsmv [43.10, 0.692, 10.83], (g) DsFWiener [45.73, 0.7028, 9.31], (h) DsFlsminsc [35.36, 0.517, 16.912], (i) FBL [45.19, 0.668, 9.61]

The visual quality in Figure 3.1 and values of IQM in Table 3.6 show that the performance of filters such as DsFlsmv, DsFWiener and FBL were superior in comparison to adaptive SAR filters. Further, it is observed that the performances of the local statistics filters are inferior for the textured images. Also, the performances of these filters drastically degraded on increase of noise levels. The performance of DsFlsmv filter in terms of IQI (0.6919), β (0.7858), FoM (0.8657) is superior compared to Lee, Kaun et al., Frost et al., and DsFlsminsc filters. DsFWiener filter had better SNR (45.73dB), SSIM (0.9169), LMSE (0.39), MSE (86.68), RMSE (9.31) and ERR3 (11.72) in comparison to other local statistics based filters. This analysis indicates that the edge and structure are better preserved using the

DsFlsmv filter, and the noise reduction is better using the DsFWiener filter. In case of the TTE images the IQM such as the IQI, FoM, SSIM and SC are almost the same for DsFlsmv and DsFWiener filters, but the visual quality obtained using the DsFlsmv filter is better compared with DsFWiener filter. Note: The values in square brackets against each filter in Figure 3.1 to Figure 3.6 represent the values of SNR, IQI and RMSE at noise variance equal to 0.01.

Table 3.7 Comparison of IQM using fuzzy and Fourier filters

Methods	**MSE**						**SNR**					
	Lena			Barbara			Lena			Barbara		
	0.01	0.05	0.1	0.01	0.05	0.1	0.01	0.05	0.1	0.01	0.05	0.1
TMED	121.8	307.3	761.99	357.0	526.0	941.93	43.23	35.20	27.31	33.43	30.07	25.01
ATMed	56.52	192.4	368.89	221.4	350.5	526.61	49.90	39.26	33.61	37.58	33.59	30.06
TMAV	66.00	154.6	375.2	254.5	344.4	563.94	48.56	41.16	33.46	36.37	33.74	29.46
FIF	134.1	636.2	1217	130.7	597.6	1126	42.40	28.88	23.24	42.20	28.97	23.45
FBF	94.26	444.1	856.8	99.62	427.8	805.2	45.46	32.00	26.29	44.52	31.86	26.37
HFBF	51.75	166.1	317.6	115.2	240.9	404.3	50.67	40.54	34.91	43.25	36.85	32.35
	IQI						**SSIM**					
TMED	0.492	0.361	0.288	0.495	0.392	0.323	0.864	0.691	0.569	0.799	0.691	0.595
ATMed	0.549	0.398	0.329	0.581	0.451	0.379	0.874	0.678	0.571	0.848	0.719	0.630
TMAV	0.598	0.463	0.385	0.590	0.496	0.423	0.921	0.794	0.684	0.857	0.780	0.699
FIF	0.495	0.304	0.229	0.671	0.455	0.354	0.808	0.574	0.467	0.881	0.695	0.590
FBF	0.536	0.345	0.267	0.705	0.498	0.396	0.828	0.602	0.494	0.892	0.715	0.608
HFBF	0.607	0.444	0.370	0.690	0.546	0.462	0.908	0.719	0.608	0.910	0.779	0.683
	Beta Metric						**FoM**					
TMED	0.078	0.008	0.024	0.015	0.027	0.031	0.747	0.440	0.358	0.817	0.575	0.474
ATMed	0.298	0.128	0.090	0.184	0.109	0.074	0.663	0.413	0.368	0.842	0.575	0.496
TMAV	0.075	0.088	0.077	0.085	0.088	0.073	0.905	0.521	0.425	0.879	0.712	0.562
FIF	0.357	0.176	0.124	0.760	0.487	0.368	0.666	0.382	0.334	0.735	0.501	0.441
FBF	0.403	0.201	0.140	0.770	0.487	0.368	0.691	0.383	0.347	0.751	0.509	0.450
HFBF	0.450	0.230	0.155	0.743	0.512	0.363	0.880	0.437	0.382	0.904	0.586	0.496
	Time						**RMSE**					
TMED	8.44	8.45	8.44	8.56	8.53	8.57	11.04	17.53	27.60	18.89	22.94	30.69
ATMed	10.24	10.11	10.17	10.18	10.20	10.13	7.52	13.87	19.21	14.88	18.72	22.95
TMAV	31.18	31.19	31.27	31.10	31.23	31.18	8.12	12.44	19.37	15.95	18.56	23.75
FIF	0.656	0.202	0.200	0.205	0.211	0.204	11.58	25.22	34.89	11.40	24.43	33.56
FBF	0.325	0.313	0.316	0.330	0.314	0.317	9.71	21.08	29.27	9.98	20.68	28.38
HFBF	0.403	0.405	0.399	0.452	0.401	0.408	7.19	12.89	17.82	10.74	15.52	20.11
	PSNR						**NCC**					
TMED	27.27	23.25	19.31	22.60	20.92	18.39	0.980	0.926	0.848	0.956	0.910	0.837
ATMed	30.60	25.28	22.46	24.67	22.68	20.91	0.992	0.975	0.952	0.977	0.956	0.931
TMAV	29.93	26.23	22.38	24.07	22.75	20.61	0.984	0.945	0.892	0.963	0.927	0.875
FIF	26.85	20.09	17.27	26.98	20.37	17.61	0.999	0.995	0.990	0.999	0.994	0.984
FBF	28.38	21.65	18.80	28.14	21.81	19.07	0.999	0.996	0.988	0.996	0.990	0.981
HFBF	30.99	25.92	23.11	27.51	24.31	22.06	0.991	0.987	0.969	0.992	0.976	0.956

Fuzzy and Fourier filters

The visual qualities of despeckled images on applications of Fuzzy and Fourier filters such as TMED, ATMED, TMAV, FIF, FBF, and HFBF filters, are shown in Figure 3.2 and Figure 3.8 respectively for noisy Barbara image and TTE image of AV in PSAX. The values of IQM

obtained using these filters are tabulated in Table 3.7. The logarithmic fuzzy filters such as the TMED, ATMED, and TMAV filters retain noise. The visual quality is improved (IQI≈0.6) using TMAV and ATMED filter. The output is smoothed on increasing the window size.

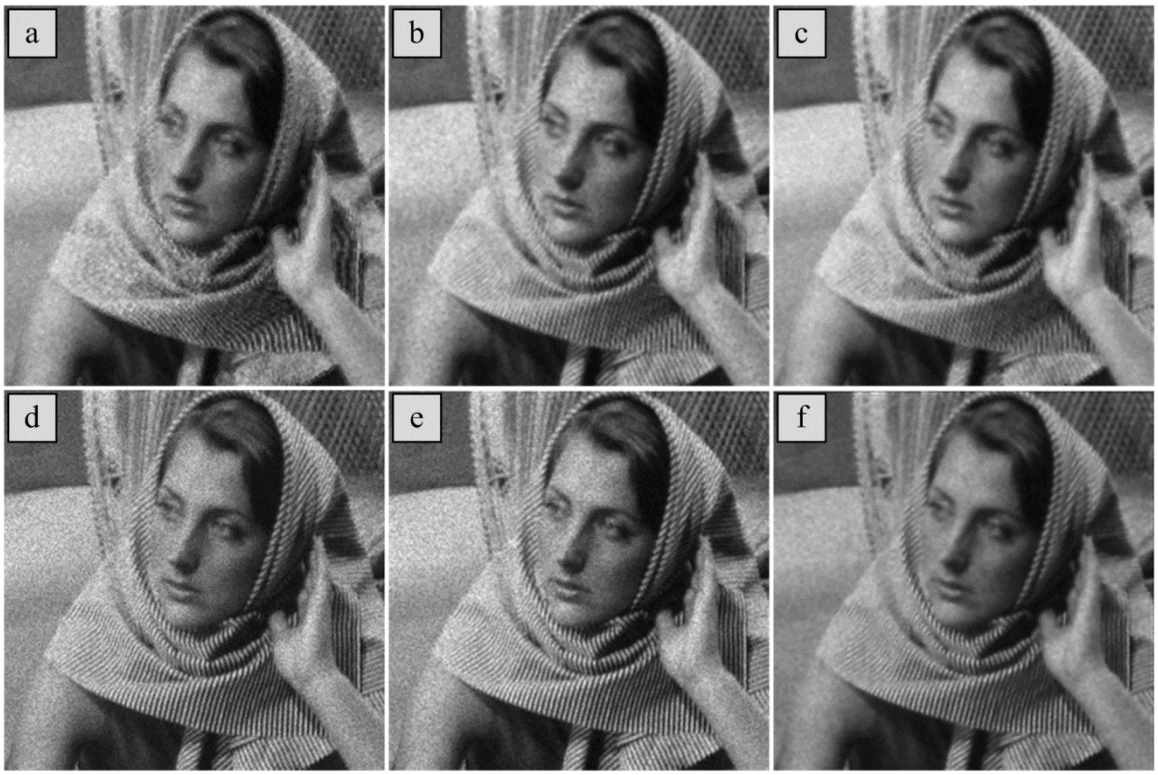

Figure 3.2 Visual quality comparisons for fuzzy and Fourier filters at σ=0.1: (a) TMED [33.43, 0.492, 11.04], (b) ATMED [37.58, 0.549, 7.52], (c) TMAV [36.37, 0.598, 8.12], (d) FIF [42.2, 0.495, 11.58], (e) FBF [44.52, 0.536, 9.71], (f) HFBF [43.25, 0.607, 7.19], whereas the noisy image has [40.06, 0.652, 12.09]

The IQM values tabulated in Table 3.7, Table 3.12, and Table 3.13 reveal that the fuzzy filters have poor β, reflecting poor edge preservation. The edges are well preserved using the TMAV filter. The IQM of Fourier filters are superior in comparison to the fuzzy filters in terms of β, IQI and SNR indicating superior edge preservation and noise suppression. The texture is not preserved using the Fourier based filters. Blurring is observed using FIF, and HFIF filters. All the Fourier filters have moderate IQI, and high SSIM, FoM and β values. The background of Barbara image is smoothed using TMAV whereas noise is retained using the TMED filter. Based on the results shown in Figure 3.2, it can be observed that the texture present in the Barbara image is only partially preserved using the TMED and ATMED filters.

Multiscale techniques: The visual qualities on application of multiscale despeckling filters such as ProbShrink, BayesShrink, PSBE, BlockShrink, NSS, GLM, OWT, RNLA, SURELET, MPT, MBR, and Bivariate filters, are shown in Figure 3.3 and Figure 3.9 respectively for noisy Barbara image and AV in PSAX. The values of IQM obtained using these filters are tabulated in Table 3.8 and Table 3.9.

Table 3.8 Comparison of IQM using multiscale filters

Methods	Beta Metric						FoM					
	Lena			Barbara			Lena			Barbara		
	0.01	0.05	0.1	0.01	0.05	0.1	0.01	0.05	0.1	0.01	0.05	0.1
ProbShrink	0.244	0.244	0.197	0.089	0.080	0.071	0.852	0.860	0.525	0.779	0.800	0.664
Bivariate	0.599	0.339	0.206	0.863	0.655	0.489	0.831	0.522	0.445	0.893	0.684	0.599
BayesShrink	0.418	0.165	0.105	0.741	0.435	0.233	0.835	0.569	0.521	0.883	0.704	0.645
PSBE	0.420	0.235	0.173	0.635	0.447	0.331	0.773	0.469	0.376	0.888	0.610	0.504
BlockShrink	0.612	0.156	0.108	0.893	0.423	0.426	0.896	0.390	0.340	0.929	0.521	0.519
Curvelets	0.316	0.147	0.105	0.678	0.383	0.280	0.688	0.377	0.336	0.707	0.487	0.442
NSS	0.634	0.159	0.108	0.899	0.423	0.291	0.912	0.391	0.331	0.930	0.525	0.448
GLM	0.392	0.160	0.105	0.795	0.453	0.272	0.833	0.490	0.422	0.863	0.756	0.737
HThreshold	0.366	0.185	0.090	0.611	0.506	0.285	0.772	0.699	0.386	0.827	0.732	0.497
SThreshold	0.489	0.189	0.108	0.759	0.533	0.326	0.758	0.656	0.430	0.787	0.828	0.546
OWT	0.313	0.149	0.106	0.678	0.383	0.281	0.685	0.376	0.330	0.719	0.485	0.448
RNLA	0.274	0.078	0.044	0.705	0.447	0.276	0.804	0.546	0.448	0.834	0.683	0.573
SURELET	0.423	0.235	0.169	0.634	0.448	0.334	0.788	0.458	0.388	0.896	0.605	0.519
MPT	0.534	0.215	0.130	0.626	0.422	0.301	0.871	0.423	0.315	0.880	0.569	0.465
MBR	0.168	0.159	0.142	0.067	0.063	0.053	0.784	0.722	0.584	0.696	0.727	0.749
	Time						**RMSE**					
ProbShrink	2.16	2.11	2.11	2.11	2.023	2.086	71.07	70.47	66.48	74.85	72.43	75.30
Bivariate	0.134	0.15	0.14	0.17	0.144	0.137	5.681	10.42	14.96	7.70	13.82	18.61
BayesShrink	0.594	0.53	0.61	0.62	0.615	0.611	7.14	11.81	15.58	9.71	16.11	20.42
PSBE	30.69	30.90	30.9	30.72	31.33	31.84	6.61	11.88	17.27	12.06	15.95	20.29
BlockShrink	6.83	8.35	8.41	6.82	8.216	8.198	5.447	24.21	37.10	6.99	23.83	23.72
Curvelets	257.0	257.2	257	256.6	256.7	257.2	13.31	29.16	40.37	12.89	28.14	38.80
NSS	10.87	11.03	11.0	10.61	10.95	10.91	5.18	24.55	37.35	6.75	24.04	35.99
GLM	5.45	5.53	5.57	5.38	5.036	5.032	7.10	14.07	18.76	8.883	15.23	17.27
HThreshold	0.12	0.12	0.14	0.12	0.1240	0.125	8.827	12.49	27.67	14.14	17.10	28.85
SThreshold	0.14	0.14	0.13	0.14	0.1390	0.143	8.837	12.56	21.28	13.04	15.59	22.49
OWT	0.90	0.91	0.90	0.91	0.9150	0.940	13.21	29.13	40.34	12.85	28.14	38.82
RNLA	1.05	0.81	0.94	0.85	0.8012	0.813	8.153	14.85	19.84	12.58	17.23	21.99
SURELET	14.35	14.45	14.5	14.48	14.39	14.3	6.57	11.91	17.13	12.07	15.91	20.33
MPT	2.71	3.30	3.60	2.76	3.36	3.05	5.60	16.87	30.06	11.22	19.11	30.15
MBR	10.32	10.35	10.3	10.11	10.41	10.3	11.34	12.18	13.24	17.98	18.53	19.22
	PSNR						**NCC**					
ProbShrink	11.09	11.17	11.67	10.64	10.93	10.59	0.975	0.975	0.974	0.963	0.963	0.963
Bivariate	33.04	27.76	24.63	30.39	25.31	22.73	0.993	0.970	0.938	0.990	0.961	0.925
BayesShrink	31.04	26.68	24.27	28.37	23.98	21.92	0.992	0.964	0.930	0.986	0.951	0.913
PSBE	31.72	26.63	23.38	26.50	24.07	21.98	0.990	0.969	0.939	0.976	0.955	0.925
BlockShrink	33.40	20.45	16.74	31.24	20.58	20.62	0.993	0.988	0.980	0.991	0.984	0.985
Curvelets	25.64	18.83	16.00	25.92	19.14	16.35	0.998	0.996	0.988	0.999	0.994	0.985
NSS	33.83	20.32	16.68	31.53	20.51	17.02	0.993	0.987	0.981	0.992	0.986	0.977
GLM	31.10	25.15	22.66	29.15	24.47	23.38	0.998	0.993	0.985	0.995	0.977	0.965
H.Threshold	29.21	26.19	19.28	25.19	23.46	18.92	0.989	0.969	0.954	0.979	0.961	0.948
SThreshold	29.20	26.14	21.57	25.81	24.27	21.09	0.978	0.958	0.935	0.965	0.946	0.923
OWT	25.71	18.84	16.01	25.94	19.14	16.31	0.999	0.996	0.989	0.999	0.994	0.985
RNLA	29.90	24.69	22.17	26.13	23.40	21.28	0.996	0.991	0.982	0.990	0.982	0.969
SURELET	31.77	26.60	23.45	26.49	24.09	21.96	0.990	0.969	0.940	0.977	0.954	0.924
MPT	33.16	23.58	18.58	27.12	22.50	18.54	0.992	0.980	0.968	0.983	0.973	0.960
MBR	27.03	26.41	25.69	23.03	22.77	22.45	0.986	0.983	0.979	0.977	0.972	0.966

The texture is well preserved on application of multiscale techniques except for the ProbShrink, MPT and MBR filters. Smoothing of noisy background is observed using the MBR and MPT filters. The shrinkage techniques result in better denoising in the homogenous regions where the performance is degraded in the edgy regions due to the generation of large coefficients. At higher values of the noise variance, SURELET and OWT filters generate large thresholds which were not suitable in denoising of TTE images. Spurious values were generated on application of the ProbShrink filter in the logarithmic domain. The performance of GLM, NSS, BlockShrink, and Bivariate stand out in terms of SSIM≥0.9, β≥0.8 and FoM≥0.9 whereas some of other methods lag in terms of one or more values like BayesShrink, and PSBE have smaller value of β. The performances of these filters are on-par to each other in terms of PSNR, RMSE, LMSE, Err3 and Err4.

Table 3.9 Comparison of performance parameters using multiscale filters

Methods	**MSE**						**SNR**					
	Lena			Barbara			Lena			Barbara		
	0.01	0.05	0.1	0.01	0.05	0.1	0.01	0.05	0.1	0.01	0.05	0.1
Probshrink	5052	4966	4419	5603	5246	5670	10.88	11.03	12.04	9.52	10.09	9.41
Bivariate	32.55	113.95	233.82	59.96	193.12	349.58	54.70	43.81	37.57	48.93	38.77	33.62
BayesShrink	51.08	139.66	242.84	94.45	259.87	417.87	50.78	42.05	37.24	44.98	36.19	32.07
PSBE	43.69	141.24	298.28	145.57	254.43	411.82	52.14	41.95	35.46	41.23	36.38	32.19
BlockShrink	29.67	586.16	1376.7	48.86	568.06	562.84	55.50	29.59	22.17	50.71	29.40	29.48
Curvelets	177.27	850.73	1630.3	166.30	792.10	1505.8	39.98	26.35	20.70	40.07	26.51	20.93
NSS	26.86	603.05	1395.2	45.65	578.17	1295.8	56.37	29.34	22.06	51.30	29.25	22.24
GLM	50.45	198.22	352.15	78.91	232.10	298.45	50.89	39.01	34.01	46.54	37.17	34.99
HThreshold	77.91	156.11	765.75	200.08	292.47	832.40	47.12	41.08	27.27	38.46	35.17	26.08
SThreshold	78.10	157.91	452.90	170.27	243.20	505.89	47.10	40.98	31.83	39.86	36.77	30.41
OWT	174.50	848.95	1627.6	165.28	792.35	1507.5	40.11	26.37	20.72	40.12	26.51	20.92
RNLA	66.47	220.72	393.69	158.26	297.01	483.58	48.50	38.07	33.05	40.50	35.03	30.80
SURELET	43.17	142.07	293.63	145.77	253.39	413.41	52.24	41.90	35.59	41.21	36.41	32.16
MPT	31.38	284.64	900.36	126.08	365.38	909.54	55.02	35.86	25.86	42.47	33.23	25.31
MBR	128.69	148.38	175.37	323.28	343.37	369.61	42.76	41.52	40.07	34.30	33.77	33.13
	IQI						**SSIM**					
ProbShrink	0.4235	0.4234	0.3275	0.3764	0.3366	0.3083	0.752	0.753	0.660	0.630	0.604	0.569
Bivariate	0.6234	0.4717	0.3919	0.7485	0.5815	0.4822	0.915	0.764	0.659	0.932	0.808	0.713
BayesShrink	0.5844	0.4319	0.3606	0.7138	0.5194	0.4093	0.879	0.757	0.697	0.916	0.790	0.708
PSBE	0.5928	0.4470	0.3700	0.6560	0.5308	0.4561	0.906	0.740	0.624	0.891	0.775	0.689
BlockShrink	0.6514	0.3108	0.2188	0.7853	0.4606	0.4615	0.941	0.620	0.486	0.950	0.732	0.730
Curvelets	0.4699	0.2779	0.2046	0.6508	0.4222	0.3183	0.806	0.573	0.466	0.882	0.695	0.588
NSS	0.6605	0.3077	0.2174	0.7943	0.4591	0.3355	0.945	0.614	0.486	0.952	0.731	0.604
GLM	0.5809	0.4200	0.3560	0.7090	0.5092	0.4513	0.912	0.752	0.662	0.927	0.807	0.756
HThreshold	0.4905	0.4194	0.2469	0.5529	0.5116	0.3526	0.875	0.791	0.536	0.831	0.782	0.625
SThreshold	0.5129	0.4179	0.2984	0.5919	0.5399	0.4223	0.891	0.805	0.640	0.855	0.816	0.711
OWT	0.4709	0.2782	0.2047	0.6514	0.4223	0.3181	0.807	0.574	0.466	0.881	0.695	0.587
RNLA	0.5107	0.3491	0.2816	0.5770	0.4566	0.3769	0.887	0.733	0.634	0.843	0.749	0.667
SURELET	0.5944	0.4453	0.3703	0.6548	0.5324	0.4563	0.907	0.738	0.626	0.891	0.778	0.689
MPT	0.6110	0.3768	0.2626	0.6703	0.4993	0.3755	0.949	0.658	0.467	0.911	0.729	0.575
MBR	0.556	0.476	0.431	0.511	0.464	0.431	0.90	0.83	0.77	0.80	0.76	0.73

Figure 3.3 Visual quality comparison for multiscale filters: (a) ProbShrink [9.52, 0.37, 74.85], (b) BayesShrink [44.98, 0.52, 9.72], (c) PSBE [41.23, 0.53, 12.06], (d) BlockShrink [50.71, 0.46, 6.99], (e) NSS [51.3,0.46, 6.75], (f)GLM [46.54, 0.51,8.88], (g) OWT [40.12, 0.65, 12.86], (h) RNLA [40.5, 0.5,12.58], (i) SURELET [41.21, 0.657, 12.07], (j) MPT [42.47,0.64, 11.22], (k) MBR [34.30,0.51,17.98], (l) Bivariate [48.93, 0.58,7.07], noisy image [40.06, 0.652, 12.09]

Table 3.10 Comparison of IQM using NLM, sparse representation and hybrid filters

	MSE						**SNR**					
	Lena			Barbara			Lena			Barbara		
	0.01	0.05	0.1	0.01	0.05	0.1	0.01	0.05	0.1	0.01	0.05	0.1
NLM	220.7	346.8	615.8	76.21	268.9	527.1	38.07	34.15	29.16	46.85	35.89	30.05
PPB	27.13	381.5	700.7	46.23	386.7	934.8	56.28	33.32	24.94	51.19	32.74	25.07
PLOW	51.94	200.0	296.7	50.44	215.6	405.0	50.63	38.92	35.49	50.32	37.70	32.22
BPFA	0.001	0.003	0.006	0.001	0.007	0.014	53.75	38.75	33.70	47.93	31.08	25.33
HTMED	89.79	216.5	609.1	312.4	431.4	807.5	45.88	38.24	29.25	34.59	31.79	26.34
HATMed	55.69	127.0	242.4	239.0	313.2	433.4	50.03	42.87	37.26	36.92	34.57	31.75
HTMAV	68.07	134.7	331.5	266.8	338.9	536.0	48.29	42.36	34.54	35.96	33.89	29.90
GW	44.15	199.3	373.5	90.13	253.9	439.1	52.05	38.96	33.50	45.39	36.39	31.64
	IQI						**SSIM**					
NLM	0.631	0.403	0.310	0.776	0.588	0.478	0.935	0.752	0.623	0.958	0.836	0.740
PPB	0.627	0.330	0.238	0.764	0.496	0.373	0.952	0.690	0.522	0.957	0.785	0.646
PLOW	0.712	0.524	0.462	0.819	0.653	0.564	0.847	0.614	0.540	0.872	0.688	0.591
BPFA	0.610	0.422	0.352	0.732	0.522	0.424	1.000	1.000	0.999	1.000	0.999	0.999
HTMED	0.580	0.454	0.376	0.545	0.463	0.393	0.897	0.773	0.665	0.811	0.735	0.654
HATMed	0.587	0.451	0.388	0.577	0.472	0.416	0.897	0.740	0.640	0.834	0.744	0.601
HTMAV	0.629	0.516	0.440	0.588	0.515	0.453	0.924	0.840	0.750	0.840	0.788	0.728
GW	0.597	0.427	0.356	0.704	0.546	0.460	0.907	0.713	0.609	0.916	0.779	0.690
	Beta Metric						**FoM**					
NLM	0.584	0.192	0.125	0.907	0.608	0.429	0.894	0.642	0.440	0.917	0.711	0.549
PPB	0.597	0.161	0.102	0.890	0.495	0.328	0.856	0.484	0.355	0.924	0.640	0.494
PLOW	0.711	0.301	0.218	0.734	0.360	0.234	0.912	0.814	0.667	0.935	0.807	0.689
BPFA	0.448	0.145	0.091	0.832	0.447	0.318	0.848	0.559	0.472	0.845	0.564	0.48
HTMED	0.099	0.110	0.110	0.081	0.095	0.082	0.875	0.518	0.417	0.844	0.666	0.560
HATMed	0.450	0.279	0.1956	0.320	0.199	0.143	0.874	0.489	0.398	0.823	0.624	0.566
HTMAV	0.330	0.255	0.209	0.236	0.191	0.153	0.867	0.677	0.487	0.847	0.819	0.643
GW	0.432	0.152	0.101	0.786	0.457	0.308	0.778	0.463	0.393	0.891	0.576	0.522
	Time						**RMSE**					
NLM	272.6	264.6	260.2	258.5	258.0	252.1	14.85	18.62	24.81	8.730	16.40	22.96
PPB	172.85	173.17	173.26	181.69	176.10	178.0	5.208	19.53	31.63	6.799	19.66	30.57
PLOW	71.68	63.90	61.05	67.01	64.14	62.28	7.207	14.144	17.227	7.102	14.683	20.126
BPFA	23.01	20.01	18.47	24.21	29.90	28.99	0.024	0.056	0.075	0.032	0.085	0.118
HTMED	8.62	8.65	8.60	8.55	8.53	8.51	9.476	14.717	24.680	17.675	20.772	28.418
HATMed	10.14	10.18	10.24	10.18	10.32	10.20	7.463	11.271	15.571	15.461	17.699	20.819
HTMAV	31.22	31.24	31.38	31.31	31.22	31.30	8.251	11.607	18.208	16.334	18.410	23.152
GW	03.64	03.60	03.67	03.62	03.61	03.60	6.644	14.117	19.327	9.494	15.934	20.955
	PSNR						**NCC**					
NLM	24.69	22.73	20.24	29.31	23.83	20.91	0.9187	0.9329	0.9373	0.9633	0.9556	0.9501
PPB	33.80	22.32	18.13	31.48	22.26	18.42	0.9993	0.9897	0.9733	0.9986	0.9889	0.9735
PLOW	30.98	25.12	23.41	31.10	24.79	22.06	0.9940	0.9791	0.9720	0.9945	0.9811	0.9638
BPFA	80.66	73.16	70.64	77.98	69.56	66.68	0.9987	0.9941	0.9852	0.9983	0.9913	0.9814
HTMED	28.60	24.77	20.28	23.18	21.78	19.06	0.9763	0.9208	0.8403	0.9516	0.9032	0.8254
HATMED	30.67	27.09	24.28	24.35	23.17	21.76	0.9886	0.9712	0.9447	0.9718	0.9503	0.9212
HTMAV	29.80	26.84	22.93	23.87	22.83	20.84	0.9812	0.9425	0.8867	0.9597	0.9226	0.8683
GW	31.68	25.14	22.41	28.58	24.08	21.70	0.9988	0.9945	0.9895	0.9973	0.9925	0.9869

Nonlocal mean filter: The values of IQM obtained using the NLM, sparse representation and hybrid filters are depicted in Table 3.10 for Barbara and Lena image at various noise

levels. The visual qualities of images on application of these filters are compared in Figure 3.4. The NLM filters results in an effective noise reduction and texture preservation. The high values β, FoM and SSIM reflect superior edge preservation using patch based filters ((FoM, SSIM and β) ≥0.9 and IQI≥0.75). The IQI for NLM filter is superior compared to that of PPB filter whereas the other parameters were better using latter filter. The performance of PLOW filter is superior in comparison to the NLM and PPB filters in terms of IQM such as the IQI, FoM, and computation time. The performance of BPFA filter stood out among the NLM, sparse and hybrid filters in terms of SSIM, RMSE, PSNR, MSE and SNR showing superior noise suppression qualities. But, observing the values of IQI, β, and FoM shows poor edge preservation in BPFA filter in comparison to NLM, PPB and PLOW filters. The performances of hybrid fuzzy filters were superior in comparison to fuzzy filters. Among hybrid filters, the performance of GW filter is superior in comparison to HTMED, HATMED and HTMAV filters.

Figure 3.4 Visual quality comparison for NLM, sparse representation and hybrid filters: (a) NLM [46.85, 0.78, 14.85], (b) PPB [51.19, 0.77, 5.21], (c) PLOW [50.32, 0.82, 7.21], (d) BPFA[47.93, 0.73, 0.03], (e) HTMED [34.59, 0.54, 9.48], (f) HATMED [36.92, 0.57, 7.46], (g) HTMAV[35.96,0.59,8.25], (h)GW[45.39, 0.71, 6.64] whereas noisy image [40.06, 0.652, 12.09]

Table 3.11 Comparison of IQM using variational and nonlinear filters

Methods	MSE						SNR					
	Lena			Barbara			Lena			Barbara		
	0.01	0.05	0.1	0.01	0.05	0.1	0.01	0.05	0.1	0.01	0.05	0.1
AFTV	143.9	759.7	1495	141.8	713.3	1391	41.79	27.34	21.45	41.45	27.42	21.62
ROF	61.62	480.5	1073	85.32	477.2	1018	49.15	31.31	24.33	45.87	30.91	24.33
ATV	38.15	192.9	533.1	115.8	262.2	564.3	53.32	39.24	30.41	43.21	36.11	29.46
Aujol	1803	1805	1811	2320	2323	2329	19.83	19.82	19.79	17.18	17.16	17.14
Shock	96.47	127.7	169.7	280.6	308.7	350.8	45.26	42.82	40.35	35.53	34.69	33.59
Median	74.63	170.1	279.2	335.2	407.1	507.8	47.49	40.33	36.03	33.98	32.29	30.37
DsFhmedian	71.80	277.9	529.5	166.7	369.7	603.6	47.83	36.07	30.47	40.05	33.13	28.87
DsFhomog	61.15	103.1	160.2	225.0	278.7	332.1	49.22	44.68	40.85	37.44	35.58	34.06
DsFhomo	80.55	141.4	214.7	284.8	345.8	415.0	46.83	41.94	38.31	35.40	33.71	32.12
DsFgf4d	323.5	1114	1932	594.7	1336	2081.2	34.75	24.01	19.23	29.00	21.97	18.12
DsFsrad	177.3	544.2	1132	116.4	549.4	1159	39.97	30.23	23.87	43.16	29.69	23.20
DsFad	139.7	153.1	221.1	239.6	257.4	333.7	42.04	41.25	38.06	36.91	36.27	34.02
DPAD	44.46	173.3	391.3	69.6	262.1	489.2	51.99	40.17	33.10	47.63	36.12	30.70
CED	93.27	179.6	279.1	260.5	316.2	386.3	45.55	39.86	36.03	36.16	34.49	32.75
Level Set	213.6	835.7	1559	403.6	979.4	1621	38.45	26.87	21.68	32.45	24.98	20.79
	IQI						**SSIM**					
AFTV	0.494	0.293	0.214	0.672	0.439	0.330	0.815	0.580	0.471	0.886	0.701	0.590
ROF	0.580	0.355	0.261	0.721	0.505	0.386	0.879	0.632	0.510	0.914	0.738	0.627
ATV	0.583	0.415	0.323	0.651	0.537	0.448	0.930	0.723	0.579	0.903	0.782	0.679
Aujol	0.092	0.090	0.09	0.096	0.095	0.095	0.532	0.531	0.531	0.394	0.394	0.394
Shock	0.593	0.489	0.430	0.563	0.495	0.452	0.913	0.816	0.737	0.833	0.776	0.727
Median	0.511	0.387	0.331	0.461	0.380	0.331	0.870	0.709	0.611	0.773	0.683	0.615
DsFhmedian	0.531	0.361	0.288	0.625	0.458	0.372	0.864	0.663	0.554	0.867	0.721	0.629
DsFhomog	0.609	0.487	0.422	0.602	0.505	0.460	0.915	0.793	0.699	0.855	0.773	0.711
DsFhomo	0.526	0.413	0.357	0.497	0.425	0.376	0.882	0.762	0.670	0.797	0.727	0.667
DsFgf4d	0.476	0.331	0.267	0.547	0.408	0.340	0.809	0.610	0.511	0.793	0.655	0.578
DsFsrad	0.593	0.367	0.286	0.726	0.506	0.390	0.904	0.638	0.520	0.912	0.732	0.623
DsFad	0.622	0.469	0.403	0.660	0.543	0.476	0.903	0.746	0.652	0.876	0.778	0.702
DPAD	0.638	0.432	0.326	0.768	0.555	0.443	0.929	0.736	0.596	0.941	0.790	0.680
CED	0.561	0.450	0.397	0.543	0.471	0.428	0.858	0.727	0.655	0.809	0.740	0.688
Level Set	0.387	0.267	0.218	0.399	0.280	0.231	0.801	0.644	0.575	0.762	0.652	0.596
	Beta Metric						**FoM**					
AFTV	0.333	0.152	0.110	0.701	0.394	0.287	0.677	0.375	0.339	0.726	0.492	0.452
ROF	0.415	0.163	0.113	0.770	0.424	0.298	0.728	0.416	0.346	0.794	0.537	0.455
ATV	0.502	0.206	0.122	0.733	0.464	0.325	0.874	0.457	0.371	0.870	0.580	0.490
Aujol	0.518	0.390	0.310	0.525	0.393	0.316	0.706	0.725	0.719	0.665	0.685	0.701
Shock	0.308	0.261	0.220	0.251	0.216	0.188	0.812	0.628	0.504	0.740	0.776	0.699
Median	0.25	0.093	0.050	0.194	0.115	0.080	0.783	0.503	0.436	0.813	0.690	0.581
DsFhmedian	0.292	0.117	0.074	0.488	0.231	0.161	0.668	0.414	0.386	0.866	0.590	0.506
DsFhomog	0.397	0.292	0.235	0.353	0.239	0.262	0.891	0.598	0.439	0.841	0.696	0.577
DsFhomo	0.296	0.165	0.098	0.127	0.071	0.048	0.795	0.592	0.507	0.772	0.763	0.705
DsFgf4d	0.281	0.162	0.123	0.408	0.290	0.246	0.750	0.476	0.407	0.797	0.594	0.518
DsFsrad	0.472	0.151	0.106	0.796	0.428	0.300	0.870	0.432	0.347	0.863	0.517	0.459
DsFad	0.471	0.280	0.211	0.681	0.483	0.375	0.883	0.528	0.416	0.868	0.647	0.544
DPAD	0.540	0.302	0.199	0.825	0.569	0.421	0.822	0.464	0.363	0.868	0.631	0.529
CED	0.181	0.088	0.066	0.345	0.205	0.153	0.785	0.447	0.406	0.767	0.699	0.644
Level Set	0.175	0.121	0.109	0.192	0.131	0.116	0.793	0.697	0.782	0.765	0.741	0.785

Total variation and bilateral filters: The visual qualities on application of variational and nonlinear filters are shown in Figure 3.5 and Figure 3.11 respectively for noisy Barbara

image and AV in PSAX. The values of IQM obtained using these filters are tabulated in Table 3.11. The performance of FBL filter stands out in comparison to the AFTV and ATV filters in terms of IQM. The edge preservation qualities of the FBL filter are moderately acceptable as the values of SSIM, β, FoM were ≥ 0.85 with IQI≥0.75. The texture of the image is well preserved using FBL filter. These observations hold good for both standard as well as TTE images. In case of noisy Barbara image, the PSNR is 9 dB higher in comparison to the TV based filters as well as the MSE is two times lesser when compared with others.

Figure 3.5 Visual quality comparison for variational and nonlinear filters: (a) AFTV [41.45,0.67, 11.71], (b) ROF [45.87, 0.72, 9.24], (c) ATV [43.21, 0.65, 10.76], (d) Aujol *et al.* [17.18, 0.1, 48.16], (e) Shock [35.53,0.56, 16.75], (f) Median [33.98,0.46, 18.30], (g) DsFhmedian [40.05, 0.63,12.91], (h) DsFhomog [37.44,0.6, 15.0], (i) DsFhomo [35.4, 0.49, 16.87] whereas the noisy image [40.06, 0.652, 12.09]

Nonlinear filters: The visual qualities on application of nonlinear iterative filters are shown in Figure 3.6 and Figure 3.12 respectively for noisy Barbara image and AV in PSAX. The values of IQM obtained using these filters are tabulated in Table 3.11. The AD filter results in

blurring of the images. Suppression of noise in the Dsfsrad and DPAD filters is quite strong. The nonlinear filters such as the DsFsrad and DsFgf4d filter preserve the texture whereas DsFmedian, and DsFad filters result in the loss of textural information. The amount of smoothing increases with increase in the number of iterations but also results in loss of finer details. The output of DsFgf4d filter contain smaller amount of noise retained in them. CED filter induces some sort of artifacts due to the enhancement of speckle pattern contours. Parameter-wise comparison between the DPAD and DsFgf4d filter showed that (β, FoM, and $PSNR)_{DPAD} \geq$ (β, FoM, and $PSNR)_{gf4d}$, $(MSE, RMSE, Err4, and NAE)_{DPAD} \leq (MSE, RMSE, Err4, and NAE)_{gf4d}$ for standard test images. The texture details were lost on application of filters such as the Aujol, and DsFhomo filters.

Figure 3.6 Visual quality comparison for iterative nonlinear filters: (a) DsFgf4d [29.02, 0.547, 24.38], (b) DsFsrad [43.16, 0.73, 10.79], (c) DsFad [36.91, 0.66, 15.47], (d) DPAD [47.63, 0.76, 8.34], (e) CED [36.16, 0.54, 16.14], (f) Level set [32.45, 0.39, 20.01] whereas the noisy image [40.06, 0.652, 12.09]

The performance parameters estimated using 1000 TTE images are presented in Table 3.13 and Table 3.14 as a combination of mean ± standard deviation for all IQM values. The visual qualities of despeckled TTE images in PSAX during diastole are compared in Figure 3.7 to Figure 3.12. The performance analysis for TTE images using the PLOW, BPFA, Aujol and Shock filters is on similar lines as that of standard test images. In case of TTE images, the IQI, FoM, SSIM and SC are almost the same for DsFlsmv and DsFWiener filter, but the visual quality obtained using the DsFlsmv is better compared with Wiener filter, as already stated in earlier paragraphs. The GLM based despeckling filter results in superior

visual quality and edge preservation for the TTE images among multiscale techniques but it has inferior IQI_{GLM}=0.64 compared to IQI_{PSBE}=0.92.

Table 3.12 Comparison of IQM for various types of filters

Method	ρ	AD	SC	MD	LMSE	NAE	ERR3	ERR4
ATMAV	**0.994**	1.68	1.04	150.7	0.98	**0.07**	**20.75**	**26.35**
ATMED	0.993	1.24	1.03	139.5	1.00	**0.07**	20.92	**26.79**
HATMAV	0.993	2.01	1.05	**116.1**	0.94	0.081	21.39	26.47
HATMED	0.993	**1.57**	1.04	122.2	**0.93**	0.081	21.22	**26.30**
HTMAV	0.992	3.04	1.07	119.9	0.96	0.083	22.46	27.93
HTMED	0.991	4.00	1.08	138.6	1.00	0.091	24.59	30.84
TMAV	0.993	2.73	1.06	128.2	1.03	0.082	22.15	27.85
TMED	0.990	3.56	1.07	148.1	1.32	0.100	26.00	32.62
HDTDWT	0.998	0.74	1.01	55.3	**0.19**	**0.04**	**9.42**	**11.17**
HDWT	0.998	0.61	1.01	58.6	0.29	0.054	10.72	12.68
BayesShrink	0.997	1.00	1.02	65.3	0.48	0.059	12.33	14.79
NSS	0.998	1.02	1.02	64.5	0.30	0.053	11.43	13.82
GLM	0.997	0.05	1.00	86.3	0.44	0.057	11.41	13.61
OWT	**1.000**	0.90	1.02	70.33	0.31	0.05	10.59	12.93
SURELET	**1.000**	0.03	0.99	**41.04**	1.18	0.09	15.02	16.79
Curvelet	0.995	2.04	1.02	44.00	1.19	0.088	15.27	17.08
PSBE	0.995	**0.01**	0.99	**41.00**	1.19	0.086	15.10	16.87
MPT	0.993	2.07	**1.05**	115.9	0.88	0.080	20.42	25.22
ProbShrink	0.992	1.79	**1.04**	121.2	0.99	0.08	22.70	27.80
MBR	0.986	-7.62	0.89	220.7	1.00	0.14	33.12	44.22
FBL	**0.999**	**0.026**	**1.01**	**30.4**	**0.09**	0.03	**6.91**	**7.99**
ROF	0.997	**0.026**	**1.00**	48.2	0.44	0.059	11.28	13.08
AFTV	0.997	0.166	**1.01**	73.3	0.46	0.061	12.64	15.12
ATV	0.997	0.006	**1.02**	67.1	0.51	0.062	14.01	16.88
FBF	0.997	0.045	1.00	**61.0**	**0.45**	0.065	**11.92**	**13.65**
FIF	0.996	0.033	0.99	67.1	0.63	0.074	13.70	15.72
HFBF	0.997	-0.22	1.00	99.3	0.61	0.068	13.52	16.65
HFIF	0.996	-0.821	0.98	80.1	0.73	0.07	14.48	16.81
FROST	0.994	0.024	1.02	103.7	0.85	0.073	18.85	23.55
KAUN	0.995	0.256	1.01	121.6	0.92	0.078	15.99	19.33
LEE	0.995	0.312	1.01	117.6	0.98	0.080	16.53	20.03
DsFlsminsc	0.991	0.193	0.31	128.0	1.11	0.090	22.57	27.36
DsFlsmv	0.997	0.196	1.01	66.0	0.40	0.057	12.74	15.54
DsFWiener	0.997	**0.002**	1.01	**62.3**	**0.39**	0.056	**11.72**	**13.91**
DsFgf4d	0.991	0.151	1.01	170.0	1.10	0.147	31.93	39.24
DsFad	0.99	0.082	1.02	98.77	0.80	0.09	19.93	23.69
DsFsrad	**1.00**	0. 013	1.08	76.80	**0.54**	**0.06**	14.93	18.29
DPAD	**1.00**	0.012	1.00	**42.49**	0.56	0.07	**11.80**	**13.35**
EED	1.00	0.002	1.01	91.65	0.56	0.06	14.64	18.13
CED	1.00	0.002	0.99	62.16	0.95	0.08	14.22	16.07
OBNLM	0.998	6.482	1.08	**56.21**	0.16	0.07	10.31	11.56
PPB	0.999	1.522	0.99	83.5	0.16	0.039	**8.25**	**10.19**
DsFhmedia	0.995	0.711	1.02	113.0	**0.81**	0.075	**17.28**	**21.64**
DsFhomog	0.993	**0.352**	1.02	**104.0**	0.94	0.079	20.63	25.36
DsFmedian	0.993	0.695	1.02	181.0	1.06	0.082	21.46	27.62

Table 3.13 Comparison of image quality metrics for TTE images (Mean±STD)

Method	MSE	RMSE	ERR3	ERR4	NAE	LMSE	MD
Lee	21.49±4.70	4.61±0.48	7.32±0.65	9.76±0.68	0.078±0.01	0.366±0.104	44.42±0.69
Kaun	202.9±2.16	14.23±0.072	22.26±0.32	28.78±1.12	0.173±0.02	0.038±0.07	240.8±2.53
Frost	314.4±4.81	17.73±0.13	23.15±0.06	26.14±0.10	0.325±0.03	0.73±0.04	163.5±30.34
DsFlsmv	90.92±4.52	9.53±0.23	18.79±0.3	28.08±0.32	0.12±0.01	0.85±0.01	171.4±5.01
DsFWiener	6.57±1.20	2.55±0.24	3.87±0.23	5.04±0.23	0.049±0.01	0.05±0.01	28.31±1.97
DsFlsminsc	201.34±15.21	14.18±0.52	27.14±0.69	40.31±0.80	0.19±0.02	1.24±0.03	234.8±2.77
FBL	11.11±1.66	3.33±0.25	6.51±0.17	4.97±0.23	0.07±0.00	0.05±0.00	54.40±13.39
TMED	309.74±11.5	17.60±0.33	50.91±0.33	34.42±0.34	0.22±0.03	1.54±0.02	250.03±0.56
ATMED	103.7±3.1	10.18±0.15	22.65±0.21	35.48±0.23	0.1±0.01	0.80±0.01	212.9±0.00
TMAV	215.50±8.29	14.68±0.28	45.75±0.33	30.23±0.32	0.17±0.02	1.00±0.01	240.19±0.83
FIF	3.24±0.17	1.80±0.05	3.44±0.05	5.27±0.06	0.04±0.01	0.10±0.01	41.7±5.12
FBF	4.89±0.22	2.21±0.05	4.57±0.06	7.06±0.06	0.026±0.01	0.09±0.01	64.0±0.01
HFBF	11.44±0.22	3.38±0.03	7.36±0.07	11.98±0.11	0.07±0.01	0.17±0.01	131.2±0.34
ProbShrink	300.67±26.2	17.32±0.74	33.96±0.81	50.42±0.79	0.21±0.05	1.007±0.01	271.79±2.1
BayesShrink	183.8±13.12	13.55±0.47	27.86±0.58	42.06±0.59	0.14±0.03	0.81±0.01	226.34±5.52
PSBE	8.38±0.36	2.89±0.06	6.64±0.11	10.66±0.19	0.03±0.01	0.06±0.01	90.3±14.83
BlockShrink	4.18±2.54	1.97±0.55	3.38±0.65	4.89±0.66	0.028±0.00	0.045±0.02	47.29±2.64
NSS	12.94±2.37	3.58±0.33	6.64±0.32	10.44±0.27	0.054±0.01	0.11±0.01	102.4±3.81
GLM	4.80±0.46	2.19±0.10	5.40±0.15	8.95±0.20	0.018±0.01	0.01±0.01	62.3±0.17
OWT	166.7±60.49	12.73±2.19	44.33±13.10	95.46±37.91	0.06±0.01	3.15±0.97	615±25.6
RNLA	43.06±7.29	6.54±0.54	9.45±0.6	12.53±0.71	0.17±0.01	0.31±0.02	108.8±11.76
SURELET	19.34±7.67	4.33±0.81	12.63±2.25	8.35±1.36	0.05±0.02	0.37±0.11	117.60±41.90
MPT	32.18±3.83	5.66±0.34	10.89±0.22	16.95±0.21	0.076±0.01	0.24±0.02	172.4±0.01
MBR	287.6±22.15	16.95±0.63	33.56±1	50.04±1.03	0.23±0.03	0.98±0.01	246.4±4.33
Bivariate	15.44±2.13	3.92±0.27	5.83±0.28	7.53±0.29	0.076±0.014	0.07±0.01	41.65±3.89
NLM	18.20±1.09	4.26±0.13	15.85±0.78	9.47±0.31	0.05±0.01	0.18±0.01	187.36±13.46
PPB	6.85±0.93	2.61±0.17	5.38±0.22	9.14±0.33	0.06±0.01	0.11±0.01	96.8±0.39
PLOW	2.47±0.41	1.56±0.13	2.44±0.17	3.23±0.19	0.027±0.01	0.036±0.01	13.10±0.36
BPFA	0.0±0.0	0.01±0.0	0.01±0.0	0.012±0.0	0.031±0.001	0.034±0.003	0.083±0.004
HTMED	301.9±11.4	17.37±0.33	34.21±0.38	50.85±0.40	0.205±0.019	1.21±0.009	249.73±0.46
HATMED	123.77±4.96	11.12±0.22	23.53±0.39	36.35±0.34	0.120±0.010	0.804±0.01	212.29±0.05
HTMAV	231.53±9.05	15.24±0.29	30.94±0.35	46.62±0.37	0.170±0.015	0.959±0.01	239.91±0.78
GW	10.57±1.14	3.24±0.17	4.69±0.17	5.94±0.17	0.065±0.004	0.071±0.01	30.74±1.74
AFTV	91.25±2.51	9.55±0.13	25.75±1.20	17.21±0.59	0.16±0.04	0.47±0.04	214.77±14.72
ROF	19.15±1.39	4.37±0.16	9.74±0.09	7.11±0.11	0.08±0.01	0.14±0.01	49.37±0.41
ATV	19.8±2.94	4.44±0.33	6.98±0.25	9.35±0.18	0.08±0.01	0.13±0.01	45.7±0.51
Aujol	569.7±94.01	23.78±2.20	38.96±2.57	51.43±2.66	0.33±0.01	0.57±0.01	168.16±0.34
Shock	196.21±7.84	14.05±0.28	25.67±0.33	37.57±0.39	0.207±0.019	0.970±0.001	219.6±12.8
DsFmedian	90.92±4.08	9.53±0.21	21.58±0.33	34.02±0.34	0.08±0.01	0.86±0.02	211.0±0
DsFhmedian	60.39±2.41	7.77±0.15	18.29±0.27	29.85±0.39	0.06±0.01	0.50±0.01	214.7±5.68
DsFhomog	0.03±0.00	0.17±0.00	0.34±0.01	0.50±0.01	0.002±0.00	0.00±0.00	4.0±0.02
DsFhomo	229.6±13.42	15.15±0.43	31.36±0.58	47.70±0.64	0.16±0.02	0.98	254.3±0.49
DsFgf4d	1.33±0.25	1.15±0.11	1.64±0.11	1.991±0.10	0.021±0.00	0.01±0.00	4.00±0.00
DsFsrad	15.12±1.02	3.89±0.13	10.12±0.06	6.96±0.08	0.06±0.00	0.14±0.01	74.33±0.26
DsFad	57.74±4.67	7.59±0.31	15.25±0.23	11.63±0.26	0.15±0.01	0.28±0.02	84.13±1.79
DPAD	0.47±0.29	0.66±0.20	2.12±0.54	1.35±0.37	0.01±0.00	0.01±0.00	19.73±4.34
CED	5.24±0.45	2.29±0.10	9.16±0.09	5.38±0.08	0.02±0.00	0.05±0.00	91.65±0.99
Level Set	138.89±3.39	11.78±0.14	26.69±0.26	42.57±0.36	0.123±0.02	0.778±0.07	256.82±0.12

Table 3.14 Comparison of parameters for TTE images

Methods	IQI	β	FOM	SSIM	PSNR	SNR	SC
Lee	0.913±0.01	0.853±0.03	0.971±0.01	0.992±0.01	34.89±0.88	41.58±1.7	0.999±0.01
Kaun	0.924±0.01	0.982±0.01	0.952±0.01	0.936±0.01	25.06±0.04	21.92±1.4	1.088±0.02
Frsot	0.803±0.02	0.625±0.02	0.835±0.03	0.890±0.01	23.15±0.06	18.11±1.3	1.246±0.05
DsFlsmv	0.85±0.02	0.60±0.01	0.94±0.02	0.98±0.02	28.55±0.21	28.40±1.8	1.09±0.02
DsFWiener	0.87±0.01	0.97±0.01	0.95±0.01	0.99±0.01	40.02±0.81	51.35±0.9	1.02±0.01
DsFlsminsc	0.74±0.01	0.10±0.01	0.88±0.02	0.93±0.01	25.10±0.31	21.51±1.9	1.12±0.03
FBL	0.78±0.02	0.97±0.00	0.82±0.04	0.98±0.01	37.72±0.64	46.22±1.0	1.03±0.01
TMED	0.75±0.02	0.06±0.01	0.87±0.01	0.92±0.01	23.22±0.16	17.41±2.2	1.26±0.07
ATMED	0.88±0.01	0.44±0.01	0.95±0.01	0.97±0.02	27.98±0.13	27.01±1.8	1.13±0.03
TMAV	0.81±0.01	0.19±0.02	0.90±0.01	0.94±0.00	24.80±0.17	20.56±2.2	1.25±0.07
FIF	0.39±0.06	0.95±0.01	1.00±0.00	1.00±0.01	43.03±0.23	57.35±1.8	1.00±0.01
FBF	0.41±0.06	0.97±0.02	1.00±0.00	1.00±0.01	41.24±0.19	53.78±1.9	1.01±0.00
HFBF	0.38±0.06	0.92±0.02	0.97±0.01	0.93±0.01	37.55±0.08	46.40±2.0	1.00±0.02
ProbShrink	0.31±0.3	0.049±0.01	0.77±0.03	0.899±0.01	23.36±0.36	19.02±3.9	1.22±0.12
BayesShrink	0.88±0.01	0.54±0.01	0.91±0.01	0.94±0.01	25.50±0.30	23.29±4.0	1.23±0.12
PSBE	0.92±0.01	0.98±0.01	0.99±0.01	0.99±0.01	38.90±0.19	49.11±2.0	1.04±0.01
BlockShrink	0.42±0.05	0.977±0.01	0.985±0.01	0.998±0.01	42.54±2.33	57.37±0.9	1.01±0.01
NSS	0.40±0.05	0.94±0.01	0.97±0.01	0.99±0.00	37.08±0.79	45.46±0.8	1.02±0.01
GLM	0.64±0.02	1.00±0.01	0.98±0.01	1.00±0.00	41.33±0.38	53.97±2.30	0.99±0.01
OWT	0.402±0.05	0.497±0.05	0.913±0.04	0.981±0.01	26.16±1.44	24.61±4.50	0.91±0.04
RNLA	0.25±0.03	0.84±0.01	0.71±0.1	0.88±0.01	31.84±0.70	34.99±1.24	1.02±0.00
SURELET	0.39±0.04	0.85±0.04	0.99±0.01	1.00±0.00	35.53±1.57	41.86±3.99	1.01±0.07
MPT	0.62±0.02	0.87±0.01	0.93±0.02	0.99±0.01	33.08±0.52	37.47±1.16	1.05±0.01
MBR	0.67±0.02	0.16±0.01	0.80±0.02	0.90±0.01	23.55±0.32	17.95±2.15	1.25±0.11
Bivariate	0.348±0.03	0.965±0.01	0.866±0.03	0.977±0.01	36.28±0.63	44.36±0.56	1.03±0.01
NLM	0.64±0.02	0.92±0.00	0.92±0.03	0.99±0.00	35.54±0.25	41.87±2.09	1.04±0.01
PPB	0.39±0.06	0.95±0.01	0.98±0.01	0.93±0.01	39.81±0.55	51.54±2.01	0.99±0.00
PLOW	0.493±0.04	0.982±0.01	0.991±0.01	0.996±0.01	44.25±0.73	59.91±0.06	0.999±0.01
BPFA	0.397±0.04	0.983±0.01	0.984±0.01	1.00±0.00	92.976±0.57	61.15±0.41	1.00±0.01
HTMED	0.755±0.02	0.012±0.01	0.848±0.015	0.910±0.006	23.33±0.16	18.46±1.48	1.28±0.054
HATMED	0.843±0.01	0.45±0.01	0.914±0.017	0.961±0.003	27.29±0.17	26.27±1.44	1.162±0.030
HTMAV	0.81±0.01	0.22±0.02	0.883±0.019	0.925±0.005	24.48±0.17	20.77±1.44	1.261±0.049
GW	0.83±0.01	0.966±0.01	0.923±0.023	0.988±0.002	37.91±0.47	47.62±0.74	0.993±0.002
AFTV	0.67±0.03	0.78±0.02	0.67±0.06	0.90±0.011	28.53±0.12	29.11±4.32	1.12±0.05
ROF	0.80±0.01	0.95±0.00	0.92±0.01	0.99±0.001	35.32±0.31	41.43±1.56	1.05±0.01
ATV	0.29±0.04	0.94±0.01	0.84±0.03	0.96±0.01	35.21±0.63	41.72±1.17	1.05±0.01
Aujol	0.35±0.04	0.79±0.005	0.930±0.015	0.907±0.011	20.69±0.81	13.08±0.28	2.93±0.096
Shock	0.32±0.02	0.24±0.004	0.779±0.036	0.920±0.007	25.27±0.17	22.21±1.41	1.17±0.032
DsFmedian	0.93±0.02	0.42±0.01	0.95±0.01	0.98±0	28.55±0.19	28.40±1.97	1.08±0.02
DsFhmedian	0.95±0.01	0.71±0.01	0.94±0.01	0.98±0	30.32±0.17	31.95±1.93	1.07±0.02
DsFhomog	0.90±0.01	1.00±0.01	1.00±0.02	1.00±0.01	63.54±0.23	98.39±1.97	1.00±0.02
DsFhomo	0.81±0.02	0.17±0.01	0.83±0.02	0.91±0.01	24.53±0.24	20.36±1.88	1.20±0.05
DsFgf4d	0.95±0.00	0.99±0.01	0.96±0.01	1.00±0.00	46.96±0.83	65.41±1.11	1.00±0.00
DsFsrad	0.61±0.02	0.95±0.02	0.97±0.01	1.00±0.00	36.35±0.29	43.48±1.53	1.04±0.01
DsFad	0.52±0.02	0.86±0.01	0.64±0.04	0.93±0.01	30.53±0.36	31.85±1.50	1.07±0.01
DPAD	0.71±0.02	1.00±0.01	1.00±0.00	1.00±0.00	52.07±2.63	74.92±3.24	1.00±0.00
CED	0.70±0.02	0.98±0.01	0.99±0.01	1.00±0.00	40.95±0.37	52.70±2.11	1.02±0.00
Level Set	0.79±0.01	0.486±0.006	0.866±0.009	0.970±0.003	26.76±0.14	24.84±1.50	1.10±0.02

The GLM filter outputs also contain a small amount of noise retained in them and appear slightly blurred. These observations holds good for all TTE and noisy standard images. The IQI of hybrid median filter is superior compared to filters such as the DsFWiener, DsFlsmv,

FBL, PSBE and DPAD filters, which normally result in good quality of denoised images, also the $(\beta)_{DsFhmedian}$ is superior compared to that of DsFlsmv and DsFlsminsc filters.

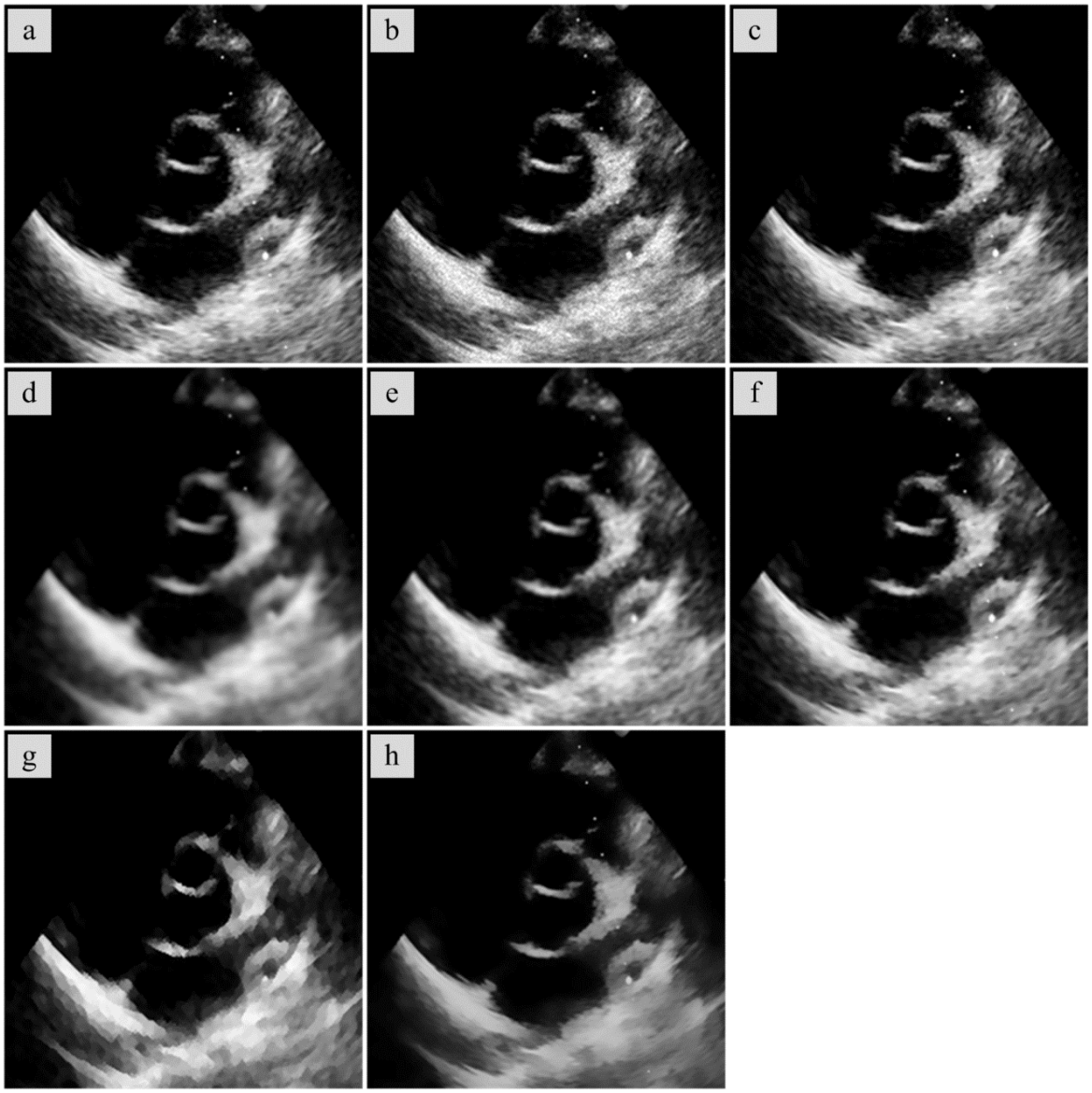

Figure 3.7 Visual qualities of TTE images using local statistics filters: (a) original TTE image in PSAX during diastole, (b) Lee, (c) Kaun *et al.*, (d) Frost *et al.*, (e) DsFlsmv, (f) DsFWiener, (g) DsFlsminsc, (h) FBL. The Frost et al. results in loss of finers details, while DsFlsminsc to blocky effects. In other filters the structure and other fine details are retained.

Clinical validation: The validation of denoised images has been carried out by grading of images by four clinical practitioners at PGI, Chandigrah. The grading of images is based on visual perception and preservation of contents in the image. The average grades of each method are tabulated in Table 3.15. The analysis reveals that despeckling methods such as the DsFlsmv, GLM, PSBE, PPB, DsFgf4d, DsFhomog, BPFA, PLOW and NLM filters are acceptable whereas the DsFca, fuzzy TMED, and RNLA filtered images are unacceptable in the clinical practice.

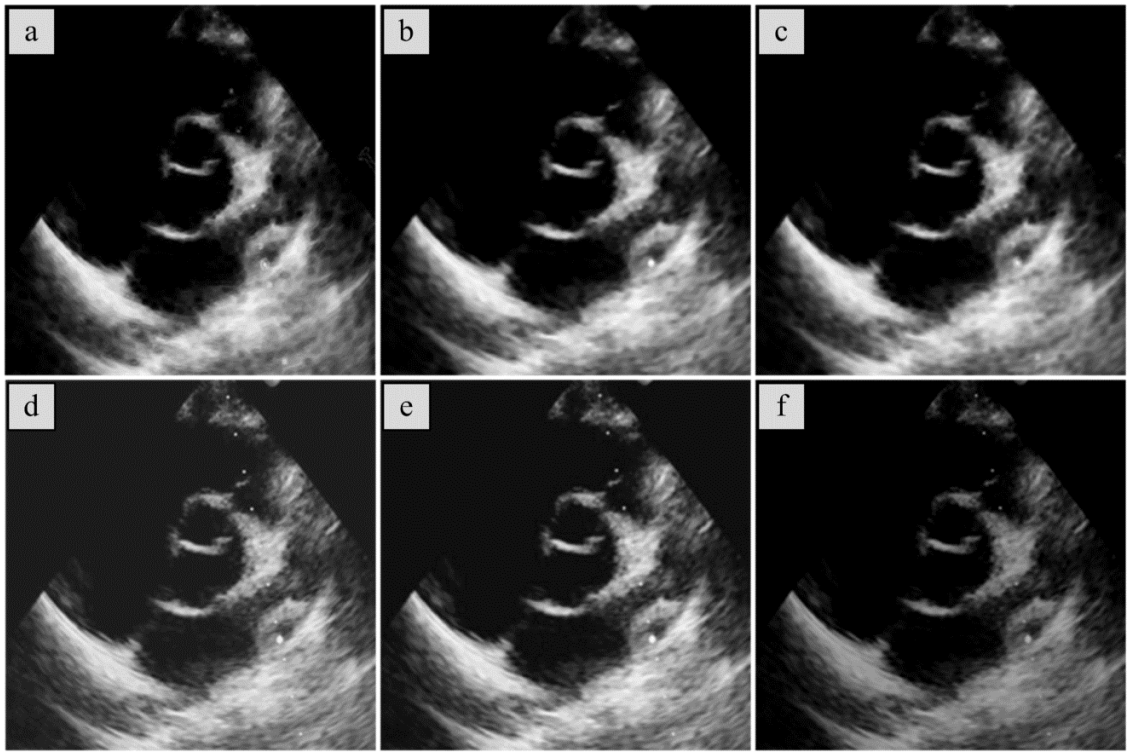

Figure 3.8 Visual qualities of TTE images on applications of fuzzy and Fourier filters: (a) TMED, (b) ATMED, (c) TMAV, (d) FIF, (e) FBF, and (f) HFBF. The Fourier filters (FIF and FBF) result in enhancement of contrast of TTE images while TMED results in blocky structures in the denoised images.

Table 3.15 Grading of despeckled images by doctors

Filter Name	Grade	Filter Name	Grade
DsFca, TMED, RNLA	4	DsFWiener, DsFhmedian, SURELET, DPAD	7
DsFad, DsFhomo, HFBF, MBR, MPT, ROF, TMAV	5	DsFlsmv, GLM, PSBE, PPB, PLOW	8
DsFsrad, FBF,FIF,NSS,ATMED, AFTV, ATV, Aujol *et al.* filter	6	DsFgf4d, DsFhomog, NLM, BPFA	9

The objective of result analysis for 48 filters is to look for the suppression of speckle noise while preserving the edges and structural information, so as to make the images more easily readable for the clinicians. It is felt, as proved in Chapter 2, the despeckling might boost up the process of automatic boundary tracing, and computer aided texture analysis, compression and classification. Based on their analysis of despeckling filters for US images of carotid artery, Loizou *et al.* [131] had concluded that the DsFhmedian and DsFlsmv filters would improve the US image quality. Similar results are observed through the analysis presented for the standard images and the TTE images in this thesis. The performance of DsFlsmv and DsFhmedian were known for high image quality index and edge preservation. The noise suppression qualities of the DsFWiener filter can be taken into account along with DsFlsmv and DsFhmedian filters. Elamvazuthi *et al.* [134] based on analysis of six despeckling filters had concluded that the hybrid combination of Wiener, wavelet and anisotropic diffusion filter would improve the quality of the US images of bone. It is observed

that the hybrid integration of fuzzy and Wiener filter improve noise suppression but with loss of texture information. Based on the analysis of 15 despeckling techniques, Finn *et al.* [22] had concluded that the performance of the DsFgf4d, DsFsrad and oriented speckle reducing AD techniques are successful in suppression of speckle noise from the TTE images.

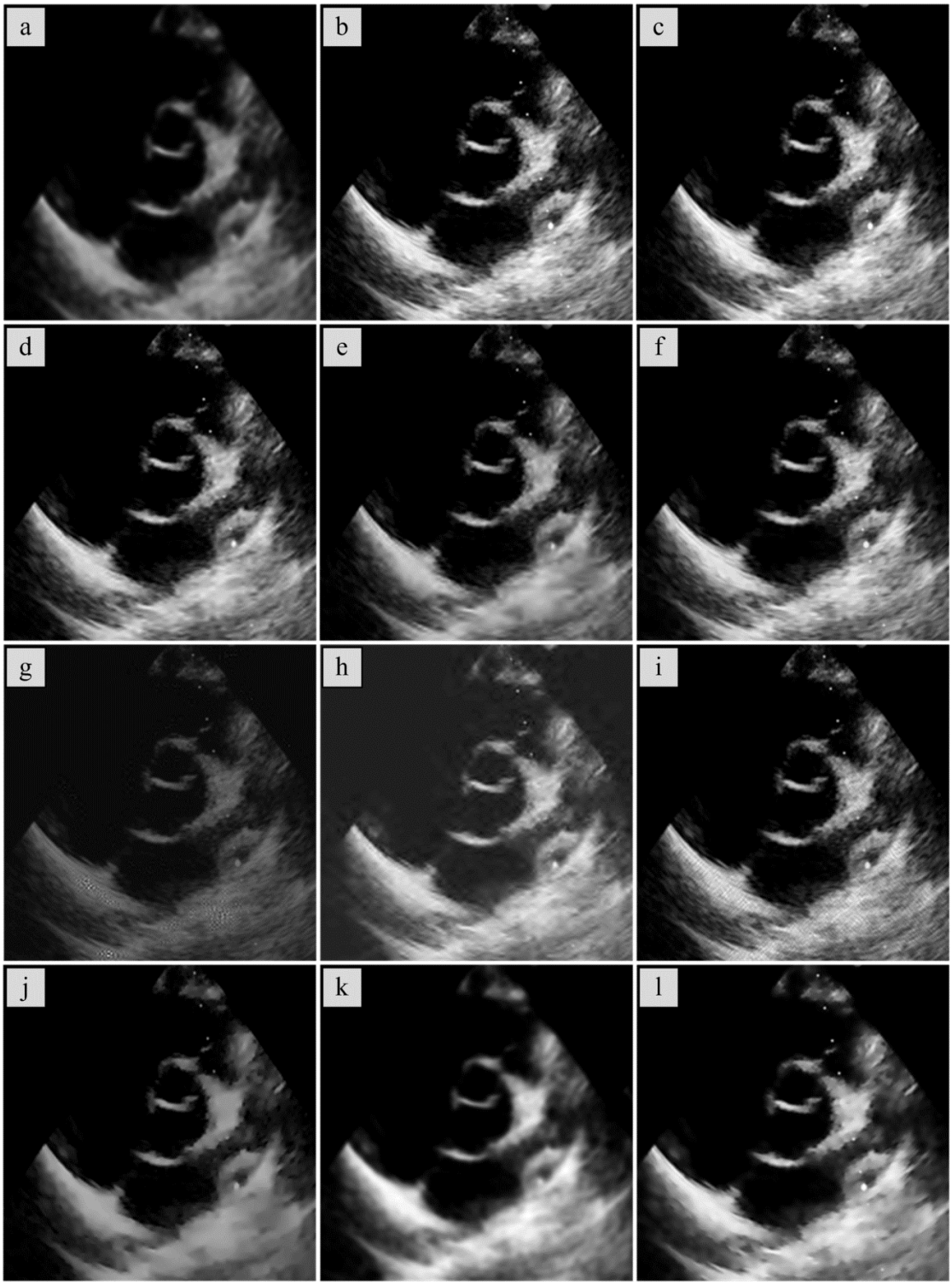

Figure 3.9 Visual quality of TTE on application of multiscale filters: (a) ProbShrink, (b) BayesShrink, (c) PSBE, (d) BlockShrink, (e) NSS, (f)GLM, (g) OWT, (h) RNLA, (i) SURELET, (j) MPT, (k) MBR, (l) Bivariate. The ProbShrink, RNLA and MBR result in reduction of contrast of the images. Spurious edges and artifacts are induced using OWT and SURELET.

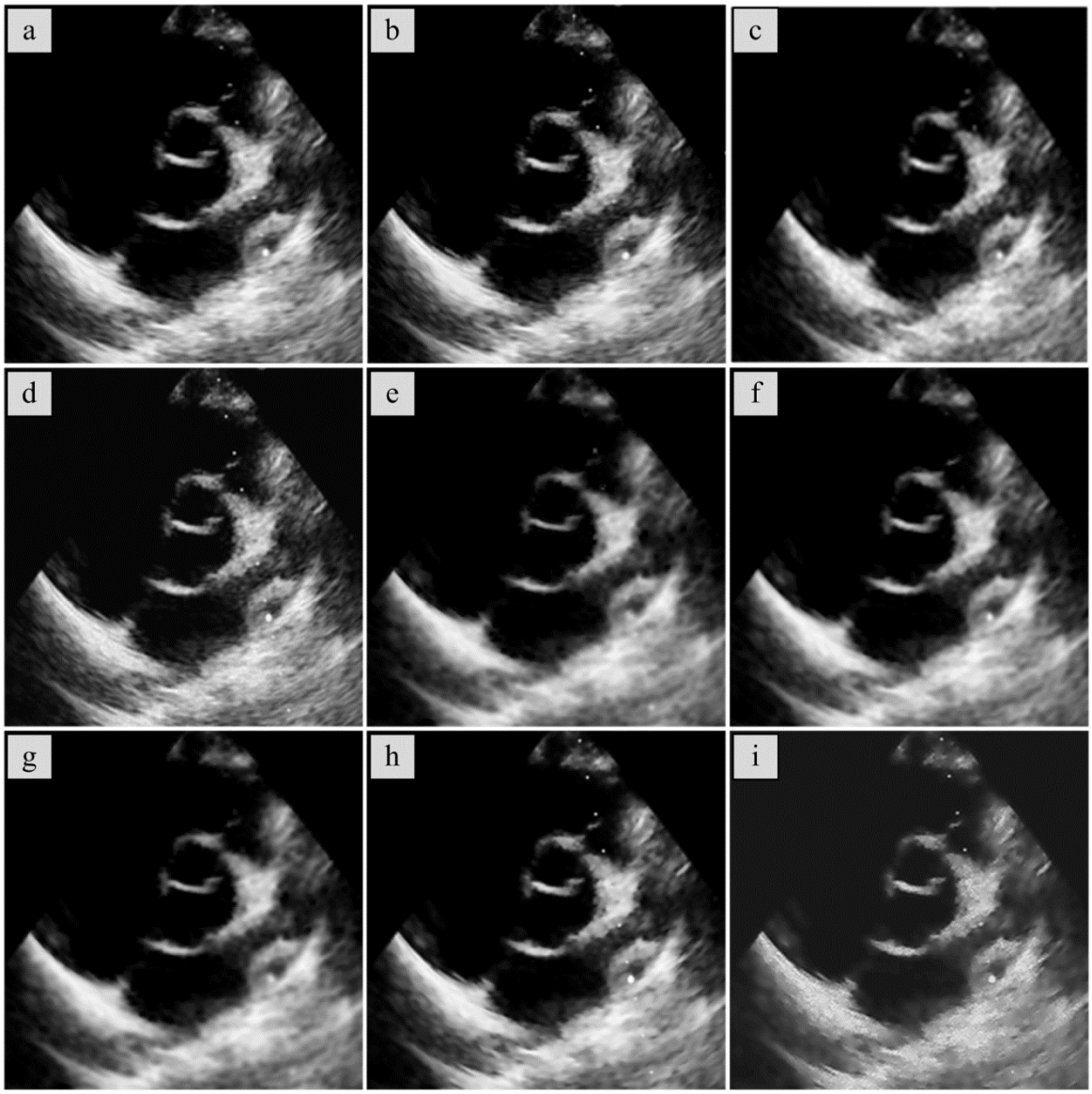

Figure 3.10 Visual quality of TTE images on application of NLM, sparse representation and hybrid filters: (a) NLM, (b) PPB, (c) PLOW, (d) BPFA, (e) HTMED, (f) HATMED, (g) HTMAV, (h) GW, (i) GHP. Blocky effects are observed in images being denoised using HTMED and gradient histogram projection (GHP) technique.

The performance of DPAD filter is superior in comparison to the DsFsrad, DsFad and DsFgf4d filters in terms of FoM, β and SSIM whereas the IQI of DsFgf4d is superior in comparison to the diffusion based despeckling techniques. Mateo *et al.* [26] compared the image quality metrics of six filters employed for the denoising of US images of kidney. It was pointed out that median filter, wavelet filters, Fourier filtering and their homomorphic counterparts are not extensively experimented on US images. Based on the analysis of these filters in this thesis, it is observed that median filter preserves the edges but noise is retained in the images. Texture is well preserved using many of the multiscale techniques. Zhang, Wang and Cheng [135] have concluded that the performance of PPB filter was superior compared to three local adaptive, two anisotropic, three multiscale techniques and a hybrid technique for reduction of noise in US image of breast.

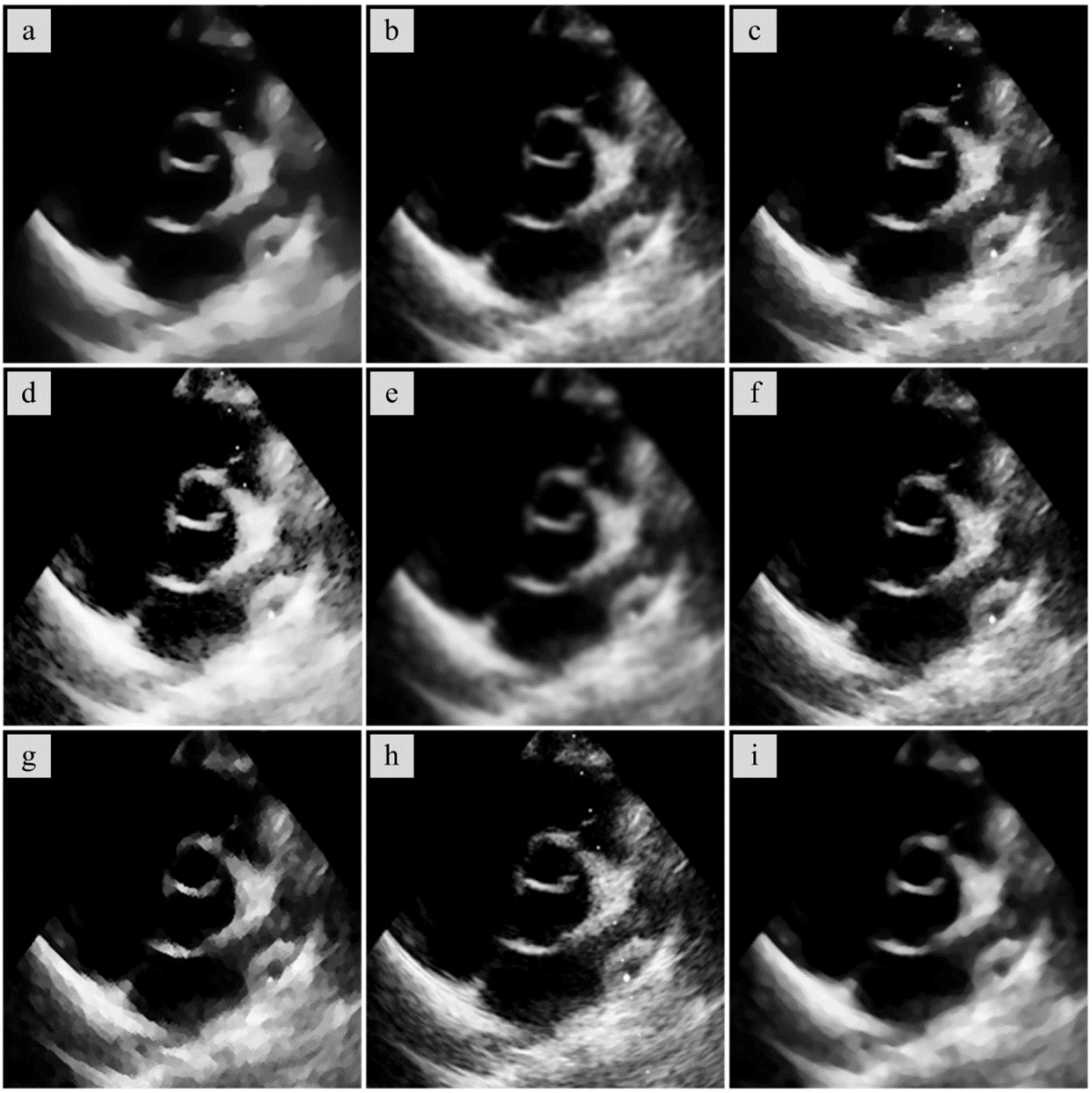

Figure 3.11 Visual quality of TTE images on applications of variational and nonlinear filters: (a) AFTV, (b) ROF, (c) ATV, (d) Aujol, (e) Shock, (f) Median, (g) DsFhmedian, (h) DsFhomog, (i) DsFhomo. The images are over-smoothed with loss of finer details using filters such as AFTV, Shock and DsFhomo filters. Blocky effects are observed in ATV and median based despeckled images.

This thesis compares the application of seven local statistics, three fuzzy, three Fourier, 12 multiscale, five variational, 10 nonlinear, three patch based, a sparse representation based dictionary and four hybrid filtering techniques. The performances of despeckling filters such as the GLM, DsFlsmv, DPAD, DsFhomog, FBL, PLOW, BPFA and PPB filters are superior among the 48 denoising techniques analyzed in terms of 16 performance parameters along with the visual quality assessment and grading by the cardiologists. Each of these filters present a set of merits and demerits tabulated in Table 3.3.

Some of the general observations based on the results in Figure 3.7 to Figure 3.12 are the visual quality of the image improves on pre-processing using the DsFgf4d filter but at the

same time, the image is considerably smoothed with noise retained. The suppression of noise using median filter is fractionally superior compared to the Lee filter in the homogeneous regions. However, the major threats with this filter are the extra computational cost needed for sorting the intensity values, blurring of the edges and loss of smaller details present in the image. The influence of median filtering is also seen on clean pixel values leading to blurring of edges. Some of the edges and finer details are lost using DsFgf4d filter. Many unwanted ripples prevailed in the CED denoised image.

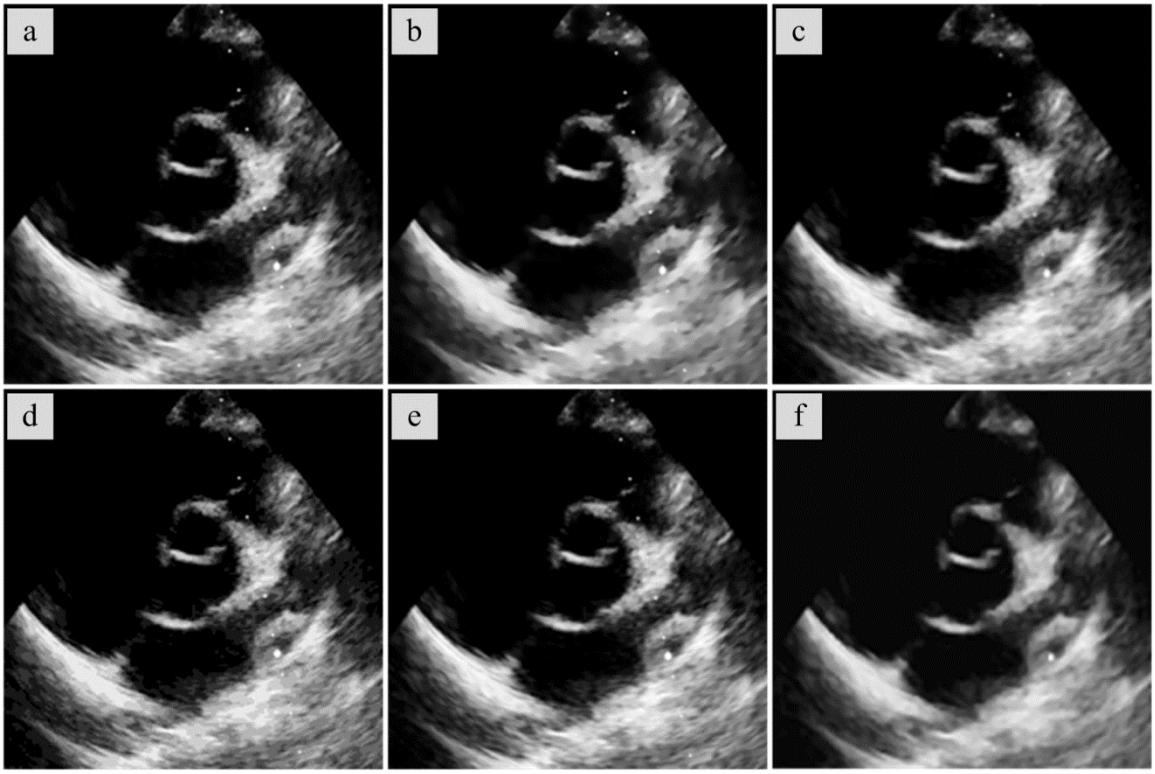

Figure 3.12 Visual quality of TTE images on application of iterative nonlinear filters: (a) DsFgf4d, (b) DsFsrad, (c) DsFad, (d) DPAD, (e) CED, (f) Level set

The DsFsrad filter is able to suppress the noise significantly but at the cost of excessive smoothing of details and higher computational time. It is also observed that it successfully eliminates noise in the background also but blurs the edges. The DPAD based filter took lesser amount of execution time in comparison to the DsFsrad filter. The issue of concern in NLM denoising is the sub-optimality in dealing with sharp edges. It failed to exploit smoothness of edge contour which can distinguish the white and black regions. The edges are well preserved using the DsFhmedian filter with increase in the visual quality of the denoised image. As no tuning of thresholds or parameters is required in DsFhomog filter, in a sense helps automatic interpretation. The sparse representation based BPFA filter results in high noise suppression but needs very high computational time. The edges are not well preserved using BPFA filter.

3.4 Performance analysis using blind quality parameters

Most of the researchers have employed standard full reference based metrics for evaluating the filter performance. The despeckling techniques and performance parameters used by various researchers are tabulated in Table 3.16. The full reference parameters such as the PSNR, MSE, SSIM, CNR, and RMSE, are computed to analyze the performances of despeckling filters. These parameters evaluate performance considering output processed and standard noise free image. But unfortunately noise free reference TTE images are not available. The traditional parameters such as the PSNR and MSE may not reflect the true performance in case of the clinical images. The possible solution to this problem would be to use parameters such as speckle suppression index (SSI) [129, 282], speckle suppression and mean preservation index (SMPI) [129, 282], and β [26]. These parameters do not require noise free image as reference for computing the performance. Mateo *et al.* [26] had employed β for evaluating edge preservation. Iqbal *et al.* [282] had used SSI and SMPI for measuring speckle suppression and the EPI for estimating edge preservation.

Table 3.16 IQM used in analysis of filters by various authors

Ref.	Types of filters	No. filters	Performance parameters	Type of image	β/ SMPI/ SSI ?
22	WLT , SAR, AD , GEO	15	FoM, SSIM, MSE, CNR, SNR	Heart US	No
134	LA, AD, MR, NLM, HYB	11	PSNR, MSE, SSIM, FoM	Breast US	No
27	DsF filters based on LS, WNR, MED, AD, GEO, HYBMED	10	MSE, SNR, PSNR, RMSE, QI, SSIM, AD, SC,NCC, MD, LMSE, NAE, Err	Carotid Artery US	No
134	MED, AD, WLT, WNR, AVG, HYB	7	PSNR	Bone fracture	No
128	WLT, AMED, AD, MAP, FF, LLS	7	SNR,ENL, CNR, EKI, CPU time	OCT Retina	No
171	AMED, WNR, LS, MBR, AD, BS	17	PSNR, SNR, SSIM, FoM, EKI, MVR	Prostate US	No
26	MED, AMED, FIF, FBF, WLT, HFIF	10	β, MSE, SNR, PSNR	Kidney US	β
76	MED, Le-Sig, LR, Lee, Frost, MAP	07	SSI, EEI, FPI, IDPC	SAR image	β ,SSI
129	Lee, Frost, MAP, WLT, BM3D, PPB	07	ENL, SSI, SMPI, CoC, ESI,	SAR image	Yes

Table 3.17 Comparison of speckle noise suppression for multiscale despeckling filters

Methods	β	SMPI	SSI	Soft threshold	β	SMPI	SSI
MPT	0.8601	2.806	0.9868	RBIO4.4	0.0084	58.59	0.9719
RNLA	0.8428	2.976	0.9627	DB2	0.0226	58.95	0.9672
OWT	0.4477	3.070	1.0409	DB4	0.0129	58.74	0.9638
MBR	0.2312	2.538	0.9341	DB8	0.0253	59.91	0.9481
NSS	0.4259	**0.962**	**0.6904**	DB45	0.0091	54.38	**0.9152**
BSHRINK	**0.9996**	2.589	0.9999	COIF1	0.0302	59.17	0.9650
SURELET	0.8958	3.967	0.9887	COIF5	0.0029	58.71	0.9454
GLM	**0.9866**	**2.238**	0.9963	SYM2	0.0226	58.95	0.9672
PSBE	**0.9805**	**2.504**	0.9960	SYM8	0.0177	55.92	0.9750
PS(DB2)	0.1939	27.61	**0.7266**	DMEY	0.0072	52.73	0.9293
PS(DB4)	0.1530	20.55	0.7281	BIOR1.1	0.2762	59.52	0.9588
PS(DB8)	0.1350	17.44	0.7287	BIOR1.5	0.0019	58.54	0.9754
PS(SYM2)	0.1939	27.61	**0.7266**	BIOR6.8	0.0136	57.11	0.9692
PS(SYM4)	0.1530	20.55	0.7281	RBIO1.1	0.2762	59.52	0.9588
PS(SYM8)	0.1350	17.44	0.7287	RBIO2.2	0.0359	58.73	0.9581

The analysis of SMPI in Table 3.17 reveals that the performance of NSS filter is best among multiscale techniques with effective noise suppression. The SMPI obtained for the NSS filter is three times more effective compared to the GLM filter and it is multi-fold higher in comparison to the ProbShrink filter also. The NSS filter and the ProbShrink filter gave best values of SSI among the multiscale techniques. The IOWT filter had SSI ≥1.1 suggesting that the noise is not suppressed. The logarithmic probShrink results in high value of SMPI which is not suitable for TTE images. All the multiscale techniques have FoM value greater than 0.8. The multiscale techniques such as the MBR, RNLA, PSBE, and GLM filter perform well compared to most of the shrinkage techniques. The GLM filter is effective in the noise suppression and the edge preservation as reflected by IQI (0.7), β (0.9), FoM (0.9), SMPI (2.5) and SSI (0.99). The PSBE and MPT filters results in effective noise suppression and edge preservation, similar to the GLM filter. It is also observed that the SMPI values for PSBE, GLM, RNLA, and MBR filters are superior in comparison to ProbShrink filter. The PSBE, GLM and BShrink result in β to be approximately equal to one. The other techniques such as MPT and RNLA filters are also on par with others with β ≤ 0.8.The issue of concern with the NSS, OWT, MBR and ProbShrink filters is β≤0.5.

The performance of the DsFlsmv, DsFWiener, DsFmedian and DsFsrad filter performance are similar in terms of IQI, FoM, SMPI and SSI as observed in Table 3.18. The SMPI of the DsFgf4d is double that of the DsFWiener, DsFmedian and DsFsrad filter, which reflects its inferiority in terms of speckle suppression. The SSI of all the DsFs (except DsFhomog) is less than one and the DsFls filter has the lowest values. The DsFls and DsFhomog had FoM which is less than 0.7 whereas all other despeckling filters has FoM which is greater than 0.8. The edges are not preserved using the DsFlsminsc and DsFhomo filter whereas the DsFlsmv, DsFWiener and DsFwaveltc filters preserved the edges as reflected in by β ≥ 0.9. The DsFmedian, DsFhomog, and DsFad filters have β ≥ 0.6.

Table 3.18 Comparison of speckle suppression by despeckling and SAR filters

Methods	**β**	**SMPI**	**SSI**	**Methods**	**β**	**SMPI**	**SSI**
DsFlsmv	**0.9301**	**2.364**	0.9810	FIF	**0.9511**	2.587	0.9994
DsFWiener	**0.9744**	**2.292**	0.9884	FBF	**0.9747**	2.575	0.9934
DsFmedian	0.7116	**2.922**	0.9899	HFIF	0.8045	3.733	0.9756
DsFlsminsi	0.1045	2.960	0.9781	HFBF	**0.9205**	3.381	**0.9645**
DsFls	0.4583	4.364	**0.8695**	CED	0.8964	**2.516**	0.9803
DsFhomog	0.6839	5.849	1.0749	LEE	**0.9906**	6.201	1.1604
DsFhomo	0.1698	3.597	0.9886	FROST	0.6164	6.019	1.1044
DsFgf4d	0.5519	7.308	0.9645	KAUN	**0.9829**	6.399	1.1704
DsFwaveltc	**1.0000**	2.588	1.0000	DPAD	**0.9837**	**2.325**	0.9966
DsFsrad	**0.9848**	**2.663**	0.9955	FBL	**0.9714**	**2.292**	0.9927
DsFlecasort	0.5258	4.002	0.9941	PPB	**0.9409**	2.931	**0.9701**
DsFca	0.5899	3.154	0.9261	NLM	0.8891	**2.367**	0.9853
DsFad	0.8111	3.358	0.9608	Med	0.0460	3.378	0.9884

Table 3.19 Comparison of speckle suppression for TV and Fuzzy filters

Method	β	SMPI	SSI	Method	β	SMPI	SSI
CGM	**0.9218**	2.113	0.9614	TMED	0.0666	3.790	1.0001
GPBB	0.8516	2.126	0.9643	ATMED	0.4438	2.881	0.9865
GPCL	**0.9077**	2.136	0.9658	TMAV	0.1681	3.767	0.9999
GPLS	0.7110	2.129	0.9652	HTMED	0.0074	4.015	0.9974
GPABB	0.8999	2.129	0.9647	HATMED	0.4467	3.082	0.9834
PDHG	**0.9123**	2.132	0.9657	HTMAV	0.2127	3.905	0.9978
SQPBBNM	**0.9219**	2.128	0.9646	GWF	**0.9634**	2.831	0.9804
AFTV	0.6672	**2.044**	0.9583	GWF1	0.1349	2.804	**0.9675**
TV	0.4390	3.085	**0.9462**	GWF2	0.4145	**2.234**	**0.9682**
ATV	**0.9433**	2.162	0.9766	GWF3	0.1249	2.755	**0.9655**

Fourier filters

The performance of the HFIF and the HFBF are superior in comparison to the FIF and FBF filters in terms of SSI as shown in Table 3.18. These results in terms of SMPI values which are superior by a factor of two compared to the SAR filters. The high value FoM suggests better denoising performance. The issue of concern using Fourier a based technique is smaller IQI. Observations revealed that the IQI is less than 0.4 using the FIF and FBF filters.

SAR filters

The SAR filters such as Frost et al., Lee, and Kaun *et al.*, over-smooth the texture in the TTE images. The values of SSI are greater than one using these filters as shown in Table 3.18 indicating poor noise suppression. The performance of SAR filters is poor in terms of SMPI; the values are almost double of the FBL, DPAD, FIF and FBF filters. The FoM is less than 0.8 using these filters. The SAR filters such as Kaun *et al.* and Lee had $\beta \geq 0.95$. IQI is greater than 0.8 using Lee, Kaun et al., and Frost et al., filters.

Fuzzy filters

The fuzzy filters perform well in terms of IQI, FoM and SSI but with higher SMPI (≤4) and small β. The fuzzy filters such as the TMED, ATMED, TMAV, GWF1, and GWF2 based denoising result in $\beta \leq 0.4$. The GW filter results in least SSI value among all the fuzzy based filters. The values of SMPI and SSI for fuzzy filters are tabulated in Table 3.19. The hybrid fuzzy filters have smaller SMPI compared to fuzzy filters. All fuzzy and hybrid fuzzy filters have FoM are greater than 0.8. The modified geometric filter preserves the edges as exhibited by the $\beta \geq 0.9$. All fuzzy based filters result in IQI≥ 0.75.

Total variation based denoising

The performance of gradient based TV denoising is moderate in terms of IQI and SMPI. The analysis based on β, FoM and SSI show the better side of these filters. The AFTV and ATV filters result in poor IQI (≤0.3), moderate β, FoM, and SMPI. These filters had SSI<1. The

values of SMPI were similar for all gradient TV, AFTV and ATV filters as shown in Table 3.19. Gradient TV methods have SMPI which is less than the SMPI of all fuzzy, DsF, and ProbShrink filter. All the variational filters have FoM are greater than 0.8 except the AFTV filter. The filters such as CGM, GPBB, GPCL, GPABB, GPPBsafe, PDHG, SQPBB, and ATV result in $\beta \geq 0.9$. Filters such as GPLS, AFTV, and TV have $\beta \leq 0.5$. The CGM, AFTV and ATV have IQI less than 0.3 whereas all other TV based techniques have values in the range 0.7 to 0.85.

Diffusion and Nonlocal means filters

The output images on application of PPB and NLM filters result in the SSI ≤1. The DPAD, FBL, NLM and PPB filters have SMPI far less compared to SAR filters proving their superior speckle suppression capabilities. The FoM using the DPAD, and PPB filters is almost equal to one and far superior compared to the SAR and OBNLM filters. The edges are well preserved using the FBL, PPB, NLM and DPAD filters with beta metric approximately equal to one. The IQI is comparatively less using the PPB (0.4), NLM (0.6), and DPAD (0.6) filters whereas FBL (0.7) is fractionally higher.

3.5 Summary

The performances forty eight filters, grouped into eight types, were analysed for despeckling of the TTE images. The thrust areas of analysis were noise suppression, edge and structure preservation, visual quality assessment and clinical grading. The performances of each filter is analysed within its own type of despeckling and also with other types of filters. The eight types of filters analysed were fuzzy filters, Fourier filters, logarithmic multiscale techniques, local statistics filters, nonlocal mean filters, variational filters, nonlinear techniques and iterative techniques. The image quality metrics consisted of traditional parameters, along with parameters which were useful in measuring edge preservation, and speckle noise suppression. Initially, the performance is analysed using traditional and edge preservation parameters along with the visual quality assessment and clinical grading. In the last part of the chapter 3 the analysis is based on the blind parameters such as SSI, SMPI and β for estimating the speckle noise suppression and edge preservation.

The performance of NSS filter in the logarithmic domain stood along with GLM filter in terms of superior noise suppression and edge preservation using the multiscale techniques. The performance of DsFlsmv, FBL and DsFWiener filters were better in the local statistics based filters both in terms noise suppression and structure preservation. The hybrid fuzzy filters performed better in comparison to the fuzzy filters in the logarithmic domain. The performance of BPFA filter stood out among the NLM, sparse and hybrid filters in terms of SSIM, RMSE, PSNR, MSE and SNR showing superior noise suppression qualities. But, observing the values of IQI, β, and FoM shows poor edge preservation in BPFA filter in

comparison to NLM, PPB and PLOW filters. The performance of FBL filter stands out in comparison to the AFTV and ATV filters in terms of IQM. The nonlinear filters such as the DsFsrad and DsFgf4d filter preserve the texture whereas DsFmedian, and DsFad filters result in the loss of textural information.

The clinical grading with experienced clinicians revealed that despeckling methods such as the DsFlsmv, GLM, PSBE, PPB, DsFgf4d, DsFhomog, BPFA, PLOW and NLM filters were acceptable whereas the DsFca, fuzzy TMED, and RNLA filtered images are unacceptable in the clinical practice.

This chapter describes the applications of despeckling filters for the CWD, M-Mode, and color Doppler echocardiographic images. The performance of the despeckling are analysed in terms of texture features, image quality metrics and visual quality assessment. The analysis attempts to bring out the characteristics of despeckling filters for images acquired in multiple views and imaging modalities through the texture features also. The texture features of the original images are compared with those obtained from the despeckled images.

4.1 Introduction

The Doppler ultrasound (US) modalities such as the continuous wave Doppler (CWD), pulse wave Doppler (PWD), and color Doppler along with B-mode echocardiographic images are employed for assessment of valvular abnormalities. Each modality has its own importance in the diagnosis of different types of abnormalities of the heart. The importance of each modality is brought out in the introductory chapter. These modalities are employed in integrated fashion in the clinical practice. The information acquired using each of the modalities is visually and intelligently combined by clinicians for making correct diagnosis. One of the important applications of the CWD echocardiographic imaging is measuring high blood flow velocities across regurgitant and stenotic valves orifices [59, 198, 282-284]. This modality is commonly used in estimation of pressure half time (PHT) and deceleration slope by manual tracing of the CWD spectrum. During the acquisition of data for measurement of the PHT it is necessary to align the Doppler sound beam as parallel as possible to the flow direction. This parallel orientation can be achieved by taking into account the qualities of 2D images and Doppler recording [10, 282, 283]. Further, as per the American Society of Echocardiography (ASE) recommendations, good quality and well defined envelopes of CWD should be employed for estimating the velocities and pressure gradients across the regurgitant and stenotic valve orifices [10].

The manual delineation of the spectrum and the presence of artifacts are the two major problems of concern in CWD spectra analysis. The manual tracing of the CWD spectrum depends on the experience of the delineator, the visual quality of the spectrum, and the acoustic viewing window employed for acquiring image [189, 191-195, 282]. Manual tracing is a time consuming task combined with inter/intra-personal variations. Most of the clinical decisions depend on the parameters derived from the manually traced spectrum [40, 189, 190-199, 201, 282]. The artifacts such as the speckle noise are also observed in the CWD images [40, 187, 190, 197, 200, 201] which need to be pre-processed as steps taken up for the B-Mode TTE images. The presence of speckle noise may lead to large variations in Doppler measurements such as the Doppler power. The peak velocity can be estimated from the Doppler spectrum using various heuristic thresholding techniques, but they are strongly influenced and prone to noise. Hence, the estimated peak power can be inaccurate [187].

Therefore, it would be desirable to suppress noise present in the CWD images with edges and the structures well preserved in the denoised image.

The problems due to the presence of noise, low contrast, and other artifacts in CWD images are identical to the issues prevailing in the B-mode TTE images [190]. The granular structures found in the CWD spectrum of gray scale are similar to those seen in B-Mode TTE images [31]. The median filter and the Gaussian low pass filter are more commonly used for reduction of noise in the CWD images [40, 189, 192, 193, 201]. Gong *et al.* [189] employed a median filter for reduction of the background noise in the CWD images. Thresholding was applied on the pre-processed image instead of direct application on the original CWD images. A Gaussian-shaped low pass filter (LPF) was employed for suppression of noise by Tschirren *et al.* [40]. Shechner *et al.* [192] used the combination of Sobel operator with a Laplacian edge detector along with the LPF, edge linking and curve fitting for automatic tracing of the mitral valve (MV) spectrograms. The essence of noise reduction and edge detection in automatic image analysis in the Doppler velocity spectrum was highlighted by Greenspan *et al.* [193] for the MV. The images were pre-processed using Gaussian kernel for noise reduction, and enhanced by application of contrast stretching [193].

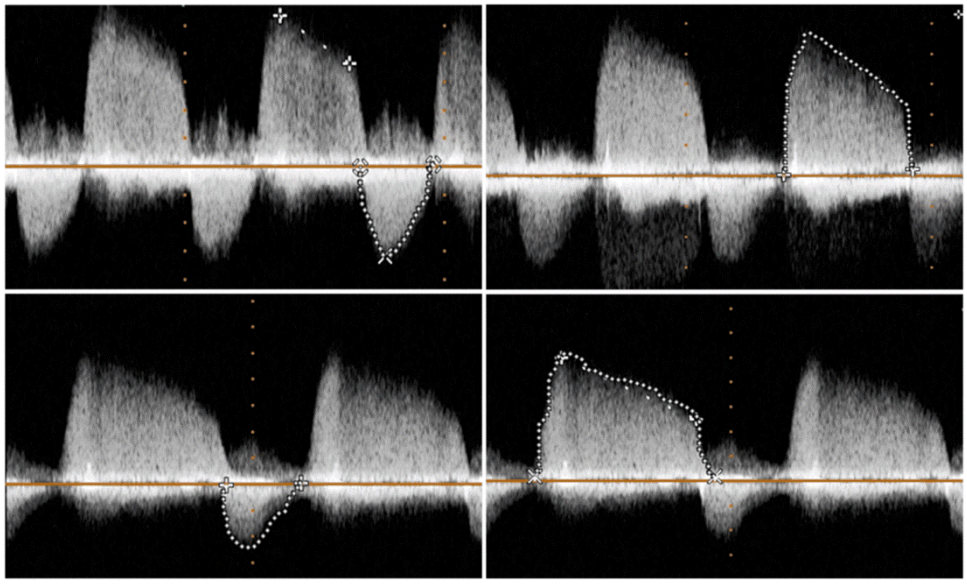

Figure 4.1 Manual tracing of the CWD images

A semi-automatic method of delineation for the PWD images of patients suffering rheumatoid arthritis was proposed by Magagnin *et al.* [195]. The outliers in the thresholded images were removed using a median filter [195]. Wang *et al.* [197] employed a Kalman filter for reduction of speckle noise in the PWD images. An adaptive pulse coupled neural network (PCNN) with adaptive thresholding was advocated by Li *et al.* [200] for removing the speckle noise from the Doppler blood flow spectrograms. They had concluded that removal of noise was essential and preliminary step in the spectrogram automation [200]. A combination of

two median filters was used for noise reduction from the spectrum image by Kalinic *et al.* [201].

Vilkomerson *et al.* [187] had observed that the peak velocity estimated using methods based on thresholding were strongly prone to the noise. Baba *et al.* [283] spoke regarding two noise sources in the cardiac Doppler US system: one, due to interaction of the signal generated across a strong cardiac wall with low velocity and second, flow signal and strong high velocity signal across the valve. The effect of second case was very high compared to the first [283]. The presence of speckle noise in the background and the aliasing effects were addressed by Zolgharni *et al.* [282] by incorporating an adaptive thresholding based on histogram analysis. Initially, the noise in the Doppler images was filtered using a first order Butterworth filter. It was said that even on performing all the said steps, some noisy spike prevailed in the extracted profiles.

Finn *et al.* [22] had compared applications of 15 denoising techniques for the B-mode echocardiographic images. The techniques considered included four types of filters such as six techniques based on anisotropic diffusion, three wavelet and five on synthetic aperture radar (SAR) techniques [22]. Zhang, Wang and Cheng [135] had compared the performances of nonlocal mean (NLM), wavelet and diffusion based techniques on the US images of breast [135]. Loizou *et al.* [131] had advocated a despeckling filter (DsF) software toolbox using MATLAB for despeckling of the US images of common carotid artery [131]. Elamvazuthi, Muhd Zain and Begam [134] had studied the applications of filters based on wavelets, median, Wiener, average, anisotropic diffusion, and combination of Daubechies–Wiener on the US images of bone. Wong *et al.* [228] compared performance of methods such as anisotropic diffusion, wavelet-domain, adaptive median, linear least square estimation, maximum a posteriori (MAP) estimation with posterior Bayesian estimation for reduction of speckle in optical coherence tomographic (OCT) images [228]. Mateo *et al.* [26] and Fernández-Caballero [12] had studied denoising applications of median filter, adaptive weighted median filter, Fourier and wavelet transform based filters and homomorphic filters for reduction of noise for the US images of kidney.

The exhaustive literature review reveals that filters based on techniques such as diffusion [22, 35, 83, 86], total variation [120, 135, 251, 252], nonlocal means [125, 127], local statistics [27, 130, 131], wavelet [94, 242, 95, 99-103, 116, 118, 135, 227, 239], bilateral [135, 256], and fuzzy [229, 250] concepts were not thoroughly being investigated and studied on the CWD images. The reason could be that impact of speckle noise is high on the B-Mode images in clinical analysis compared to its adverse impact on the CWD images. The literature review reveals that no exhaustive analysis of despeckling technique is reported for the CWD images in terms of image quality metrics (IQM) and visual analysis. This thesis

presents an exhaustive analysis of despeckling characteristics of eight type's filters for the CWD images in terms of visual quality and IQM and clinical validation.

The despeckling techniques are compared for the B-Mode images in Chapter 3 and these filters also employed for speckle noise reduction in CWD images in this chapter. An overview of despeckling filters is tabulated in Table 3.1. The concepts, merits and demerits of various filters are tabulated in Table 3.3. Each CWD image is observed after pre-processing to verify if the finer details necessary for diagnosis are retained or taken off.

4.2 Feature extraction

The texture present in an image is considered to be an affluent source of visual information perceived by humans in appreciating the visual outlook of that image [284-286]. The textures are often complex visual patterns made up of different entities, or sub-patterns characterized in terms of brightness, color, slope, size, and others. Thus the texture can be considered as a similarity grouping in an image [284]. The sub-pattern present in the local region may bring out the perceived uniformity, lightness, roughness, density, linearity, regularity, directionality, frequency, coarseness, phase, fineness, randomness, granulation, and smoothness, of the texture altogether [285]. The texture present in the image provides information on the spatial arrangement of intensities. The spatial arrangements and interrelationships of image pixels visually seen are reflected as intensity variations in the intensity patterns or gray tones. The ability of human in recognition of texture is commendable compared to the ability of digital computers. The texture of an image would be a vital characteristic in analysis of the image. The texture characteristic plays important role in analysis of images acquired in remote sensing and medical imaging.

There are numerous approaches for feature extraction from an image. The feature and feature extraction techniques would be important in the successful classification, and segmentation of images. Various methods have been advocated for extraction of texture descriptor. Some of texture extraction techniques employed in this thesis are first order statistics, gray level difference matrix (GLDM), gray level difference statistics (GLDS), statistical feature matrix, Laws textures energy measure (Laws TEM) and fractal dimension texture analysis. The texture features employed by Liozou *et al.* [27, 130, 131] for analysis of despeckling filters are employed for analysis filter performance for the TTE images in this thesis. The performance analysis of despeckling filters for the US images of carotid artery was presented in terms of texture features by [27, 130, 131]. Sixty one texture features and ten image quality metrics were computed to bring out the performance of ten despeckling filters by Liozou *et al.* [27, 130, 131] whereas in this thesis performance analysis is extended to 48 filters. In this thesis this particular exercise is carried out for the B-Mode, M-Mode, CWD, and PWD based echocardiographic images. The B-Mode images are acquired in multiple views such as A4C, A2C, A5C, PLAX and PSAX.

The first order statistics features computed for specifying the performance of despeckling filters are mean, median, standard deviation, skewness and kurtosis. The spatial gray level dependence matrices (SGLDM) were advocated by Haralick *et al.* [286]. These features were based on the computation of second order conditional probability density functions. Based on the probability density functions the following features are estimated: the angular second moment, correlation, entropy, difference entropy, inverse difference moment, contrast, variance, sum average, sum entropy, difference variance, sum variance and information measures of correlation. For any assumed distance *d* (the value of d is set to one using a 3×3 matrices) at angles θ=($0^0, 45^0, 90^0 \; and \; 135^0$) four values were estimated for all texture measures.

The gray level difference statistics (GDLS) technique use the first order statistics based on the absolute difference between pair of gray levels using the local property, with an objective to determine the texture measures such as entropy, angular second moment, contrast and mean. The GDLS based texture features are estimated for the displacement δ = (0, 1) (1, 1), (1, 0), (1, -1), with $\delta \equiv (\Delta x, \Delta y)$, and their mean values are taken into consideration. The visual properties of the texture in the image were employed in the extraction of the neighborhood gray tone difference matrix (NGTDM) based features. NGTDM based features consists of the following features: contrast, complexity, coarseness, strength and busyness. The statistical properties, at several distances for a pair of pixel pair for an image were taken into account while estimating features based on statistical feature matrix (SFM). The SFM class of features consisted of contrast, roughness, periodicity, and coarseness. The values of constants which estimate the inter-sample distance are set as L_r = L_c = 4.

The Laws texture energy measures (Laws TEM) employed convolution between the image and its statistics with defined masks for extraction of texture features from the image. The Laws TEM were used to describe the texture information present in the image. The extraction vectors with length *l*=4, L = (1, 6, 15, 20, 15, 6, 1), E = (-1, -4, -5, 0, 5, 4, 1) and S = (-1, -2, 1, 4, 1, -2, -1) were employed, where local averaging was performed which will behave as an edge detector and spot detector. The texture features extracted using various kernels are as follows: LL stands for texture energy from LL kernel, EE—texture energy from EE kernel, SS—texture energy from SS kernel, LE—average texture energy from LE and EL kernels, ES—average texture energy from ES and SE kernels and LS—average texture energy from LS and SL kernels. The fractional Brownian motion model is employed in the extraction of fractal dimension texture analysis.

4.3 Results:

The results tabulated in Table 4.1 reflect the moderate edge preservation and high structural similarity on application of wavelet shrinkage techniques. The applications of shrinkage techniques for the echocardiographic images result in spurious thresholds, which are tackled by embedding a Wiener filter sequentially. The size of the mask in the Wiener filter is set to be 3×3. The performances of Fourier filters for noisy Barbara image are shown in Figure 4.2. The performances of the Fourier filters namely Fourier Ideal filter, Fourier Butterworth filter (FBF), homomorphic FIF and homomorphic FBF, are superior at cut-off frequency equal to 500. The values of β and IQI are quite small at cut-off frequency equal to 100, but the values improved at cut-off frequency equal to 500. The values of these parameters are less than 0.7 which show that the edges are partially preserved.

Table 4.1 Performance of wavelet filtering techniques

Methods		IQI	SSIM	NCC	β	FoM	PSNR	SNR	MSE	LMSE	ERR3	RMSE
Wavelet thresholding	OWT	0.6515	0.8812	0.9997	0.6786	0.7488	25.95	40.12	165.3	1.17	15.03	12.86
	SURELET	0.6511	0.8829	0.9995	0.6759	0.7087	25.93	40.10	165.8	1.18	15.05	12.88
	BayesShrink	0.7140	0.9120	0.9868	0.7413	0.9074	28.38	44.99	94.3	0.47	12.33	9.72
	BlockShrink	0.7851	0.9502	0.9916	0.8930	0.9261	31.22	50.67	49.6	0.29	8.85	7.00
Wavelet [24, 26]	HL	0.5840	0.8823	0.9925	0.4130	0.7388	24.15	36.53	250.4	1.53	19.87	15.81
	LH	0.6531	0.8815	0.9979	0.6559	0.7259	26.19	40.60	156.4	1.15	15.09	12.51
	HH	0.6552	0.8814	0.9978	0.6470	0.7182	26.22	40.66	155.3	0.93	15.15	12.46
	LH-HH	0.6631	0.8831	0.9963	0.6250	0.8127	26.54	41.31	144.2	0.87	14.82	12.01
Homomorphic wavelet	HL	0.5830	0.8818	0.9942	0.4082	0.7440	24.05	36.33	255.8	1.57	20.30	15.99
	LH	0.6515	0.8810	0.9961	0.6533	0.7890	26.07	40.36	160.8	1.13	15.44	12.68
	HH	0.6544	0.8817	0.9971	0.6427	0.7020	26.12	40.47	158.8	0.96	15.42	12.60
	LH-HH	0.6616	0.8813	0.9988	0.6263	0.7670	26.51	41.25	145.1	0.87	14.85	12.05

The performances of the filters namely the probabilistic patch based (PPB) filter, NLM filter, anisotropic total variation (ATV) filter, fast bilateral (FBL) filter, posterior Bayesian estimation (PSBE), generalized likelihood method (GLM), NeighshrinkSURE (NSS), multiscale product thresholding (MPT) and M-Band ridgelet (MBR) filter, are shown in Figure 4.3. The details of each filter are discussed in Chapter 2 and Chapter 3. It is observed from Figure 4.3 that the edge preservation specified using β is greater than 0.9 for PPB, NLM and FBL filters, indicating good edge preservation using these filters. The images are over-smoothed using the MBR filter and the MPT filter as reflected by the values of β which is less than 0.2. The values of IQM such as FoM, SSIM, NCC, and β are greater than 0.85 on application of the PPB, NLM, and FBL filters indicating superior edge preservation, structural preservation and lesser distortion induced.

The performance of wavelet thresholding techniques such as the orthogonal wavelet thresholding (OWT), SURE with linear estimation of thresholds (SURELET), BayesShrink, BlockShrink, wavelet soft thresholding and homomorphic wavelet thresholding using various

sub-bands are tabulated in Table 4.1. The performance of BlockShrink based filter stands out compared to all techniques in Table 4.1.

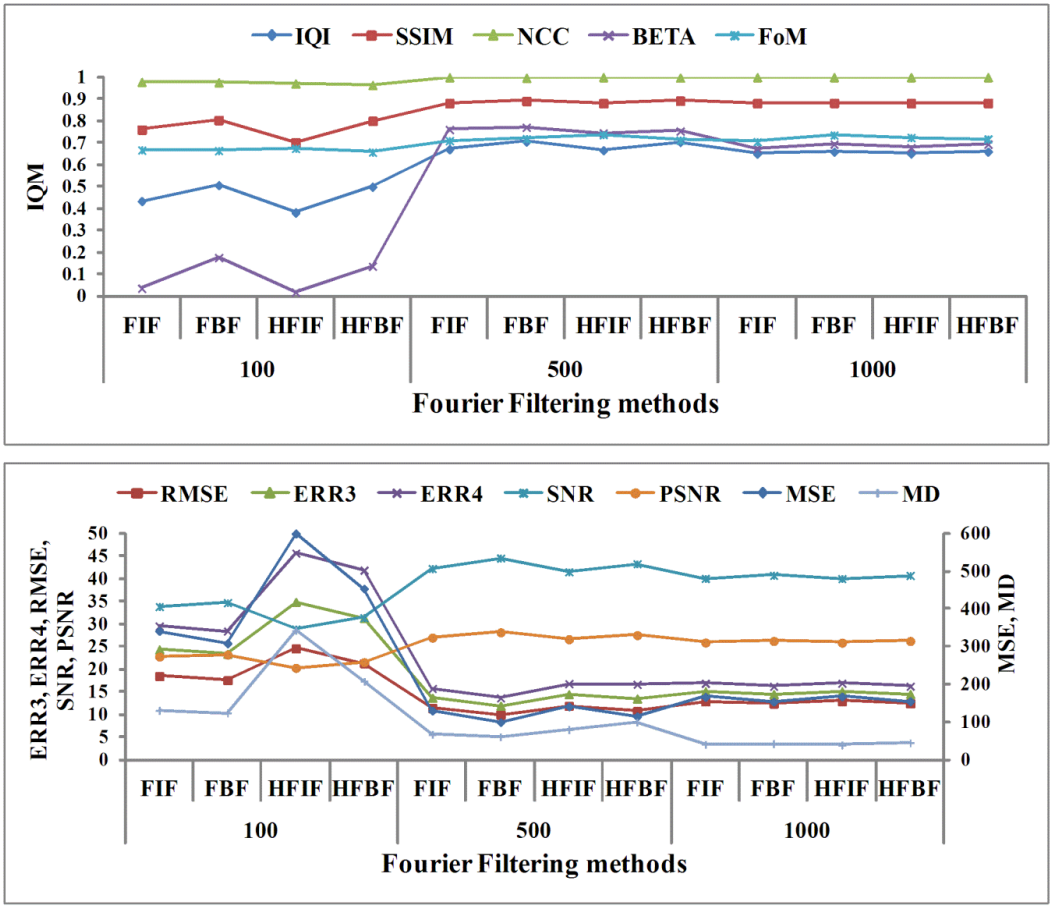

Figure 4.2 Performance of Fourier filters at various cut-off frequencies

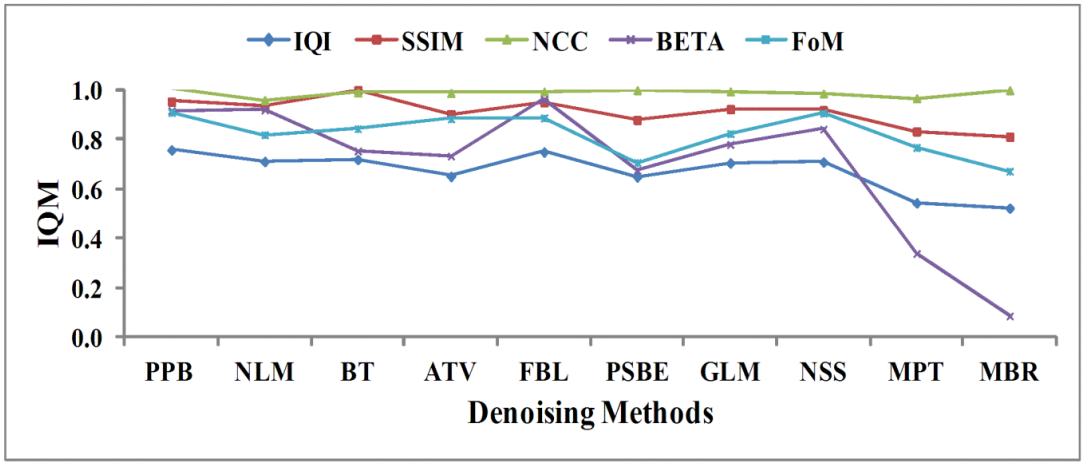

Figure 4.3 Performance of PPB, NLM, ATV, FBL, PSBE, GLM, NSS, MPT, MBR filters

Table 4.2 Performance of despeckling filters using masks of various sizes

Metrics	Mask size	DsF med	TMAV	ATMAV	DsF lsmv	DsF Wiener	DsF ls	DsF homog	DsF gf4d
MSE	3×3	234.20	253.6	219.46	**94.51**	**86.21**	282.32	230.57	596.37
	5×5	334.96	351.2	320.06	117.55	116.98	409.66	307.51	598.12
	7×7	317.48	417.97	219.46	119.64	138.04	531.44	354.77	594.28
SNR(dB)	3×3	37.10	36.40	37.66	**44.98**	**45.78**	35.47	37.23	28.98
	5×5	33.99	33.57	34.38	43.08	43.12	32.24	34.73	28.95
	7×7	34.45	32.06	37.66	42.93	41.69	29.98	33.49	29.01
PSNR(dB)	3×3	24.44	24.09	24.72	**28.38**	**28.78**	23.62	24.50	20.38
	5×5	22.88	22.67	23.08	27.43	27.45	22.01	23.25	20.36
	7×7	23.11	21.92	24.72	27.35	26.73	20.88	22.63	20.39
RMSE	3×3	15.30	15.93	14.81	**9.72**	**9.29**	16.80	15.18	24.42
	5×5	18.30	18.74	17.89	10.84	10.82	20.24	17.54	24.46
	7×7	17.82	20.44	14.81	10.94	11.75	23.05	18.84	24.38
ERR3	3×3	21.46	22.15	20.75	**12.74**	**11.72**	22.80	20.63	31.99
	5×5	25.28	25.25	24.45	14.12	13.67	26.37	23.10	32.01
	7×7	24.05	26.89	20.75	14.05	14.67	29.23	24.27	31.93
ERR4	3×3	27.62	27.85	26.35	**15.54**	**13.91**	28.25	25.36	39.31
	5×5	31.44	30.99	30.20	16.98	16.10	32.07	27.80	39.34
	7×7	29.56	32.53	26.35	16.77	17.16	35.00	28.88	39.24
LMSE	3×3	1.06	1.03	0.98	0.40	0.39	0.94	0.94	1.11
	5×5	1.18	1.06	1.09	0.45	0.44	1.01	1.01	1.10
	7×7	1.01	1.01	0.98	0.43	0.47	0.99	0.98	1.10
NAE	3×3	0.0824	0.0820	0.0773	0.0565	0.0565	0.0882	0.0794	0.1462
	5×5	0.0941	0.0989	0.0928	0.0618	0.0641	0.1140	0.0950	0.1466
	7×7	0.0942	0.1120	0.0773	0.0635	0.0706	0.1368	0.1063	0.1460
IQI	3×3	0.5657	0.5929	0.5949	**0.7240**	**0.7037**	0.5779	0.5965	0.5447
	5×5	0.4614	0.4877	0.4893	0.6932	0.6378	0.4468	0.4996	0.5463
	7×7	0.4554	0.4171	0.5949	0.6837	0.5950	0.3530	0.4354	0.5460
SSIM	3×3	0.8343	0.8576	0.8595	**0.9133**	**0.9181**	0.8371	0.8515	0.7938
	5×5	0.7744	0.7868	0.7947	0.9046	0.8921	0.7465	0.7957	0.7931
	7×7	0.7737	0.7270	0.8595	0.8995	0.8654	0.6622	0.7507	0.7935
NCC	3×3	0.9821	0.9640	0.9734	**0.9903**	**0.9932**	0.9848	0.9812	1.1135
	5×5	0.9736	0.9504	0.9618	0.9872	0.9887	0.9788	0.9742	1.1138
	7×7	0.9700	0.9399	0.9734	0.9848	0.9857	0.9728	0.9683	1.1131
BETA	3×3	0.1734	0.0878	0.1890	**0.8132**	**0.7811**	0.2506	0.2976	0.4052
	5×5	0.1954	0.1233	0.2442	**0.7857**	**0.7533**	0.1579	0.0385	0.4074
	7×7	0.0631	0.0192	0.1890	0.7890	0.7403	0.1214	0.1434	0.4074
FoM	3×3	0.7693	**0.8870**	**0.8900**	**0.8889**	**0.8525**	0.7753	0.8053	0.7714
	5×5	0.7796	0.7778	0.8071	0.8227	0.7909	0.6212	0.6854	0.7781
	7×7	0.6893	0.6339	0.8900	0.7861	0.7520	0.6541	0.5939	0.7632

Initially, the performance of ten despeckling filters namely DsFWiener, DsFlsmv, DsFhmedian, DsFlsminsc, DsFhomog, DsFgf4d, DsFsrad, DsFad, DsFhomo, and DsFmedian are analysed for the CWD images. These ten filters were analysed by Loizou *et al.* [131] for the US images of carotid artery. The CWD images are embedded with speckle noise to show the impact of these despeckling filters. The speckle noise is artificially added to the images using the MATLAB inbuilt "*imnoise*" to highlight the importance of pre-processing the noisy images. It is to be noted that artificial noise added only during this study of ten filters in this section. The performances of these filters are also analysed without adding any noise to the CWD images. The region of interest (ROI) is selected and noise is added to this ROI. The noisy ROIs are despeckled using ten despeckling filters. The results obtained for these noisy images using ten despeckling filters are shown in Figure 4.4. The

visual of despeckled images are shown in Figure 4.5. The IQM are computed using the original and despeckled ROI.

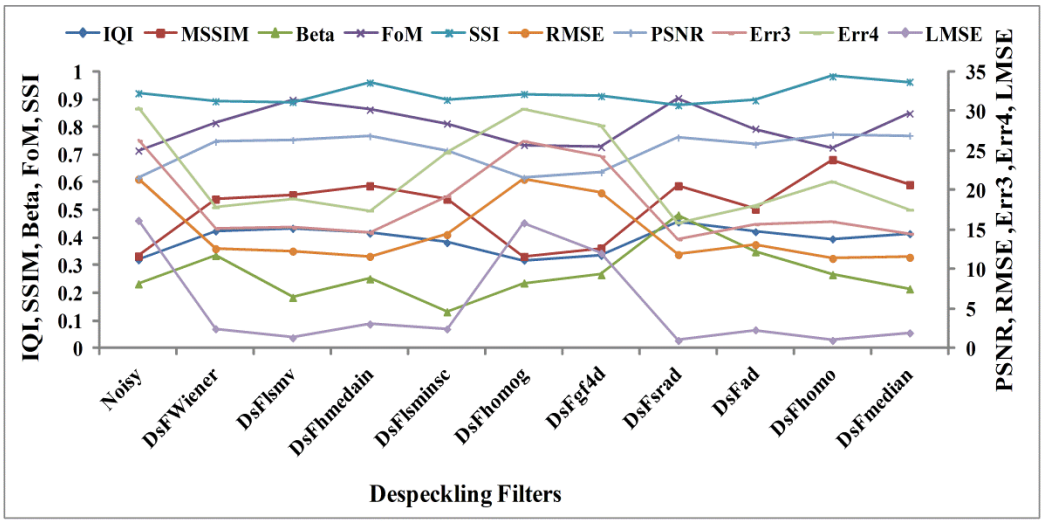

Figure 4.4 Comparison of IQM using ten despeckling filters

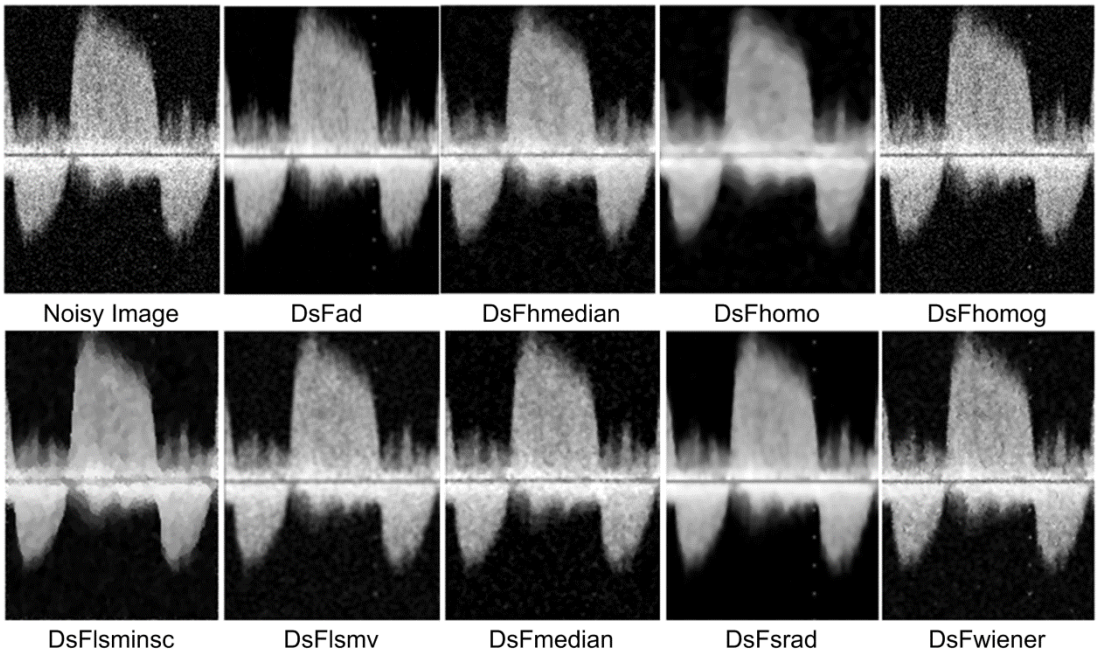

Figure 4.5 Visual qualities of CWD images on application of despeckling filters

The performance of the DsFsrad filter is superior compared to the DsFgf4d filter, DsFhomog filter, DsFlsminsc, DsFhmedian and DsFad filter in terms of IQM such as Err3, Err4, LMSE and NAE. The visual quality of despeckled images obtained using the DsFlsmv, DsFWiener, DsFad and DsFsrad are able to retain structure and edge details. The outer boundaries are blurred on application of the DsFhomo and DsFlsminsc filters. The performances of window based filters such as the DsFmed, TMAV, ATMAV, DsFlsmv,

DsFWiener, DsFhomog, and DsFgf4d filters are analyzed with the window size as 3×3, 5×5 and 7×7. The IQM of these filters are tabulated in Table 4.2. Analysis of results shown in Table 4.2 reveals that the performances of the DsFlsmv and DsFWiener filter stand out in comparison to all other techniques. The values of SNR, PSNR, IQI, SSIM, NCC, β and FoM are highest for these two filters which indicate better edge and structure preservation accompanied with noise reduction. The MSE of Wiener filter with 3×3 windows is less compared to all other filters in Table 4.2 also with highest SNR (dB).

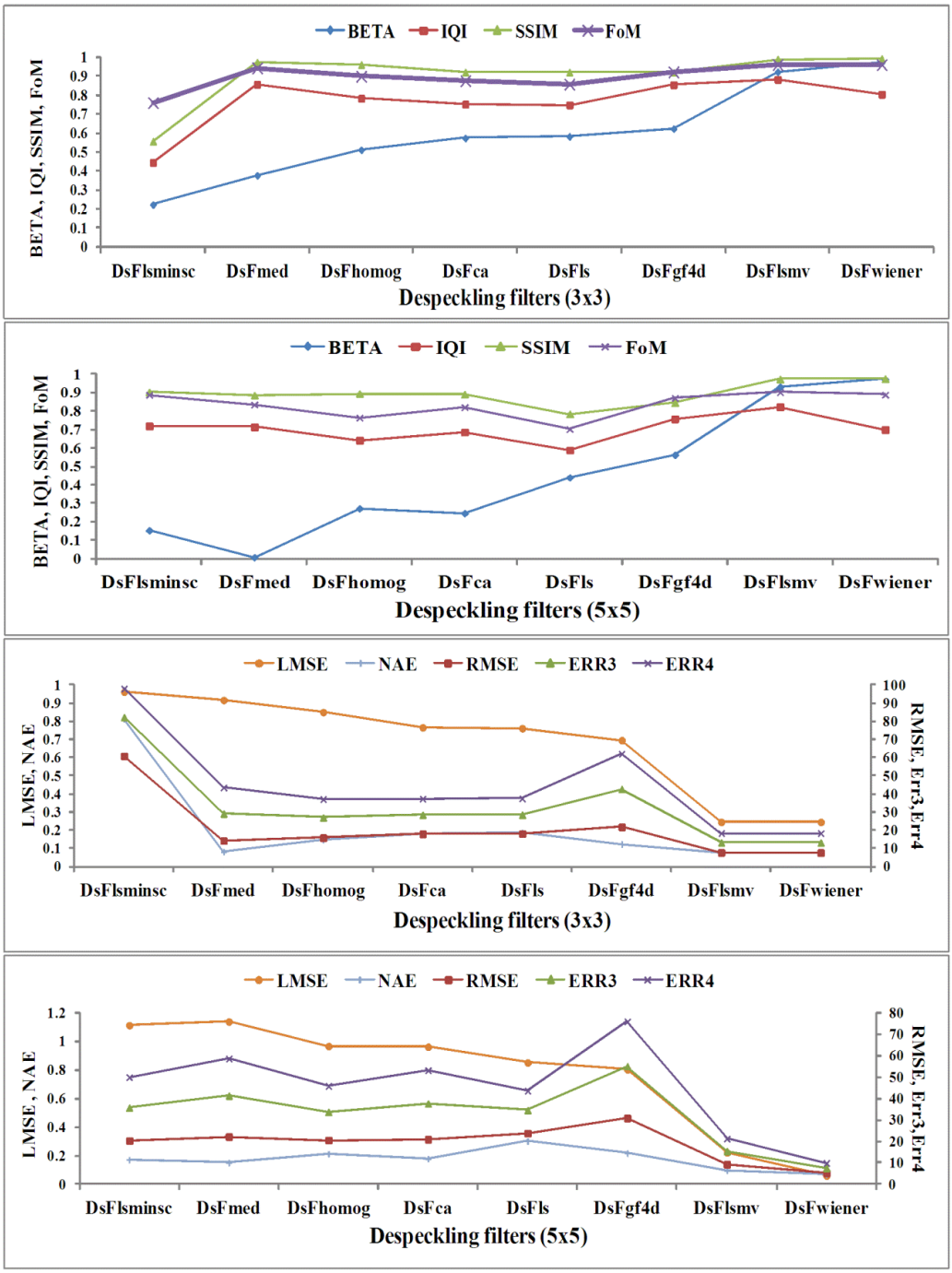

Figure 4.6 Comparison of IQM for despeckling filters with mask size of 3×3 and 5×5

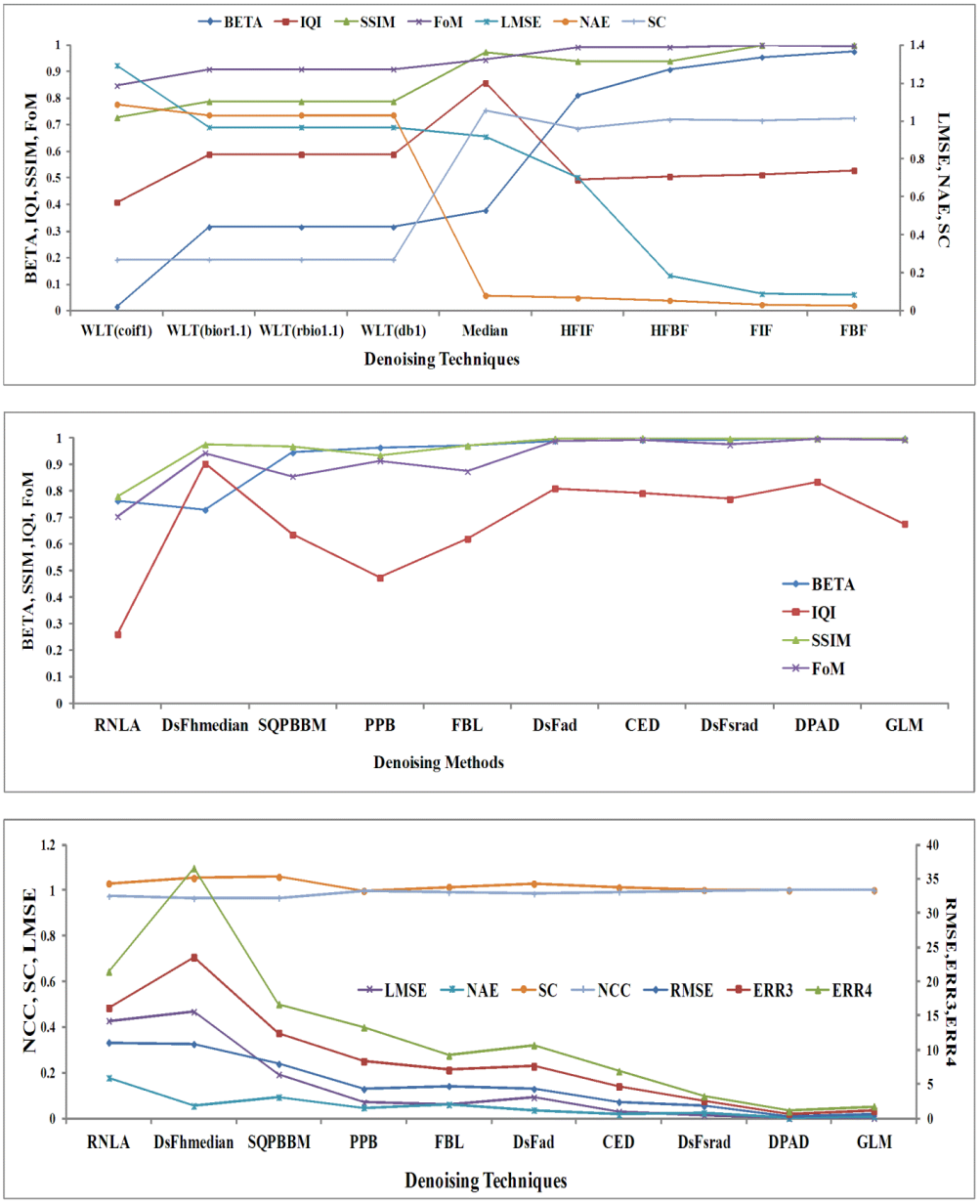

Figure 4.7 Comparison of IQM for wavelet-domain, Fourier, RNLA, DsFhmedian, SQPBBM, PPB, FBL, DsFad, CED, DsFsrad, DPAD, GLM

The FoM obtained using the fuzzy filters such as the TMAV and ATMAV filter along with the DsFlsmv filter are high (>0.89) and superior compared to all other filters. The values of β for most of the filters tabulated in Table 4.2 are quite small except for the DsFlsmv and DsFWiener filters. Also, the values of NCC are also higher for these two filters. The issue of concern using filters such as the TMAV, ATMAV, DsFmed filters and others is poor value of β whereas the other parameters are moderate, in the middle range. With the increase in the window size, the values of IQM such as SNR, PSNR, IQI, SSIM, and FoM decrease, whereas the values of parameters like MSE, LMSE, ERR3 and ERR4 show an increase. The

results obtained for the CWD images are shown in Figure 4.6 to Figure 4.13, and Table 4.3 to Table 4.5. The results tabulated in Table 4.3 to Table 4.5 are in terms of mean and standard deviation obtained using 200 CW Doppler images whereas the results shown in Figure 4.6 to Figure 4.13 are for one image using various types of filters. The performances of the DsFlsmv and DsFWiener filter are superior compared to filters such as the DsFgf4d, DsFhomog filters and others, as observed in Figure 4.6, for various window sizes. The drawbacks of the filters such as the DsFlsminsc, DsFmed, DsFhomog, DsFca and DsFgf4d filter are poor β and IQI. It is also observed that the values of IQI for the DsFlsmv filter is superior compared to the DsFWiener filter.

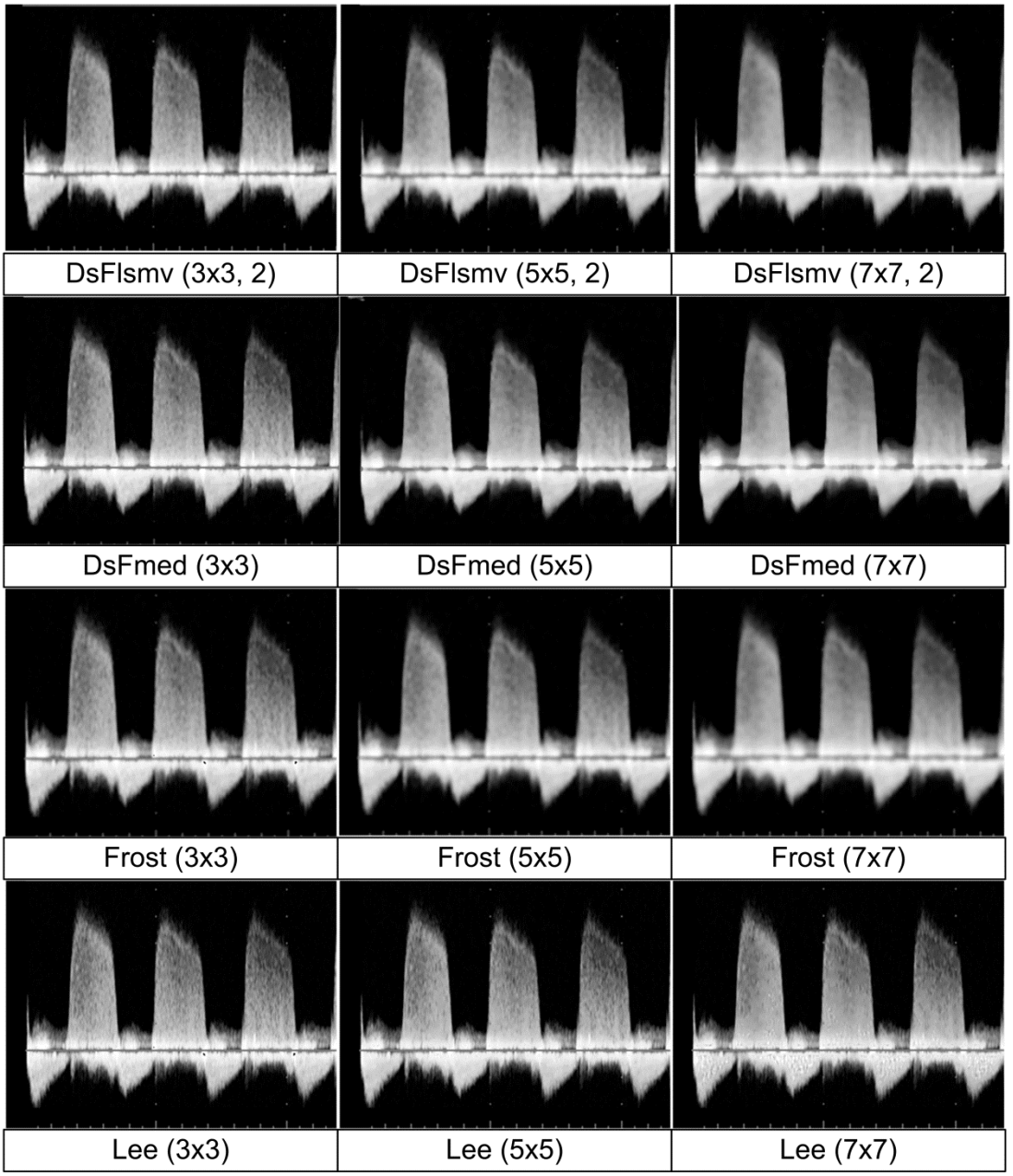

Figure 4.8 Visual qualities using filters such as DsFlsmv, DsFmed, DsFWiener, Frost *et al.,* and Lee filter with mask size 3×3, 5×5, 7×7

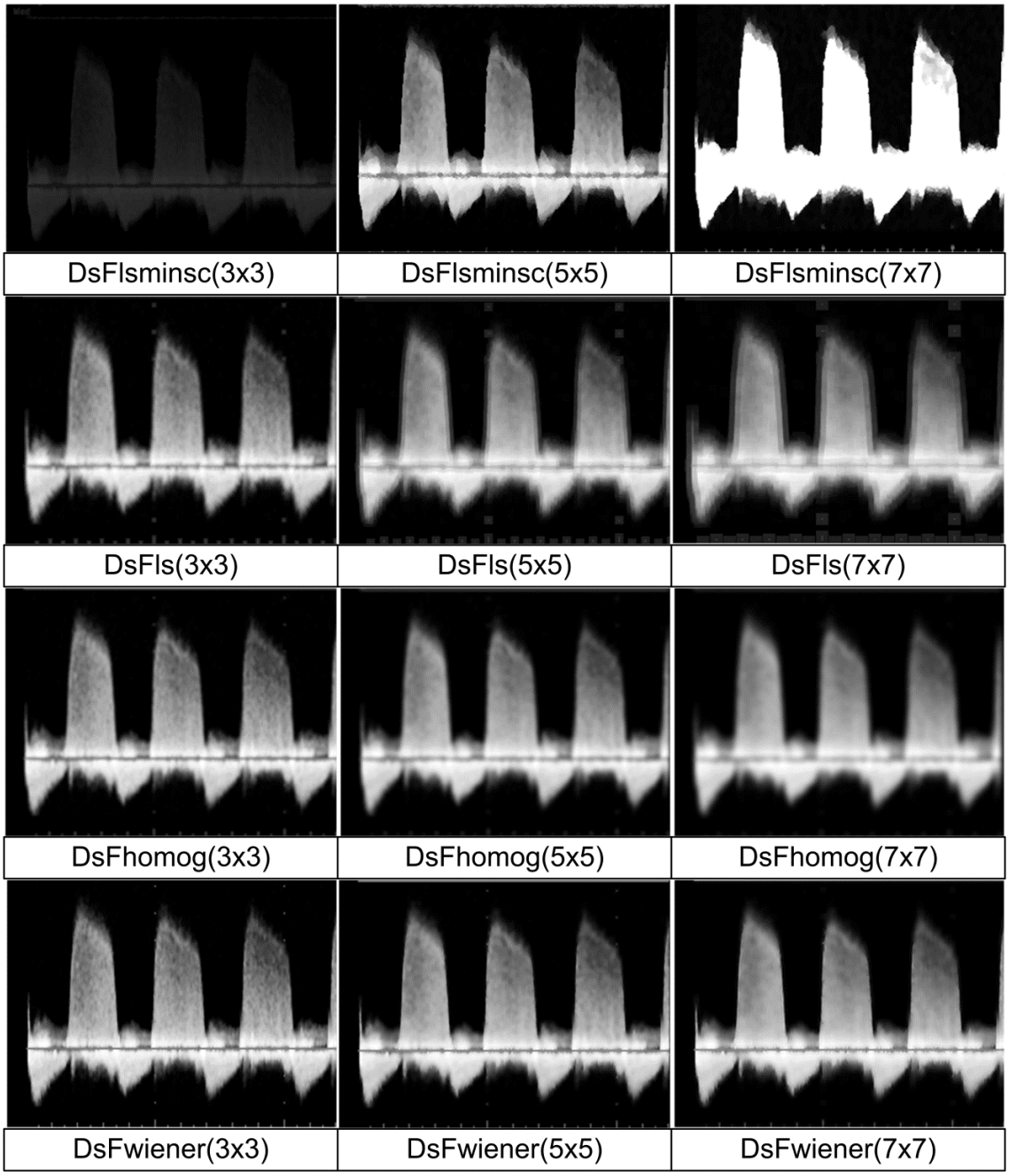

Figure 4.9 Visual qualities on application of Fourier, GLM, and RNLA based filters

The performance analysis of Doppler images is similar to the noisy standard test images as described in the earlier paragraphs. The values of the LMSE, RMSE, Err3 and Err4 are the least for the DsFlsmv and DsFWiener filters compared to other filter shown in Figure 4.6. The performances of the wavelet based filters, Fourier filters, Ripplet based filter, gradient projection filters, hybrid median, diffusion based filter, GLM and PPB filter are shown in Figure 4.7. The wavelet and Fourier filters resulted in FoM> 0.85, which shows lesser distortion induced in images during pre-processing. The error estimation like the LMSE and NAE are quite small for the Fourier filter in comparison to wavelet based noise reduction, but

the IQI is the same for both types of filters. The IQI for hybrid median filter is superior compared to RNLA, PPB, CED, DsFsrad, and other filters.

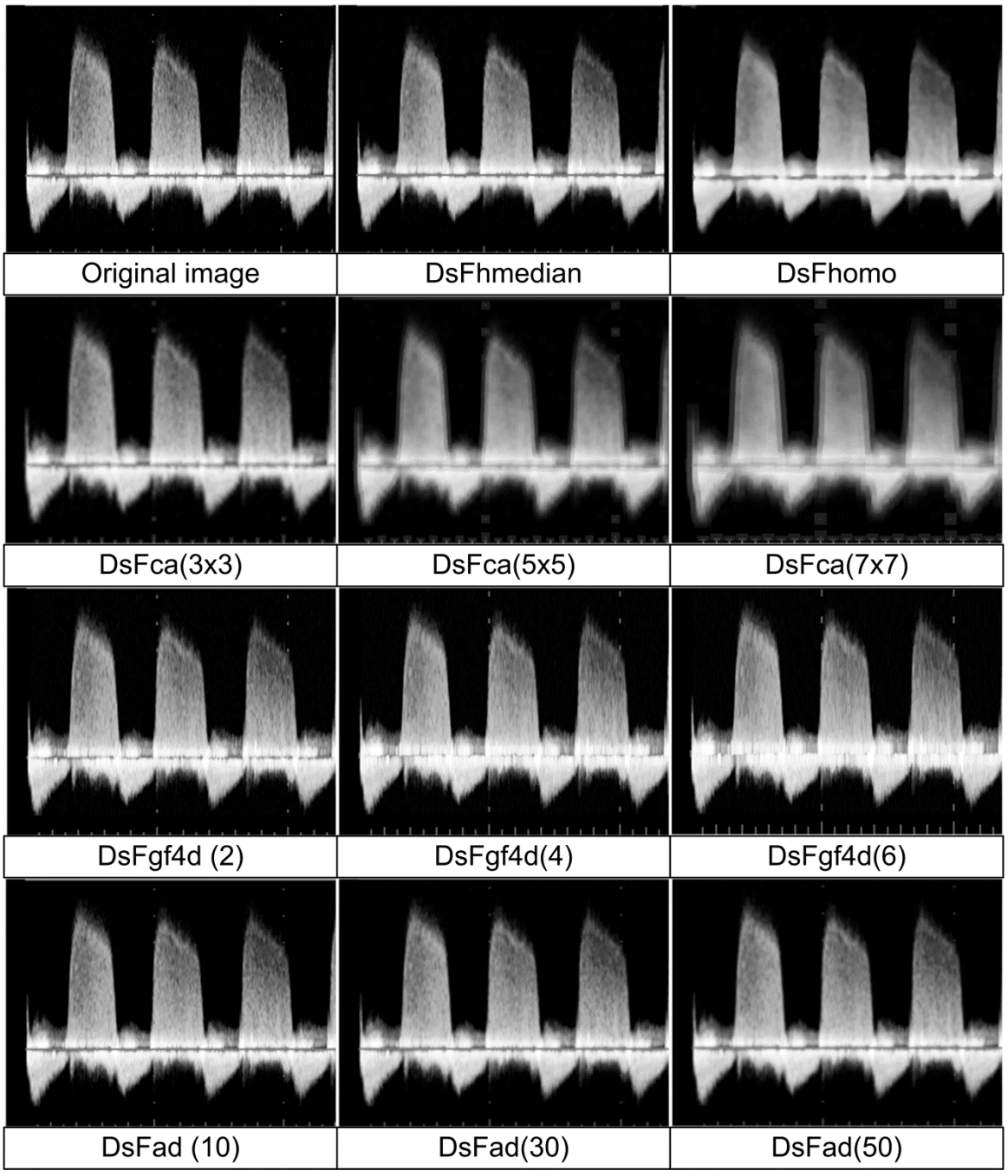

Figure 4.10 Comparison of visual quality of CWD image on application of filters such as DsFhmedian, DsFhomo, DsFca, DsFgf4d, and DsFad filters at various numbers of iterations

The performance of GLM filter is superior in terms of all parameters except IQI. The performances of the DsFsrad, DPAD and GLM filter are superior compared to filters such as the RNLA, DsFhmedian, SQPBBM, PPB, FBL and DsFad in terms of parameters like Err3, Err4, LMSE, and NAE. The visual quality of denoised images employing three different window sizes are compared in Figure 4.8 and Figure 4.9. The first, second, and third

columns show the denoised images obtained using window size of 3×3, 5×5 and 7×7, respectively. The despeckled images obtained using the Dsflsmv, DsFmed, Frost *et al.*, and Lee filter are shown in Figure 4.8. The results of filters such as DsFlsminsc, DsFls, DsFhomog, and DsFWiener filter are shown in Figure 4.9.

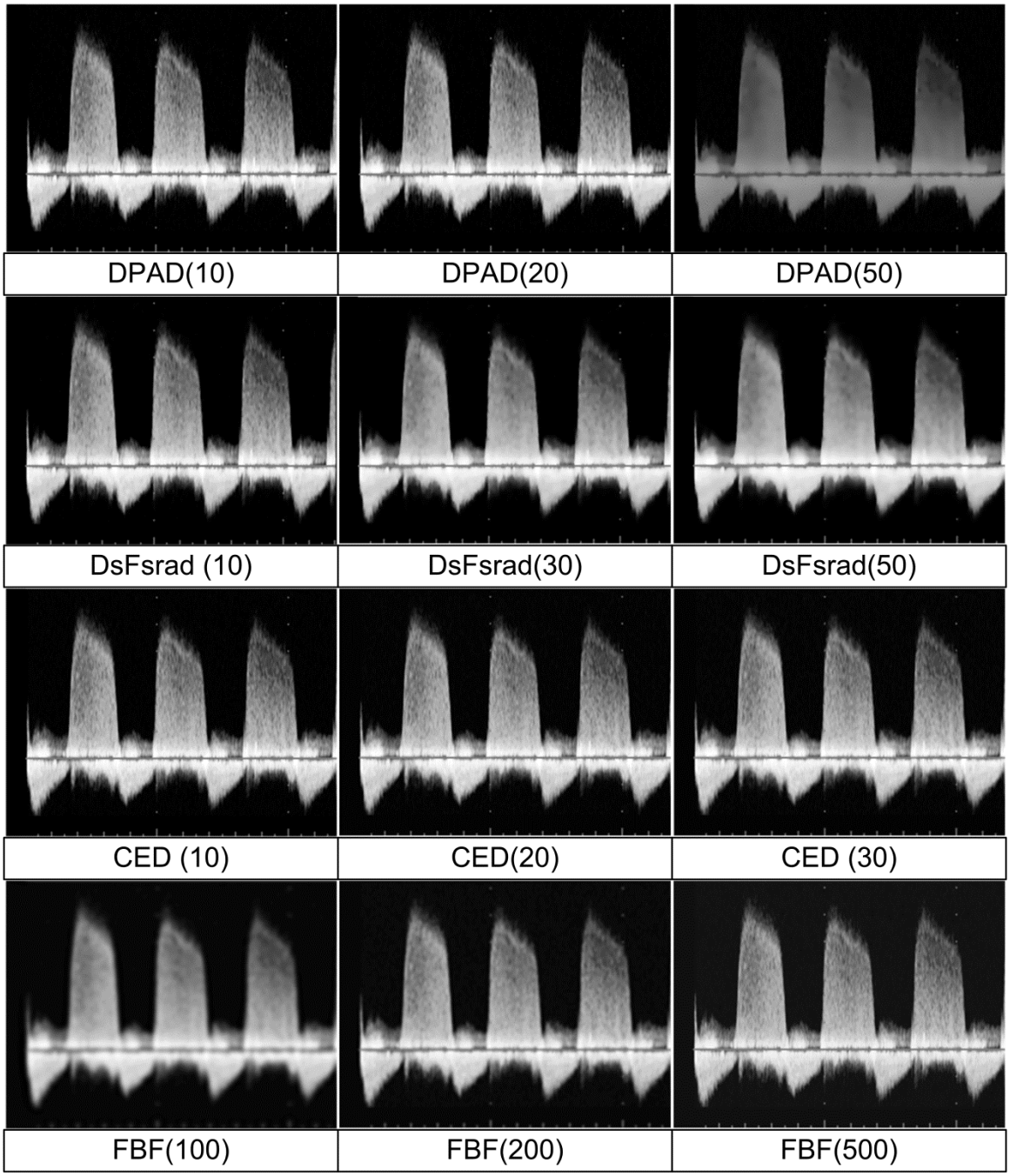

Figure 4.11 Visual qualities on application of DPAD, DsFsrad, CED and FBF filters

The first image in Figure 4.10 is the original image used in all the figures also. The visual outlook of results obtained using hybrid median filter and DsFhomo filter are shown in the first row of Figure 4.10. The results for DsFgf4d and Dsfad filter with different number of

iterations are shown in second and third row of Figure 4.10, respectively. The despeckled images obtained using DPAD filter, DsFsrad, CED and FBF are shown in Figure 4.11. The structure and finer details are mostly preserved using the DsFlsmv, DsFWiener, DsFmed, and DsFhmedian filters. The denoised images become smoother on increase of window size for most of the filters. The performance of filters such as the DsFlsminsc filter with window size 3×3 and 7×7 are not acceptable as all necessary details are completely lost.

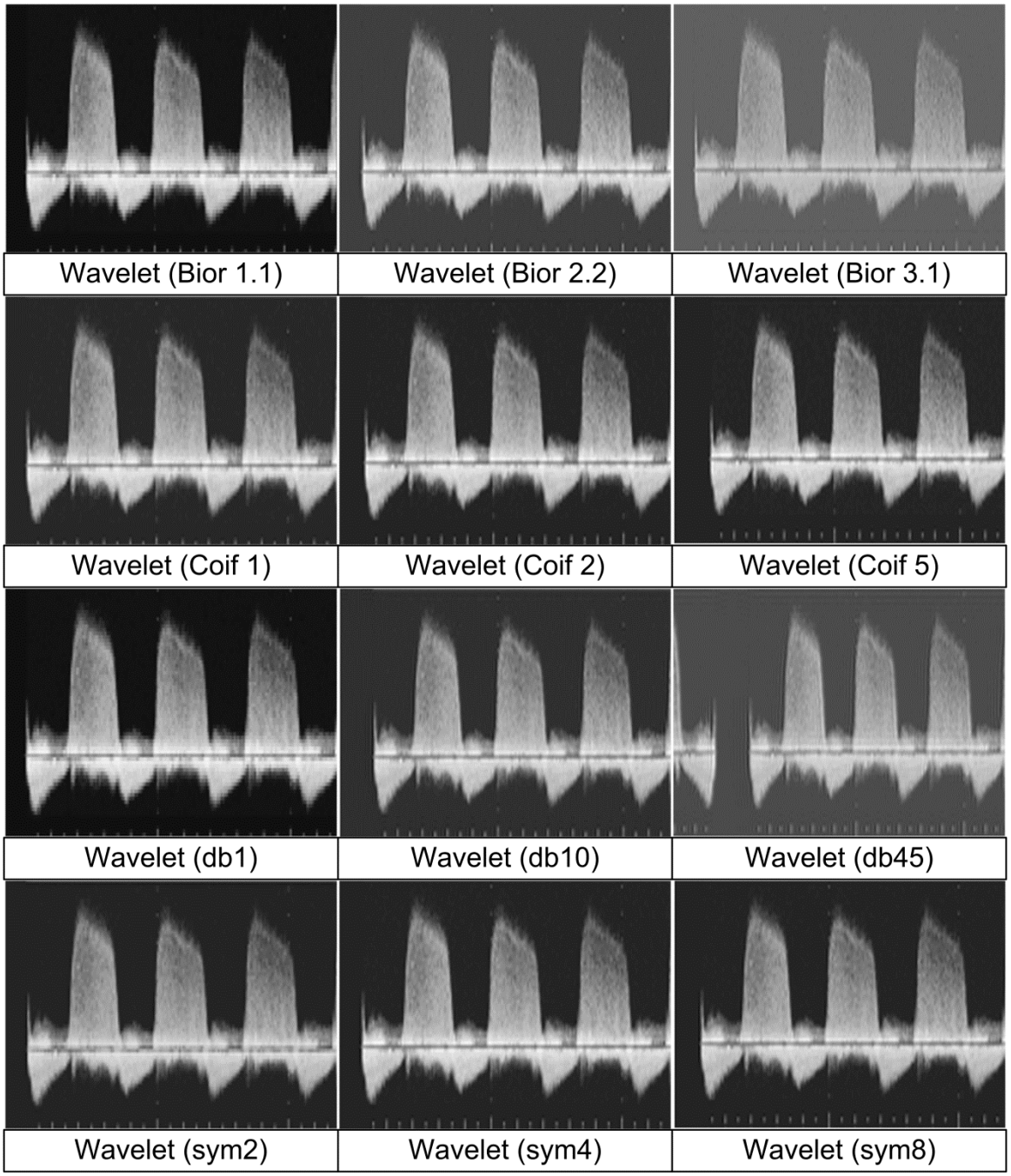

Figure 4.12 Comparison of visual quality on application of wavelets based filters

The contrast of images is considerably reduced on application of filters with window size 3×3 and 7×7 window size, respectively. Similarly, the performances of filters such as DsFls (5×5, 7×7), and DsFhomog (7×7) filter are also not acceptable for the practicing clinician. The visual outlook of images on application of methods such as the DsFgf4d, DsFad, DsFsrad, CED, and PPB filter are shown in Figure 4.10 are acceptable except the DPAD filter. The denoising applications of various wavelet-domain filters are depicted in Figure 4.12. The results of gradient projection based methods in terms of visual quality are shown in Figure 4.13. The visual quality obtained using wavelet (Bior 3.1), wavelet (db45), SQPBB, Frost (7×7) filters are not acceptable to the doctors.

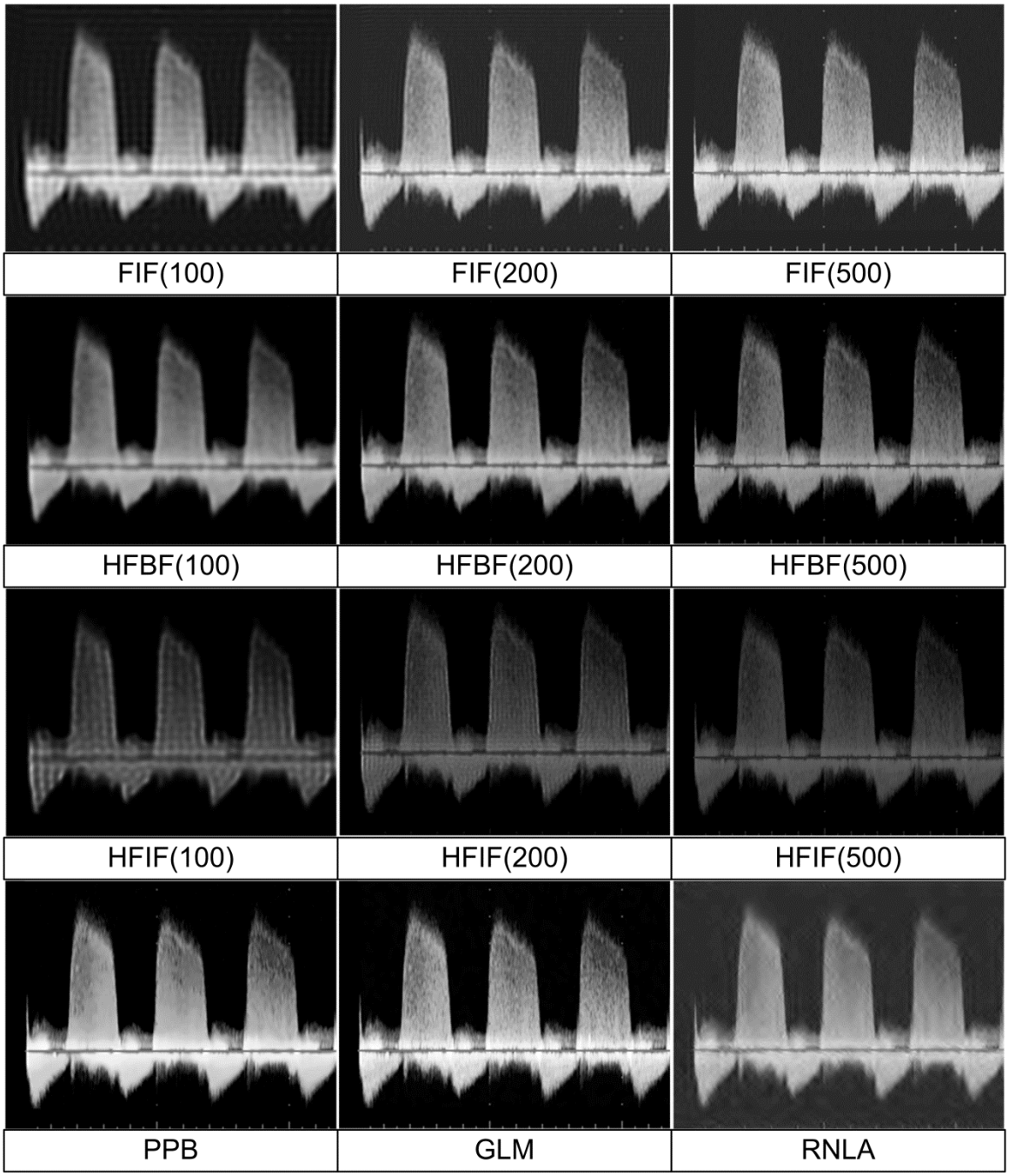

Figure 4.13 Comparison of visual quality using Fourier, GLM, and RNLA based filters

Table 4.3 Comparison of LMSE and other parameters for CWD images (Mean±STD)

Methods	**LMSE**	**MD**	**NCC**	**SC**	**ERR4**	**ERR3**	**RMSE**
DsFad	0.34±0.03	117.5±0.52	0.963±0.01	1.06±0.01	22.42±0.88	16.38±0.9	9.72±0.80
DsFgf4d	0.11±0.01	4.02±1.78	0.997±0.02	1.00±0.03	1.86±0.06	1.53±0.07	1.10±0.07
DsFhmed	0.49±0.02	238.4±0.5	0.954±0.02	1.07±0.03	38.26±1.73	25.28±1.63	12.22±1.23
DsFhomo	0.99±0.01	255.0±2.53	0.874±0.04	1.18±0.07	62.10±2.28	44.57±2.30	24.86±1.96
DsFhomog	0.02±0.02	5.89±2.16	0.994±0.01	1.00±0.03	0.68±0.02	0.50±0.03	0.30±0.02
DsFlsminsc	1.09±0.02	245.3±3.08	0.894±0.03	1.14±0.05	52.17±1.86	37.95±1.85	22.28±1.55
DsFlsmv	0.89±0.05	95.25±0.29	0.984±0.02	1.09±0.03	36.88±1.44	26.96±1.48	15.97±1.29
DsFmed	0.91±0.01	224.2±2.14	0.943±0.02	1.08±0.03	45.09±1.69	30.93±1.73	15.88±1.45
DsFsrad	0.80±0.01	93.63±2.71	0.876±0.03	1.23±0.07	30.79±2.11	25.99±2.12	9.88±1.74
DsFWiener	0.06±0.05	26.36±3.11	0.992±0.02	1.02±0.02	7.77±0.67	6.11±0.59	4.25±0.50
Methods	**FoM**	**β**	**SSIM**	**IQI**	**PSNR**	**SNR**	**MSE**
DsFad	0.96±0.01	0.74±0.04	0.99±0.05	0.75±0.03	28.41±0.71	35.47±2.54	95.02±15.6
DsFgf4d	0.99±0.01	1.00±0.04	1.00±0.03	0.91±0.02	47.29±0.57	53.23±2.26	10.22±0.1
DsFhmed	0.93±0.01	0.72±0.01	0.96±0.01	0.87±0.02	26.43±0.86	31.51±2.87	150.8±30.7
DsFhomo	0.77±0.02	0.16±0.03	0.83±0.03	0.57±0.05	20.25±0.68	19.15±2.63	621.6±98.5
DsFhomog	0.98±0.01	1.00±0.03	1.00±0.01	0.90±0.01	58.76±0.72	56.18±2.61	20.09±0.01
DsFlsminsc	0.76±0.01	0.15±0.01	0.88±0.01	0.59±0.03	21.19±060	21.04±2.42	498.4±69.0
DsFlsmv	0.97±0.02	0.44±0.01	0.97±0.01	0.84±0.02	24.09±0.70	46.84±0.57	16.52±1.77
DsFmed	0.94±0.01	0.38±0.01	0.96±0.01	0.82±0.02	24.15±0.79	26.95±2.77	254.1±46.7
DsFsrad	0.90±0.01	0.52±0.01	0.90±0.02	0.67±0.08	22.19±0.75	33.04±2.66	398.2±70.2
DsFWiener	0.95±0.02	0.97±0.01	0.99±0.07	0.81±0.02	35.63±0.99	49.91±2.10	18.27±4.5

Table 4.4 Comparison of FoM and other parameters for CWD images (Mean±STD)

Methods	FoM	Beta	SSIM	IQI	PSNR	SNR	MSE
DsFad	0.96±0.01	0.74±0.04	0.99±0.05	0.75±0.03	28.41±0.71	35.47±2.54	95.02±15.6
ATMED	0.94±0.03	0.38±0.01	0.95±0.02	0.73±0.02	23.45±0.81	25.13±1.82	299.5±58.2
ATV	0.91±0.02	0.97±0.02	0.97±0.04	0.39±0.04	33.11±0.75	44.49±1.72	12.33±5.94
DsFcasort	0.92±0.03	0.98±0.03	0.99±0.01	0.65±0.04	36.75±0.85	42.15±1.67	14.00±2.84
FBF	0.97±0.04	0.98±0.05	1.00±0.06	0.62±0.06	36.88±0.72	42.41±2.63	13.52±2.27
FIF	0.96±0.03	0.96±0.03	1.00±0.04	0.59±0.06	39.05±0.78	46.76±2.75	11.21±1.5
DsFgf4d	0.99±0.01	1.00±0.04	1.00±0.03	0.91±0.02	47.29±0.57	53.23±2.26	10.22±0.15
GLM	0.99±0.03	1.00±0.06	1.00±0.05	0.58±0.05	40.14±0.63	58.94±2.68	6.35±0.83
HFBF	0.98±0.02	0.91±0.03	0.95±0.01	0.59±0.07	32.78±0.65	44.22±2.54	14.61±5.03
HFIF	0.99±0.03	0.81±0.02	0.95±0.01	0.58±0.07	29.22±0.80	37.09±2.71	79.07±14.2
DsFhmed	0.93±0.01	0.72±0.01	0.96±0.01	0.87±0.02	26.43±0.86	31.51±2.87	150.8±30.7
DsFhomo	0.77±0.02	0.16±0.03	0.83±0.03	0.57±0.05	20.25±0.68	19.15±2.63	621.69±98.5
DsFhomog	0.98±0.01	1.00±0.03	1.00±0.01	0.90±0.01	58.76±0.72	56.18±2.61	20.09±0.01
DsFls	0.83±0.04	0.58±0.01	0.90±0.02	0.63±0.03	22.18±0.67	23.01±2.51	398.5±62.2
DsFlsminsc	0.76±0.01	0.15±0.01	0.88±0.01	0.59±0.03	21.19±060	21.04±2.42	498.4±69.0
DsFlsmv	0.97±0.02	0.44±0.01	0.97±0.01	0.84±0.02	24.09±0.70	46.84±0.57	16.50±1.77
MBR	0.76±0.03	0.14±0.01	0.80±0.03	0.46±0.06	19.32±0.64	17.29±2.36	768.92±112.38
DsFmed	0.94±0.01	0.38±0.01	0.96±0.01	0.82±0.02	24.15±0.79	26.95±2.77	254.18±46.75
MPT	0.84±0.05	0.88±0.05	0.97±0.01	0.63±0.04	29.25±0.60	37.16±2.17	77.94±11.26
NSS	0.92±0.04	0.96±0.01	0.98±0.01	0.59±0.06	34.28±0.68	47.22±1.31	24.54±4.01
PPB	0.96±0.02	0.97±0.01	0.96±0.01	0.60±0.06	37.37±0.62	53.29±1.25	12.05±1.82
PSBE	0.99±0.01	0.98±0.08	0.99±0.06	0.94±0.01	34.04±0.65	46.74±2.55	35.91±3.88
RNLA	0.74±0.06	0.73±0.03	0.73±0.03	0.28±0.02	25.91±1.17	30.24±2.74	172.77±49.24
DsFsrad	0.90±0.01	0.52±0.01	0.90±0.02	0.67±0.08	22.19±0.75	33.04±2.66	398.21±70.26
DsFwlt2	0.94±0.04	0.84±0.07	0.97±0.02	0.44±0.02	36.89±24.36	32.43±7.47	80.18±93.85
DsFWiener	0.95±0.02	0.97±0.01	0.99±0.07	0.81±0.02	35.63±0.99	49.91±2.10	18.27±4.54

The results obtained using PPB, GLM and RNLA are shown in Figure 4.13. The visual quality of denoised images on application of FIF, FBF, HFIF and HFBF are shown in Figure 4.13. The results obtained for FIF, FBF, HFBF and HFIF at 500Hz are acceptable along with the

GLM, and PSBE filters. The visual qualities obtained using FIF, HFBF and HFIF are not acceptable as the finer details. The images are over-smoothed using Fast Bilateral filter, FBF (100), FIF (100), RNLA and HFBF (100). The contrast and brightness of images are reduced using HFIF at all frequencies, RNLA and FIF (100) filters.

Table 4.5 Comparison of LMSE and other parameters for CWD images (Mean ± STD)

	LMSE	MD	NCC	SC	ERR4	ERR3	RMSE
DsFad	0.34±0.03	117.5±0.51	0.963±0.01	1.00±0.05	22.42±0.88	16.38±0.9	9.72±0.80
DsFcasort	0.14±0.01	30.61±1.76	0.985±0.01	1.00±0.04	6.66±0.41	5.29±0.4	3.72±0.37
FBF	0.18±0.03	56.55±0.01	0.998±0.02	1.00±0.03	9.18±0.35	6.46±0.35	3.66±0.31
FIF	0.19±0.02	68.75±6.28	0.998±0.03	1.00±0.02	7.04±0.20	4.82±0.25	2.85±0.26
DsFgf4d	0.11±0.01	4.01±1.78	0.997±0.02	1.00±0.03	1.86±0.06	1.53±0.07	1.10±0.07
GLM	0.02±0.01	62.75±0.17	0.987±0.01	1.00±0.04	9.69±0.40	5.95±0.30	2.51±0.17
HFBF	0.19±0.02	133.4±4.25	0.996±0.02	1.00±0.01	17.05±0.57	11.33±0.55	5.87±0.43
HFIF	0.71±0.03	441.5±13.1	0.997±0.03	0.95±0.01	37.52±1.63	21.37±1.20	8.86±0.81
DsFhmed	0.49±0.02	238.4±0.5	0.954±0.02	1.00±0.03	38.26±1.73	25.28±1.63	12.22±1.23
DsFhomo	0.99±0.01	255.0±2.5	0.874±0.04	1.00±0.07	62.10±2.28	44.57±2.30	24.86±1.96
DsFhomog	0.02±0.02	5.89±2.16	0.994±0.01	1.00±0.03	0.68±0.02	0.50±0.03	0.30±0.02
DsFls	0.77±0.01	178.6±22.7	0.923±0.02	1.00±0.02	39.13±1.48	30.37±1.60	19.91±1.55
DsFlsminsc	1.09±0.02	245.3±3.08	0.894±0.03	1.04±0.05	52.17±1.86	37.95±1.85	22.28±1.55
DsFlsmv	0.89±0.05	95.25±0.29	0.984±0.02	1.00±0.03	36.88±1.44	26.96±1.48	15.97±1.29
MBR	0.99±0.05	248.5±0.18	0.835±0.04	1.00±0.06	65.92±2.43	48.03±2.45	27.66±2.02
DsFmed	0.91±0.01	224.4±2.14	0.943±0.02	1.00±0.03	45.09±1.69	30.93±1.73	15.88±1.45
MPT	0.23±0.03	196.2±11.1	0.974±0.01	1.00±0.01	23.59±0.88	15.92±0.80	8.81±0.62
NSS	0.08±0.01	108.5±2.95	0.993±0.02	1.00±0.02	11.95±0.37	8.25±0.39	4.94±0.39
PSBE	0.07±0.02	98.43±6.15	0.975±0.01	1.00±0.02	14.48±0.44	9.88±0.45	5.08±0.38
RNLA	0.48±0.05	178.5±16.8	0.963±0.01	1.00±0.01	25.13±3.20	18.91±2.52	13.03±1.80
DsFsrad	0.80±0.01	93.63±2.71	0.876±0.03	1.00±0.07	30.79±2.11	25.99±2.12	9.88±1.74
Wavelet	0.14±0.15	65.43±48.9	0.935±0.04	1.00±0.09	43.73±9.07	30.80±6.97	17.65±4.78
DsFWiener	0.06±0.05	26.36±3.11	0.992±0.02	1.02±0.02	7.77±0.67	6.11±0.59	4.25±0.50
DsFwlt2	1.31±0.04	542.28±11.22	0.864±0.07	0.28±0.02	147.64±7.31	121.38±8.0	89.68±8.31
DsFca	1.07±0.05	176.91±25.03	0.403±0.15	6.72±2.25	79.49±10.91	67.04±8.48	49.78±6.52

The values in the parenthesis indicate the cut-off frequency employed in these filters. The IQM reflecting the edge and structure preservation along with noise reduction for the CWD images are tabulated in Table 4.3, Table 4.4 and Table 4.5. The following observations are made based on results tabulated. The LMSE of the CWD images is less than 0.1±0.01 using filters such as FBF, FIF, DsFgf4d, DsFhomog, NSS, PSBE and DsFWiener filter. The mean difference (MD) for the DsFgf4d and DsFhomog filters is less than 6 and all other methods greater than 30. The NCC value is least for the MBR and DsFlsminsc filters. The filters such as Fourier, DsFgf4d, GLM, DsFhomog, NSS, DsFlsmv and DsFWiener are better in terms of Err3, Err4 and RMSE.

The filters such as the DsFWiener, PPB, DsFlsmv, DsFhomog, DsFgf4d, FIF, and FBF has smaller MSE along with higher SNR and PSNR compared to other techniques. It reveals that considerable amount of noise is taken off from the image using these filters. Based on the analysis of results tabulated in Table 4.3 and Table 4.4, the IQI of denoised

images on application of filters like DsFgf4d, PSBE, DsFhmedian, DsFhomog and DsFWiener filter is greater than 0.8, which implies that the image quality are well retained. The issue of concern in application of filters such as DsFsrad, DsFmed, MBR, DsFlsmv, DsFlsminsc, DsFhomo and ATMED filter is poor value of β. The filters such as ATV, Fourier filters, DsFgf4d, GLM, PPB, NSS, PPB, PSBE, and DsFWiener result in $\beta \geq 0.9$ showing better edge preservation.

The analysis reveals the following with regard to denoising applications of eight types of filters for the CWD images.

i. The issues to be addressed using Fourier based filters is to improve IQI and MD.
ii. The filters such as the DsFmed, DsFhomo, DsFhmedian, ATMED and TMAV filters retain certain amount of noise in despeckled images. This observation is based on the high values of MSE, Err3, Err4, MD and poor SNR, PSNR, and β.
iii. The performance of local statistics filters such as the DsFls and DsFlsminsc filers are inferior in terms of β, and IQI showing that edges are not well preserved. These filters also retain noise in the denoised images as the SNR and PSNR are far less compared to other filters with high values of MSE, Err3, Err4, and RMSE.
iv. The versatile wavelet filter based on GLM delivers good results in terms of β, SSIM, and others but point of concern with this filter is poor IQI. All the wavelet domain filters experimented in this paper have this problem of low IQI along with high Err3, Err4 and MD.
v. The hybrid median filter (DsFhmedian) retains noise as reflected by high values of MSE, MD, Err3 and Err4 with poor value of β, SNR and PSNR.
vi. The nonlinear iterative denoising technique such as DsFad, DsFsrad have drawbacks such as poor β, IQI, along with high values of MD and MSE. The performance of techniques like DsFgf4d, DsFhomog are acceptable in terms of both IQM and visual quality.
vii. The anisotropic total variation filter and nonlocal means based PPB filters have poor IQI. The performances of these two filters are acceptable in terms of visual and image quality metrics except have fractionally inferior IQI.
viii. Denoising application of nonlinear approximation based Ripplet transformations are hampred by poor FoM, SSIM, IQI and β. The IQM, visual quality and clinical validation reveal that the performances of filters such as DsFWiener, PSBE, DsFhomog and DsFgf4d are acceptable.

The texture features are extracted from B-Mode TTE images acquired in five views using two windows. The texture of B-Mode images are compared with texture features extracted using the CWD, color Doppler (CD) and M-Mode images. The images are pre-

processed using various despeckling filters. The texture features of the despeckled images are compared with the original images. The features are extracted by converting all images to gray scale. All texture features of the original B-Mode, M-Mode, CWD and CD, are compared with features obtained from the denoised images.

Table 4.6 Comparison of FOS features for B-Mode, CD, CWD and MM modality

Mean	**PSAX**	**PLAX**	**A4C**	**A5C**	**A2C**	**CD**	**CWD**	**MM**
Original	25.5±11.4	25.1±7.6	19.24±3.4	19.28±2.8	24.49±4.5	26.2±5.6	36.8±7.0	37.09±8.8
DsFlsmv	25.4±11.3	25.6±7.6	19.17±3.4	19.22±2.8	24.49±5.1	26.3±5.6	37.2±7.1	36.9±8.8
DsFgf4d	29.1±12.5	28.9±8.3	22.43±3.8	22.50±3.2	28.39±4.8	30.9±6.2	41.2±7.2	45.4±9.3
DsFWiener	25.6±11.3	25.307.6	19.40±3.4	19.44±2.8	24.73±5.1	26.7±5.6	37.5±7.0	37.7±8.8
NLM	25.4±11.4	25.1±7.7	19.22±3.4	19.27±2.8	24.45±4.4	26.3±5.6	37.0±7.0	37.1±8.8
PSBE	23.8±11.3	23.3±7.5	17.54±3.4	17.66±2.7	22.82±4.9	23.4±5.6	33.2±6.9	32.0±8.7
ATV	25.6±11.3	25.2±7.6	19.3±3.4	19.4±2.8	24.68±4.9	26.6±5.6	37.4±7.0	37.5±8.8
Skewness	**PSAX**	**PLAX**	**A4C**	**A2C**	**A5C**	**CD**	**CW**	**MM**
Original	2.59±0.71	2.8±0.45	2.99±0.34	2.92±0.22	2.66±0.26	2.4±0.35	1.8±0.33	1.6±0.30
DsFlsmv	2.45±0.61	2.4±0.41	2.84±0.30	2.75±0.17	2.55±0.25	2.2±0.29	1.7±0.31	1.2±0.26
DsFgf4d	2.40±0.70	2.3±0.43	2.77±0.32	2.70±0.23	2.43±0.24	2.1±0.33	1.6±0.31	1.3±0.26
DsFWiener	2.61±0.74	2.5±0.45	2.99±0.34	2.92±0.24	2.67±0.27	2.4±0.37	1.8±0.33	1.6±0.31
NLM	2.59±0.72	2.5±0.45	2.99±0.34	2.92±0.23	2.67±0.26	2.4±0.36	1.8±0.33	1.6±0.30
PSBE	2.47±0.51	2.5±0.43	2.96±0.33	2.80±0.13	2.65±0.25	2.4±0.27	1.9±0.34	1.7±0.27
TV	2.58±0.71	2.5±0.45	2.97±0.34	2.90±0.22	2.65±0.26	2.9±0.36	1.8±0.33	1.6±0.30
Variance	**PSAX**	**PLAX**	**A4C**	**A5C**	**A2C**	**CD**	**CW**	**MM**
Original	46.9±12.8	48.3±8.8	41.50±3.6	40.27±4.2	43.93±4.8	49.3±6.6	62.6±6.3	56.6±7.3
DsFlsmv	45.8±12.9	47.8±8.8	40.2±3.6	39.06±4.2	42.84±5.2	47.9±6.7	61.2±6.3	54.3±7.5
DsFgf4d	51.6±12.7	53.5±8.5	46.45±3.5	45.22±4.2	48.54±4.6	55.0±6.6	67.0±5.7	63.9±7.1
DsFWiener	46.8±12.7	48.2±8.7	41.4±3.56	40.2±4.14	43.8±5.28	49.6±6.5	62.8±6.1	55.9±7.3
NLM	46.9±12.8	48.3±8.8	41.50±3.6	40.25±4.2	43.86±4.7	49.4±6.6	62.9±6.3	56.6±7.4
PSBE	43.1±13.8	44.4±9.3	37.17±4.1	35.95±4.5	40.06±5.5	43.5±7.6	57.4±7.1	48.9±8.7
TV	46.7±12.8	48.1±8.7	41.3±3.59	40.1±4.18	43.7±5.15	49.5±6.5	62.9±6.2	56.3±7.3
Kurtosis	**PSAX**	**PLAX**	**A4C**	**A5C**	**A2C**	**CD**	**CW**	**MM**
Original	11.03±5.8	9.98±2.9	12.89±2.6	12.69±2.0	11.05±1.9	8.81±2.4	5.47±1.5	4.98±1.2
DsFlsmv	9.84±4.54	9.33±2.5	11.74±2.2	11.34±1.4	10.36±1.7	7.88±1.8	5.13±1.3	4.44±0.9
DsFgf4d	9.52±5.12	8.52±2.4	10.98±2.1	10.84±1.7	9.32±1.57	7.21±1.8	4.77±1.2	3.84±0.8
DsFWiener	11.20±6.1	9.99±2.9	12.91±2.6	12.79±2.1	11.16±2.0	8.84±2.5	5.38±1.4	5.00±1.2
NLM	11.02±5.8	9.97±2.9	12.87±2.6	12.69±2.0	11.09±1.9	8.81±2.4	5.45±1.5	5.00±1.2
PPB	10.95±5.9	9.89±2.9	12.73±2.6	12.55±2.0	10.96±1.9	8.70±2.4	5.37±1.4	4.91±1.2
PSBE	10.05±3.8	10.2±2.9	12.97±2.6	12.03±1.3	11.44±1.9	9.08±1.9	6.16±1.7	5.36±1.2
TV	10.92±5.8	9.87±2.8	12.70±2.5	12.52±2.0	11.00±1.9	8.73±2.4	5.37±1.4	4.97±1.2

The statistical features such as mean, skewness, and variance are tabulated in Table 4.6 for the B-Mode images in PSAX, PLAX, A4C, A5C, and A2C views along with CD, CWD and MM imaging modality images. The mean values of the original TTE images in multiple views are same on application of despeckling filters such as the DsFlsmv filter, DsFWiener filter, and ATV filters whereas filters like DsFgf4d result in larger variations as observed in Table 4.6. The mean values are higher for the CWD and M-mode images when compared to the images acquired in A4C and A5C. Large variations are also observed between images in A4C and A5C when compared with A2C. Clear distinction is observed between images acquired using B-Mode, M-Mode and CWD based echocardiographic imaging. The difference between FOS parameters is small for images acquired in A4C

compared with A5C, PSAX compared with PLAX whereas large variations are observed between A4C compared with A2C, PLAX compared with A4C and A5C views.

The SGLDM features for TTE images in B-Mode, M-Mode, CWD and CD are depicted in Table 4.7. The values of f1 are least for CWD images whereas A4C and A5C are highest. There is huge gap between the values of f1 between A4C and A5C when compared with A2C, similarly PLAX and PSAX compared with CWD images. The analysis of f1 multi mode view images holds good for the other SGLDM features such as f2, f3 and f5 also. The texture features based on GLDS are compared in Table 4.8. The energy values of A4C and A5C are quite distinct compared to A2C, similarly, PLAX and PSAX compared with A4C and A5C.

Table 4.7 Comparison of SGLDM features for B-Mode, CD, CWD and MM modality

f1	**PSAX**	**PLAX**	**A4C**	**A5C**	**A2C**	**CD**	**CW**	**MM**
Original	0.35±0.06	0.35±0.07	0.40±0.07	0.41±0.04	0.26±0.04	0.34±0.05	0.18±0.06	0.23±0.03
DsFlsmv	0.34±0.06	0.33±0.07	0.39±0.07	0.39±0.04	0.25±0.04	0.32±0.05	0.16±0.06	0.21±0.03
DsFgf4d	0.33±0.06	0.32±0.07	0.38±0.07	0.39±0.04	0.25±0.04	0.31±0.05	0.16±0.06	0.19±0.03
DsFWiener	0.34±0.06	0.33±0.07	0.39±0.07	0.39±0.04	0.25±0.04	0.32±0.05	0.16±0.06	0.20±0.03
NLM	0.35±0.07	0.35±0.08	0.41±0.08	0.41±0.04	0.27±0.04	0.34±0.05	0.18±0.06	0.23±0.03
PSBE	0.34±0.06	0.34±0.07	0.39±0.07	0.40±0.04	0.26±0.04	0.32±0.05	0.16±0.06	0.20±0.03
TV	0.32±0.06	0.32±0.07	0.37±0.07	0.38±0.04	0.25±0.04	0.30±0.05	0.15±0.06	0.18±0.03
f2	**PSAX**	**PLAX**	**A4C**	**A5C**	**A2C**	**CD**	**CW**	**MM**
Original	301.6±27.2	306.3±27.5	298.3±14.4	289.6±19.5	299.9±15.2	555.2±31.6	729±127	892±192.7
DsFlsmv	167.1±11.6	167.9±13.3	165.7±7.2	162.8±9.2	171.4±11.8	314.6±14.4	389±66.1	489±106.3
DsFgf4d	281.2±22.4	286.2±24.4	280.3±13.6	271.03±18.2	277.6±18.4	525.6±29.5	705±131.3	843±200.6
DsFWiener	277.8±18.9	282.3±20.43	279.1±11.8	270.63±15.2	275.64±13.10	522.4±24.7	663.3±91.9	711.8±136.7
NLM	289.7±25.5	293.3±26.7	285.1±13.5	276.35±18.3	283.40±19.13	542.9±30.4	716±121.6	843±184.1
PSBE	52.4±12.5	59.1±10.03	52.6±4.11	50.54±4.92	57.08±21.19	74.79±8.99	96.8±12.8	130.4±25.3
TV	259.3±21.8	263.9±22.5	258.8±11.7	250.73±16.3	257.47±18.03	506.3±26.5	669±106.4	769±164.9
f3	**PSAX**	**PLAX**	**A4C**	**A5C**	**A2C**	**CD**	**CW**	**MM**
original	0.92±0.04	0.93±0.02	0.91±0.02	0.91±0.02	0.92±0.01	0.88±0.03	0.90±0.02	0.86±0.04
DsFlsmv	0.95±0.03	0.96±0.01	0.95±0.01	0.95±0.01	0.95±0.01	0.93±0.02	0.95±0.01	0.91±0.03
DsFgf4d	0.94±0.03	0.95±0.01	0.93±0.01	0.93±0.01	0.94±0.01	0.91±0.02	0.92±0.02	0.89±0.03
DsFWiener	0.92±0.04	0.94±0.02	0.92±0.02	0.91±0.01	0.93±0.01	0.89±0.03	0.91±0.02	0.88±0.03
NLM	0.92±0.04	0.93±0.02	0.92±0.02	0.91±0.01	0.92±0.01	0.88±0.03	0.91±0.02	0.86±0.04
PSBE	0.98±0.01	0.98±0.00	0.98±0.00	0.98±0.00	0.98±0.00	0.98±0.01	0.98±0.00	0.97±0.01
TV	0.93±0.03	0.94±0.01	0.92±0.01	0.92±0.01	0.93±0.01	0.89±0.03	0.91±0.02	0.88±0.04
f5	**PSAX**	**PLAX**	**A4C**	**A5C**	**A2C**	**CD**	**CW**	**MM**
original	0.73±0.05	0.73±0.05	0.77±0.05	0.77±0.03	0.67±0.05	0.72±0.04	0.62±0.04	0.61±0.03
DsFlsmv	0.74±0.05	0.73±0.05	0.77±0.04	0.77±0.03	0.68±0.05	0.71±0.04	0.66±0.04	0.61±0.03
DsFgf4d	0.75±0.04	0.75±0.04	0.78±0.04	0.79±0.02	0.70±0.05	0.74±0.03	0.65±0.04	0.64±0.02
DsFWiener	0.73±0.05	0.73±0.05	0.77±0.04	0.77±0.03	0.68±0.05	0.71±0.04	0.66±0.04	0.61±0.03
NLM	0.74±0.05	0.74±0.05	0.78±0.05	0.78±0.03	0.68±0.05	0.72±0.04	0.68±0.04	0.62±0.03
PSBE	0.74±0.05	0.74±0.05	0.78±0.04	0.78±0.03	0.69±0.05	0.72±0.04	0.67±0.04	0.62±0.03
TV	0.75±0.05	0.74±0.05	0.78±0.04	0.78±0.02	0.69±0.05	0.73±0.04	0.69±0.04	0.62±0.03

The features based on NGTDM and SFM are being tabulated in Table 4.9 and Table 4.11, respectively. The contrast and coarseness are abbreviated as “CONTR” and “COARS” in Table 4.9. The results show that the values of CONTR are quite high for the M-Mode and CWD images in comparison to the B-Mode images in multiple views. The values of CONTR are higher for PLAX and PSAX images in comparison to images acquired in the apical

windows. The value of coarseness is higher for B-Mode images in comparison to the CD, MM and CWD images. The texture features based on FDTA are tabulated in Table 4.10. The results shows that the Hoarest coefficient is fractionally higher for the images acquired in B-mode compared to the M-Mode images. In other images this parameter is almost the same. The Fourier power spectrum features are shown in Table 4.12. The values of f_r and f_a are higher for the CWD and M-Mode images in comparison to the images in the apical and parasternal windows.

Table 4.8 Comparison of GLDS features for B-Mode, CD, CWD and MM modality

Contrast	**PSAX**	**PLAX**	**A4C**	**A5C**	**A2C**	**CD**	**CW**	**MM**
original	301±27.2	306.3±27.5	298.2±14.4	289.5±19.5	299±15.2	555±31.6	729±127.6	892±192.4
DsFlsmv	167±11.7	167.8±13.3	165.6±7.2	162.8±9.2	171±11.8	314±14.4	388±66.1	489±106.6
DsFgf4d	281±22.6	286.1±24.4	280.2±13.6	270.9±18.2	277±18.4	525±29.5	705±131.2	843±200.4
DsFWiener	277±18.9	281.9±20.4	279.1±11.8	270.5±15.2	275±13.1	522±24.7	663±91.3	711±136.7
NLM	289±25.5	293.3±26.7	285 ±13.5	276±18.3	283±19.1	542±30.4	716±121.6	843±184.9
PSBE	52.4±12.5	59.9±10.3	52.5±4.1	50.5±4.9	57.1±21.1	74.7±8.9	96±12.8	130±25.3
TV	258±21.2	263±22.5	258±11.7	250±16.3	257±18.1	506±26.5	669±106.3	769±164.8
Energy	**PSAX**	**PLAX**	**A4C**	**A5C**	**A2C**	**CD**	**CW**	**MM**
original	0.49±0.07	0.49±0.08	0.55±0.08	0.55±0.04	0.40±0.05	0.46±0.06	0.32±0.06	0.33±0.03
DsFlsmv	0.49±0.07	0.48±0.08	0.54±0.07	0.54±0.04	0.40±0.05	0.46±0.05	0.36±0.05	0.33±0.03
DsFgf4d	0.52±0.06	0.52±0.07	0.57±0.07	0.58±0.04	0.44±0.05	0.49±0.05	0.35±0.06	0.37±0.03
DsFWiener	0.49±0.07	0.48±0.08	0.54±0.07	0.54±0.04	0.40±0.05	0.46±0.05	0.36±0.05	0.32±0.03
NLM	0.50±0.07	0.50±0.08	0.56±0.08	0.56±0.04	0.41±0.05	0.47±0.06	0.39±0.06	0.35±0.03
PSBE	0.49±0.07	0.49±0.08	0.55±0.07	0.55±0.04	0.41±0.05	0.46±0.05	0.37±0.05	0.33±0.03
TV	0.49±0.07	0.49±0.07	0.54±0.07	0.55±0.04	0.41±0.05	0.46±0.05	0.39±0.05	0.32±0.03
Entropy	**PSAX**	**PLAX**	**A4C**	**A5C**	**A2C**	**CD**	**CW**	**MM**
original	1.66±0.24	1.68±0.24	1.50±0.23	1.50±0.13	1.93±0.17	1.80±0.18	2.21±0.20	2.42±0.15
DsFlsmv	1.58±0.21	1.61±0.22	1.44±0.19	1.44±0.11	1.80±0.14	1.75±0.16	2.00±0.17	2.29±0.15
DsFgf4d	1.54±0.20	1.57±0.20	1.42±0.19	1.41±0.11	1.79±0.16	1.69±0.16	2.11±0.20	2.26±0.14
DsFWiener	1.59±0.21	1.61±0.21	1.45±0.19	1.45±0.11	1.80±0.14	1.76±0.16	2.01±0.18	2.32±0.16
NLM	1.61±0.24	1.63±0.24	1.44±0.22	1.46±0.13	1.87±0.16	1.77±0.18	2.02±0.21	2.35±0.16
PSBE	1.50±0.21	1.52±0.21	1.35±0.18	1.36±0.11	1.70±0.16	1.65±0.16	1.86±0.16	2.12±0.14
TV	1.56±0.22	1.58±0.21	1.41±0.18	1.42±0.11	1.77±0.15	1.73±0.16	1.91±0.18	2.32±0.16

Table 4.9 Comparison of NGTDM features for B-Mode, CD, CWD and MM modality

Coarseness	**PSAX**	**PLAX**	**A4C**	**A5C**	**A2C**	**CD**	**CW**	**MM**
Original	6.71±0.80	6.80±0.55	6.27±0.86	6.61±0.70	8.61±2.15	2.69±0.26	2.71±0.35	2.14±0.54
DsFlsmv	67.86±14.04	67.55±8.69	62.23±8.54	71.61±5.97	72.07±6.86	33.36±3.42	24.73±4.25	23.13±5.67
DsFgf4d	13.82±1.75	14.09±1.38	12.72±1.48	13.48±0.92	16.67±2.99	5.28±0.59	5.10±0.76	3.67±1.11
DsFWiener	58.86±11.13	58.66±6.74	54.58±8.32	62.98±6.07	66.12±7.24	28.30±2.44	23.16±1.95	17.74±4.43
NLM	8.54±1.02	8.71±0.74	8.20±1.20	8.50±0.87	10.84±2.50	3.12±0.30	3.63±0.53	2.81±0.74
PSBE	98.50±19.66	98.35±12.95	90.22±14.28	103.75±8.6	108.39±10.7	68.48±6.70	49.85±7.94	47.56±9.09
TV	82.44±11.93	81.94±8.37	77.74±8.99	89.64±5.71	80.51±6.25	48.14±4.47	22.86±6.75	28.87±7.28
Contrast	**PSAX**	**PLAX**	**A4C**	**A5C**	**A2C**	**CD**	**CW**	**MM**
Original	0.21±0.16	0.21±0.12	0.14±0.04	0.13±0.04	0.18±0.06	0.30±0.10	0.63±0.18	0.73±0.29
DsFlsmv	0.13±0.09	0.14±0.07	0.09±0.02	0.08±0.02	0.11±0.03	0.22±0.07	0.43±0.11	0.46±0.17
DsFgf4d	0.22±0.14	0.23±0.11	0.15±0.04	0.14±0.04	0.19±0.05	0.33±0.10	0.69±0.19	0.83±0.30
DsFWiener	0.17±0.11	0.17±0.09	0.12±0.03	0.11±0.03	0.14±0.04	0.30±0.09	0.58±0.14	0.56±0.21
NLM	0.20±0.14	0.20±0.11	0.13±0.03	0.12±0.03	0.16±0.05	0.30±0.10	0.63±0.18	0.68±0.27
PSBE	0.07±0.06	0.07±0.05	0.04±0.01	0.04±0.01	0.06±0.03	0.08±0.04	0.17±0.05	0.18±0.08
TV	0.18±0.12	0.18±0.10	0.12±0.03	0.11±0.03	0.15±0.06	0.31±0.09	0.63±0.15	0.66±0.25

Table 4.10 Comparison of FDTA features for B-Mode, CD, CWD and MM modality

h1	PSAX	PLAX	A4C	A5C	A2C	CD	CW	MM
Original	0.39±0.01	0.40±0.01	0.39±0.01	0.39±0.01	0.40±0.01	0.37±0.01	0.33±0.01	0.33±0.01
DsFlsmv	0.48±0.02	0.49±0.01	0.48±0.01	0.48±0.01	0.49±0.01	0.46±0.01	0.45±0.02	0.45±0.01
DsFgf4d	0.49±0.01	0.50±0.01	0.49±0.01	0.49±0.01	0.49±0.01	0.46±0.01	0.38±0.01	0.44±0.01
DsFWiener	0.44±0.02	0.45±0.01	0.44±0.01	0.44±0.01	0.45±0.01	0.41±0.01	0.40±0.02	0.42±0.01
NLM	0.41±0.02	0.42±0.01	0.41±0.01	0.41±0.01	0.42±0.01	0.39±0.01	0.35±0.01	0.36±0.01
PSBE	0.52±0.01	0.53±0.00	0.53±0.01	0.52±0.01	0.53±0.00	0.51±0.01	0.49±0.01	0.49±0.01
TV	0.45±0.02	0.46±0.01	0.45±0.01	0.45±0.01	0.46±0.01	0.42±0.01	0.40±0.02	0.40±0.01

Table 4.11 Comparison of SFM features for B-Mode, CD, CWD and MM modality

Coardness	PSAX	PLAX	A4C	A5C	A2C	CD	CW	MM
Original	12.35±2.37	11.64±1.65	12.87±1.37	12.97±1.26	10.91±0.77	8.77±0.90	7.39±0.91	5.50±0.88
DsFlsmv	14.19±2.54	13.33±1.83	14.60±1.42	14.79±1.39	12.63±0.95	9.85±0.97	8.44±0.96	6.42±1.02
DsFgf4d	11.69±1.98	11.02±1.39	11.88±1.00	12.08±1.11	10.48±0.62	8.11±0.71	6.98±0.92	5.18±0.94
DsFWiener	13.34±2.36	12.52±1.62	13.62±1.22	13.85±1.27	12.00±0.89	9.07±0.85	7.70±0.86	6.06±0.96
NLM	12.70±2.41	11.98±1.70	13.24±1.36	13.38±1.29	11.31±0.78	8.87±0.90	7.52±0.94	5.66±0.92
PSBE	18.97±4.54	17.15±2.74	19.40±2.47	19.54±2.23	16.23±1.55	14.76±2.18	12.52±1.41	9.50±1.32
TV	13.50±2.52	12.66±1.69	13.83±1.29	14.04±1.34	12.14±1.00	9.11±0.89	7.70±0.90	5.87±0.97
Contrast	**PSAX**	**PLAX**	**A4C**	**A5C**	**A2C**	**CD**	**CW**	**MM**
Original	24.54±1.10	24.73±1.08	24.42±0.59	24.06±0.79	24.48±0.65	33.31±0.95	38.06±3.31	42.00±4.84
DsFlsmv	18.27±0.64	18.31±0.72	18.20±0.40	18.04±0.50	18.51±0.59	25.08±0.57	27.80±2.34	31.11±3.63
DsFgf4d	23.70±0.94	23.91±1.00	23.67±0.57	23.27±0.76	23.55±0.86	32.41±0.91	37.42±3.45	40.78±5.25
DsFWiener	23.56±0.80	23.74±0.84	23.62±0.50	23.26±0.64	23.47±0.54	32.31±0.76	36.34±2.51	37.56±3.84
NLM	24.03±1.06	24.20±1.08	23.87±0.56	23.50±0.76	23.79±0.88	32.94±0.92	37.73±3.19	40.82±4.77
PSBE	10.18±1.19	10.84±0.88	10.25±0.41	10.04±0.48	10.59±1.41	12.21±0.74	13.89±0.92	16.06±1.58
TV	22.74±0.93	22.96±0.96	22.75±0.51	22.38±0.71	22.68±0.74	31.81±0.83	36.48±2.89	39.01±4.47
Periodicity	**PSAX**	**PLAX**	**A4C**	**A5C**	**A2C**	**CD**	**CW**	**MM**
Original	0.56±0.02	0.57±0.02	0.56±0.01	0.55±0.01	0.54±0.01	0.54±0.01	0.62±0.03	0.53±0.02
DsFlsmv	0.63±0.02	0.64±0.02	0.63±0.01	0.62±0.01	0.62±0.01	0.61±0.01	0.64±0.02	0.62±0.03
DsFgf4d	0.69±0.01	0.69±0.01	0.71±0.01	0.71±0.01	0.71±0.01	0.68±0.01	0.73±0.02	0.68±0.01
DsFWiener	0.60±0.01	0.61±0.02	0.61±0.01	0.60±0.01	0.61±0.01	0.58±0.01	0.62±0.02	0.59±0.02
NLM	0.58±0.02	0.59±0.02	0.58±0.01	0.57±0.01	0.56±0.02	0.55±0.01	0.63±0.03	0.56±0.03
PSBE	0.67±0.01	0.68±0.01	0.66±0.01	0.65±0.01	0.65±0.01	0.66±0.01	0.66±0.02	0.69±0.02
TV	0.61±0.01	0.61±0.02	0.61±0.01	0.60±0.01	0.61±0.01	0.58±0.01	0.63±0.02	0.58±0.03

Table 4.12 Comparison of FPS features for B-Mode, CD, CWD and MM modality

fa ($x10^3$)	PSAX	PLAX	A4C	A5C	A2C	CD	CW	MM
original	16.88±7.2	17.85±4.7	14.86±2.0	13.76±2.2	16.08±1.4	16.39±3.08	21.71±2.93	19.51±2.96
DsFlsmv	17.12±7.2	18.08±4.7	15.17±2.0	14.08±2.2	16.34±1.7	17.58±3.63	24.10±3.49	18.76±4.75
DsFgf4d	18.11±7.5	19.28±4.9	16.24±2.2	15.01±2.3	17.34±1.4	18.21±3.16	22.79±2.87	22.01±2.84
DsFWiener	17.48±7.1	18.44±4.6	15.59±1.9	14.50±2.2	16.70±1.7	18.18±3.55	24.64±3.44	19.32±4.72
NLM	17.05±7.3	18.04±4.7	15.11±2.4	13.98±2.2	16.25±1.6	16.92±3.19	22.84±3.22	19.28±3.42
PPB	16.94±7.3	17.95±4.7	15.02±2.6	13.90±2.3	16.19±1.6	16.76±3.29	23.08±3.14	19.50±3.66
PSBE	16.12±7.5	17.12±4.8	14.06±2.5	12.93±2.3	15.29±1.4	16.02±3.91	22.80±3.64	16.89±4.96
TV	17.43±7.2	18.41±4.6	15.53±1.9	14.43±2.2	16.62±1.3	18.19±3.58	24.81±3.436	19.49±4.73
fr ($x10^3$)	**PSAX**	**PLAX**	**A4C**	**A5C**	**A2C**	**CD**	**CW**	**MM**
original	20.14±5.0	20.14±3.5	16.53±1.4	16.80±1.3	18.22±1.8	18.44±2.89	22.94±2.90	23.44±2.75
DsFlsmv	20.68±4.8	20.55±3.5	17.06±1.4	17.27±1.3	18.88±1.7	21.69±2.58	27.29±2.99	27.95±3.29
DsFgf4d	22.29±4.9	22.22±3.4	18.49±1.4	18.95±1.3	20.30±1.9	20.77±2.89	24.47±2.77	27.03±2.67
DsFWiener	21.05±4.7	20.92±3.4	17.49±1.3	17.68±1.2	19.26±1.7	22.30±2.50	27.92±2.91	28.62±3.19
NLM	20.46±4.9	20.39±3.5	16.86±1.4	17.08±1.3	18.62±1.8	19.53±2.78	24.46±3.21	24.75±2.91
PPB	20.60±5.1	20.57±3.6	17.01±1.5	17.20±1.4	18.86±1.8	19.53±2.90	24.55±3.25	24.78±3.81
PSBE	19.40±4.9	19.32±3.5	15.66±1.4	15.90±1.3	17.45±1.8	19.56±2.91	25.08±3.19	24.75±3.12
TV	21.00±3.5	20.88±2.9	17.43±1.5	17.62±1.2	19.08±1.7	22.32±2.73	28.08±2.40	28.72±3.10

4.4 Summary

The performance of the despeckling techniques are analysed for the CWD images in terms of image quality metrics, visual quality assessment and clinical validation. The objective of despeckling is suppression of noise with retention of edge and structural information necessary in the clinical validation. The performance analysis of despeckling is carried at various mask size and number of iterations with suitable combination of the input parameters for each of the filter. The performance of the DsFsrad filter are superior compared to the DsFgf4d filter, DsFhomog filter, DsFlsminsc, DsFhmedian and DsFad filter in terms of IQM such as Err3, Err4, LMSE and NAE. The visual quality of despeckled images obtained using the DsFlsmv, DsFWiener, DsFad and dsFsrad are able to retain structure and edge details. The issues of concern in despeckling of CWD images using various filters are discussed at length highlighted in this chapter.

The texture features of the B-Mode, M-Mode, CWD, and CD based echocardiographic modality images are extracted using sixty one texture features along with sixteen image quality metrics for analysis of despeckling filter performances. The features are extracted for B-Mode images acquired in two parasternal and three apical views. Features extracted using the despeckled images showed marked difference in images acquired in A4C and A5C in comparison to A2C, and A4C compared with PLAX view images. Similarly, the features of CWD, M-Mode, color Doppler and B-Mode images are quite distinct. The features extracted can be employed in classification of severity of the valvular diseases.

CHAPTER 5: SEGMENTATION OF ECHOCARDIGRAPHIC IMAGES

This chapter describes segmentation of B-Mode, continuous wave Doppler (CWD), color Doppler (CD) images and synthetic test images with intensity in-homogeneity. The segmentation techniques employed are based on concepts edge, region, watershed, fuzzy and active contour. The Gaussian and median filters used in the methods such as the Kiruthika, Magagnin and reaction diffusion based active contour are replaced by the despeckling filters. The manually segmented B-Mode images are compared with images delineated using the local region based active contour. The images acquired in two parasternal and three apical views along with CWD and color Doppler images are used in the analysis of segmentation techniques to high the importance of integrated analysis multi-view images.

5.1 Introduction

Echocardiographic images are acquired in B-Mode (brightness-Mode), and M-Mode (motion mode) along with Doppler based modalities namely continuous wave Doppler (CWD), pulse wave Doppler (PWD) and color Doppler (CD). The B-Mode images are visually observed using windows such as apical, parasternal or sub-costal [3, 6, 8, 9, 10, 12, 16, 18]. As stated in the earlier chapters each modality and view provides specific information, each acts as an additional tool to the other but not as a substitute [3, 62, 65, 66, 68, 216-226]. In this thesis, the images acquired from patients diagnosed with aortic regurgitation (AR) are employed for analysis of despeckling filter performances. All of them are also used for performance analysis of segmentation techniques. The B-Mode images are viewed in apical four chamber (A4C), apical five chamber (A5C), apical two chamber (A2C), parasternal long axis (PLAX) and parasternal short axis (PSAX) during the diagnosis of AR. The B-Mode, M-Mode, CWD, PWD and CD images are together used in the study of anatomy and diagnosis of AR. Chapter 2, Chapter 3 and Chapter 4 addressed the issues of despeckling TTE images in multiple views and modalities. This chapter presents an analysis of segmentation techniques for the CWD, B-Mode and CD images acquired in various views. The chapter begins with looking for segmentation techniques for the CWD images followed by B-Mode and CD images.

An overview of segmentation techniques analysed for the CWD, B-Mode, and color Doppler images are tabulated in Table 5.1. These methods are employed in delineation of various types of images as highlighted in Table 5.1. In the available literature it is highlighted that the methods in Table 5.1 can be used to delineate images with intensity in-homogeneity and low contrast. The applications of these methods are analysed for different echocardiography modality images. The methods are implemented by making use of the procedure and codes provided by the authors specified in the references in Table 5.1. In addition to these implementations, certain modifications are incorporated in methods such as reaction diffusion based active contour [184], Magagnin [195] and Kirtuthika [199] method of segmentation.

In addition to these, texture based segmentation is proposed and analysed for the echocardiographic images. The usefulness of denoising and enhancement in edge, region, multi-stage watershed [25, 170, 296, 297] and Chan-Vese [64,161] based segmentation was brought out in Chapter 2. This chapter describes segmentation of CWD, B-Mode and color Doppler images. The segmentation techniques are first analysed for the CWD images followed by B-Mode images and color Doppler images. The steps employed in the implementations of ten methods are shown in Figure 5.1 and Figure 5.2.

5.2 CWD image segmentation

Continuous wave Doppler (CWD) echocardiography is employed for measuring the high blood flow velocities across regurgitant and stenotic valves orifices [59, 197-201, 282]. The measured velocities are converted into pressure gradients using simplified version of Bernoulli equation. It is necessary to align the Doppler sound beam as parallel as possible to the flow direction for accurate measurements. The parallel orientation is achieved by taking into account the qualities of 2D image and Doppler recording. An angular deviation of 20 degrees or less can result in less than 10% errors in velocity measurements. But these smaller errors in velocity measurement reflect in huge variations in pressure gradients due to the quadratic relationship between velocity and pressure gradients [10, 282]. The outer boundaries of CWD image reflect the fast moving blood cells and hence all measurements are made taking into account the outer boundary [10].

The current US machines have inbuilt software which can provide accurate peak velocity, velocity time integral and gradients from a manually traced velocity envelope [10, 198]. The manual tracing is the major issue of concern in the CW spectra analysis because tracing depends on the experience of the operator, visual quality of the spectrum, and the viewing acoustic window [189, 190, 192-201, 282]. It is a time consuming activity embedded with inter- and intra-personal variations. The clinical outcome depends on the conclusions derived from the manual tracing of the spectrum [40, 189, 190, 192, 200, 282]. The peak velocity estimated from the manually traced envelope can result in an error of approximately larger than 25%, even by the most experienced clinicians [187]. The Doppler spectra exhibit large variations in the envelope shape and image appearance under various disease conditions and state of the cardiac valves. The automation of CW Doppler images would result in faster processing, uniformity in results with increased objectivity, and more accurate estimation of valvular abnormalities [40, 189, 192, 282].

The peak velocity was estimated from the Doppler spectrum using various thresholding techniques, but these techniques are strongly influenced by noise, hence the estimated peak value would be inaccurate [187]. Therefore, it would be desirable to suppress noise with the edges and the structures well preserved. The CW Doppler images inherit speckle noise having an adverse impact on automatic segmentation process. This problem of CW Doppler

images is identical to the issues prevailing in the B-Mode images [190]. The impact of despeckling filters on various segmentation techniques for automatic envelope extraction of CW Doppler images is being presented.

Gong *et al.* [189] had compared fuzzy based adaptive thresholding with Ostu's thresholding. Thresholding was applied on the denoised CWD images. Doherty *et al.* [194] used the Doppler signal as components of multidimensional time series infected with noise for estimation of velocity spectrum curve. Greenspan *et al.* [193] have proposed a method for automatic image analysis of Doppler velocity spectrum and it included the following steps such as enhancement of images, edge detection, extraction of envelope, linking of edges and parameter extraction. The images are enhanced using contrast stretching followed by the detection of thresholds [193].

Table 5.1 Overview of segmentation techniques for B-Mode, CWD and color Doppler images

Ref.	Year	Type	Abbreviation	Method	Application of the method
[195]	2006	Edge	Magagnin	Histogram and thresholding	Pulsed Doppler images
[287][h]	2005	Edge	SMED	Scale multiplication	Synthetic and natural
[288]	2008	Fuzzy	IFD	Intuitionistic fuzzy divergence	CT and standard images
[289][b]	2010	Fuzzy	FTS	Fuzzy soft thresholding	Head MRI, X-ray, TTE
[46, 289][a]	2005	Topological derivative	DTD	Discrete topological derivative	CT angiography, head MRI
[199]	2006	Edge	Kiruthika	Edge based segmentation	CW Doppler images
[184][c]	2013	Level set	RD	Reaction diffusion	Synthetic and MRI image
[184][c]	2013	Level set	GDRLSE1	Generalized distance regularized level set evolution	Synthetic and MRI image
[184][c]	2013	Level set	GDRLSE2		Synthetic and MRI image
[184][c]	2013	Level set	GDRLSE3		Synthetic and MRI image
[154][d]	2008	Level set	RSF	Region scalable fitting	Brain MR, Vessel image
[304][c]	2010	Active contour	LIF	Local image fitting energy	Synthetic and MRI image
[292][d]	2011	Level set	LSEBFE	Intensity inhomogeneities	CT image of Vessel
[293][e]	2010	Active contour	IVC	Regularized level set	MRI
[183][f]	2007	Active contour	GMAC	Global minimization of active	Synthetic images
[294][g]	2009	Active contour	LFE	Laplacian fitting energy	synthetic images
[175][d]	2010	Level set	SVMLS	Multiphase level set	MRI image
[295]	2007	Clustering	FCM	Fuzzy C-means	US Carotid artery
[25, 296, 297]	2009, 2011	Region	Region	Region growing	Ultrasound images, weld images
		Edge	Adaptive canny	Canny edge detection	
		Watershed	Multiwater	Multistage watershed	

a.http://www.mathworks.in/MATLABcentral/fileexchange/14224-image-segmentation-via-topological- derivative
b.http://www.mathworks.in/MATLABcentral/fileexchange/36918-soft-thresholding-for-image-segmentation
c. http://www4.comp.polyu.edu.hk/~cslzhang/
d. http://www.engr.uconn.edu/~cmli/
e. http://www4.comp.polyu.edu.hk/~cslzhang/RD/IVC_webpage/
f. https://9d5b76582b7871444743f5d0bbd439c802a638d7.googledrive.com/host/ 0B3BTLeCYLunCc1o4YzV1Ui1SeVE/codes.html
g. http://smart.nuist.edu.cn/People/khzhang/khzhang.html
h.http://www.mathworks.in/MATLABcentral/fileexchange/44141-Canny-edge-detection-enhancement-by- scale-multiplication

Magagnin *et al.* [195] had proposed a semi-automatic method for the tracing of pulsed Doppler spectrum images. The baseline and scale factor were determined using a Sobel

horizontal and vertical filters, respectively. The Doppler images were segmented using a "probabilistic, hierarchical, and discriminant" i.e. the PHD framework by Zhou *et al.* [196]. Park *et al.* [198] employed a series of detector for locating objects and shape information to segment the mitral valve inflow patterns. Syeda-Mahmood *et al.* [202] proposed a clinical decision support system for identification of spectrum shape patterns for various valvular diseases using content based image retrieval. Kalinic *et al.* [201] proposed a model-based segmentation scheme incorporating prior knowledge for extraction of spectrum envelope of Doppler images acquired at the AV during systole. The method consisted of detection of base line, maximal velocity line, and selection of threshold along with fitting of velocity curve.

Vilkomerson *et al.* [187] observed that peak velocity estimated using methods based on thresholding are strongly prone to noise. An automatic method for tracing for the outer borders of the PWD echocardiographic velocity spectrum images acquired at the aortic valve was proposed by Zolgharni *et al.* [282]. The envelope of the filtered image was obtained using biggest-gap method followed by superimposing it on the original image. The methods depicted in Figure 5.1 and Figure 5.2, employed for delineation of the outer boundaries of CWD spectrum, are described in the next few sub-sections.

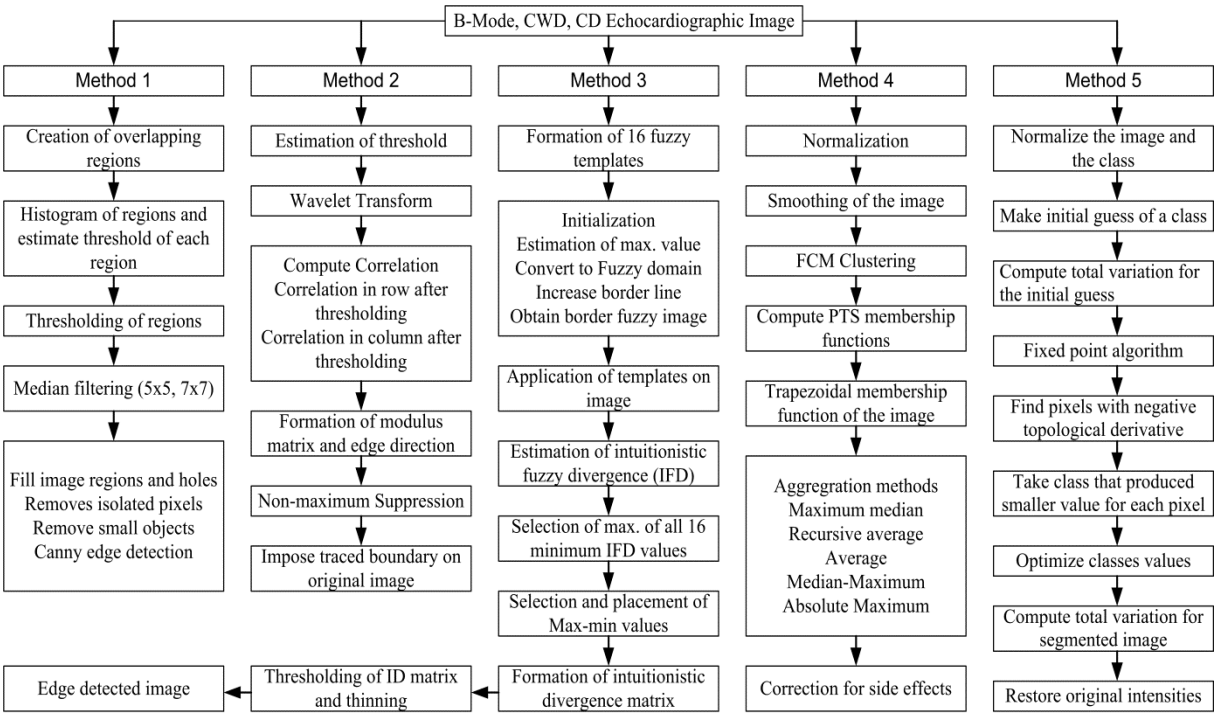

Figure 5.1 Segmentation techniques for B-Mode, CWD and CD images- Method 1 to Method 5

5.2.1 Magagnin method

Magagnin *et al.* [195] had proposed a semi-automatic method for segmentation of coronary flow Doppler images. This method is employed for segmentation of CWD, B-Mode, and color Doppler images to study their applications and suitability. The technique employed

combination of histogram, thresholding and median filter for tracing the boundaries. The steps employed in the implementation of the Magagnin's method are shown in Figure 5.1 and the method is referred to as "Method-1". The overlapping regions can be manually selected. The histogram and thresholds of each overlapping region are estimated. The thresholded images are filtered using a median filter with 7×7 windows. The image regions and holes were filled using function "*imfill*". The isolated pixels and smaller objects were removed using the function "*bwmorph*" and "*bwareaopen*". The edges in the resultant image are computed using the canny edge detection. The details of this approach are available in Magagnin *et al.* [195]. Prior to application of steps shown in Figure 5.1, the images were converted to gray scale and resized to 512×512. These steps were employed in all the ten methods shown in Figure 5.1 and Figure 5.2.

5.2.2 Scale multiplication edge detection (SMED)

A wavelet based scale multiplication edge detection (SMED) method was advocated by Bao *et al.* [287] for improving accuracy of edge detection. The location accuracy of edge detection was improved by incorporating the SMED technique [287]. The technique was analysed using the noisy synthetic, house and flower images. In this thesis the SMED method is employed for outer boundary detection in the TTE images. The fundamental steps of this technique are shown in Figure 5.1 as "Method-2". The approach includes estimation of threshold at each scale and wavelet transforms of the input image. The steps employed consist of computing the thresholds and estimating the correlation between the pixels. The correlations between pixels row-wise and column-wise are estimated on application of wavelet transform. Before estimating correlation, the wavelet coefficients are thresholded. This is followed by construction of modulus matrix and direction estimation. The estimated pixels in various directions are subjected to non-maximum suppression. The resultant image is filtered for suppression of noise. The boundaries are traced and superimposed on the original image. Details of the SMED method and its implementation steps are brought out in [287].

5.2.3 Intuitionistic fuzzy divergence (IFD)

Charia and Ray [288] proposed a distance measure called as "intuitionistic fuzzy divergence" (IFD) for edge detection in "Brain" image, "Rice" image, "Lung" image, "Aorta" image, "Pepper" image, and "cameraman" images. The IFD was based on hesitation degree, non-membership degree and membership degree. The IFD based edge detection approach is employed for tracing the boundaries of the CWD images. The approach consists of formation of sixteen templates, initialization, finding the hesitation degree, estimation of the maximum divergence, transforming fuzzy domain image to pixel domain, thresholding and morphological operations [173, 274, 288]. All the steps are shown in Figure 5.1. The

stepwise details of this approach were provided by Chaira and Ray in [289]. This method is referred to as Method-3 in Figure 5.1. The major steps of IFD techniques are: i) formation of edge-detected templates, ii) application of edge templates over the image, iii) computation of IFD between each element of every template and the image window, iv) selection of maximum of templates among the minimum IFD values, v) positioning of the maximum value, vi) selection and positioning of max-min value, vii) construction of new divergence matrix and viii) thresholding of divergence matrix and obtain edge detected image.

5.2.4 Fuzzy soft thresholding based segmentation

The fuzzy soft thresholding approach based on fuzzy aggregation methods were proposed for the medical images by Aja-Fernandez *et al.* [289]. The core idea of soft thresholding was to relate each pixel of the image with other in terms of fuzzy membership functions. This membership function was derived from the histograms of various regions in the image. Each of the pixels would thus belong to various regions with different membership functions. Thus the pixels are segregated from the noisy ones easily in any given noisy image. These aggregation methods are employed for segmentation of the CWD images. The steps used in the implementation of this method are shown in Figure 5.1. Every pixel is correlated to other pixels in various parts of the image using fuzzy membership functions instead of hard decisions like wavelet based thresholding. The fuzzy C-means (FCM) clustering is employed for sorting the pixels followed by computation of the pseudo trapezoidal shaped membership functions. Various aggregration approaches such as maximum median, recursive average, average aggregration, median maximum aggregration and absolute maximum aggregration are employed in the experimentations. This method is referred to as Method-4 in Figure 5.1.

5.2.5 Topological derivative based segmentation

The topological sensitivity provides information of the edges in the image and derivative speaks about the incremental changes in the topology. Larrabide *et al.* [46, 290] had advocated this technique to overcome iterative processing of the images. The technique was employed for segmentation of computed tomographic and magnetic resonance images. The topological derivative based segmentation is currently employed for tracing the outer boundaries of the CWD spectrum acquired from patient diagnosed with AR. The major steps of the topological derivative based segmentation are shown in Figure 5.1. The images are normalized and an initial guess is made regarding the class of the image. The total variation of the initial guess is computed followed by application of fixed point algorithm. The pixels with negative topological derivative are traced. A class is formed with smaller values for each of the pixel. The class is optimized resulting in the required segmented image. The total variation for the segmented image is estimated and the original intensities are restored. This method is referred to as Method-5 in Figure 5.1.

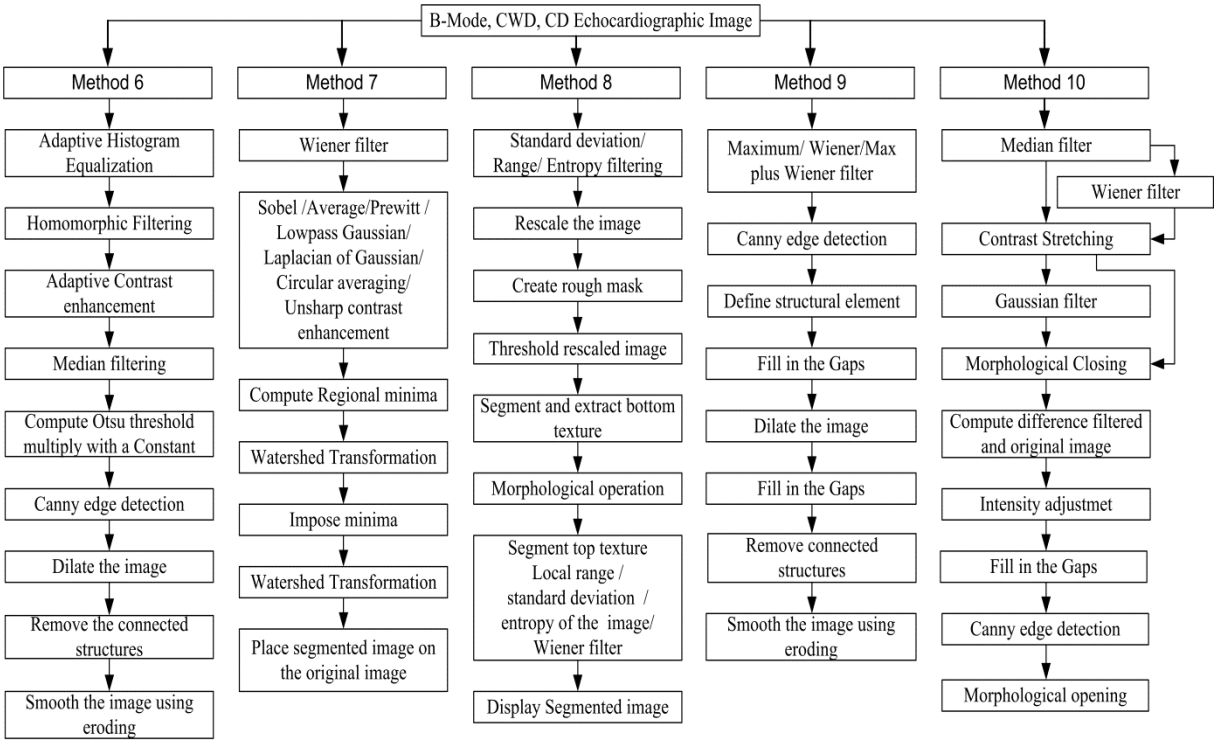

Figure 5.2 Segmentation techniques for B-Mode, CWD and CD images - Method 6 to Method 10

5.2.6 Segmentation using histogram equalization

The histogram equalization enhances the contrast of image by redistributing the gray values equally over the entire image. It enhances the contrast for the values close to histogram maxima and decreases contrast near minima [299, 300]. The histogram equalization, homomorphic filter and canny edge detection are employed for tracing the outer boundaries of the CWD images. The brightness levels of the image are equally distributed for full scale by using MATLAB function "*histeq*". The enhanced images are filtered using the homomorphic filter. On application of filtering the contrast of the image reduced and to compensate for this, adaptive contrast enhancement is performed. The enhancement is based on the difference between each pixel value and its deviation. The enhanced images are filtered using median filter with window size 7×7. The edges in the images are detected using canny edge detection. The obtained boundaries had discontinuities and unwanted objects connected to the boundary which are addressed using the morphological operations such as dilation and erosion. The resultant image is superimposed on the enhanced image. The steps incorporated in the algorithm are shown in Figure 5.2 for quick reference and better understanding. This method is referred to as Method-6 in Figure 5.2.

5.2.7 Multistage watershed transform based segmentation

The watershed transform comes under the family of region-based segmentation. It is based

on mathematical morphology. This technique combines concepts such as the shareholding, detection of discontinuities and region processing. The advantage of using watershed is, when employed at on another level will assist in forging the fragmented regions [25, 296, 297]. The images are converted to gray scale and resized to 512x512. These images are pre-processed using adaptive Wiener filter employing MATLAB inbuilt function "*Wiener2*". The pre-processed image is employed for computing the gradient where various gradient operators such as the Sobel, Prewitt, Roberts or Gaussian derivative are employed. The gradient image is sub-divided into initial regions employing gradient magnitude. The obtained edges are grouped to form a contour. The initial watershed may results in many smaller regions, often reflecting over segmentation or generating undesired smaller regions. The boundaries traced at this stage may not have same weights. The boundaries within the homogeneous regions are weaker. The neighborhood relation is employed to compare these boundaries. The neighborhood relation is in terms of the connectivity graph from the mosaic image.

The mosaic image is further thresholded by using the Otsu's thresholding approach. The thresholded image is converted into a binary image. The morphological operations and watershed top hat transformation are employed to compute the bright objects present in the image. The peak values which significantly differ from the local background are estimated. The partially overlapping regions are separated using the Watershed. The smaller objects are weeded out using morphological operations. The Euclidean distance map (EDM) is computed for the resultant image. At the point of overlap in the resultant binary image, the inverse EDM has a ridge with the overlapping of two catchment objects. Hence, every basin is labelled uniquely and ridge separating them as watershed. The resultant labelled image is eroded to match the content and background borders. This also overcomes the false separation of the overlapping segments. The marked region provided the shape of ROI with the boundaries marked. The smaller regions with some homogenous intensity characteristics are merged. Thus, the multistage watershed transform based segmentation provided better tracing in comparison to the edge and region growing based delineation.

5.2.8 Segmentation using texture filters

The texture based filters play important role in the boundary detection of the images [300, 301]. The three texture filters available in MATLAB namely "*stdfilt"*, "*rangefilt"* and "*entropyfilt"*, are employed for CWD image segmentation. The steps employed in implementation of texture filter based segmentation are shown in Figure 5.2 as Method-8. This method is implemented in two stages. The bottom and top textures are extracted in two stages using the texture filters like the range filter, standard deviation filter and entropy filters. The resized, gray scale input image is filtered using one of the texture filters and then image is rescaled followed by thresholding.

A rough mask for the bottom texture is created and the rescaled image is thresholded. The extracted bottom texture is morphologically processed using the MATLAB function "*imopen"*. The rough mask is employed to segment the top texture using one the texture filters. Various combination of the texture filters such as "rangefilt + rangefilt", "stdfilt + stdfilt", "entropyfilt + entropyfilt", "rangefilt + stdfilt", "entropyfilt + rangefilt" and other combinations are used in the experimentation to find which combination results in the best results.

5.2.9 Segmentation using adaptive and maximum filter

The combination of maximum filter, adaptive Wiener and canny edge detection are employed for segmentation of the CWD images. The CWD images are denoised using the combination of maximum and adaptive Wiener filter. Implementation steps of this approach are shown in Figure 5.2 as Method-9. The despeckled images are subjected to canny edge detection and morphological operations for tracing the outer boundaries. The other edge detection techniques such as Sobel, Prewitt and Roberts are also tested. It is observed that performance using canny edge is better; hence results based on this are presented. The results of sequential combination of adaptive Wiener and maximum filter followed by canny edge detection stood out. The morphological operations are performed for the reasons already discussed in watershed based segmentation.

5.2.10 Kiruthika method of segmentation

Kiruthika *et al.* [199] had proposed a method for tracing outer boundaries of the CWD images during AR. This method employed the combination of median filter, contrast enhancement, Gaussian filter, morphological operations, intensity adjustment and canny edge detection for tracing the outer boundaries of CWD spectrum. The performance of adaptive Wiener filter is superior compared to Gaussian filter in terms of speckle noise suppression and edge preservation. The necessities of Gaussian filter after contrast enhancement is overcome in this thesis. The images are initially filtered using a median filter followed by the Wiener filter. The images are processed using the morphological closing operation and then the intensities are adjusted using inbuilt function "*imadjust*" and "*imfill*" operations. The edges in the resultant image are obtained using canny edge detection combined with morphological opening operation. Finally the output image is superimposed on the enhanced image. The steps employed in implementation of modified Kiruthika's method are shown in are shown Figure 5.2 as Method-10.

5.3 Proposed delineation techniques for CWD images

The performances of three methods namely Kiruthika *et al.* [199], Magagnin *et al.* [195], and reaction diffusion (RD) [184] are improved by replacing the Gaussian filter with despeckling

filters. The major steps employed in implementation of these techniques [195], [199], [184] are shown in Figure 5.3 to Figure 5.5 highlighting the changes incorporated.

5.3.1 Modified Magagnin method

The semi-automatic method advocated by Magagnin *et al.* [195] consisted of dividing the image into overlapping regions and these regions are manually selected. The histogram and threshold of each overlapping region are being computed. The thresholded images are filtered using a 7×7 window based median filter. Further, the image regions and holes are filled followed by removing the isolated pixels and smaller objects. The edges in the resultant image are computed using the canny edge detection. The boundaries of CWD images are not fully traced using the Magagnin's [195] method. The median filter preserves the texture while retaining the noise. To improve the performance of this method, the median filter is sequentially combined despeckling techniques as shown in Figure 5.3. The noise retained in the median filtered image is suppressed using the despeckling techniques discussed in the earlier section.

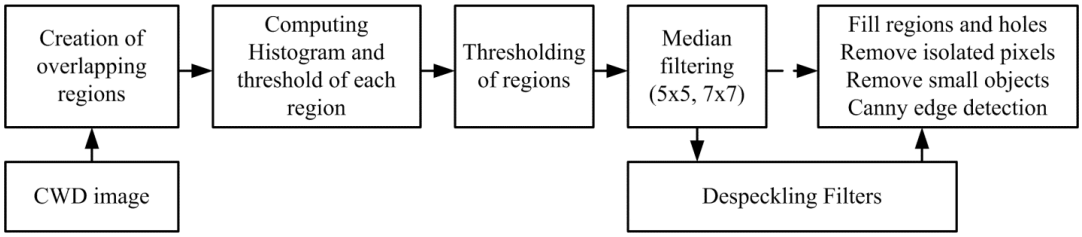

Figure 5.3 Modified Magagnin's method for delineation of CWD images

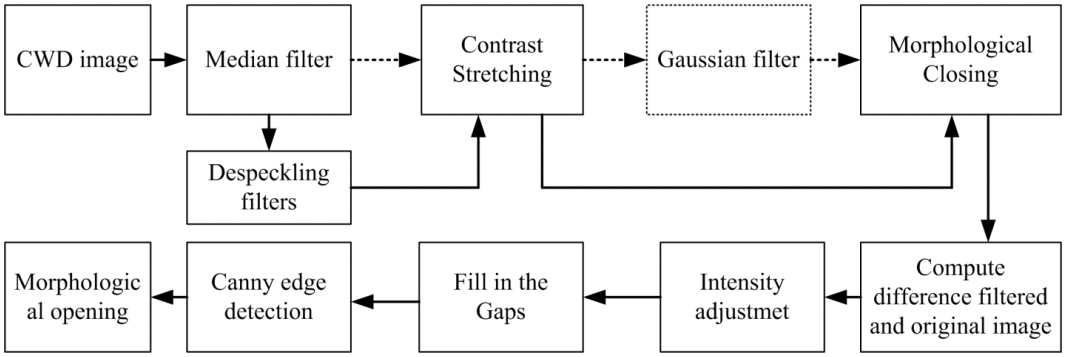

Figure 5.4 Modified Kiruthika's method for delineation of CWD images

5.3.2 Modified Kiruthika method

Kiruthika *et al.* [199] had proposed an automatic method for delineation of the boundaries of CWD images during aortic regurgitation. This method is modified and proposed modifications are shown in Figure 5.4 where the output is further refined using despeckling filters in-place of median filter. This step can be visualized in Fig.3. The need of Gaussian filter is overcome in the modified Kiruthika's method. The images are processed using the morphological operations and then the intensities are adjusted. The edges in the resultant image are

obtained using the Canny edge detection combined with morphological opening operation. Finally the boundary traced is superimposed on the original image.

The active contours are commonly used in the segmentation of medical images [184, 291, 303]. The computational burden of re-initialization was overcome by embedding diffusion term in the level set evolution process by Zhang *et al.* [184]. The reaction-diffusion (RD) based active contour technique is free from re-initialization and can be employed for delineation of images in the presence of intensity in-homogeneity. The need for re-initialization is overcome using the RD based segmentation technique. A diffusion based term was introduced into the level set evolution. The solution is a piecewise constant. A two step splitting method is employed in estimation of stable solution of the RD based LSE. The two steps are iterating the level set evolution, solving the diffusion equation, and regularizing the level set function to ensure stability. The CWD images have intensity in-homogeneity and poor contrast. Therefore, it is proposed to analyze the application of RD based active contour for segmentation of CWD images. The only modification is usage of despeckling techniques in place of the Gaussian convolution filter. All the steps are on similar lines as advocated by the authors in [184] and the MATLAB code provided by the authors are being used in implementations.

5.4 Segmentation in the presence of intensity in-homogeneity

5.4.1 Local image fitting (LIF) energy

An active contour based segmentation technique was proposed by Zhang, Song and Zhang [304] to smooth the level set function (LSF), overcome re-initialization, and reduce computational burden in the presence of intensity in-homogeneity. The technique embedded the local information of the image into region based active contour. A local image fitting energy function was introduced for extraction of local image information. The Gaussian filtering was embedded in the technique for smoothening of the LSF. The major steps incorporated in the implantation of the technique were initialization of the LSF to be binary function, evolution of the LSF, regularization of the LSF using Gaussian filtering, and verification whether the evolution is stationary. If the evolution is not stationary the steps are repeated. This technique was analysed by Zhang, Song and Zhang [304] for the hand phantom, synthetic and brain MR images in the presence of intensity in-homogeneity.

5.4.2 Level set evolution and bias field estimation (LSE-BFE)

Li *et al.* [292] proposed a level set method for segmentation of images with intensity in-homogeneities. A region based level set method was advocated for segmentation of images and corrections in the intensity in-homogeneity. The method had advocated a clustering objective function for handling the image intensity in-homogeneities in neighbourhood around

every point, and this function was integrated over the entire domain. This was incorporated in a variational level set formulation. A local intensity clustering property is derived taking into account the intensities of neighbourhood of every pixel. The energy function is defined based on the local clustering criterion integrated over neighbourhood center. The energy function is transformed into the level set framework. The minimization of energy is achieved by the interleaving procedure of the LSE and bias field estimation (BFE). The method is analysed by using the synthetic images, and Doppler images. This technique was employed for MRI and synthetic images segmentation by Li *et al.* [292]. In this thesis, B-Mode, CWD and color Doppler images are used to study the applications and suitability of LSE-BFE.

5.4.3 Image Laplacian fitting (ILF)

A variational level set formulation for segmentation of noisy synthetic and real vessel images, in the presence of intensity in-homogeneity was advocated by Zhang *et al.* [294]. The image Laplacian was employed in constructing the energy functional. The zero crossing of the image Laplacian was considered as the desired boundary of the object segmented. To further improve the performance in the presence of noise total variation for the image Laplacian was integrated into the delineation process.

5.4.4 Statistical and variational multiphase level set (SVLMS)

A variational level set based on simultaneous segmentation and bias correction was put-forth by Zhang, Zhang and Zhang [175] for the MR images. The technique was considered to be robust to initialization. The technique was based on the concept of simultaneous segmentation and bias correction. The intensity distribution in an image was modelled as the Gaussian distribution with varying mean and the variance. The image transformations to another domain with overlapping distribution are significantly curtailed. A maximum likelihood objective function is defined for each point in the transformed domain. The integration of this function defined the variational level set function.

5.4.5 Two phase locally statistical method (2phaseLSM)

A statistical active contour model was advocated by Zhang *et al.* [305] for segmentation of images in the presence of intensity in-homogeneity. The in-homogeneous objects were modelled in the algorithm as Gaussian distributions of different mean and variance. A moving window was being employed to project the image into another domain. The intensities in the projected domain exhibited Gaussian characteristics but were better segregated also. The mean of Gaussian distribution in the transformed space is estimated as the product of bias field and the original values in the window. The energy function of each region is defined based on the combination of bias field, level function and constant approximation of true values.

5.5 Region based active contour

5.5.1 Selective Binary and Gaussian filtering level set

The image segmentation is an important computer vision problem. The geodesic active contours employ the image gradients in construction of edge stopping function to stop the contour evolution process. Some of the active contour techniques employ a balloon force term for shrinkage and expansion of the contour. But, it is quite difficult to construct a balloon force. The placement of initial contour, size of the balloon and local minima estimation decide how accurately the inner and outer boundaries are traced. To overcome drawbacks of these methods, region based active contours were proposed and analysed by various authors. The Chan-Vese method can detect all the objects in the image. The geodesic active contour (GAC) can be employed for extraction of objects when the initial contour surrounds the boundary. Hence, it fails to detect the interior contours without setting the initial one side of the object. Zhang *et al.* [293] had proposed a region based active contour method using selectively penalization and Gaussian filtering to regularize the LSF. Both inner and outer boundaries of the region of interest and all other objects were delineated. The signed pressure force (SPF) function was constructed by using statistical information of the contour, both inside and outside. The SPF was employed for contouring the direction of evolution. This technique avoids computing signed distance function and re-initialization. It employs selective step in penalizing the level set function to be binary and employ Gaussian filter to regularize it. The Gaussian filter was employed for smoothening of level set evolution and making evolution stable. This technique is also known as IVC in this thesis.

5.5.2 Local region based active contour

The region based active contour method was reformulated in local way by Lankton and Tannenbaum [174] for segmentation of synthetic and MR images. An initial mask is defined. The local variables were computed by filtering operations instead of iterative procedures. A square window is being used for localization. The initializations were represented by a binary image. The coefficients necessary for balancing the image fidelity and curvature regularization are estimated. The assumed framework for segmentation took into account both foreground and background instead of the global region models. This allowed the analysis of smaller local regions, removing assumption of global representation using the global statistics.

5.5.3 Global minimization of active contour model (GMAC)

The major issue of local minima in the active contour energy in the variational framework was addressed by Bresson *et al.* [183] through global minimization of active contour model (GMAC). This method is the integration of image denoising and segmentation approaches in

a global minimization framework. It was the unification of snake model, total variation denoising and Mumford-Shah segmentation. It was observed that the snakes are highly sensitive to initialization. A good initial condition was related to non-convexity of the energy function to be minimized and the prevalence of local minima. The presence of local minima prevents meaningful segmentation. To address these issues the global minimization of active contour models are advocated. The unification of denoising with segmentation results in the global minimization solution in the presence of intensity in-homogeneity. The traditional issue of contour propagation was resolved using the dual formulation of total variation norm. The distance function was computed as a solution of the LSF that does not remain stationary during evolution process. The GAC model was unified with the active contour in the global minimization framework for detection of same time object edges. The method is fast, easy to implement, independent of initialization and behaves as an improved version of the Chan and Vese (CV) model.

5.5.4 Active contour without edges

The CV model is regarded as the special case of the Mumford-Shah model based on minimum partition problem. The model is based on attempting to separate the image into various regions based on the intensities. The active contour is sensitive to the initial positions. It is useful to determine the LSF not for the whole image domain but in a narrow band near the contour. The cartoon version of the MS model is the Chan-Vese model, where image intensities are assumed to be piece-wise constant. It is a region based geometric active contour based method of image segmentation. As the snakes are highly dependent on the image gradient they perform poorly on the smooth images. The CV model does not depend on the edges. It divides the image into two regions namely the region inside the curve and region outside the curve. The curve is said to be at the boundary of the object if no differences are observed between the curve inside and outside. The CV method divides the image into the regions and each region is represented as piecewise constant. The CV seeks the desired segmentation as best piecewise constant approximated to the given image. The good performance of the CV model is because of its ability to obtain a larger convergence range and handle topologically changes naturally. The built in masks such as the “small”, “medium”, “whole”, and “whole + small” are used in experimentations.

5.5.5 Level set evolution without (LSW) re-initialization

Li *et al.* [306] advocated a level set evolution (LSE) technique without re-initialization. This was based on variational formulation using the geometric active contours. The level set function was brought very close to the signed distance function. The method consisted of internal and external energy terms. The internal energy term was employed for penalizing the deviation of the level set function from the signed distance function. The external energy term

drives the zero level set towards the desired features in the image. The method is referred to as “LSW” in the result analysis. The LSW technique was employed for segmentation of synthetic and the US carotid artery images. This technique is employed for segmentation of CWD, MM, CD and B-Mode images acquired in multi-views.

5.6 Results

The TTE images acquired using B-Mode, color Doppler and CWD imaging modalities are used in the comparative analysis of segmentation techniques. The basic objective of this exercise is to study the suitability of various segmentation techniques in tracing the boundaries of images acquired in multiple views.

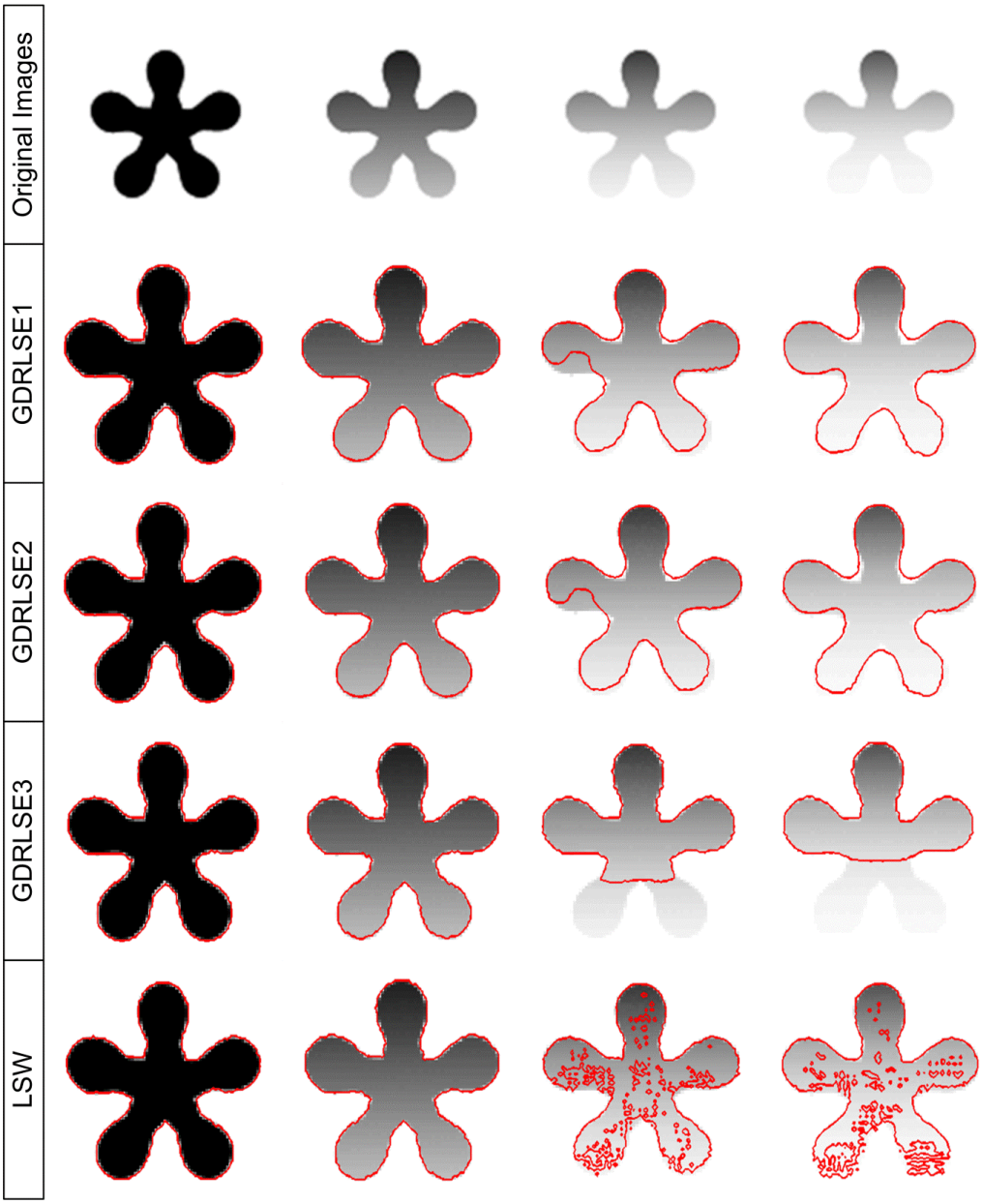

Figure 5.5 Segmentation of synthetic images using GDRLSE techniques

The performances of texture filter based segmentation, modified Kiruthika's method, modified Magagnin's method and modified RD based methods are proposed and analysed for the TTE images in this thesis. The results obtained for the synthetic images with different amount of intensity in-homogeneity are shown in Figure 5.5 to Figure 5.11. These images consisted of increasing amount of intensity in-homogeneity starting with full homogeneous image. The objective of segmenting the CD images is to effectively trace the regurgitant area in the left ventricle out flow tract.

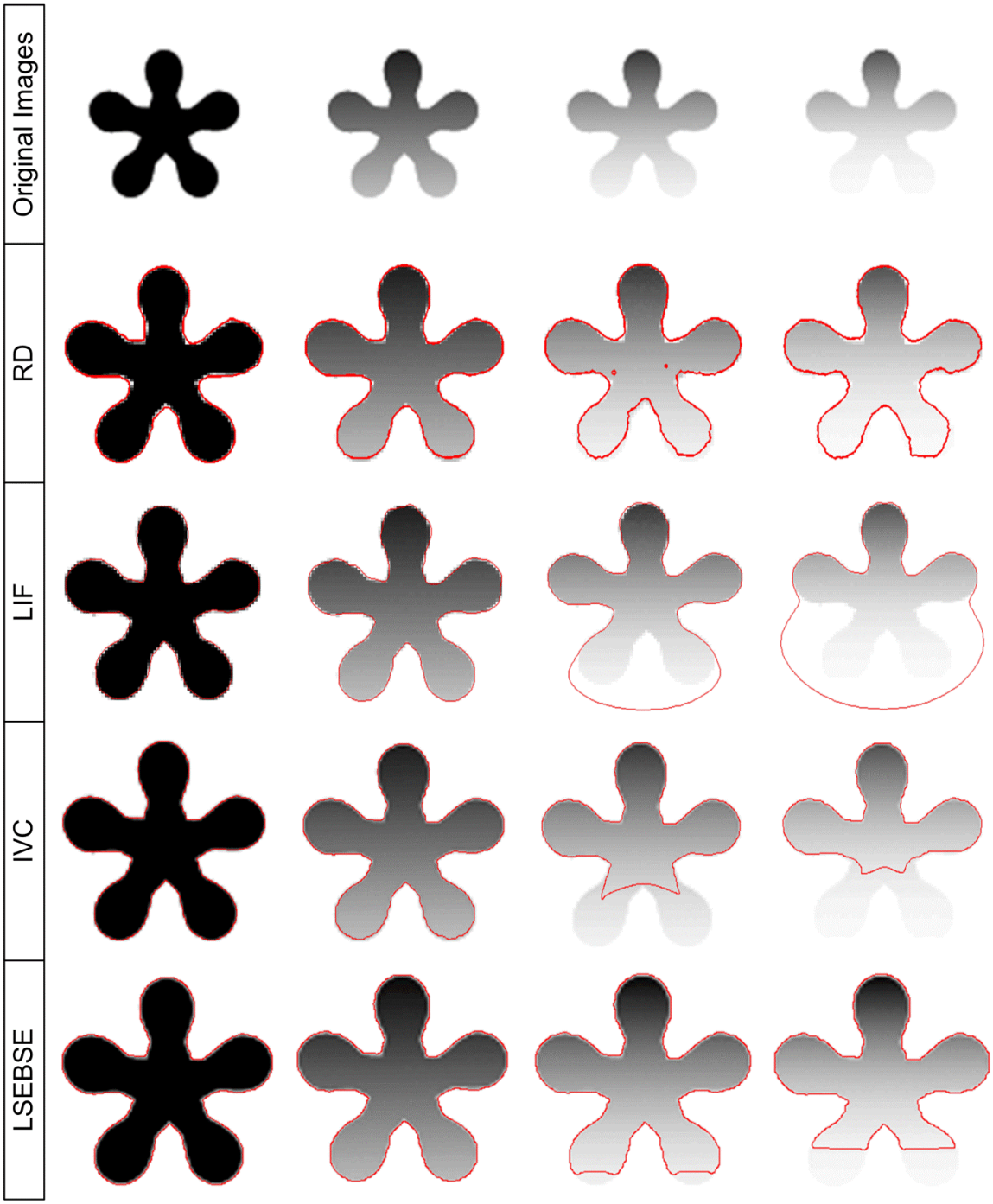

Figure 5.6 Segmentation of synthetic images using RD and other techniques

The effective regurgitant orifice area reflects the severity of regurgitation. The results obtained by employing the methods are shown in Table 5.1 for the CD images are shown in Figure 5.12 to Figure 5.16. The color Doppler images acquired in the apical five chamber (A5C) and parasternal long axis (PLAX) are employed for analysis of the segmentation techniques. The B-Mode images acquired in two parasternal and three apical windows are employed in the analysis of segmentation techniques. The objective of segmenting the images acquired in apical window namely A4C, A5C and A2C is to trace the inner boundary of the left ventricle. The left ventricle gets dilated during AR. The PLAX images are segmented to trace the boundaries of aortic and mitral valve leaflets. The inner and outer boundaries of aortic valve, which will aid in computing the aortic valve area, are traced using the images acquired in the PSAX.

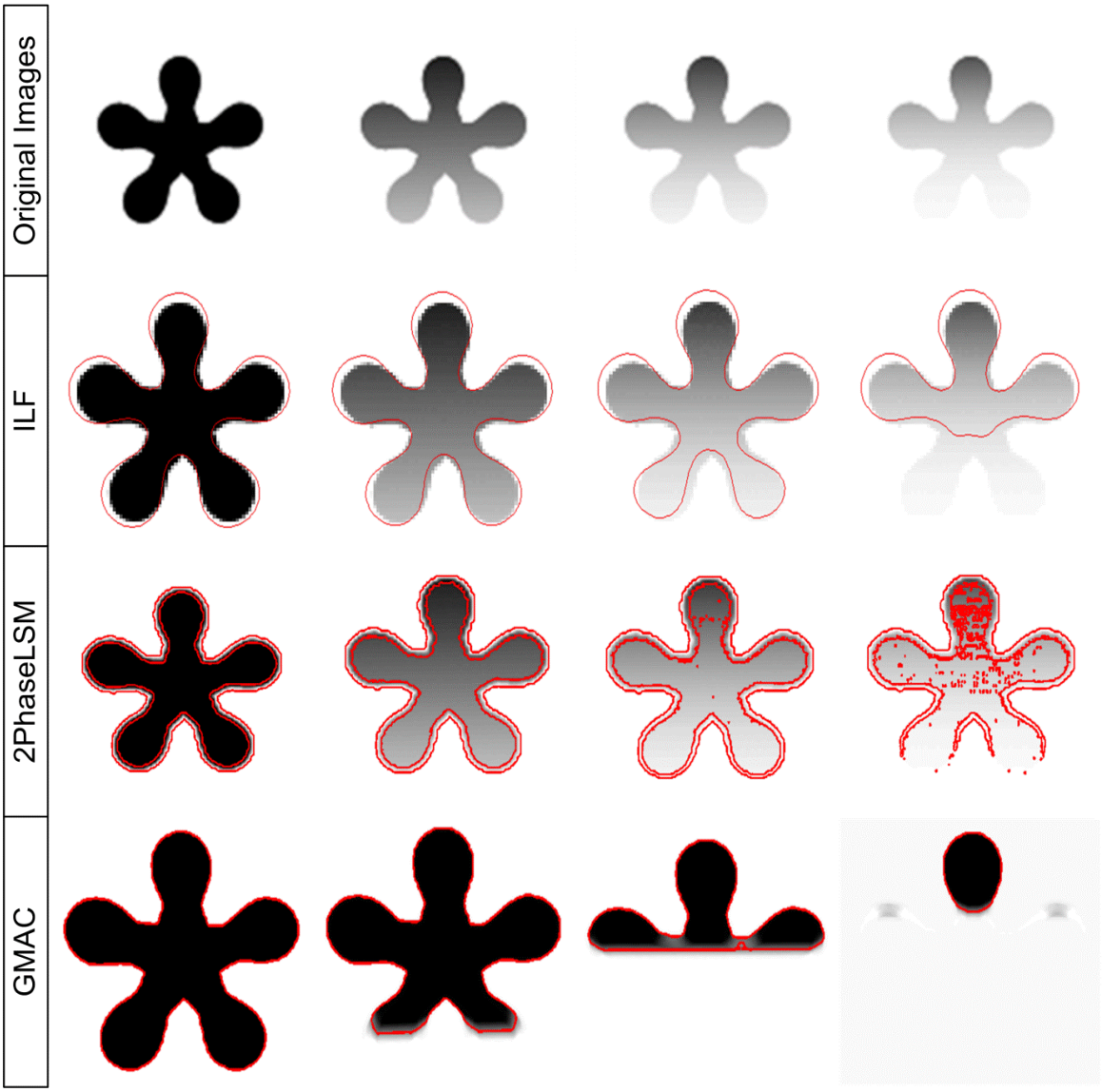

Figure 5.7 Segmentation of synthetic images using ILF and other techniques

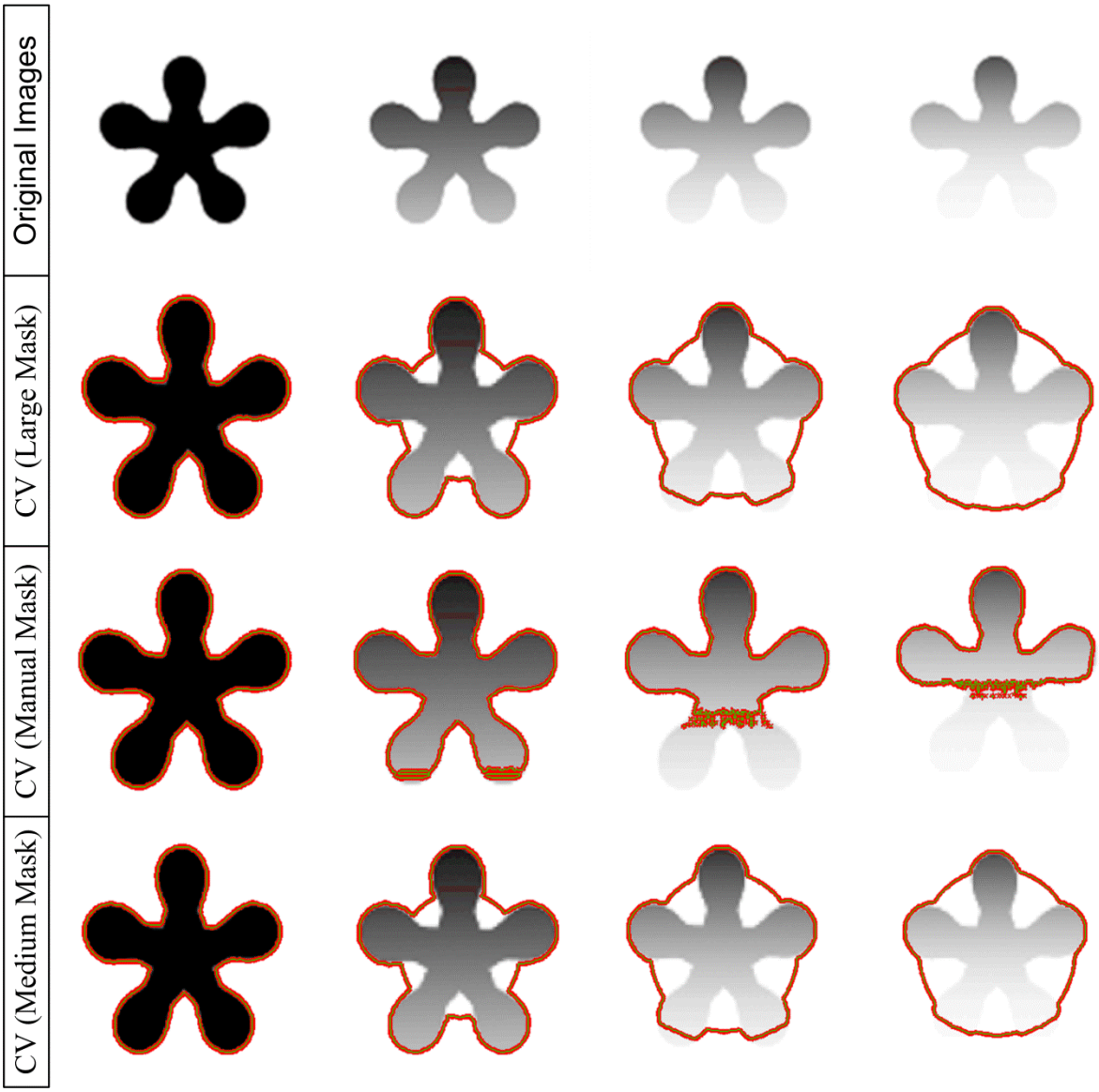

Figure 5.8 Segmentation of synthetic images using CV techniques

The results obtained on application of various segmentation techniques on B-Mode TTE images are shown in Figure 5.17 to Figure 5.25. The manually traced images are compared with boundaries delineated using the local region active contour technique in Figure 5.26 and Figure 5.27. The clinicians are requested to trace the boundaries using the MATLAB free hand tool. The clinical manually traced images are compared with boundaries of images on application of region based active contour and reaction diffusion based segmentation. The CWD images acquired from the adult patients diagnosed with AR are used for the applications of segmentation techniques on Doppler images. The results obtained using various segmentation techniques for the CWD images are shown in Figure 5.28 to Figure 5.33.

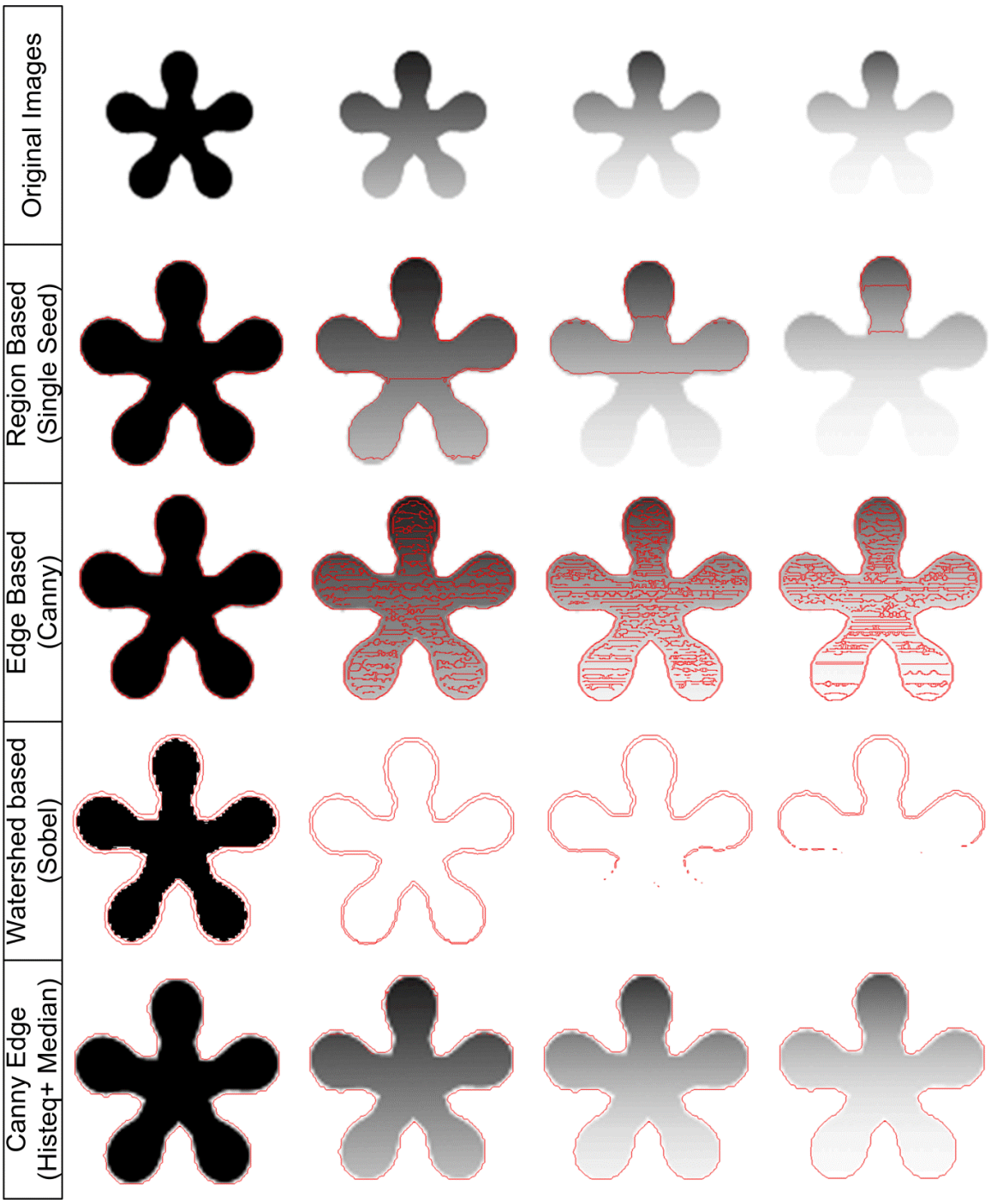

Figure 5.9 Segmentation of synthetic images using region based and other techniques

The performance of segmentation technique based on the combination of texture filters for CWD images are presented in Figure 5.34 and Figure 5.35. The results of modified Magagnin and modified Kiruthika method are shown in Figure 5.36 to Figure 5.38. The performances of modified RD method using various despeckling methods are shown in Figure 5.39 to Figure 5.40. The results obtained for synthetic images using GDRLSE, and LSW techniques are shown in Figure 5.5. The performance of GDRLSE technique is superior in comparison to the LSW techniques.

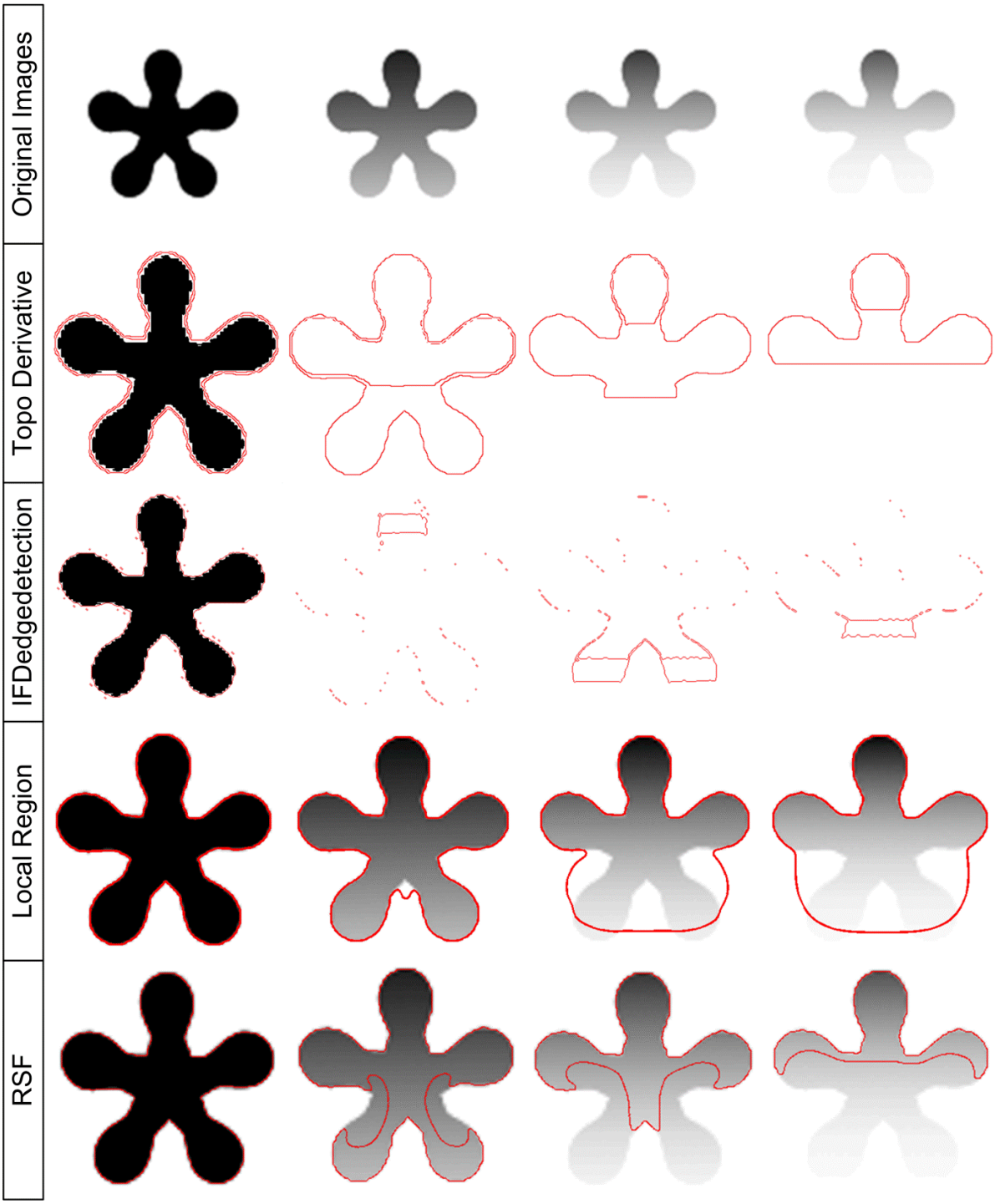

Figure 5.10 Segmentation of synthetic images using topological derivative and other techniques

Complete boundaries are traced even in the presence of intensity in-homogeneity. The segmentation results for RD, LIF, IVC and LSEBFE technique are shown in Figure 5.6. The performance of RD and LSEBFE technique are better in comparison to LIF and IVC techniques. The performance of LSEBFE and RD is degraded when the intensity in-homogeneity is high as observed in segmented images shown in third and fourth column of Figure 5.6.

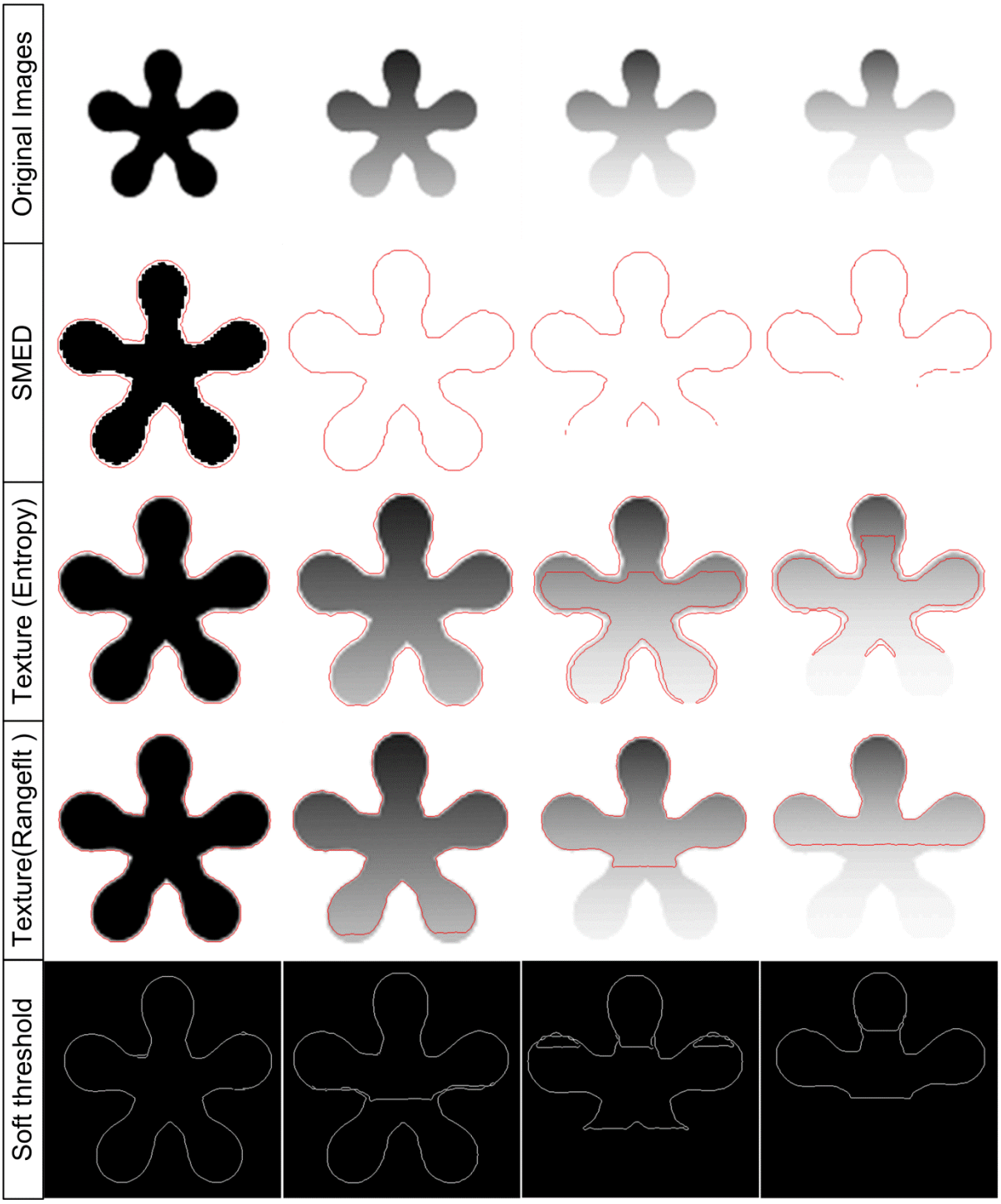

Figure 5.11 Segmentation of synthetic images using SMED and other techniques

The segmentation results on application of ILF, 2phaseLSM and GMAC techniques are depicted in Figure 5.7 for synthetic images with various amount of intensity in-homogeneity. The performances of these techniques are superior for the images with homogeneous intensity. The performance is drastically degraded as observed in third and fourth column of Figure 5.7 due to the intensity in-homogeneity. The boundaries traced using the ILF technique are slightly away from the actual image boundaries as observed in the

second row of Figure 5.7. The results of CV technique using inbuilt and manual selected mask are shown in Figure 5.8. The technique fails to trace the boundaries in the images with intensity in-homogeneity. The boundaries of the homogenous ROI are fully traced as seen in the first column of Figure 5.8. It fails in the presence of intensity in-homogeneity as observed in last three columns of Figure 5.8.

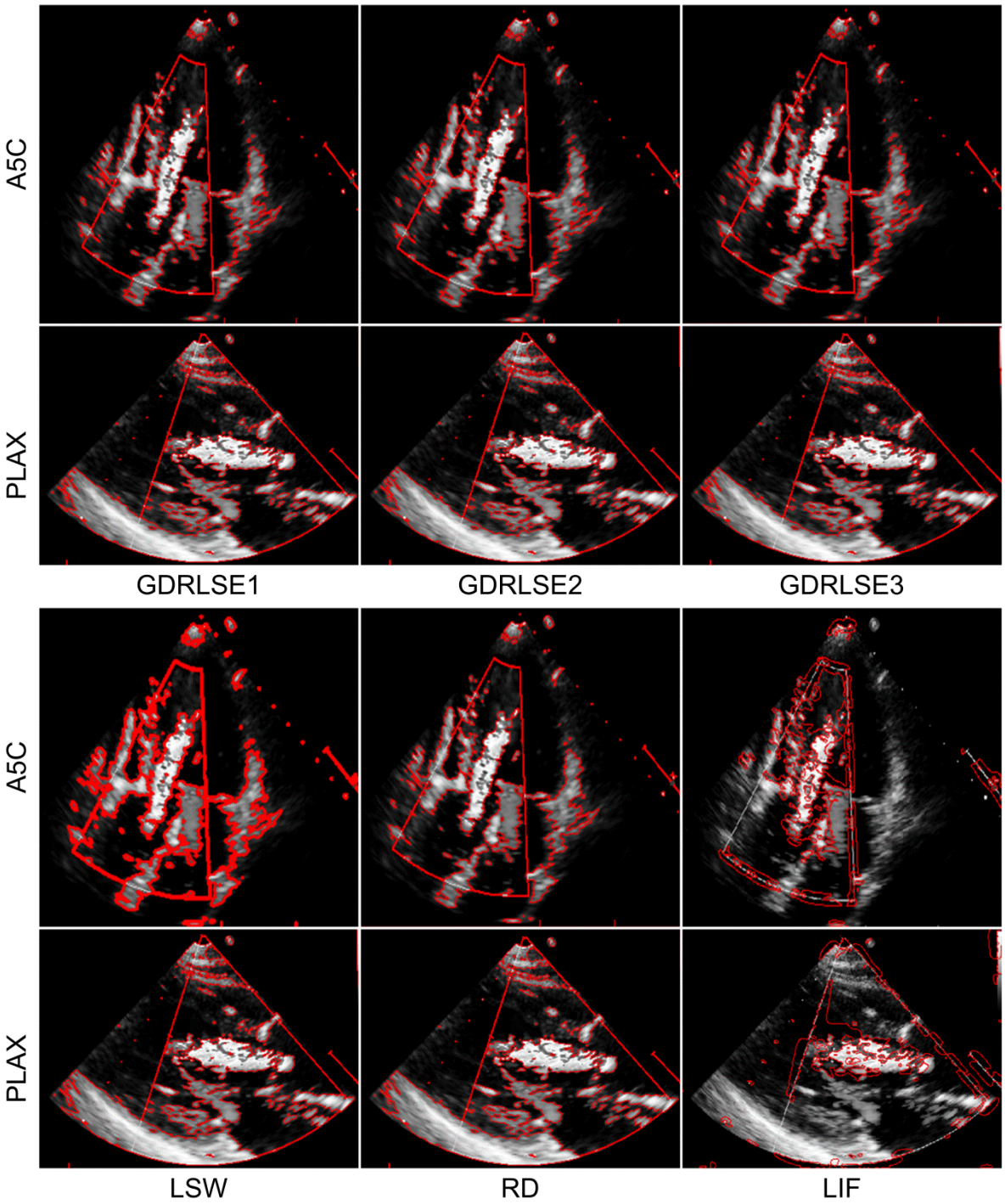

Figure 5.12 Segmentation of color Doppler images using ILF and other techniques

The application of region based, edge based, watershed and adaptive edge detection are shown in Figure 5.9. A seed is manually passed on the region based technique. Canny edge

detection and morphological operations are used in the edge based techniques. The results of watershed transform with Sobel edge detection are shown in fourth row of Figure 5.9. The adaptive edge detection which combines histogram equalization and median filtering are shown in last row of Figure 5.9. The boundaries traced using the adaptive edge detection is superior in comparison to all techniques in Figure 5.9.

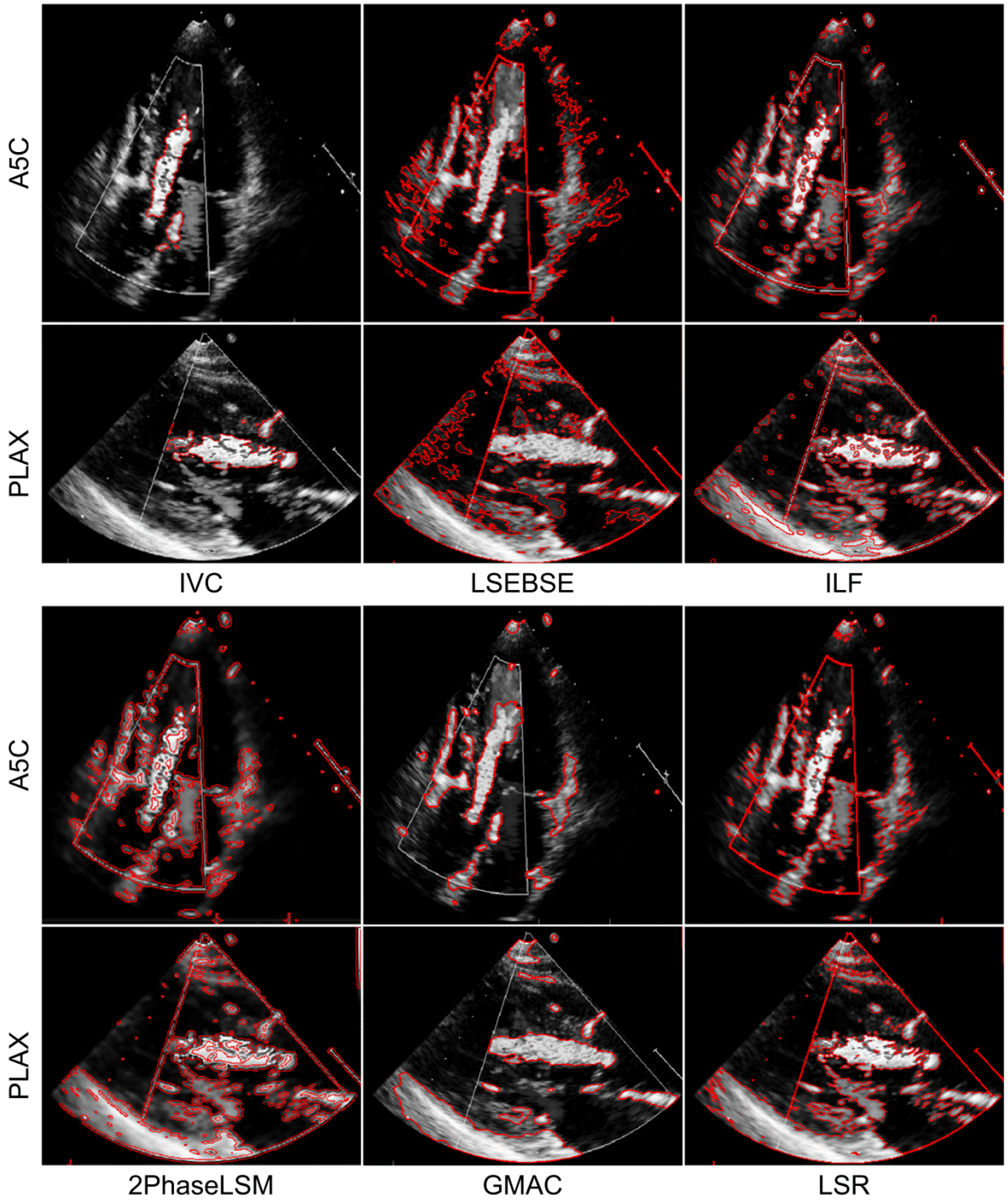

Figure 5.13 Segmentation of color Doppler images using IVC and other techniques

The performances of techniques such as topological derivative, IFD edge detection, local region active contour and region scale fitting techniques are shown in Figure 5.10. The

results reveal that these techniques fail to trace complete boundaries in the images with non-uniform intensities. It is further observed that the local region based active contour can trace complete boundaries but the number of iterations and computational time required is quite high. The performance of the techniques such as the SMED, texture based, and soft thresholding using fuzzy aggregation are shown in Figure 5.11 for the synthetic test images. The borders traced are complete in the first and second column of figure 5.11. These techniques cannot be used when the intensity variations are non-homogeneous.

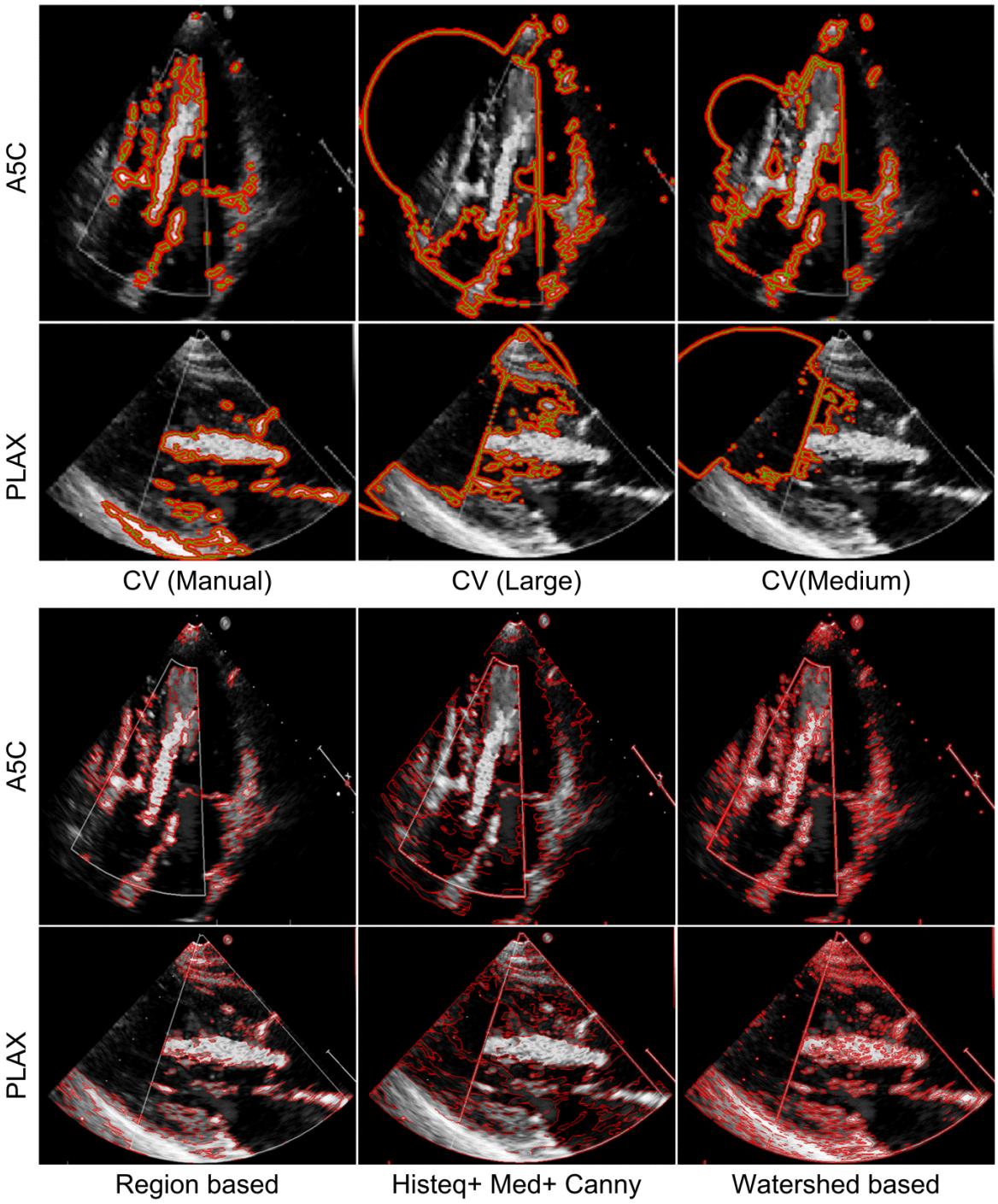

Figure 5.14 Segmentation of color Doppler images using CV and other techniques

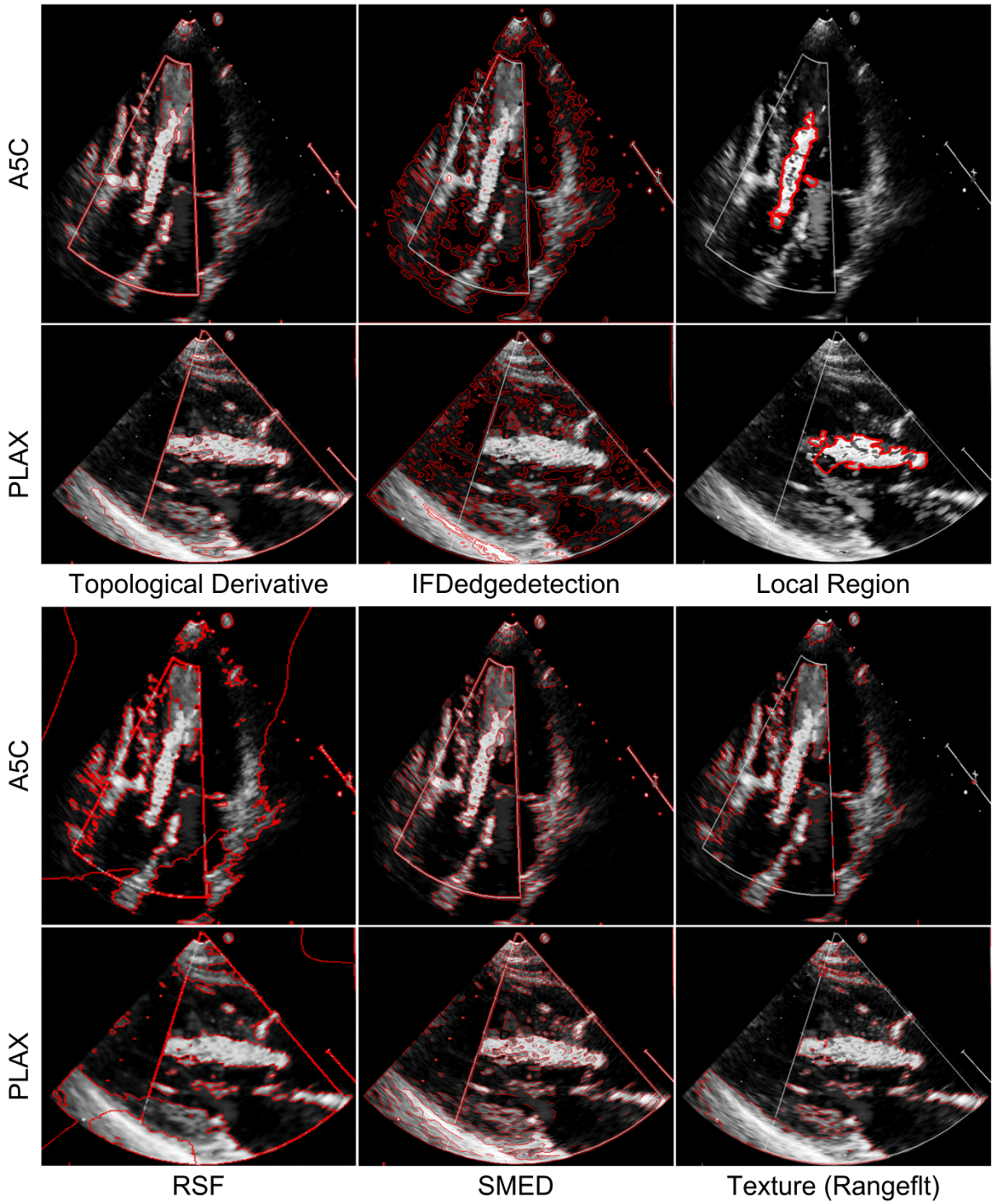

Figure 5.15 Segmentation of color Doppler images using topological derivative and other techniques

During AR there is leakage of blood in the reverse direction from the aortic valve into the left ventricle. The severity of leakage is assessed by measuring the extent of flow in backward directions. The regurgitant area is traced from the images in PLAX and A5C and the results are shown in Figure 5.12 to Figure 5.16. The results of GDRLSE, LSW, RD and LIF are shown in Figure 5.12. The outer boundary of the regurgitant area and LV are traced using the GDRLSE and RD techniques.

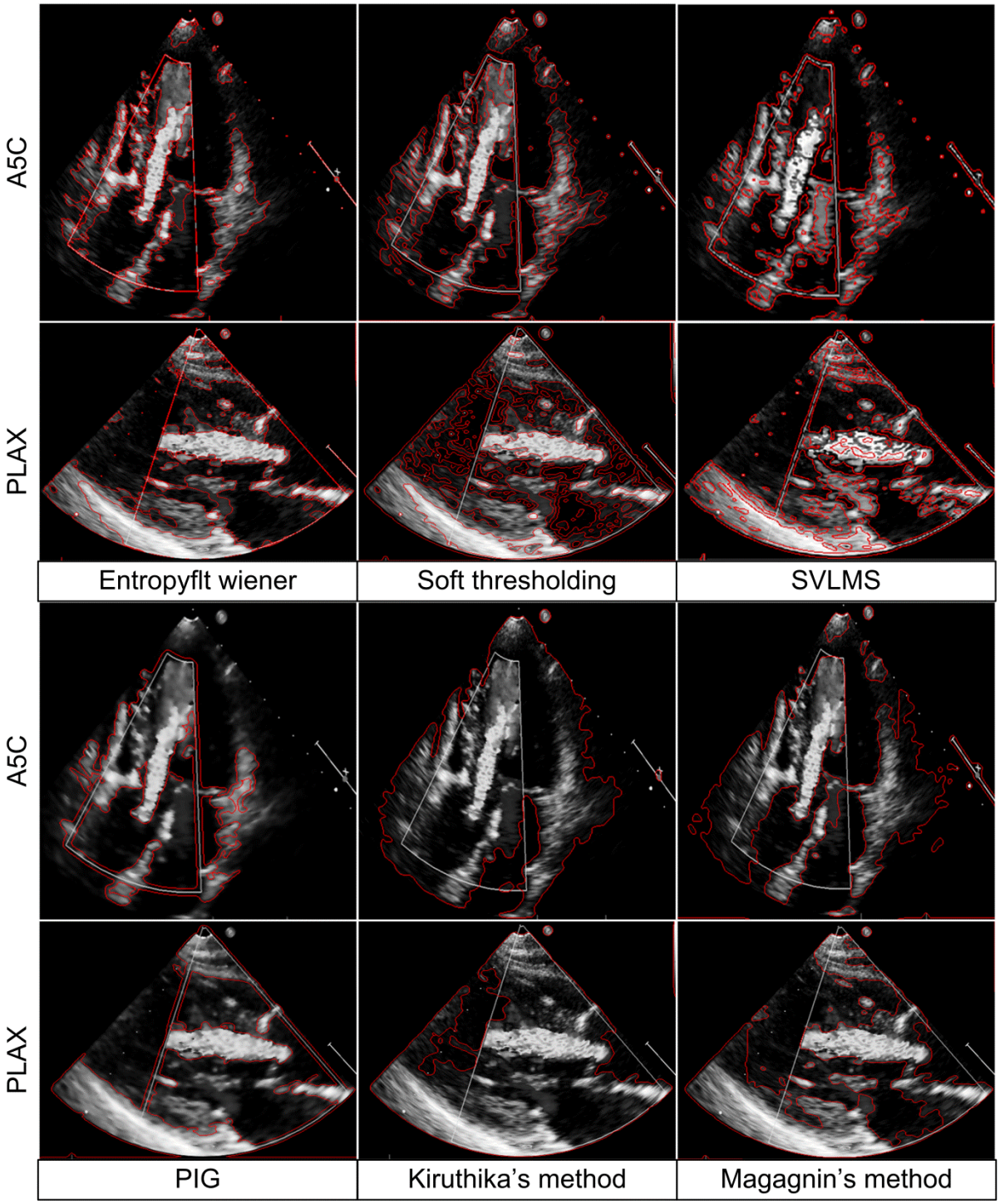

Figure 5.16 Segmentation of color Doppler images using SVLMS and other techniques

If only regurgitant region is to be traced then these techniques fail. The performance of IVC, LSEBSE, ILF, GMAC, 2phaseLSM and LSR techniques are shown in Figure 5.13. The IVC and GMAC techniques are able to trace the regurgitant area better and completely in comparison to techniques shown in Figure 5.13. The performance of CV and other techniques are shown in Figure 5.14. The region based technique with one seed and CV with manual mask selection are able to trace the region of interest better compared to other

techniques. The regurgitant area traced using the local region based active contour (LRAC) is the best result observed in Figure 5.15.

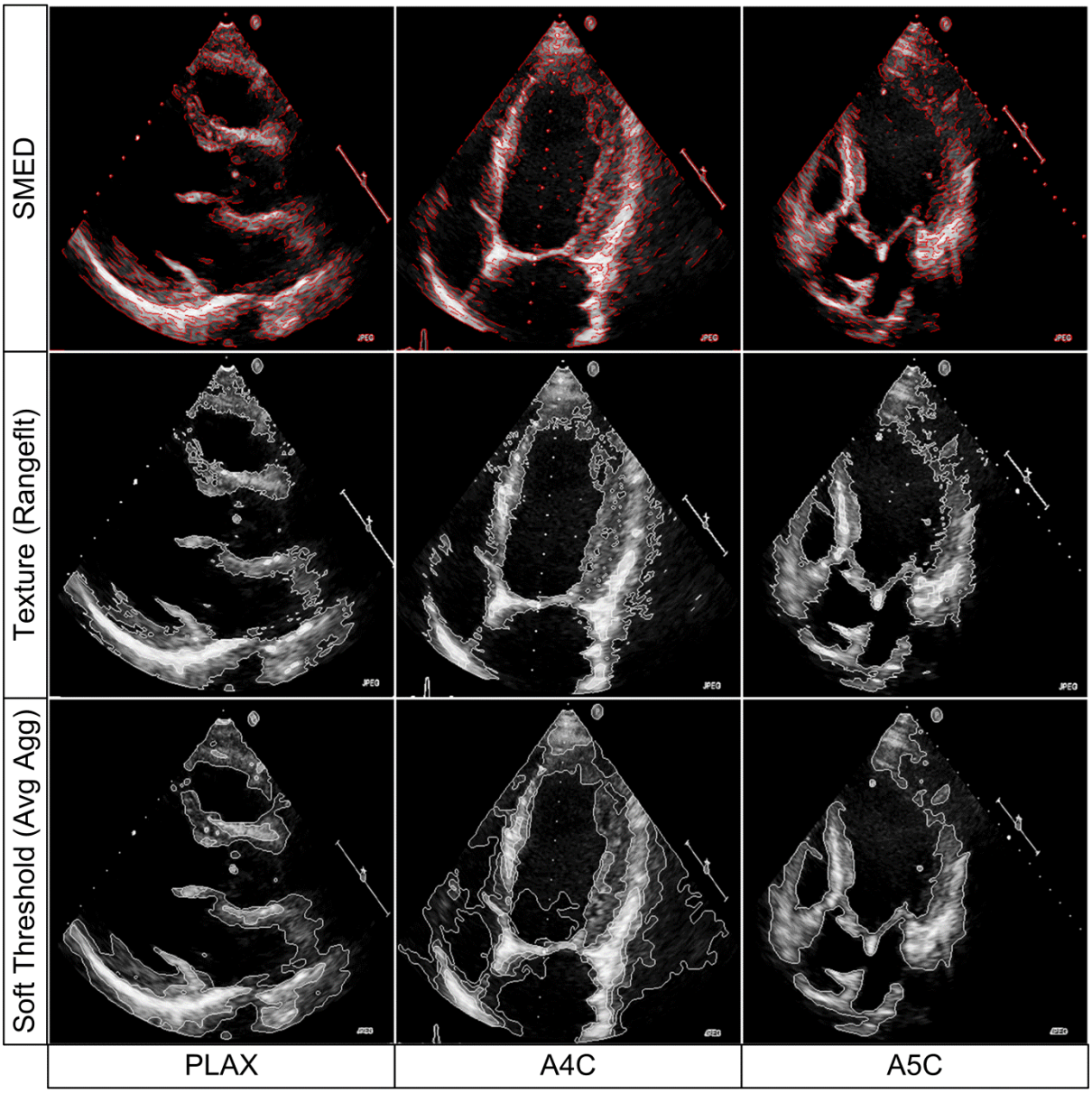

Figure 5.17 Segmentation of B-Mode images using SMED and other techniques

The performance of LRCA stands out in comparison to the topological derivative, IFD edge detection, RSF, SMED and texture filter based segmentation techniques shown in Figure 5.15. The results shown in Figure 5.16 reveal that the methods such as entropyfilt, soft thresholding, SVLMS, PIG, Kiruthika and Magagnin, all fail in tracing the regurgitant area. The performance of SMED, texture filter and soft thresholding in segmenting the B-Mode images in PLAX, A4C and A5C, are shown in Figure 5.17. The MV and AV leaflets are traced using the soft thresholding based segmentation.

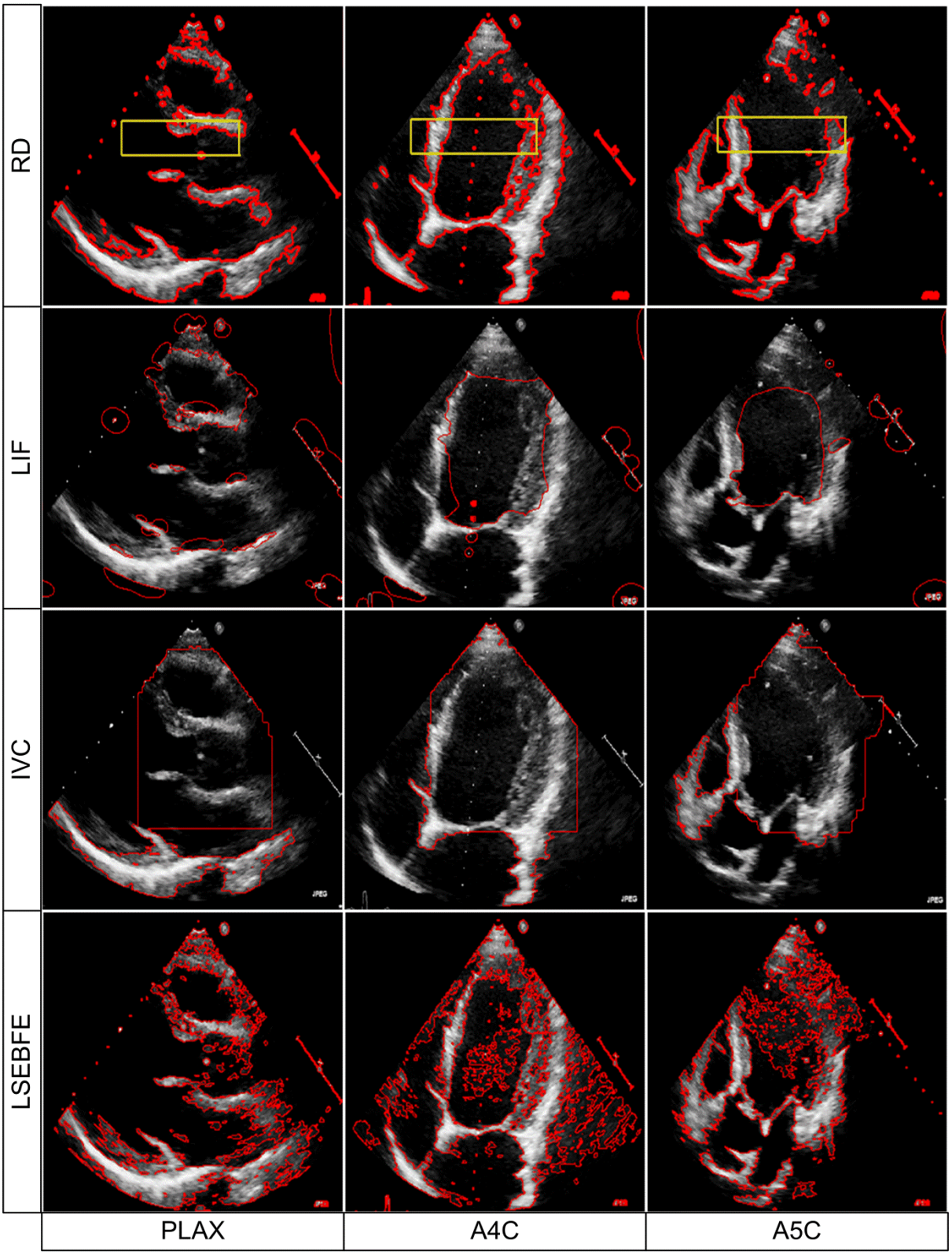

Figure 5.18 Segmentation of B-Mode images using RD and other techniques

However, this technique fails in tracing the complete inner boundaries of the left ventricle. The techniques such as SMED and texture filters fail to trace the boundaries of MV and AV leaflets and LV boundaries. The performance of RD based technique traces the inner and

outer boundaries of LV, traces the leaflets of MV and AV but these boundaries contain discontinuities. The methods such as the LIF, IVC, and LSEBFE fail to segment the region of interest. The placement of an initial mask for RD method is shown in the first row of Figure 5.18. It is noticed that irrespective of selection of any type and size of the mask, no change in the boundaries tracing is observed. This reflects that this technique is not dependent on the initial mask selection. Irrespective of initial mask size and shape, the contour traced is identical using the RD segmentation.

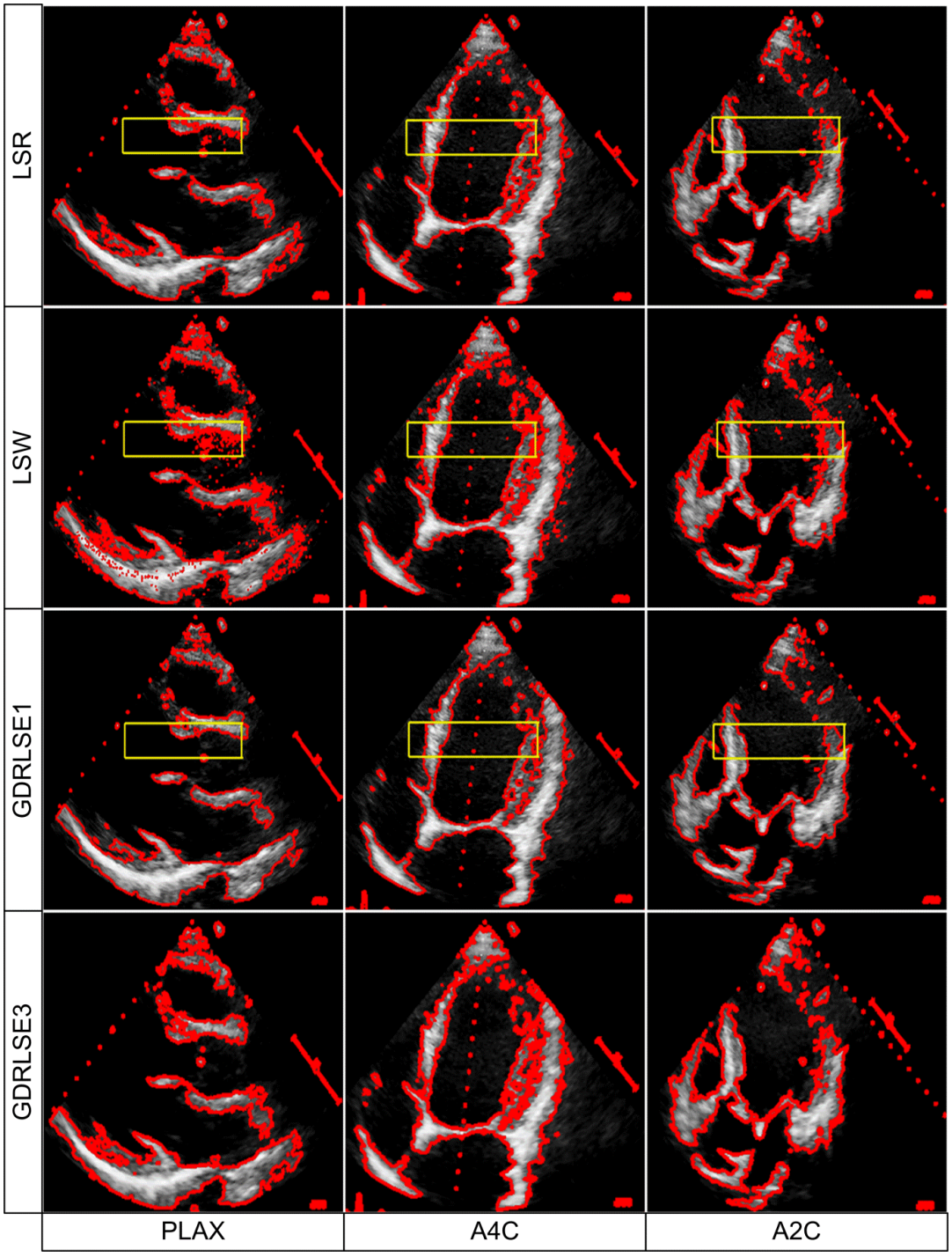

Figure 5.19 Segmentation of B-Mode images using LSR and other techniques

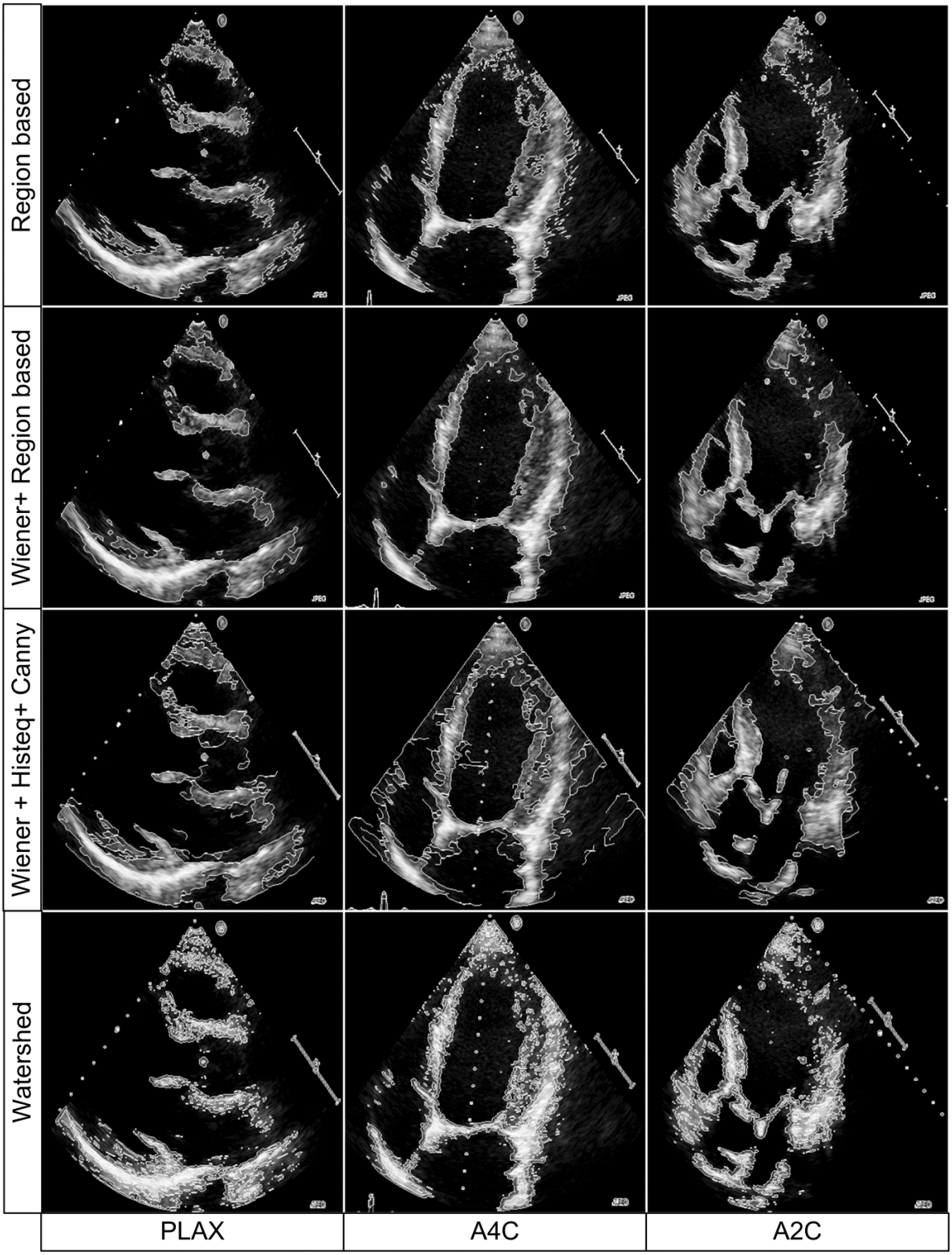

Figure 5.20 Segmentation of B-Mode images using Region and other techniques

The performance of LSR, LSW, and GDRLSE based segmentation are shown in Figure 5.19 for B-Mode images in multiple views. The placements of initial mask are shown to show the importance of initial mask in these methods. These techniques produced same results

irrespective of mask placements. The LSW technique shows that the noise present in the image hampers the boundary tracing. Boundaries traced using the method shown in Figure 5.19 have discontinues.

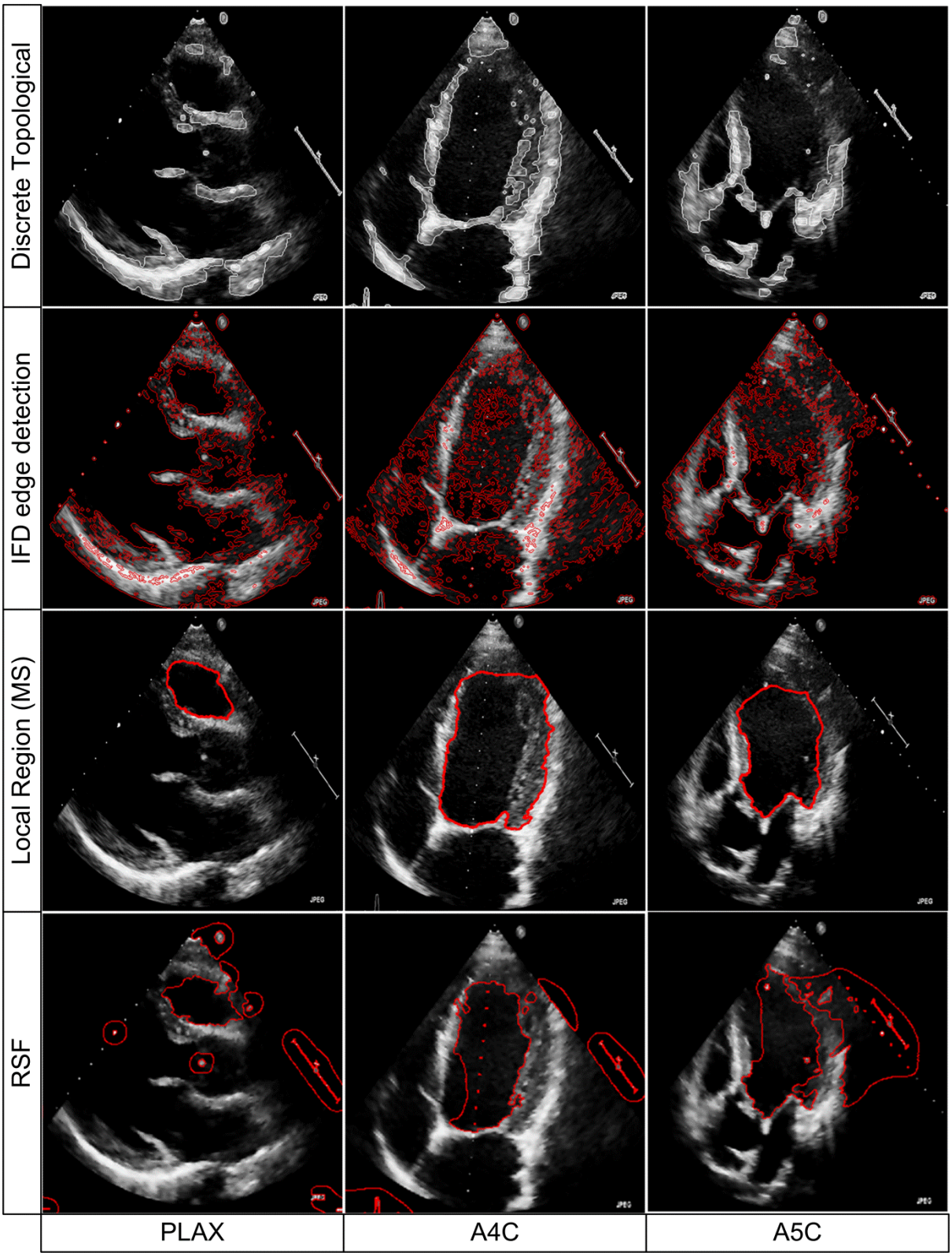

Figure 5.21 Segmentation of B-Mode images using discrete topological derivative and other techniques

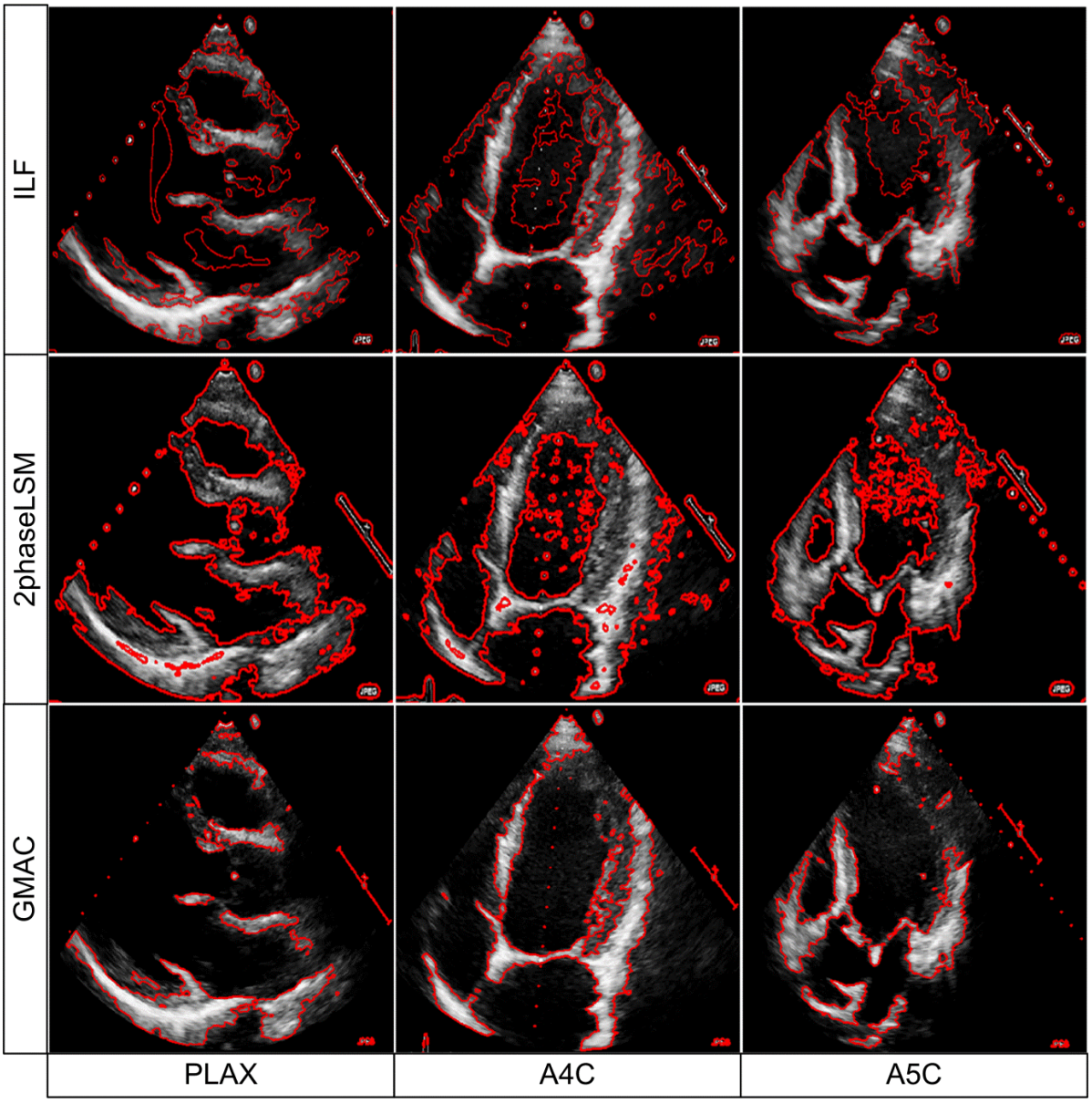

Figure 5.22 Segmentation of B-Mode images using ILF and other techniques

The results obtained on application of techniques namely region based, Wiener filter embedded in region based method, adaptive edge detection, and watershed based segmentation are shown in Figure 5.20. All the techniques result in incomplete boundaries and are prone to noise. The boundary tracing shown in Figure 5.21 reveal that the local region based segmentation results in complete boundary tracing of the LV and RV. The only issue with this technique is the higher amount of computational time required. The other methods shown in Figure 5.21 fail in delineation of LV and leaflet boundaries. The results in Figure 5.22 show that the 2phaseLSM technique is prone to noise and also result complete boundary tracing. The GMAC technique fails to trace LV and leaflet boundaries in the presence of intensity in-homogeneity. The basic snake based method whose results shown

in Figure 5.23, result in complete boundary tracing but proper selection of initialization is necessary.

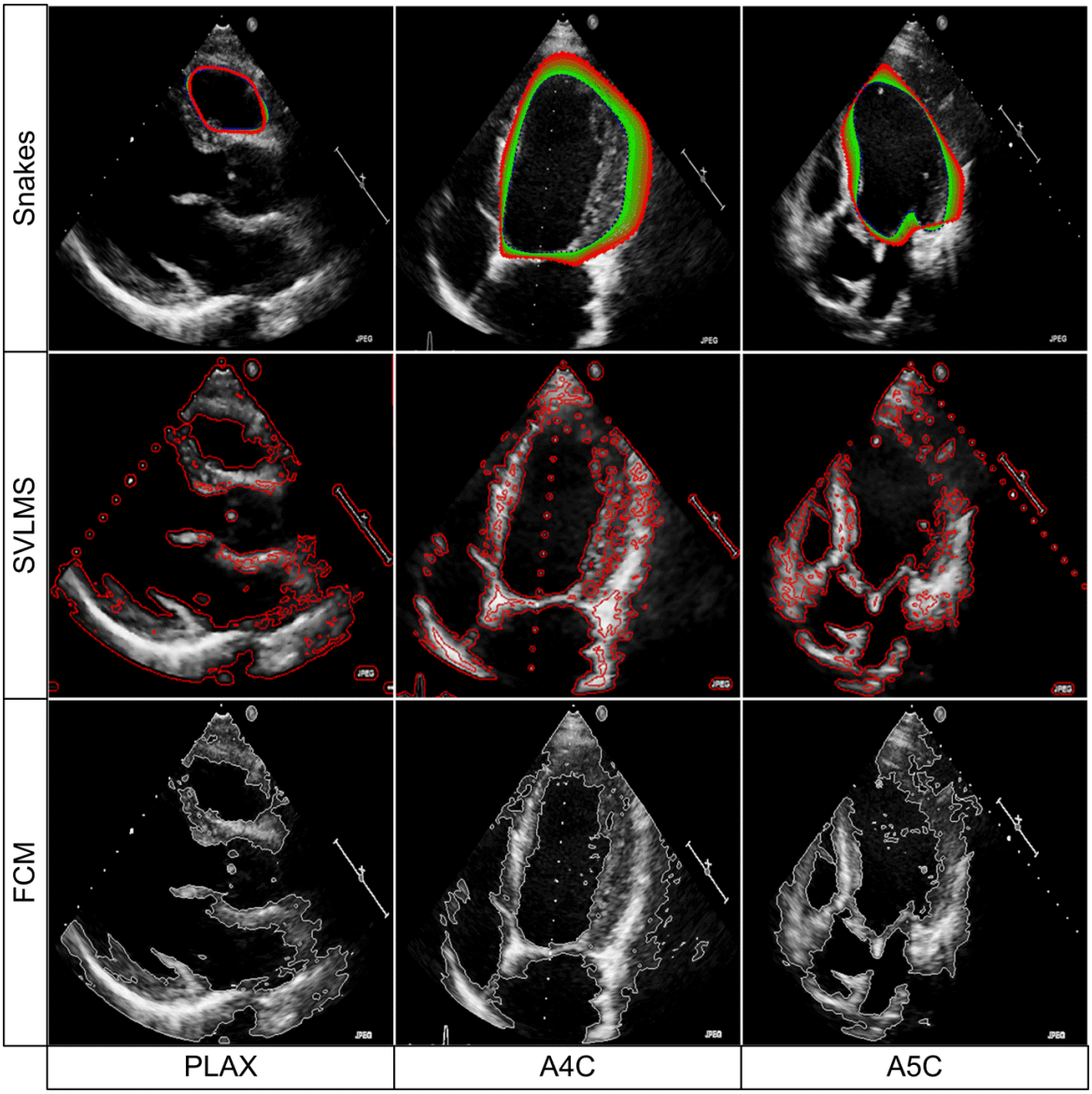

Figure 5.23 Segmentation of B-Mode images using Snakes and other techniques

Table 5.2 Comparison of manual and LRAC based segmentation for A4C, A5C, A2C

Parameter	A4C			A5C			A2C		
	LRAC	Manual 1	Manual 2	LRAC	Manual 1	Manual 2	LRAC	Manual 1	Manual 2
Area	26270	26973	27053	14520	15001	15560	28746	32205	29488
Major axis	229.62	252.69	254.69	193.88	191.35	193.78	239.51	275.38	256.739
Minor axis	151.13	139.57	138.75	101.24	104.92	109.06	155.96	150.55	147.78
Eccentricity	0.7528	0.8336	0.8386	0.8528	0.8362	0.8265	0.7589	0.8373	0.8177
Convex area	27871	27697	27947	16733	17065	17226	29937	32653	29857
Filled area	26288	26973	27053	14520	15001	15560	28746	32205	28488
Solidity	0.9426	0.9739	0.968	0.8677	0.8791	0.9091	0.9602	0.9863	0.9876
Extent	0.7725	0.7805	0.8096	0.6796	0.7022	0.7754	0.8046	0.7812	0.7867
Perimeter	722.27	648.12	677.61	562.02	566.96	560.81	707.36	733.87	691.62

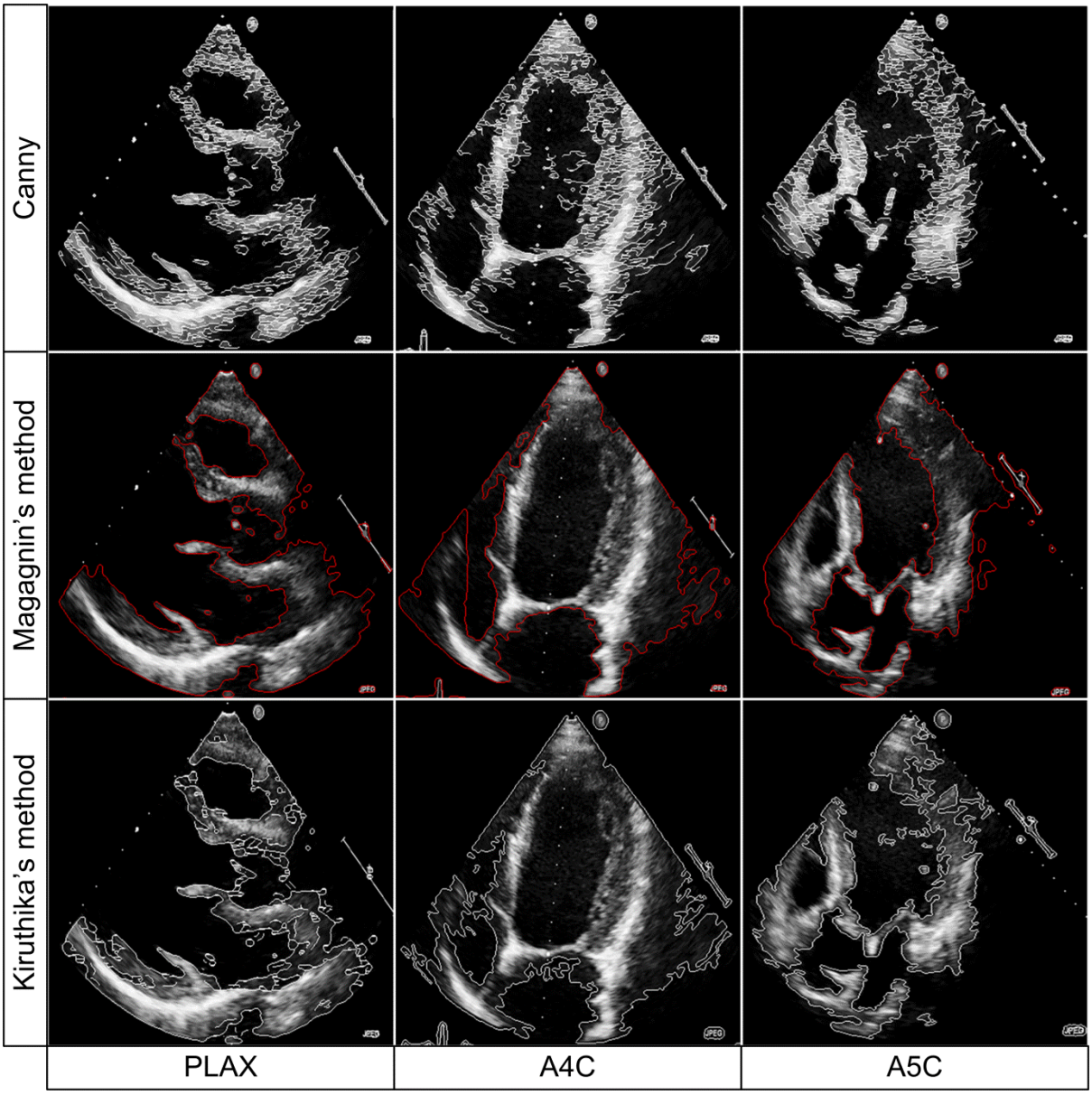

Figure 5.24 Segmentation of B-Mode images using Canny and other techniques

The results shown in Figure 5.24 reveal that the methods like Canny edge detection, Magagnin and Kiruthika do not find applications in delineation of the B-Mode images whereas these techniques are suitable in tracing the outer boundary of the CWD spectrum. It is attempted to improve the performance of some techniques such as IFD edge detection, LRAC, GMAC, 2phaseLSM and Magagnin methods by embedding Wiener filter prior to segmentation. The results obtained on combining Wiener filter with segmentation techniques are shown in Figure 5.25. The results reveal that the performance improves on combining despeckling with segmentation. The boundaries traced using the LRAC technique are compared with manual traced in Figure 5.26 and Figure 5.27 and the results show complete boundary tracing using this technique. The parameters computed using the MATLAB inbuilt functions are tabulated in Table 5.2 and Table 5.3.

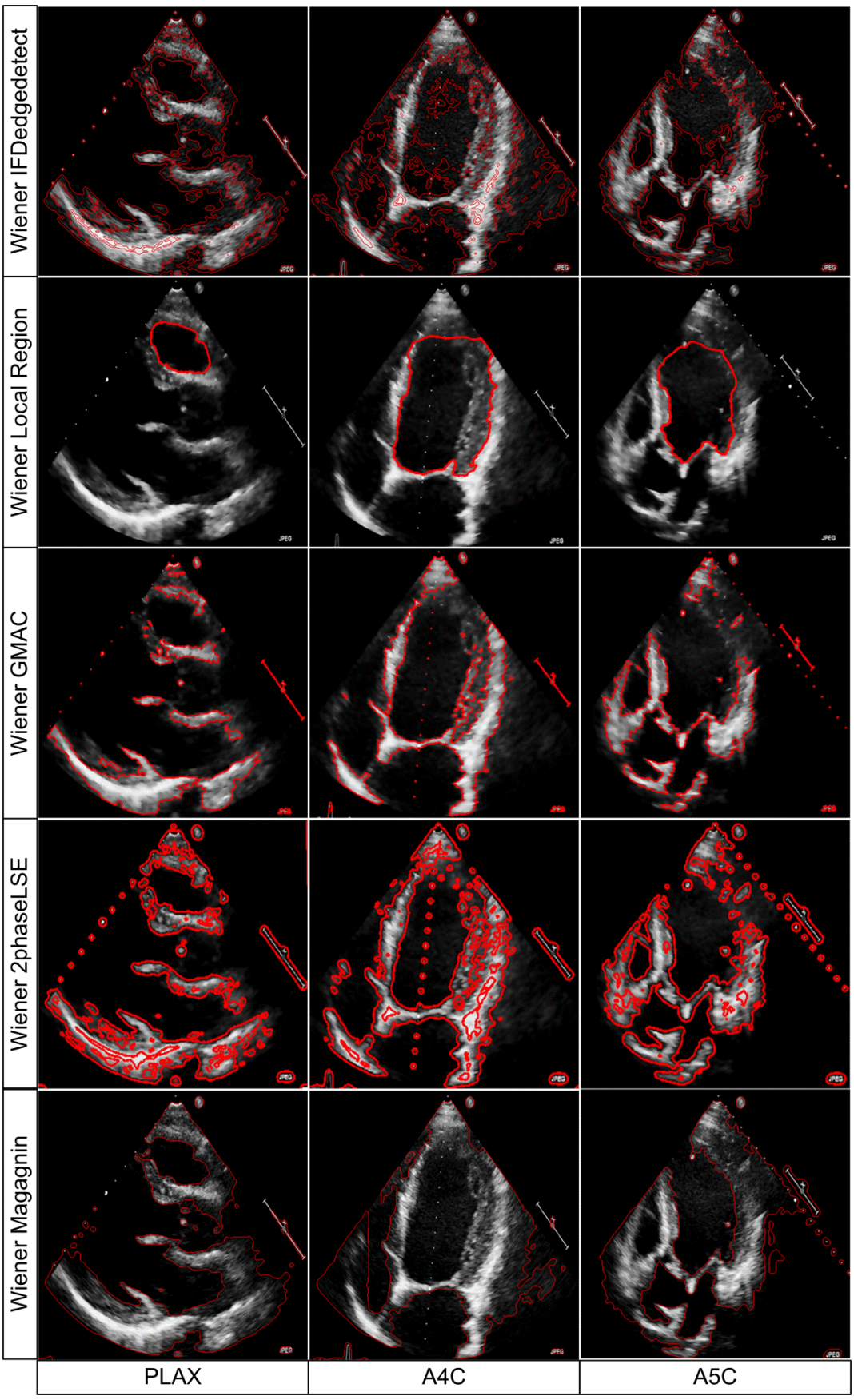

Figure 5.25 Segmentation of B-Mode images using IFD and other techniques

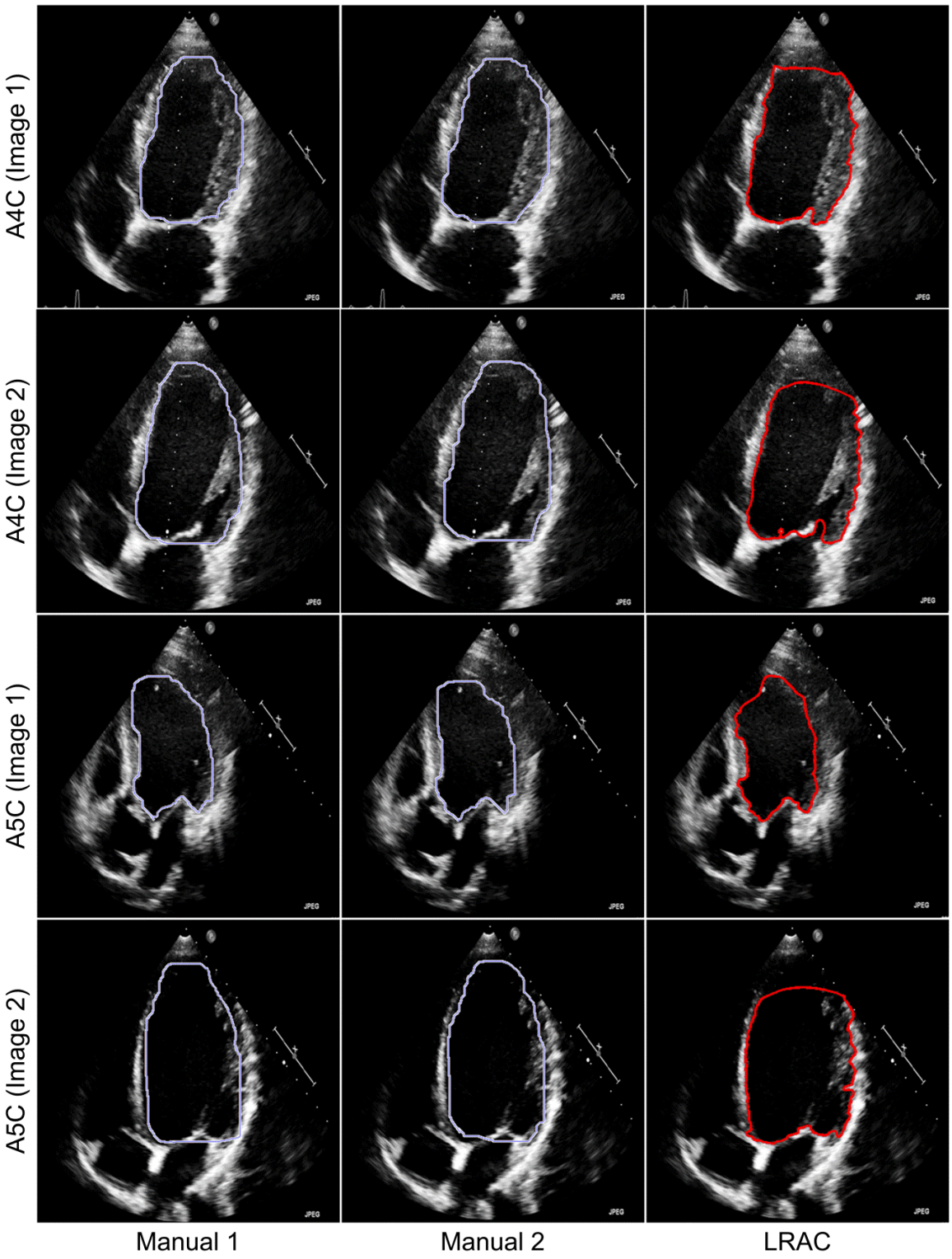

Figure 5.26 Comparison of manual tracing with LRAC based segmentation

The parameters such as area are in terms of number of pixels in these two tables. The analysis of results reveals that the results of both manual delineation and LRAC method are almost identical with fractional variations in terms of area and other parameters in terms of centimetres. The segmentation techniques analysed using the synthetic, color Doppler and

B-Mode images are also experimented using the CWD images. The results for the CWD images are shown in Figure 5.28 to 5.33. The performances of the techniques such as GDRLSE, IVC, CV, RSF, edge, region, watershed, local region, IFD edge detection and adaptive edge detection are improved on using a pre-processed image in-place of the original image.

Table 5.3 Comparison of manual and LRAC based segmentation for PLAX and CD

Parameter	PLAX			CD		
	LRAC	Manual 1	Manual 2	LRAC	Manual 1	Manual 2
Area	14715	14971	14968	5074	5113	5168
Major axis	178.76	186.84	182.23	142.07	147.37	136.62
Minor axis	106.48	105.48	104.65	46.98	47.69	44.79
Eccentricity	0.8035	0.8475	0.8487	0.9437	0.9462	0.9447
Convex area	15232	16366	15765	5554	5718	5341
Filled area	14715	15974	15068	5074	5214	4568
Solidity	0.9661	0.9759	0.9558	0.9136	0.9117	0.8553
Extent	0.783	0.7891	0.7485	0.6712	0.6712	0.5893
Perimeter	500.47	531.32	526.35	341.72	341.73	365.81

The results for all the methods are presented for the original and pre-processed images using the Wiener and median filters. The boundaries of the CWD image are completely and accurately traced using the methods namely IVC, region, watershed, adaptive edge and GDRLSE based methods. The methods such as the GDRLSE, LSW, IFL, and GMAC are prone to noise. The methods like IFL, 2phaseLSM, GMAC and topological derivative fail to trace the complete boundaries. In next paragraphs results of the modified methods are discussed using the CWD images.

The simulation results are initially analyzed for modified versions of delineation methods. All the simulations based experiments are being performed using MATLAB environment. The first case is Magagnin's method. The outliers resulting from the thresholded images are removed using median filter and the filter is implemented using the MATLAB inbuilt function "*medfilt"* with window size of 3x3, and 5x5. The results are optimal for 5x5 mask. The next experiment is modified Kiruthika's method. The performance of adaptive Wiener filter is better in comparison to Gaussian filter hence it is used as replacement. The filter is implemented using the function "*Wiener2"*. Three texture filters and the Wiener filter are used in combination for segmenting bottom and top texture separately.

The performances are evaluated by visually inspecting the traced boundary. The traced boundary using different combinations of texture filters are shown in Figure 5.34 and Figure 5.35. The results of all the three methods are compared in Figure 5.36. The results presented in Figure 5.34 and Figure 5.35 reveal that the combination of "*entorpyflt"*, "*rangeflt"* and "*stdflt"* with both "*rangeflt"* and "*stdflt"* fail in tracing the outer boundaries of CWD images.

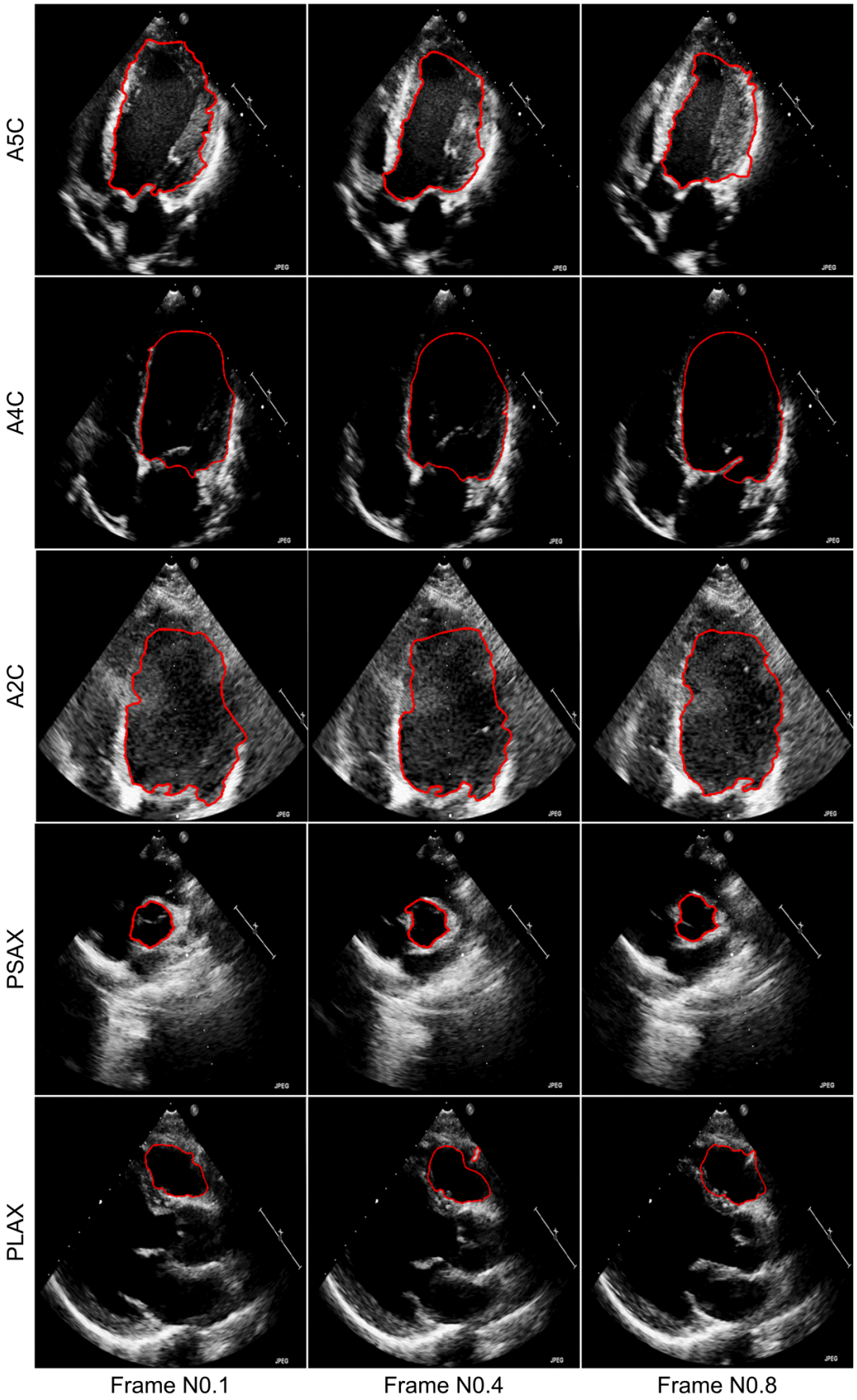

Figure 5.27 Segmentation of B-Mode images using RD and other techniques

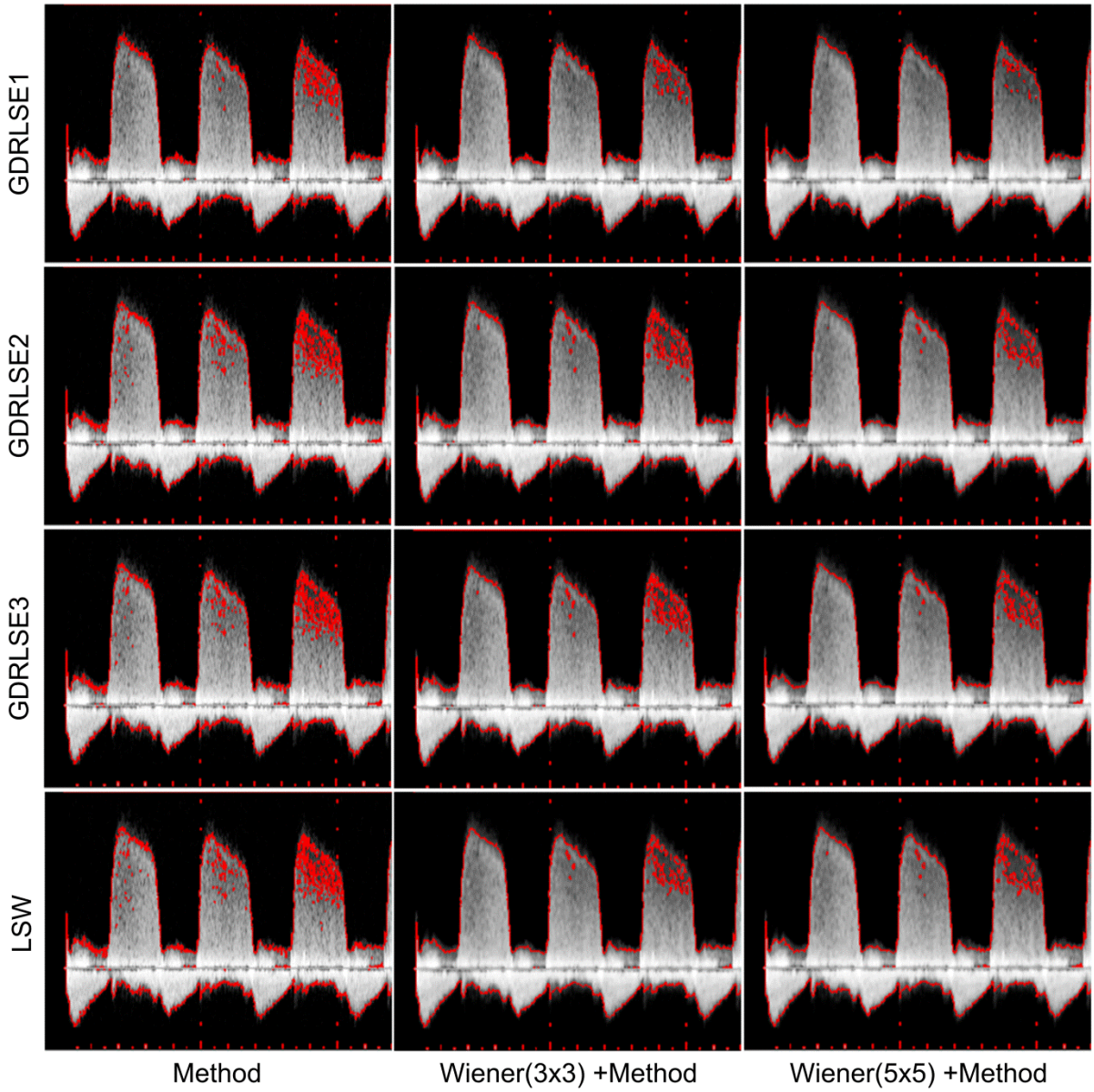

Figure 5.28 Segmentation of CWD images using GDRLSE and other techniques

The combination of "*rangeflt"* and "*stdflt"* with Wiener filter result in complete contouring of the outer boundaries but fail when the contrast is low. The fourth column and first row of Figure 5.34 and Figure 5.35 reveal that the usage of "*entropyflt"* for delineation of both top and bottom texture results in over-segmentation. Similarly, using "*stdflt"* and "*rangeflt"* for delineation of both top and bottom texture also result in incomplete boundary tracing. Hence, the use of same filter for top and bottom texture delineation fails in the CWD images. The combination of *"rangeflt"* and "*stdflt"* with "*entropyflt"* result in accurate and complete boundary contouring. In order to show adaptabilty and versatality of these techniques, the results are shown for both good and low contrast images in Figure 5.34 and Figure 5.35, respectively.

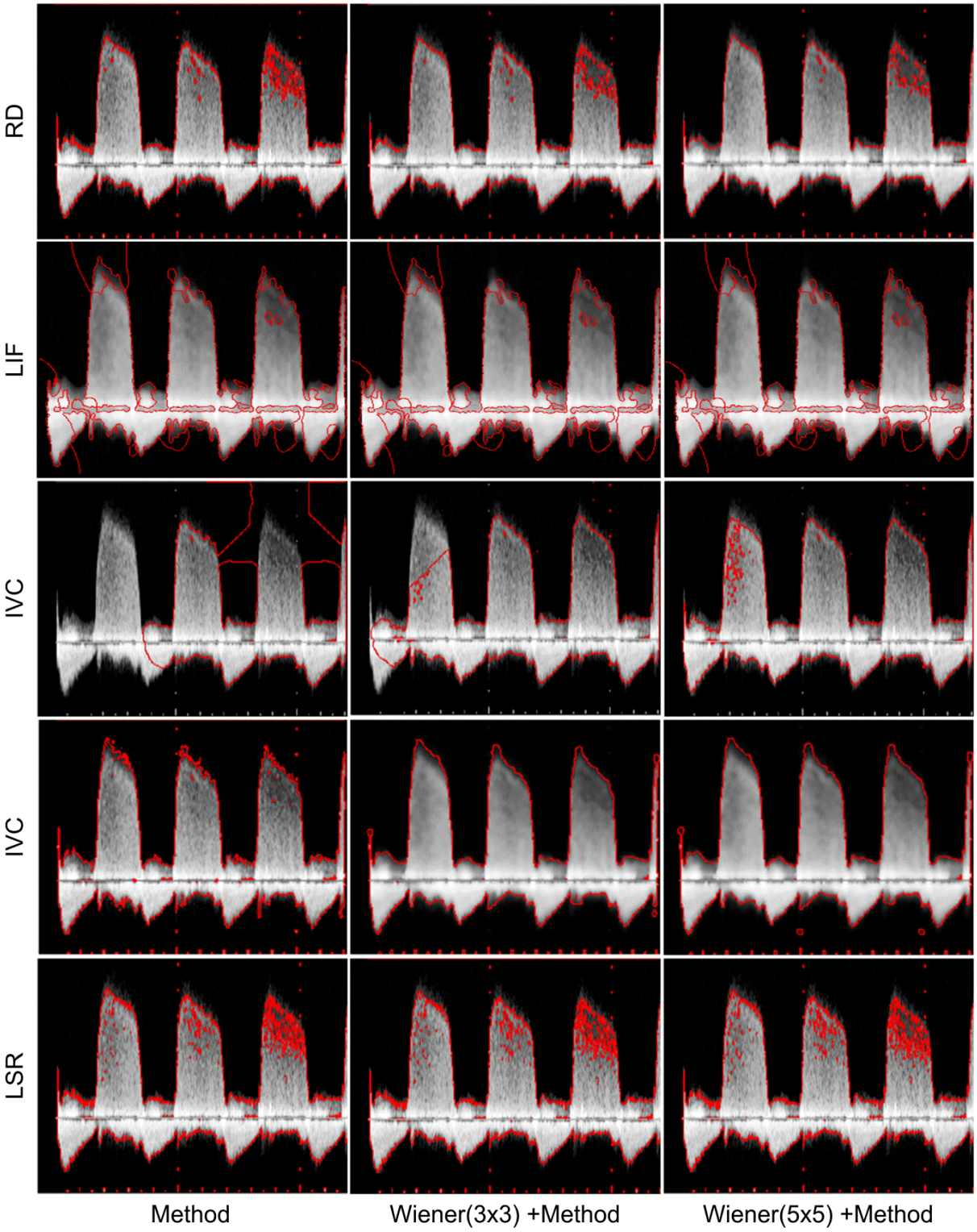

Figure 5.29 Segmentation of CWD images using RD and other techniques

The boundaries traced by the proposed method are compared with Magagnin's and modified Kiruthika's method in Figure 5.36. The top texture is not completely traced in Magagnin's method. The modified Kiruthika method also fails when contrast is low as evident from the

second row and second column image compared with the third image in the second row. The median and Wiener filters in the Kiruthika, Magagnin and RD methods are replaced by despeckling filters namely DsFlsmv, DsFad, DsFsrad, DsFlsminsc, DsFWiener, DsFhomog, DsFhmedian, and DsFgf4d filters. The boundaries delineated using modified Kiruthika's method are shown in Figure 5.38.

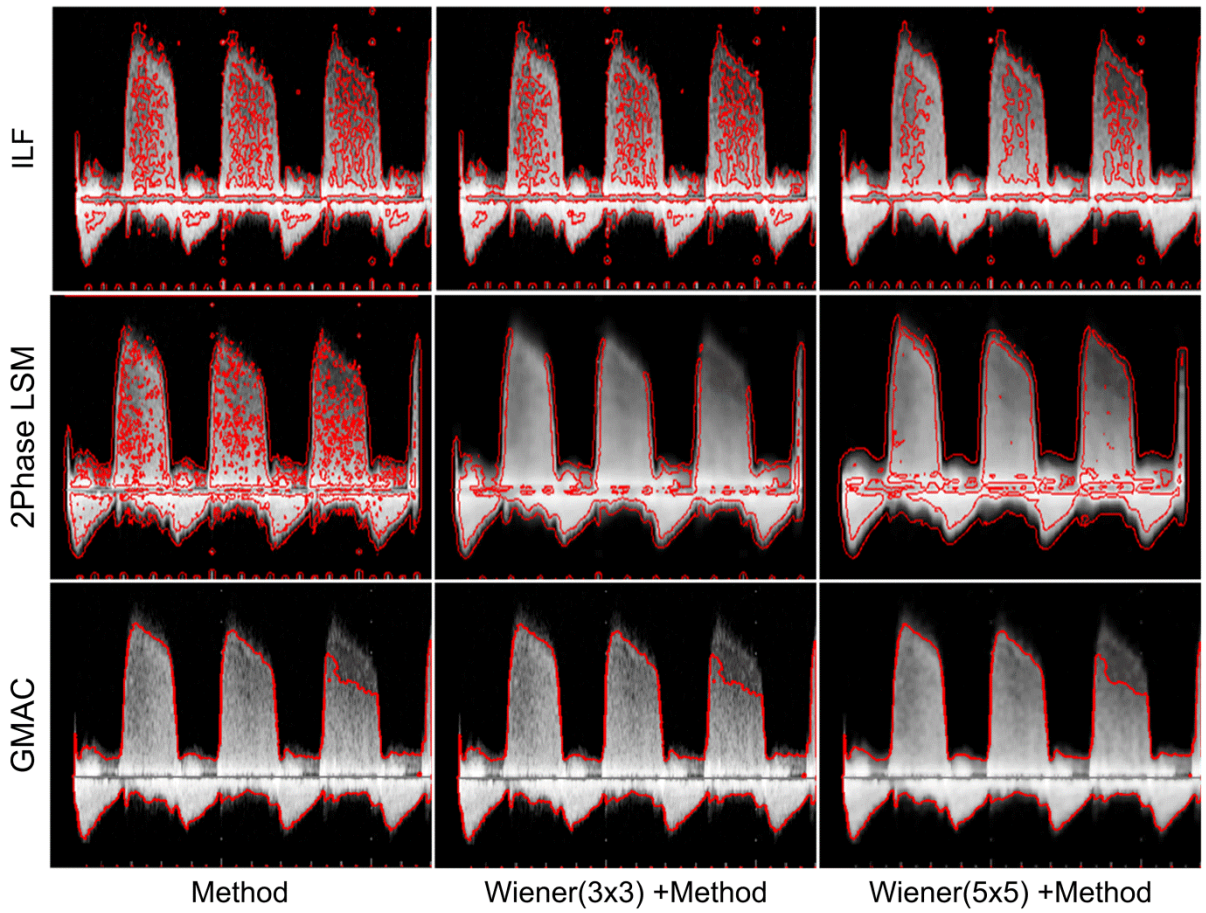

Figure 5.30 Segmentation of CWD images using ILF and other techniques

The boundaries are completely contoured when images are less contaminated. But the method failed for noisy images. The first row of Figure 5.38 shows the need for additional filtering in the Kiruthika's method [199]. The second and third rows of Figure 5.38 are results obtained for noisy CWD images (noise variance=0.1). The noise in the background is successfully taken off by sequentially combining the median filter with either DsFsrad or DsFWiener filter. Noise is retained in the background in all cases shown in Figure 5.38 expect for the DsFsrad and the DsFWiener filter. The results of modified Magagnin's scheme are shown in Figure 5.37. The results are similar to those of modified Kiruthika's method. The major drawback of the Magagnin's method is incomplete boundary tracing. Noise is fully removed on sequential integration of the median filter and the despeckling filters in Magagnin method but the technique fails in the presence of intensity in-homogeneity as seen in Figure

5.37. The results in second row of Figure 5.37 are for images embedded with Gaussian noise of zero mean and 0.1 variance.

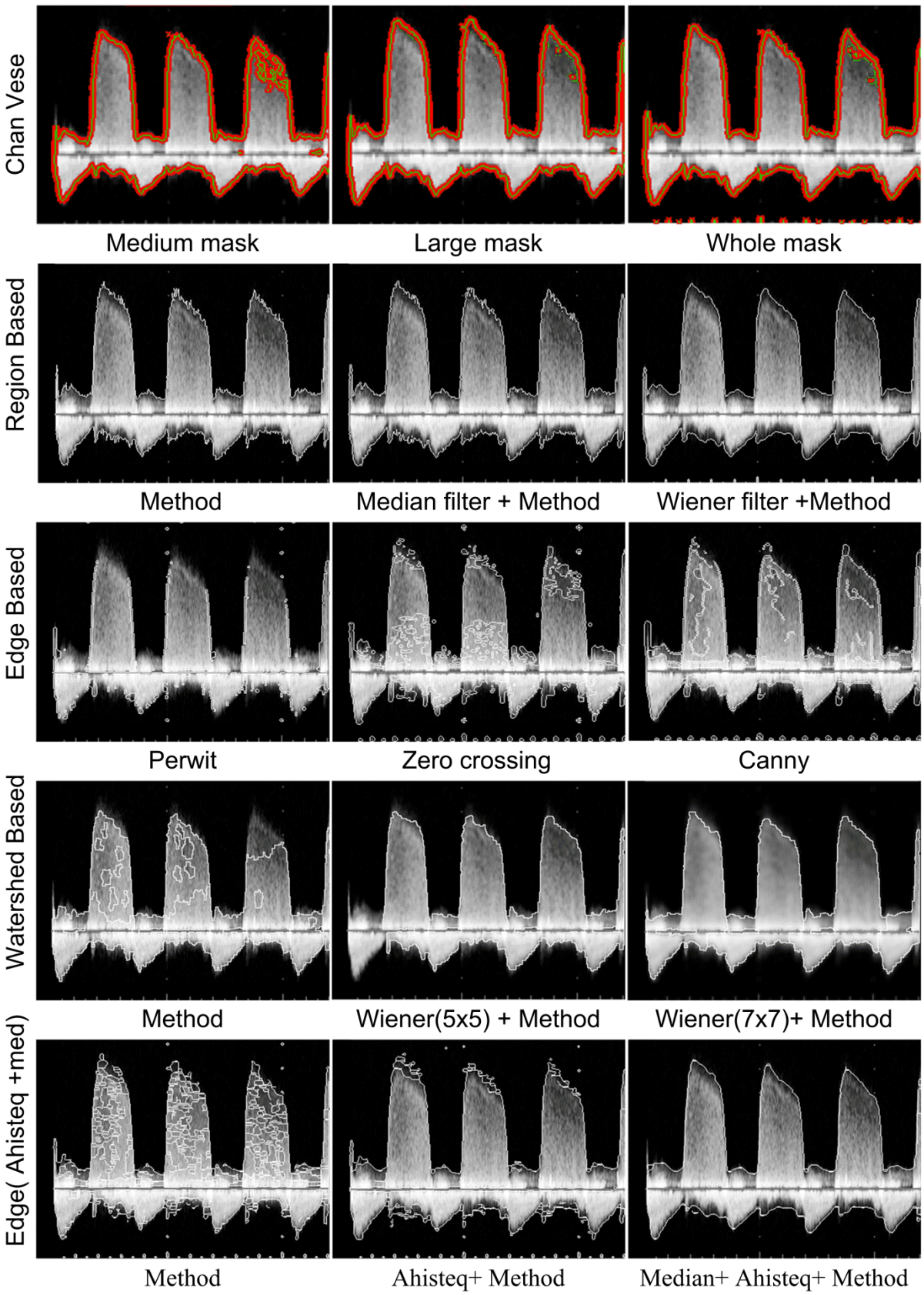

Figure 5.31 Segmentation of CWD images using GDRLSE and other techniques

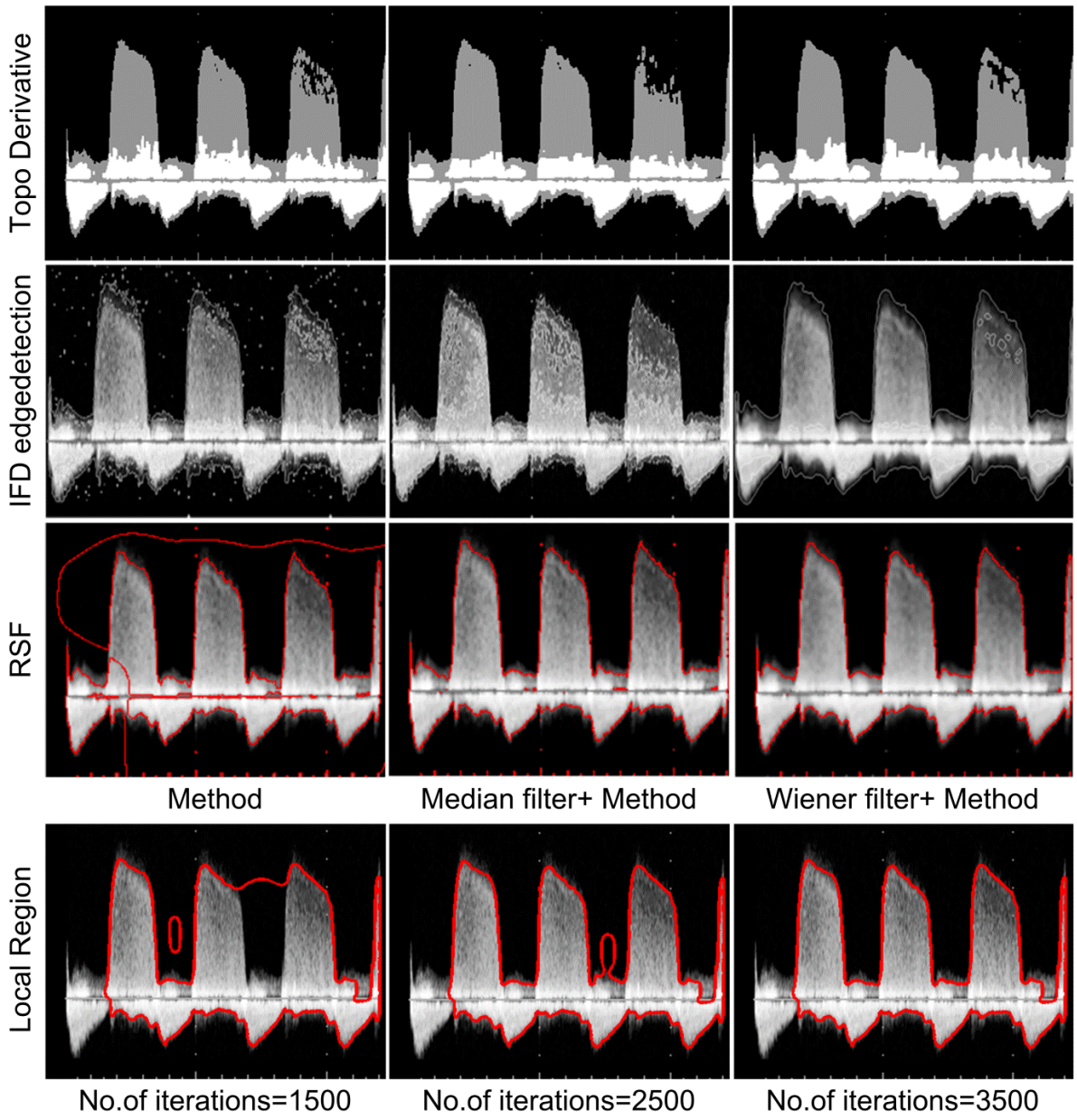

Figure 5.32 Segmentation of CWD images using Topological derivative and other techniques

The results obtained using RD method with Gaussian convolution filter and other filters is shown in Figure 5.39. The outer boundaries are traced using modified Kiruthika's method. But for segmenting the region of interest in a CWD image it is necessary to crop image in modified Kiruthika's method. This issue of cropping image is overcome in RD based segmentation. The boundaries are traced by placing a square mask as the region of interest. The number of iterations required in contouring CWD images is reduced on use of despeckling filters in-place of the Gaussian filter. The number of iteration required for using various filters are specified in parenthesis in Figure 5.39. The boundaries traced using the RD methods with DsFsrad are smooth, complete and accurate in comparison to all other combinations in Figure 5.39.

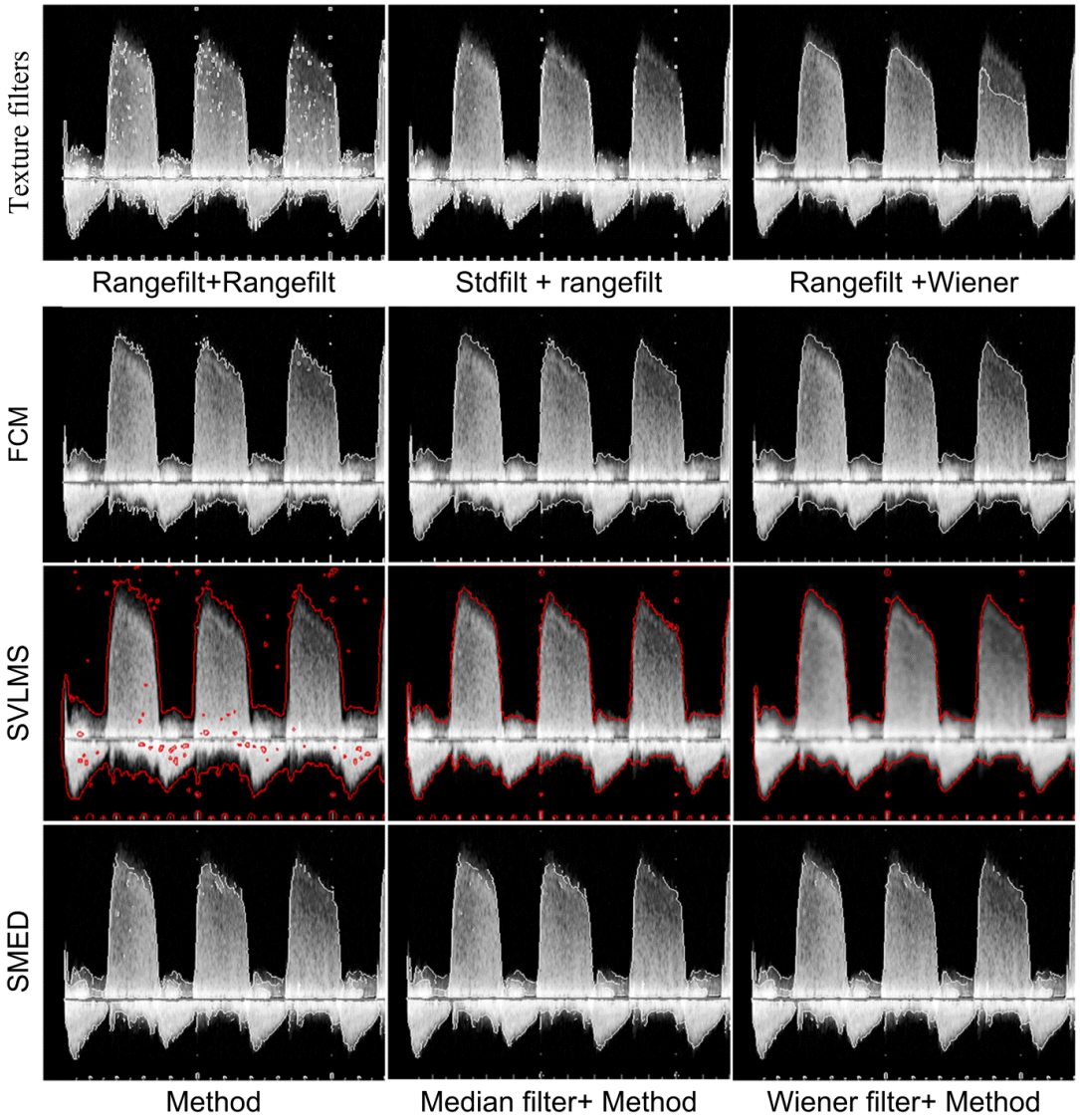

Figure 5.33 Segmentation of CWD images using Texture filters and other techniques

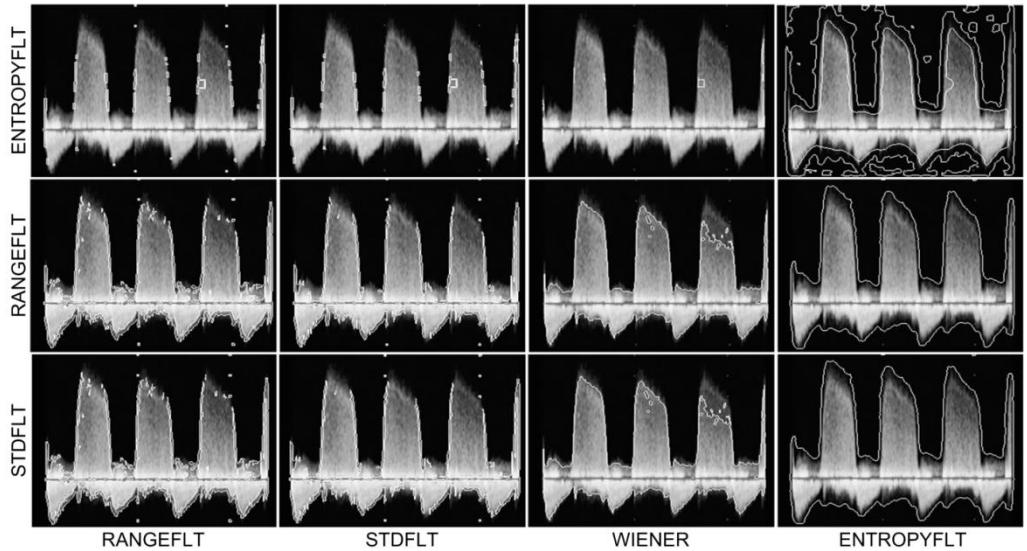

Figure 5.34 Delineation of CWD images using proposed combination of texture filters: column-wise-first-Rangeflt, second- stdflt, third-Wiener and fourth-entroplyflt

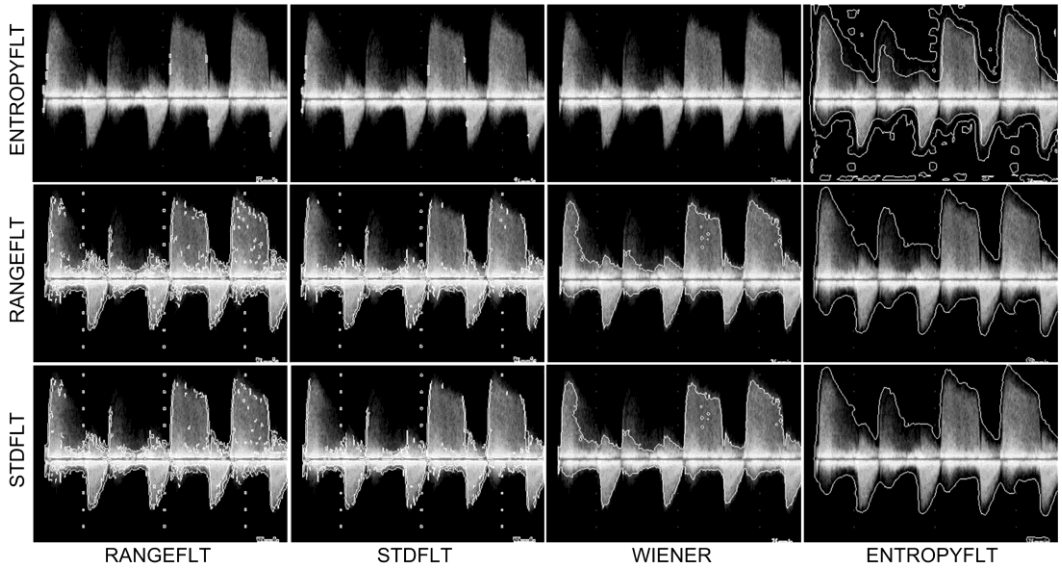

Figure 5.35 Delineation of CWD images using proposed combination of texture filters: column-wise-first-Rangeflt, second- stdflt, third-Wiener and fourth-entropyflt for second image

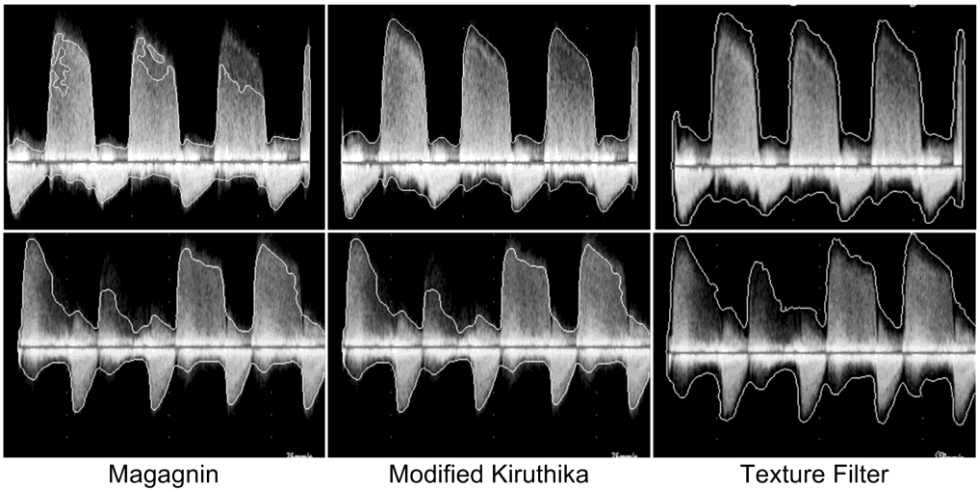

Figure 5.36 Comparison of proposed delineation technique with modified Kiruthika and Magagnin method

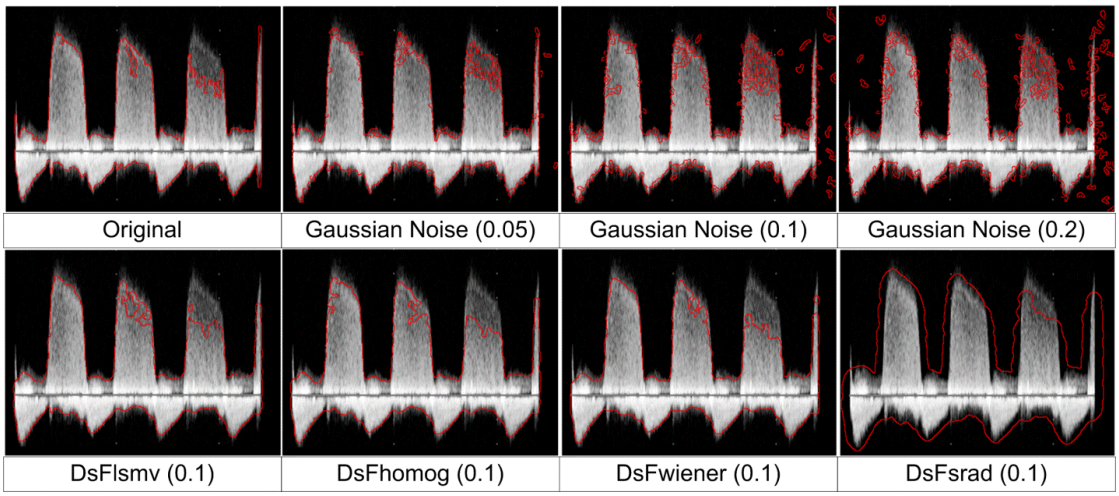

Figure 5.37 Delineation of CWD image using modified Magagnin method

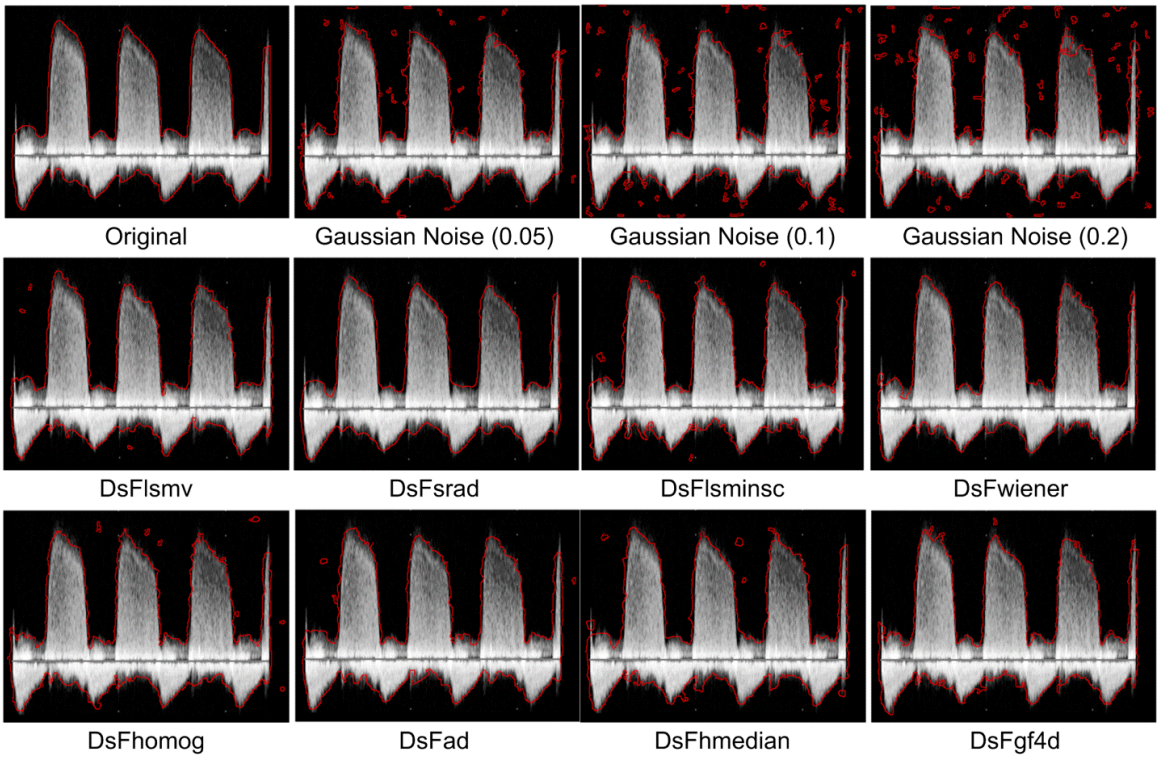

Figure 5.38 Delineation of CWD image using modified Kiruthika method

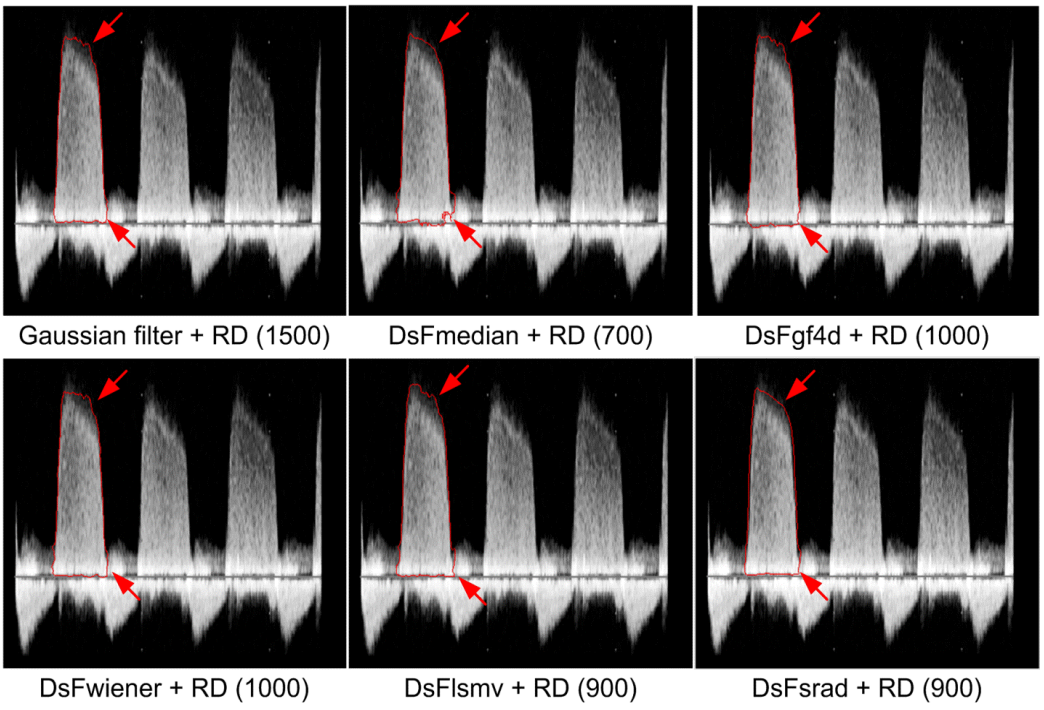

Figure 5.39 Delineation of CWD image using modified RD method

Boundary leakages are observed when the RD method is combined with the DsFmedian filter. The points to be observed are highlighted using an arrow head pointer in Figure 5.39. Further, performances of the modified RD method with various despeckling filters are tested using low contrast images with higher amount of intensity in-homogeneity in

Figure 5.40. The boundaries traced in Figure 5.40 show that embedding of despeckling filter as replacement for the Gaussian filter in the RD method can be employed in the delineation of CWD images even in the presence of intensity in-homogeneity.

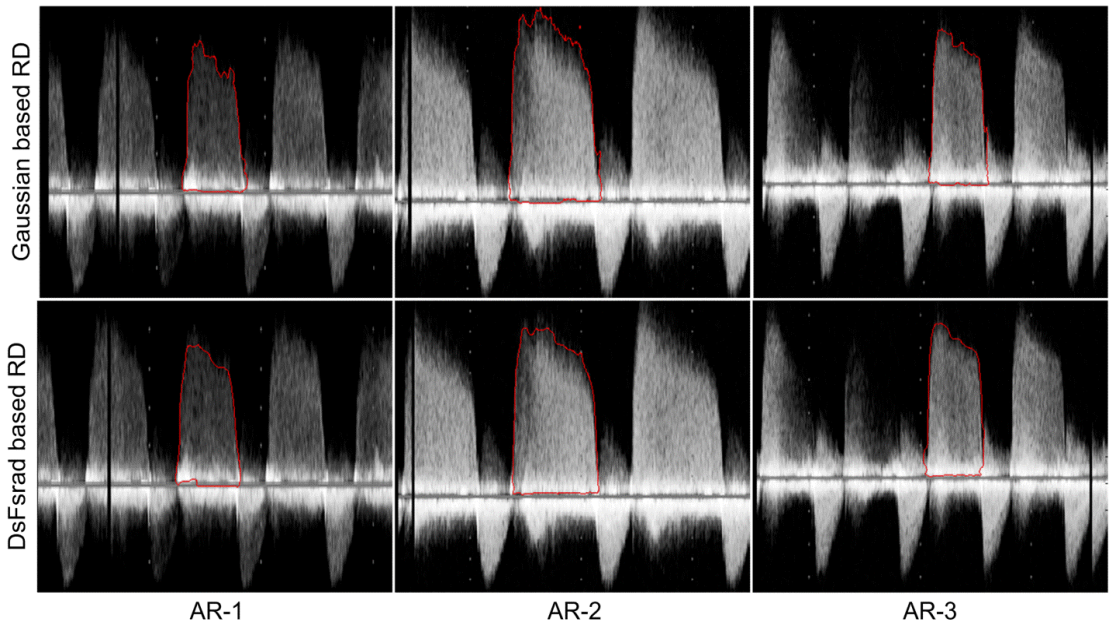

Figure 5.40 Delineation of low contrast CWD image using modified RD method where AR-1 to AR-3 are the three patient's

5.7 Summary

The CWD, CD, and B-Mode are segmented using techniques based on edge, region, watershed, fuzzy and active contour. The images acquired in multiple views are delineated in the presence of intensity in-homogeneity. The synthetic images with homogenous region throughout and with varying amount intensity in-homogeneity are first segmented prior to segmentation of multi-modality echocardiographic images. The original and pre-processed images are used in the analysis of segmentation of techniques.

The segmentation techniques are analysed to test their suitability in tracing the regurgitant jet area in the LVOT from the CD images. The study revealed that the techniques such as local region based active contour (LRAC), GMAC, and IVC techniques can be used for segmenting the regurgitant jet area. The leaflets of the AV and the MV in the parasternal long axis can be traced using soft thresholding, RD, GDRLSE and 2phaseLSM based segmentation techniques. The techniques such as RD, GMAC and LRAC can be employed for segmenting the images in A4C, A2C and A5C for tracing the inner boundaries of the LV. The inner boundaries of RV in PLAX view can be traced using the techniques like snakes, SVLMS, 2phaseLSM and LRAC.

The outer boundaries of CWD images are completely traced using GDRLSE, IVC, region based, CV, FCM and SVLMS using the original CWD images. The performance of

techniques such as edge, watershed, adaptive edge, IFD edge detection, LRAC and RSF techniques are improved on embedding the median and Wiener filters. These techniques also resulted in complete boundary tracing. The performance of Kiruthika method, Magagnin method and RD based delineation improved on replacing the Gaussian filter and median filter with despeckling filters such as the DsFsrad and DsFlsmv filters, also resulting in complete boundary delineation.

6.1 Conclusions

The echocardiographic images acquired in multiple views and windows are employed in the analysis of valvular abnormalities in the heart. The aetiologies and consequences are studied by integrated visualization of B-Mode, continuous wave Doppler (CWD), pulse wave Doppler (PWD) and color Doppler (CD) images. Each of the modality provides a particular piece of information necessary in accurate diagnosis of the diseases. The images acquired in apical and parasternal view help in observing various parts of the cardiac structure better than the other. The cross sectional images acquired in multiple views aid in precise location of the abnormality in the valvular and chambers of the heart but they are prone to noise.

The computer aided visualization and analysis are critical portion of the clinical diagnosis. The quality of the image is crucial in arriving at a concrete decision of a critical state of abnormality in the heart. The transthoracic echocardiographic (TTE) images are known to be of low contrast and also suffer due to shadowing, reverberations, and speckle noise. Many researchers are putting in efforts to improve the quality of the TTE images and computer aided diagnosis by advocating despeckling, enhancement and segmentation techniques. The research is more concentrated on the images acquired in one view using B-Mode echocardiography. But it is necessary to process the images acquired in multiple views and modalities as they are used hand-in-hand, not as a substitute for each other. Hence, this current research work is taken up to despeckle and segment images acquired in multiple views using the B-Mode, CWD, and color Doppler images. The TTE images acquired from the adult patients diagnosed with AR are used in analysis of 48 despeckling and twenty five segmentation techniques in this thesis. Aortic regurgitation is the backward flow of blood from the aortic valve into the left ventricle during the diastole. The aetiologies and consequences of AR are diagnosed by visually observing the B-Mode images in parasternal long axis (PLAX), parasternal short axis (PSAX), apical four chamber (A4C), apical five chamber (A5C) and apical two chamber (A2C) along with CD, CWD, and PWD images.

In an attempt to address the issue of speckle noise in the clinical TTE images, six despeckling filters were proposed. The first set of techniques consisted of multiple multiscale methods implemented in the logarithmic domain for edge preserved despeckling; the performance analysis was in terms of image quality metrics, visual quality assessment and clinical validation. The performances of multiscale techniques are compared with two adaptive and four iterative techniques. It is concluded that the neighbourhood shrinkage combined with SURE known as NeighShrinkSURE, represented as LM7E stands out among multiscale techniques along with the GLM based filter. The posterior sampling based Bayesian estimation (PSBE) was combined with adaptive Wiener filter in the second proposed method. The performance of the PSBE filter was enhanced by integrating Wiener

filter for despeckling of noisy TTE images. It is concluded that the combination of PSBE filter with Wiener filter improves despeckling when the amount of noise present in the images is high otherwise PSBE alone will be sufficient. The triangulation moving average (TMAV) fuzzy filter was employed in the logarithmic domain for speckle noise reduction. The noise suppression and edge preservation of TMAV filter were fine tuned by combining it with the adaptive Wiener filter. The fourth proposed scheme was based on integration of geometric, fuzzy and the adaptive Wiener filter. The performance of fuzzy filter was further refined with higher noise suppression and edge preservation using the integrated fuzzy filters. The fifth method advocated was the hybrid homomorphic fuzzy (HHF) filter, which is the sequential integration of fuzzy and speckle reducing anisotropic diffusion filter. The performance is analysed using the standard test images and TTE images in multiple views. The fuzzy filters implemented go to show that the fuzzy filter will find their applications for speckle noise which is multiplicative in nature. Earlier the fuzzy filters were proven to be effective in additive noise reduction. The final proposed despeckling technique was based on the replacement of the regularization term of the total variation filter with the bilateral term. This technique was known as the extreme total variation bilateral (ETVB) filter. Along with these techniques the duality based denoising techniques were also analysed for the TTE images.

A comparative analysis of 48 filters is carried out for the B-Mode, CWD and color Doppler images. These filters were grouped into eight types namely the local statistics, fuzzy, Fourier, multiscale, nonlocal mean, total variation, nonlinear iterative and hybrid filters. The performance analysis was in terms of speckle noise suppression, visual quality and clinical validation. The analysis was also in terms of blind assessment parameters along with the traditional parameters. The merits, demerits and concepts of 48 filters are studied for the quality improvement of the TTE images. It work shows that the performance of despeckling filters such as the GLM, DsFlsmv, DPAD, DsFhomog, FBL, PLOW, BPFA and PPB filters are superior among the 48 denoising techniques analyzed in terms of 16 performance parameters along with the visual quality assessment and grading by the cardiologists. It is concluded that these filters can be employed for noise reduction in the TTE images. The performances of the despeckling techniques were analysed for the CWD images. The performance of the DsFsrad filter is superior in comparison to the DsFgf4d, DsFhomog, DsFlsminsc, DsFhmedian and DsFad filter in terms of IQM such as Err3, Err4, LMSE and NAE. The visual quality of despeckled images obtained using the DsFlsmv, DsFWiener, DsFad and dsFsrad are able to retain structure and edge details. The texture features of the B-Mode, M-mode, CWD and CD based echocardiographic modality images are extracted. Features extracted from despeckled images showed marked difference for images acquired using A4C and A5C in comparison to A2C, and A4C compared with PLAX view images.

Similarly, the features of CWD, M-Mode, Color Doppler and B-mode images were quite distinct.

The CWD, CD and B-Mode were segmented using techniques based on edge, region, watershed, fuzzy, and active contour. The images acquired in multiple views were delineated in the presence of intensity in-homogeneity. The segmentation techniques were analysed to test their suitability in tracing the regurgitant jet area in the LVOT from the CD images. The study has revealed that the techniques such as local region based active contour (LRAC), GMAC and IVC techniques can be employed for segmenting the regurgitant jet area. The leaflets of the AV and the MV in the parasternal long axis can be traced using soft thresholding, RD, GDRLSE and 2phaseLSM based segmentation techniques. The techniques such as RD, GMAC and LRAC are suitable for segmenting the LV in A4C, A2C and A5C. The boundaries of RV in PLAX view can be traced using snakes, SVLMS, 2phaseLSM and LRAC. It is concluded that among the twenty segmentation techniques analysed the LRAC is the most suitable technique for tracing the boundaries in the B-Mode TTE images.

The outer boundaries of CWD images can be delineated using GDRLSE, IVC, region based, CV, FCM and SVLMS using the original CWD images. The performance of techniques such as the watershed, adaptive edge, IFD edge detection, LRAC and RSF techniques can be improved on embedding the median and Wiener filters. The performance of Kiruthika method, Magagnin method and RD based delineation are improved on replacing the Gaussian filter and median filter with despeckling filters such as the DsFsrad and DsFlsmv filters, also resulting in complete boundary delineation.

6.2 Future scope

The limitation of the current research work is that the pre-processed and segmented images were not employed for AR severity classification. The thesis concentrated for despeckling and segmentation of the TTE images in multiple views. The second limitation is the texture features were employed in specifying the filter performance whereas the texture features might be used in classification of severity of the valvular regurgitation and stenosis. These two limitations reflect the possible scope of the current research topic. As a future scope:

1) Analysis of the despeckling techniques for 3D TTE images shall be taken up in multiple views after the collection of 3D data from various sources.

2) The texture features extracted from the images in multiple views and modalities should be analysed for classification of AR severity. This shall overcome the need for manual or automatic delineation of cardiac structure for deciding on the severity of diseases based on parameters estimated.

3) Efforts should be made to reduce the computation time required in execution of local region based active contour segmentation for the TTE images acquired in multiple view and modalities.

4) The segmentation techniques can be used for segmentation and analysis of the right ventricle, mitral valve and other parts of the cardiac structure acquired from patients suffering from aortic stenosis, mitral stenosis and mitral regurgitation.

5) Disease specific analysis such as mitral regurgitation, aortic stenosis and other valvular diseases can also be taken up. Integration of images acquired in different views would be necessary in each case.

PUBLICATIONS FROM THE WORK

Journals

1. **Nagashettappa Biradar**, M.L.Dewal, M.K.Rohit, “Speckle noise reduction in echocardiographic images of aortic valve and cardiac chambers”, *Optik-Int.J.Light Electron Opt.* (2014), vol.126, pp.153-163, **Elsevier**, 2015.
2. **Nagashettappa Biradar**, M.L.Dewal, M.K.Rohit, "Speckle noise reduction in B-mode Echocardiographic images: A comparison", *IETE Technical Review*, pp. 1-19, **Taylor and Francis**, 2015. DOI:10.1080/02564602.2015.1031714.
3. **Nagashettappa Biradar**, M.L.Dewal, M.K.Rohit, “Comparative analysis of Despeckling filters for Continuous Wave Doppler images”, *Biomedical Engineering Letters*, vol. 5, pp. 33-44, **Springer,** 2015.
4. **Nagashettappa Biradar**, M. L. Dewal, and M. K. Rohit, "A novel hybrid homomorphic fuzzy filter for speckle noise reduction," *Biomedical Engineering Letters*, vol. 4, pp. 176-185, **Springer,** 2014.
5. **Nagashettappa Biradar**, M. Dewal, and M. Rohit, "Edge preserved speckle noise reduction using integrated fuzzy filters,"*International Scholarly Research Notices,* vol. 2014, Article ID 876434, 11 pages, **Hindawi**, 2014. doi:10.1155/2014/876434.
6. **Nagashettappa Biradar**, M.L. Dewal, and M. K. Rohit, "Speckle noise reduction using Hybrid TMAV based fuzzy filter," *International Journal of Research in Engineering and Technology,* vol. 3, pp. 113-118, 2014.
7. **Nagashettappa Biradar**, M.L.Dewal, M.K.Rohit, “Denoising of Transthoracic Echocardiographic images using Multiple Multiscale Techniques”, Sadhana, **Springer** (under revision).
8. **Nagashettappa Biradar**, M.L.Dewal, M.K.Rohit, "Echocardiographic image denoising using extreme total variation bilateral filter", *Optik-Int.J.Light Electron Opt.*, **Elsevier**, (Under review).
9. **Nagashettappa Biradar**, M.L.Dewal, M.K.Rohit, "Evaluation of despeckling filters for Echocardiographic images", *International Journal of Biomedical Imaging,* **Hindawi**, (Under review).

Conference

10. **Nagashettappa Biradar**, M.L.Dewal, M.K.Rohit, “M-Band Ridgelet based Speckle Noise Reduction in Transthoracic Echocardiographic images”, in *proceeding of National conference on Recent advances in Science and Technology,* 2014, pp.555-558.

11. **Nagashettappa Biradar**, M.L.Dewal, M.K.Rohit, "Challenges in contouring of cardiac chambers and valves in different views", in *Proceeding of International Conference on HealthTech Innovations* 2015, abstract no.5, pp.56.

12. **Nagashettappa Biradar,** M.L.Dewal, M.K.Rohit, "Automated Delineation of Doppler Echocardiographic images using Texture Filters", in *IEEE Proceedings of the 9th INDIACom,* 2nd International Conference on Computing for Sustainable Global Development, 2015, pp. 293-297.

BIBLIOGRAPHY

[1] A. S. Go, D. Mozaffarian, V. L. Roger, E. J. Benjamin, J. D. Berry, W. B. Borden, D. M. Bravata, S. Dai, E. S. Ford, C. S. Fox, S. Franco, H. J. Fullerton, C. Gillespie, S. M. Hailpern, J. A. Heit, V. J. Howard, M. D. Huffman, B. M. Kissela, S. J. Kittner, D. T. Lackland, J. H. Lichtman, L. D. Lisabeth, D. Magid, G. M. Marcus, A. Marelli, D. B. Matchar, D. K. McGuire, E. R. Mohler, C. S. Moy, M. E. Mussolino, G. Nichol, N. P. Paynter, P. J. Schreiner, P. D. Sorlie, J. Stein, T. N. Turan, S. S. Virani, N. D. Wong, D. Woo, and M. B. Turner, "Heart Disease and Stroke Statistics—2013 Update: A Report From the American Heart Association," *Circulation,* vol. 127, pp. e6-e245, 2013.

[2] P. Lancellotti, C. Tribouilloy, A. Hagendorff, B. A. Popescu, T. Edvardsen, L. A. Pierard, L. Badano, and J. L. Zamorano, "Recommendations for the echocardiographic assessment of native valvular regurgitation: an executive summary from the European Association of Cardiovascular Imaging," *European Heart Journal–Cardiovascular Imaging,* vol. 14, pp. 611-644, 2013.

[3] S. Kaddoura, *Echo made easy*: Elsevier Health Sciences, 2012.

[4] J. A. Noble, N. Navab, and H. Becher, "Ultrasonic image analysis and image-guided interventions," *Interface focus,* vol. 1, pp. 673-685, 2011.

[5] J. Noble, "Ultrasound image segmentation and tissue characterization," *Proceedings of the Institution of Mechanical Engineers, Part H: Journal of Engineering in Medicine,* vol. 224, pp. 307-316, 2010.

[6] P. Lancellotti, C. Tribouilloy, A. Hagendorff, L. Moura, B. A. Popescu, J. L. Monin, L. A. Pierard, L. Badano, J. L. Zamorano, and R. Sicari, "European Association of Echocardiography recommendations for the assessment of valvular regurgitation. Part 1: aortic and pulmonary regurgitation (native valve disease)," *European Journal of Echocardiography,* vol. 11, pp. 223-244, 2010.

[7] M. Halliwell, "A tutorial on ultrasonic physics and imaging techniques," *Proceedings of the Institution of Mechanical Engineers, Part H: Journal of Engineering in Medicine,* vol. 224, pp. 127-142, 2010.

[8] R. M. Lang, M. Bierig, R. B. Devereux, F. A. Flachskampf, E. Foster, P. A. Pellikka, M. H. Picard, M. J. Roman, J. Seward, J. Shanewise, S. Solomon, K. T. Spencer, M. St. John Sutton, and W. Stewart, "Recommendations for chamber quantification," *European Journal of Echocardiography,* vol. 7, pp. 79-108, 2006.

[9] W. A. Zoghbi, M. Enriquez-Sarano, E. Foster, P. A. Grayburn, C. D. Kraft, R. A. Levine, P. Nihoyannopoulos, C. M. Otto, M. A. Quinones, H. Rakowski, W. J. Stewart, A. Waggoner, and N. J. Weissman, "American Society of Echocardiography: recommendations for evaluation of the severity of native valvular regurgitation with two-dimensional and Doppler echocardiography: A report from the American Society of

Echocardiography's Nomenclature and Standards Committee and The Task Force on Valvular Regurgitation, developed in conjunction with the American College of Cardiology Echocardiography Committee, The Cardiac Imaging Committee, Council on Clinical Cardiology, The American Heart Association, and the European Society of Cardiology Working Group on Echocardiography, represented by," *European Journal of Echocardiography,* vol. 4, pp. 237-261, 2003.

[10] M. A. Quiñones, C. M. Otto, M. Stoddard, A. Waggoner, and W. A. Zoghbi, "Recommendations for quantification of Doppler echocardiography: a report from the Doppler Quantification Task Force of the Nomenclature and Standards Committee of the American Society of Echocardiography," *Journal of the American Society of Echocardiography,* vol. 15, pp. 167-184, 2002.

[11] T. Misaridis and J. A. Jensen, "Use of modulated excitation signals in medical ultrasound. Part I: basic concepts and expected benefits," *IEEE Transactions on, Ultrasonics, Ferroelectrics and Frequency Control,* vol. 52, pp. 177-191, 2005.

[12] A. Fernández-Caballero and J. M. Vega-Riesco, "Determining heart parameters through left ventricular automatic segmentation for heart disease diagnosis," *Expert Systems with Applications,* vol. 36, pp. 2234-2249, 2009.

[13] T. Guha and Q. J. Wu, "Curvelet Based Feature Extraction," *Face Recognition,* pp. 35-46, 2010.

[14] S. H. Contreras Ortiz, T. Chiu, and M. D. Fox, "Ultrasound image enhancement: a review," *Biomedical Signal Processing and Control,* vol. 7, pp. 419-428, 2012.

[15] C. Eswaran, A. W. Reza, and S. Hati, "Extraction of the contours of optic disc and exudates based on marker-controlled watershed segmentation," *Proceedings of International Conference on Computer Science and Information Technology,* pp. 719-723, 2008.

[16] O. Dössel, D. Farina, M. B. Mohr, M. Reumann, G. Seemann, and D. L. Weiss, "Computer-assisted Planning of Cardiac Interventions and Heart Surgery," in *GI Jahrestagung (1)*, pp. 499-506, 2006.

[17] E. Parvizi and Q. J. Wu, "Multiple object tracking based on adaptive depth segmentation," *Proceeding of Canadian Conference on Computer and Robot Vision,* pp. 273-277, 2008.

[18] R. F. Schulte, G. B. Sands, F. B. Sachse, O. Dössel, and A. J. Pullan, "Creation of a Human Heart, Model and its Customisation using Ultrasound Images," *Biomedizinische Technik / Biomedical Engineering,* vol. 46, pp. 26-28, 2001.

[19] R. Hanna, H. Barschdorf, T. Klinder, F. M. Weber, M. W. Krueger, O. Dössel, and C. Lorenz, "A hybrid method for automatic anatomical variant detection and segmentation," *Functional Imaging and Modeling of the Heart*, pp. 333-340, 2011.

[20] B. Prasad, S. Gupta, and K. K. Biswas, "Color and shape index for region-based image retrieval," in *Visual Form*, pp. 716-725, 2001.

[21] L. Christodoulou, C. P. Loizou, C. Spyrou, T. Kasparis, and M. Pantziaris, "Full-automated system for the segmentation of the common carotid artery in ultrasound images," *Proceeding of Communications Control and Signal Processing*, pp. 1-6, 2012.

[22] S. Finn, M. Glavin, and E. Jones, "Echocardiographic speckle reduction comparison," *IEEE Transactions on Ultrasonics, Ferroelectrics and Frequency Control,* vol. 58, pp. 82-101, 2011.

[23] D. Mittal, V. Kumar, S. C. Saxena, N. Khandelwal, and N. Kalra, "Enhancement of the ultrasound images by modified anisotropic diffusion method," *Medical & biological engineering & computing,* vol. 48, pp. 1281-1291, 2010.

[24] A. Khare, M. Khare, Y. Jeong, H. Kim, and M. Jeon, "Despeckling of medical ultrasound images using Daubechies complex wavelet transform," *Signal Processing,* vol. 90, pp. 428-439, 2010.

[25] V. Shrimali, R. Anand, and V. Kumar, "Current trends in segmentation of medical ultrasound b-mode images: a review," *IETE Technical Review,* vol. 26, p. 8, 2009.

[26] J. L. Mateo and A. Fernández-Caballero, "Finding out general tendencies in speckle noise reduction in ultrasound images," *Expert Systems with Applications,* vol. 36, pp. 7786-7797, 2009.

[27] C. P. Loizou and C. S. Pattichis, "Despeckle filtering algorithms and software for ultrasound imaging," *Synthesis lectures on algorithms and software in engineering,* vol. 1, pp. 1-166, 2008.

[28] A. Pizurica, A. M. Wink, E. Vansteenkiste, W. Philips, and B. J. Roerdink, "A review of wavelet denoising in MRI and ultrasound brain imaging," *Current medical imaging reviews,* vol. 2, pp. 247-260, 2006.

[29] D. L. Parker, T. A. Pryor, and J. D. Ridges, "Enhancement of two-dimensional echocardiographic images by lateral filtering," *Computers and Biomedical Research,* vol. 12, pp. 265-277, 1979.

[30] J. Bamber and C. Daft, "Adaptive filtering for reduction of speckle in ultrasonic pulse-echo images," *IEEE Transactions on Ultrasonics,* vol. 24, pp. 41-44, 1986.

[31] L. Y. Mo and R. Cobbold, "" Speckle" in Continuous Wave Doppler Ultrasound Spectra: A Simulation Study," *IEEE Transactions on Ultrasonics, Ferroelectrics and Frequency Control, ,* vol. 33, pp. 747-753, 1986.

[32] X. Zong, E. A. Geiser, A. F. Laine, and D. C. Wilson, "Homomorphic wavelet shrinkage and feature emphasis for speckle reduction and enhancement of echocardiographic images," in *IEEE Transactions on Medical Imaging*, pp. 658-667, 1996.

[33] X. Zong, A. F. Laine, and E. A. Geiser, "Speckle reduction and contrast enhancement of echocardiograms via multiscale nonlinear processing," *IEEE Transactions on Medical Imaging,* vol. 17, pp. 532-540, 1998.

[34] A. Achim, A. Bezerianos, and P. Tsakalides, "Novel Bayesian multiscale method for speckle removal in medical ultrasound images," *IEEE Transactions on Medical Imaging,,* vol. 20, pp. 772-783, 2001.

[35] Y. Yu and S. T. Acton, "Speckle reducing anisotropic diffusion," *IEEE Transactions on Image Processing,* vol. 11, pp. 1260-1270, 2002.

[36] Y. Yue, M. M. Croitoru, A. Bidani, J. B. Zwischenberger, and J. W. Clark Jr, "Nonlinear multiscale wavelet diffusion for speckle suppression and edge enhancement in ultrasound images," *IEEE Transactions on Medical Imaging,* vol. 25, pp. 297-311, 2006.

[37] A. Hammoude, "Endocardial border identification in two-dimensional echocardiographic images: review of methods," *Computerized Medical Imaging and Graphics,* vol. 22, pp. 181-193, 1998.

[38] M. Mulet-Parada and J. A. Noble, "2D+ T acoustic boundary detection in echocardiography," *Medical Image Analysis,* vol. 4, pp. 21-30, 2000.

[39] R. Jadon, S. Chaudhury, and K. Biswas, "A fuzzy theoretic approach for video segmentation using syntactic features," *Pattern Recognition Letters* vol. 22, pp. 1359-1369, 2001.

[40] J. Tschirren, R. M. Lauer, and M. Sonka, "Automated analysis of Doppler ultrasound velocity flow diagrams," *IEEE Transactions on Medical Imaging,* vol. 20, pp. 1422-1425, 2001.

[41] R. S. Sengar, A. Upadhyay, P. G. Patwardhan, M. Singh, and V. M. Gadre, "Approaches based on non-separable filter banks in 2D Gel electrophoresis image analysis," *Proceedings of International Conference on Asia Pacific Signal and Information Processing Association*, pp. 387-392, 2010.

[42] T. Shiota, "Automated cardiac flow measurement by digital colour Doppler echocardiography," *Heart,* vol. 88, pp. 211-212, 2002.

[43] N. Lin, W. Yu, and J. S. Duncan, "Combinative multi-scale level set framework for echocardiographic image segmentation," *Medical Image Analysis,* vol. 7, pp. 529-537, 2003.

[44] J. Yan and T. Zhuang, "Applying improved fast marching method to endocardial boundary detection in echocardiographic images," *Pattern Recognition Letters,* vol. 24, pp. 2777-2784, 2003.

[45] Y. Shang, X. Yang, M. Zhu, B. Jin, and M. Liu, "Prior based cardiac valve segmentation in echocardiographic sequences: geodesic active contour guided by region and shape prior," *Pattern Recognition and Image Analysis*, pp. 447-454, 2005.

[46] I. Larrabide, R. Feijóo, A. Novotny, and E. Taroco, "Topological derivative: a tool for image processing," *Computers & Structures,* vol. 86, pp. 1386-1403, 2008.

[47] W. Fang, K. L. Chan, S. Fu, and S. M. Krishnan, "Incorporating temporal information into active contour method for detecting heart wall boundary from echocardiographic image sequence," *Computerized Medical Imaging and Graphics,* vol. 32, pp. 590-600, 2008.

[48] E. J. H. Wu, M. L. De Andrade, D. E. Nicolosi, and S. C. Pontes Jr, "Artificial neural network: border detection in echocardiography," *Medical & biological engineering & computing,* vol. 46, pp. 841-848, 2008.

[49] R. J. Schneider, D. P. Perrin, N. V. Vasilyev, G. R. Marx, P. J. del Nido, and R. D. Howe, "Mitral annulus segmentation from 3D ultrasound using graph cuts," *IEEE Transactions on Medical Imaging,* vol. 29, pp. 1676-1687, 2010.

[50] S. G. Antunes, J. S. Silva, J. B. Santos, P. Martins, and E. Castela, "Phase Symmetry Approach Applied to Children Heart Chambers Segmentation: A Comparative Study," *IEEE Transactions on Biomedical Engineering,* vol. 58, pp. 2264-2271, 2011.

[51] P. Bansod, U. Desai, S. Merchant, and N. Burkule, "Segmentation of left ventricle in short-axis echocardiographic sequences by weighted radial edge filtering and adaptive recovery of dropout regions," *Computer methods in biomechanics and biomedical engineering,* vol. 14, pp. 603-613, 2011.

[52] A. Belaid, D. Boukerroui, Y. Maingourd, and J. F. Lerallut, "Phase-Based Level Set Segmentation of Ultrasound Images," *IEEE Transactions on Information Technology in Biomedicine,* vol. 15, pp. 138-147, 2011.

[53] F. A. A. Dawood, R. W. Rahmat, M. Z. Dimon, L. Nurliyana, and S. B. Kadiman, "Automatic Boundary Detection of Wall Motion in Two-dimensional Echocardiography Images," *Journal of Computer Science,* vol. 7, 2011.

[54] A. Skalski and P. Turcza, "Heart segmentation in echo images," *Metrology and Measurement Systems,* vol. 18, pp. 305-314, 2011.

[55] G. Carneiro, J. C. Nascimento, and A. Freitas, "The segmentation of the left ventricle of the heart from ultrasound data using deep learning architectures and derivative-based search methods," *IEEE Transactions on Image Processing,* vol. 21, pp. 968-982, 2012.

[56] J. Weese, J. Peters, C. Meyer, I. Wächter, R. Kneser, H. Lehmann, O. Ecabert, H. Barschdorf, R. Hanna, and F. M. Weber, "The generation of patient-specific heart models for diagnosis and interventions," in *Statistical Atlases and Computational Models of the Heart*, ed: Springer, 2010, pp. 25-35.

[57] S. D. Solomon, *Essential Echocardiography: A Practical Guide With DVD*: Springer, 2007.

[58] T. M. Nguyen, Q. J. Wu, and S. Ahuja, "An extension of the standard mixture model for image segmentation," *IEEE Transactions on Neural Networks,* vol. 21, pp. 1326-1338, 2010.

[59] A. Ebangelista, H. García del Castillo, F. Calvo, G. Permanyer-Miralda, C. Brotons, J. Angel, T. González-Alujas, P. Tornos, and J. Soler-Soler, "Strategy for optimal aortic regurgitation quantification by Doppler echocardiography: agreement among different methods," *American heart journal,* vol. 139, pp. 773-781, 2000.

[60] D. Detaint, D. Messika-Zeitoun, J. Maalouf, C. Tribouilloy, D. W. Mahoney, A. J. Tajik, and M. Enriquez-Sarano, "Quantitative Echocardiographic Determinants of Clinical Outcome in Asymptomatic Patients With Aortic RegurgitationA Prospective Study," *JACC: Cardiovascular Imaging,* vol. 1, pp. 1-11, 2008.

[61] E. van der Wall, "Evaluation of Valve Disease with Novel Imaging Techniques," in *Valve Surgery at the Turn of the Millennium*, pp. 93-104, 2004.

[62] M. V. Burri, D. Gupta, R. E. Kerber, and R. M. Weiss, "Review of novel clinical applications of advanced, real-time, 3-dimensional echocardiography," *Translational Research,* vol. 159, pp. 149-164, 2012.

[63] K. Ray, Q. J. Wu, G. Basu, and P. K. Panigrahi, "Random matrix route to image denoising," *Proceedings* of *International Conference on Systems and Informatics* pp. 1975-1980, 2012.

[64] T. F. Chan and L. A. Vese, "Active contours without edges," *IEEE Transactions on Image Processing,* vol. 10, pp. 266-277, 2001.

[65] M. Ishii, M. Jones, T. Shiota, I. Yamada, R. S. Heinrich, S. R. Holcomb, A. P. Yoganathan, and D. J. Sahn, "Quantifying Aortic Regurgitation by Using the Color Doppler–Imaged Vena Contracta A Chronic Animal Model Study," *Circulation,* vol. 96, pp. 2009-2015, 1997.

[66] R. Massay, R. Logan-Sinclair, J. Bamber, and D. Gibson, "Quantitative effects of speckle reduction on cross sectional echocardiographic images," *British heart journal,* vol. 62, pp. 298-304, 1989.

[67] J. W. Goodman, "Some fundamental properties of speckle," *Journal of the Optical Socity of America,* vol. 66, pp. 1145-1150, 1976.

[68] P. Atkinson and M. Berry, "Random noise in ultrasonic echoes diffracted by blood," *Journal of Physics A: Mathematical, Nuclear and General,* vol. 7, pp. 1293-1302, 1974.

[69] J. Dainty, "I The statistics of speckle patterns," *Progress in optics,* vol. 14, pp. 1-46, 1977.

[70] J. G. Abbott and F. Thurstone, "Acoustic speckle: Theory and experimental analysis," *Ultrasonic Imaging,* vol. 1, pp. 303-324, 1979.

[71] G. Traney, J. Allison, S. Smith, and O. Von Ramm, "A quantitative approach to speckle reduction via frequency compounding," *Ultrasonic Imaging,* vol. 8, pp. 151-164, 1986.

[72] R. S. Sengar, A. Upadhyay, P. G. Patwardhan, M. Singh, and V. M. Gadre, "Approaches based on non-separable filter banks in 2D Gel electrophoresis image analysis," in *Proceedings of Asia Pacific Signal and Information Processing Association (APSIPA) International Conference, Biopolis, Singapore*, 2010, pp. 387-392.

[73] T. Loupas, W. McDicken, and P. Allan, "An adaptive weighted median filter for speckle suppression in medical ultrasonic images," *IEEE Transactions on Circuits and Systems,* vol. 36, pp. 129-135, 1989.

[74] C. Tao and W. Hong Ren, "Adaptive impulse detection using center-weighted median filters," *IEEE Letters on Signal Processing, ,* vol. 8, pp. 1-3, 2001.

[75] R. N. Czerwinski, D. L. Jones, and W. D. O'Brien Jr, "Ultrasound speckle reduction by directional median filtering," *Proceeding of International Conference on Image Processing,* pp. 358-361, 1995.

[76] F. Qiu, J. Berglund, J. R. Jensen, P. Thakkar, and D. Ren, "Speckle noise reduction in SAR imagery using a local adaptive median filter," *GI Science & Remote Sensing,* vol. 41, pp. 244-266, 2004.

[77] J.-S. Lee, "Speckle analysis and smoothing of synthetic aperture radar images," *Computer graphics and image processing,* vol. 17, pp. 24-32, 1981.

[78] D. T. Kuan, A. A. Sawchuk, T. C. Strand, and P. Chavel, "Adaptive noise smoothing filter for images with signal-dependent noise," *IEEE Transactions on Pattern Analysis and Machine Intelligence,* pp. 165-177, 1985.

[79] V. S. Frost, J. A. Stiles, K. S. Shanmugam, J. C. Holtzman, and S. A. Smith, "An adaptive filter for smoothing noisy radar images," *Proceedings of the IEEE Communications and Radar,* vol. 69, pp. 133-135, 1981.

[80] Z. Shi and K. B. Fung, "A comparison of digital speckle filters," *Proceedings of Geoscience and Remote Sensing Symposium, IGARSS'94. Surface and Atmospheric Remote Sensing: Technologies, Data Analysis and Interpretation., International*, pp. 2129-2133, 1994.

[81] J.-S. Lee, "Digital image enhancement and noise filtering by use of local statistics," *IEEE Transactions on Pattern Analysis and Machine Intelligence,* pp. 165-168, 1980.

[82] A. Ozcan, A. Bilenca, A. E. Desjardins, B. E. Bouma, and G. J. Tearney, "Speckle reduction in optical coherence tomography images using digital filtering," *Journal of the Optical Society of America,* vol. 24, pp. 1901-1910, 2007.

[83] P. Perona and J. Malik, "Scale-space and edge detection using anisotropic diffusion," *IEEE Transactions on Pattern Analysis and Machine Intelligence,* vol. 12, pp. 629-639, 1990.

[84] J. Weickert, "Coherence-enhancing diffusion filtering," *International Journal of Computer Vision,* vol. 31, pp. 111-127, 1999.

[85] K. Z. Abd-Elmoniem, A. Youssef, and Y. M. Kadah, "Real-time speckle reduction and coherence enhancement in ultrasound imaging via nonlinear anisotropic diffusion," *IEEE Transactions on Biomedical Engineering,* vol. 49, pp. 997-1014, 2002.

[86] S. Aja-Fernández and C. Alberola-López, "On the estimation of the coefficient of variation for anisotropic diffusion speckle filtering," *IEEE Transactions on Image Processing* vol. 15, pp. 2694-2701, 2006.

[87] K. Krissian, C.-F. Westin, R. Kikinis, and K. G. Vosburgh, "Oriented speckle reducing anisotropic diffusion," *IEEE Transactions on Image Processing,* vol. 16, pp. 1412-1424, 2007.

[88] F. Liu and J. Liu, "Anisotropic diffusion for image denoising based on diffusion tensors," *Journal of Visual Communication and Image Representation,* vol. 23, pp. 516-521, 2012.

[89] K. Saini, M. Dewal, and M. Rohit, "Modified nonlinear complex diffusion filter (MNCDF)," *Journal of Echocardiography,* vol. 10, pp. 48-55, 2012.

[90] S. Nirmala, S. Dandapat, and P. Bora, "Wavelet weighted blood vessel distortion measure for retinal images," *Biomedical Signal Processing and Control* vol. 5, pp. 282-291, 2010.

[91] P. Gorgel, A. Sertbas, and O. N. Ucan, "A wavelet-based mammographic image denoising and enhancement with homomorphic filtering," *Journal of medical systems,* vol. 34, pp. 993-1002, 2010.

[92] C. S. Anand and J. S. Sahambi, "Wavelet domain non-linear filtering for MRI denoising," *Magnetic Resonance Imaging* vol. 28, pp. 842-861, 2010.

[93] A. Rojas Domínguez and A. K. Nandi, "Detection of masses in mammograms via statistically based enhancement, multilevel-thresholding segmentation, and region selection," *Computerized Medical Imaging and Graphics,* vol. 32, pp. 304-315, 2008.

[94] Y.-L. Qiao, C.-Y. Song, and C.-H. Zhao, "M-band ridgelet transform based texture classification," *Pattern Recognition Letters,* vol. 31, pp. 244-249, 2010.

[95] J. Xu, L. Yang, and D. Wu, "Ripplet: A new transform for image processing," *Journal of Visual Communication and Image Representation,* vol. 21, pp. 627-639, 2010.

[96] D. Gupta, R. Anand, and B. Tyagi, "Ripplet domain non-linear filtering for speckle reduction in ultrasound medical images," *Biomedical Signal Processing and Control,* vol. 10, pp. 79-91, 2014.

[97] D. L. Donoho and I. M. Johnstone, "Threshold selection for wavelet shrinkage of noisy data," in *Engineering in Medicine and Biology Society, 1994. Engineering Advances: New Opportunities for Biomedical Engineers. Proceedings IEEE International Conference*, pp. A24-A25 vol. 1, 1994.

[98] D. L. Donoho, "De-noising by soft-thresholding," *IEEE Transactions on Information Theory,* vol. 41, pp. 613-627, 1995.

[99] A. Pizurica and W. Philips, "Estimating the probability of the presence of a signal of interest in multiresolution single-and multiband image denoising," *IEEE Transactions on Image Processing,* vol. 15, pp. 654-665, 2006.

[100] P. Bao and L. Zhang, "Noise reduction for magnetic resonance images via adaptive multiscale products thresholding," *Image Processing Medical Imaging,* vol. 22, pp. 1089-1099, 2003.

[101] T. Blu and F. Luisier, "The SURE-LET approach to image denoising," *IEEE Transactions on Image Processing,* vol. 16, pp. 2778-2786, 2007.

[102] F. Luisier, T. Blu, and M. Unser, "A new SURE approach to image denoising: Interscale orthonormal wavelet thresholding," *IEEE Transactions on Image Processing,* vol. 16, pp. 593-606, 2007.

[103] Z. Dengwen and C. Wengang, "Image denoising with an optimal threshold and neighbouring window," *Pattern Recognition Letters,* vol. 29, pp. 1694-1697, 2008.

[104] S. Solbo and T. Eltoft, "Homomorphic wavelet-based statistical despeckling of SAR images," *IEEE Transactions on Geoscience and Remote Sensing,* vol. 42, pp. 711-721, 2004.

[105] H. Rabbani, M. Vafadust, P. Abolmaesumi, and S. Gazor, "Speckle Noise Reduction of Medical Ultrasound Images in Complex Wavelet Domain Using Mixture Priors," *IEEE Transactions on Biomedical Engineering,* vol. 55, pp. 2152-2160, 2008.

[106] S. Gupta, R. Chauhan, and S. Saxena, "Homomorphic wavelet thresholding technique for denoising medical ultrasound images," *Journal of Medical Engineering & Technology* vol. 29, pp. 208-214, 2005.

[107] V. Dutt and J. F. Greenleaf, "Adaptive speckle reduction filter for log-compressed B-scan images," *IEEE Transactions on Medical Imaging,* vol. 15, pp. 802-813, 1996.

[108] A. K. Jain and C. R. Christensen, "Digital Processing Of Images In Speckle Noise," 1980, pp. 46-50.

[109] V. Badalyan and E. Bazulin, "Use of homomorphic filtering for upgrading flaw imaging in the expert examination of welded joints of atomic power plant pipelines," *Russian Journal of Nondestructive Testing* vol. 39, pp. 266-272, 2003.

[110] S. Gupta, R. Chauhan, and S. Sexana, "Wavelet-based statistical approach for speckle reduction in medical ultrasound images," *Medical and Biological Engineering and computing,* vol. 42, pp. 189-192, 2004.

[111] D. Zhang, Q. Li, and J. You, "A modified matched filter with double-sided thresholding for screening proliferative diabetic retinopathy," *IEEE Transactions on Information Technology in Biomedicine,* vol. 13, pp. 528-534, 2009.

[112] B. Zhang, X. Wu, J. You, Q. Li, and F. Karray, "Hierarchical detection of red lesions in retinal images by multiscale correlation filtering," *SPIE medical imaging*, 2009, pp. 72601L-72601L-12.

[113] O. V. Michailovich and A. Tannenbaum, "Despeckling of medical ultrasound images," *IEEE Transactions on Ultrasonics, Ferroelectrics and Frequency Control,* vol. 53, pp. 64-78, 2006.

[114] S. Sudha, G. Suresh, and R. Sukanesh, "Speckle noise reduction in ultrasound images using context-based adaptive wavelet thresholding," *IETE Journal of Research,* vol. 55, p. 135, 2009.

[115] X. Hao, S. Gao, and X. Gao, "A novel multiscale nonlinear thresholding method for ultrasonic speckle suppressing," *IEEE Transactions on Medical Imaging,* vol. 18, pp. 787-794, 1999.

[116] A. Pizurica, W. Philips, I. Lemahieu, and M. Acheroy, "A versatile wavelet domain noise filtration technique for medical imaging," *IEEE Transactions on Medical Imaging,* vol. 22, pp. 323-331, 2003.

[117] R. G. Dantas and E. T. Costa, "Ultrasound speckle reduction using modified Gabor filters," *IEEE Transactions on Ultrasonics, Ferroelectrics and Frequency Control,* vol. 54, pp. 530-538, 2007.

[118] A. S. Saad, "Simultaneous speckle reduction and contrast enhancement for ultrasound images: Wavelet versus Laplacian pyramid," *Pattern Recognition and Image Analysis,* vol. 18, pp. 63-70, 2008.

[119] G. Aubert and J.-F. Aujol, "A variational approach to removing multiplicative noise," *SIAM Journal on Applied Mathematics* vol. 68, pp. 925-946, 2008.

[120] G. Gilboa, N. Sochen, and Y. Y. Zeevi, "Texture preserving variational denoising using an adaptive fidelity term," *Proceedings of VLsM*, 2003.

[121] C. Sheng, Y. Xin, Y. Liping, and S. Kun, "Total variation-based speckle reduction using multi-grid algorithm for ultrasound images," in *Image Analysis and Processing–ICIAP,* pp. 245-252, 2005.

[122] C. Tomasi and R. Manduchi, "Bilateral filtering for gray and color images," *Proceedings of International Conference on Computer Vision,* pp. 839-846, 1998.

[123] J. Tang, S. Guo, Q. Sun, Y. Deng, and D. Zhou, "Speckle reducing bilateral filter for cattle follicle segmentation," *BMC genomics,* vol. 11, p. S9, 2010.

[124] W. Zhang, Q. Zhang, and C. Yang, "Improved bilateral filtering for SAR image despeckling," *Electronics Letters* vol. 47, pp. 286-288, 2011.

[125] P. Coupé, P. Hellier, C. Kervrann, and C. Barillot, "Nonlocal means-based speckle filtering for ultrasound images," *IEEE Transactions on Image Processing,* vol. 18, pp. 2221-2229, 2009.

[126] A. Buades, B. Coll, and J.-M. Morel, "A non-local algorithm for image denoising," *Proceedings of IEEE Computer Society Conference on Computer Vision and Pattern Recognition,* pp. 60-65, *2005.*

[127] C. A. Deledalle, L. Denis, and F. Tupin, "Iterative weighted maximum likelihood denoising with probabilistic patch-based weights," *IEEE Transactions on Image Processing, ,* vol. 18, pp. 2661-2672, 2009.

[128] Y. Guo, Y. Wang, and T. Hou, "Speckle filtering of ultrasonic images using a modified non local-based algorithm," *Biomedical Signal Processing and Control,* vol. 6, pp. 129-138, 2011.

[129] Y. Sheng and Z.-G. Xia, "A comprehensive evaluation of filters for radar speckle suppression," *Proceedings of International Symposium of Geoscience and Remote Sensing. Remote Sensing for a Sustainable Future,* pp. 1559-1561, 1996.

[130] C. P. Loizou, C. S. Pattichis, C. I. Christodoulou, R. S. Istepanian, M. Pantziaris, and A. Nicolaides, "Comparative evaluation of despeckle filtering in ultrasound imaging of the carotid artery," *IEEE Transactions on Ultrasonics, Ferroelectrics and Frequency Control, ,* vol. 52, pp. 1653-1669, 2005.

[131] C. P. Loizou, C. Theofanous, M. Pantziaris, and T. Kasparis, "Despeckle filtering software toolbox for ultrasound imaging of the common carotid artery," *Computer methods and programs in biomedicine,* vol. 114, pp. 109-124, 2014.

[132] R. Srivastava, J. Gupta, and H. Parthasarthy, "Comparison of PDE based and other techniques for speckle reduction from digitally reconstructed holographic images," *Optics and Lasers in Engineering* vol. 48, pp. 626-635, 2010.

[133] P. C. Tay, C. D. Garson, S. T. Acton, and J. A. Hossack, "Ultrasound despeckling for contrast enhancement," *IEEE Transactions on Image Processing,* vol. 19, pp. 1847-1860, 2010.

[134] I. Elamvazuthi, M. L. B. Muhd Zain, and K. Begam, "Despeckling of ultrasound images of bone fracture using multiple filtering algorithms," *Mathematical and Computer Modelling,* vol. 57, pp. 152-168, 2013.

[135] J. Zhang, C. Wang, and Y. Cheng, "Comparison of Despeckle Filters for Breast Ultrasound Images," *Circuits, Systems, and Signal Processing,* pp. 1-24, 2014.

[136] V. Chalana, D. T. Linker, D. R. Haynor, and Y. Kim, "A multiple active contour model for cardiac boundary detection on echocardiographic sequences," *IEEE Transactions on Medical Imaging,* vol. 15, pp. 290-298, 1996.

[137] S. Kumar Maurya, P. Kumar Mishra, R. Kumar Singh, and A. Kumar Misra, "Image Enhancement by Intensity Based Interpolation and Selective Threshold," *Proceedings of International Conference on Communication Systems and Network Technologies,* pp. 174-178, 2012.

[138] E. J. H. Wu and D. E. Nicolosi, "A comparison of left ventricular border detection techniques applied to 2D echocardiograms," *Revista Brasileira de Engenharia Biomédica,* vol. 29, pp. 309-318, 2013.

[139] Q. Li, J. You, and D. Zhang, "Vessel segmentation and width estimation in retinal images using multiscale production of matched filter responses," *Expert Systems with Applications* vol. 39, pp. 7600-7610, 2012.

[140] T. Grosser, O. Hellwich, and A. Wendemuth, "Analysis of merge criteria within a watershed based segmentation algorithm," *Proceedings of International Conference on Adaptive Science & Technology*, pp. 250-256, *2009*.

[141] A. Rojas Domínguez and A. K. Nandi, "Toward breast cancer diagnosis based on automated segmentation of masses in mammograms," *Pattern Recognition* vol. 42, pp. 1138-1148, 2009.

[142] C. Lamberti, A. Martelli, and A. Guidazzoli, "Postprocessing techniques for 2-D echocardiographic imaging," *Proceedings of the Annual International Conference of the IEEE Engineering in Medicine and Biology Society, 1988.*, 1988, pp. 450-451.

[143] C. Xu and J. L. Prince, "Snakes, shapes, and gradient vector flow," *IEEE Transactions on Image Processing,* vol. 7, pp. 359-369, 1998.

[144] A. Giachetti, "On-line analysis of echocardiographic image sequences," *Medical Image Analysis,* vol. 2, pp. 261-284, 1998.

[145] C.-M. Chen, H. H.-S. Lu, and Y.-C. Lin, "An early vision-based snake model for ultrasound image segmentation," *Ultrasound in medicine & biology,* vol. 26, pp. 273-285, 2000.

[146] G. Hamarneh and T. Gustavsson, "Combining snakes and active shape models for segmenting the human left ventricle in echocardiographic images," in *Computers in Cardiology*, pp. 115-118, 2000.

[147] G. Jacob, J. A. Noble, C. Behrenbruch, A. D. Kelion, and A. P. Banning, "A shape-space-based approach to tracking myocardial borders and quantifying regional left-ventricular function applied in echocardiography," *IEEE Transactions on Medical Imaging,* vol. 21, pp. 226-238, 2002.

[148] P. Abolmaesumi and M. R. Sirouspour, "An interacting multiple model probabilistic data association filter for cavity boundary extraction from ultrasound images," *IEEE Transactions on Medical Imaging,* vol. 23, pp. 772-784, 2004.

[149] X. Hang, N. Greenberg, and J. Thomas, "Left ventricle quantification in 3D echocardiography using a geometric deformable model," *Computers in cardiology,* vol. 31, p. 649, 2004.

[150] J. Cheng, S. W. Foo, and S. M. Krishnan, "Echocardiographic image sequence segmentation by multiscale directional snake," *Proceedings of the Fourth IEEE International Symposium on Signal Processing and Information Technology,* pp. 26-29 2004.

[151] S. Martin, V. Daanen, O. Chavanon, and J. Troccaz, *Fast segmentation of the mitral valve leaflet in echocardiography*: Springer, 2006.

[152] B. Li and S. T. Acton, "Active contour external force using vector field convolution for image segmentation," *IEEE Transactions on Image Processing,* vol. 16, pp. 2096-2106, 2007.

[153] J. Stoitsis, S. Golemati, S. Kendros, and K. Nikita, "Automated detection of the carotid artery wall in B-mode ultrasound images using active contours initialized by the Hough transform," *Proceedings of Annual International Conference of the IEEE on Engineering in Medicine and Biology Society,* pp. 3146-3149, 2008.

[154] C. Li, C.-Y. Kao, J. C. Gore, and Z. Ding, "Minimization of region-scalable fitting energy for image segmentation," *IEEE Transactions on Image Processing,* vol. 17, pp. 1940-1949, 2008.

[155] M. Marsousi, A. Eftekhari, A. Kocharian, and J. Alirezaie, "Endocardial boundary extraction in left ventricular echocardiographic images using fast and adaptive B-spline snake algorithm," *International journal of computer assisted radiology and surgery,* vol. 5, pp. 501-513, 2010.

[156] S. G. Antunes, Jos, S. Silva, and J. B. Santos, "A level set segmentation method of the four heart cavities in pediatric ultrasound images," *Proceedings of* the 7th international conference on Image Analysis and Recognition - Volume Part II, voa de Varzim, Portugal, 2010.

[157] S. G. Antunes, J. S. Silva, and J. B. Santos, "A level set segmentation method of the four heart cavities in pediatric ultrasound images," in *Image Analysis and Recognition*, pp. 99-107, 2010.

[158] M. Agarwal, M. Hanmandlu, and K. K. Biswas, "Generalized intuitionistic fuzzy soft set and its application in practical medical diagnosis problem," *Proceedings of IEEE International Conference on Fuzzy Systems*, pp. 2972-2978, 2011.

[159] S. Osher and R. Fedkiw, *Level set methods and dynamic implicit surfaces* vol. 153: Springer Science & Business Media, 2003.

[160] D. Mumford and J. Shah, "Optimal approximations by piecewise smooth functions and associated variational problems," *Communications on pure and applied mathematics,* vol. 42, pp. 577-685, 1989.

[161] S. P. Dakua and J. Sahambi, "Automatic left ventricular contour extraction from cardiac magnetic resonance images using cantilever beam and random walk approach," *Cardiovascular Engineering,* vol. 10, pp. 30-43, 2010.

[162] S. P. Dakua and J. Sahambi, "Modified active contour model and Random Walk approach for left ventricular cardiac MR image segmentation," *International Journal for Numerical Methods in Biomedical Engineering,* vol. 27, pp. 1350-1361, 2011.

[163] V. Caselles, R. Kimmel, and G. Sapiro, "Geodesic active contours," *International Journal of Computer Vision,* vol. 22, pp. 61-79, 1997.

[164] R. Malladi, J. A. Sethian, and B. C. Vemuri, "Shape modeling with front propagation: A level set approach," *IEEE Transactions on Pattern Analysis and Machine Intelligence,* vol. 17, pp. 158-175, 1995.

[165] S. Dakua and J. Sahambi, "A level set method for cardiac magnetic resonance image segmentation: an adaptive approach," *Proceedings of IEEE international Conference on Industrial and Information Systems,* pp. 1-6, 2008.

[166] R. S. Sengar, A. K. Upadhyay, M. Singh, and V. M. Gadre, "Segmentation of two dimensional electrophoresis gel image using the wavelet transform and the watershed transform," *Proceedings of National Conference on Communications (NCC),* pp. 1-5, 2012.

[167] C. Kotropoulos and I. Pitas, "Optimum nonlinear signal detection and estimation in the presence of ultrasonic speckle," *Ultrasonic Imaging,* vol. 14, pp. 249-275, 1992.

[168] C. Kotropoulos, X. Magnisalis, I. Pitas, and M. G. Strintzis, "Nonlinear ultrasonic image processing based on signal-adaptive filters and self-organizing neural networks," *IEEE Transactions on Image Processing,* vol. 3, pp. 65-77, 1994.

[169] J. W. Klingler Jr, C. L. Vaughan, T. D. Fraker Jr, and L. T. Andrews, "Segmentation of echocardiographic images using mathematical morphology," *IEEE Transactions on Biomedical Engineering,* vol. 35, pp. 925-934, 1988.

[170] D. L. Pham, C. Xu, and J. L. Prince, "Current methods in medical image segmentation 1," *Annual review of biomedical engineering,* vol. 2, pp. 315-337, 2000.

[171] F. Shao, K. V. Ling, W. S. Ng, and R. Y. Wu, "Prostate boundary detection from ultrasonographic images," *Journal of ultrasound in medicine,* vol. 22, pp. 605-623, 2003.

[172] J. Cheng, S. W. Foo, and S. M. Krishnan, "Watershed-presegmented snake for boundary detection and tracking of left ventricle in echocardiographic images," 2006.

[173] T. Chaira and S. Anand, "A Novel Intuitionistic Fuzzy Approach For Tumor / Hemorrhage Detection in Medical Images," *Journal of Scientific and Industrial Research* vol. 70, 2011.

[174] S. Lankton and A. Tannenbaum, "Localizing region-based active contours," *IEEE Transactions on Image Processing,* vol. 17, pp. 2029-2039, 2008.

[175] K. Zhang, D. Zhang, and S. Zhang, "A variational multiphase level set approach to simultaneous segmentation and bias correction," *Proceedings of IEEE International Conference on Image Processing,* pp. 4105-4108 2010.

[176] C. Sheng, Y. Xin, Y. Liping, and S. Kun, "Segmentation in echocardiographic sequences using shape-based snake model combined with generalized Hough transformation," *The international journal of cardiovascular imaging,* vol. 22, pp. 33-45, 2006.

[177] S. G. Lacerda, A. F. da Rocha, D. F. Vasconcelos, J. L. de Carvalho, I. Sene, and J. F. Camapum, "Left ventricle segmentation in echocardiography using a radial-search-based image processing algorithm," *IEEE International Conference on Engineering in Medicine and Biology Society,* pp. 222-225, 2008.

[178] H. Zheng and O. Hellwich, "Double regularized Bayesian estimation for blur identification in video sequences," in *Computer Vision–ACCV 2006*, pp. 943-952, 2006.

[179] C. Li, C. Xu, C. Gui, and M. D. Fox, "Distance regularized level set evolution and its application to image segmentation," *IEEE Transactions on Image Processing,* vol. 19, pp. 3243-3254, 2010.

[180] K. Saini, M. Dewal, and M. Rohit, "A Fast Region-Based Active Contour Model for Boundary Detection of Echocardiographic Images," *Journal of digital imaging,* vol. 25, pp. 271-278, 2012.

[181] J. Silvestre Silva, J. B. Santos, D. Roxo, P. Martins, E. Castela, and R. Martins, "Algorithm Versus Physicians Variability Evaluation in the Cardiac Chambers Extraction," *IEEE Transactions on Information Technology in Biomedicine,* vol. 16, pp. 835-841, 2012.

[182] T. Dietenbeck, M. Alessandrini, D. Barbosa, J. D'hooge, D. Friboulet, and O. Bernard, "Detection of the whole myocardium in 2D-echocardiography for multiple orientations using a geometrically constrained level-set," *Medical Image Analysis,* vol. 16, pp. 386-401, 2012.

[183] X. Bresson, S. Esedoḡlu, P. Vandergheynst, J.-P. Thiran, and S. Osher, "Fast global minimization of the active contour/snake model," *Journal of Mathematical Imaging and vision,* vol. 28, pp. 151-167, 2007.

[184] K. Zhang, L. Zhang, H. Song, and D. Zhang, "Re-initialization free level set evolution via reaction diffusion," *IEEE Transactions on Image Processing,* vol. 22, pp. 258-271, 2013.

[185] J. A. Noble and D. Boukerroui, "Ultrasound image segmentation: a survey," *IEEE Transactions on Medical Imaging,* vol. 25, pp. 987-1010, 2006.

[186] B. Das and S. Banerjee, "Parametric contour model in medical image segmentation," *Deformable Models*, 2007, pp. 31-74.

[187] D. Vilkomerson, S. Ricci, and P. Tortoli, "Finding the peak velocity in a flow from its doppler spectrum," *IEEE Transactions on, Ultrasonics, Ferroelectrics and Frequency Control,* vol. 60, pp.2079-2088, 2013.

[188] A. F. Hall and S. J. Kovács, "Automated method for characterization of diastolic transmitral Doppler velocity contours: early rapid filling," *Ultrasound in medicine & biology,* vol. 20, pp. 107-116, 1994.

[189] J. Gong, R. Kirsner, A. MacIsaac, C. Drossos, and J. Cameron, "Computer processing of CW Doppler trans-valvular spectrograms," *Proceedings of Conference on Intelligent Information Systems, The Seventh Australian and New Zealand*, pp. 335-340, 2001.

[190] T. Jansson, R. Jurkonis, T. D. Mast, H. W. Persson, and K. Lindstrom, "Frequency dependence of speckle in continuous-wave ultrasound with implications for blood perfusion measurements," *IEEE Transactions on Ultrasonics, Ferroelectrics and Frequency Control,* vol. 49, pp. 715-725, 2002.

[191] M. A. von Krger and D. H. Evans, "Doppler ultrasound tracking instrument for monitoring blood flow velocity," *Ultrasound in medicine & biology,* vol. 28, pp. 1499-1508, 2002.

[192] P. Shechner, M. Sheinovitz, M. Feinberg, and H. Greenspan, "Image analysis of Doppler echocardiography for patients with atrial fibrillation," *Proceedings of IEEE International Symposium on Biomedical Imaging: Nano to Macro,* pp. 488-491, 2004.

[193] H. Greenspan, O. Shechner, M. Scheinowitz, and M. S. Feinberg, "Doppler echocardiography flow-velocity image analysis for patients with atrial fibrillation," *Ultrasound in medicine & biology,* vol. 31, pp. 1031-1040, 2005.

[194] D. A. Doherty, I. R. James, and J. P. Newnham, "Estimation of the Doppler ultrasound maximal umbilical waveform envelope: I. Estimation method," *Ultrasound in medicine & biology,* vol. 28, pp. 1251-1259, 2002.

[195] V. Magagnin, E. Caiani, L. Delfino, C. Champlon, S. Cerutti, and M. Turiel, "Semi-Automated Analysis of Coronary Flow Doppler Images: Validation with Manual Tracings," *Proceedings of IEEE International Conference on Engineering in Medicine and Biology Society,* pp. 719-722, 2006.

[196] S. K. Zhou, F. Guo, J. Park, G. Carneiro, J. Jackson, M. Brendel, C. Simopoulos, J. Otsuki, and D. Comaniciu, "A probabilistic, hierarchical, and discriminant framework for rapid and accurate detection of deformable anatomic structure," *Proceedings of IEEE International Conference on Computer Vision,* pp. 1-8, 2007.

[197] Z. Wang, G. Slabaugh, M. Zhou, and T. Fang, "Automatic tracing of blood flow velocity in pulsed Doppler images," *Proceedings of IEEE International Conference on Automation Science and Engineering,* pp. 218-222, 2008.

[198] J. Park, S. K. Zhou, J. Jackson, and D. Comaniciu, "Automatic mitral valve inflow measurements from Doppler echocardiography," in *Medical Image Computing and Computer-Assisted Intervention–MICCAI 2008*, pp. 983-990, 2008.

[199] N. Kiruthika, B. Prabhakar, and M. R. Reddy, "Automated assessment of aortic regurgitation using 2D Doppler Echocardiogram," *Proceedings of IEEE International Workshop Imagining Systems and Techniques, on Imagining read Imaging*, pp. 95-99, 2006.

[200] H. Li, Y. Zhang, and D. Xu, "Noise and speckle reduction in Doppler blood flow spectrograms using an adaptive pulse-coupled neural network," *EURASIP Journal on Advances in Signal Processing,* vol. 2010, p. 2, 2010.

[201] H. Kalinic, S. Loncaric, M. Cikes, D. Milicic, and B. Bijnens, "Model-based segmentation of aortic ultrasound images," *Proceedings of International Symposium on Image and Signal Processing and Analysis,* pp. 739-743, 2011.

[202] T. Syeda-Mahmood, P. Turaga, D. Beymer, F. Wang, A. Amir, H. Greenspan, and K. Pohl, "Shape-based similarity retrieval of doppler images for clinical decision support," *Proceedings of IEEE Conference on Computer Vision and Pattern Recognition,* pp. 855-862, 2010.

[203] E. R. Wolfe, E. J. Delp, C. R. Meyer, F. L. Bookstein, and A. J. Buda, "Accuracy of automatically determined borders in digital two-dimensional echocardiography using a cardiac phantom," *IEEE Transactions on Medical Imaging, ,* vol. 6, pp. 292-296, 1987.

[204] I. Mikic, S. Krucinski, and J. D. Thomas, "Segmentation and tracking in echocardiographic sequences: active contours guided by optical flow estimates," *IEEE Transactions on Medical Imaging,* vol. 17, pp. 274-284, 1998.

[205] G. I. Sanchez-Ortiz, J. Declerck, M. Mulet-Parada, and J. A. Noble, "Automating 3D echocardiographic image analysis," *Medical Image Computing and Computer-Assisted Intervention–MICCAI 2000*, pp. 687-696, 2000.

[206] M. L. Siqueira, J. Scharcanski, and P. O. Navaux, "Echocardiographic image sequence segmentation and analysis using self-organizing maps," *Journal of VLSI signal processing systems for signal, image and video technology,* vol. 32, pp. 135-145, 2002.

[207] E. Boonchieng, W. Boonchieng, and R. Kanjanavanit, "Edge-detection and segmentation methods for two-dimensional echocardiograms," *Computers in Cardiology,* pp. 541-544, 2004.

[208] S. Chan and G. Sainarayanan, "Fuzzy-based boundary enhancement for echocardiogram using local image characteristics," *Malaysian Journal of Computer Science,* vol. 19, p. 151, 2006.

[209] C. Sheng, Y. Xin, Y. Liping, and S. Kun, "Segmentation in echocardiographic sequences using shape-based snake model," *Image Analysis and Processing–ICIAP 2005*, pp. 375-382, 2005.

[210] M. Nillesen, R. Lopata, I. Gerrits, L. Kapusta, H. Huisman, J. Thijssen, and C. De Korte, "Three dimensional segmentation of the heart muscle in real-time 3D echocardiographic sequences using image statistics," *Computers in Cardiology,* pp. 129-132, 2006.

[211] E. Humada and S. Abu-Bakar, "Automatic Coronary Artery Detection in Echocardiogram Image," *Proceedings of IEEE International Conference on Signal Processing and Communications,* pp. 584-587, 2007.

[212] M. M. Nillesen, R. G. Lopata, I. H. Gerrits, L. Kapusta, H. J. Huisman, J. M. Thijssen, and C. L. de Korte, "Segmentation of the heart muscle in 3-D pediatric echocardiographic images," *Ultrasound in medicine & biology,* vol. 33, pp. 1453-1462, 2007.

[213] M. Mora, J. Leiva, and M. Olivares, "Heart Cavity Segmentation in Ultrasound Images Based on Supervised Neural Networks," in *Computer Vision/Computer Graphics CollaborationTechniques*, pp. 58-68, 2009.

[214] M. Hassanzadeh, G. Ardeshir, and M. Karami Mollaei, "Two new methods for finding eondocardial and epicardial boundaries in echocardiographic images using wavelet analysis," *European Journal of Scientific Research,* vol. 27, pp. 264-274, 2009.

[215] A. Karamalis, W. Wein, T. Klein, and N. Navab, "Ultrasound confidence maps using random walks," *Medical Image Analysis,* vol. 16, pp. 1101-1112, 2012.

[216] C. M. Tribouilloy, M. E. Sarano, Kent R. Bailey, James B.Seward, and A. Jamil Tajik, "Assessment of Severity of Aortic Regurgitation Using the Width of the Vena Contracta : A Clinical Color Doppler Imaging Study," *Circulation Journal of American Heart Association,* pp. 558-564, 2000.

[217] H. W. Benjamin Shipton, "Valvular Heart Disease: Review and Update," *American Family Physician,* pp. 2201-2208 2001.

[218] S. A. H. DuWayne L. Willett, Michael E. Jessen, Michael A. Wait, Paul A. Grayburn, "Assessment of Aortic Regurgitation by Transesophageal Color Doppler Imaging of the

Vena Contracta: Validation Against an Intraoperative Aortic Flow Probe," *Journal of the American College of Cardiology,* pp. 1450-1455, 2001.

[219] A. A. I. D Vinereanu, A. G. Fraser, "Assessment of left ventricular long axis contraction can detect early myocardial dysfunction in asymptomatic patients with severe aortic regurgitation," *Heart,* pp. 30-36, 2001.

[220] I. S. Paul A. Heidenreich, Steven L. Hancock, J. Edwinatwood, "A Systolic Murmur is a Common Presentation of Aortic Regurgitation Detected by Echocardiography," *Clinical Cardiology,* pp. 502-506, 2004.

[221] Enriquez-Sarano , A. J. T. Maurice, , "Aortic Regurgitation," *The New England Journal of Medicine,* pp. 1539-1546, 2004.

[222] Nisha Surenderanath, Faris Al-Mousily, Douglas Theriaque, Jonathan Shuster, Carolyn Spencer,Margaret M Samyn, "1060 Evaluation of aortic valve regurgitation by cardiac magnetic resonance imaging: a comparison with echocardiography," *Journal of Cardiovascular Magnetic,* 2008.

[223] Kameswari Maganti, Vera H. Rigolin, Maurice Enriquez Sarano, Robert O. Bonow, "Valvular Heart Disease: Diagnosis and Management," in *Symposium on cardiovascular diseases*, pp. 483-500, 2009.

[224] Victoria Delgado, Nico R. van de Veire, Frank van der Kley, Joanne D. Schuijf,, "Transcatheter aortic valve implantation: role of multi-detector row computed tomography to evaluate prosthesis positioning and deployment in relation to valvefunction," *European Heart Journal,* pp. 477-493, 2010.

[225] S. H. Recke, "Left Ventricular function-conduction impairment as reflected by the ECG in chornic aortic regurgitation," *Wiener Klinische Wochenschrift,* pp. 502-507, 2011.

[226] J. Simpson, O. Miller, and A. Bell, "Three-dimensional echocardiography in congenital heart disease ," *International Journal of Cardiovascular Imaging, pp. 743-753,* 2012.

[227] S. G. Chang, B. Yu, and M. Vetterli, "Adaptive wavelet thresholding for image denoising and compression," *IEEE Transactions on Image Processing,* vol. 9, pp. 1532-1546, 2000.

[228] A. Wong, A. Mishra, K. Bizheva, and D. A. Clausi, "General Bayesian estimation for speckle noise reduction in optical coherence tomography retinal imagery," *Optics Express,* vol. 18, pp. 8338-8352, 2010.

[229] H. K. Kwan, "Fuzzy filters for noise reduction in images," in *Fuzzy Filters for Image Processing*, pp. 25-53, 2003.

[230] M. Zhu, S. J. Wright, and T. F. Chan, "Duality-based algorithms for total-variation-regularized image restoration," *Computational Optimization and Applications,* vol. 47, pp. 377-400, 2010.

[231] G. Bhutada, R. Anand, and S. Saxena, "Edge preserved image enhancement using adaptive fusion of images denoised by wavelet and curvelet transform," *Digital Signal Processing,* vol. 21, pp. 118-130, 2011.

[232] M. Szkulmowski, I. Gorczynska, D. Szlag, M. Sylwestrzak, A. Kowalczyk, and M. Wojtkowski, "Efficient reduction of speckle noise in optical coherence tomography," *Optics Express,* vol. 20, pp. 1337-1359, 2012.

[233] H. Guo, J. E. Odegard, M. Lang, R. A. Gopinath, I. W. Selesnick, and C. S. Burrus, "Wavelet based speckle reduction with application to SAR based ATD/R," *Proceedings of IEEE International Conference on Image Processing,* pp. 75-79, 1994.

[234] B. B. Saevarsson, J. R. Sveinsson, and J. A. Benediktsson, "Speckle reduction of SAR images using adaptive curvelet domain," *Proceedings of IEEE International Symposium on Geoscience and Remote Sensing,* pp. 4083-4085, 2003.

[235] A. KHARE and U. S. Tiwary, "Soft-thresholding for denoising of medical images — a multiresolution approach," *International Journal of Wavelets, Multiresolution and Information Processing,* vol. 03, pp. 477-496, 2005.

[236] X. Hua, L. E. Pierce, and F. T. Ulaby, "SAR speckle reduction using wavelet denoising and Markov random field modeling," *IEEE Transactions on Geoscience and Remote Sensing,* vol. 40, pp. 2196-2212, 2002.

[237] R. R. Coifman and D. L. Donoho, *Translation-invariant de-noising*: Springer, 1995.

[238] L. Zhang and P. Bao, "Denoising by spatial correlation thresholding," *IEEE Transactions on Circuits and Systems for Video Technology,* vol. 13, pp. 535-538, 2003.

[239] D. Zhou and X. Shen, "Image denoising using block thresholding," *Proceedings of Congress on Image and Signal Processing,* pp. 335-338, 2008.

[240] R. Jirik and T. Taxt, "High-resolution ultrasonic imaging using two-dimensional homomorphic filtering," *IEEE Transactions on Ultrasonics, Ferroelectrics and Frequency Control,* vol. 53, pp. 1440-1448, 2006.

[241] L. Sendur and I. W. Selesnick, "Bivariate shrinkage functions for wavelet-based denoising exploiting interscale dependency," *IEEE Transactions on Signal Processing, ,* vol. 50, pp. 2744-2756, 2002.

[242] J. L. Starck, E. J. Candès, and D. L. Donoho, "The curvelet transform for image denoising," *IEEE Transactions on Image Processing,* vol. 11, pp. 670-684, 2002.

[243] G. Gilboa, N. Sochen, and Y. Y. Zeevi, "Estimation of optimal PDE-based denoising in the SNR sense," *Image Processing, IEEE Transactions on,* vol. 15, pp. 2269-2280, 2006.

[244] T. R. Crimmins, "Geometric filter for speckle reduction," *Applied optics,* vol. 24, pp. 1438-1443, 1985.

[245] A. Madabhushi and D. N. Metaxas, "Combining low-, high-level and empirical domain knowledge for automated segmentation of ultrasonic breast lesions," *IEEE Transactions on Medical Imaging,* vol. 22, pp. 155-169, 2003.

[246] H. D. Liang, J. A. Noble, and P. N. Wells, "Recent advances in biomedical ultrasonic imaging techniques," *Interface Focus,* pp. 475-476, 2011.

[247] E. Candes, L. Demanet, D. Donoho, and L. Ying, "Fast discrete curvelet transforms," *Multiscale Modeling & Simulation,* vol. 5, pp. 861-899, 2006.

[248] R. C. Gonzalez, R. E. Woods, and S. L. Eddins, *Digital image processing using MATLAB* vol. 2: Gatesmark Publishing Knoxville, 2009.

[249] T. T. Cai and B. W. Silverman, "Incorporating information on neighbouring coefficients into wavelet estimation," *Sankhyā: The Indian Journal of Statistics, Series B,* pp. 127-148, 2001.

[250] H. Kwan and Y. Cai, "Fuzzy filters for image filtering," *Proceedings of Midwest Symposium Circuits and Systems,* pp. 672-675, 2002.

[251] T. Goldstein and S. Osher, "The split Bregman method for L1-regularized problems," *SIAM Journal on Imaging Sciences,* vol. 2, pp. 323-343, 2009.

[252] L. I. Rudin, S. Osher, and E. Fatemi, "Nonlinear total variation based noise removal algorithms," *Physica D: Nonlinear Phenomena,* vol. 60, pp. 259-268, 1992.

[253] C. Louchet and L. Moisan, "Total variation as a local filter," *SIAM Journal on Imaging Sciences,* vol. 4, pp. 651-694, 2011.

[254] H. Zheng and O. Hellwich, "An edge-driven total variation approach to image deblurring and denoising," *Proceedings of International Conference on Innovative Computing, Information and Control,* pp. 705-710, 2006.

[255] S. Paris, P. Kornprobst, J. Tumblin, and F. Durand, "A gentle introduction to bilateral filtering and its applications," *ACM SIGGRAPH, pp. 1-45, 2007*.

[256] K. N. Chaudhury, D. Sage, and M. Unser, "Fast bilateral filtering using trigonometric range kernels," *IEEE Transactions on Image Processing,* vol. 20, pp. 3376-3382, 2011.

[257] M. Elad, "On the origin of the bilateral filter and ways to improve it," *IEEE Transactions on Image Processing,* vol. 11, pp. 1141-1151, 2002.

[258] M. Ertas, I. Yildirim, M. Kamasak, and A. Akan, "An iterative tomosynthesis reconstruction using total variation combined with non-local means filtering," *Biomedical engineering online,* vol. 13, p. 65, 2014.

[259] T. Chan, S. Esedoglu, F. Park, and A. Yip, "Recent developments in total variation image restoration," *Mathematical Models of Computer Vision,* vol. 17, 2005.

[260] P. Kornprobst and J. Tumblin, *Bilateral filtering: Theory and applications*: Now Publishers Inc, 2009.

[261] O. D'Hondt, S. Guillaso, and O. Hellwich, "Iterative bilateral filtering of polarimetric SAR data," *Selected Topics in Applied Earth Observations and Remote Sensing, IEEE Journal of,* vol. 6, pp. 1628-1639, 2013.

[262] S. Kaur, "How Medical Robots are going to Affect Our Lives," *IETE Technical Review (Medknow Publications & Media Pvt. Ltd.),* vol. 29, 2012.

[263] A. K. Tripathi and S. Mukhopadhyay, "Removal of Fog from Images: A Review," *IETE Technical Review (Medknow Publications & Media Pvt. Ltd.),* vol. 29, 2012.

[264] K. Basak, M. Manjunatha, and P. K. Dutta, "Review of laser speckle-based analysis in medical imaging," *Medical & biological engineering & computing,* vol. 50, pp. 547-558, 2012.

[265] V. S. Frost, J. A. Stiles, K. S. Shanmugan, and J. C. Holtzman, "A model for radar images and its application to adaptive digital filtering of multiplicative noise," *IEEE Transactions on Pattern Analysis and Machine Intelligence,* pp. 157-166, 1982.

[266] A. Bini and M. Bhat, "Despeckling low SNR, low contrast ultrasound images via anisotropic level set diffusion," *Multidimensional Systems and Signal Processing* vol. 25, pp. 41-65, 2014.

[267] D. Gupta, R. Anand, and B. Tyagi, "Despeckling of ultrasound images of bone fracture using M-band ridgelet transform," *Optik-International Journal for Light and Electron Optics,* vol. 125, pp. 1417-1422, 2014.

[268] J. Weickert, "Coherence-enhancing shock filters," in *Pattern Recognition*, pp. 1-8, 2003.

[269] M. Zhou, H. Chen, J. Paisley, L. Ren, L. Li, Z. Xing, D. Dunson, G. Sapiro, and L. Carin, "Nonparametric Bayesian dictionary learning for analysis of noisy and incomplete images," *IEEE Transactions on Image Processing,* vol. 21, pp. 130-144, 2012.

[270] V. Frost, J. Stiles, K. S. Shanmugam, J. Holtzman, and S. Smith, "An adaptive filter for smoothing noisy radar images," *Proceedings of the IEEE,* vol. 69, pp. 133-135, 1981.

[271] P. Chatterjee and P. Milanfar, "Patch-based near-optimal image denoising," *IEEE Transactions on Image Processing,* vol. 21, pp. 1635-1649, 2012.

[272] B. Deka and P. K. Bora, "Removal of correlated speckle noise using sparse and overcomplete representations," *Biomedical Signal Processing and Control* vol. 8, pp. 520-533, 2013.

[273] C. S. Anand and J. Sahambi, "MRI denoising using bilateral filter in redundant wavelet domain," *Proceedings of IEEE Region 10 Conference TENCON*, pp. 1-6, 2008.

[274] M. Agarwal, K. K. Biswas, and M. Hanmandlu, "Generalized intuitionistic fuzzy soft sets with applications in decision-making," *Applied Soft Computing* vol. 13, pp. 3552-3566, 2013.

[275] B. Deka and P. Bora, "A versatile statistical model for despeckling of medical ultrasound images," *Proceedings of Annual IEEE India Conference (INDICON),* pp. 1-4, 2009.

[276] K. M. Singh and P. K. Bora, "Adaptive vector median filter for removal impulses from color images," *Proceedings of the International Symposium on*, *Circuits and Systems,* pp. II-396-II-399 vol. 2, 2003.

[277] B. Deka and P. Bora, "Despeckling of medical ultrasound images using sparse representation," *Proceedings of International Conference on Signal Processing and Communications (SPCOM),* pp. 1-5, 2010.

[278] K. Basak, M. Mahadevappa, and P. K. Dutta, "Multiscale noise-adaptive homomorphic filtering based speckle denoising in laser speckle imaging," *Proceedings of National Conference on Computer Vision, Pattern Recognition, Image Processing and Graphics (NCVPRIPG),* pp. 1-5, 2013.

[279] A. Talukdar, B. Deka, and P. Bora, "Wavelet based adaptive bayesian despeckling for medical ultrasound images," *Proceedings of IEEE Region 10 Conference, TENCON,* pp. 1-6, 2010.

[280] R. Mukkavilli, J. Sahambi, and P. Bora, "Modified homomorphic wavelet based despeckling of medical ultrasound images," *Proceedings of Canadian Conference on Electrical and Computer Engineering, CCECE* pp. 000887-000890, 2008.

[281] M. Iqbal, J. Chen, W. Yang, P. Wang, and B. Sun, "SAR image despeckling by selective 3D filtering of multiple compressive reconstructed images," *Progress In Electromagnetics Research,* vol. 134, pp. 209-226, 2013.

[282] M. Zolgharni, N. M. Dhutia, G. D. Cole, M. R. Bahmanyar, S. Jones, S. A. Sohaib, S. B. Tai, K. Willson, J. A. Finegold, and D. P. Francis, "Automated aortic Doppler flow tracing for reproducible research and clinical measurements," *IEEE Transaction on Medical Imaging,* vol. 33, pp. 1071-1082, 2014.

[283] T. Baba, S. Adachi, and M. Taiko, "Automatic Valve-Rejection Algorithm for Cardiac Doppler Ultrasound Systems," *ISRN Biomedical Imaging,* vol. 2013, 2013.

[284] A. Rosenfeld and A. C. Kak, *Digital Picture Processing: Vol.: 1*: Academic Press, Incorporated, 1982.

[285] M. D. Levine, *Vision in man and machine* vol. 574: McGraw-Hill New York, 1985.

[286] R. M. Haralick, K. Shanmugam, and I. H. Dinstein, "Textural features for image classification," *IEEE Transactions on Systems, Man and Cybernetics,* pp. 610-621, 1973.

[287] P. Bao, D. Zhang, and W. Xiaolin, "Canny edge detection enhancement by scale multiplication," *IEEE Transactions on Pattern Analysis and Machine Intelligence,* vol. 27, pp. 1485-1490, 2005.

[288] T. Chaira and A. Ray, "A new measure using intuitionistic fuzzy set theory and its application to edge detection," *Applied Soft Computing,* vol. 8, pp. 919-927, 2008.

[289] S. Aja-Fernandez, G. Vegas-Sanchez-Ferrero, and M. Fernandez, "Soft thresholding for medical image segmentation," *Proceedings of* IEEE *International Conference on Engineering in Medicine and Biology Society*, pp. 4752-4755, 2010.

[290] I. Larrabide, R. Feijóo, A. Novotny, E. Taroco, and M. Masmoudi, "An image segmentation method based on a discrete version of the topological derivative," in *World Congress Structural and Multidisciplinary Optimization*, 2005, pp. 1-11.

[291] A. Mishra, P. Dutta, and M. Ghosh, "A GA based approach for boundary detection of left ventricle with echocardiographic image sequences," *Image and vision Computing,* vol. 21, pp. 967-976, 2003.

[292] C. Li, R. Huang, Z. Ding, J. Gatenby, D. N. Metaxas, and J. C. Gore, "A level set method for image segmentation in the presence of intensity inhomogeneities with application to MRI," *IEEE Transactions on Image Processing,* vol. 20, pp. 2007-2016, 2011.

[293] K. Zhang, L. Zhang, H. Song, and W. Zhou, "Active contours with selective local or global segmentation: a new formulation and level set method," *Image and vision Computing,* vol. 28, pp. 668-676, 2010.

[294] K. Zhang, S. Xu, W. Zhou, and B. Liu, "Active Contours Based on Image Laplacian Fitting Energy," *Chinese Journal of Electronics,* vol. 18, pp. 281-284, 2009.

[295] A. R. Abdel-Dayem and M. R. El-Sakka, "Fuzzy c-means clustering for segmenting carotid artery ultrasound images," in *Image Analysis and Recognition*, pp. 935-948, 2007.

[296] V. R. Rathod, R. Anand, and A. Ashok, "Comparative analysis of NDE techniques with image processing," *Nondestructive Testing and Evaluation,* vol. 27, pp. 305-326, 2012.

[297] V. R. Rathod and R. Anand, "A comparative study of different segmentation techniques for detection of flaws in nde weld images," *Journal of Nondestructive Evaluation,* vol. 31, pp. 1-16, 2012.

[298] A. K. Hamou and M. R. El-Sakka, "A novel segmentation technique for carotid ultrasound images," *Proceedings of IEEE International Conference on Acoustics, Speech, and Signal Processing,* pp. iii-521-4 vol. 3, 2004.

[299] J. Fu, H. C. Lien, and S. Wong, "Wavelet-based histogram equalization enhancement of gastric sonogram images," *Computerized Medical Imaging and Graphics,* vol. 24, pp. 59-68, 2000.

[300] A. Adelkhani, B. Beheshti, S. Minaei, P. Javadikia, and M. Ghasemi-Varnamkhasti, "Taste characterization of orange using image processing combined with ANFIS," *Measurement,* vol. 46, pp. 3573-3580, 2013.

[301] W. M. Hafizah and E. Supriyanto, "Automatic generation of region of interest for kidney ultrasound images using texture analysis," *International Journal of Biology and Biomedical Engineering,* vol. 6, pp. 26-34, 2012.

[302] K. Maganti, V. H. Rigolin, M. E. Sarano, and R. O. Bonow, "Valvular heart disease: diagnosis and management," *Proceedings of Mayo Clinic,* pp. 483-500, 2010.

[303] A. R. Domínguez and A. K. Nandi, "Improved dynamic-programming-based algorithms for segmentation of masses in mammograms," *Medical physics,* vol. 34, pp. 4256-4269, 2007.

[304] K. Zhang, H. Song, and L. Zhang, "Active contours driven by local image fitting energy," *Pattern recognition,* vol. 43, pp. 1199-1206, 2010.

[305] K. Zhang, L. Zhang, K.-M. Lam, and D. Zhang, "A Local Active Contour Model for Image Segmentation with Intensity Inhomogeneity," *arXiv preprint arXiv:1305.7053,* 2013.

[306] C. Li, C. Xu, C. Gui, and M. D. Fox, "Level set evolution without re-initialization: a new variational formulation," *Proceedings of IEEE Computer Society Conference on Computer Vision and Pattern Recognition*, pp. 430-436, 2005.